

# **Initial Evaluation of the Albedo and Solar-Radiation Flux of Asphalt Pavements**

FINAL REPORT  
May 2017

Submitted by:

John Hencken  
Research Engineer

The Center for Advanced Infrastructure and Transportation (CAIT)  
Rutgers Asphalt Pavement Laboratory  
93 Road 1, Piscataway, NJ 08854

Primary Customer  
Robert Blight , Project Engineer  
NJDOT Pavement Design Unit

In cooperation with

Rutgers, The State University of New Jersey  
And  
State of New Jersey  
Department of Transportation  
And  
U.S. Department of Transportation  
Federal Highway Administration

## **Disclaimer Statement**

The contents of this report reflect the views of the authors, who are responsible for the facts and the accuracy of the information presented herein. This document is disseminated under the sponsorship of the Department of Transportation, University Transportation Centers Program, in the interest of information exchange. The U.S. Government assumes no liability for the contents or use thereof.

The Center for Advanced Infrastructure and Transportation (CAIT) is a National UTC Consortium led by Rutgers, The State University. Members of the consortium are the University of Delaware, Utah State University, Columbia University, New Jersey Institute of Technology, Princeton University, University of Texas at El Paso, Virginia Polytechnic Institute, and University of South Florida. The Center is funded by the U.S. Department of Transportation.

1. Report No. CAIT-UTC-NC 10	2. Government Accession No.	3. Recipient's Catalog No.	
4. Title and Subtitle <b>Initial Evaluation of the Albedo and Solar-Radiation Flux of Asphalt Pavements</b>		5. Report Date May 2017	
		6. Performing Organization Code CAIT	
7. Author(s) John Hencken		8. Performing Organization Report No. CAIT-UTC-NC 10	
9. Performing Organization Name and Address The Center for Advanced Infrastructure and Transportation (CAIT)/Rutgers University 93 Road 1, Piscataway, New Jersey, 08902		10. Work Unit No.	
		11. Contract or Grant No. DTRT13-G-UTC28	
12. Sponsoring Agency Name and Address Center for Advanced Infrastructure and Transportation Rutgers, The State University of New Jersey 100 Brett Road Piscataway, NJ 08854		13. Type of Report and Period Covered Final Report 12/1/2014 – 6/30/2016	
		14. Sponsoring Agency Code	
15. Supplementary Notes U.S. Department of Transportation/OST-R 1200 New Jersey Avenue, SE Washington, DC 20590-0001			
16. Abstract There is a perception that asphalt pavements utilized for highways and parking lots are contributing to increased temperatures in urban areas known as the urban heat island effect. Due to its dark color, asphalt is known to have low albedo, but the research conducted to determine the dialing heating and cooling has been limited. The majority of research conducted to date has focused on freshly paved asphalt samples without accounting for changes in age, wearing, lift thickness, or aggregate types associated with different asphalt mix designs. Each of these parameters are known to affect the amount of light reflected, the amount of heat absorbed, and the amount of heat retained. This paper will show results from a revised methodology to simultaneously test repeatable one meter samples which can easily be conducted in other laboratories to help compare results evenly.			
17. Key Words Asphalt Pavement, Urban Thermal Loading, Urban Heat Island Effect, UHI, Environmental Radiation, Albedo, Sustainability		18. Distribution Statement	
19. Security Classification (of this report) Unclassified	20. Security Classification (of this page) Unclassified	21. No. of Pages Total # 422	22. Price

## **Acknowledgements**

The authors would like to acknowledge Mike Jopko from Trap Rock Industries for their gracious donation of asphalt loose-mix buckets of 9.5M64V, without which, this project would never have been possible.

The author would also like to acknowledge Michael Tulanowski who helped creating the slabs and wiring the measurement systems for this project, and Robert Jarrett who helped reduce and analyze the data generated throughout this project.



## Table of Contents

DESCRIPTION OF THE PROBLEM .....	1
APPROACH .....	2
METHODOLOGY .....	3
TEST SITE LOCATION AND SITE SETUP .....	3
EQUIPMENT .....	7
Hukseflux Net Radiometer .....	7
Thermocouples .....	9
Asphalt Slab Compaction and Electromagnetic Density Gauge Verification .....	13
ASPHALT MIX SELECTION AND DESIGN PARAMETERS .....	17
DERIVED DATA .....	19
DATA SELECTION PROCESS .....	21
FINDINGS.....	25
SLAB DENSITY .....	25
ENVIRONMENTAL PARAMETERS .....	27
Solar .....	27
Meteorological .....	41
THERMOCOUPLE DATA .....	57
ALBEDO .....	102
SOLAR RADIATION.....	109
CONCLUSIONS.....	134
THERMOCOUPLES .....	134
ALBEDO .....	136
SOLAR RADIATION.....	137
RECOMMENDATIONS .....	141
CUSTOMER QUESTIONS AND ANSWERS.....	142
REFERENCES.....	147
APPENDIX.....	148
APPENDIX A – NJDOT PERVIOUS CONCRETE FOR SIDEWALK USE TASK 3 .....	148
Table of Contents.....	149
Table of Figures.....	152

Objective.....	158
Test Description.....	160
Background of Energy Budget .....	160
Radiation (Shortwave, Longwave, Net) .....	160
Sensible Heat.....	161
Latent Heat.....	162
Ground Heat Flux.....	162
Total Energy Balance .....	162
Pervious Concrete.....	163
Benefits and Limitations .....	164
Site Description.....	164
Location .....	164
Site Setup .....	168
Field Sample Creation .....	188
Construction Environmental Conditions.....	197
Field Mix Aggregate Characterization .....	198
Soil Characterization.....	211
Equipment .....	212
Test Setup .....	212
Sensors.....	212
Anemometers and Weather Vane .....	213
Barometric Pressure .....	213
Tipping Bucket Rain Gauge.....	213
Ambient Temperature and Relative Humidity .....	214
Rotronic Hygroclip2 HC2S3.....	214
HMP45C .....	214
Net Radiometers.....	214
Kipp & Zonen CNR2 Net Radiometer .....	214
Kipp & Zonen CNR4 Net Radiometer .....	215
Hukseflux NR01 Net Radiometer.....	215
Load Cells.....	216
Load Cell Central Model SWCM-2.5K .....	216

Thermocouples.....	218
Campbell Scientific FW05 Type E Thermocouples.....	218
Omega Type K Thermocouples .....	219
Model 108 Temperature Probe .....	221
Time-Domain Reflectometers.....	224
Campbell Scientific CS616 .....	224
Campbell Scientific CS650 .....	225
Data Loggers and Multiplexers .....	228
Campbell Scientific CR10X Datalogger (1) .....	228
Campbell Scientific CR1000 Datalogger (3) .....	229
Campbell Scientific CR3000 Datalogger (2) .....	231
Campbell Scientific AM25T Thermocouple Multiplexer (1).....	233
Campbell Scientific AM16/32B Multiplexer (1) .....	233
Equipment Setup.....	234
Equipment Location and Orientation.....	239
Rooftop Weather Station.....	239
Ground Weather Station .....	240
Type-E Air Column Thermocouples .....	242
Slab Temperature Probes.....	243
Net Radiometers.....	244
Measurement Protocol .....	245
Data Derived from Outside Sources.....	261
Sky Condition Data .....	262
Zenith Data.....	263
Initial Data.....	264
Net Radiometers.....	264
Thermocouples.....	267
Type E.....	270
Type K.....	273
Rain Buckets .....	280
Barometric Pressure .....	281
Relative Humidity .....	282

Time-Domain Reflectometers.....	283
Anemometers.....	287
Load Cells.....	288
Density Determination .....	326
Final Analysis and Results.....	328
Mass H2O Slab .....	328
Volumetric Water Content Slab.....	329
Total Energy Budget .....	329
Sensible Heat Flux Calculations .....	329
Latent Heat Flux Calculations .....	331
Albedo .....	334
Conclusions.....	335
Future Research.....	337
Acknowledgements.....	339
References .....	340
A: NJDOT Section 606 - Sidewalks, Driveways, and Islands .....	341
B: NJDOT Section 903- Concrete.....	342
C: Soil Characterization: USDA .....	344
C1: Map .....	344
C2: USDA Soil Classification - Description .....	347
D: Tipping Bucket (2) & HMP45C - Wire Diagram.....	351
E: Wind (2) & Tipping Bucket (1) & Setra 278 - Wire Diagram .....	352
F: NR01 Green Ext. - Wire Diagram.....	353
G: NR01 Black Ext. - Wire Diagram .....	354
H: Rotronic Hygroclip2 HC2S3 and CNR4 - Wire Diagram.....	355
I: Load Cells - Wire Diagram .....	356
J: CNR2 & Young Wind (1) - Wire Diagram.....	357
K: COM - Wire Diagrams .....	358
L: CR3000 Thermo - Campbell DAQ Wire Diagram/Text .....	359
M: CR_AM25T Campbell Multiplexer Wire Diagram/Text .....	363
N: CR3000 Load Cell - Campbell DAQ Wire Diagram/Text .....	368
O: CR10X Weather - Campbell DAQ Wire Diagram/Text.....	374

P: CR1000 TDR - Campbell DAQ Wire Diagram/Text .....	376
Q: CR1000 Inside Temp - Campbell DAQ Wire Diagram/Text .....	378
R: CR1000 Inside Solar - Campbell DAQ Wire Diagram/Text .....	382
APPENDIX B - HUKSEFLUX NET RADIOMETERS .....	385
Probe 1945 .....	385
Probe 2346 .....	385
Probe 2347 .....	387
APPENDIX C - THERMOCOUPLES .....	388
Probe 1 .....	388
Probe 2 .....	393
Probe 3 .....	398

## List of Figures

Figure 1: The Rutgers Asphalt Paving Laboratory; showing the location where the 1 sq. m. samples would be tested.....	3
Figure 2: Initial site survey and site conditions facing West.....	4
Figure 3: Initial Site Conditions after cleaning up the existing debris, facing North.....	4
Figure 4: Removing debris to prepare the testing site .....	5
Figure 5: Preparing the testing surface by spreading Reclaimed Asphalt Pavement (RAP) to normalize the reflective surfaces.....	6
Figure 6: Back scraping the RAP base to prepare for rolling the surface with a vibratory drum roller .....	6
Figure 7: Rolling the base surface to ensure a stable surface to place the test specimens .....	7
Figure 8: Hukseflux NR01 net radiometer.....	8
Figure 9: Preparing the thermocouple extension wire to be conjoined into a single probe .....	10
Figure 10: Initial J-Type thermocouple probe assembly.....	10
Figure 11: Layout of the proposed area of measurement and locations where thermocouple testing was conducted .....	12
Figure 12: Thermocouple placement verification data at 12.5mm depth.....	12
Figure 13: Thermocouple placement verification data at 76.2mm depth.....	13
Figure 14: New 1 sq. m. asphalt compaction mold created in-house .....	14
Figure 15: Freshly compacted 1 sq. m. asphalt sample .....	15
Figure 16: The Transtech PQI380 electromagnetic density gauge .....	16
Figure 17: Asphalt verification slab utilized to practice compaction and verify the offset for the PQI380.....	17
Figure 18: Mix gradation of the 9.5M64V asphalt mixture selected for use in this project.....	19
Figure 19: Initial and Final PQI density compared to AASHTO T-166 bulk density results for test specimen 2 ..	25
Figure 20: Initial and Final PQI density compared to AASHTO T-166 bulk density results for test specimen 3 ..	26
Figure 21: Initial and Final PQI density compared to AASHTO T-166 bulk density results for test specimen 3 ..	26
Figure 22: Comparison of zenith angles utilized for calculation of albedo.....	27
Figure 23: The zenith angle utilized for the July 31 – August, 2015 albedo calculations for this report.....	30
Figure 24: The zenith angle utilized for the January, 4 – January 6, 2016 albedo calculations for this report ..	33
Figure 25: The zenith angle utilized for the February 6 – February 8, 2016 albedo calculations for this report	36
Figure 26: The zenith angle utilized for the April 16 – April 18, 2016 albedo calculations for this report .....	40
Figure 27: Diurnal pattern of thermocouple probe 1 in slab sample 2 for testing period July 31 - August 2, 2015 compared to 4" soil depth, NR01 infrared surface temp, and ambient temp.....	58
Figure 28: Diurnal pattern of thermocouple probe 2 in slab sample 3 for testing period July 31 - August 2, 2015 compared to 4" soil depth, NR01 infrared surface temp, and ambient temp.....	59
Figure 29: Diurnal pattern of thermocouple probe 3 in slab sample 4 for testing period July 31 - August 2, 2015 compared to 4" soil depth, NR01 infrared surface temp, and ambient temp.....	60
Figure 30: Maximum and minimum temperatures for each thermocouple probe at each depth for testing period July 31, 2015- August 2, 2015.....	61
Figure 31: Diurnal pattern of the ¼ inch depth thermocouple temperature for each probe (probe 1/blue/slab 2; probe 2/orange/slab 3; probe 3/gray/slab 4) for test period July 31, 2015 – August 2, 2015 .....	62
Figure 32: Diurnal pattern of the ½ inch depth thermocouple temperature for each probe (probe 1/blue/slab 2; probe 2/orange/slab 3; probe 3/gray/slab 4) for test period July 31, 2015 – August 2, 2015 .....	63
Figure 33: Diurnal pattern of the ¾ inch depth thermocouple temperature for each probe (probe 1/blue/slab 2; probe 2/orange/slab 3; probe 3/gray/slab 4) for test period July 31, 2015 – August 2, 2015 .....	63

Figure 34: Diurnal pattern of the 1 inch depth thermocouple temperature for each probe (probe 1/blue/slab 2; probe 2/orange/slab 3; probe 3/gray/slab 4) for test period July 31, 2015 – August 2, 2015 .....	64
Figure 35: Diurnal pattern of the 1 ½ inch depth thermocouple temperature for each probe (probe 1/blue/slab 2; probe 2/orange/slab 3; probe 3/gray/slab 4) for test period July 31, 2015 – August 2, 2015 ...	65
Figure 36: Diurnal pattern of the 2 inch depth thermocouple temperature for each probe (probe 1/blue/slab 2; probe 2/orange/slab 3; probe 3/gray/slab 4) for test period July 31, 2015 – August 2, 2015 .....	65
Figure 37: Diurnal pattern of the 2 ½ inch depth thermocouple temperature for each probe (probe 1/blue/slab 2; probe 2/orange/slab 3; probe 3/gray/slab 4) for test period July 31, 2015 – August 2, 2015 ...	66
Figure 38: Diurnal pattern of the 3 inch depth thermocouple temperature for each probe (probe 1/blue/slab 2; probe 2/orange/slab 3; probe 3/gray/slab 4) for test period July 31, 2015 – August 2, 2015 .....	67
Figure 39: Diurnal pattern of the 3 ½ inch depth thermocouple temperature for each probe (probe 1/blue/slab 2; probe 2/orange/slab 3; probe 3/gray/slab 4) for test period July 31, 2015 – August 2, 2015 ...	67
Figure 40: Diurnal pattern of the 4 inch depth thermocouple temperature for each probe (probe 1/blue/slab 2; probe 2/orange/slab 3; probe 3/gray/slab 4) for test period July 31, 2015 – August 2, 2015 .....	68
Figure 41: Diurnal pattern of thermocouple probe 1 in slab sample 2 for testing period January 4 - January 6, 2016 compared to 4" soil depth, NR01 infrared surface temp, and ambient temp.....	69
Figure 42: Diurnal pattern of thermocouple probe 2 in slab sample 3 for testing period January 4 - January 6, 2016 compared to 4" soil depth, NR01 infrared surface temp, and ambient temp.....	70
Figure 43: Diurnal pattern of thermocouple probe 3 in slab sample 4 for testing period January 4 - January 6, 2016 compared to 4" soil depth, NR01 infrared surface temp, and ambient temp.....	71
Figure 44: Maximum and minimum temperatures for each thermocouple probe at each depth for testing period January 4, 2016- January 6, 2016 .....	72
Figure 45: Diurnal pattern of the ¼ inch depth thermocouple temperature for each probe (probe 1/blue/slab 2; probe 2/orange/slab 3; probe 3/gray/slab 4) for test period January 4, 2016 – January 6, 2016 .....	73
Figure 46: Diurnal pattern of the ½ inch depth thermocouple temperature for each probe (probe 1/blue/slab 2; probe 2/orange/slab 3; probe 3/gray/slab 4) for test period January 4, 2016 – January 6, 2016 .....	74
Figure 47: Diurnal pattern of the ¾ inch depth thermocouple temperature for each probe (probe 1/blue/slab 2; probe 2/orange/slab 3; probe 3/gray/slab 4) for test period January 4, 2016 – January 6, 2016 .....	74
Figure 48: Diurnal pattern of the 1 inch depth thermocouple temperature for each probe (probe 1/blue/slab 2; probe 2/orange/slab 3; probe 3/gray/slab 4) for test period January 4, 2016 – January 6, 2016 .....	75
Figure 49: Diurnal pattern of the 1 ½ inch depth thermocouple temperature for each probe (probe 1/blue/slab 2; probe 2/orange/slab 3; probe 3/gray/slab 4) for test period January 4, 2016 – January 6, 2016 .....	76
Figure 50: Diurnal pattern of the 2 inch depth thermocouple temperature for each probe (probe 1/blue/slab 2; probe 2/orange/slab 3; probe 3/gray/slab 4) for test period January 4, 2016 – January 6, 2016 .....	76
Figure 51: Diurnal pattern of the 2 ½ inch depth thermocouple temperature for each probe (probe 1/blue/slab 2; probe 2/orange/slab 3; probe 3/gray/slab 4) for test period January 4, 2016 – January 6, 2016 .....	77
Figure 52: Diurnal pattern of the 3 inch depth thermocouple temperature for each probe (probe 1/blue/slab 2; probe 2/orange/slab 3; probe 3/gray/slab 4) for test period January 4, 2016 – January 6, 2016 .....	78
Figure 53: Diurnal pattern of the 3 ½ inch depth thermocouple temperature for each probe (probe 1/blue/slab 2; probe 2/orange/slab 3; probe 3/gray/slab 4) for test period January 4, 2016 – January 6, 2016 .....	78
Figure 54: Diurnal pattern of the 4 inch depth thermocouple temperature for each probe (probe 1/blue/slab 2; probe 2/orange/slab 3; probe 3/gray/slab 4) for test period January 4, 2016 – January 6, 2016 .....	79

Figure 55: Diurnal pattern of thermocouple probe 1 in slab sample 2 for testing period February 6 - February 8, 2016 compared to 4" soil depth, NR01 infrared surface temp, and ambient temp.....	80
Figure 56: Diurnal pattern of thermocouple probe 2 in slab sample 3 for testing period February 6 - February 8, 2016 compared to 4" soil depth, NR01 infrared surface temp, and ambient temp.....	81
Figure 57: Diurnal pattern of thermocouple probe 3 in slab sample 4 for testing period February 6 - February 8, 2016 compared to 4" soil depth, NR01 infrared surface temp, and ambient temp.....	82
Figure 58: Maximum and minimum temperatures for each thermocouple probe at each depth for testing period February 6, 2016- February 8, 2016 .....	83
Figure 59: Diurnal pattern of the ¼ inch depth thermocouple temperature for each probe (probe 1/blue/slab 2; probe 2/orange/slab 3; probe 3/gray/slab 4) for test period February 6, 2016 – February 8, 2016 .....	84
Figure 60: Diurnal pattern of the ½ inch depth thermocouple temperature for each probe (probe 1/blue/slab 2; probe 2/orange/slab 3; probe 3/gray/slab 4) for test period February 6, 2016 – February 8, 2016 .....	84
Figure 61: Diurnal pattern of the ¾ inch depth thermocouple temperature for each probe (probe 1/blue/slab 2; probe 2/orange/slab 3; probe 3/gray/slab 4) for test period February 6, 2016 – February 8, 2016 .....	85
Figure 62: Diurnal pattern of the 1 inch depth thermocouple temperature for each probe (probe 1/blue/slab 2; probe 2/orange/slab 3; probe 3/gray/slab 4) for test period February 6, 2016 – February 8, 2016 .....	86
Figure 63: Diurnal pattern of the 1 ½ inch depth thermocouple temperature for each probe (probe 1/blue/slab 2; probe 2/orange/slab 3; probe 3/gray/slab 4) for test period February 6, 2016 – February 8, 2016 .....	86
Figure 64: Diurnal pattern of the 2 inch depth thermocouple temperature for each probe (probe 1/blue/slab 2; probe 2/orange/slab 3; probe 3/gray/slab 4) for test period February 6, 2016 – February 8, 2016 .....	87
Figure 65: Diurnal pattern of the 2 ½ inch depth thermocouple temperature for each probe (probe 1/blue/slab 2; probe 2/orange/slab 3; probe 3/gray/slab 4) for test period February 6, 2016 – February 8, 2016 .....	88
Figure 66: Diurnal pattern of the 3 inch depth thermocouple temperature for each probe (probe 1/blue/slab 2; probe 2/orange/slab 3; probe 3/gray/slab 4) for test period February 6, 2016 – February 8, 2016 .....	88
Figure 67: Diurnal pattern of the 3 ½ inch depth thermocouple temperature for each probe (probe 1/blue/slab 2; probe 2/orange/slab 3; probe 3/gray/slab 4) for test period February 6, 2016 – February 8, 2016 .....	89
Figure 68: Diurnal pattern of the 4 inch depth thermocouple temperature for each probe (probe 1/blue/slab 2; probe 2/orange/slab 3; probe 3/gray/slab 4) for test period February 6, 2016 – February 8, 2016 .....	90
Figure 69: Diurnal pattern of thermocouple probe 1 in slab sample 2 for testing period April 16 - April 18, 2016 compared to 4" soil depth, NR01 infrared surface temp, and ambient temp.....	91
Figure 70: Diurnal pattern of thermocouple probe 2 in slab sample 3 for testing period April 16 - April 18, 2016 compared to 4" soil depth, NR01 infrared surface temp, and ambient temp.....	92
Figure 71: Diurnal pattern of thermocouple probe 3 in slab sample 4 for testing period April 16 - April 18, 2016 compared to 4" soil depth, NR01 infrared surface temp, and ambient temp.....	93
Figure 72: Maximum and minimum temperatures for each thermocouple probe at each depth for testing period April 16, 2016- April 18, 2016.....	94
Figure 73: Diurnal pattern of the ¼ inch depth thermocouple temperature for each probe (probe 1/blue/slab 2; probe 2/orange/slab 3; probe 3/gray/slab 4) for test period April 16, 2016 – April 18, 2016 .....	95
Figure 74: Diurnal pattern of the ½ inch depth thermocouple temperature for each probe (probe 1/blue/slab 2; probe 2/orange/slab 3; probe 3/gray/slab 4) for test period April 16, 2016 – April 18, 2016 .....	95
Figure 75: Diurnal pattern of the ¾ inch depth thermocouple temperature for each probe (probe 1/blue/slab 2; probe 2/orange/slab 3; probe 3/gray/slab 4) for test period April 16, 2016 – April 18, 2016 .....	96



Figure 76: Diurnal pattern of the 1 inch depth thermocouple temperature for each probe (probe 1/blue/slab 2; probe 2/orange/slab 3; probe 3/gray/slab 4) for test period April 16, 2016 – April 18, 2016 .....	97
Figure 77: Diurnal pattern of the 1 ½ inch depth thermocouple temperature for each probe (probe 1/blue/slab 2; probe 2/orange/slab 3; probe 3/gray/slab 4) for test period April 16, 2016 – April 18, 2016 ...	97
Figure 78: Diurnal pattern of the 2 inch depth thermocouple temperature for each probe (probe 1/blue/slab 2; probe 2/orange/slab 3; probe 3/gray/slab 4) for test period April 16, 2016 – April 18, 2016 .....	98
Figure 79: Diurnal pattern of the 2 ½ inch depth thermocouple temperature for each probe (probe 1/blue/slab 2; probe 2/orange/slab 3; probe 3/gray/slab 4) for test period April 16, 2016 – April 18, 2016 ...	99
Figure 80: Diurnal pattern of the 3 inch depth thermocouple temperature for each probe (probe 1/blue/slab 2; probe 2/orange/slab 3; probe 3/gray/slab 4) for test period April 16, 2016 – April 18, 2016 .....	99
Figure 81: Diurnal pattern of the 3 ½ inch depth thermocouple temperature for each probe (probe 1/blue/slab 2; probe 2/orange/slab 3; probe 3/gray/slab 4) for test period April 16, 2016 – April 18, 2016 .	100
Figure 82: Diurnal pattern of the 4 inch depth thermocouple temperature for each probe (probe 1/blue/slab 2; probe 2/orange/slab 3; probe 3/gray/slab 4) for test period April 16, 2016 – April 18, 2016 .....	101
Figure 83: Comparison of 3 slabs albedo measurements for July 31, 2015 .....	102
Figure 84: Comparison of 3 slabs albedo measurements for August 1, 2015 .....	103
Figure 85: Comparison of 3 slabs albedo measurements for August 2, 2015 .....	103
Figure 86: Comparison of 3 slabs albedo measurements for January 4, 2016 .....	104
Figure 87: Comparison of 3 slabs albedo measurements for January 5, 2016 .....	104
Figure 88: Comparison of 3 slabs albedo measurements for January 6, 2016 .....	105
Figure 89: Comparison of 3 slabs albedo measurements for February 6, 2016 .....	105
Figure 90: Comparison of 3 slabs albedo measurements for February 7, 2016 .....	106
Figure 91: Comparison of 3 slabs albedo measurements for February 8, 2016 .....	106
Figure 92: Comparison of 3 slabs albedo measurements for April 16, 2016 .....	107
Figure 93: Comparison of 3 slabs albedo measurements for April 17, 2016 .....	108
Figure 94: Comparison of 3 slabs albedo measurements for April 18, 2016 .....	108
Figure 95: Solar radiation measured for sample 1 (slab 2) for testing period July 31, 2015 - August 2, 2015 .	109
Figure 96: Solar radiation measured for sample 2 (slab 3) for testing period July 31, 2015 - August 2, 2015 .	110
Figure 97: Solar radiation measured for sample 3 (slab 4) for testing period July 31, 2015 - August 2, 2015 .	111
Figure 98: Infrared radiation measured for sample 1 (slab 2) for testing period July 31, 2015 - August 2, 2015 .....	111
Figure 99: Infrared radiation measured for sample 2 (slab 3) for testing period July 31, 2015 - August 2, 2015 .....	112
Figure 100: Infrared radiation measured for sample 3 (slab 4) for testing period July 31, 2015 - August 2, 2015 .....	113
Figure 101: Net radiation measured for sample 1 (slab 2) for testing period July 31, 2015 - August 2, 2015 .	113
Figure 102: Net radiation measured for sample 2 (slab 3) for testing period July 31, 2015 - August 2, 2015 .	114
Figure 103: Net radiation measured for sample 3 (slab 4) for testing period July 31, 2015 - August 2, 2015 .	115
Figure 104: Solar radiation measured for sample 1 (slab 2) for testing period January 31, 2016 - January 6, 2016 .....	116
Figure 105: Solar radiation measured for sample 2 (slab 3) for testing period January 31, 2016 - January 6, 2016 .....	116
Figure 106: Solar radiation measured for sample 3 (slab 4) for testing period January 31, 2016 - January 6, 2016 .....	117

Figure 107: Infrared radiation measured for sample 1 (slab 2) for testing period January 31, 2016 - January 6, 2016 .....	118
Figure 108: Infrared radiation measured for sample 2 (slab 3) for testing period January 31, 2016 - January 6, 2016 .....	118
Figure 109: Infrared radiation measured for sample 3 (slab 4) for testing period January 31, 2016 - January 6, 2016 .....	119
Figure 110: Net radiation measured for sample 1 (slab 2) for testing period January 31, 2016 - January 6, 2016 .....	120
Figure 111: Net radiation measured for sample 2 (slab 3) for testing period January 31, 2016 - January 6, 2016 .....	120
Figure 112: Net radiation measured for sample 3 (slab 4) for testing period January 31, 2016 - January 6, 2016 .....	121
Figure 113: Solar radiation measured for sample 1 (slab 2) for testing period February 6, 2016 - February 8, 2016 .....	122
Figure 114: Solar radiation measured for sample 2 (slab 3) for testing period February 6, 2016 - February 8, 2016 .....	122
Figure 115: Solar radiation measured for sample 3 (slab 4) for testing period February 6, 2016 - February 8, 2016 .....	123
Figure 116: Infrared radiation measured for sample 1 (slab 2) for testing period February 6, 2016 - February 8, 2016 .....	124
Figure 117: Infrared radiation measured for sample 2 (slab 3) for testing period February 6, 2016 - February 8, 2016 .....	124
Figure 118: Infrared radiation measured for sample 3 (slab 4) for testing period February 6, 2016 - February 8, 2016 .....	125
Figure 119: Net radiation measured for sample 1 (slab 2) for testing period February 6, 2016 - February 8, 2016 .....	126
Figure 120: Net radiation measured for sample 2 (slab 3) for testing period February 6, 2016 - February 8, 2016 .....	126
Figure 121: Net radiation measured for sample 3 (slab 4) for testing period February 6, 2016 - February 8, 2016 .....	127
Figure 122: Solar radiation measured for sample 1 (slab 2) for testing period April 16, 2016 - April 18, 2016 .....	128
Figure 123: Solar radiation measured for sample 2 (slab 3) for testing period April 16, 2016 - April 18, 2016 .....	128
Figure 124: Solar radiation measured for sample 3 (slab 4) for testing period April 16, 2016 - April 18, 2016 .....	129
Figure 125: Infrared radiation measured for sample 1 (slab 2) for testing period April 16, 2016 - April 18, 2016 .....	130
Figure 126: Infrared radiation measured for sample 2 (slab 3) for testing period April 16, 2016 - April 18, 2016 .....	130
Figure 127: Infrared radiation measured for sample 3 (slab 4) for testing period April 16, 2016 - April 18, 2016 .....	131
Figure 128: Net radiation measured for sample 1 (slab 2) for testing period April 16, 2016 - April 18, 2016 .....	132
Figure 129: Net radiation measured for sample 2 (slab 3) for testing period April 16, 2016 - April 18, 2016 .....	132
Figure 130: Net radiation measured for sample 3 (slab 4) for testing period April 16, 2016 - April 18, 2016 .....	133

Figure 131: Reduced thermocouple measurements for the top, middle, and bottom of the slab for April 16, 2016 .....	134
Figure 132: Reduced thermocouple measurements for the top, middle, and bottom of the slab for February 8, 2016 .....	135
Figure 133: Annual albedo comparison across each of the three slabs .....	136
Figure 134: Average albedo values per sample .....	137
Figure 135: Sample comparison of the total net radiation measured for testing period July 31, 2015 – August 2, 2015 .....	138
Figure 136: Sample comparison of the total net radiation measured for testing period January 4 2016 – January 6, 2016 .....	139
Figure 137: Sample comparison of the total net radiation measured for testing period February 6, 2016 – February 8, 2016 .....	139
Figure 138: Sample comparison of the total net radiation measured for testing period April 16 2016 – April 18, 2016 .....	140
Figure 139: Net Surface Radiation Flux (Wallace & Hobbs 2006).....	161
Figure 140: The total energy balance .....	163
Figure 141: The Rutgers Asphalt Pavement Laboratory’s location in New Jersey.....	165
Figure 142: The testing site.....	166
Figure 143: Proposed Test Slab Locations .....	167
Figure 144: Existing site layout prior to Pervious Concrete.....	168
Figure 145: Research Wall that was required to be re-sited .....	169
Figure 146: Bobcat E85 Excavator .....	170
Figure 147: Preparing to move wall footing .....	171
Figure 148: Moving the footing with the E85 Excavator .....	172
Figure 149: Rough foundations for pervious test samples, looking ESE.....	173
Figure 150: Rough foundations for pervious test samples, looking WNW.....	174
Figure 151: Bobcat E50 with 1ft (0.30m) bucket attachment .....	175
Figure 152: Auger attachment on Bobcat E50.....	176
Figure 153: Footing tubes in place inside rough foundations .....	177
Figure 154: Prepared subgrades for drainage with footing tubes exposed .....	178
Figure 155: Drainage Pipe with Wyle ‘Y’ .....	179
Figure 156: Non-woven geotextile fabric covering drainage pipe.....	180
Figure 157: Stockpile of ¾in (19mm) aggregate .....	181
Figure 158: Placing and compacting base course aggregate .....	182
Figure 159: Leveling the base course.....	183
Figure 160: Applying the final level of base course aggregate. Note the excessive dust in the aggregate.....	184
Figure 161: Testing the viability of the air bags.....	185
Figure 162: Layout of slab molds prior to geo-textile fabric.....	186
Figure 163: Verification of the final slab grade.....	187
Figure 164: Final layout of concrete molds prior to pouring.....	188
Figure 165: <i>Aggregate, water, admixtures and tools prepared to mix concrete slabs</i> .....	189
Figure 166: First batch pour of the pervious concrete sample awaiting final batch .....	190
Figure 167: Hand work and rodding to create concrete field samples.....	191
Figure 168: Preparing flexural, compressive, and permeability samples .....	192
Figure 169: Final field sample prior to curing .....	193

Figure 170: Wet curing samples .....	194
Figure 171: Prepared samples curing under plastic sheeting .....	195
Figure 172: Final layout of field slabs after curing procedure and prior to backfilling .....	196
Figure 173: Preparing aggregate for splitting .....	200
Figure 174: Quartering aggregate for sampling .....	201
Figure 175: Aggregate gradations compiled (0.45 Power) .....	205
Figure 176: Conceptual diagram showing equipment setup .....	212
Figure 177: Load Cell calibration curves .....	217
Figure 178: Type E Calibration Data .....	219
Figure 179: Type K Calibration Values .....	221
Figure 180: USP Calibrations .....	223
Figure 181: CS616 (6 inches) Calibration Curve .....	224
Figure 182: CS616 (9 inches) Calibration Curve .....	225
Figure 183: CS650 (3 inches) Calibration Curve .....	226
Figure 184: Dry TDR calibration sample, manifold is hanging on right after stemming from gravity fed bucket .....	227
Figure 185: Wet TDR calibration sample, manifold is hanging on right after stemming from gravity fed bucket .....	228
Figure 186: Laboratory setup to test individual equipment .....	235
Figure 187: Rough equipment siting plan .....	236
Figure 188: Preparing an Extension Line for Soldering .....	237
Figure 189: Insulation of signal extension wires .....	238
Figure 190: Rooftop weather station .....	239
Figure 191: Ground Weather Station, Left Foreground .....	241
Figure 192: Type-E close proximity air column thermocouples .....	242
Figure 193: <i>In-Slab temperature probe location</i> .....	244
Figure 194: Net Radiometer location .....	245
Figure 195: Final Sensor Layout by DAQ and Location .....	246
Figure 196: Outside equipment environmental containment box location .....	247
Figure 197: Almost completed wiring inside environmental containment boxes .....	248
Figure 198: In laboratory setup of additional DAQs and Multiplexer .....	249
Figure 199: Computer, power supply, and communications .....	250
Figure 200: Zenith Angles used for Albedo Calculations .....	264
Figure 201: Radiation for July 20 - July 22, 2017 at Slab 1 .....	265
Figure 202: Radiation for July 20, 2017 at Slab 1 .....	265
Figure 203: Net Radiation for July 20 - July 22, 2017 at Slab 1 .....	266
Figure 204: Net Radiation for July 20 - July 22, 2017 at Slabs 1, 3, 4, 6, & 8 .....	266
Figure 205: Net Radiation for July 20 - July 22, 2017 at Slabs 1, 3, 4, 6, & 8 with Rain Bucket Readings on the Right Axis .....	267
Figure 206: Internal Slab Temperatures at 0.5 inches of embedment .....	268
Figure 207: Internal Slab Temperatures at 0.5 inches of embedment on July 20, 2017 .....	268
Figure 208: Internal Slab Temperatures at 0.5 inches of embedment on July 21, 2017 .....	269
Figure 209: Internal Slab Temperatures at 0.5 inches of embedment on July 22, 2017 .....	269
Figure 210: Under Slab Temperature at 4 inches Below Slab 3 on July 20, 2017 .....	270
Figure 211: Type E Temperatures at heights 25 cm, 13 cm, 6 cm, and 1 cm above Slab 4 .....	271

Figure 212: Type E Temperatures at heights 25 cm, 13 cm, 6 cm, and 1 cm above Slab 4 on July 20, 2017 ...	271
Figure 213: Ambient and Type E Temperatures at a height of 2 m and 25 cm above Slab 1 and Slab 4, respectively.....	272
Figure 214: Ambient Temperature at 2 m above Slab 1, Type E Temperature at 25 cm above Slab 4, Under Slab Temperature at 4" below Slab 4, and Soil T at a depth of 3" with Rain Bucket Data on the Right Axis ...	273
Figure 215: Slab 1 Internal, Under Slab, and Ambient Temperature Readings .....	274
Figure 216: Slab 2 Internal, Under Slab, and Ambient Temperature Readings .....	275
Figure 217: Slab 3 Internal, Under Slab, and Ambient Temperature Readings .....	276
Figure 218: Slab 4 Internal, Under Slab, and Ambient Temperature Readings .....	276
Figure 219: Slab 5 Internal, Under Slab, and Ambient Temperature Readings .....	277
Figure 220: Slab 6 Internal, Under Slab, and Ambient Temperature Readings .....	278
Figure 221: Slab 7 Internal, Under Slab, and Ambient Temperature Readings .....	279
Figure 222: Slab 8 Internal, Under Slab, and Ambient Temperature Readings .....	280
Figure 223: Rain Bucket Readings at the Roof Weather Station .....	281
Figure 224: Barometric Pressure Readings at the Roof Weather Station for July 20 - July 22, 2017 .....	282
Figure 225: Relative Humidity Readings at the Roof Weather Station for July 20 - July 22, 2017 .....	283
Figure 226: Soil VWC Unfiltered from 7/20-7/22 .....	284
Figure 227: Soil VWC 3" Filtered vs Unfiltered Measurement .....	285
Figure 228: Soil VWC 6" Filtered vs Unfiltered Measurement .....	286
Figure 229: Volumetric Water Content in Soil at a Depth of 3 and 6 inches with Rain Bucket Data on the Right Axis.....	287
Figure 230: Wind Speed at Roof Weather Station.....	287
Figure 231: Load Cell 1 Response vs Measured Rain Events .....	289
Figure 232: Load Cell 2 Response vs Measured Rain Events .....	290
Figure 233: Load Cell 3 vs Measured Rain Events.....	291
Figure 234: Load Cell 4 Response vs Measured Rain Events .....	292
Figure 235: Load Cell 5 Response vs Measured Rain Events .....	293
Figure 236: Load Cell 6 Response vs Measured Rain Events .....	294
Figure 237: Load Cell 7 Response vs Measured Rain Events .....	295
Figure 238: Load Cell 8 Response vs Measured Rain Events .....	296
Figure 239: Load Cell 9 Response vs Measured Rain Events .....	297
Figure 240: Load Cell 10 Response vs Measured Rain Events .....	298
Figure 241: Load Cell 11 Response vs Measured Rain Events .....	299
Figure 242: Load Cell 12 Response vs Measured Rain Events .....	300
Figure 243: Load Cell 13 Response vs Measured Rain Events .....	301
Figure 244: Load Cell 14 Response vs Measured Rain Events .....	302
Figure 245: Load Cell 15 Response vs Measured Rain Events .....	303
Figure 246: Load Cell 16 Response vs Measured Rain Events .....	304
Figure 247: Load Cell 1 Unfiltered vs Load Cell 1 Filtered .....	305
Figure 248: Load Cell 2 Unfiltered vs Load Cell 2 Filtered .....	305
Figure 249: Load Cell 3 Filtered vs Load Cell 3 Unfiltered .....	306
Figure 250: Load Cell 4 Filtered vs Load Cell 4 Unfiltered .....	306
Figure 251: Load Cell 5 Filtered vs Load Cell 5 Unfiltered .....	307
Figure 252: Load Cell 6 Filtered vs Load Cell 6 Unfiltered .....	307
Figure 253: Load Cell 7 Filtered vs Load Cell 7 Unfiltered .....	308

Figure 254: Load Cell 8 Filtered vs Load Cell 8 Unfiltered .....	308
Figure 255: Load Cell 9 Filtered vs Load Cell 9 Unfiltered .....	309
Figure 256: Load Cell 10 Filtered vs Load Cell 10 Unfiltered .....	309
Figure 257: Load Cell 11 Filtered vs Load Cell 11 Unfiltered .....	310
Figure 258: Load Cell 13 Filtered vs Load Cell 13 Unfiltered .....	310
Figure 259: Load Cell 14 Filtered vs Load Cell 14 Unfiltered .....	311
Figure 260: Load Cell 15 Filtered vs Load Cell 15 Unfiltered .....	311
Figure 261: Load Cell 16 Filtered vs Load Cell 16 Unfiltered .....	312
Figure 262: Slab 1 Mass Original vs Corrected.....	313
Figure 263: Slab 2 Mass Original vs Corrected.....	314
Figure 264: Slab 3 Mass Original vs Corrected.....	314
Figure 265: Slab 4 Mass Original vs Corrected.....	315
Figure 266: Slab 5 Mass Original vs Corrected.....	315
Figure 267: Slab 6 Mass Original vs Corrected.....	316
Figure 268: Slab 7 Mass Original vs Corrected.....	316
Figure 269: Slab 8 Mass Original vs Corrected.....	317
Figure 270: Slab 1 Mass vs Measured Rain events .....	317
Figure 271: Slab 2 Mass vs Measured Rain Events .....	318
Figure 272: Slab 3 Mass vs Measured Rain Events .....	318
Figure 273: Slab 4 Mass vs Measured Rain Events .....	319
Figure 274: Slab 5 Mass vs Measured Rain Events .....	319
Figure 275: Slab 6 Mass vs Measured Rain Events .....	320
Figure 276: Slab 7 Mass vs Measured Rain Events .....	321
Figure 277: Slab 8 Mass vs Measured Rain Events .....	321
Figure 278: Mass of Water in Slab 1 for July 20, 2017 through July 22, 2017 with Rain Bucket Readings on the Right Axis .....	322
Figure 279: Mass of Water in Slab 2 for July 20, 2017 through July 22, 2017 with Rain Bucket Readings on the Right Axis .....	322
Figure 280: Mass of Water in Slab 3 for July 20, 2017 through July 22, 2017 with Rain Bucket Readings on the Right Axis .....	323
Figure 281: Mass of Water in Slab 4 for July 20, 2017 through July 22, 2017 with Rain Bucket Readings on the Right Axis .....	323
Figure 282: Mass of Water in Slab 5 for July 20, 2017 through July 22, 2017 with Rain Bucket Readings on the Right Axis .....	324
Figure 283: Mass of Water in Slab 6 for July 20, 2017 through July 22, 2017 with Rain Bucket Readings on the Right Axis .....	324
Figure 284: Mass of Water in Slab 7 for July 20, 2017 through July 22, 2017 with Rain Bucket Readings on the Right Axis .....	325
Figure 285: Mass of Water in Slab 8 for July 20, 2017 through July 22, 2017 with Rain Bucket Readings on the Right Axis .....	325
Figure 286: The sensible heat flux for July 20 - 22, 2017.....	330
Figure 287: The latent heat flux for July 20 - 22, 2017 .....	332
Figure 288: Calculated Albedo for each Pervious Mix Field Sample.....	334

## List of Tables

Table 1: Measured and calculated values provided by the Hukseflux NR01 net radiometer .....	9
Table 2: Thermocouple placement and spacing to create a single sample probe .....	11
Table 3: Electromagnetic density gauge and AASHTO T-166 bulk density comparison and offset calculation .	16
Table 4: Mixture design of dense graded 9.5M64V HMA utilized for this project .....	18
Table 5: Sources of climatological data derived for regional locations as close proximity to the test site as possible .....	20
Table 6: Definitions of nomenclature utilized throughout this report .....	21
Table 7: List of dates for which the initial thermocouple and net radiometer data was compiled .....	22
Table 8: List of dates for which full thermocouple and net radiometer data was available .....	23
Table 9: Date ranges selected from Table 8 above for further analysis related the temperature and relative humidity.....	24
Table 10: Zenith and Azimuth Angles; July 31, 2015 - Aug 2, 2015 (NAD 83: 40°30'44.7"; -74°25'7.3") .....	28
Table 11: Zenith and Azimuth Angles; January 4, 2016 - January 6, 2016 (NAD 83: 40°30'44.7"; -74°25'7.3").	31
Table 12: Zenith and Azimuth Angles; February 6, 2016 - February 8, 2016 (NAD 83: 40°30'44.7"; -74°25'7.3") .....	34
Table 13: Zenith and Azimuth Angles; April 16, 2016 – April 18, 2016 (NAD 83: 40°30'44.7"; -74°25'7.3").....	37
Table 14: Wunderground climatological data for the test period of July 31 - August 2, 2015.....	41
Table 15: NOAA record of climatological observations for the test period of July 31 - August 2, 2015 .....	41
Table 16: NCDC quality controlled local climatological data for the test period on July 31, 2015.....	42
Table 17: NCDC quality controlled local climatological data for the test period on August 1, 2015.....	43
Table 18: NCDC quality controlled local climatological data for the test period on August 2, 2015.....	44
Table 19: Wunderground climatological data for the test period of January 4 - January 6, 2016 .....	45
Table 20: NOAA record of climatological observations for the test period of January 4 - January 6, 2016.....	45
Table 21: NCDC quality controlled local climatological data for the test period on January 4, 2016 .....	46
Table 22: NCDC quality controlled local climatological data for the test period on January 5, 2016 .....	47
Table 23: NCDC quality controlled local climatological data for the test period on January 6, 2016 .....	48
Table 24: Wunderground climatological data for the test period of February 6 - February 8, 2016 .....	49
Table 25: NOAA record of climatological observations for the test period of February 6 - February 8, 2016...	49
Table 26: NCDC quality controlled local climatological data for the test period on February 6, 2016 .....	50
Table 27: NCDC quality controlled local climatological data for the test period on February 7, 2016 .....	51
Table 28: NCDC quality controlled local climatological data for the test period on February 8, 2016 .....	52
Table 29: Wunderground climatological data for the test period of April 16 - April 18, 2016.....	53
Table 30: NOAA record of climatological observations for the test period of April 16 - April 18, 2016 .....	53
Table 31: NCDC quality controlled local climatological data for the test period on April 16, 2016 .....	54
Table 32: NCDC quality controlled local climatological data for the test period on April 17, 2016 .....	55
Table 33: NCDC quality controlled local climatological data for the test period on April 18, 2016 .....	56
Table 34: Base/Subgrade Threshold Materials .....	178
Table 35: Environmental parameters collected during construction .....	197
Table 36: Aggregates utilized for pervious concrete project.....	198
Table 37: Mass of source aggregates utilized .....	199
Table 38: Aggregate Specific Gravities.....	201
Table 39: Results from Ignition Oven Test.....	203
Table 40: Clayton #57 Gradation .....	205

Table 41: Weldon ½" Gradation .....	206
Table 42: Weldon ¾" gradation .....	207
Table 43: Weldon ¼" gradation .....	207
Table 44: NJ Gravel ¼" White Washed Gradation .....	209
Table 45: Weldon Concrete Sand .....	209
Table 46: Aggregate Moisture Content .....	210
Table 47: Load Cell calibration curve equations .....	217
Table 48: Calibration equations for Type-E Thermocouples .....	218
Table 49: Calibration equations for Type-E Thermocouples .....	219
Table 50: USP Calibration Equations.....	222
Table 51: CR1000 Datalogger Equipment used .....	231
Table 52: CR3000 Datalogger Equipment used .....	233
Table 53: Type E close proximity air column thermocouple heights.....	243
Table 54: In-slab thermocouple depth arrangement .....	243
Table 55: Field sample 1 sensors .....	250
Table 56: Field sample 2 sensors .....	252
Table 57: Field sample 3 sensors .....	253
Table 58: Field sample 4 sensors .....	254
Table 59: Field sample 5 sensors .....	256
Table 60: Field sample 6 sensors .....	257
Table 61: Field sample 7 sensors .....	258
Table 62: Field sample 8 sensors .....	259
Table 63: Sources of climatological data derived for regional locations Near the test site .....	262
Table 64: Sky conditions utilized for albedo calculations .....	262
Table 65: Load Cells utilized for Final Slab Mass.....	312
Table 66: The Sensible and Latent Heat Flux for Each Slab .....	332
Table 67: The energy budget and savings for each slab .....	334



## DESCRIPTION OF THE PROBLEM

Due to concerns about Urban Heat Island effect and the desire for energy efficiency, different land cover types including natural, agricultural, and most building materials, such as roofing have been studied extensively (Yang, 2013). Major infrastructure components, such as concrete and asphalt road surfaces, parking lots, and sidewalks have more recently become a topic of interest (Li, 2013). Due to its dark color, asphalt is known to have a low albedo or low level of reflectivity, but the majority of albedo and solar radiation research conducted in the asphalt and concrete industry to date has highlighted freshly paved asphalt or concrete samples without accounting for changes in aged pavements, varying lift thickness, aggregate types, or structural parameters associated with widely varying asphalt mix designs. The asphalt parameters are known to affect the amount of light reflected, the amount of heat absorbed, the amount of heat retained, and the amount of heat expunged throughout the nighttime hours. Several studies have been completed to evaluate the benefits of more reflective surfaces, such as Portland Cement Concrete and chip seals using lightly colored aggregates (Li, 2013). Another recent study was conducted to determine if “cool” pavements provided any benefit to the environment (Li, 2012). Since the aggregates, mix designs, and climate are different from location to location, it is important to measure the solar radiation and albedo for state specific asphalt parameters.

The State of New Jersey currently holds over 39,000 miles of public roadways (of which 8410 lane miles are controlled by the state DOT), and 24 public use airports. As of 2007, the land cover of the state comprised of 800 sq. mi. of impervious surface which was increasing at a rate of 6.67 sq. mi. per day (Hasse, 2010). This results in an 11% total impervious land cover as of 2007. Arnold and Gibbons (1996) showed that an increase of 10% in impervious surface area results in an increase of land surface temperature by 1-1.5 C, which was expanded upon by Xu in 2010 (Xu, 2010, Arnold, 1996). It should be noted that this relationship does not correlate with a linear scaling, but rather an exponential rate, resulting in a more rapid increase in temperature of urban areas than those of rural landscapes. Due to these NJ statistics, the need for research about impervious surface, albedo, and solar radiation flux for asphalt and concrete pavements in New Jersey is paramount.

## APPROACH

Unfortunately, urban heat island effect is not a problem that only New Jersey needs to be concerned with, but fortunately the issue has been gaining recognition around the country. The studies that have been conducted thus far have been primarily focused on fresh new pavement, typically with only one sample of each mix tested, which excludes the capability of analyzing results from repeatable samples (Li, 2013). Albedo and solar radiation flux has been measured on asphalt pavements utilizing two techniques, the solar spectrum reflectance measurement test, ASTM C1549, and the Pyranometer test method, ASTM E1918, the latter of which provides better measurements for pavement surfaces and gravel (Tran, 2009). ASTM E1918 requires the measurement surface to have a circular diameter of 4m or a square with at least 4 meters per side (ASTM, 2015). To evaluate multiple pavement types or to change mix parameters utilizing 4m x 4m square pavement plots would require considerable amount of space, have high cost and require significant time to produce. This method is beneficial because it allows ample testing surface for the ASTM E1918 test methodology and is easy to pave with a paver and roller, but the pitfalls make it difficult to measure multiple similar samples as well as multiple mix parameters simultaneously. There is a need to create a better test procedure that can be conducted with multiple samples to statistical repeatability. The procedure should be easily reproducible by other practitioners and should be able to be utilized on field aged and traffic loaded samples. This is an important parameter to consider because the surface characteristic of both asphalt and concrete, from binder film thickness to texture, which will affect the albedo and solar radiation flux. The goal of this research is to replicate the asphalt albedo results compiled by Li, 2012, to conduct outdoor field measurements on asphalt slabs with two major differences; smaller samples and measurements conducted on 3 samples simultaneously to provide data that could be statistically analyzed. One of the main goals of this study is to determine if a 1m by 1m sample area size would be sufficient to replicate albedo and solar radiation measurements of in-service pavements.

## METHODOLOGY

Testing should be conducted for at least 48 hours simultaneously for a set of 3 similar samples. This testing should be conducted 4 times annually to represent the effects of seasonal data. By utilizing similar mix parameters and monitoring the samples for a year in the same location with the same environmental loading, the three samples can be evaluated to determine if the statistical variability between the measurements is significant.

### *TEST SITE LOCATION AND SITE SETUP*

The testing site for the three samples used for this study is located behind the Rutgers Asphalt Pavement Laboratory, as can be seen in Figure 1. The ideal area would be a wide open area non-influenced by buildings or trees with a completely open view of the sky, so the use of the space behind the lab provided an inherent problem to the project due to the variation in the angle of the sun that intrinsically would impart a direct effect on the quality of the measurements over an annual period.

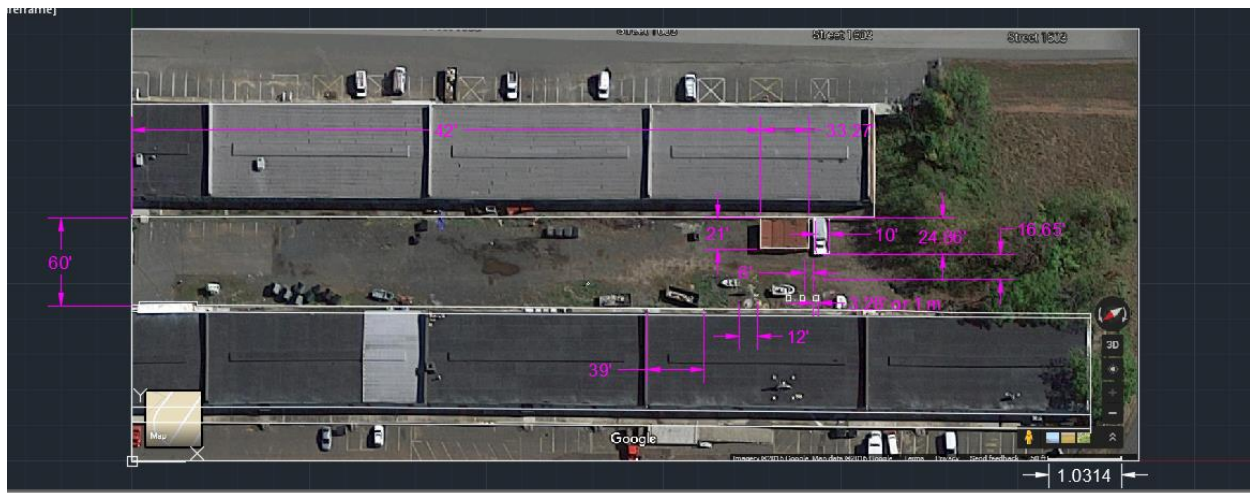


Figure 1: The Rutgers Asphalt Paving Laboratory; showing the location where the 1 sq. m. samples would be tested

In Figure 1, it is important to point out that there are a few constraints to the area that were required to design around. The two primary constraints were that there must remain a minimum of 12' fire lane access to both buildings. There was a currently existing set of shipping containers stored there that were unable to be moved as well as a concrete wall that was being utilized for a separate project. The testing area used for this study is not the ideal, but it was considered acceptable to provide relative results to compare values from sample to sample. The initial condition behind the lab was and remained a community area, so additional considerations were required to ensure the safety and accessibility to the area which also required mitigation as part of the project. Figure 2 and 3 show the condition of the testing area from the Northwest, then from the Southwest respectively, prior to the beginning of the project once the dense brush had been removed.



Figure 2: Initial site survey and site conditions facing West



Figure 3: Initial Site Conditions after cleaning up the existing debris, facing North



Figure 3 emphasizes the close proximity of the buildings to the testing location. To ensure that any reflected radiation not associated with the samples directly being measured and to ensure the surrounding material would not “white wash” the sensors, 120 tons of reclaimed asphalt pavement (RAP) was placed on the test site. To clean the site and spread the rap a bobcat skid-steer was utilized. The RAP was then compacted to provide a flat working surface using a 1.5 ton vibratory drum roller. Figure 4 shows the removal of pre-existing ground imperfections, Figure 5 shows the spreading of the RAP, Figure 6 shows the back-scraping used to finalize the spreading of the rap, and finally, Figure 7 shows the vibratory compactor utilized to compact the final surface.



Figure 4: Removing debris to prepare the testing site





Figure 5: Preparing the testing surface by spreading Reclaimed Asphalt Pavement (RAP) to normalize the reflective surfaces



Figure 6: Back scraping the RAP base to prepare for rolling the surface with a vibratory drum roller





Figure 7: Rolling the base surface to ensure a stable surface to place the test specimens

After these procedures were completed, the site was considered ready to place the 1 sq. m. slab samples that were to be tested. This surface, albeit similar in color to the asphalt samples being tested in this study, created an even and minimally reflective surface to conduct albedo and solar radiative flux measurements.

### ***EQUIPMENT***

This project was considered to be a pilot project to show that creating the necessary samples and testing utilizing this method is viable. To ensure its viability several different pieces of equipment were required to collect enough information about the albedo, solar radiation flux, and to ensure the asphalt being tested was constructed similar to in-service asphalt pavement. To conduct this study the equipment required included pyranometer, pyrgeometer, thermocouples, and an electromagnetic density gauge. The pyranometer is a sensor utilized to measure short wave radiation. The pyrgeometer is a sensor that measures long wave radiation. The thermocouples were needed to measure multiple depths of the asphalt slab to evaluate the influence of the solar radiation on the test slab. The electromagnetic density gauge is a non-destructive sensor utilized to measure the density of materials to ensure the asphalt slabs were constructed to the proper density.

*Hukseflux Net Radiometer*

Since this study was intended to measure solar radiation flux in addition to albedo, the Hukseflux NR01 net radiometer, which is a four component instrument that incorporates four separate sensors including two pyranometers (up and down facing) for measuring short-wave radiation flux as well as 2 pyrgeometers (up and down facing) for measuring far infrared radiation flux, was selected. Figure 8 shows the Hukseflux unit displayed over a mock sample from the top down. The domed sensor facing up on the right side of the NR01 is the up facing pyranometer and the flat sensor on the left side of the Figure 8 is the upward facing pyrgeometer.



Figure 8: Hukseflux NR01 net radiometer

How the net radiometer was utilized in this experiment was what defined the difference between the standard ASTM E1918 and this methodology. ASTM E1918 specifies that the net radiometer should be placed at a height of 0.5m above the testing surface (ASTM, 2015). This is determined by the sensors typical view window measurement of influence. On the NR01, both pyranometers have a view window of  $180^\circ$ , the upward facing pyrgeometer has a view of  $180^\circ$  and the downward facing pyrgeometer has a field of view of  $150^\circ$ . However, although the viewing angle of the sensors are between  $150^\circ$  and  $180^\circ$  the sensors operate in a directional, or cosine response. Therefore the unit is sensitive to direction of light and will only provide a response relative to the cosine of the angle of incidence. The manufacturer suggested that although the field of view was  $180^\circ$ , the majority of the radiation captured in the measurement was a  $90^\circ$  field of view from the center of the sensor. By applying this metric, the sample size was able to be reduced to a 1m by 1m square which leaves a 0.0856m extra material on each side of the cone of measurement, while utilizing the same height for the sensor as is required in the specification.



The parameters that are collected by the net radiometer are shown in Table 1.

Table 1: Measured and calculated values provided by the Hukseflux NR01 net radiometer

Measurement Name	Measurement Type	Measured or Calculated	Units
PTemp_C_Avg	Instrument Body Temperature	Measured	°C
SR01Up_Avg	Global Solar Radiation	Measured	W/m <sup>2</sup>
SR01Dn_Avg	Reflected Solar Radiation	Measured	W/m <sup>2</sup>
IR01Up_Avg	Downward Longwave Radiation	Measured	W/m <sup>2</sup>
IR01Dn_Avg	Upward Longwave Radiation	Measured	W/m <sup>2</sup>
NR01TC_Avg	Surface Temperature	Measured	°C
NR01TK_Avg	Surface Temperature	Measured	K
NetRs_Avg	Net Solar Radiation	SR01Up_Avg - SR01Dn_Avg	W/m <sup>2</sup>
NetRl_Avg	Net Longwave Radiation	IR01Up_Avg - IR01Dn_Avg	W/m <sup>2</sup>
Albedo_Avg	Albedo or Solar Reflectance	SR01Dn_Avg / SR01Up_Avg	N/A
UpTot_Avg	Downward Total	SR01Up_Avg + IR01Up_Avg	W/m <sup>2</sup>
DnTot_Avg	Upward Total	SR01Dn_Avg + IR01Dn_Avg	W/m <sup>2</sup>
NetTot_Avg	Net Total	NetRs_Avg + NetRl_Avg	W/m <sup>2</sup>

#### *Thermocouples*

To measure the internal heat absorption, temperature of the asphalt slab at different depths was measured utilizing thermocouples. The thermocouples that were utilized for the experiment were made in-house by carbon rod arc welding 8 inch lengths of Type K measurement wire to 100 feet long separately shielded thermocouple extension wire as shown in Figure 9.



Figure 9: Preparing the thermocouple extension wire to be conjoined into a single probe

Prior to switching to Type K thermocouples, which are comprised of Chromel and Alumel wires, experiments were conducted with J-Type thermocouples which are comprised Constatan and Iron wires, which means they have the capability to rust when in wet environments. The J-Type wire that was utilized is shown in figure 10 along with a probe that was designed and manufactured in the lab.



Figure 10: Initial J-Type thermocouple probe assembly

The J-Type thermocouples inevitably failed due to the amount of signal noise generated in the 100-foot long extension wire which had 12 sets of thermocouple wires (24 wires) within one grounded shield, without the use a signal amplifier on each probe.

Once the thermocouples had been created they were each separately tested for a five-minute period while the data was visually verified to have sufficient welds, calibration was conducted referencing a calibrated name-brand thermocouple, using linear regression to normalize the probes to 0°C (32°F) an ice water bath, a middle temperature using an ambient temperature water bath, and a 100°C (212°F) water bath. After the testing had been conducted, post calibrations were also conducted to verify that the calibrations remained valid throughout the testing period. The thermocouple calibration records are provided for reference in Appendix C of this paper.

To conduct the measurements to utilize for comparisons of albedo and solar flux within this project, 10 Type K thermocouples were taped to a piece of PVC pipe which could then be inserted into a cored one inch (25.4mm) diameter hole in the slab sample. The depth profile of the thermocouple locations within one temperature “probe” is shown in Table 2 below.

**Table 2: Thermocouple placement and spacing to create a single sample probe**

<b>Thermocouple ID</b>	<b>Thermocouple Depth (in.)</b>	<b>Thermocouple depth (mm)</b>
10	0.25	6.35
9	0.5	12.7
8	0.75	19.05
7	1	25.4
6	1.5	38.1
5	2	50.8
4	2.5	63.5
3	3	76.2
2	3.5	88.9
1	4	101.6

Since the best configuration of thermocouples utilized to travel long distance requires the use of a conditioned signal amplifier for each thermocouple, a work around was devised to reduce ambient noise to a sufficient level by increasing the sampling rate to 30 samples per 100 Hz measurement frequency. The signal was then conditioned with applying a low pass Butterworth filter with a cutoff frequency of 2 Hz and a smoothing filter with a rectangular moving average that had a half width of 600 points, before the data was recorded into 15-minute time blocks.

To determine the proper location to place the temperature probes in the slab samples to avoid influencing the albedo and heat flux measurements as much as possible, while still ensuring viable data without excessive wind loading effects on the sides of the sample, a verification was conducted on a test slab. Figure 11 shows the arrangement of the thermocouples utilized for this verification.

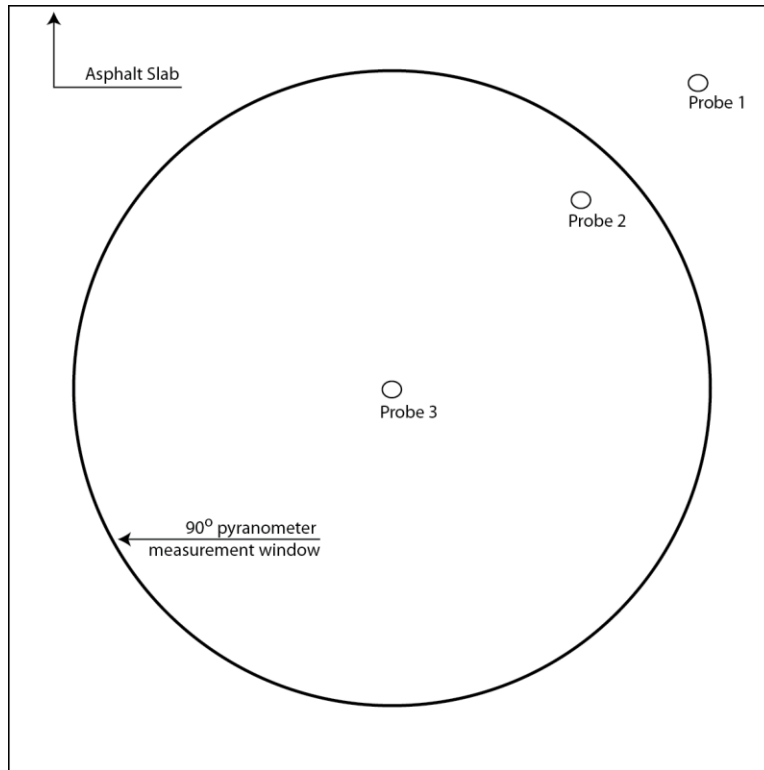


Figure 11: Layout of the proposed area of measurement and locations where thermocouple testing was conducted

The sides of the hole were filled with mineral filler to ensure a tight fit with no air gaps remaining. One probe was placed in the center of the slab, one was placed 254mm in on the 45° from the corner of the slab, and one was placed 101.6mm in on the 45° from the corner of the slab. The data shown in Figure 12 and Figure 13 shows the 0.5in 12.5mm (0.5in) and 76.2mm (3in) depth respectively, temperature measurements from each thermocouple at the three locations in the asphalt slab over a week period.

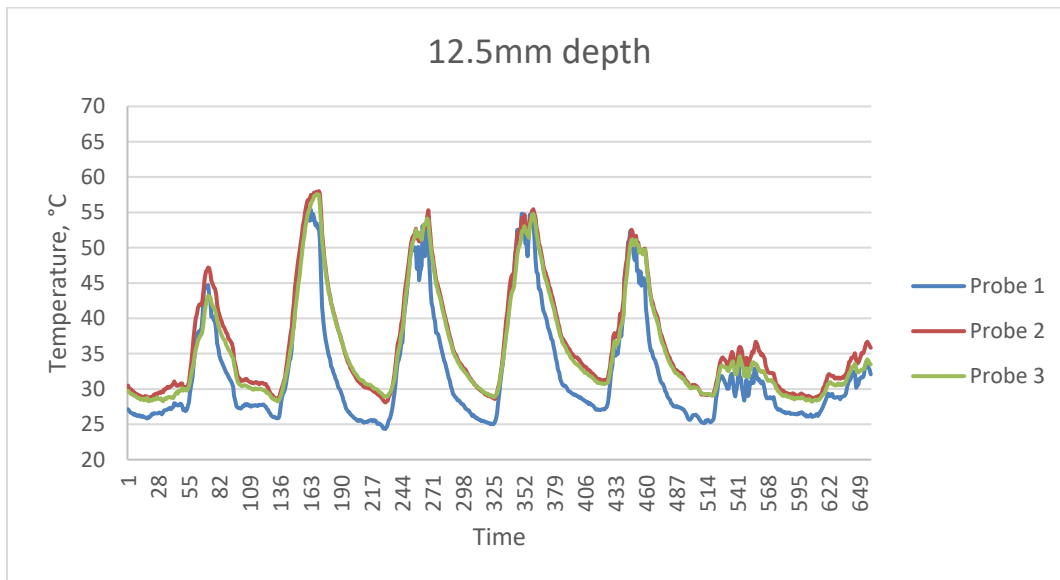


Figure 12: Thermocouple placement verification data at 12.5mm depth

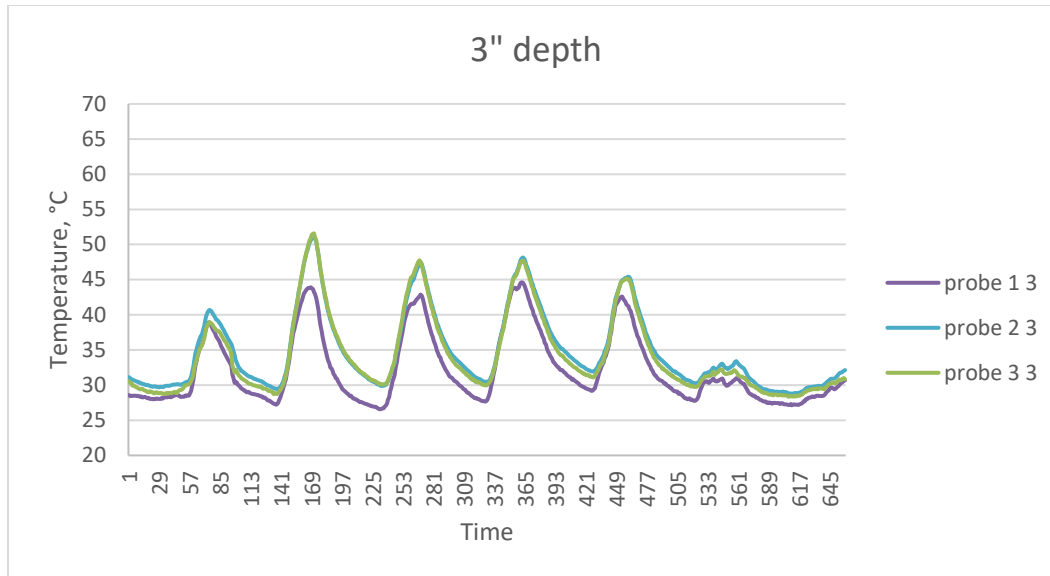


Figure 13: Thermocouple placement verification data at 76.2mm depth

Probe 1 was nearest to the corner, probe two was half of the distance to the center of the slab, and probe 3 was in the center of the slab. It was clear to see that probe 2 and 3 were more closely matched than probe 1. Since probe 3 was not practical, as it was in the center of the slab, the probe 2 location, which was still 106mm inside the measurement window, was utilized for further testing. Although no localized wind speed was measured, it is likely that the edge of the sample was more impacted by wind loading on the exposed sides of the sample.

#### *Asphalt Slab Compaction and Electromagnetic Density Gauge Verification*

The creation of the asphalt slabs was a new experience for our laboratory due to the size of the sample. To create the samples a new mold, which is shown in Figure 14, was designed, machined, and welded in-house. The mold provides removable and interchangeable sides to allow for different lift thicknesses if desired.



Figure 14: New 1 sq. m. asphalt compaction mold created in-house

The plate of the steel mold was 2.38mm thick, supported by 3.175mm wall 50mm by 50mm wall square stock. The walls of the mold were 3.175mm wall C-channel. Each corner of the sidewalls were welded and the base was bolted to the sidewalls to ensure the volume of the sample would not change during compaction. As Figure 14 clearly depicts, the initial slab was compacted utilizing Gilson specimen compaction papers that are utilized for other methods of compaction of asphalt in the laboratory. Due to the size of the sample and the number of papers required the remaining slabs utilized a talc based release agent, typically used in asphalt binder research, which could be spread with a paint brush. The compaction of the sample was conducted with a vibratory plate compactor on the steel mold, which was followed by rolling with a 90kg (200lb) water filled manual roller. An example of the steel mold with a compacted asphalt sample previous to being demolded is shown in Figure 15.





Figure 15: Freshly compacted 1 sq. m. asphalt sample

Part of the project was to create repeatable samples and provide the opportunity to eventually evaluate how the density and air void percentage of different mix types affected the albedo and solar radiation. To ensure the desired density of the samples was met before albedo and solar radiation testing began, an electromagnetic density gauge was used to verify the compaction density of each slab. This alleviated the need to core or cut part of the slab to conduct standard asphalt density in the laboratory, which is typically conducted using the AASHTO T-166 Specification, “Bulk Specific Gravity of Compacted Asphalt Mixtures Using Saturated Surface-Dry Specimens.”

A dedicated test slab was created prior to creating the test slabs, which used the same asphalt mix to verify the volumetrically designed batch weight and to determine the offset for the electromagnetic density gauge. An example of the electromagnetic density gauge can be seen in Figure 16.

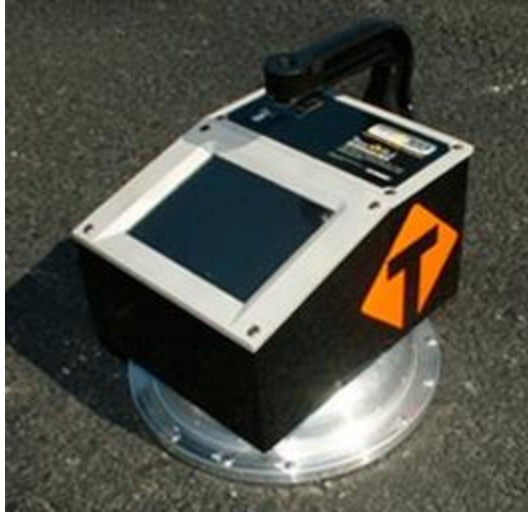


Figure 16: The Transtech PQI380 electromagnetic density gauge

The initial slabs were designed to be 101.6mm thick with an initial batch weight of 2,623kg to a target 4.4 percent air voids. After compaction, the slab was measured with the electric density gauge in 9 locations then cut, cored, and bulk density tested. The initial results from the electric density gauge, the results from the bulk density test, and the calculated offset are shown in Table 3, an illustration of the cut and cored asphalt slab is shown in Figure 17 respectively. The average offset which was  $-107.3\text{kg/m}^3$  ( $-6.9\text{lbs/ft}^3$ ), is shown in Table 3 was selected to verify the final slab specimens.

Table 3: Electromagnetic density gauge and AASHTO T-166 bulk density comparison and offset calculation

TRI_9.5M64V			
Core #	EDG Density (lbs/ft <sup>3</sup> )	T-166 Density (lbs/ft <sup>3</sup> )	Calculated Offset
1	153.8	152.9	0.9
2	147.6	149.9	-2.3
3	142.0	152.4	-10.4
4	154.3	155.3	-1.0
5	138.6	152.4	-13.8
6	146.3	153.6	-7.3
7	149.7	154.8	-5.1
8	136.1	152.1	-16.0
9	144.5	152.1	-7.6
Average	<b>145.9</b>	<b>152.8</b>	<b>-6.9</b>





Figure 17: Asphalt verification slab utilized to practice compaction and verify the offset for the PQI380

#### ***ASPHALT MIX SELECTION AND DESIGN PARAMETERS***

Based on the size of the samples and the needs of the project, it was determined that approximately 2 tons would be required to produce the test specimens as well as the verification samples. One of the state's largest asphalt aggregate and mix suppliers offered to sample loose mix while they were producing a dense graded asphalt which featured a virgin 64-22 asphalt binder (9.5M64V), which is the standard basic mix utilized in the State of New Jersey. Given this opportunity, the authors agreed to utilize the mix for this project, alleviating the need to create the mix in the laboratory. While this saved a significant amount of time, it also ensured that the mix was authentic to New Jersey, both in regards to aggregate sourcing and binder selection, but was also representative of drum plant produced mix that was being utilized in Hillsborough Township, NJ. Table 4 shows the aggregate gradation, optimal asphalt content percentage (AC%), and maximum bulk specific gravity (G<sub>mm</sub>).

Table 4: Mixture design of dense graded 9.5M64V HMA utilized for this project

Sieve Size (mm)	% Passing
50.00	100
37.50	100
25.00	100
19.00	100
12.50	100
9.50	95.3
4.75	67.5
2.36	50
1.18	35.1
0.60	26.3
0.30	18.3
0.15	11.1
0.08	6.7
% AC	5.39
Gmm	2.701

The gradation met the standard dense graded aggregate blend as required by NJDOT. The gradation set within New Jersey standard limits on a 0.45 power chart is shown in Figure 18 below. As a 9.5mm nominal aggregate size blend, which is one of the most widely utilized blends for wearing courses, the sample thickness of 4" (101.6mm) thick was 10 times the nominal aggregate size. This suggests that assuming the mixture was homogenous, the sample size was sufficient to conduct viable measurements. The typical minimum sample size utilized in asphalt performance testing is required to be a minimum of 2.5 times the nominal aggregate size.

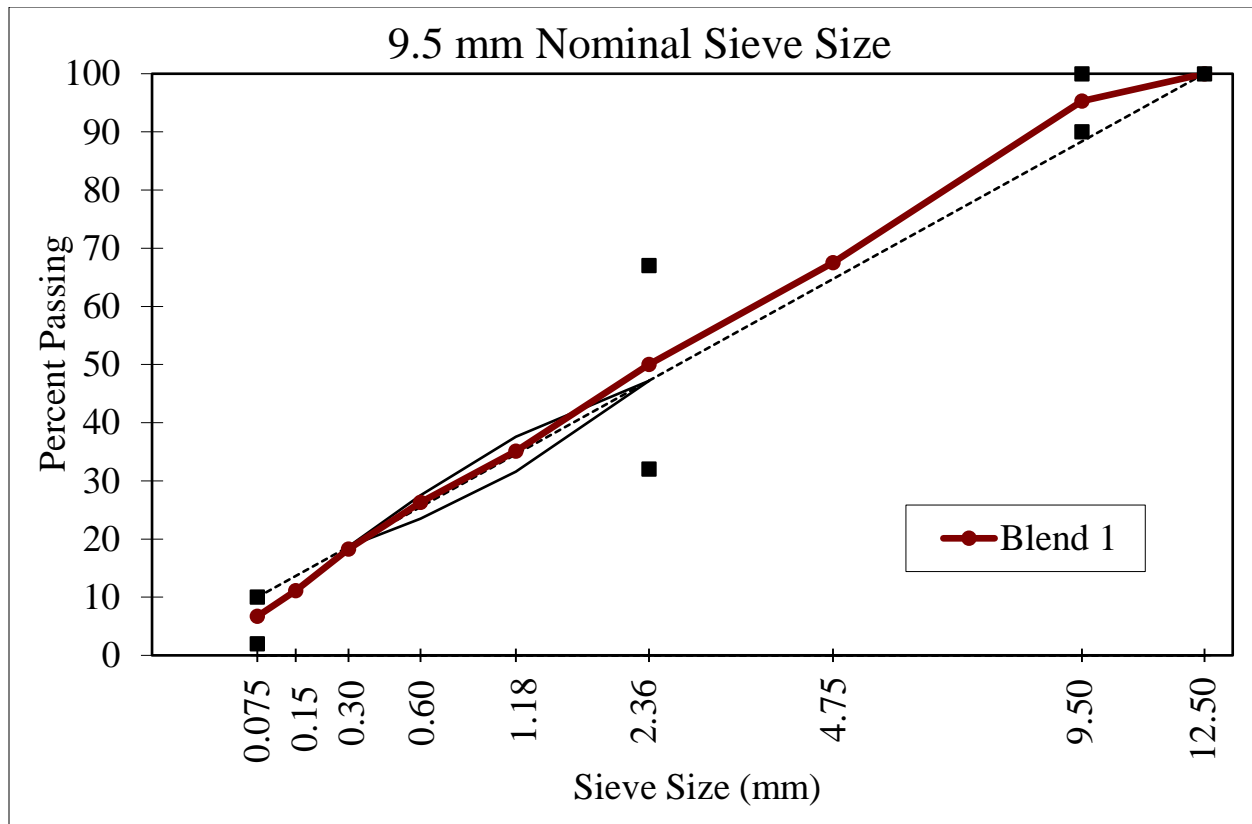


Figure 18: Mix gradation of the 9.5M64V asphalt mixture selected for use in this project

#### DERIVED DATA

Since this project did not include funding for a local weather station, the environmental data was derived from government sponsored climatological databases. Based on the local availability data was derived from three different primary sources. Each source provided slightly different datasets. Table 5 shows the information source, the location it was derived from, and the data that was provided by the dataset for each of the three sources.

**Table 5: Sources of climatological data derived for regional locations as close proximity to the test site as possible**

<b>Source</b>	<b>Location</b>	<b>Data Provided</b>
NOAA Record of Climatological Observations	New Brunswick, NJ	Temperature Min (°F)
NOAA Record of Climatological Observations	New Brunswick, NJ	Temperature Max (°F)
NOAA Record of Climatological Observations	New Brunswick, NJ	Precipitation Rain/Melted (inches)
NOAA Record of Climatological Observations	New Brunswick, NJ	Precipitation Snow/Ice(inches)
NOAA Record of Climatological Observations	New Brunswick, NJ	Evaporation (inches)
NOAA Record of Climatological Observations	New Brunswick, NJ	Soil Temperature 4" Depth Min (°F)
NOAA Record of Climatological Observations	New Brunswick, NJ	Soil Temperature 4" Depth Max (°F)
NOAA Record of Climatological Observations	New Brunswick, NJ	Soil Temperature 6" Depth Min (°F)
NOAA Record of Climatological Observations	New Brunswick, NJ	Soil Temperature 6" Depth Max (°F)
NCDC Quality Controlled Local Climatological Data	Somerville: Somerset Airport	Resultant Wind Speed (MPH)
NCDC Quality Controlled Local Climatological Data	Somerville: Somerset Airport	Resultant Wind Direction
NCDC Quality Controlled Local Climatological Data	Somerville: Somerset Airport	Average Wind Speed (MPH)
NCDC Quality Controlled Local Climatological Data	Somerville: Somerset Airport	Sky Conditions <sup>1</sup>
NCDC Quality Controlled Local Climatological Data	Somerville: Somerset Airport	Weather Type <sup>1</sup>
Wunderground	Pluckemin, NJ	Relative Humidity Min (%)
Wunderground	Pluckemin, NJ	Relative Humidity Avg (%)
Wunderground	Pluckemin, NJ	Relative Humidity Max (%)
Wunderground	Pluckemin, NJ	Temperature Min (°F)
Wunderground	Pluckemin, NJ	Temperature Max (°F)
Wunderground	Pluckemin, NJ	Precipitation (inches)

Each of these sources provided slightly different datasets and were considered important to analyze for this project since there was no local weather station to provide microclimate data. Each regional source could then be cross referenced to assume the most accurate climatological circumstances that was possible. Since each dataset has its own nomenclature, Table 6 below shows the pattern of labeling and the abbreviations utilized throughout the remaining set of climatological data within this paper.

Table 6: Definitions of nomenclature utilized throughout this report

Qualifier		Weather Phenomena		
Intensity or Proximity	Descriptor	Precipitation	Obscuration	Other
1	2	3	4	5
- Light	MI Shallow	DZ Drizzle	BR Mist	PO Well-
Moderate	PR Partial	RA Rain	FG Fog	Developed
(see note 2)	BC Patches	SN Snow	FU Smoke	Dust/Sand
+ Heavy	DR Low Drifting	SG Snow Grains	VA Volcanic Ash	Whirls
VC In the Vicinity (see note 3)	BL Blowing	IC Ice Crystals	DU Widespread Dust	SQ Squalls
	SH Shower(s)	PL Ice Pellets		FC Funnel Cloud
	TS Thunderstorm	GR Hail	SA Sand	Tornado
	FZ Freezing	GS Small Hail	HZ Haze	Waterspout
		and/or Snow	PY Spray	(see note 3)
		Pellets		SS Sandstorm
		UP Unknown Precipitation		SS Duststorm
<b>1.</b> The weather groups shall be constructed by considering columns 1 to 5 in the table above in sequence, i.e. intensity, followed by description, followed by weather phenomena, e.g. heavy rain shower(s) is coded as +SHRA				
<b>2.</b> To denote moderate intensity no entry or symbol is used.				
<b>3.</b> Tornadoes and waterspouts shall be coded as +FC.				
‡ CLR (clear), FEW (few), SCT (scattered), BKN (broken), or OVC (overcast), VV (vertical visibility)				

The data that was derived from the NOAA Record of Climatological Observations- New Brunswick Station was downloaded from the website:

[web/datasets/GHCND/stations/GHCND:USC00286055/detail](http://web/datasets/GHCND/stations/GHCND:USC00286055/detail)

The data that was derived from the NCDC Quality Controlled Local Climatological Data was downloaded from the website:

<http://www.ncdc.noaa.gov/qclcd/QCLCD?prior=N>

The data that was derived from Wunderground.com was downloaded from the website:

[https://www.wunderground.com/history/airport/KSMQ/2016/5/26/MonthlyCalendar.html?req\\_city=Pluckemin&req\\_state=NJ&reqdb.zip=07978&reqdb.magic=1&reqdb.wmo=99999#calendar](https://www.wunderground.com/history/airport/KSMQ/2016/5/26/MonthlyCalendar.html?req_city=Pluckemin&req_state=NJ&reqdb.zip=07978&reqdb.magic=1&reqdb.wmo=99999#calendar).

#### DATA SELECTION PROCESS

The final data selection process was determined initially by the desired environmental conditions and then reduced to match available data. Originally in the project proposal, testing was to be conducted for

a 48h window at least one time per season. Due to the availability of the equipment, 10 partial to mostly full months were collected; occasionally the equipment required service.

The initial step in data reduction was conducted by searching the climatological records described in the derived data section of the report. When possible, 72 hour segments were defined based on the following criteria: 1) less than 95% cloud cover and 2) less than 25% relative humidity. Both of these criteria were difficult to meet in the New Jersey climate, which led to the selection of the best possible data per month. Table 7 summarizes the dates that were selected for the initial reduction of data.

**Table 7: List of dates for which the initial thermocouple and net radiometer data was compiled**

<b>2015</b>		<b>2016</b>	
<b>Month</b>	<b>Day</b>	<b>Month</b>	<b>Day</b>
July	31	January	4
August	1	January	5
August	2	January	6
September	5	February	6
September	6	February	7
September	7	February	8
September	15	February	26
September	16	February	27
September	17	February	28
October	10	March	6
October	11	March	7
October	12	March	8
October	18	March	29
October	19	March	30
October	20	March	31
November	14	April	16
November	15	April	17
November	16	April	18
November	23		
November	24		
November	25		
December	19		
December	20		
December	21		

The second step in the data reduction process was to cross reference the derived data from Table 7 with the data measured by the thermocouples and net radiometers. Any dates that were missing full measured datasets were discarded, which resulted in the following list shown in Table 8 below.

**Table 8: List of dates for which full thermocouple and net radiometer data was available**

<b>2015</b>		<b>2016</b>	
<b>Month</b>	<b>Day</b>	<b>Month</b>	<b>Day</b>
July	31	January	4
August	1	January	5
August	2	January	6
October	10	February	6
October	11	February	7
October	12	February	8
October	18	February	26
October	19	February	27
October	20	February	28
November	14	March	6
November	15	March	7
November	16	March	8
November	23	March	29
November	24	March	30
November	25	March	31
December	19	April	16
December	20	April	17
December	21	April	18

To fulfill the requirements of the project, four data sets were required for additional data reduction and analysis. To reduce the datasets further, the Wunderground.com minimum/maximum temperatures and minimum/maximum percent relative humidity were utilized. An attempt was made to evaluate both seasonal data and varying temperature range data. The dates that were selected for further analysis including the % relative humidity and temperatures are shown in Table 9 below.

Table 9: Date ranges selected from Table 8 above for further analysis related the temperature and relative humidity

Date			Season	Relative Humidity (%)	Temperature (°F)		Precipitation
Year	Month	Day		Average	Minimum	Maximum	(inches)
2015	July	31	Summer	76	63	90	0.00
2015	August	1	Summer	66	61	90	0.00
2015	August	2	Summer	60	57	89	0.00
2016	January	4	Winter	48	12	33	0.00
2016	January	5	Winter	47	9	30	0.00
2016	January	6	Winter	60	7	42	0.00
2016	February	6	Winter	70	19	41	0.00
2016	February	7	Winter	64	18	46	0.00
2016	February	8	Winter	59	30	41	0.00
2016	April	16	Spring	47	32	70	0.00
2016	April	17	Spring	51	32	73	0.00
2016	April	18	Spring	45	37	82	0.00



## FINDINGS

### SLAB DENSITY

When constructing the asphalt slabs for this experiment, which was to be conducted for a year, one of the most critical components was to create samples that were similar in mix proportions, binder type, density, mass, and thickness. To create such a large sample, the required mass of material was determined by volume. Since the samples were designed to utilize the minimum measurement window possible to test with the net radiometer, coring the slab to verify the density was determined to be detrimental to the sample. As thus, to avoid conducting measurements over an annual period without the knowledge of whether the samples were of similar density, the PQI380 electromagnetic density gauge was utilized. To provide the most accurate measurements, the gauge required laboratory verified cores that could be utilized to calculate an instrument offset. One test slab of the project mix was constructed and cored as shown above in the Asphalt Slab Compaction section of the paper. The results from the PQI gauge for each slab are shown in Figures 19, 20, and 21 below. The data utilized for the T-166 bulk data was available for these three slabs because after the solar radiation measurements had been completed, each slab was cut, cored, and bulked to verify the final density of each slab and to check the accuracy of the gauge. Due to the fact that the slabs were compacted utilizing a vibratory plate compactor, the slabs did not finish up with a perfectly flat surface, which shows in the measured data provided by the PQI380. The two most common spots for humps were in the center of the slab and/or near the corners.

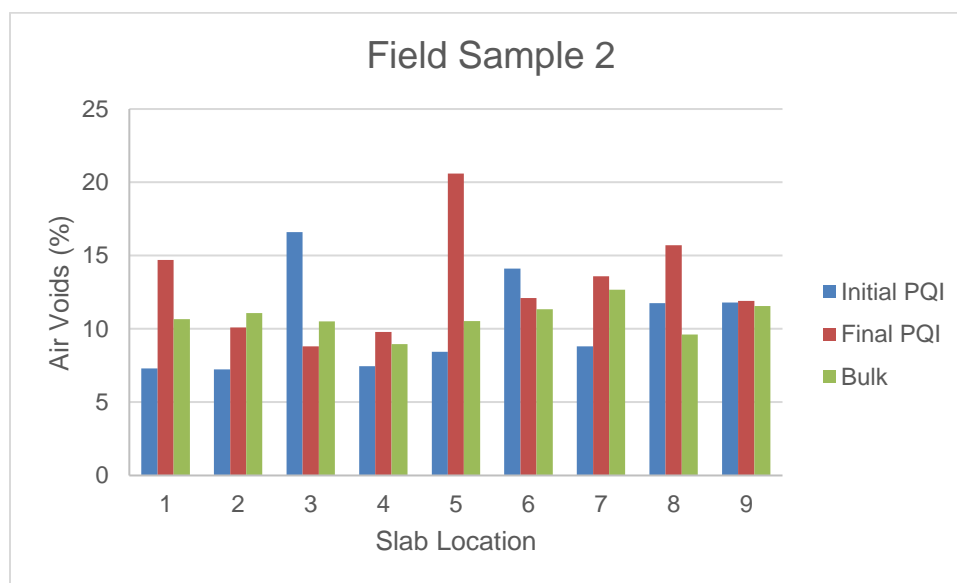


Figure 19: Initial and Final PQI density compared to AASHTO T-166 bulk density results for test specimen 2

Sample 2 originally did not have a hump in the center, but one formed throughout the year while resting on the RAP surface. Proper subbase would provide a significantly better product if it were available.

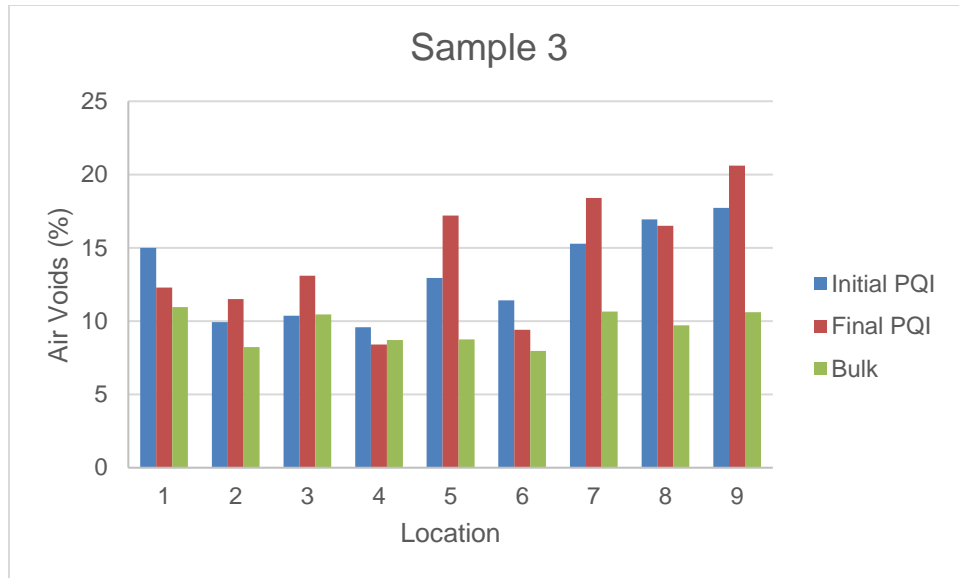


Figure 20: Initial and Final PQI density compared to AASHTO T-166 bulk density results for test specimen 3

Sample 3, shown in Figure 20, was compacted with a hump near the center and right edge of the slab, which was in the portion of the slab that was less frequently traveled by the vibratory compactor, as well as the portion of the slab that was difficult to reach with the vibratory compactor due to compacting inside the asphalt laboratory as opposed to outside due to a rain event.

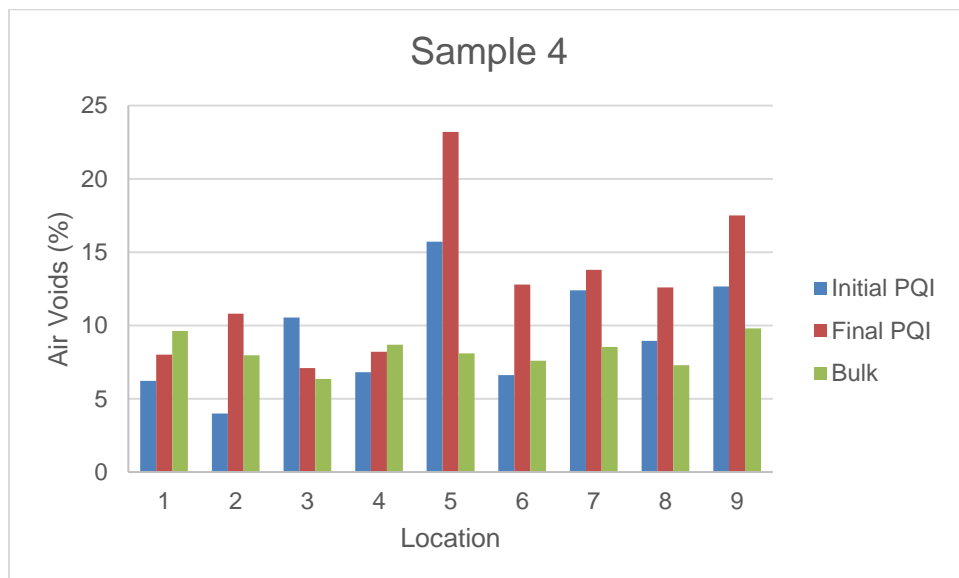


Figure 21: Initial and Final PQI density compared to AASHTO T-166 bulk density results for test specimen 3

Sample 4 had some edge humping as well as a very large center hump as part of a reaction to too much mix loaded in the center of the slab. This slab also settled on slightly on the RAP base while testing was being conducted.

## ENVIRONMENTAL PARAMETERS

### Solar

One component of calculating albedo measurements requires the input of the zenith angle of the sun, which should be a minimum of 45 degrees from the highest elevation the sun will attain that day (CC). The azimuth angle plays a less important role in the calculation, but is important when obstructions shade different test samples at different times throughout an annual period. The zenith and azimuth data was collected from solar topo online from the website:

<http://solartopo.com/solar-orbit.htm>.

The zenith angle is important to normalize for measurements of albedo to ensure the incident angle of incoming solar radiation is reflecting in a similar manner across all test samples throughout time. It is also increasingly important in the space where this project was conducted, because of the close proximity of the buildings. A comparison of the zenith angles utilized for calculating albedo for this experiment is shown in Figure 22 below. Anecdotal evidence provided by the authors support the variation in the effect of the zenith and azimuth angles, where the sample sunrise, where the sunlight began to touch the samples, was approximately 9:30 AM in January compared to 6:30 AM in July. The sample sunset, or time at which the sunlight faded from direct contact with the samples was more angular and would begin with sample 4, then progress to 3 and finally 2. The sample sunset in January was approximately 3 PM while in July the sample sunset was closer to 6 PM.

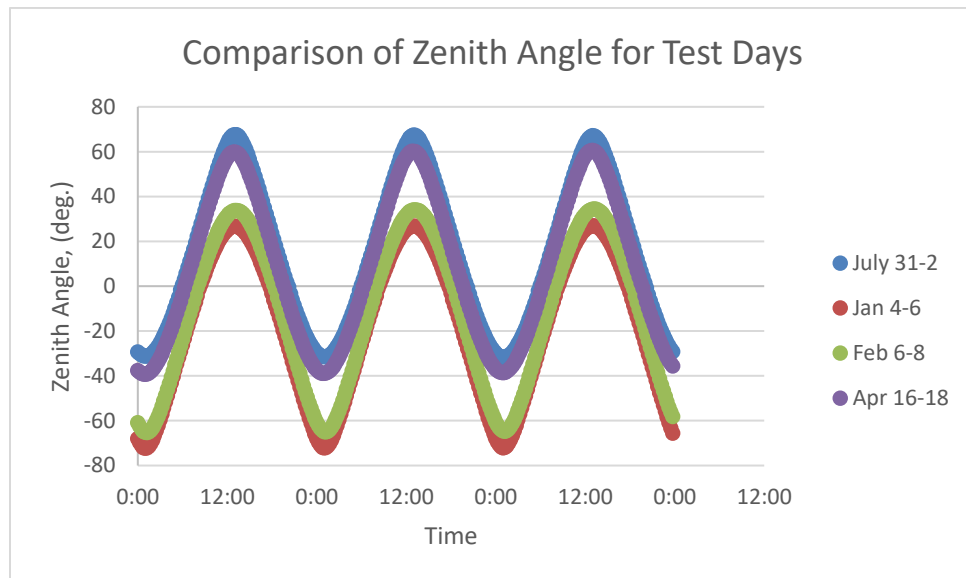


Figure 22: Comparison of zenith angles utilized for calculation of albedo

## July 31, 2015 – August 2, 2015

The zenith and azimuth angles for the period of July 31 – August 2 are shown in Table 10 below.

Table 10: Zenith and Azimuth Angles; July 31, 2015 - Aug 2, 2015 (NAD 83: 40°30'44.7"; -74°25'7.3")

Time	31-Jul		1-Aug		2-Aug	
UTC -5	Zenith	Azimuth	Zenith	Azimuth	Zenith	Azimuth
0:00	-29.2734	342.504	-29.5164	342.4498	-29.7648	342.3966
0:15	-30.0377	346.5045	-30.2831	346.4654	-30.5337	346.4278
0:30	-30.6068	350.5751	-30.8537	350.552	-31.1058	350.5309
0:45	-30.9749	354.6966	-31.2226	354.69	-31.4753	354.6858
1:00	-31.138	358.8474	-31.3857	358.8577	-31.6383	358.8709
1:15	-31.0945	3.005046	-31.3412	3.032193	-31.5928	3.062583
1:30	-30.8447	7.146401	-31.0898	7.190113	-31.3395	7.237465
1:45	-30.3914	11.24923	-30.634	11.30895	-30.881	11.37267
2:00	-29.7393	15.2929	-29.9787	15.36783	-30.2223	15.44709
2:15	-28.895	19.25922	-29.1305	19.34839	-29.37	19.44215
2:30	-27.8664	23.13295	-28.0975	23.23524	-28.3324	23.34236
2:45	-26.663	26.90215	-26.8892	27.01638	-27.1191	27.13563
3:00	-25.2947	30.55821	-25.5158	30.68319	-25.7402	30.81332
3:15	-23.7723	34.09577	-23.9879	34.23032	-24.2067	34.37013
3:30	-22.1065	37.5124	-22.3166	37.65542	-22.5296	37.80377
3:45	-20.3081	40.80827	-20.5126	40.95875	-20.7198	41.1146
4:00	-18.3879	43.98573	-18.5867	44.14277	-18.7881	44.30519
4:15	-16.3558	47.04891	-16.5491	47.21172	-16.7448	47.37992
4:30	-14.2216	50.00332	-14.4095	50.17123	-14.5996	50.34452
4:45	-11.9945	52.85555	-12.1772	53.02801	-12.3619	53.20584
5:00	-9.68312	55.61294	-9.86072	55.78952	-10.0403	55.97144
5:15	-7.29538	58.28342	-7.46817	58.46378	-7.64281	58.64946
5:30	-4.81269	60.87528	-5.00697	61.05919	-5.17696	61.24839
5:45	-1.61022	63.39709	-1.80703	63.5844	-2.01602	63.77697
6:00	0.70182	65.8576	0.563685	66.04825	0.425509	66.24413
6:15	3.111134	68.26575	2.962447	68.45974	2.812777	68.65895
6:30	5.694517	70.63061	5.544916	70.82801	5.394041	71.03063
6:45	8.35921	72.96144	8.211129	73.1624	8.061724	73.36857
7:00	11.07513	75.26777	10.9291	75.47248	10.78174	75.68242
7:15	13.82872	77.55948	13.68471	77.7682	13.53939	77.98216
7:30	16.61163	79.84689	16.46944	80.05993	16.32594	80.27824
7:45	19.41756	82.14097	19.27689	82.3587	19.1349	82.58172
8:00	22.24105	84.4535	22.10154	84.67632	21.9607	84.90448
8:15	25.07704	86.7973	24.93829	87.02566	24.79819	87.25943
8:30	27.92052	89.18653	27.7821	89.42095	27.64228	89.66084

8:45	30.76637	91.63708	30.62779	91.8781	30.48776	92.12466
9:00	33.60916	94.16698	33.46991	94.41517	33.32913	94.66898
9:15	36.44298	96.79693	36.30246	97.05289	36.16035	97.31456
9:30	39.26119	99.55103	39.11878	99.81535	38.97467	100.0855
9:45	42.05622	102.4576	41.9112	102.7308	41.76435	103.0099
10:00	44.81916	105.55	44.67073	105.8326	44.52034	106.1211
10:15	47.53939	108.8682	47.38668	109.1603	47.23184	109.4586
10:30	50.20403	112.4596	50.04605	112.7612	49.88575	113.069
10:45	52.79722	116.3808	52.63288	116.6913	52.46602	117.0079
11:00	55.29923	120.6982	55.12736	121.016	54.95275	121.34
11:15	57.68542	125.4889	57.50479	125.8111	57.32118	126.1394
11:30	59.92498	130.8378	59.73439	131.1596	59.54055	131.4872
11:45	61.97977	136.8327	61.77815	137.1463	61.57302	137.4657
12:00	63.8036	143.5509	63.59028	143.8453	63.37319	144.1452
12:15	65.34289	151.0372	65.11787	151.2977	64.88881	151.5635
12:30	66.53966	159.2724	66.30393	159.4817	66.06392	159.6962
12:45	67.33813	168.1406	67.09396	168.2816	66.84523	168.4278
13:00	67.69457	177.4149	67.44536	177.4748	67.19134	177.5403
13:15	67.58744	186.7811	67.33732	186.756	67.08211	186.7364
13:30	67.02332	195.9037	66.77632	195.7994	66.52398	195.7005
13:45	66.035	204.5026	65.7944	204.3326	65.54821	204.1673
14:00	64.67307	212.4016	64.44097	212.1825	64.2031	211.9674
14:15	62.99535	219.5325	62.77271	219.2806	62.54419	219.0316
14:30	61.05838	225.91	60.84528	225.6385	60.62625	225.3691
14:45	58.91253	231.5971	58.70846	231.3162	58.49846	231.0364
15:00	56.60025	236.6782	56.40437	236.3948	56.2026	236.1117
15:15	54.15618	241.2407	53.96752	240.9593	53.77302	240.6778
15:30	51.60814	245.3664	51.42568	245.09	51.23746	244.8128
15:45	48.97837	249.1276	48.80113	248.8577	48.61822	248.5867
16:00	46.28467	252.5861	46.11176	252.3235	45.93324	252.0595
16:15	43.54145	255.7941	43.37202	255.5391	43.19706	255.2826
16:30	40.76046	258.7954	40.59376	258.548	40.4216	258.2989
16:45	37.95147	261.6268	37.7868	261.3868	37.61675	261.1449
17:00	35.12271	264.3192	34.95947	264.0862	34.7909	263.8513
17:15	32.28128	266.8989	32.11891	266.6726	31.95126	266.4442
17:30	29.43346	269.3883	29.27144	269.1682	29.1042	268.946
17:45	26.5849	271.8068	26.42277	271.5925	26.25546	271.3761
18:00	23.74085	274.1715	23.57819	273.9626	23.4104	273.7515
18:15	20.90635	276.4973	20.74278	276.2934	20.5741	276.0874
18:30	18.08639	278.7978	17.92157	278.5986	17.75167	278.3973
18:45	15.28619	281.0853	15.11982	280.8905	14.9484	280.6935

19:00	12.51149	283.3712	12.34335	283.1805	12.1702	282.9877
19:15	9.769356	285.6661	9.599382	285.4793	9.424434	285.2905
19:30	7.070008	287.9802	6.898476	287.7972	6.722064	287.6122
19:45	4.432558	290.3232	4.260851	290.1439	4.084547	289.9626
20:00	1.907641	292.7045	1.741518	292.5288	1.571861	292.3513
20:15	-0.36245	295.1333	-0.51669	294.9613	-0.67847	294.7875
20:30	-3.25372	297.6188	-3.50169	297.4505	-3.7498	297.2805
20:45	-6.06475	300.1696	-6.2566	300.0054	-6.45359	299.8393
21:00	-8.49799	302.7948	-8.6941	302.6347	-8.89536	302.4729
21:15	-10.8594	305.5026	-11.06	305.3471	-11.2657	305.19
21:30	-13.1413	308.3015	-13.3465	308.151	-13.5568	307.999
21:45	-15.3354	311.1991	-15.5453	311.0542	-15.7604	310.9079
22:00	-17.4328	314.2027	-17.6475	314.064	-17.8675	313.9241
22:15	-19.4241	317.3185	-19.6437	317.1868	-19.8686	317.0541
22:30	-21.2993	320.5515	-21.5237	320.4277	-21.7535	320.3032
22:45	-23.048	323.9054	-23.2772	323.7905	-23.5117	323.6751
23:00	-24.6594	327.3816	-24.8932	327.2767	-25.1323	327.1715
23:15	-26.1227	330.9793	-26.3607	330.8856	-26.6042	330.7919
23:30	-27.4268	334.6949	-27.6688	334.6136	-27.9162	334.5325
23:45	-28.5614	338.5218	-28.8069	338.4539	-29.0576	338.3868

The zenith angles utilized to calculate the albedo results for this paper are shown as a plot in Figure 23 below.

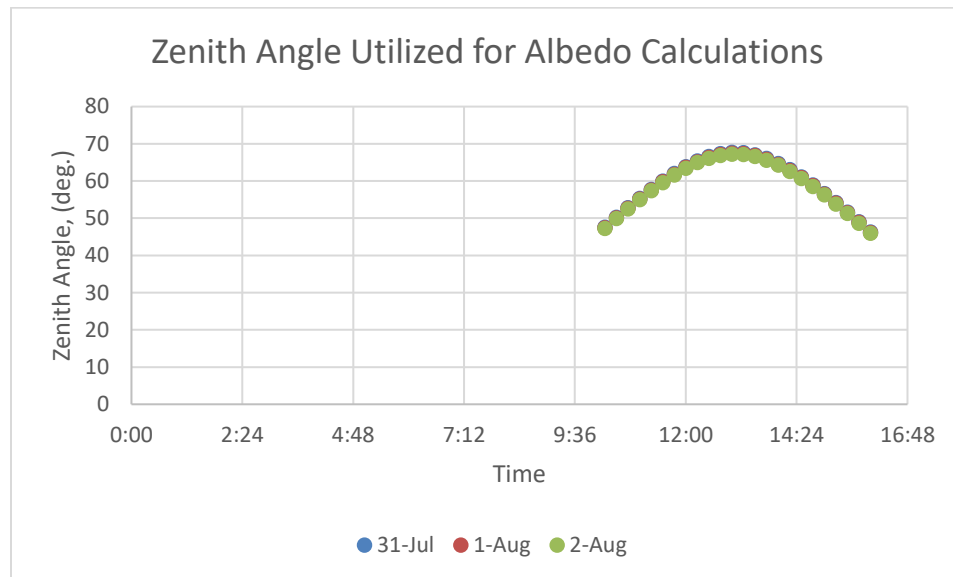


Figure 23: The zenith angle utilized for the July 31 – August, 2015 albedo calculations for this report

Due to the higher azimuth of the sun in July in the Northeastern United States, the sun's Zenith is more even from morning to afternoon than it is in the winter.

## January 4, 2016 – January 6, 2016

The zenith and azimuth angles for the period of January 4 – January 6 are shown in Table 11 below.

**Table 11: Zenith and Azimuth Angles; January 4, 2016 - January 6, 2016 (NAD 83: 40°30'44.7"; -74°25'7.3")**

<b>Time</b>	<b>4-Jan</b>		<b>5-Jan</b>		<b>6-Jan</b>	
<b>UTC -5</b>	<b>Zenith</b>	<b>Azimuth</b>	<b>Zenith</b>	<b>Azimuth</b>	<b>Zenith</b>	<b>Azimuth</b>
0:00	-67.9363	318.7826	-67.7917	318.6991	-67.6416	318.6304
0:15	-69.6555	327.0848	-69.5152	326.9501	-69.3687	326.8301
0:30	-71.0031	336.5545	-70.8699	336.3564	-70.73	336.1723
0:45	-71.894	347.0668	-71.7718	346.7985	-71.6422	346.5426
1:00	-72.2582	358.2513	-72.1508	357.9175	-72.0354	357.593
1:15	-72.0632	9.532055	-71.9735	9.149887	-71.8755	8.772835
1:30	-71.3265	20.30006	-71.2558	19.89391	-71.1766	19.48856
1:45	-70.1092	30.1114	-70.0567	29.70424	-69.996	29.29413
2:00	-68.494	38.77027	-68.4579	38.37811	-68.4138	37.98027
2:15	-66.5648	46.2847	-66.5426	45.91597	-66.5127	45.5398
2:30	-64.3945	52.77535	-64.3837	52.43287	-64.3656	52.082
2:45	-62.0416	58.40132	-62.0401	58.08466	-62.0315	57.75916
3:00	-59.5511	63.31881	-59.5569	63.02594	-59.556	62.72415
3:15	-56.957	67.66422	-56.9686	67.39254	-56.9737	67.11206
3:30	-54.2849	71.55028	-54.301	71.29715	-54.3108	71.03545
3:45	-51.5544	75.06792	-51.574	74.83086	-51.5874	74.58551
4:00	-48.7806	78.28974	-48.8028	78.06654	-48.819	77.83536
4:15	-45.9754	81.27374	-45.9994	81.06247	-46.0176	80.84352
4:30	-43.1483	84.06647	-43.1736	83.86545	-43.1931	83.65706
4:45	-40.3072	86.7056	-40.3332	86.5134	-40.3536	86.31411
5:00	-37.4586	89.22197	-37.485	89.03733	-37.5056	88.84588
5:15	-34.6084	91.64109	-34.6346	91.46294	-34.6551	91.27824
5:30	-31.7614	93.98439	-31.7871	93.81179	-31.8073	93.63288
5:45	-28.9224	96.27011	-28.9474	96.10223	-28.9667	95.92827
6:00	-26.0957	98.51399	-26.1195	98.35012	-26.1377	98.18037
6:15	-23.2854	100.7298	-23.3078	100.5693	-23.3246	100.4032
6:30	-20.4955	102.93	-20.5162	102.7723	-20.5313	102.6091
6:45	-17.73	105.1255	-17.7488	104.9701	-17.7619	104.8094
7:00	-14.993	107.3266	-15.0096	107.1731	-15.0204	107.0144
7:15	-12.2887	109.5429	-12.3028	109.3908	-12.3112	109.2337
7:30	-9.62144	111.7832	-9.63289	111.6322	-9.63843	111.4763
7:45	-6.99583	114.0562	-7.00431	113.9059	-7.00681	113.751
8:00	-4.32442	116.3699	-4.33064	116.2201	-4.32968	116.0658
8:15	-1.14509	118.7324	-1.14683	118.5828	-1.14245	118.4289
8:30	0.988302	121.1512	0.990083	121.0017	0.997379	120.848

8:45	3.216681	123.634	3.222466	123.4843	3.234297	123.3306
9:00	5.480081	126.1877	5.490232	126.0378	5.506668	125.884
9:15	7.70338	128.8193	7.718171	128.6691	7.739405	128.5152
9:30	9.858808	131.5352	9.878511	131.3846	9.904785	131.2305
9:45	11.93107	134.3412	11.95596	134.1904	11.98753	134.0362
10:00	13.90864	137.2425	13.93899	137.0915	13.97614	136.9373
10:15	15.78128	140.2433	15.81735	140.0922	15.86032	139.9383
10:30	17.5391	143.3466	17.58114	143.1958	17.63018	143.0424
10:45	19.17233	146.554	19.22058	146.4038	19.27592	146.2512
11:00	20.67128	149.8653	20.72593	149.7161	20.78775	149.5649
11:15	22.02634	153.2784	22.08756	153.1308	22.15602	152.9814
11:30	23.22819	156.789	23.29609	156.6434	23.3713	156.4965
11:45	24.26797	160.39	24.34263	160.2472	24.42464	160.1035
12:00	25.13753	164.0723	25.21894	163.933	25.30773	163.7932
12:15	25.82966	167.8239	25.91776	167.6888	26.01326	167.5537
12:30	26.33835	171.6307	26.43302	171.5006	26.53507	171.3709
12:45	26.65902	175.4766	26.76005	175.3522	26.86844	175.2286
13:00	26.78873	179.3441	26.89586	179.2261	27.01028	179.1093
13:15	26.72626	183.2149	26.83915	183.1038	26.95926	182.9945
13:30	26.47218	187.0705	26.59046	186.9669	26.71587	186.8655
13:45	26.02887	190.893	26.15211	190.7972	26.28236	190.704
14:00	25.40035	194.6659	25.5281	194.5781	25.66273	194.4934
14:15	24.59214	198.3741	24.72394	198.2945	24.86246	198.2183
14:30	23.61106	202.0052	23.74644	201.9336	23.88837	201.866
14:45	22.46497	205.5487	22.60347	205.4852	22.74832	205.4258
15:00	21.16251	208.997	21.30367	208.9413	21.451	208.89
15:15	19.71286	212.3449	19.85626	212.2966	20.00564	212.2532
15:30	18.12555	215.5894	18.27079	215.5483	18.4218	215.5122
15:45	16.41025	218.7297	16.55695	218.6954	16.70923	218.6663
16:00	14.57671	221.7669	14.72453	221.739	14.87772	221.7165
16:15	12.63476	224.7035	12.78335	224.6815	12.93711	224.6652
16:30	10.59447	227.5433	10.74347	227.5269	10.89744	227.5163
16:45	8.466739	230.2911	8.615712	230.28	8.769472	230.2747
17:00	6.265054	232.9527	6.413311	232.9464	6.566193	232.9461
17:15	4.010965	235.5342	4.156993	235.5324	4.307545	235.5367
17:30	1.755474	238.0424	1.894613	238.0448	2.038415	238.0534
17:45	-0.36765	240.4844	-0.24217	240.4907	-0.11362	240.5033
18:00	-3.19785	242.8674	-2.99388	242.8774	-2.78241	242.8937
18:15	-6.08659	245.1992	-5.93588	245.2126	-5.78135	245.2324
18:30	-8.6963	247.4876	-8.54584	247.5041	-8.39171	247.5273
18:45	-11.3493	249.7406	-11.1991	249.7602	-11.0454	249.7865



19:00	-14.0408	251.9668	-13.8909	251.9892	-13.7376	252.0185
19:15	-16.7665	254.1749	-16.6169	254.2	-16.464	254.2322
19:30	-19.5221	256.3742	-19.3728	256.402	-19.2203	256.4368
19:45	-22.3034	258.5748	-22.1544	258.605	-22.0023	258.6425
20:00	-25.1065	260.7875	-24.9578	260.82	-24.8059	260.86
20:15	-27.9273	263.0241	-27.7787	263.0588	-27.6271	263.1012
20:30	-30.7616	265.2979	-30.6132	265.3347	-30.4618	265.3794
20:45	-33.6053	267.6241	-33.457	267.6628	-33.3057	267.7096
21:00	-36.4539	270.02	-36.3056	270.0604	-36.1543	270.1091
21:15	-39.3023	272.5059	-39.154	272.5476	-39.0026	272.5981
21:30	-42.1452	275.1058	-41.9966	275.1486	-41.8451	275.2004
21:45	-44.9761	277.8486	-44.8273	277.892	-44.6754	277.9447
22:00	-47.7877	280.7697	-47.6385	280.8128	-47.4862	280.8658
22:15	-50.571	283.9121	-50.4214	283.954	-50.2684	284.0063
22:30	-53.315	287.3297	-53.1647	287.3689	-53.0111	287.419
22:45	-56.0056	291.0897	-55.8547	291.1241	-55.7002	291.17
23:00	-58.6249	295.276	-58.4733	295.3025	-58.318	295.3412
23:15	-61.1494	299.993	-60.9973	300.0074	-60.8411	300.0346
23:30	-63.5481	305.3684	-63.3958	305.3644	-63.2391	305.374
23:45	-65.7801	311.5508	-65.6283	311.5201	-65.4716	311.5034

The zenith angles utilized to calculate the albedo results for this paper are shown as a plot in Figure 24 below.

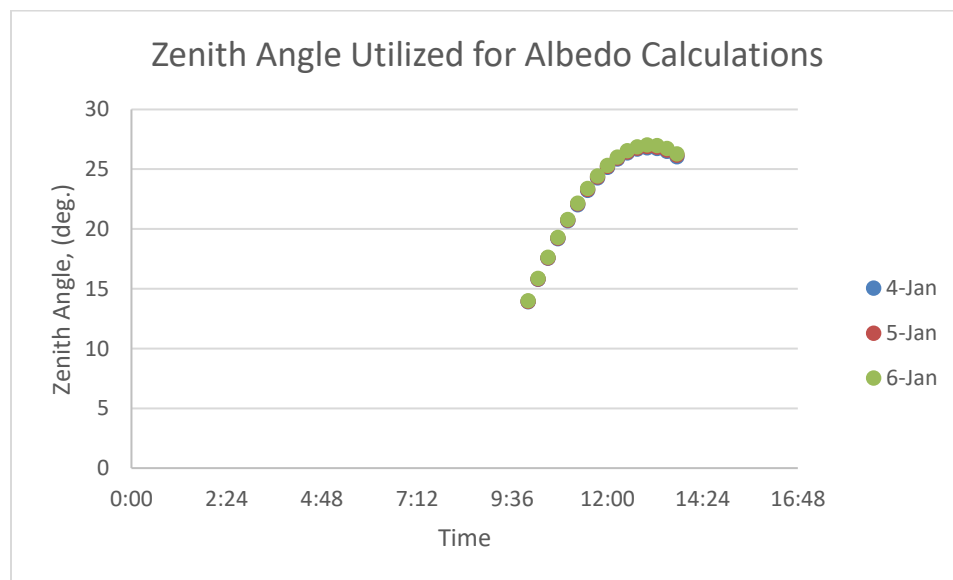


Figure 24: The zenith angle utilized for the January, 4 – January 6, 2016 albedo calculations for this report

The effect of the lower azimuth is pronounced in January, which imparts an uneven sun loading at peak zenith compared to the summer months. None of the zenith angles were higher than 45° to conduct the January measurements, which led to the selection of the angles listed above in Figure 24. These led to discrepancies in the data that will be discussed later in the paper in the Albedo section.

## February 6 – February 8, 2016

The zenith and azimuth angles for the period of February 6 – February 8 are shown in Table 12 below.

**Table 12: Zenith and Azimuth Angles; February 6, 2016 - February 8, 2016 (NAD 83: 40°30'44.7"; -74°25'7.3")**

Time UTC -5	6-Feb		7-Feb		8-Feb	
	Zenith	Azimuth	Zenith	Azimuth	Zenith	Azimuth
0:00	-60.799	322.6099	-60.5206	322.8796	-60.2393	323.1545
0:15	-62.3909	329.4217	-62.1021	329.6529	-61.8101	329.8895
0:30	-63.6772	336.8615	-63.3792	337.0389	-63.0778	337.2222
0:45	-64.6099	344.8597	-64.3052	344.9681	-63.9967	345.0832
1:00	-65.1484	353.2701	-64.8402	353.2977	-64.528	353.3329
1:15	-65.2661	1.876549	-64.9586	1.818017	-64.6467	1.767895
1:30	-64.957	10.42517	-64.6545	10.28352	-64.3471	10.15076
1:45	-64.2367	18.67356	-63.9428	18.45929	-63.6435	18.25389
2:00	-63.139	26.43437	-62.8562	26.16258	-62.5677	25.89909
2:15	-61.7087	33.59641	-61.4385	33.2833	-61.1623	32.97755
2:30	-59.9947	40.12098	-59.7375	39.78124	-59.4741	39.44773
2:45	-58.0443	46.02344	-57.7997	45.66897	-57.5487	45.31955
3:00	-55.8998	51.35191	-55.6669	50.99155	-55.4276	50.63516
3:15	-53.5976	56.16971	-53.3753	55.80964	-53.1465	55.45256
3:30	-51.168	60.5438	-50.955	60.18806	-50.7356	59.83449
3:45	-48.636	64.53815	-48.4311	64.18923	-48.2198	63.84181
4:00	-46.022	68.21068	-45.8239	67.86998	-45.6195	67.53021
4:15	-43.3426	71.61228	-43.1503	71.28042	-42.9517	70.94905
4:30	-40.6116	74.78689	-40.4239	74.46402	-40.2301	74.1413
4:45	-37.8403	77.77222	-37.6564	77.45818	-37.4664	77.144
5:00	-35.0384	80.60053	-34.8573	80.29496	-34.6702	79.98903
5:15	-32.2139	83.29952	-32.0349	83.00195	-31.85	82.70383
5:30	-29.3741	85.89308	-29.1964	85.60298	-29.013	85.3122
5:45	-26.5251	88.40197	-26.3481	88.11881	-26.1654	87.83484
6:00	-23.6727	90.84444	-23.4958	90.56767	-23.3132	90.29
6:15	-20.822	93.23667	-20.6445	92.96577	-20.4615	92.69391
6:30	-17.9779	95.59319	-17.7994	95.32769	-17.6154	95.06117
6:45	-15.1452	97.92726	-14.9651	97.66671	-14.7796	97.4051
7:00	-12.3284	100.2511	-12.1463	99.99509	-11.9587	99.73801
7:15	-9.53212	102.5761	-9.34749	102.3243	-9.15748	102.0714
7:30	-6.76109	104.9131	-6.57348	104.6653	-6.38053	104.4163

7:45	-3.84124	107.2726	-3.5982	107.0285	-3.34137	106.7832
8:00	-0.61821	109.6647	-0.45303	109.424	-0.28618	109.1823
8:15	1.681849	112.0992	1.864811	111.862	2.053893	111.6237
8:30	4.16132	114.5859	4.358668	114.3521	4.561473	114.1173
8:45	6.669027	117.1345	6.874571	116.9043	7.085392	116.673
9:00	9.146123	119.7547	9.358411	119.5281	9.575912	119.3006
9:15	11.56992	122.4559	11.78867	122.2333	12.01259	122.0098
9:30	13.92687	125.2475	14.15212	125.0293	14.38254	124.8103
9:45	16.20602	128.1386	16.43794	127.9254	16.67502	127.7114
10:00	18.39708	131.1378	18.63587	130.9303	18.87981	130.7221
10:15	20.48972	134.2531	20.73554	134.0522	20.9865	133.8507
10:30	22.47323	137.4914	22.72622	137.2981	22.98432	137.1043
10:45	24.33649	140.8584	24.59669	140.6738	24.862	140.4891
11:00	26.06796	144.3576	26.33534	144.1832	26.60781	144.0089
11:15	27.65578	147.9906	27.93021	147.8279	28.2097	147.6656
11:30	29.088	151.7559	29.3692	151.6066	29.65545	151.458
11:45	30.35277	155.6486	30.64036	155.5145	30.93296	155.3813
12:00	31.43872	159.6604	31.73217	159.543	32.03056	159.4271
12:15	32.33532	163.7787	32.63394	163.6797	32.93742	163.5826
12:30	33.03328	167.9869	33.33626	167.9079	33.64399	167.8311
12:45	33.52498	172.265	33.83138	172.207	34.1424	172.1519
13:00	33.80484	176.5896	34.11361	176.5536	34.42686	176.5209
13:15	33.86957	180.9354	34.17963	180.9218	34.49397	180.912
13:30	33.71842	185.2759	34.02864	185.2848	34.34294	185.2979
13:45	33.35318	189.5851	33.66245	189.616	33.97559	189.6516
14:00	32.77808	193.8382	33.08535	193.8904	33.39626	193.9476
14:15	31.99957	198.0131	32.30389	198.0854	32.6116	198.1631
14:30	31.02599	202.0912	31.32652	202.1822	31.63017	202.2788
14:45	29.86719	206.0574	30.16321	206.1656	30.46209	206.2796
15:00	28.53409	209.901	28.82502	210.0246	29.11856	210.1543
15:15	27.0383	213.6148	27.32369	213.7524	27.61146	213.896
15:30	25.39173	217.1956	25.67129	217.3455	25.95299	217.5014
15:45	23.60635	220.6432	23.87988	220.8038	24.15532	220.9705
16:00	21.69391	223.9598	21.96131	224.1299	22.23042	224.306
16:15	19.66579	227.1502	19.92705	227.3285	20.18984	227.5128
16:30	17.53295	230.2204	17.78813	230.406	18.04467	230.5974
16:45	15.30594	233.1779	15.55513	233.3698	15.80553	233.5675
17:00	12.99503	236.0309	13.23834	236.2285	13.48272	236.4318
17:15	10.61065	238.7884	10.84812	238.991	11.08657	239.1992
17:30	8.164424	241.4595	8.395908	241.6667	8.62832	241.8794
17:45	5.672266	244.0537	5.897013	244.2651	6.122736	244.4821

18:00	3.165507	246.5806	3.38055	246.7961	3.596956	247.017
18:15	0.739467	249.0498	0.932897	249.2693	1.129195	249.494
18:30	-1.68517	251.4712	-1.4356	251.6945	-1.20479	251.9231
18:45	-5.10265	253.8546	-4.86956	254.0818	-4.62471	254.3143
19:00	-7.85448	256.2099	-7.64342	256.4412	-7.43188	256.6776
19:15	-10.6342	258.5476	-10.4256	258.783	-10.2166	259.0236
19:30	-13.4369	260.8781	-13.2304	261.118	-13.0235	261.3629
19:45	-16.2581	263.2126	-16.0532	263.4572	-15.8479	263.7068
20:00	-19.093	265.5629	-18.8893	265.8125	-18.6851	266.0671
20:15	-21.937	267.9416	-21.734	268.1966	-21.5305	268.4565
20:30	-24.7853	270.3627	-24.5824	270.6233	-24.379	270.889
20:45	-27.6327	272.8412	-27.4295	273.108	-27.2256	273.3797
21:00	-30.4739	275.3943	-30.2697	275.6676	-30.0647	275.9458
21:15	-33.3029	278.0413	-33.097	278.3214	-32.8903	278.6064
21:30	-36.113	280.8041	-35.9048	281.0913	-35.6955	281.3835
21:45	-38.8966	283.7082	-38.6852	284.0027	-38.4727	284.3023
22:00	-41.6448	286.7831	-41.4295	287.0849	-41.2129	287.3917
22:15	-44.3472	290.0629	-44.127	290.3717	-43.9055	290.6856
22:30	-46.9914	293.5878	-46.7654	293.9029	-46.5378	294.223
22:45	-49.5623	297.4041	-49.3295	297.724	-49.0949	298.0489
23:00	-52.0417	301.5648	-51.801	301.8872	-51.5583	302.2146
23:15	-54.4073	306.1296	-54.1575	306.4508	-53.9056	306.7768
23:30	-56.6318	311.1623	-56.3721	311.4768	-56.1101	311.7961
23:45	-58.6825	316.7272	-58.4122	317.0271	-58.1392	317.3319

The zenith angles utilized to calculate the albedo results for this paper are shown as a plot in Figure 25 below.

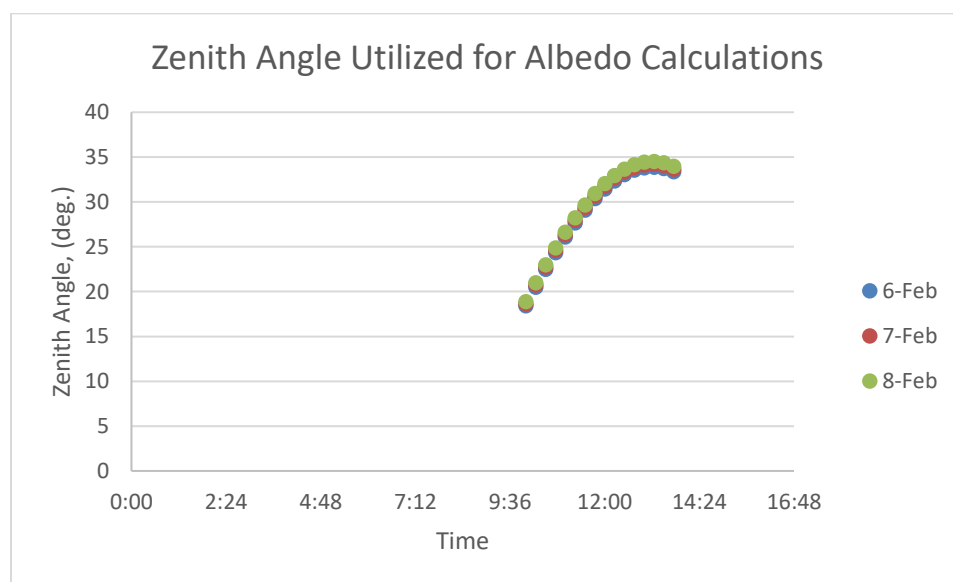


Figure 25: The zenith angle utilized for the February 6 – February 8, 2016 albedo calculations for this report

The effect of the lower azimuth is pronounced in February, which imparts an uneven sun loading at peak zenith compared to the summer months. None of the zenith angles were higher than 45° to conduct the February measurements, which led to the selection of the angles listed above in Figure 25. These led to discrepancies in the data that will be discussed later in the paper in the Albedo section.

### April 16, 2016 – April 18, 2016

The zenith and azimuth angles for the period of April 16 – April 18 are shown in Table 13 below.

**Table 13: Zenith and Azimuth Angles; April 16, 2016 – April 18, 2016 (NAD 83: 40°30'44.7"; -74°25'7.3")**

Time UTC -5	16-Apr		17-Apr		18-Apr	
	Zenith	Azimuth	Zenith	Azimuth	Zenith	Azimuth
0:00	-37.5173	342.0575	-37.1887	342.2322	-36.8623	342.4024
0:15	-38.2834	346.6332	-37.947	346.784	-37.613	346.9307
0:30	-38.8255	351.3017	-38.4824	351.4265	-38.1419	351.5476
0:45	-39.1365	356.0328	-38.7879	356.1298	-38.4421	356.2236
1:00	-39.2118	0.79273	-38.8592	0.860947	-38.5094	0.926419
1:15	-39.0504	5.546137	-38.6951	5.585119	-38.3429	5.621891
1:30	-38.6546	10.25802	-38.2982	10.26806	-37.9449	10.27644
1:45	-38.0299	14.89571	-37.6737	14.87777	-37.3207	14.85869
2:00	-37.1847	19.43055	-36.83	19.38614	-36.4785	19.34108
2:15	-36.1297	23.83903	-35.7776	23.77009	-35.4288	23.70094
2:30	-34.8773	28.10341	-34.5288	28.01215	-34.1837	27.92107
2:45	-33.4411	32.21179	-33.0971	32.10056	-32.7563	31.98983
3:00	-31.8355	36.15774	-31.4964	36.02888	-31.1606	35.90078
3:15	-30.0747	39.9396	-29.741	39.79536	-29.4106	39.65209
3:30	-28.1727	43.5597	-27.8447	43.40218	-27.5198	43.24577
3:45	-26.143	47.02354	-25.8208	46.85461	-25.5017	46.6869
4:00	-23.9984	50.33894	-23.6819	50.16025	-23.3685	49.98286
4:15	-21.7508	53.51536	-21.4399	53.32835	-21.1322	53.14268
4:30	-19.4111	56.5634	-19.1057	56.36926	-18.8034	56.17649
4:45	-16.9894	59.49426	-16.6893	59.29399	-16.3923	59.0951
5:00	-14.4952	62.31948	-14.2	62.1139	-13.9079	61.90967
5:15	-11.9367	65.05069	-11.6461	64.84044	-11.3587	64.63152
5:30	-9.32178	67.69947	-9.03551	67.48505	-8.75237	67.27192
5:45	-6.65756	70.27725	-6.37519	70.05904	-6.09598	69.84206
6:00	-3.75362	72.79535	-3.39295	72.5736	-3.02361	72.35304
6:15	-0.52688	75.26491	-0.29621	75.0398	-0.07035	74.81582
6:30	1.880613	77.69702	2.133614	77.46863	2.385639	77.24132
6:45	4.546058	80.10273	4.809279	79.87111	5.069885	79.64048
7:00	7.30937	82.49322	7.574642	82.25834	7.836859	82.02437
7:15	10.11502	84.87987	10.3805	84.64167	10.64275	84.4043
7:30	12.9431	87.27445	13.20846	87.03284	13.47049	86.79196

7:45	15.78299	89.68926	16.04839	89.44413	16.31038	89.19963
8:00	18.62709	92.13731	18.89288	91.88856	19.15518	91.64033
8:15	21.46884	94.63258	21.73545	94.38013	21.99853	94.12806
8:30	24.30191	97.19026	24.56988	96.93406	24.83424	96.67809
8:45	27.11985	99.82701	27.38973	99.56707	27.65594	99.3072
9:00	29.91574	102.5613	30.18813	102.2977	30.4568	102.0341
9:15	32.68195	105.4137	32.95751	105.1468	33.22928	104.8796
9:30	35.40994	105.4137	35.68935	108.1377	35.96491	107.8674
9:45	38.08992	105.4137	38.37388	111.2967	38.65395	111.024
10:00	40.71055	105.4137	40.99981	114.6534	41.28513	114.3795
10:15	43.25859	105.4137	43.55388	118.2411	43.84521	117.9677
10:30	45.71846	105.4137	46.02051	122.0965	46.31858	121.826
10:45	48.07184	105.4137	48.38129	126.2593	48.68677	125.9952
11:00	50.29718	105.4137	50.61456	130.7712	50.928	130.518
11:15	52.36939	105.4137	52.69499	135.6729	53.01672	135.4366
11:30	54.25968	105.4137	54.59348	141.0002	54.9235	140.7884
11:45	55.93586	105.4137	56.27734	146.7775	56.61517	146.5994
12:00	57.36329	105.4137	57.71133	153.0093	58.05587	152.875
12:15	58.50679	105.4137	58.85955	159.6705	59.20896	159.5905
12:30	59.33353	105.4137	59.68845	166.6983	60.04014	166.6817
12:45	59.81675	105.4137	60.17065	173.9898	60.52142	174.0429
13:00	59.93947	105.4137	60.28886	181.4078	60.63518	181.5324
13:15	59.69724	105.4137	60.0387	188.7976	60.37712	188.9902
13:30	59.09887	105.4137	59.42946	196.0084	59.75701	196.2612
13:45	58.16498	105.4137	58.4825	202.914	58.79699	203.2162
14:00	56.92478	105.4137	57.22792	209.4257	57.52804	209.7654
14:15	55.41228	105.4137	55.70055	215.4951	55.98584	215.861
14:30	53.66278	105.4137	53.93637	221.1089	54.20705	221.4912
14:45	51.71029	105.4137	51.96988	226.2799	52.22666	226.6706
15:00	49.58594	105.4137	49.83255	231.0374	50.07647	231.4307
15:15	47.31733	105.4137	47.55214	235.4197	47.78439	235.8113
15:30	44.92836	105.4137	45.15262	239.4681	45.37448	239.8553
15:45	42.43948	105.4137	42.65445	243.224	42.86717	243.6048
16:00	39.86807	105.4137	40.07497	246.7259	40.27978	247.0995
16:15	37.22889	105.4137	37.42889	250.0095	37.62694	250.3753
16:30	34.53452	105.4137	34.7287	253.1066	34.92108	253.4645
16:45	31.79577	105.4137	31.98514	256.0457	32.17285	256.3959
17:00	29.02199	105.4137	29.20749	258.8519	29.39145	259.1948
17:15	26.22141	105.4137	26.40391	261.5477	26.585	261.8837
17:30	23.40141	105.4137	23.58171	264.1529	23.76072	264.4826
17:45	20.56874	105.4137	20.74759	266.6855	20.92525	267.0093

18:00	17.72979	105.4137	17.90787	269.1616	18.08487	269.4801
18:15	14.89092	105.4137	15.06885	271.596	15.24579	271.9097
18:30	12.05889	105.4137	12.2372	274.0022	12.4146	274.3116
18:45	9.241965	105.4137	9.420979	276.393	9.599189	276.6986
19:00	6.452534	105.4137	6.632126	278.7804	6.811055	279.0826
19:15	3.716586	105.4137	3.895014	281.1761	4.073106	281.4753
19:30	1.115326	105.4137	1.283872	283.5911	1.453259	283.8877
19:45	-1.29255	105.4137	-1.09774	286.0367	-0.91584	286.3309
20:00	-4.72055	105.4137	-4.49422	288.5237	-4.26357	288.8157
20:15	-7.44309	105.4137	-7.24165	291.0631	-7.04087	291.3531
20:30	-10.0828	105.4137	-9.8759	293.666	-9.66963	293.9539
20:45	-12.6704	105.4137	-12.4573	296.3435	-12.245	296.6293
21:00	-15.1983	105.4137	-14.9786	299.1068	-14.7597	299.3903
21:15	-17.6586	105.4137	-17.4318	301.9673	-17.2057	302.2482
21:30	-20.0426	105.4137	-19.808	304.9364	-19.5743	305.214
21:45	-22.3407	105.4137	-22.0979	308.0249	-21.8559	308.2986
22:00	-24.5425	105.4137	-24.291	311.2436	-24.0404	311.5124
22:15	-26.6367	105.4137	-26.376	314.6022	-26.1164	314.8649
22:30	-28.6112	105.4137	-28.3411	318.1091	-28.0721	318.3643
22:45	-30.453	105.4137	-30.1732	321.7708	-29.8947	322.0166
23:00	-32.1486	105.4137	-31.859	325.5911	-31.5709	325.8257
23:15	-33.6839	105.4137	-33.3846	329.5706	-33.0869	329.7917
23:30	-35.0448	105.4137	-34.7359	333.7056	-34.429	333.9108
23:45	-36.2174	105.4137	-35.8995	337.9875	-35.5836	338.1743

The zenith angles utilized to calculate the albedo results for this paper are shown as a plot in Figure 26 below.



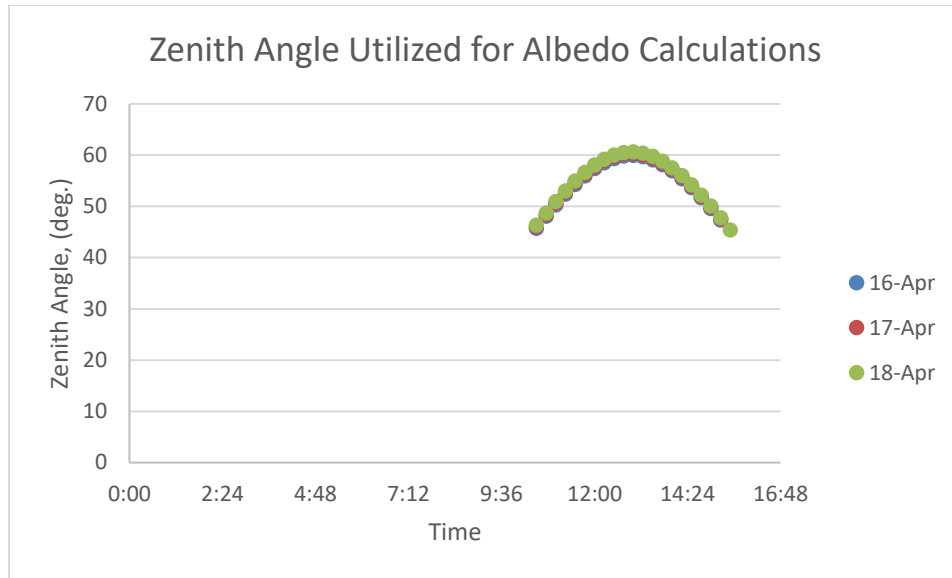


Figure 26: The zenith angle utilized for the April 16 – April 18, 2016 albedo calculations for this report

Due to the higher azimuth of the sun in April, the sun's Zenith was more similar to the July conditions represented in Figure 23 and was more even from morning to afternoon than was shown in January and February.

## July 31, 2015 – August 2, 2015

As described in the Derived Data section of the paper, the climatological information for different local sources were derived from publicly available databases. The Wunderground data from the Pluckemin, NJ station for the July 31 – August 2, 2015 test period is shown in Table 14 below. The relative humidity during this period fluctuated between 31%RH to 97%RH with minimum temperatures at night reaching as low as 13.9°C (57°F) and maximum daytime temperatures reaching as high as 0.0°C (32.2°F).

**Table 14: Wunderground climatological data for the test period of July 31 - August 2, 2015**

<b><u>Wunderground Data</u></b>						
Pluckemin, NJ						
<b>Date (2015)</b>		<b>Relative Humidity (%)</b>			<b>Temperature (°F)</b>	
Month	Day	Minimum	Average	Maximum	Minimum	Maximum
July	31	31	76	97	63	90
August	1	29	66	97	61	90
August	2	29	60	93	57	89

The NOAA record of climatological observation data from the New Brunswick, NJ station for the July 31 – August 2, 2015 test period is shown in Table 15 below. The temperature data from this dataset shows that the minimum temperature recorded was 18.9°C (66°F) and the maximum was 32.8°C (91°F) with a short rain event on July 31<sup>st</sup>. The soil temperatures at both 4 inch and 8 inch depths remained fairly constant between 22.8°C (73°F) to 25°C (77°F).

**Table 15: NOAA record of climatological observations for the test period of July 31 - August 2, 2015**

<b><u>NOAA Record of Climatological Observations</u></b>											
New Brunswick, NJ											
<b>Date (2015)</b>		<b>Temperature (°F)</b>		<b>Precipitation (in.)</b>			<b>Evaporation (in.)</b>	<b>Soil Temperature (°F)</b>			
Month	Day	Min	Max	Rain	Frozen	Frozen/ Ground		4" depth		8" depth	
								Min	Max	Min	Max
July	31	66	90	0.94	0	0	0.2	75	76	74	75
August	1	66	91	trace	0	0	0.3	74	77	73	78
August	2	61	91	0	0	0	0.2	74	76	73	74

The NCDC quality controlled local climatological data from the Somerville: Somerset Airport, NJ station for the July 31 test period is shown in Table 16 below. This dataset showed that the early morning had potential fog by the Somerset Airport, but there was none noted at the Asphalt Laboratory that morning. The wind speed for the day remained below 10 mph, which was considered sufficient for testing conditions for this project.

Table 16: NCDC quality controlled local climatological data for the test period on July 31, 2015

NCDC Quality Controlled Local Climatological Data				
Somerville: Somerset Airport				
Sunday, July 31, 2016				
Time	Sky Conditions	Weather Type	Wind Speed (MPH)	Wind Direction
0003	BKN009 BKN080	BR	3	330
0020	BKN007 OVC080	FG	0	0
0029	BKN005 OVC080	FG	0	0
0037	VV004	FG	0	0
0053	VV003	FG	3	320
0153	VV003	FG	0	0
0253	VV003	FG	0	0
0317	VV003	FG	0	0
0353	VV003	FG	0	0
0400	VV003	FG	0	0
0422	VV003	FG	0	0
0435	VV003	FG	0	0
0453	VV003	BR	0	0
0508	VV003	FG		M
0532	VV003	BR	0	0
0539	SCT003	BR	0	0
0546	SCT003	BR	0	0
0553	FEW003		0	0
0653	CLR		0	0
0753	CLR		0	0
0853	CLR		0	0
0953	CLR		5	VR
1053	CLR		6	VR
1153	FEW070		5	VR
1253	SCT065		7	VR
1353	FEW065		6	VR
1453	CLR		8	330
1553	SCT070		6	VR
1653	FEW		3	320
1753	CLR		3	290
1853	CLR		0	0

<b>1953</b>	CLR		0	0
<b>2053</b>	CLR		0	0
<b>2153</b>	CLR		0	0
<b>2253</b>	CLR		0	0
<b>2353</b>	CLR		0	0

The NCDC quality controlled local climatological data from the Somerville: Somerset Airport, NJ station for the August 1 test period is shown in Table 17 below. The dataset reveals that there was broken and scattered cloud cover throughout the day. There was an overage in wind speed, with winds reaching up to 13 mph, but at a direction that would have been blocked by the building. One benefit the close proximity of the buildings did provide was as a wind block on two sides.

**Table 17: NCDC quality controlled local climatological data for the test period on August 1, 2015**

<b>NCDC Quality Controlled Local Climatological Data</b>				
<b>Somerville: Somerset Airport</b>				
<b>Monday, August 01, 2016</b>				
<b>Time</b>	<b>Sky Conditions</b>	<b>Weather Type</b>	<b>Wind Speed (MPH)</b>	<b>Wind Direction</b>
0053	CLR		0	0
0153	BKN080		0	0
0253	CLR		0	0
0333	CLR	BR	0	0
0341	CLR	BR	0	0
0353	CLR		0	0
0453	FEW075		0	0
0553	CLR		0	0
0653	CLR		0	0
0753	FEW110		0	0
0853	OVC110		3	VR
0953	SCT120		3	VR
1053	CLR			M
1153	FEW065			M
1253	FEW070		6	VR
1353	FEW070		9	280
1453	FEW070 BKN120		6	VR
1553	FEW120		13	310
1653	CLR		8	310
1753	BKN110		6	VR
1853	BKN110		0	0
1953	CLR		0	0

2053	CLR		0	0
2153	CLR		0	0
2253	SCT120		0	0
2353	CLR		0	0

The NCDC quality controlled local climatological data from the Somerville: Somerset Airport, NJ station for the August 2 test period is shown in Table 18 below. The dataset revealed that the sky conditions were clear for most of the day, with winds at or below 10 mph.

**Table 18: NCDC quality controlled local climatological data for the test period on August 2, 2015**

<b>NCDC Quality Controlled Local Climatological Data</b>				
<b>Somerville: Somerset Airport</b>				
<b>Tuesday, August 02, 2016</b>				
<b>Time</b>	<b>Sky Conditions</b>	<b>Weather Type</b>	<b>Wind Speed (MPH)</b>	<b>Wind Direction</b>
0053	CLR		0	0
0153	FEW110		0	0
0253	FEW120		0	0
0353	CLR		0	0
0453	CLR	BR	0	0
0553	CLR		0	0
0653	CLR		0	0
0753	CLR			M
0853	CLR		0	0
0953	CLR		0	0
1053	CLR		8	160
1153	SCT075 SCT090		6	VR
1253	FEW075 SCT090		3	VR
1353	BKN085		6	VR
1453	FEW080		3	VR
1553	CLR		10	180
1653	CLR		0	0
1753	CLR		3	VR
1853	CLR		0	0
1953	CLR		0	0
2053	CLR		0	0
2153	CLR		0	0
2253	CLR		0	0
2353	CLR		0	0

## January 4, 2016 – January 6, 2016

As described in the Derived Data section of the paper, the climatological information for different local sources were derived from publicly available databases. The Wunderground data from the Pluckemin, NJ station for the January 4 – January 6, 2016 test period is shown in Table 19 below. The dataset shows that the minimum relative humidity recorded was 19%RH on January 6<sup>th</sup> and up to a maximum of 88%RH on January 4<sup>th</sup>. The minimum temperature recorded from this dataset was -13°C (7°F) and the maximum temperature recorded was 5.6°C (42°F).

**Table 19: Wunderground climatological data for the test period of January 4 - January 6, 2016**

<b><u>Wunderground Data</u></b>						
Pluckemin, NJ						
<b>Date (2016)</b>		<b>Relative Humidity (%)</b>			<b>Temperature (°F)</b>	
Month	Day	Minimum	Average	Maximum	Minimum	Maximum
January	4	29	48	88	12	33
January	5	21	47	80	9	30
January	6	19	60	87	7	42

The NOAA record of climatological observation data from the New Brunswick, NJ station for the January 4 – January 6, 2016 test period is shown in Table 20 below. This dataset showed the lowest temperature to be on January 5<sup>th</sup>, recorded at -12.8°C (9°F), and the maximum temperature to be 9.4°C (49°F) recorded the day prior. The soil temperatures ranged from 2.2°C (36°F) to 6.7°C (44°F).

**Table 20: NOAA record of climatological observations for the test period of January 4 - January 6, 2016**

<u><i>NOAA Record of Climatological Observations</i></u>											
<i>New Brunswick, NJ</i>											
Date (2016)		Temperature (°F)		Precipitation (in.)			Evaporation (in.)	Soil Temperature (°F)			
Month	Day	Min	Max	Rain	Frozen	Frozen /Grou		4" depth		8" depth	
								Min	Max	Min	Max
January	4	28	49	0	0	0		42	44	42	43
January	5	9	33	0	0	0		40	43	39	41
January	6	14	43	0	0	0		37	40	36	38

The NCDC quality controlled local climatological data from the Somerville: Somerset Airport, NJ station for the January 4, 2016 test period is shown in Table 21 below. This dataset shows that other than in the early morning, the majority of the day had clear skies, but the wind was over 10 mph for a good portion of the day. Depending on the local wind angle, there is potential for high wind loading on the samples for the January 4<sup>th</sup> measurements.

**Table 21: NCDC quality controlled local climatological data for the test period on January 4, 2016**

<b>NCDC Quality Controlled Local Climatological Data</b>				
		<b>Somerville: Somerset Airport</b>		
<b>4-Jan</b>				
<b>Time</b>	<b>Sky Conditions</b>	<b>Weather Type</b>	<b>Wind Speed (MPH)</b>	<b>Wind Direction</b>
53	CLR		0	0
153	CLR		0	0
253	OVC055		0	0
353	OVC049		16	340
453	FEW055		14	340
553	CLR		11	320
653	SCT039		10	310
753	CLR		16	330
853	CLR			M
953	CLR		13	340
1053	CLR		16	330
1153	CLR		10	350
1253	CLR		18	330
1353	CLR		17	330
1453	CLR		14	350
1553	CLR		16	340
1653	CLR		14	330
1753	CLR		18	330
1853	CLR		15	360
1953	CLR		13	350
2053	CLR		8	350
2153	CLR		16	330
2253	CLR		11	330
2353	CLR		7	350

The NCDC quality controlled local climatological data from the Somerville: Somerset Airport, NJ station for the January 5, 2016 test period is shown in Table 22 below. The wind from the day prior continued to be above 10 mph until the 4:53 AM recording. The entire day had clear skies.



Table 22: NCDC quality controlled local climatological data for the test period on January 5, 2016

NCDC Quality Controlled Local Climatological Data				
		Somerville: Somerset Airport		
5-Jan				
Time	Sky Conditions	Weather Type	Wind Speed (MPH)	Wind Direction
53	CLR		13	340
153	CLR		10	340
253	CLR		9	350
353	CLR		10	350
453	CLR		6	340
553	CLR		6	350
653	CLR		7	350
753	CLR		6	330
853	CLR		8	350
953	CLR		0	0
1053	CLR		7	10
1153	CLR		8	10
1253	CLR		6	30
1353	CLR		5	340
1453	CLR		5	VR
1553	CLR		3	320
1653	CLR		0	0
1753	CLR		0	0
1853	CLR		0	0
1953	CLR		3	310
2053	CLR		0	0
2153	CLR		0	0
2253	CLR		0	0
2353	CLR		0	0

The NCDC quality controlled local climatological data from the Somerville: Somerset Airport, NJ station for the January 6, 2016 test period is shown in Table 23 below. This dataset shows that the winds on January 6<sup>th</sup> were light and variable with clear skies all day.

Table 23: NCDC quality controlled local climatological data for the test period on January 6, 2016

NCDC Quality Controlled Local Climatological Data				
		Somerville: Somerset Airport		
6-Jan				
Time	Sky Conditions	Weather Type	Wind Speed (MPH)	Wind Direction
53	CLR		0	0
153	CLR		0	0
253	CLR		0	0
353	CLR		0	0
453	CLR		0	0
553	CLR		0	0
653	CLR		0	0
753	CLR		0	0
853	CLR		0	0
953	CLR		3	180
1053	CLR		0	0
1153	CLR		5	VR
1253	CLR		3	VR
1353	CLR		6	300
1453	CLR		3	VR
1553	CLR		5	170
1653	CLR		5	220
1753	CLR		0	0
1853	CLR		0	0
1953	CLR		0	0
2053	CLR		0	0
2153	CLR		0	0
2253	CLR		3	320
2353	CLR		0	0

## February 6 – February 8, 2016

As described in the Derived Data section of the paper, the climatological information for different local sources were derived from publicly available databases. The Wunderground data from the Pluckemin, NJ station for the February 6 – February 8, 2016 test period is shown in Table 24 below. This dataset shows that the relative humidity fluctuated between 33%RH and 89%RH. The temperatures recorded ranged from a minimum of -7.8 (18°F) to 7.8°C (46°F).

**Table 24: Wunderground climatological data for the test period of February 6 - February 8, 2016**

<u><b>Wunderground Data</b></u>						
Pluckemin, NJ						
<b>Date (2016)</b>		<b>Relative Humidity (%)</b>			<b>Temperature (°F)</b>	
Month	Day	Minimum	Average	Maximum	Minimum	Maximum
February	6	36	70	89	19	41
February	7	33	64	89	18	46
February	8	43	59	79	30	41

The NOAA record of climatological observation data from the New Brunswick, NJ station for the February 6 – February 8, 2016 test period is shown in Table 25 below. The New Brunswick dataset showed slightly higher temperatures than the Wunderground data, with a recorded minimum of -6.7°C (20°F) and a recorded maximum of 8.3°C (47°F). The soil temperatures at both the 4 inch depth and 8 inch depth fluctuated between 1.7°C (35°F) and 3.3°C (38°F) for a high. There was a minimal amount of precipitation recorded on February 6<sup>th</sup>. This minimal amount of precipitation was the remnants of an ice/snow event that was undergoing melting on February 6<sup>th</sup>, which became apparent when analyzing the albedo data. The results from this issue will be discussed later in the paper.

**Table 25: NOAA record of climatological observations for the test period of February 6 - February 8, 2016**

<u><i>NOAA Record of Climatological Observations</i></u>											
<i>New Brunswick, NJ</i>											
Date (2016)		Temperature (°F)		Precipitation (in.)			Evaporation (in.)	Soil Temperature (°F)			
Month	Day	Min	Max	Rain	Frozen	Frozen/ Ground		4" depth		8" depth	
								Min	Max	Min	Max
February	6	20	41	0.08	0.7	3		37	38	36	38
February	7	22	42	0	0	2		36	38	36	36
February	8	25	47	0	0	trace	0	35	36	35	36

The NCDC quality controlled local climatological data from the Somerville: Somerset Airport, NJ station for the February 6, 2016 test period is shown in Table 26 below. This dataset shows that the sky conditions were clear for the day, with some light winds that remained below 10 mph.

Table 26: NCDC quality controlled local climatological data for the test period on February 6, 2016

NCDC Quality Controlled Local Climatological Data				
		Somerville: Somerset Airport		
Saturday, February 06, 2016				
Time	Sky Conditions	Weather Type	Wind Speed (MPH)	Wind Direction
53	CLR		0	0
153	CLR		0	0
253	CLR		0	0
353	CLR		0	0
453	CLR		0	0
553	CLR		0	0
653	CLR		3	320
753	CLR		0	0
853	CLR			M
953	CLR		0	0
1053	CLR		3	40
1153	CLR		3	VR
1253	CLR		8	220
1353	CLR		7	210
1453	CLR		7	190
1553	CLR		5	210
1653	CLR		5	200
1753	CLR		0	0
1853	CLR		0	0
1953	CLR		0	0
2053	CLR		0	0
2153	CLR		0	0
2253	CLR		0	0
2353	CLR		0	0

The NCDC quality controlled local climatological data from the Somerville: Somerset Airport, NJ station for the February 7, 2016 test period is shown in Table 27 below. This dataset shows that February 7<sup>th</sup> had clear sky conditions for the entire day. There were light winds that were variable in direction that began in the early afternoon around 3 mph that built to about 8 mph in the late afternoon.

Table 27: NCDC quality controlled local climatological data for the test period on February 7, 2016

NCDC Quality Controlled Local Climatological Data				
		Somerville: Somerset Airport		
Sunday, February 07, 2016				
Time	Sky Conditions	Weather Type	Wind Speed (MPH)	Wind Direction
53	CLR		0	0
153	CLR		0	0
253	CLR		0	0
353	CLR		0	0
453	CLR		0	0
553	CLR		0	0
653	CLR		0	0
753	CLR		0	0
853	CLR		0	0
953	CLR		0	0
1053	CLR		5	350
1153	CLR		0	0
1253	CLR		3	VR
1353	CLR		3	VR
1453	CLR		3	150
1553	CLR		3	150
1653	CLR		0	0
1753	CLR		0	0
1853	CLR		0	0
1953	CLR		0	0
2053	CLR		5	360
2153	CLR		6	10
2253	CLR		6	20
2353	CLR		8	30

The NCDC quality controlled local climatological data from the Somerville: Somerset Airport, NJ station for the February 8, 2016 test period is shown in Table 28 below. The February 8<sup>th</sup> dataset shows that there were scattered clouds that eventually became more overcast. The wind angle rotated significantly throughout the day, but did not exceed 10 mph.

Table 28: NCDC quality controlled local climatological data for the test period on February 8, 2016

NCDC Quality Controlled Local Climatological Data				
		Somerville: Somerset Airport		
Monday, February 08, 2016				
Time	Sky Conditions	Weather Type	Wind Speed (MPH)	Wind Direction
53	CLR		7	20
153	CLR		7	20
253	CLR		8	20
353	CLR		10	50
453	SCT035		7	40
553	OVC032		5	VR
653	OVC034		3	360
753	OVC032		3	10
853	OVC033		6	10
953	OVC036		7	50
1053	OVC034		7	40
1153	FEW034 OVC060		8	30
1253	FEW037 BKN060 OVC075		8	50
1353	OVC075		6	VR
1453	SCT049 OVC075		8	80
1553	SCT041 SCT050 OVC070		5	VR
1653	OVC043		3	90
1753	OVC039		6	90
1853	OVC042		3	120
1953	OVC037		6	120
2053	OVC036		6	110
2153	OVC034		6	110
2253	SCT019 OVC030		7	VR
2304	BKN018 OVC030		7	VR
2353	OVC018		3	100

## April 16, 2016 – April 18, 2016

As described in the Derived Data section of the paper, the climatological information for different local sources were derived from publicly available databases. The Wunderground data from the Pluckemin, NJ station for the April 16 – April 18, 2016 test period is shown in Table 29 below. The minimum recorded relative humidity provided in the Wunderground dataset was 12%RH and the maximum was 89%RH. The ambient temperature ranged from a minimum of 0.0°C (32°F) to a maximum of 27.8°C (82°F).

**Table 29: Wunderground climatological data for the test period of April 16 - April 18, 2016**

<b><u>Wunderground Data</u></b>						
Pluckemin, NJ						
<b>Date (2016)</b>		<b>Relative Humidity (%)</b>			<b>Temperature (°F)</b>	
Month	Day	Minimum	Average	Maximum	Minimum	Maximum
April	16	12	47	89	32	70
April	17	24	51	89	32	73
April	18	12	45	89	37	82

The NOAA record of climatological observation data from the New Brunswick, NJ station for the April 16 – April 18, 2016 test period is shown in Table 30 below. This dataset showed a recorded minimum ambient temperature of 1.7°C (35°F) and a maximum of 23.3°C (74°F). There was no recorded precipitation. The soil temperatures in the 4 inch depth fluctuated between 8.9°C (48°F) to 19.4°C (67°F). The 8 inch depth soil temperature had less fluctuation, from 9.4°C (49°F) to 12.8°C (55°F).

**Table 30: NOAA record of climatological observations for the test period of April 16 - April 18, 2016**

<u><i>NOAA Record of Climatological Observations</i></u>											
<i>New Brunswick, NJ</i>											
Date (2016)		Temperature (°F)		Precipitation (in.)			Evaporation	Soil Temperature (°F)			
Month	Day	Min	Max	Rain	Frozen	Frozen/in.		4" depth		8" depth	
								Min	Max	Min	Max
April	16	35	65	0	0			48	67	49	53
April	17	36	68	0	0	0		48	51	49	55
April	18	41	74	0	0	0	0	49	51	49	55

The NCDC quality controlled local climatological data from the Somerville: Somerset Airport, NJ station for the April 16, 2016 test period is shown in Table 31 below. This dataset shows that there was some light wind that fluctuated between 3-7 mph with varying wind angles. The max recorded wind speed for the day was 9 mph. The sky conditions were clear for the entire day.



**Table 31: NCDC quality controlled local climatological data for the test period on April 16, 2016**

<b>NCDC Quality Controlled Local Climatological Data</b>				
		<b>Somerville: Somerset Airport</b>		
<b>Saturday, April 16, 2016</b>				
<b>Time</b>	<b>Sky Conditions</b>	<b>Weather Type</b>	<b>Wind Speed (MPH)</b>	<b>Wind Direction</b>
53	CLR		0	0
153	CLR		0	0
253	CLR		3	330
353	CLR		0	0
453	CLR		0	0
553	CLR		0	0
653	CLR		0	0
753	CLR		6	VR
853	CLR		9	40
953	CLR		7	VR
1053	CLR		0	0
1153	CLR		7	60
1253	CLR		3	20
1353	CLR		7	VR
1453	CLR		7	VR
1553	CLR		8	30
1653	CLR		3	110
1753	CLR		6	80
1853	CLR		0	0
1953	CLR		6	110
2053	CLR		3	90
2153	CLR		3	130
2253	CLR		0	0
2353	CLR		0	0

The NCDC quality controlled local climatological data from the Somerville: Somerset Airport, NJ station for the April 17, 2016 test period is shown in Table 32 below. The sky conditions for April 17<sup>th</sup> were clear all day. Afternoon winds ranged from 3 mph to 9 mph predominantly out of the East-southeast.

Table 32: NCDC quality controlled local climatological data for the test period on April 17, 2016

NCDC Quality Controlled Local Climatological Data				
		Somerville: Somerset Airport		
Sunday, April 17, 2016				
Time	Sky Conditions	Weather Type	Wind Speed (MPH)	Wind Direction
53	CLR		0	0
153	CLR		0	0
253	CLR		0	0
353	CLR		0	0
453	CLR		5	310
553	CLR		0	0
653	CLR		0	0
753	CLR		0	0
853	CLR		0	0
953	CLR		0	0
1053	CLR		0	0
1153	CLR		6	VR
1253	CLR		3	VR
1353	CLR		7	170
1453	CLR		9	160
1553	CLR		3	170
1653	CLR		5	160
1753	CLR		5	190
1853	CLR		0	0
1953	CLR		0	0
2053	CLR		0	0
2153	CLR		0	0
2253	CLR		0	0
2353	CLR		0	0

The NCDC quality controlled local climatological data from the Somerville: Somerset Airport, NJ station for the April 18, 2016 test period is shown in Table 33 below. This dataset shows that the sky conditions as well as the wind speed and direction were relatively similar for April 18<sup>th</sup> as they were for April 17<sup>th</sup>.

Table 33: NCDC quality controlled local climatological data for the test period on April 18, 2016

NCDC Quality Controlled Local Climatological Data				
		Somerville: Somerset Airport		
Monday, April 18, 2016				
Time	Sky Conditions	Weather Type	Wind Speed (MPH)	Wind Direction
53	CLR		0	0
153	CLR		3	310
253	CLR		3	310
353	CLR		0	0
453	CLR		0	0
553	CLR		0	0
653	CLR		0	0
753	CLR		0	0
853	CLR			M
953	CLR		7	310
1053	CLR		5	VR
1153	CLR		3	VR
1253	CLR			M
1353	CLR		5	VR
1453	CLR		5	VR
1553	CLR		6	180
1653	CLR		5	190
1753	CLR		3	190
1853	CLR		7	130
1953	CLR		7	120
2053	CLR		5	160
2153	CLR		0	0
2253	CLR		0	0
2353	CLR		0	0

### ***THERMOCOUPLE DATA***

The embedded thermocouples provided temperature data at 15 minute intervals throughout the entire testing period. The type K thermocouples described in the Equipment: Thermocouple section provided the unique opportunity to monitor each of the slabs temperatures at 10 different depths throughout a vertical profile. The spacing utilized provided 4 measurements within the top inch, then every half inch to the base of the slab. The section format includes an overview plot for the combined thermocouples for each of the slabs, a plot of the maximum and minimum temperatures, then a comparison of the three slabs at each depth for each of the testing periods highlighted in this paper. Within this section Probe 1 is associated with Slab 2, Probe 2 is associated with Slab 3, and Probe 3 is associated with Slab 4. In addition to the thermocouple data, the overview plots contain the surface temperature measured by the net radiometers, the ambient temperature acquired from the Wunderground - Pluckemin station derived data, and the ground temperature measured at 4 inch depth from the NOAA New Brunswick Records as explained in Table 5.

## July 31, 2015 – August 2, 2015

Within this section, the data compiled for the thermocouples for the testing period from July 31 - August 2, 2015. As expected, there is a noticeable diurnal pattern to the heating and cooling of the slab and surrounding ground surface, shown in Figures 27, 28, and 29. The ground surface temperature for the three-day period fluctuated between 26.6°C (79.9°F) nighttime to 29.4°C (84.9°F) daytime. The ambient temperature fluctuated between 16.1°C (61°F) nighttime to 31.6°C (88.9°F) daytime. There is a noticeable lag in both the heating and cooling portion of the temperature plots, due to the coefficient of thermal conductivity of the asphalt slab. The cooling takes longer than the heating for this testing period, as expected, but the rate of heating influence is the fastest and most significant during this testing period in the hot summer months. The 0.25" embedded thermocouple recorded temperature as high as 56.3°C (133.3°F) on August 2, 2015. Since this is the hottest measurement period, it is important to note that the temperature at the hottest point of the slab did not exceed the binder high temperature performance grade rating.

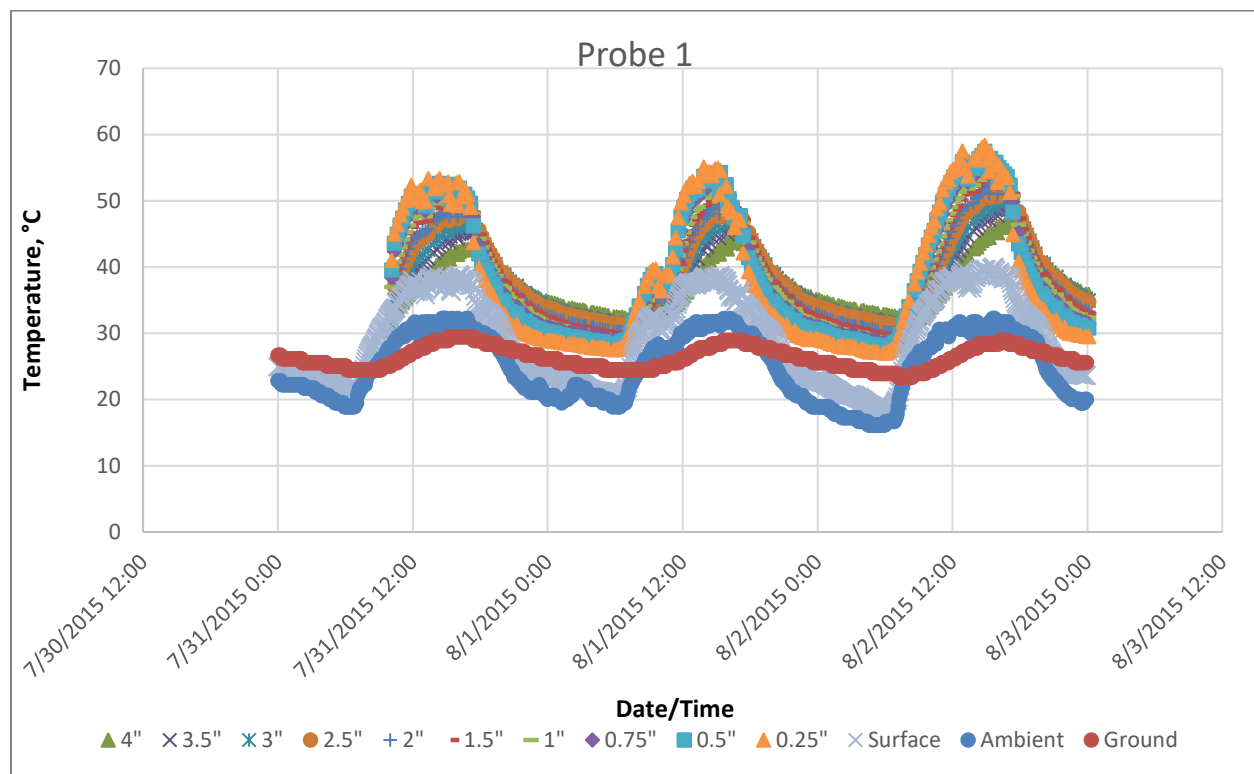
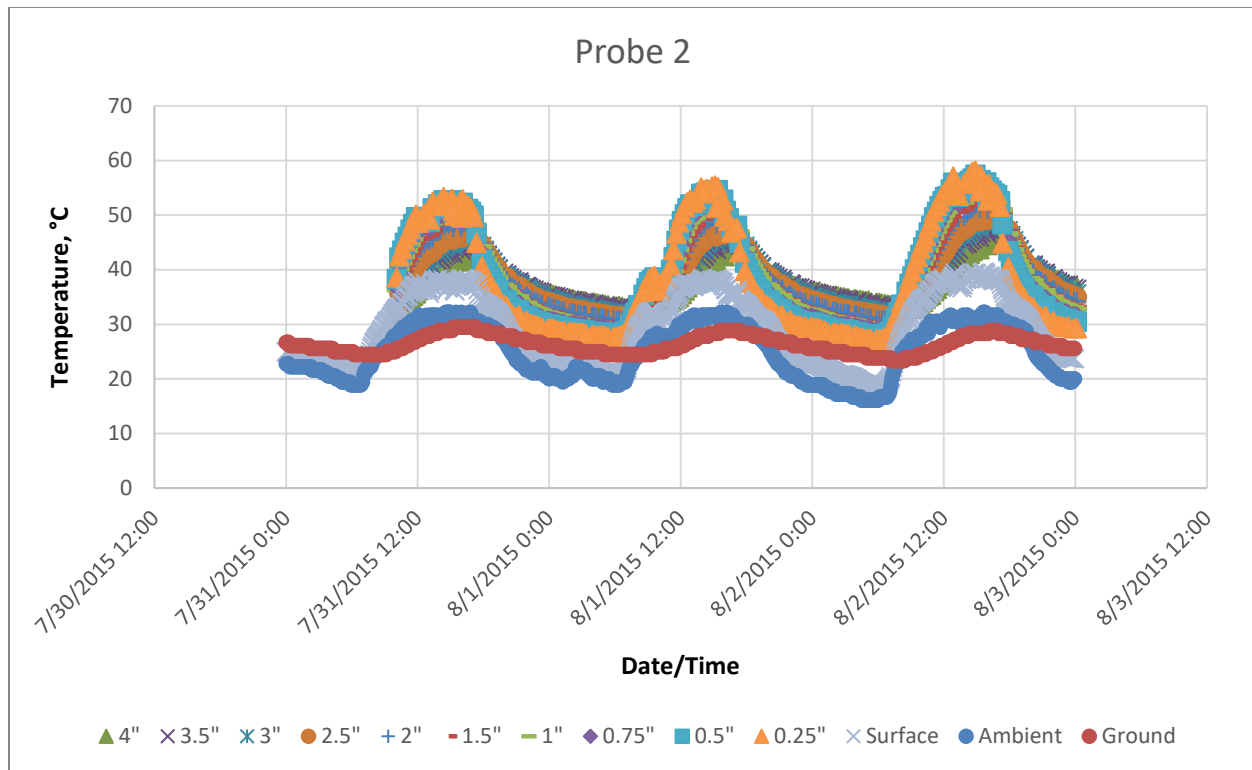
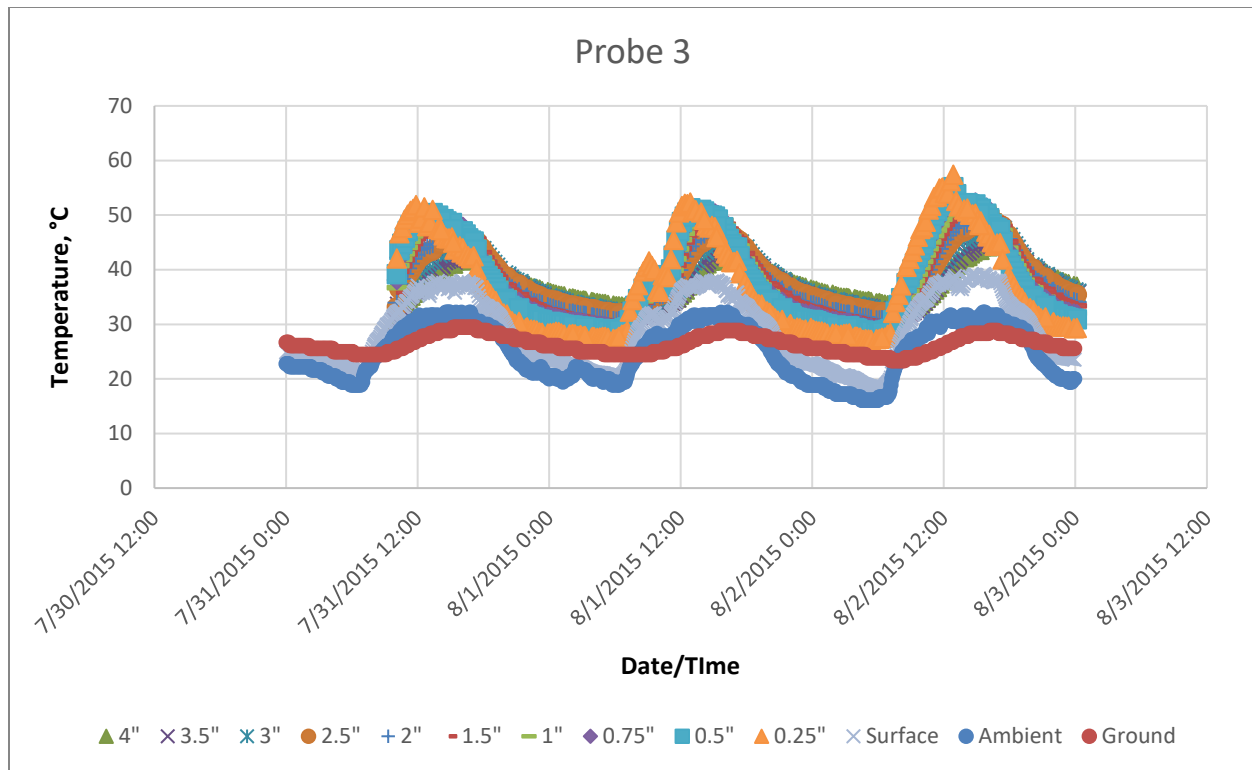


Figure 27: Diurnal pattern of thermocouple probe 1 in slab sample 2 for testing period July 31 - August 2, 2015 compared to 4" soil depth, NR01 infrared surface temp, and ambient temp



**Figure 28: Diurnal pattern of thermocouple probe 2 in slab sample 3 for testing period July 31 - August 2, 2015 compared to 4" soil depth, NR01 infrared surface temp, and ambient temp**

The July 31 – August 2 test period temperature analysis revealed that the 4" ground temperature did not cool as much as the ambient temperature throughout the night but did rise to a temperature similar to the ambient as the day progressed. The surface temperature dipped as low as the ambient temperature, but during the daytime increased by as much as 6 degrees higher than the ambient temperature, as shown in Figure 28. The surface temperature always remained cooler than the interior slab temperatures.



**Figure 29: Diurnal pattern of thermocouple probe 3 in slab sample 4 for testing period July 31 - August 2, 2015 compared to 4" soil depth, NR01 infrared surface temp, and ambient temp**

Although the three slabs were under similar conditions, slab three was shaded by the building in the morning for a period of less than half an hour. That short period of time had a noticeable effect on the rate of cooling, shown in Figure 29. The rate of cooling in the slab thermocouples compared to the other two slabs shows the pronounced influence that the solar energy had on the slab. To further evaluate the differences between the slab temperatures, the maximum and minimum for each slab was calculated for each depth and shown in Figure 30.



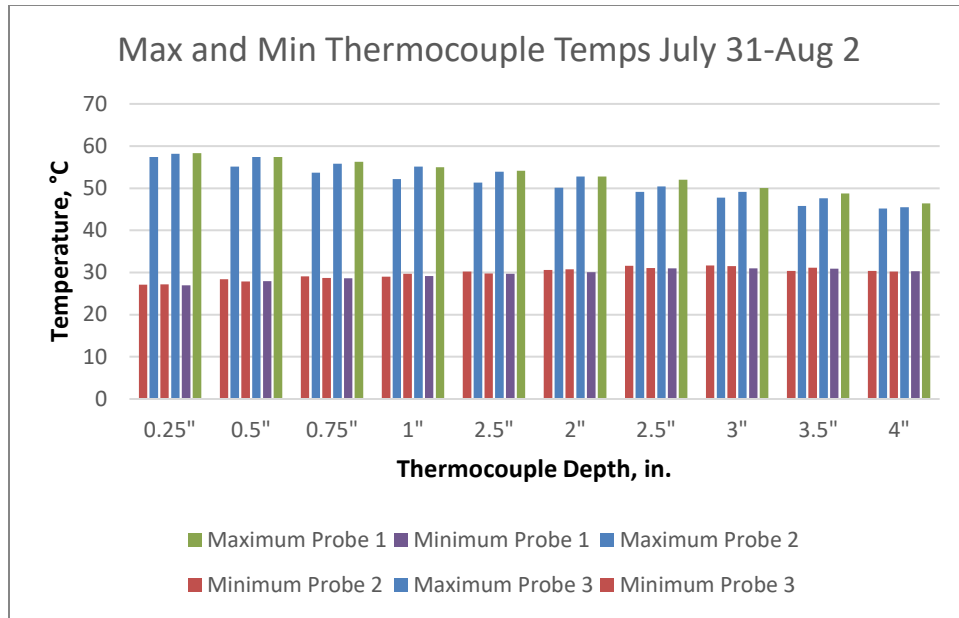
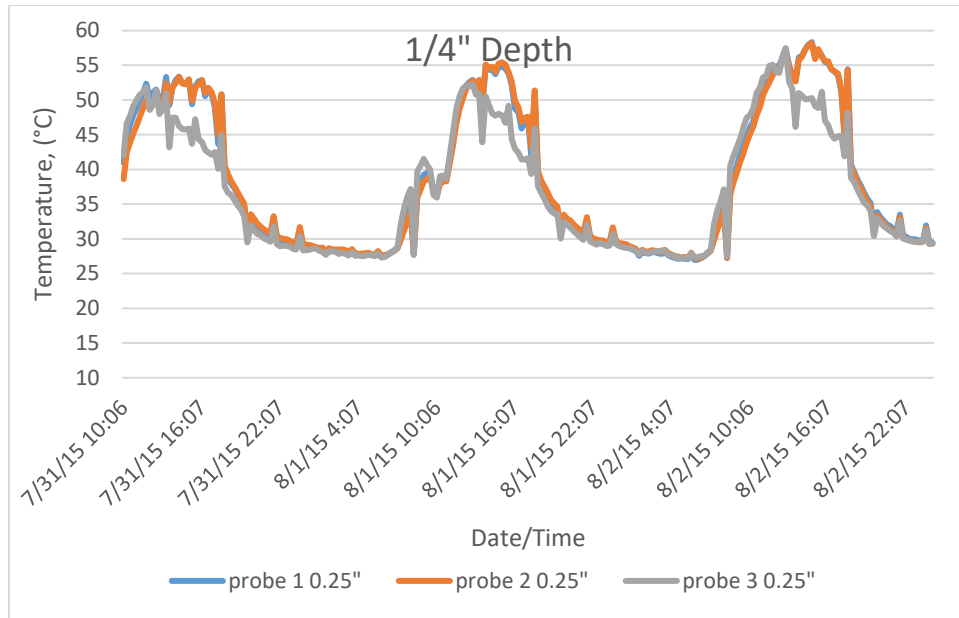


Figure 30: Maximum and minimum temperatures for each thermocouple probe at each depth for testing period July 31, 2015- August 2, 2015

Figure 30 shows that for a four-inch thick slab measuring one meter square, with the sides and top exposed will retain heat above ambient levels throughout the night. Measurements from 1-inch depth through 4-inch depth indicate that the temperature from that portion of the slab remained approximately 10°C (18°F) more than the ambient temperature throughout the nighttime. The 4 inch depth was the least susceptible to temperature fluctuations, but still had a daily variability of over 15°C. The top portion of the slab had a higher overall variability at approximately 31°C (87.8°F), which was both seen in the nighttime and daytime levels. The minimum measured temperature for the 0.25-inch depth thermocouple was 26.9°C (80.4°F), approximately seven degrees higher than the ambient temperature.



**Figure 31: Diurnal pattern of the 1/4 inch depth thermocouple temperature for each probe (probe 1/blue/slab 2; probe 2/orange/slab 3; probe 3/gray/slab 4) for test period July 31, 2015 – August 2, 2015**

Figure 31 shows the diurnal pattern of the 0.25" deep thermocouple for the testing period July 31, 2015 – Aug 2, 2015. The maximum temperature for the three-day period was 57.9°C (136.2°F) and the minimum temperature was 27.3°C (81.1°F). Two of the slabs, Slab 2 and Slab 3, exhibited similar results. Slab 4 had similar results for the warming phase but cooled off significantly earlier than the other two slabs. This is likely as a result of the building shading related to the zenith angle of the sun. The similarity between the three slabs at 0.25", other than the shading anomaly, shows that the material properties influenced the temperature of the mix significantly. Since each of the three slabs had the same aggregate gradation and binder type, there was good coherence between the slabs.

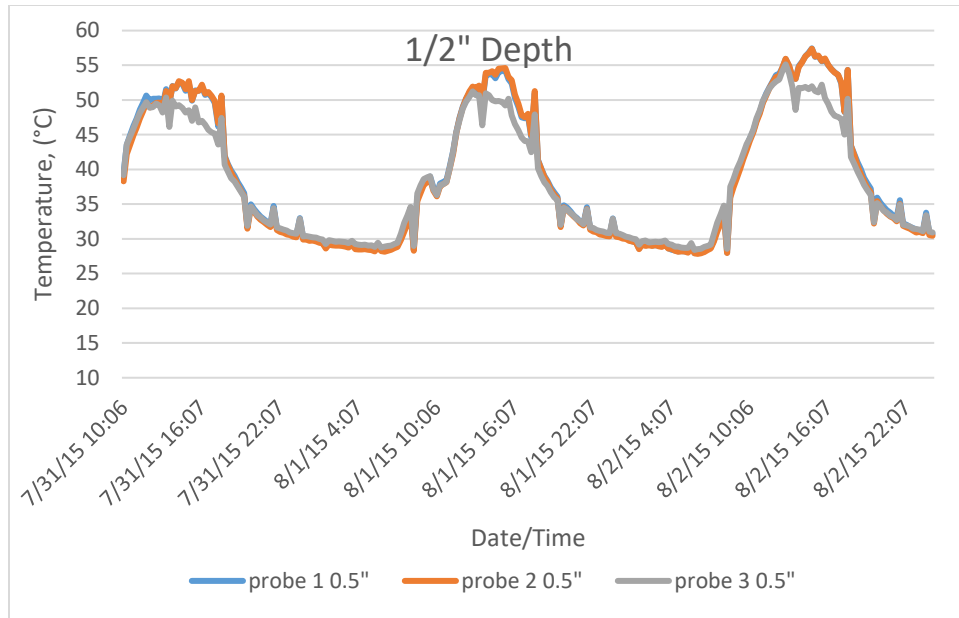


Figure 32: Diurnal pattern of the ½ inch depth thermocouple temperature for each probe (probe 1/blue/slab 2; probe 2/orange/slab 3; probe 3/gray/slab 4) for test period July 31, 2015 – August 2, 2015

Figure 32 shows the diurnal pattern of the 0.5" deep thermocouple for the testing period July 31, 2015 – Aug 2, 2015. The maximum temperature for the three-day period was 56.2°C (133.2°F) and the minimum temperature was 28.4°C (83.1°F). The variability within the measurements at this depth was as much as 27.8°C (50.1°F).

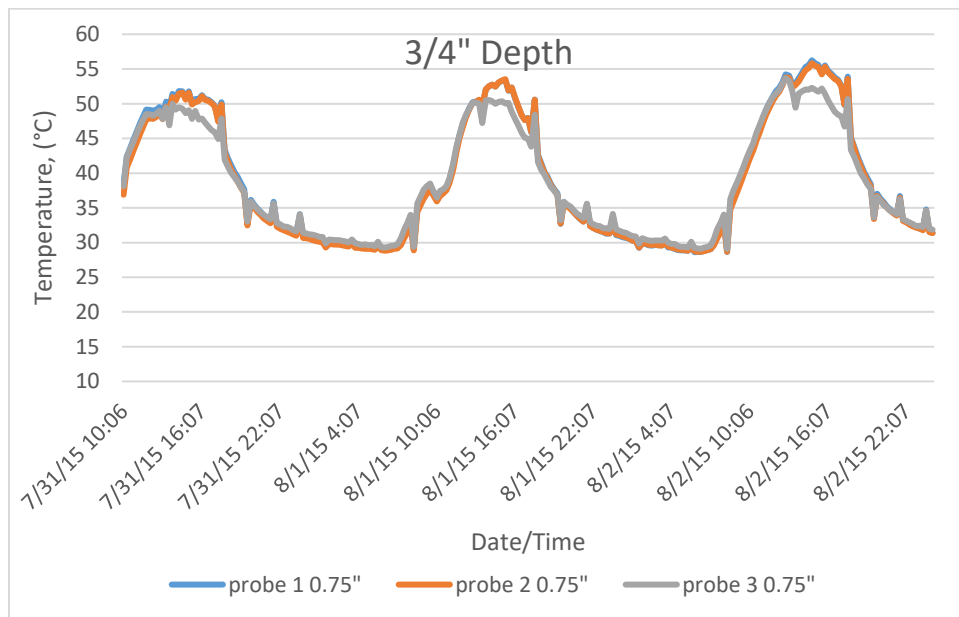


Figure 33: Diurnal pattern of the ¾ inch depth thermocouple temperature for each probe (probe 1/blue/slab 2; probe 2/orange/slab 3; probe 3/gray/slab 4) for test period July 31, 2015 – August 2, 2015

Figure 33 shows the diurnal pattern of the 0.75" deep thermocouple for the testing period July 31, 2015 – Aug 2, 2015. The maximum temperature for the three-day period was 55.4°C (131.7°F) and the minimum temperature was 29.0°C (84.2°F). The variability within the measurements at this depth was as much as 26.4°C (47.5°F).

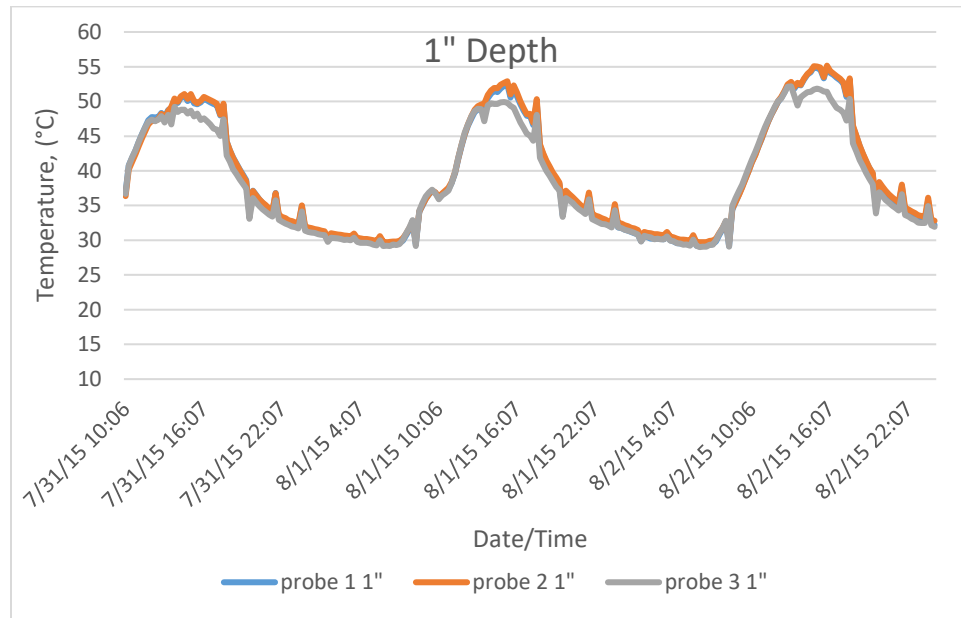


Figure 34: Diurnal pattern of the 1 inch depth thermocouple temperature for each probe (probe 1/blue/slab 2; probe 2/orange/slab 3; probe 3/gray/slab 4) for test period July 31, 2015 – August 2, 2015

Figure 34 shows the diurnal pattern of the 1.0" deep thermocouple for the testing period July 31, 2015 – Aug 2, 2015. The maximum temperature for the three-day period was 54.8°C (130.6°F) and the minimum temperature was 29.3°C (84.7°F). The variability within the measurements at this depth was as much as 25.5°C (45.9°F).

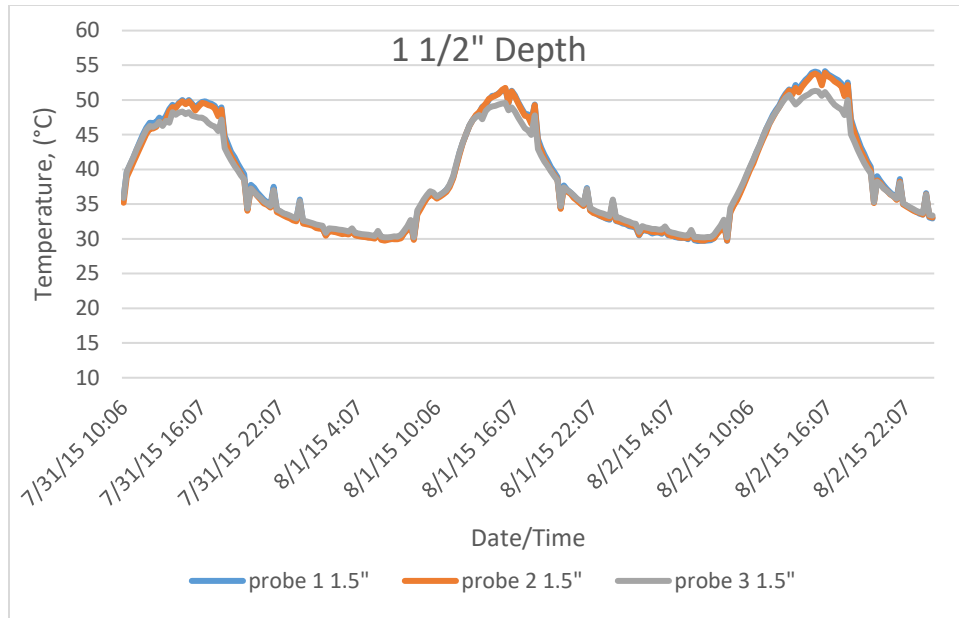


Figure 35: Diurnal pattern of the 1 1/2 inch depth thermocouple temperature for each probe (probe 1/blue/slab 2; probe 2/orange/slab 3; probe 3/gray/slab 4) for test period July 31, 2015 – August 2, 2015

Figure 35 shows the diurnal pattern of the 1.5" deep thermocouple for the testing period July 31, 2015 – Aug 2, 2015. The maximum temperature for the three-day period was 53.9°C (129.0°F) and the minimum temperature was 30.2°C (86.4°F). The variability within the measurements at this depth was as much as 23.7°C (42.6°F).

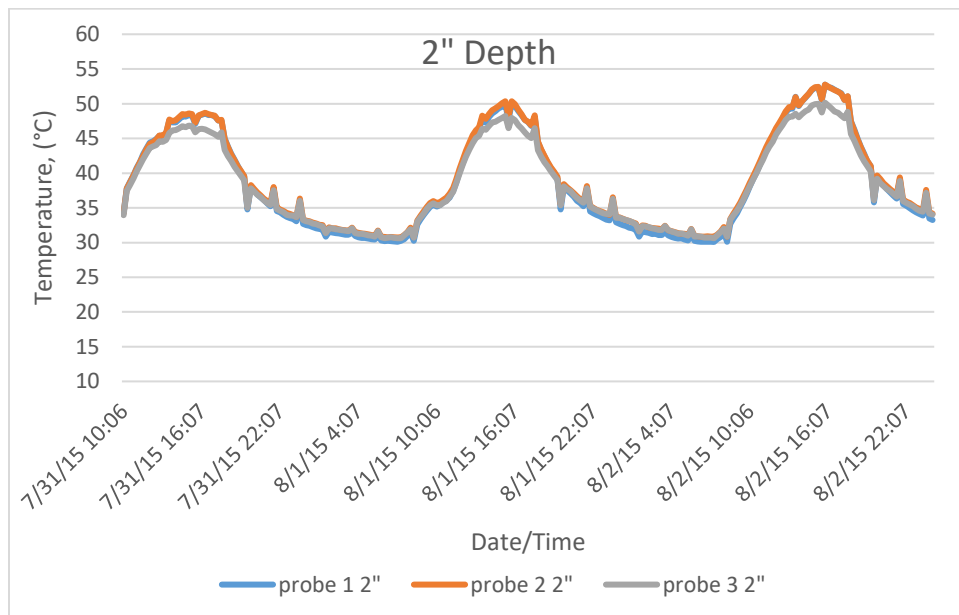
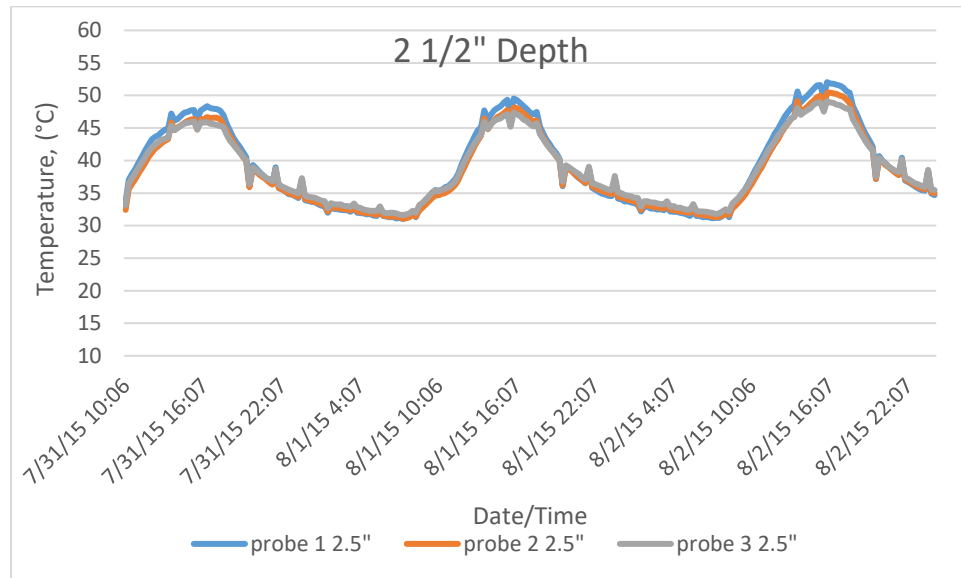


Figure 36: Diurnal pattern of the 2 inch depth thermocouple temperature for each probe (probe 1/blue/slab 2; probe 2/orange/slab 3; probe 3/gray/slab 4) for test period July 31, 2015 – August 2, 2015

Figure 36 shows the diurnal pattern of the 2.0" deep thermocouple for the testing period July 31, 2015 – Aug 2, 2015. The maximum temperature for the three-day period was 52.7°C (126.9°F) and the minimum temperature was 30.6°C (87.1°F). The variability within the measurements at this depth was as much as 22.1°C (39.8°F).



**Figure 37: Diurnal pattern of the 2 ½ inch depth thermocouple temperature for each probe (probe 1/blue/slab 2; probe 2/orange/slab 3; probe 3/gray/slab 4) for test period July 31, 2015 – August 2, 2015**

Figure 37 shows the diurnal pattern of the 2.5" deep thermocouple for the testing period July 31, 2015 – Aug 2, 2015. The maximum temperature for the three-day period was 50.3°C (122.5°F) and the minimum temperature was 31.8°C (89.2°F). The variability within the measurements at this depth was as much as 18.5°C (33.3°F).

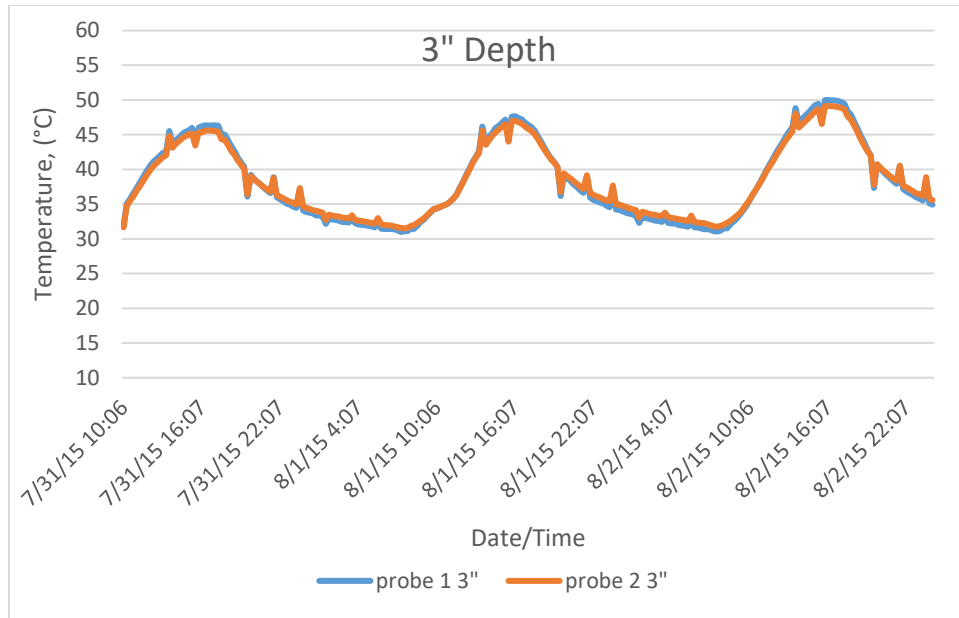


Figure 38: Diurnal pattern of the 3 inch depth thermocouple temperature for each probe (probe 1/blue/slab 2; probe 2/orange/slab 3; probe 3/gray/slab 4) for test period July 31, 2015 – August 2, 2015

Figure 38 shows the diurnal pattern of the 3.0" deep thermocouple for the testing period July 31, 2015 – Aug 2, 2015. The maximum temperature for the three-day period was 49.1°C (120.4°F) and the minimum temperature was 31.6°C (88.9°F). The variability within the measurements at this depth was as much as 23.6°C (31.5°F).

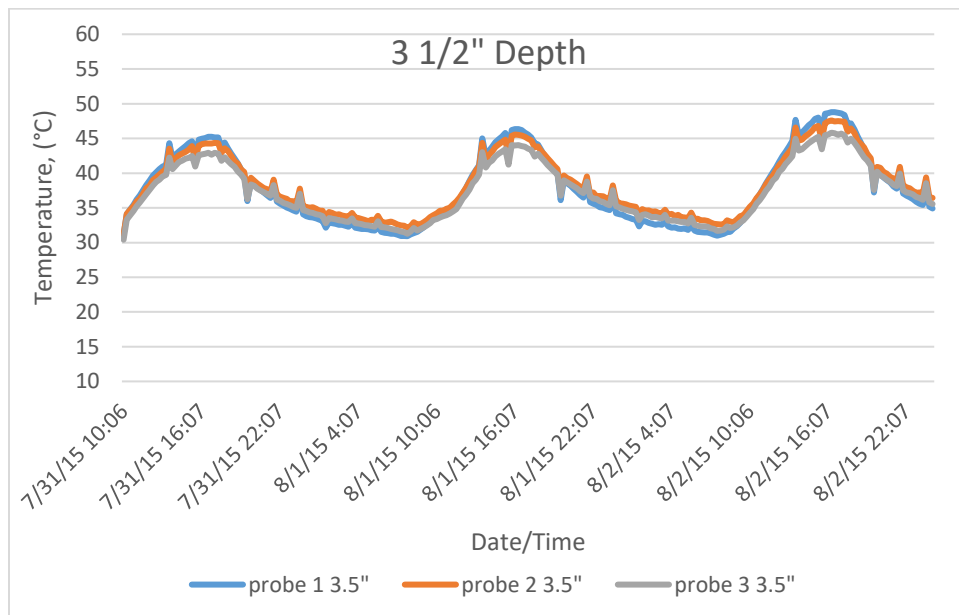
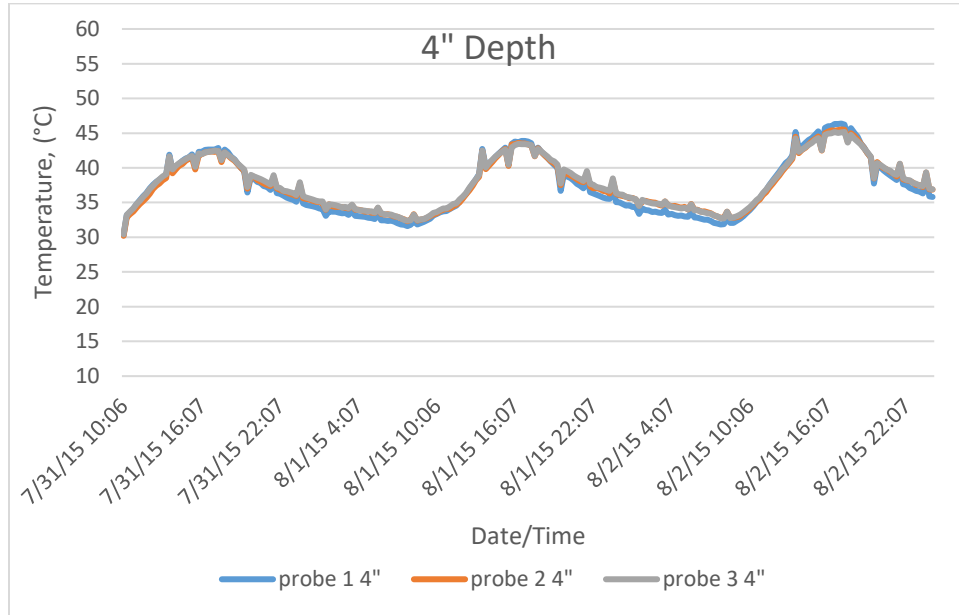


Figure 39: Diurnal pattern of the 3 ½ inch depth thermocouple temperature for each probe (probe 1/blue/slab 2; probe 2/orange/slab 3; probe 3/gray/slab 4) for test period July 31, 2015 – August 2, 2015

Figure 39 shows the diurnal pattern of the 3.5" deep thermocouple for the testing period July 31, 2015 – Aug 2, 2015. The maximum temperature for the three-day period was 47.5°C (117.5°F) and the minimum temperature was 31.2°C (88.2°F). The variability within the measurements at this depth was as much as 16.3°C (29.3°F).



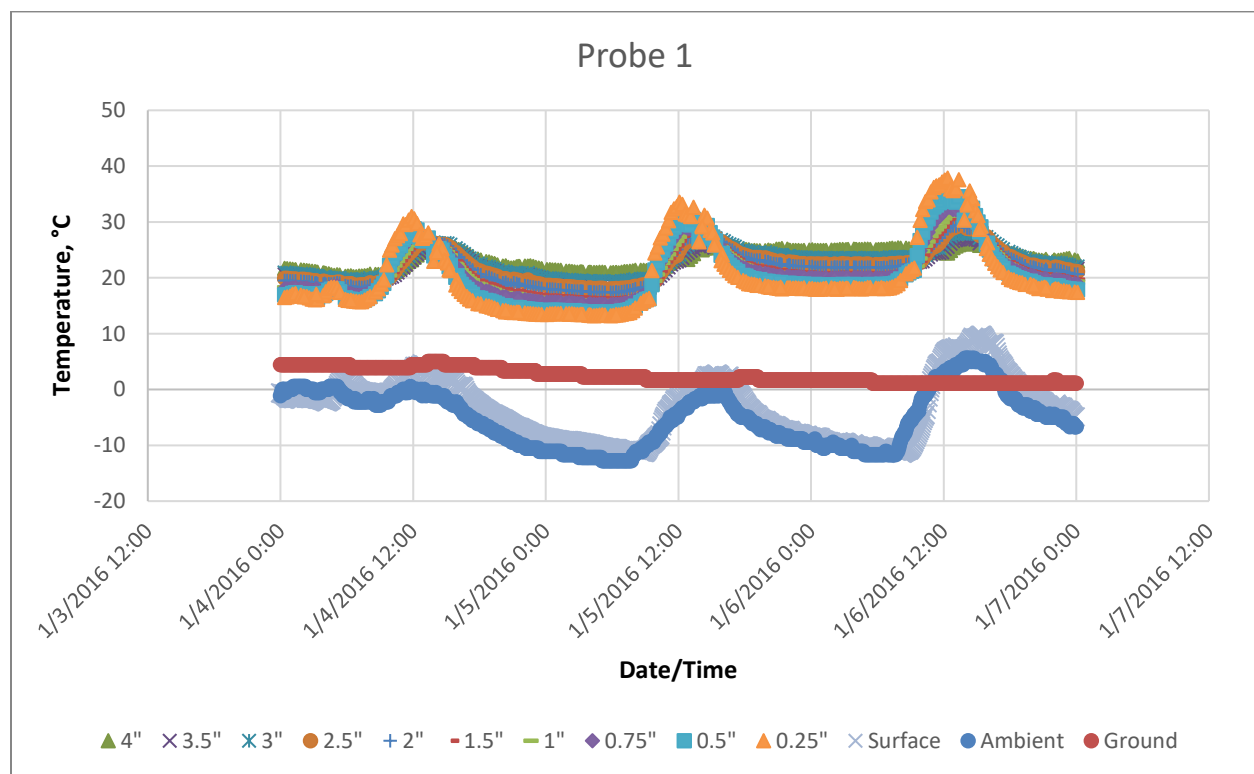
**Figure 40: Diurnal pattern of the 4 inch depth thermocouple temperature for each probe (probe 1/blue/slab 2; probe 2/orange/slab 3; probe 3/gray/slab 4) for test period July 31, 2015 – August 2, 2015**

Figure 40 shows the diurnal pattern of the 4.0" deep thermocouple for the testing period July 31, 2015 – Aug 2, 2015. The maximum temperature for the three-day period was 45.2°C (113.4°F) and the minimum temperature was 32.4°C (90.3°F). The variability within the measurements at this depth was as much as 12.8°C (23.1).



## January 4, 2016 – January 6, 2016

Within this section, the data compiled for the thermocouples for the testing period from January 4 - January 6, 2016. As expected, there is a noticeable diurnal pattern to the heating and cooling of the slab and surrounding ground surface, shown in Figures 41, 42, and 43. The ground surface temperature for the three-day period fluctuated minimally between 1.1°C (33.9°F) to 4.4°C (39.9°F) throughout the three day period. The ambient temperature fluctuated between -12.7°C (9.1°F) nighttime to 5.5°C (41.9°F) daytime. There is a noticeable lag in both the heating and cooling portion of the temperature plots, due to the coefficient of thermal conductivity of the asphalt slab. Due to the significantly cold ambient temperature and soil temperature, the asphalt slab did not heat as much as in the summer months. The 0.25" embedded thermocouple recorded temperature as high as 37.1°C (98.8°F) on January 6, 2016. Since this is the coldest measurement period, it is important to note that the temperature at the coldest point of the slab did not exceed the binder low temperature performance grade rating.



**Figure 41: Diurnal pattern of thermocouple probe 1 in slab sample 2 for testing period January 4 - January 6, 2016 compared to 4" soil depth, NR01 infrared surface temp, and ambient temp**

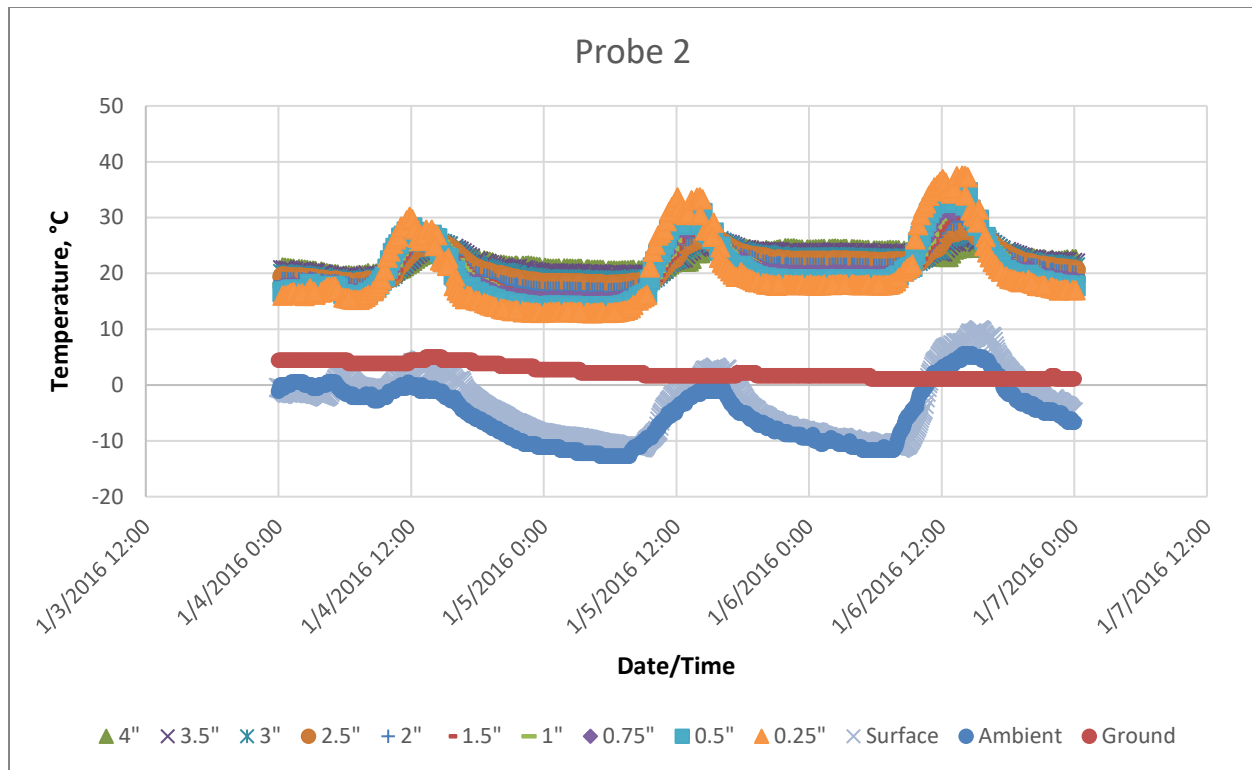


**Figure 42: Diurnal pattern of thermocouple probe 2 in slab sample 3 for testing period January 4 - January 6, 2016 compared to 4" soil depth, NR01 infrared surface temp, and ambient temp**

The January 4 – January 6 test period temperature analysis revealed that the 4" ground temperature did not fluctuate as much as it had in the July test period. The slab surface temperature dipped as low as -12.7°C (54.9°F) throughout the night, but remained to a temperature slightly warmer than the ambient temperature for the majority of the time, with the exception being during the early morning hours, presumably as frost occurred. The surface temperature dipped as low as the ambient temperature, but during the daytime increased by as much as 4 degrees higher than the ambient temperature, as shown in Figure 42. The surface temperature always remained cooler than the interior slab temperatures.

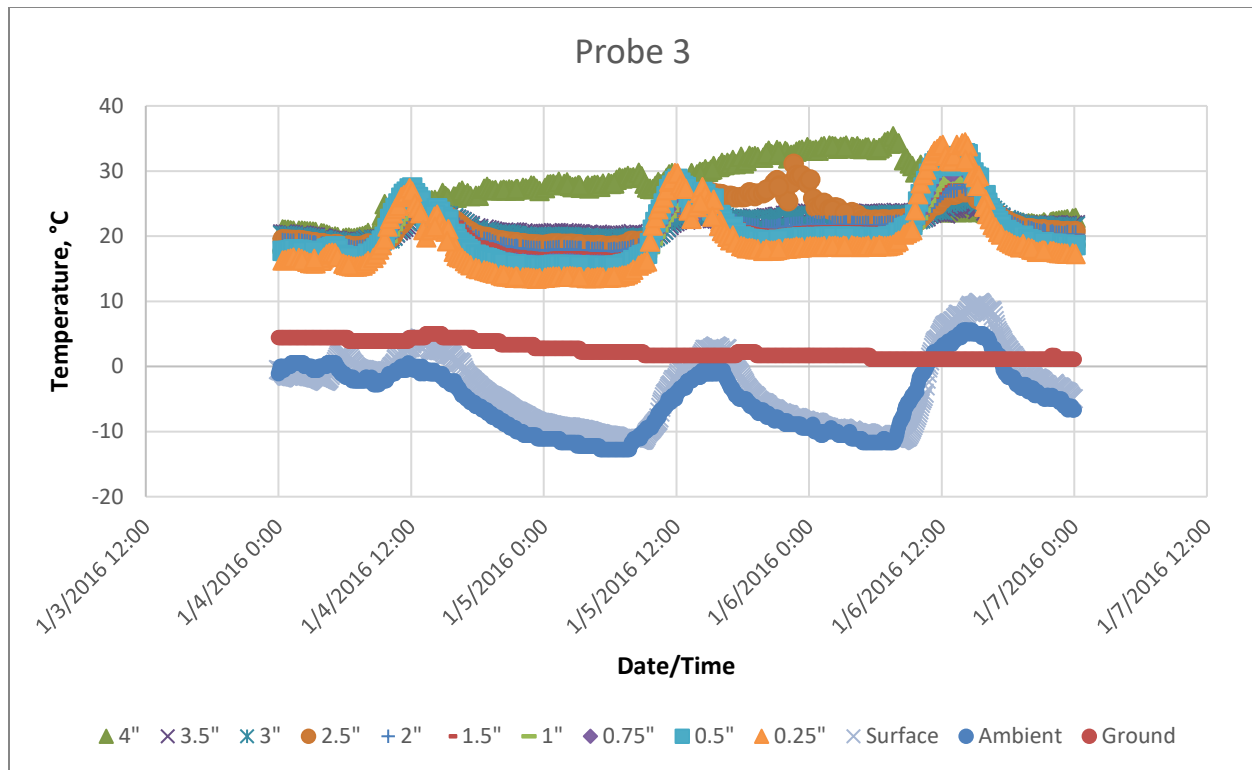


**Figure 43: Diurnal pattern of thermocouple probe 3 in slab sample 4 for testing period January 4 - January 6, 2016 compared to 4" soil depth, NR01 infrared surface temp, and ambient temp**

Although the three slabs were under similar conditions, slab three was shaded by the building in the morning for a period of less than half an hour. That short period of time had a noticeable effect on the rate of cooling, shown in Figure 43. The rate of cooling in the slab thermocouples compared to the other two slabs shows the pronounced influence that the solar energy had on the slab. Figure 43 also shows two temperature probe malfunctions, one at the 2.5" depth and a second at the 4" depth. To further evaluate the differences between the slab temperatures, the maximum and minimum for each slab was calculated for each depth and shown in Figure 44.

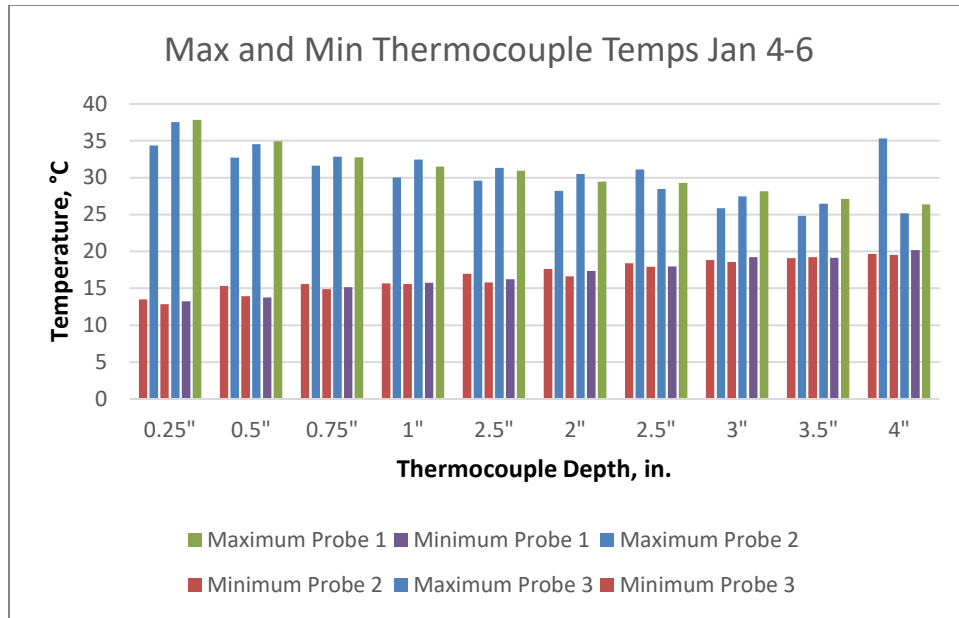


**Figure 44: Maximum and minimum temperatures for each thermocouple probe at each depth for testing period January 4, 2016- January 6, 2016**

Figure 44 shows that a four-inch thick slab measuring one meter square, with the sides and top exposed will retain heat above ambient levels throughout the night. Measurements from 1-inch depth through 4-inch depth indicate that the temperature from that portion of the slab remained approximately 30°C (27°F) more than the ambient temperature throughout the nighttime. The 4 inch depth was the least susceptible to temperature fluctuations, but still had a daily variability of over 6.3°C (10.8°F). The top portion of the slab had a higher overall variability at approximately 24°C (38.7°F), which was seen from nighttime and daytime levels. The minimum measured temperature for the 0.25-inch depth thermocouple was 13.6°C (56.5°F), approximately 20 degrees higher than the ambient temperature.

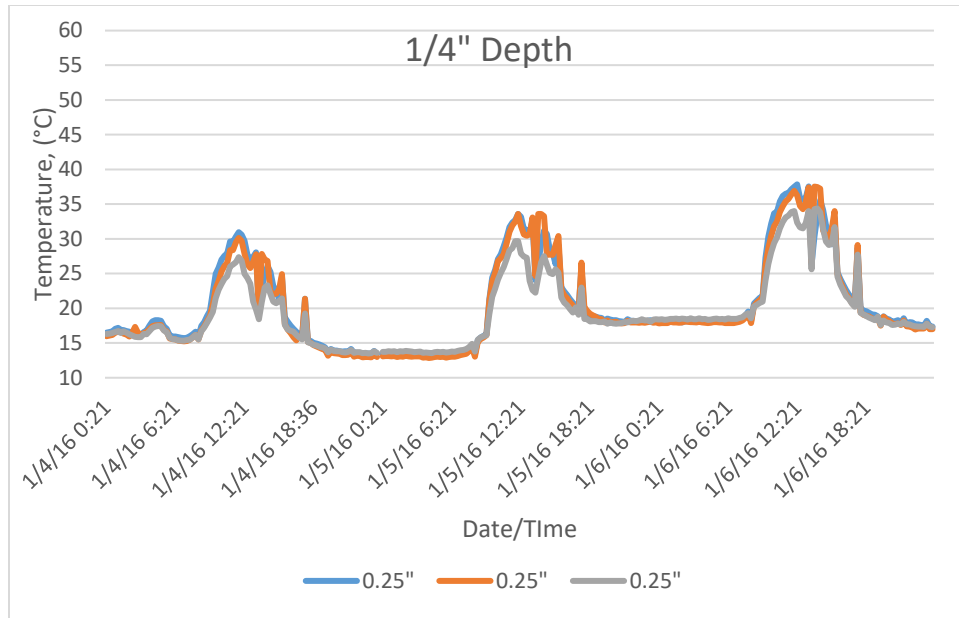


**Figure 45: Diurnal pattern of the 1/4 inch depth thermocouple temperature for each probe (probe 1/blue/slab 2; probe 2/orange/slab 3; probe 3/gray/slab 4) for test period January 4, 2016 – January 6, 2016**

Figure 45 shows the diurnal pattern of the 0.25" deep thermocouple for the testing period January 4, 2016 – January 6, 2016. The maximum temperature for the three-day period was 36.8°C (98.2°F) and the minimum temperature was 13.6°C (56.5°F). Each of the three slabs exhibited similar results. The noise in the data is likely as a result of the cloud shading causing rapid surface temperature fluctuations. The similarity between the three slabs at 0.25", other than the shading anomaly, shows that the material properties influenced the temperature of the mix significantly. Since each of the three slabs had the same aggregate gradation and binder type, there was good coherence between the slabs.

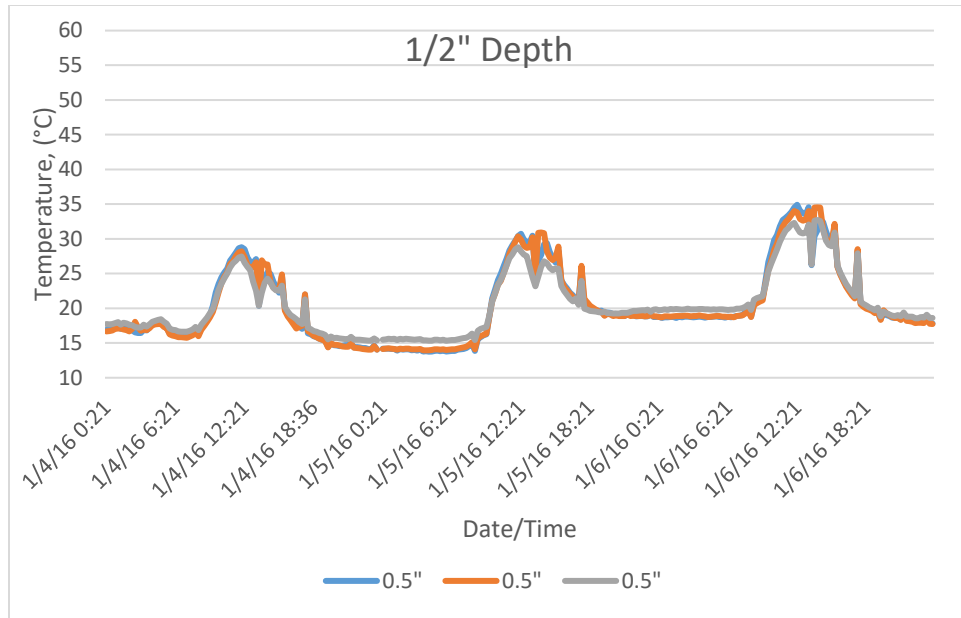


Figure 46: Diurnal pattern of the ½ inch depth thermocouple temperature for each probe (probe 1/blue/slab 2; probe 2/orange/slab 3; probe 3/gray/slab 4) for test period January 4, 2016 – January 6, 2016

Figure 46 shows the diurnal pattern of the 0.5" deep thermocouple for the testing period January 4, 2016 – January 6, 2016. The maximum temperature for the three-day period was 34.0°C (93.2°F) and the minimum temperature was 15.5°C (59.9°F). The variability within the measurements at this depth was as much as 18.5°C (33.3°F).

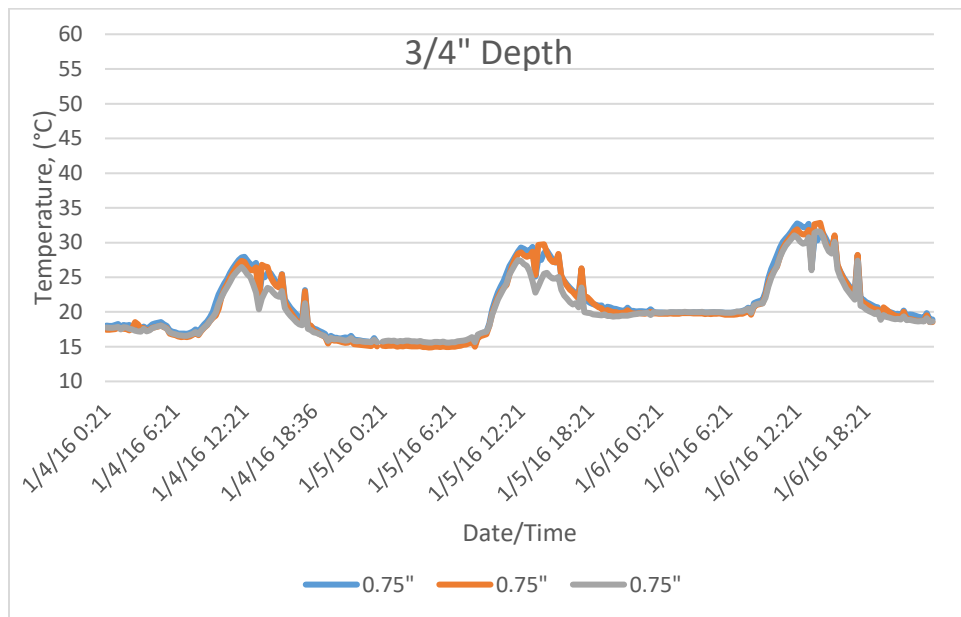
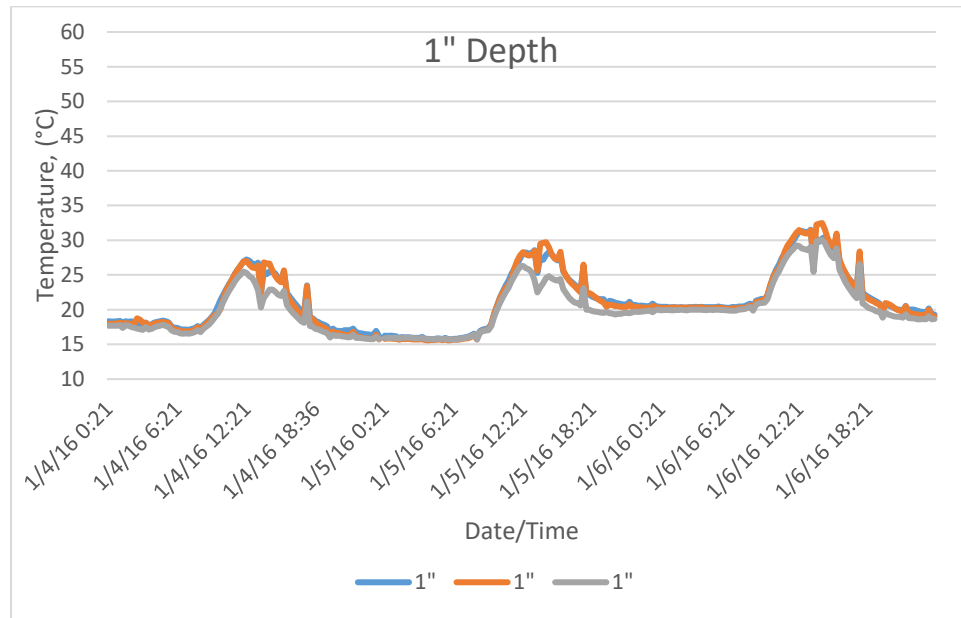


Figure 47: Diurnal pattern of the ¾ inch depth thermocouple temperature for each probe (probe 1/blue/slab 2; probe 2/orange/slab 3; probe 3/gray/slab 4) for test period January 4, 2016 – January 6, 2016

Figure 47 shows the diurnal pattern of the 0.75" deep thermocouple for the testing period January 4, 2016 – January 6, 2016. The maximum temperature for the three-day period was 31.6°C and the minimum temperature was 15.6°C. The variability within the measurements at this depth was as much as 16.0°C.



**Figure 48: Diurnal pattern of the 1 inch depth thermocouple temperature for each probe (probe 1/blue/slab 2; probe 2/orange/slab 3; probe 3/gray/slab 4) for test period January 4, 2016 – January 6, 2016**

Figure 48 shows the diurnal pattern of the 1" deep thermocouple for the testing period January 4, 2016 – January 6, 2016. The maximum temperature for the three-day period was 32.5°C (90.5°F) and the minimum temperature was 15.6°C (60.8°F). The variability within the measurements at this depth was as much as 16.9°C (29.7°F).

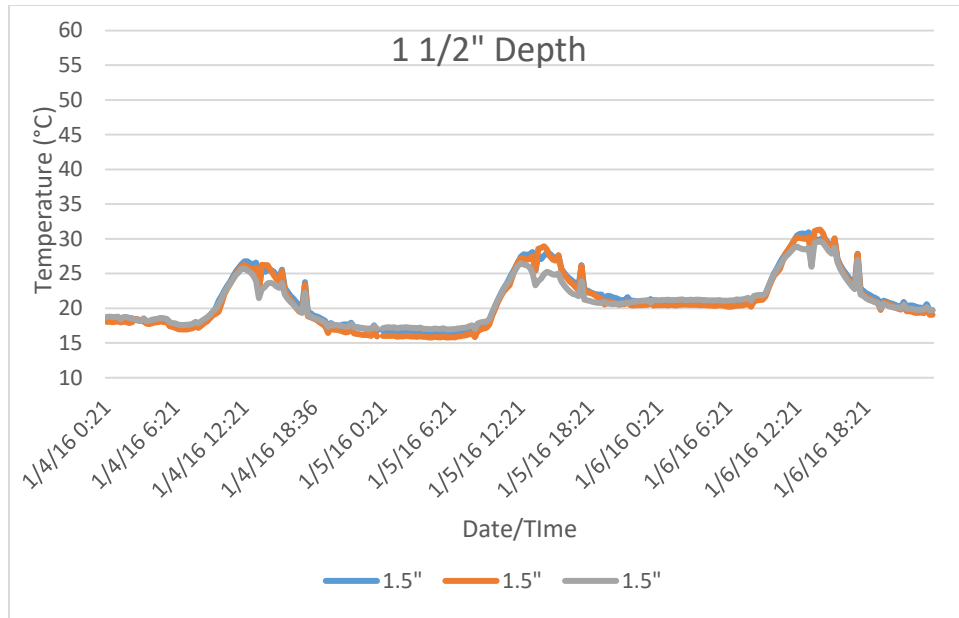


Figure 49: Diurnal pattern of the 1 1/2 inch depth thermocouple temperature for each probe (probe 1/blue/slab 2; probe 2/orange/slab 3; probe 3/gray/slab 4) for test period January 4, 2016 – January 6, 2016

Figure 49 shows the diurnal pattern of the 1.5" deep thermocouple for the testing period January 4, 2016 – January 6, 2016. The maximum temperature for the three-day period was 29.6°C (85.3°F) and the minimum temperature was 17.0°C (62.6°F). The variability within the measurements at this depth was as much as 12.6°C (22.7°F).

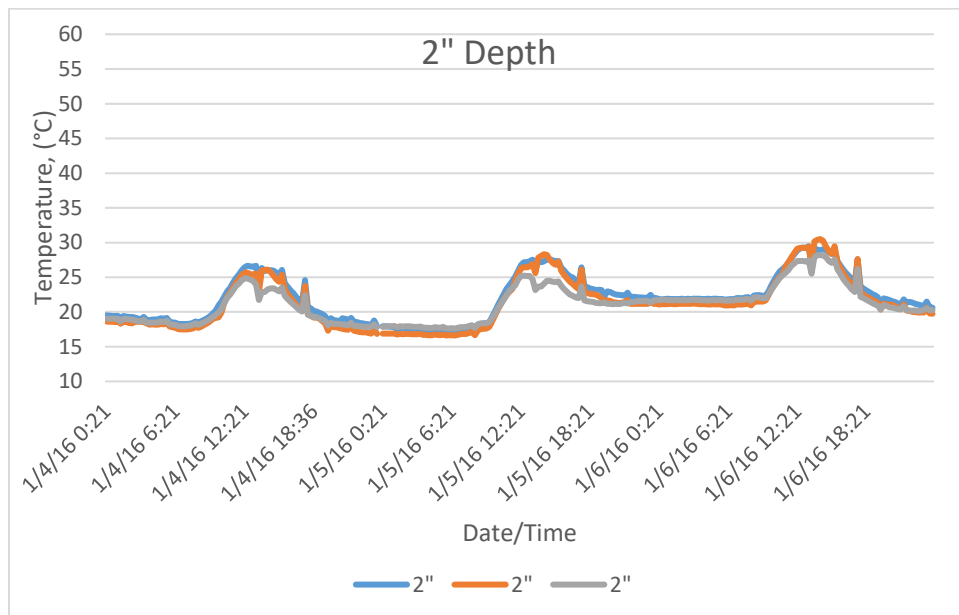
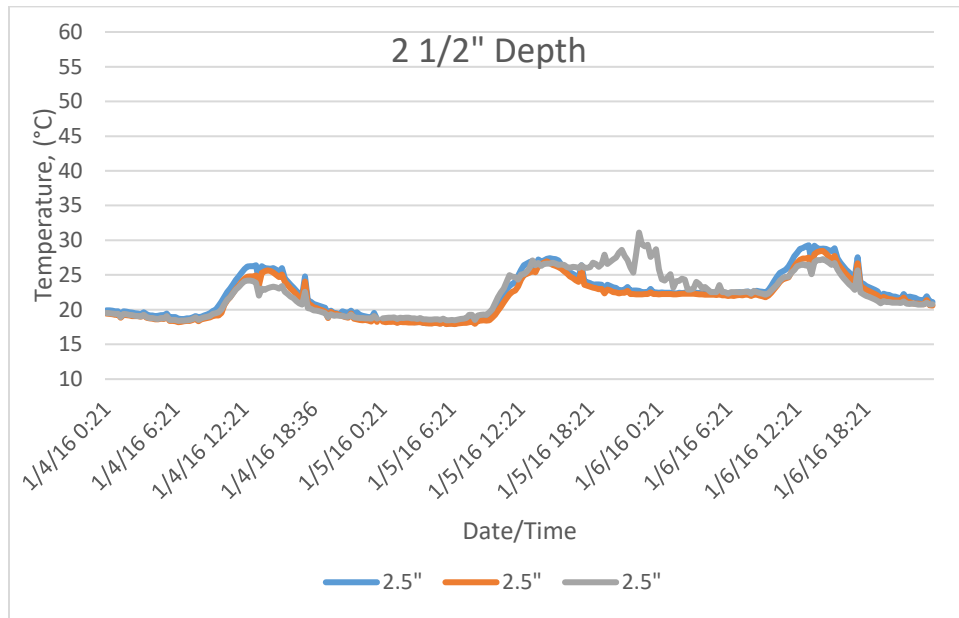


Figure 50: Diurnal pattern of the 2 inch depth thermocouple temperature for each probe (probe 1/blue/slab 2; probe 2/orange/slab 3; probe 3/gray/slab 4) for test period January 4, 2016 – January 6, 2016



Figure 50 shows the diurnal pattern of the 2" deep thermocouple for the testing period January 4, 2016 – January 6, 2016. The maximum temperature for the three-day period was 30.4°C (86.7°F) and the minimum temperature was 17.8°C (64.0°F). The variability within the measurements at this depth was as much as 12.6°C (22.7°F).



**Figure 51: Diurnal pattern of the 2 ½ inch depth thermocouple temperature for each probe (probe 1/blue/slab 2; probe 2/orange/slab 3; probe 3/gray/slab 4) for test period January 4, 2016 – January 6, 2016**

Figure 47 shows the diurnal pattern of the 2.5" deep thermocouple for the testing period January 4, 2016 – January 6, 2016. The maximum temperature for the three-day period was 28.5°C (83.3°F) and the minimum temperature was 18.5°C (65.3°F). The variability within the measurements at this depth was as much as 10.0°C (3.4°F).

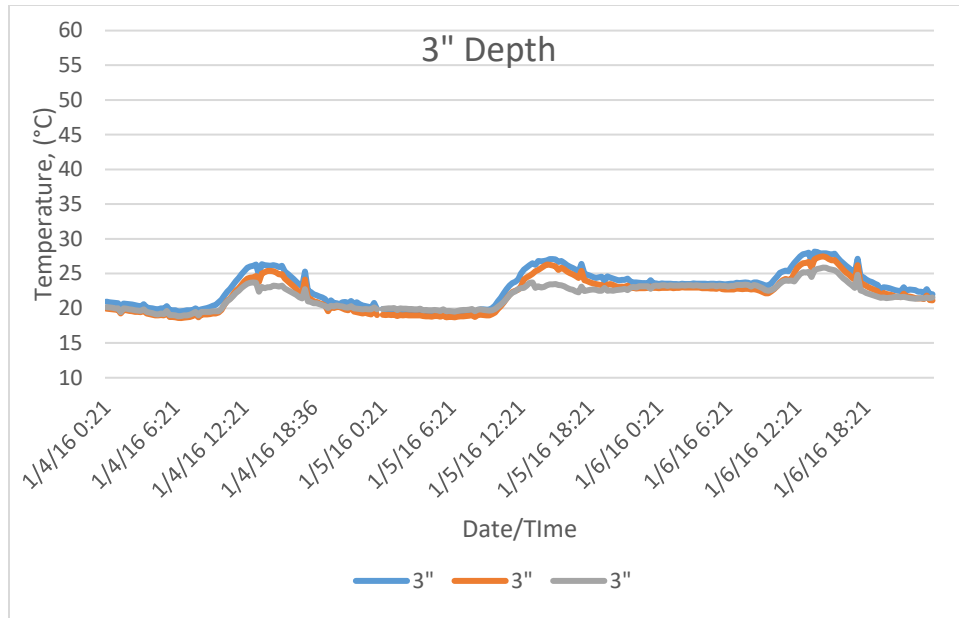


Figure 52: Diurnal pattern of the 3 inch depth thermocouple temperature for each probe (probe 1/blue/slab 2; probe 2/orange/slab 3; probe 3/gray/slab 4) for test period January 4, 2016 – January 6, 2016

Figure 52 shows the diurnal pattern of the 3" deep thermocouple for the testing period January 4, 2016 – January 6, 2016. The maximum temperature for the three-day period was 25.8°C (78.4°F) and the minimum temperature was 19.7°C (67.5°F). The variability within the measurements at this depth was as much as 6.1°C (10.9°F).

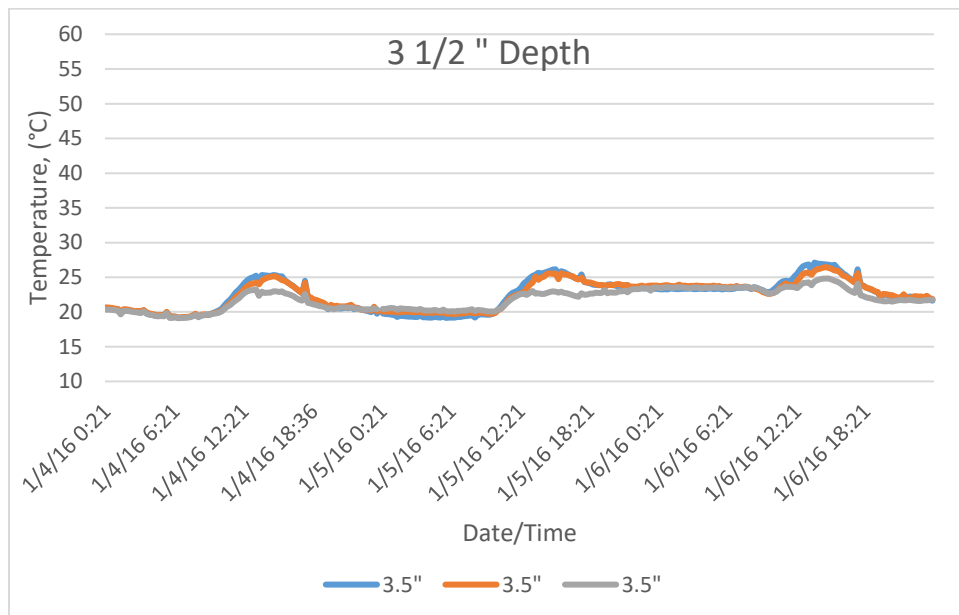
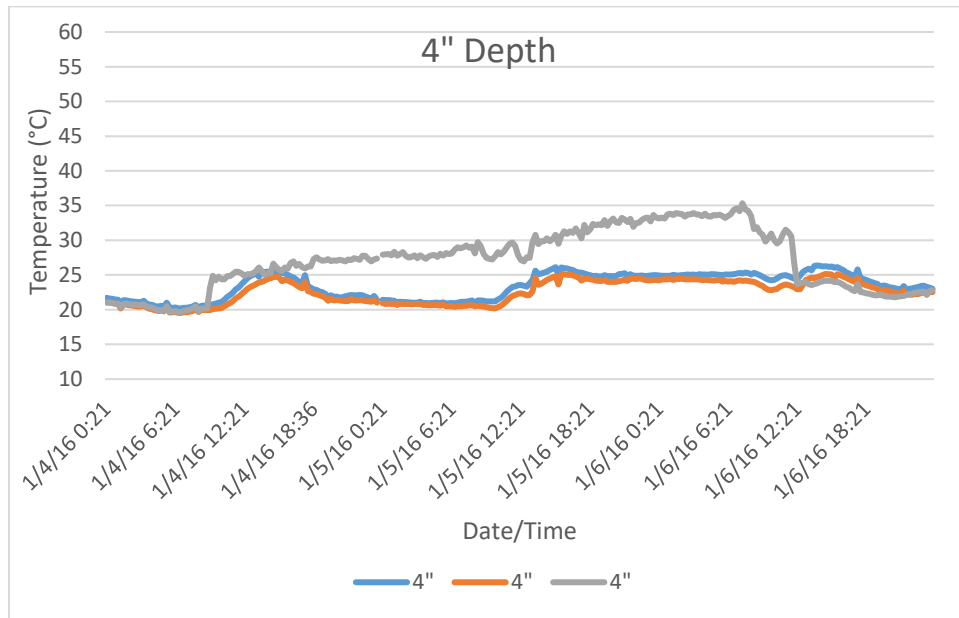


Figure 53: Diurnal pattern of the 3 1/2 inch depth thermocouple temperature for each probe (probe 1/blue/slab 2; probe 2/orange/slab 3; probe 3/gray/slab 4) for test period January 4, 2016 – January 6, 2016

Figure 53 shows the diurnal pattern of the 3.5" deep thermocouple for the testing period January 4, 2016 – January 6, 2016. The maximum temperature for the three-day period was 25.6°C (78.0°F) and the minimum temperature was 20.1°C (68.2°F). The variability within the measurements at this depth was as much as 5.5°C (9.8°F).



**Figure 54: Diurnal pattern of the 4 inch depth thermocouple temperature for each probe (probe 1/blue/slab 2; probe 2/orange/slab 3; probe 3/gray/slab 4) for test period January 4, 2016 – January 6, 2016**

Figure 54 shows the diurnal pattern of the 4" deep thermocouple for the testing period January 4, 2016 – January 6, 2016. The maximum temperature for the three-day period was 25.1°C (77.1°F) and the minimum temperature was 20.2°C (68.4°F). The variability within the measurements at this depth was as much as 4.9°C (8.7°F).

## February 6 – February 8, 2016

Within this section, the data compiled for the thermocouples for the testing period from February 6 - February 8, 2016. As expected, there is a noticeable diurnal pattern to the heating and cooling of the slab and surrounding ground surface, shown in Figures 55, 56, and 57. The ground surface temperature for the three-day period fluctuated minimally between 1.6°C (34.9°F) to 2.2°C (36°F) throughout the three day period. The ambient temperature fluctuated between -6.7°C (19.94°F) nighttime to 7.2°C (45°F) daytime. There is a noticeable lag in both the heating and cooling portion of the temperature plots, due to the coefficient of thermal conductivity of the asphalt slab. Due to the significantly cold ambient temperature and soil temperature, the asphalt slab did not heat as much as in the summer months. The 0.25" embedded thermocouple recorded temperature as high as 31.1°C (88°F) on February 6, 2016.

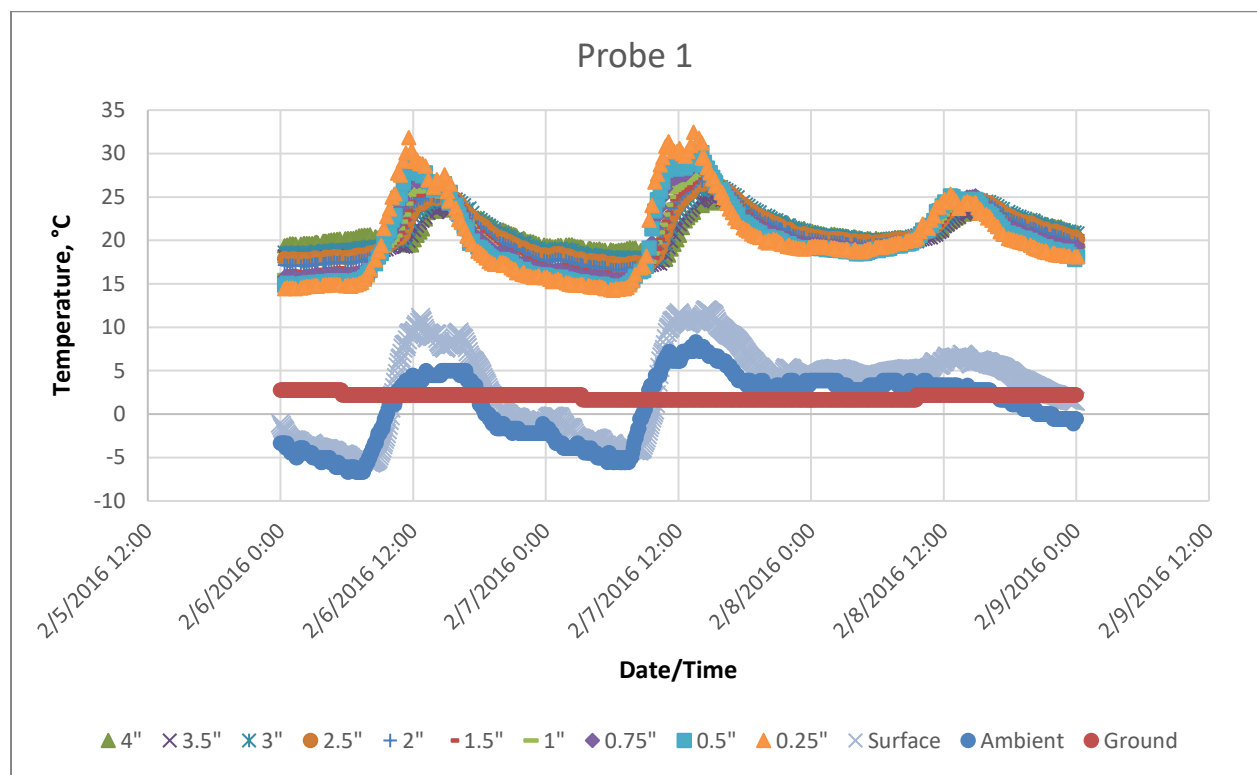


**Figure 55: Diurnal pattern of thermocouple probe 1 in slab sample 2 for testing period February 6 - February 8, 2016 compared to 4" soil depth, NR01 infrared surface temp, and ambient temp**

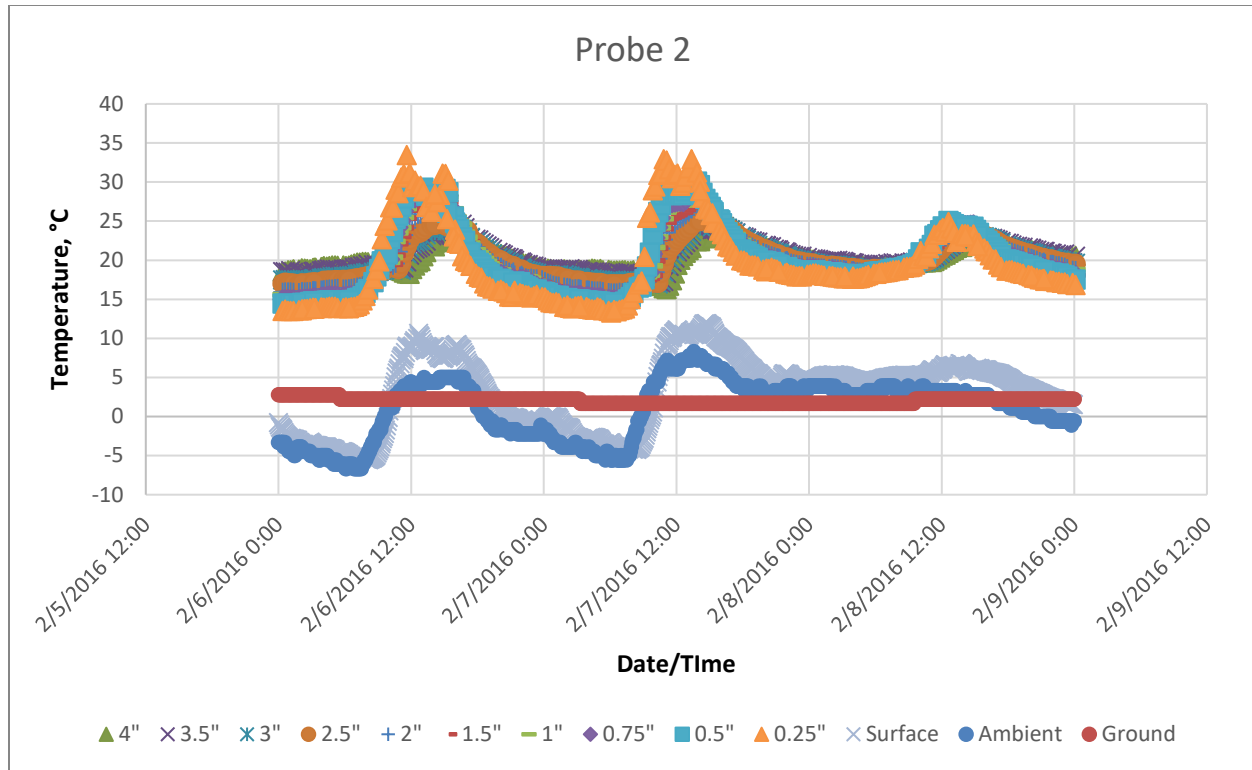


**Figure 56: Diurnal pattern of thermocouple probe 2 in slab sample 3 for testing period February 6 - February 8, 2016 compared to 4" soil depth, NR01 infrared surface temp, and ambient temp**

The February 6 – February 8 test period temperature analysis revealed that the 4" ground temperature did not fluctuate as much as it had in the summer test period. The slab surface temperature dipped as low as -4.4°C (24.1°F) throughout the night, but remained slightly warmer than the ambient temperature for the majority of the time, with the exception being during the early morning hours. The surface temperature dipped as low as the ambient temperature, but during the daytime increased by as much as 3.8 degrees Celsius higher than the ambient temperature, as shown in Figure 56. The surface temperature always remained cooler than the interior slab temperatures.

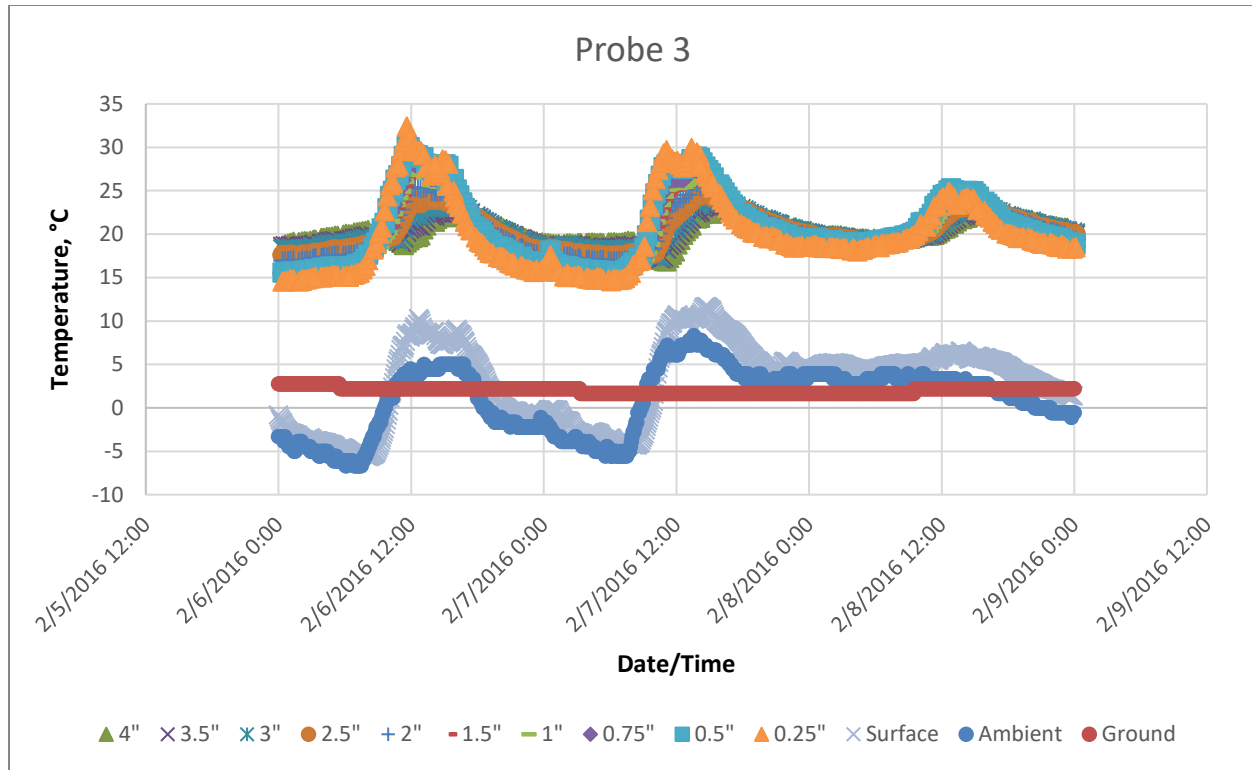


**Figure 57: Diurnal pattern of thermocouple probe 3 in slab sample 4 for testing period February 6 - February 8, 2016 compared to 4" soil depth, NR01 infrared surface temp, and ambient temp**

Although the three slabs were under similar conditions, slab three was shaded by the building in the morning for a period of about half an hour. That short period of time had a noticeable effect on the rate of cooling, shown in Figure 57. The rate of cooling in the slab thermocouples compared to the other two slabs shows the pronounced influence that the solar energy had on the slab. To further evaluate the differences between the slab temperatures, the maximum and minimum for each slab was calculated for each depth and shown in Figure 58.

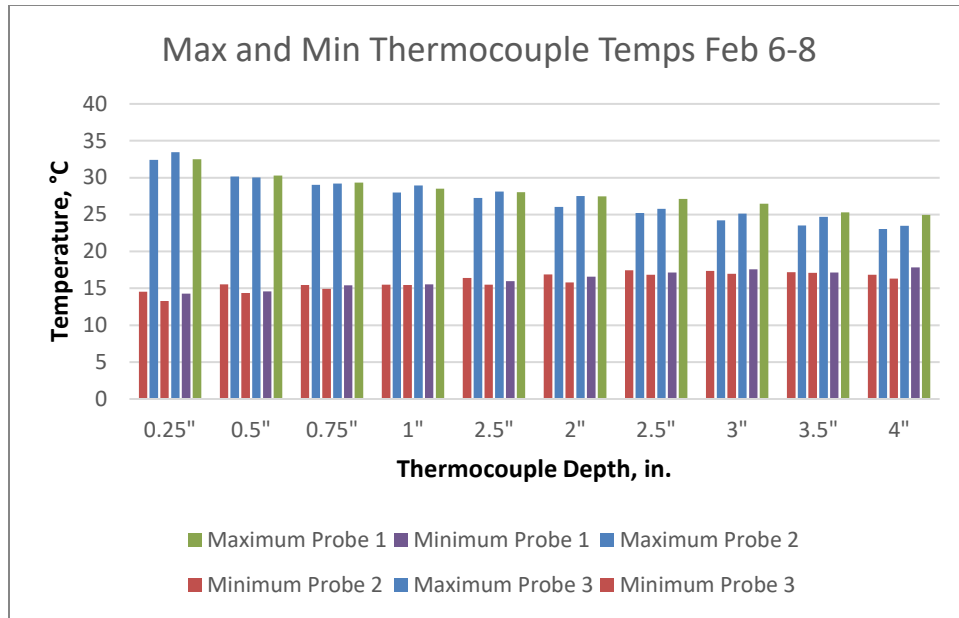


Figure 58: Maximum and minimum temperatures for each thermocouple probe at each depth for testing period February 6, 2016- February 8, 2016

Figure 58 shows that a four-inch thick slab measuring one meter square, with the sides and top exposed will retain heat above ambient levels throughout the night. Measurements from 1-inch depth through 4-inch depth indicate that the temperature from that portion of the slab remained approximately 12.8°C (36°F) more than the ambient temperature throughout the nighttime. The 4 inch depth was the least susceptible to temperature fluctuations, but still had a daily variability of over 7.1°C (12.8°F). The top portion of the slab had a higher overall variability at approximately 24°C (32.4°F), which was seen from nighttime and daytime levels. The minimum measured temperature for the 0.25-inch depth thermocouple was 20.2°C (68.4°F), approximately 15 degrees higher than the ambient temperature.

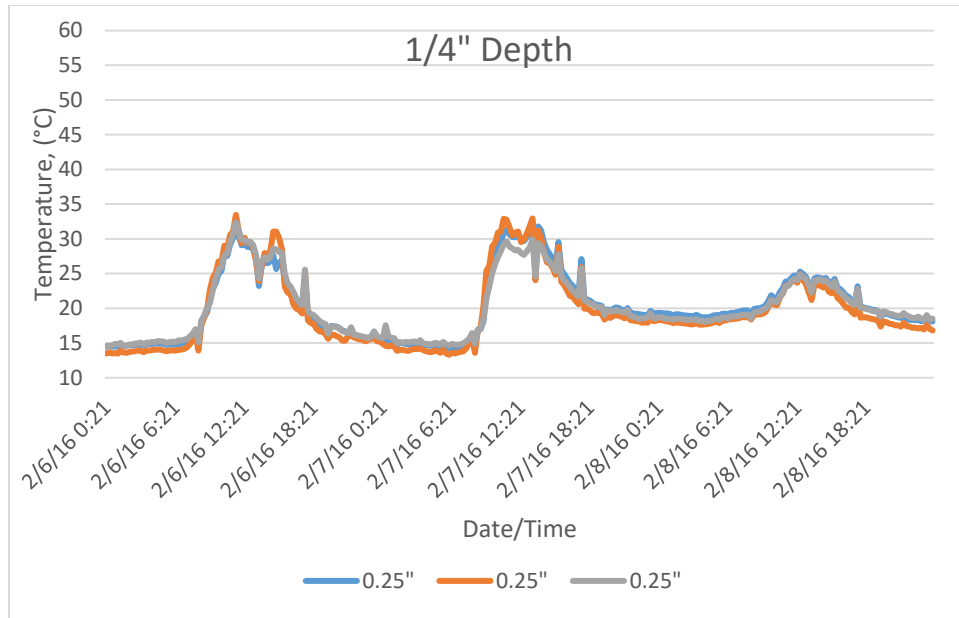


Figure 59: Diurnal pattern of the ¼ inch depth thermocouple temperature for each probe (probe 1/blue/slab 2; probe 2/orange/slab 3; probe 3/gray/slab 4) for test period February 6, 2016 – February 8, 2016

Figure 59 shows the diurnal pattern of the 0.25" deep thermocouple for the testing period February 6, 2016 – February 8, 2016. The maximum temperature for the three-day period was 31.2°C (88.2°F) and the minimum temperature was 14.5°C (58.1°F). Each of the three slabs exhibited similar results. The similarity between the three slabs at 0.25" shows that the material properties influenced the temperature of the mix significantly. Since each of the three slabs had the same aggregate gradation and binder type, there was good coherence between the slabs.

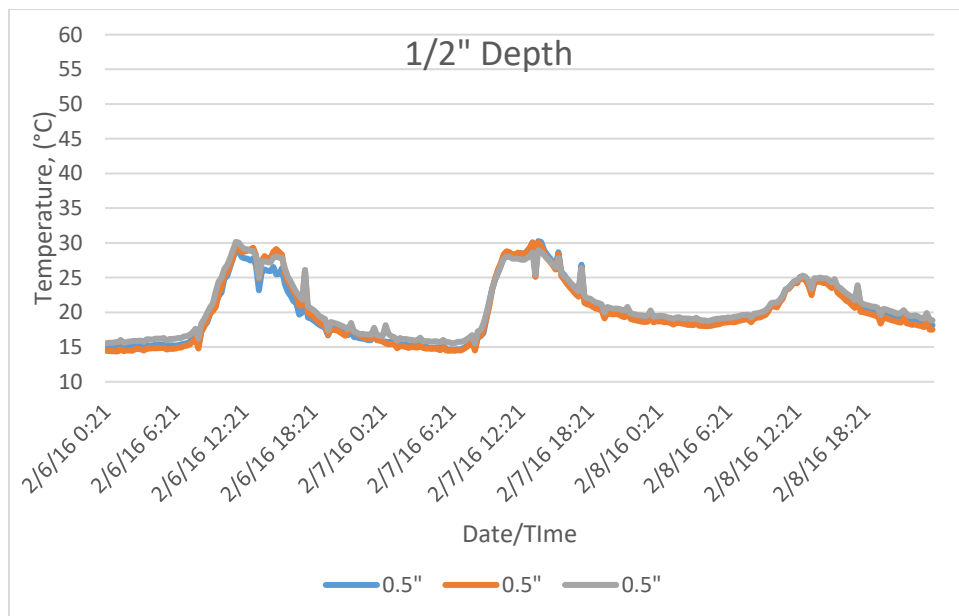
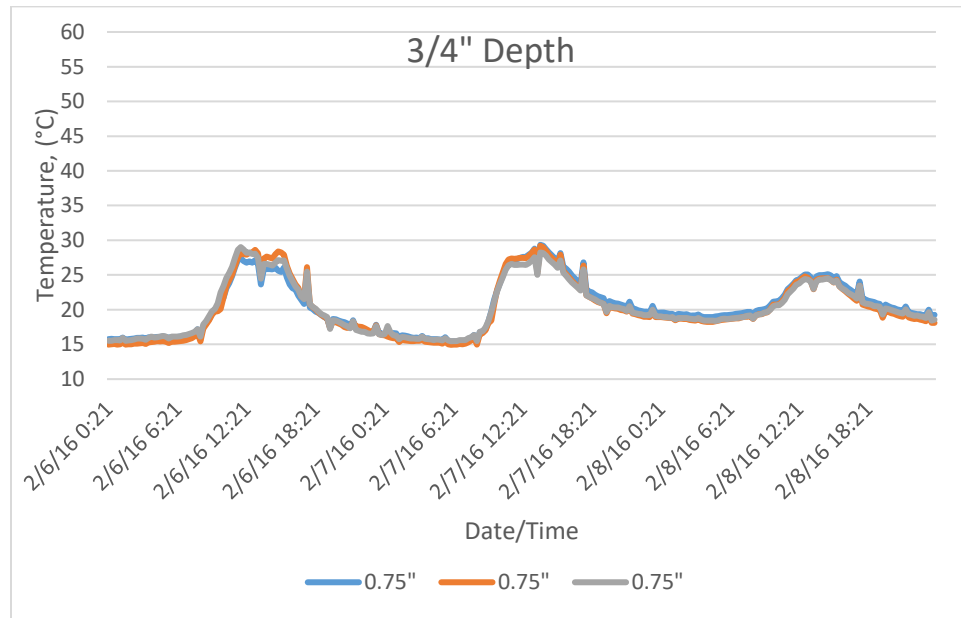


Figure 60: Diurnal pattern of the ½ inch depth thermocouple temperature for each probe (probe 1/blue/slab 2; probe 2/orange/slab 3; probe 3/gray/slab 4) for test period February 6, 2016 – February 8, 2016



Figure 60 shows the diurnal pattern of the 0.5" deep thermocouple for the testing period February 6, 2016 – February 8, 2016. The maximum temperature for the three-day period was 29.4°C (84.9°F) and the minimum temperature was 15.9°C (60.6°F). The variability within the measurements at this depth was as much as 13.5°C (24.3°F).



**Figure 61: Diurnal pattern of the ¾ inch depth thermocouple temperature for each probe (probe 1/blue/slab 2; probe 2/orange/slab 3; probe 3/gray/slab 4) for test period February 6, 2016 – February 8, 2016**

Figure 61 shows the diurnal pattern of the 0.75" deep thermocouple for the testing period February 6, 2016 – February 8, 2016. The maximum temperature for the three-day period was 28.2°C (82.8°F) and the minimum temperature was 15.6°C (60.8°F). The variability within the measurements at this depth was as much as 12.6°C (22°F).

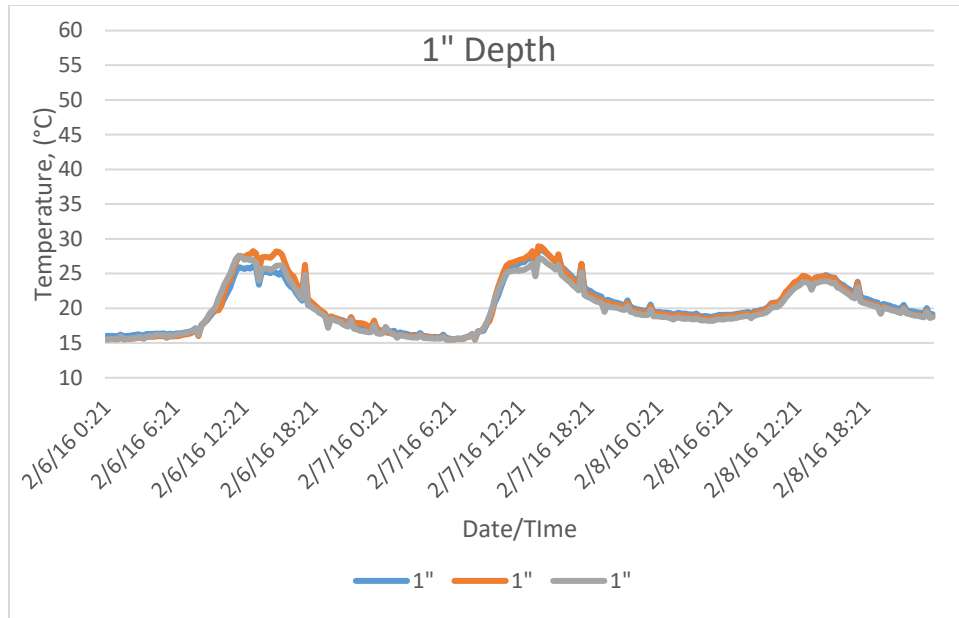


Figure 62: Diurnal pattern of the 1 inch depth thermocouple temperature for each probe (probe 1/blue/slab 2; probe 2/orange/slab 3; probe 3/gray/slab 4) for test period February 6, 2016 – February 8, 2016

Figure 62 shows the diurnal pattern of the 1" deep thermocouple for the testing period February 6, 2016 – February 8, 2016. The maximum temperature for the three-day period was 26.1°C (79°F) and the minimum temperature was 15.6°C (60.1°F). The variability within the measurements at this depth was as much as 10.5°C (18.9°F).

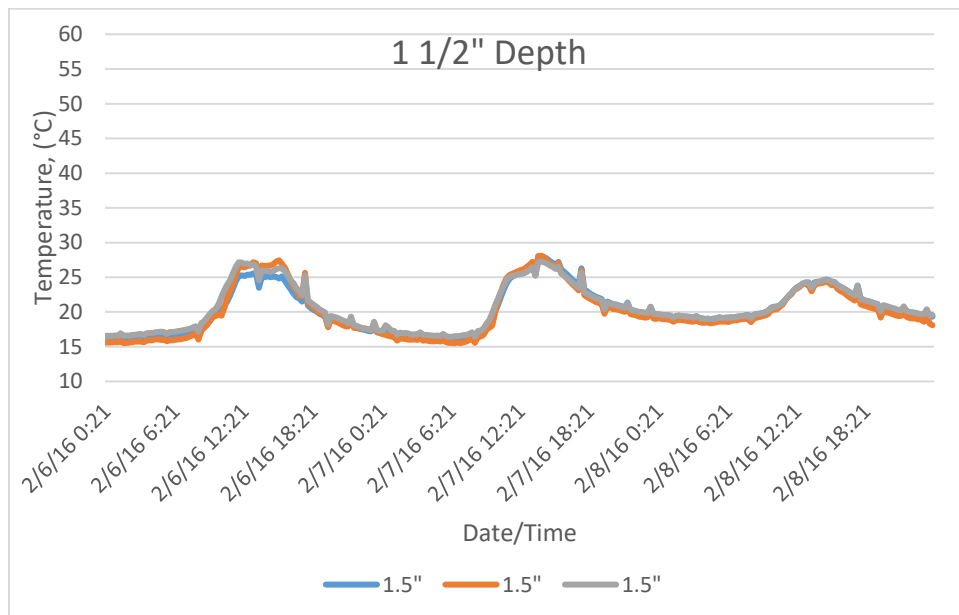
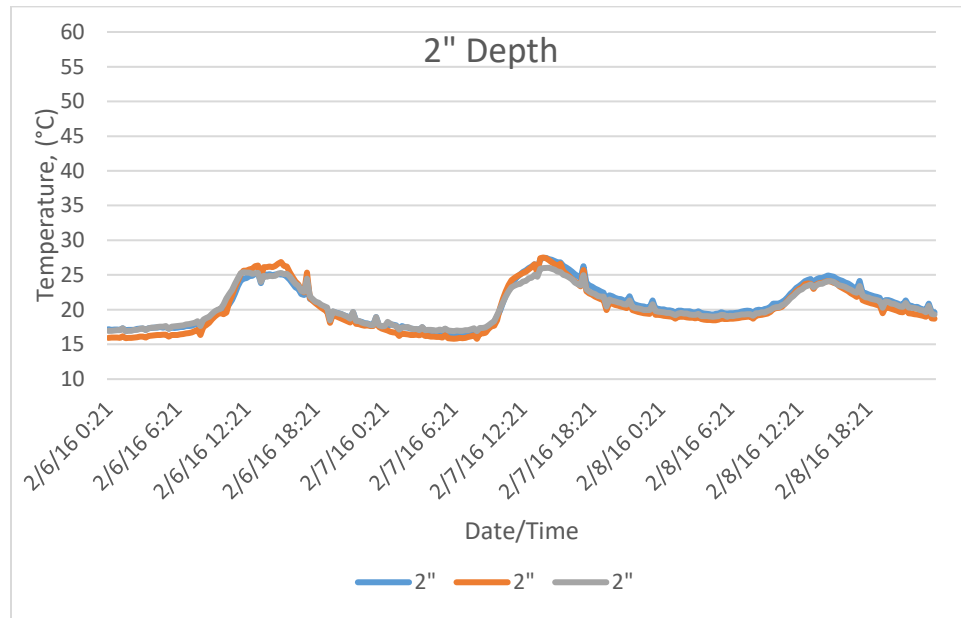


Figure 63: Diurnal pattern of the 1 ½ inch depth thermocouple temperature for each probe (probe 1/blue/slab 2; probe 2/orange/slab 3; probe 3/gray/slab 4) for test period February 6, 2016 – February 8, 2016

Figure 63 shows the diurnal pattern of the 1.5" deep thermocouple for the testing period February 6, 2016 – February 8, 2016. The maximum temperature for the three-day period was 26.9°C (80.4°F) and the minimum temperature was 16.6°C (61.9°F). The variability within the measurements at this depth was as much as 10.3°C (18.5°F).



**Figure 64: Diurnal pattern of the 2 inch depth thermocouple temperature for each probe (probe 1/blue/slab 2; probe 2/orange/slab 3; probe 3/gray/slab 4) for test period February 6, 2016 – February 8, 2016**

Figure 64 shows the diurnal pattern of the 2" deep thermocouple for the testing period February 6, 2016 – February 8, 2016. The maximum temperature for the three-day period was 26.8°C (80.2°F) and the minimum temperature was 16.9°C (64.4°F). The variability within the measurements at this depth was as much as 13.3°C (15.8°F).

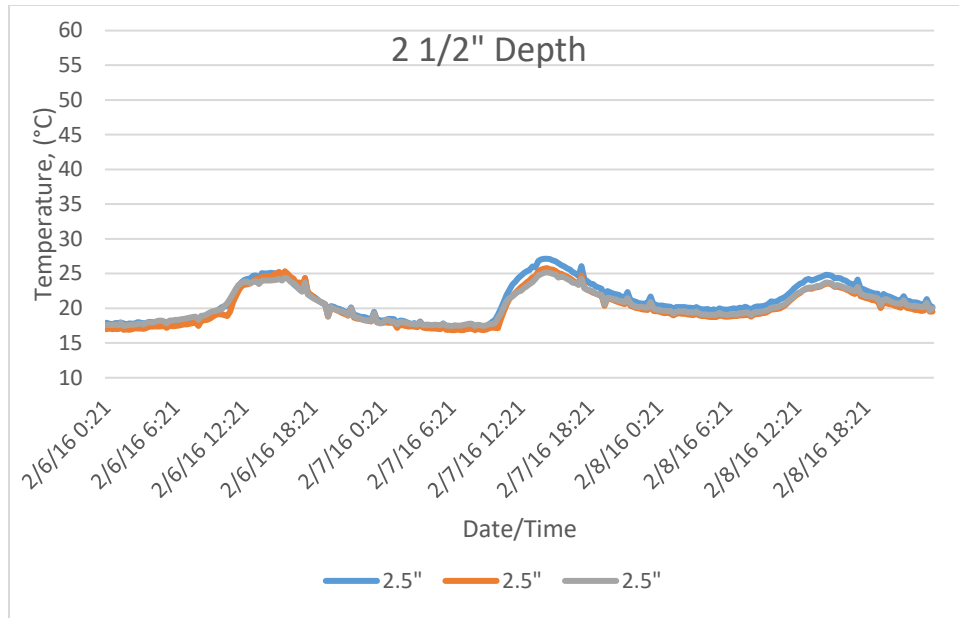


Figure 65: Diurnal pattern of the 2 1/2 inch depth thermocouple temperature for each probe (probe 1/blue/slab 2; probe 2/orange/slab 3; probe 3/gray/slab 4) for test period February 6, 2016 – February 8, 2016

Figure 65 shows the diurnal pattern of the 2.5" deep thermocouple for the testing period February 6, 2016 – February 8, 2016. The maximum temperature for the three-day period was 25.1°C (77.2°F) and the minimum temperature was 17.4°C (63.3°F). The variability within the measurements at this depth was as much as 7.7°C (13.9°F).

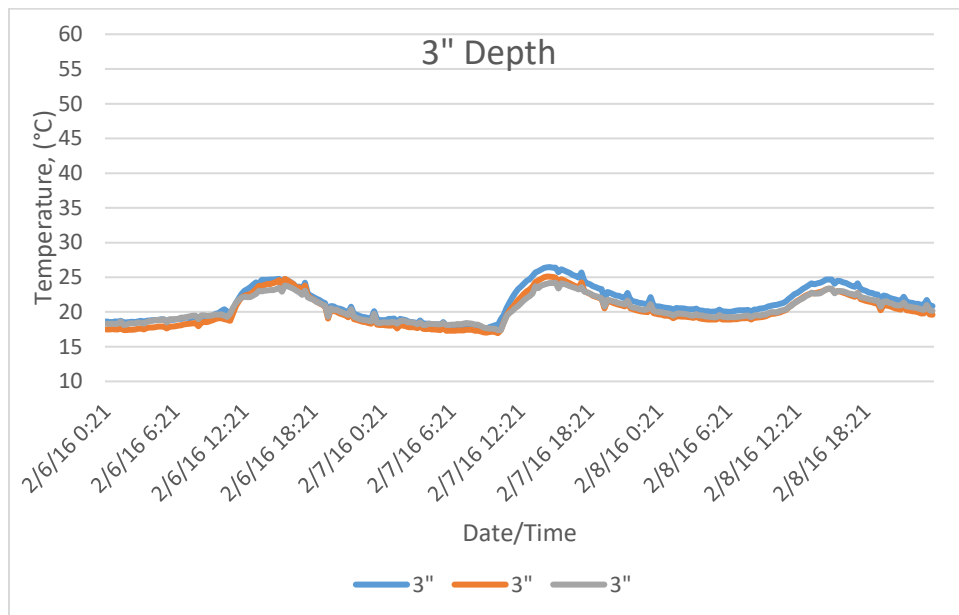


Figure 66: Diurnal pattern of the 3 inch depth thermocouple temperature for each probe (probe 1/blue/slab 2; probe 2/orange/slab 3; probe 3/gray/slab 4) for test period February 6, 2016 – February 8, 2016

Figure 66 shows the diurnal pattern of the 3" deep thermocouple for the testing period February 6, 2016 – February 8, 2016. The maximum temperature for the three-day period was 24.1°C (75.4°F) and the minimum temperature was 17.6°C (63.7°F). The variability within the measurements at this depth was as much as 6.5°C (11.7°F).

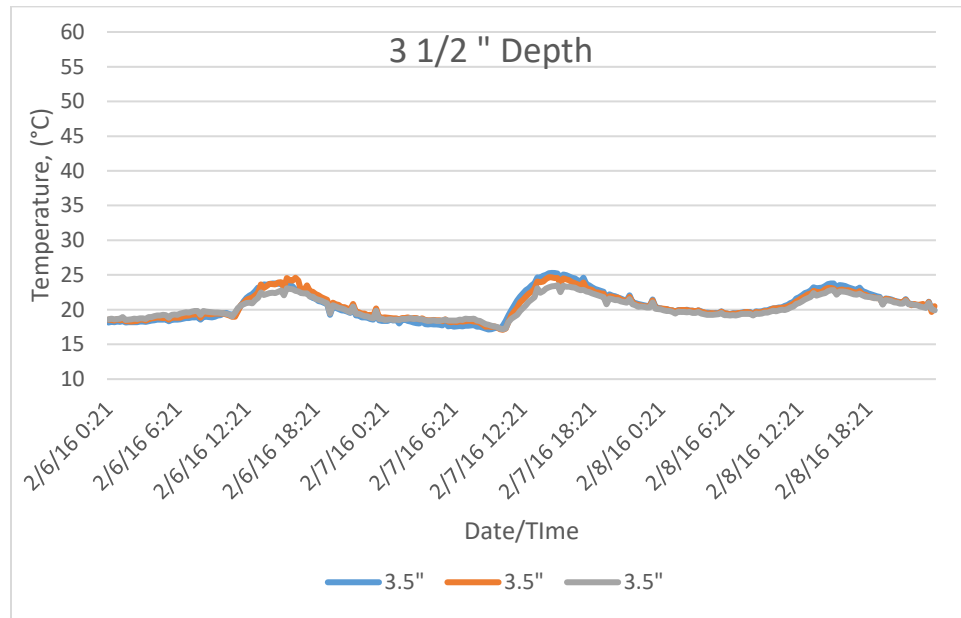
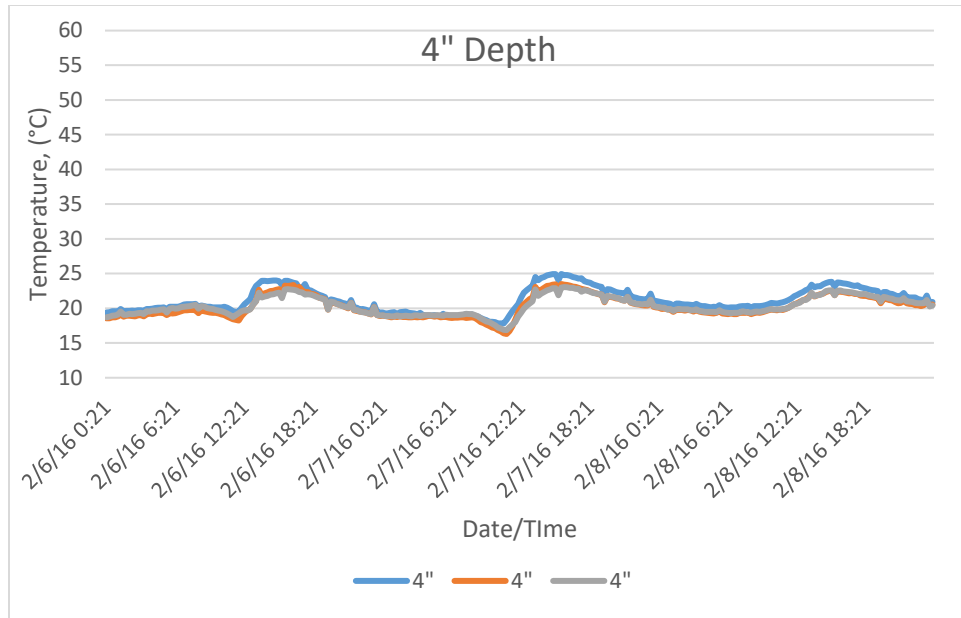


Figure 67: Diurnal pattern of the 3 ½ inch depth thermocouple temperature for each probe (probe 1/blue/slab 2; probe 2/orange/slab 3; probe 3/gray/slab 4) for test period February 6, 2016 – February 8, 2016

Figure 67 shows the diurnal pattern of the 3.5" deep thermocouple for the testing period February 6, 2016 – February 8, 2016. The maximum temperature for the three-day period was 24.1°C (75.4°F) and the minimum temperature was 17.2°C (63°F). The variability within the measurements at this depth was as much as 6.9°C (12.4°F).



**Figure 68: Diurnal pattern of the 4 inch depth thermocouple temperature for each probe (probe 1/blue/slab 2; probe 2/orange/slab 3; probe 3/gray/slab 4) for test period February 6, 2016 – February 8, 2016**

Figure 68 shows the diurnal pattern of the 4" deep thermocouple for the testing period February 6, 2016 – February 8, 2016. The maximum temperature for the three-day period was 24.8°C (76.6°F) and the minimum temperature was 17.0°C (62.6°F). The variability within the measurements at this depth was as much as 7.8°C (14°F).

## April 16, 2016 – April 18, 2016

Within this section, the data compiled for the thermocouples for the testing period from April 16 - April 18, 2016. As expected, there is a noticeable diurnal pattern to the heating and cooling of the slab and surrounding ground surface, shown in Figures 69, 70, and 71. The ground surface temperature for the three-day period fluctuated between 1.1°C (34°F) to 16.7°C (62.1°F) throughout the three day period. The ambient temperature fluctuated between -12.7°C (9.1°F) nighttime to 8.8°C (47.8°F) daytime. There is a noticeable lag in both the heating and cooling portion of the temperature plots, due to the coefficient of thermal conductivity of the asphalt slab. The 0.25" embedded thermocouple recorded temperature as high as 54.6°C (130.2°F) on April 18, 2016. This measurement period was chosen to evaluate as a mid-range temperature scenario.

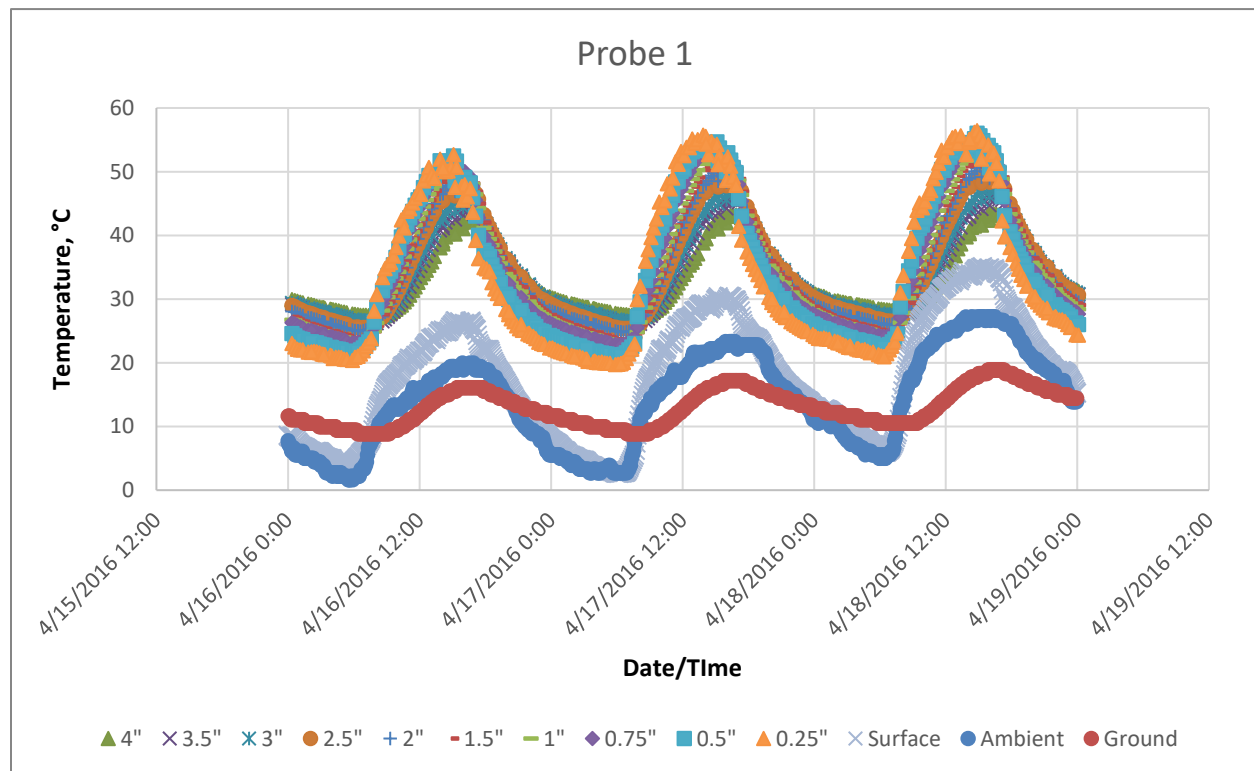
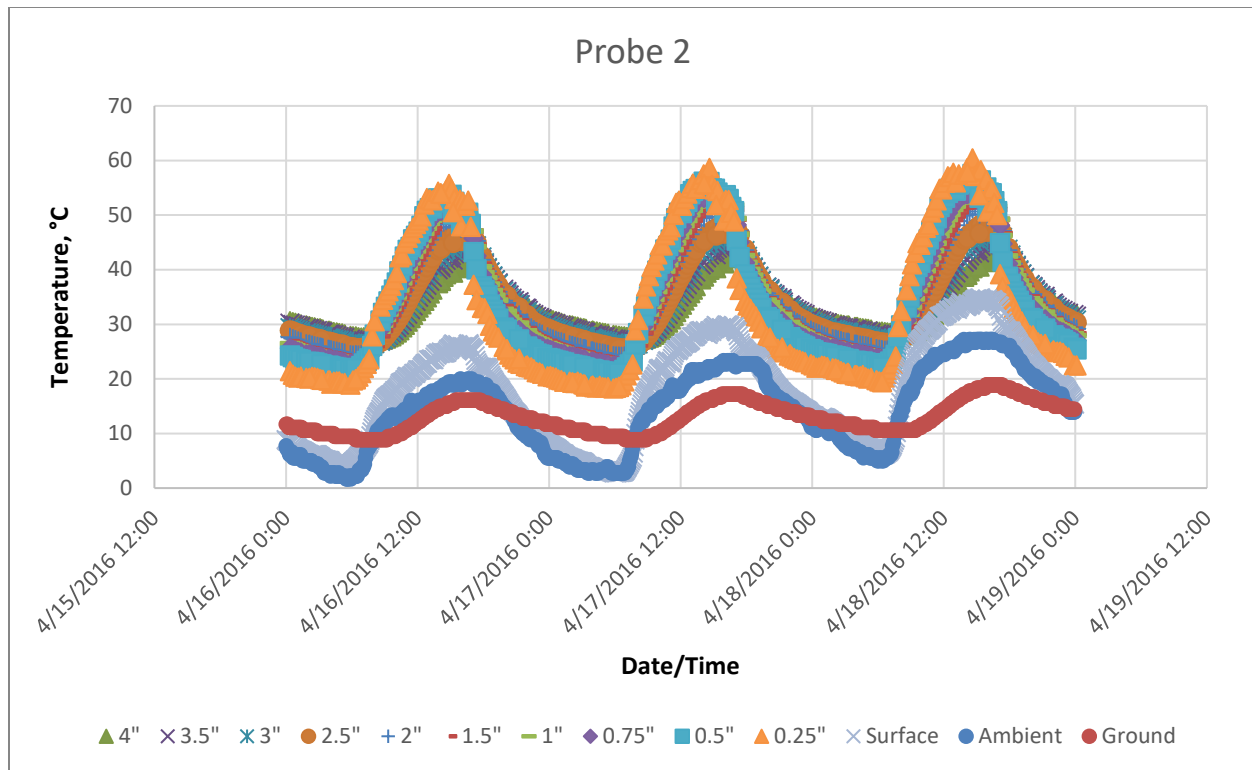


Figure 69: Diurnal pattern of thermocouple probe 1 in slab sample 2 for testing period April 16 - April 18, 2016 compared to 4" soil depth, NR01 infrared surface temp, and ambient temp



**Figure 70: Diurnal pattern of thermocouple probe 2 in slab sample 3 for testing period April 16 - April 18, 2016 compared to 4" soil depth, NR01 infrared surface temp, and ambient temp**

The April 16 – April 18 test period temperature analysis revealed that the 4" ground temperature did not fluctuate as much as it had in the July test period. The slab surface temperature dipped as low as 4.7°C (40.6°F) throughout the night, but remained to a temperature slightly warmer than the ambient temperature throughout the test period. The surface temperature dipped as low as the ambient temperature, but during the daytime increased by as much as 6.9 degrees higher than the ambient temperature, as shown in Figure 70. The surface temperature always remained cooler than the interior slab temperatures.



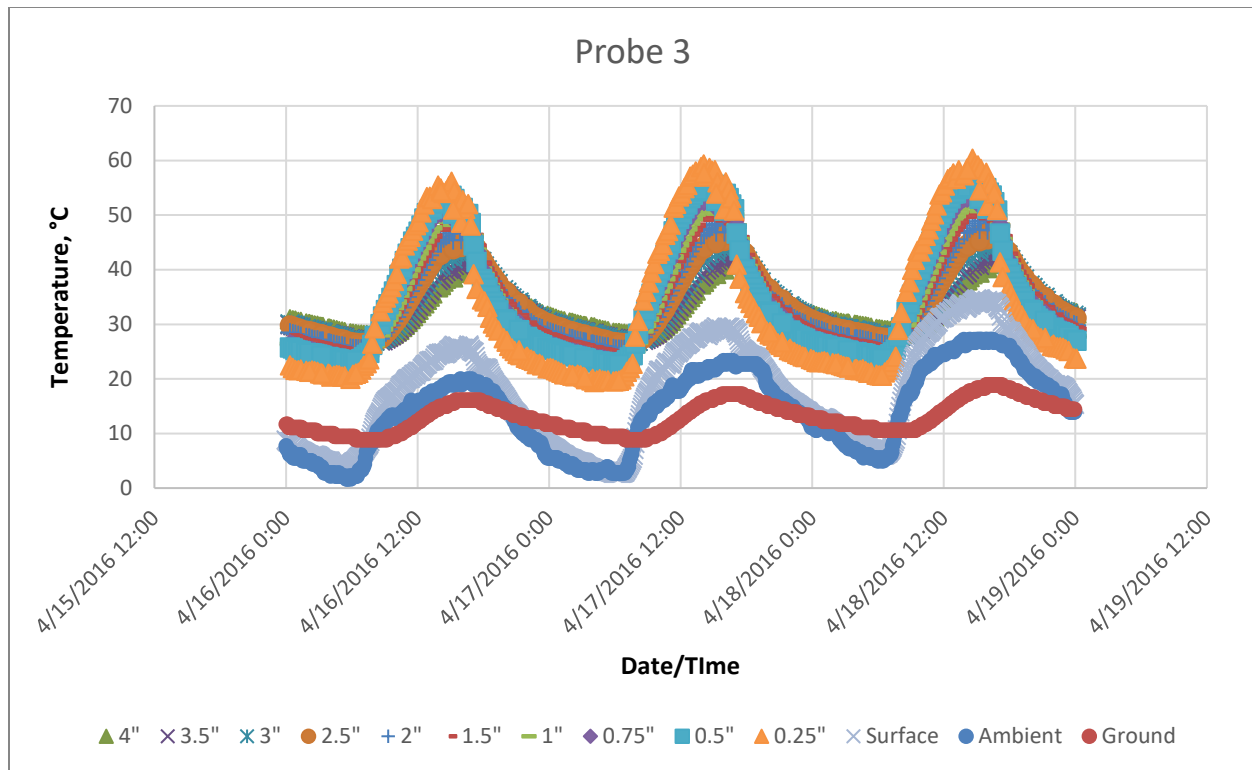


**Figure 71: Diurnal pattern of thermocouple probe 3 in slab sample 4 for testing period April 16 - April 18, 2016 compared to 4" soil depth, NR01 infrared surface temp, and ambient temp**

Although the three slabs were under similar conditions, slab three was shaded by the building in the morning for a period of less than half an hour. That short period of time had a noticeable effect on the rate of cooling, shown in Figure 71. The rate of cooling in the slab thermocouples compared to the other two slabs shows the pronounced influence that the solar energy had on the slab. To further evaluate the differences between the slab temperatures, the maximum and minimum for each slab was calculated for each depth and shown in Figure 72.

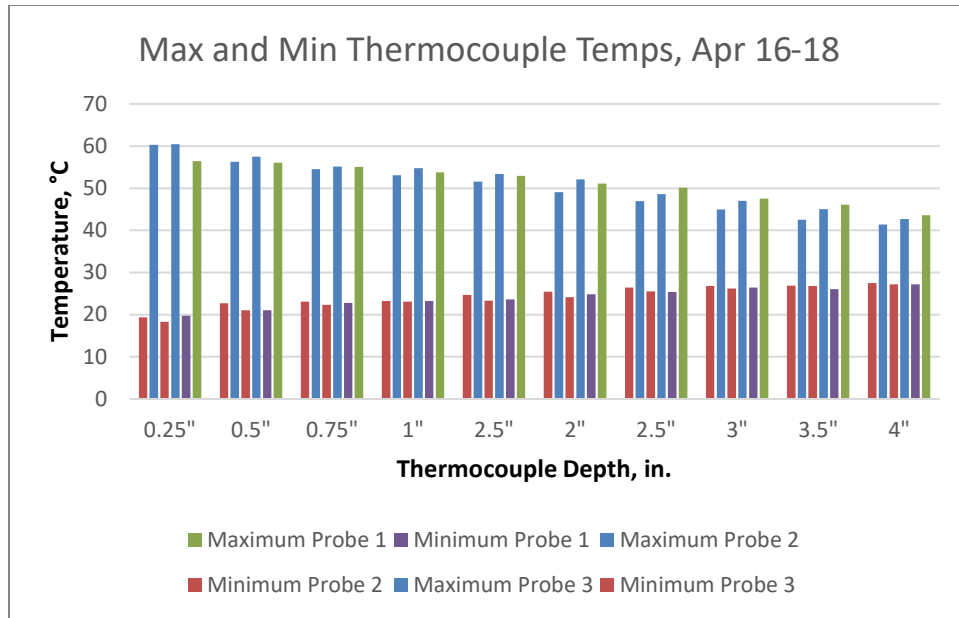


Figure 72: Maximum and minimum temperatures for each thermocouple probe at each depth for testing period April 16, 2016- April 18, 2016

Figure 72 shows that a four-inch thick slab measuring one meter square, with the sides and top exposed will retain heat above ambient levels throughout the night. Measurements from 2-inch depth through 4-inch depth indicate that the temperature from that portion of the slab became similar to the ambient temperature throughout the nighttime. The 4 inch depth was the least susceptible to temperature fluctuations, but still had a daily variability of over 16.3°C (27.5°F). The top portion of the slab had a higher overall variability at approximately 40.9°C (73.8°F), which was seen from nighttime and daytime levels. The minimum measured temperature for the 0.25-inch depth thermocouple was 18.2°C (64.8°F), approximately 17 degrees higher than the ambient temperature.

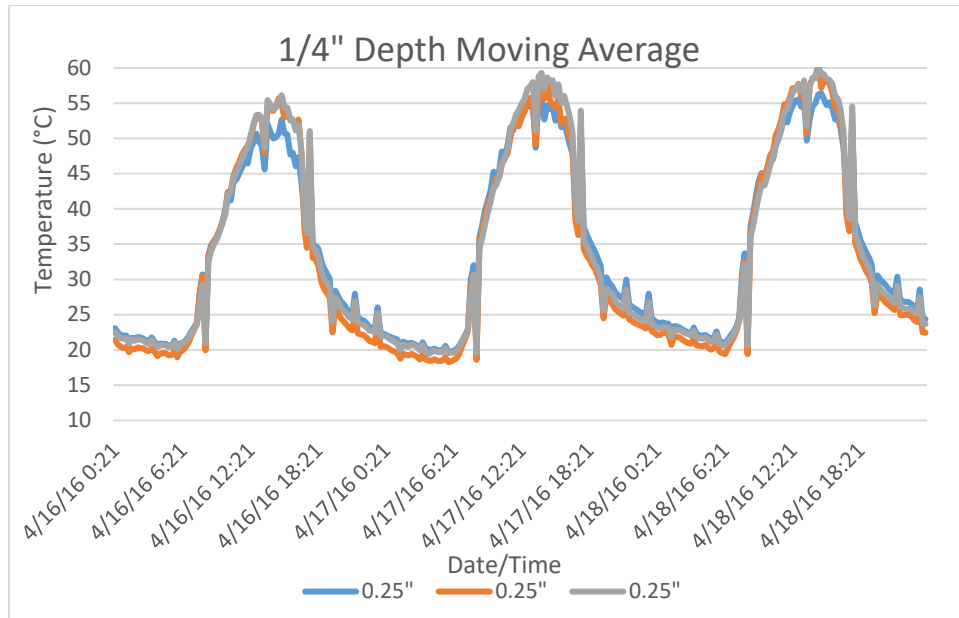


Figure 73: Diurnal pattern of the ¼ inch depth thermocouple temperature for each probe (probe 1/blue/slab 2; probe 2/orange/slab 3; probe 3/gray/slab 4) for test period April 16, 2016 – April 18, 2016

Figure 73 shows the diurnal pattern of the 0.25" deep thermocouple for the testing period April 16, 2016 – April 8, 2018. The maximum temperature for the three-day period was 59.1°C (138.4°F) and the minimum temperature was 19.6°C (67.3°F). Each of the three slabs exhibited similar results. The similarity between the three slabs at 0.25" shows that the material properties influenced the temperature of the mix significantly. Since each of the three slabs had the same aggregate gradation and binder type, there was good coherence between the slabs.

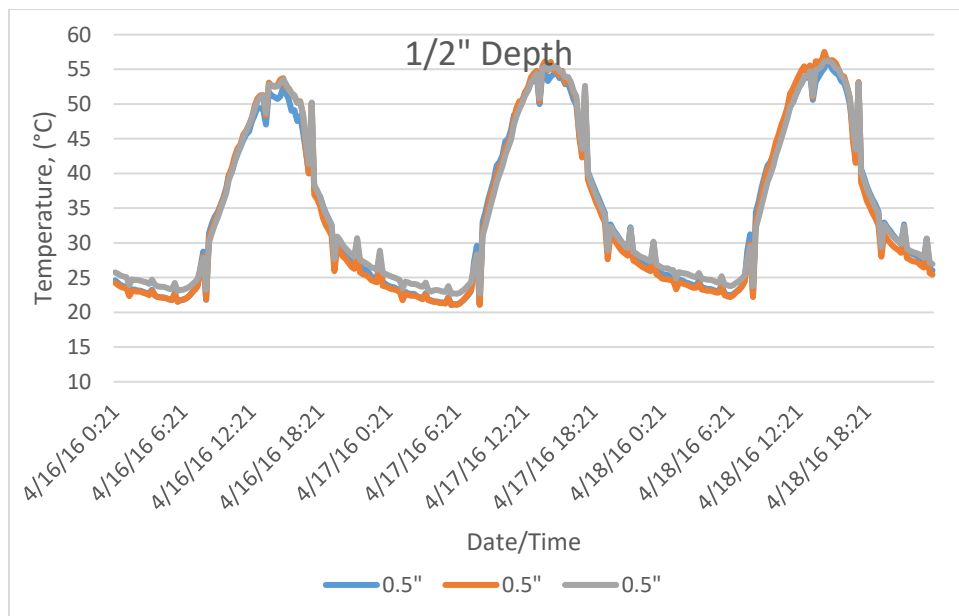
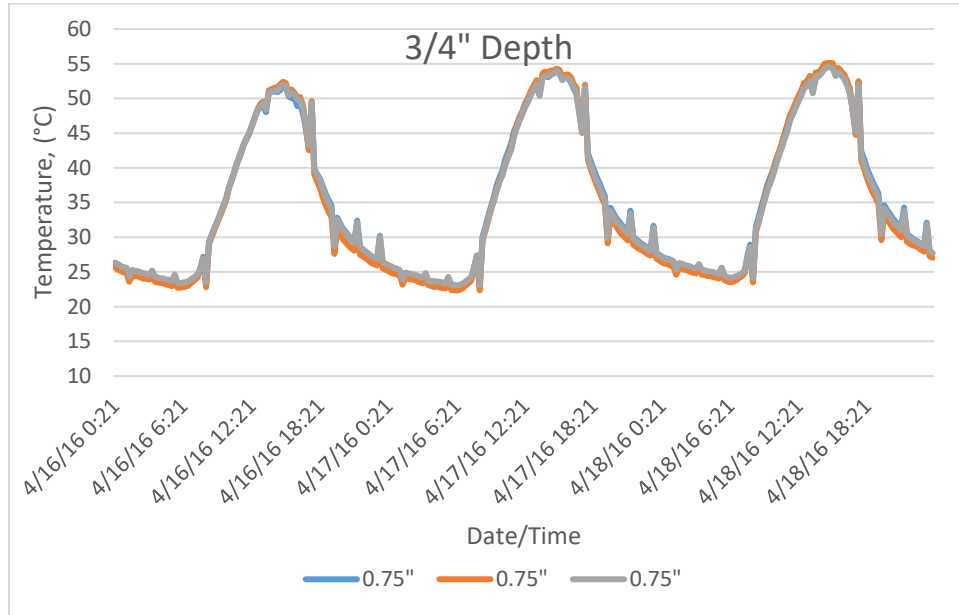


Figure 74: Diurnal pattern of the ½ inch depth thermocouple temperature for each probe (probe 1/blue/slab 2; probe 2/orange/slab 3; probe 3/gray/slab 4) for test period April 16, 2016 – April 18, 2016

Figure 74 shows the diurnal pattern of the 0.5" deep thermocouple for the testing period April 16, 2016 – April 18, 2016. The maximum temperature for the three-day period was 55.9°C (132.6°F) and the minimum temperature was 22.8°C (73.0°F). The variability within the measurements at this depth was as much as 33.1°C (59.6°F).



**Figure 75: Diurnal pattern of the ¾ inch depth thermocouple temperature for each probe (probe 1/blue/slab 2; probe 2/orange/slab 3; probe 3/gray/slab 4) for test period April 16, 2016 – April 18, 2016**

Figure 75 shows the diurnal pattern of the 0.75" deep thermocouple for the testing period April 16, 2016 – April 18, 2016. The maximum temperature for the three-day period was 54.4°C (129.9°F) and the minimum temperature was 23.1°C (73.6°F). The variability within the measurements at this depth was as much as 31.3°C (56.3°F).

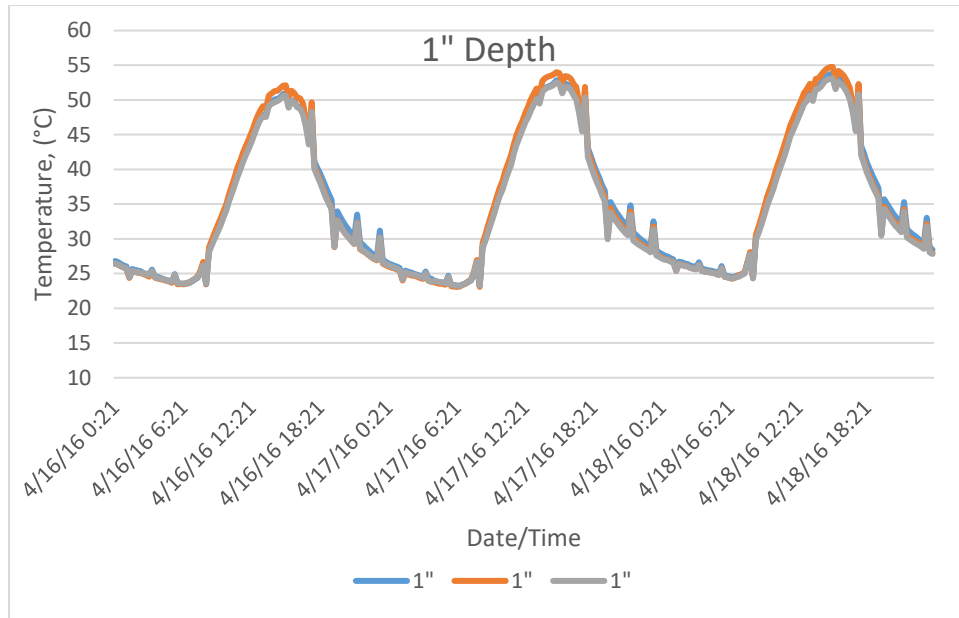


Figure 76: Diurnal pattern of the 1 inch depth thermocouple temperature for each probe (probe 1/blue/slab 2; probe 2/orange/slab 3; probe 3/gray/slab 4) for test period April 16, 2016 – April 18, 2016

Figure 76 shows the diurnal pattern of the 1" deep thermocouple for the testing period April 16, 2016 – April 18, 2016. The maximum temperature for the three-day period was 52.6°C (126.7°F) and the minimum temperature was 23.4°C (74.1°F). The variability within the measurements at this depth was as much as 29.2°C (52.6°F).

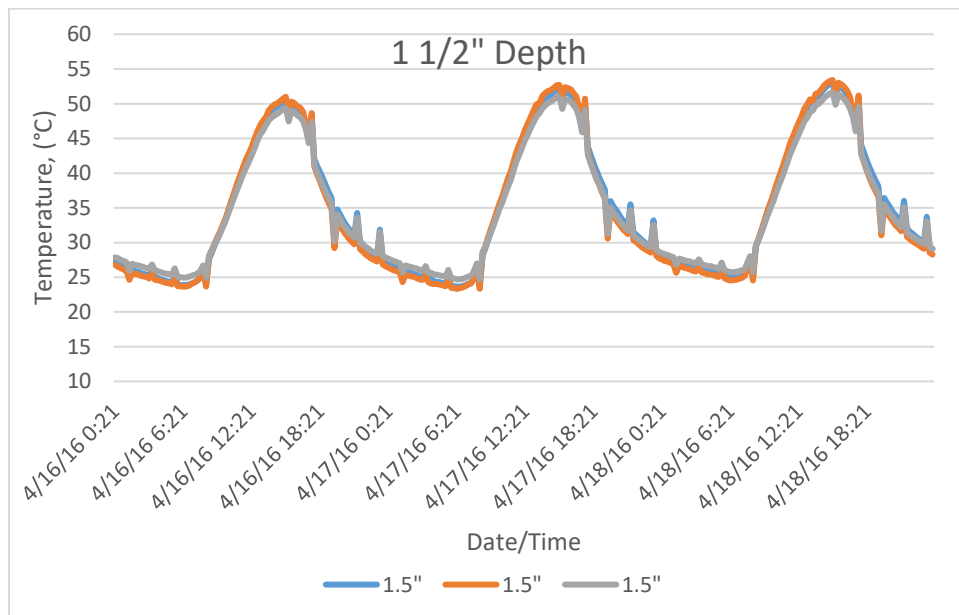
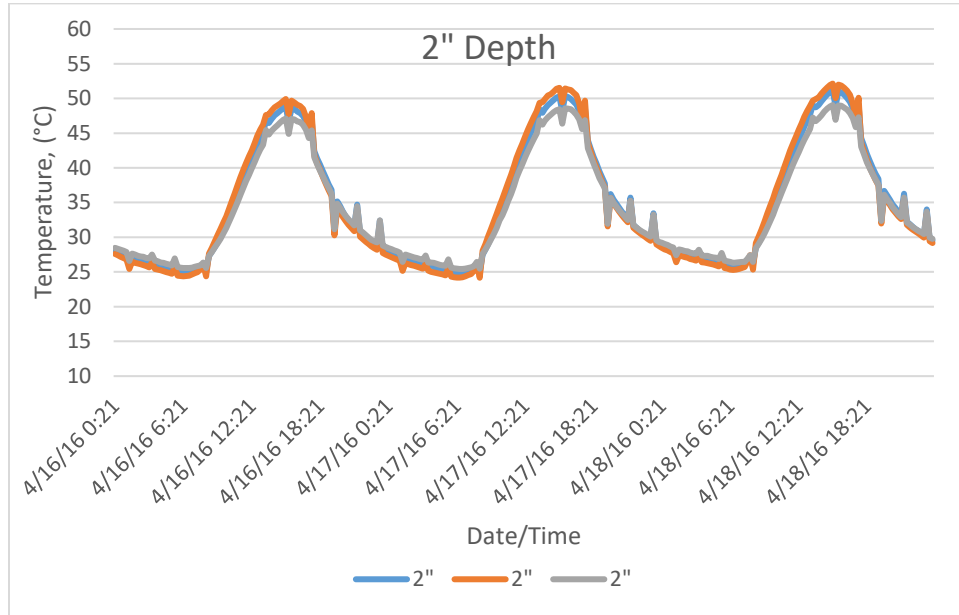


Figure 77: Diurnal pattern of the 1 ½ inch depth thermocouple temperature for each probe (probe 1/blue/slab 2; probe 2/orange/slab 3; probe 3/gray/slab 4) for test period April 16, 2016 – April 18, 2016

Figure 77 shows the diurnal pattern of the 1.5" deep thermocouple for the testing period April 16, 2016 – April 18, 2016. The maximum temperature for the three-day period was 53.4°C (128.1°F) and the minimum temperature was 24.7°C (76.5°F). The variability within the measurements at this depth was as much as 28.7°C (51.6°F).



**Figure 78: Diurnal pattern of the 2 inch depth thermocouple temperature for each probe (probe 1/blue/slab 2; probe 2/orange/slab 3; probe 3/gray/slab 4) for test period April 16, 2016 – April 18, 2016**

Figure 78 shows the diurnal pattern of the 2" deep thermocouple for the testing period April 16, 2016 – April 18, 2016. The maximum temperature for the three-day period was 52.0°C (125.6°F) and the minimum temperature was 25.5°C (77.9°F). The variability within the measurements at this depth was as much as 26.5°C (45.7°F).

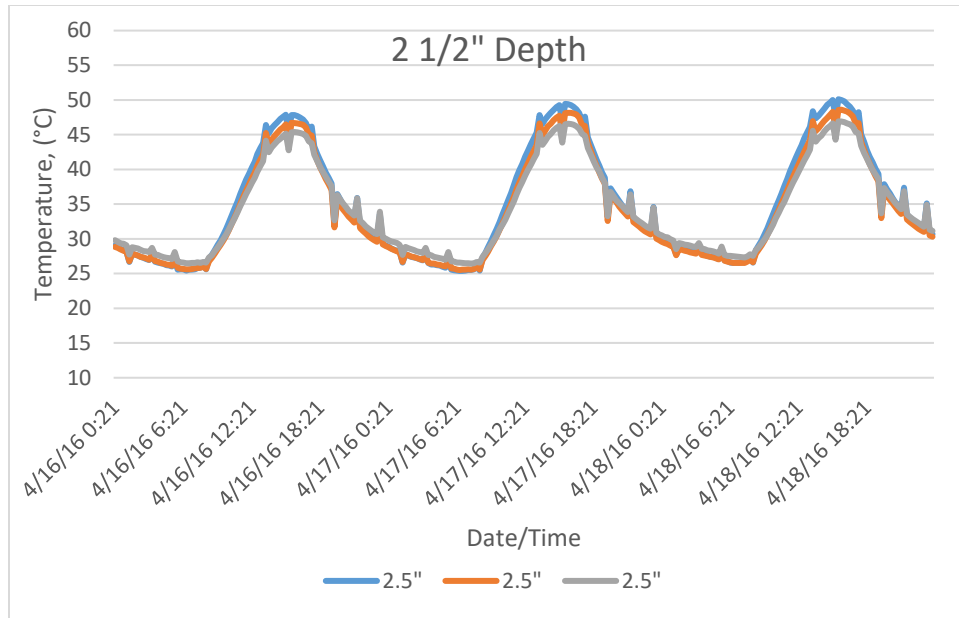


Figure 79: Diurnal pattern of the 2 1/2 inch depth thermocouple temperature for each probe (probe 1/blue/slab 2; probe 2/orange/slab 3; probe 3/gray/slab 4) for test period April 16, 2016 – April 18, 2016

Figure 79 shows the diurnal pattern of the 2.5" deep thermocouple for the testing period April 16, 2016 – April 18, 2016. The maximum temperature for the three-day period was 48.3°C (118.9°F) and the minimum temperature was 26.6°C (79.9°F). The variability within the measurements at this depth was as much as 21.7°C (39°F).

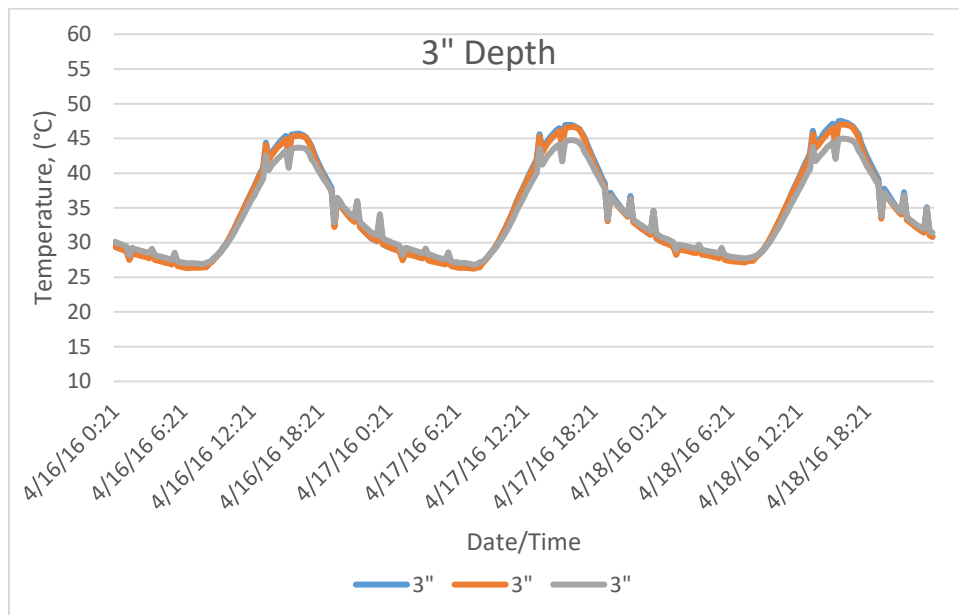
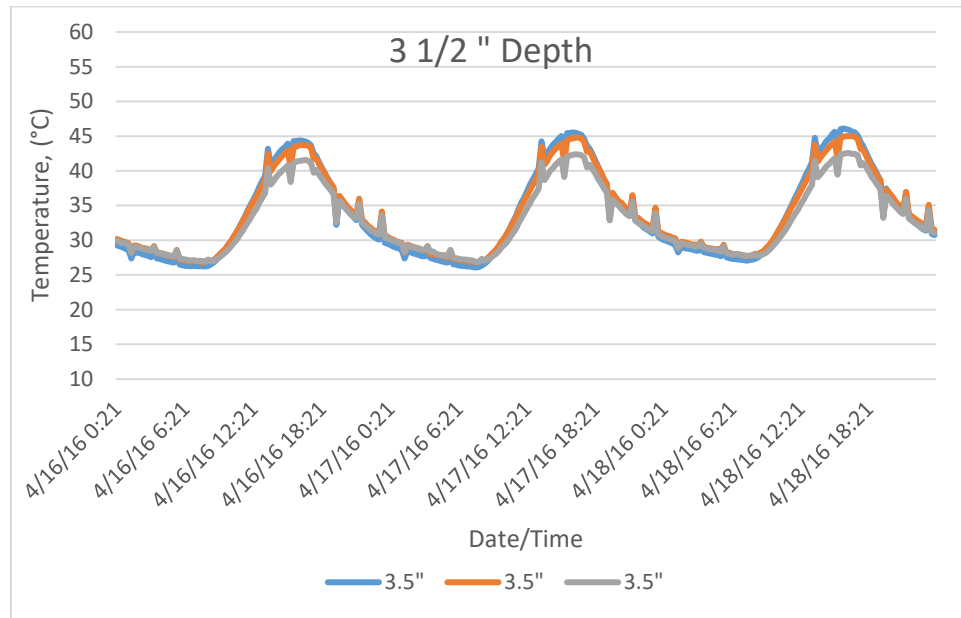


Figure 80: Diurnal pattern of the 3 inch depth thermocouple temperature for each probe (probe 1/blue/slab 2; probe 2/orange/slab 3; probe 3/gray/slab 4) for test period April 16, 2016 – April 18, 2016

Figure 80 shows the diurnal pattern of the 3" deep thermocouple for the testing period April 16, 2016 – April 18, 2016. The maximum temperature for the three-day period was 46.9°C (116.4°F) and the minimum temperature was 26.9°C (80.4°F). The variability within the measurements at this depth was as much as 20.0°C (36°F).



**Figure 81: Diurnal pattern of the 3 ½ inch depth thermocouple temperature for each probe (probe 1/blue/slab 2; probe 2/orange/slab 3; probe 3/gray/slab 4) for test period April 16, 2016 – April 18, 2016**

Figure 81 shows the diurnal pattern of the 3.5" deep thermocouple for the testing period April 16, 2016 – April 18, 2016. The maximum temperature for the three-day period was 45.0°C (113°F) and the minimum temperature was 26.9°C (80.4°F). The variability within the measurements at this depth was as much as 18.1°C (32.6°F).



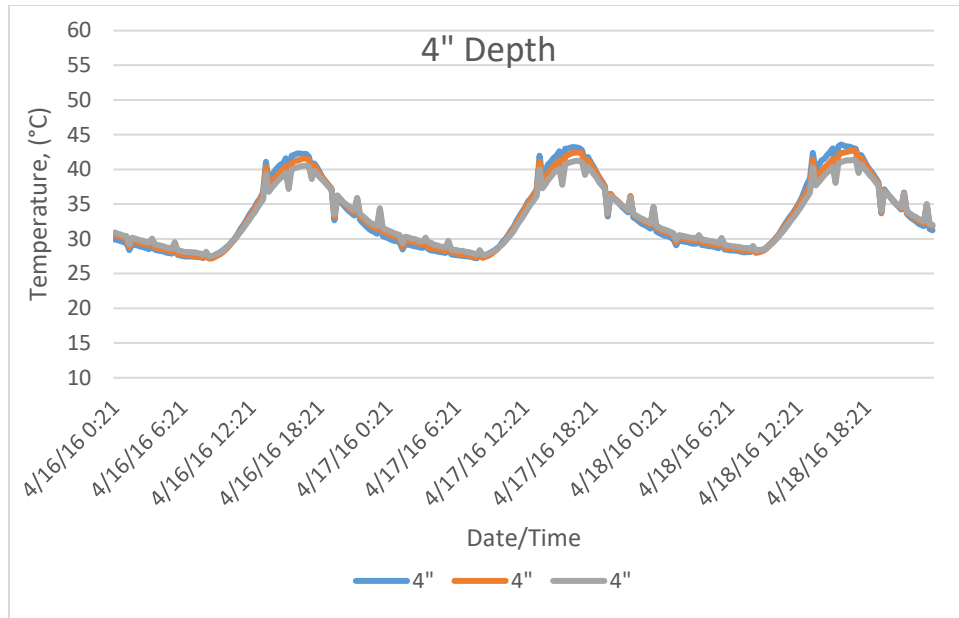


**Figure 82: Diurnal pattern of the 4 inch depth thermocouple temperature for each probe (probe 1/blue/slab 2; probe 2/orange/slab 3; probe 3/gray/slab 4) for test period April 16, 2016 – April 18, 2016**

Figure 82 shows the diurnal pattern of the 4" deep thermocouple for the testing period April 16, 2016 – April 18, 2016. The maximum temperature for the three-day period was 41.5°C (106.7°F) and the minimum temperature was 28.1°C (82.6°F). The variability within the measurements at this depth was as much as 13.4°C (24.1°F).

## ALBEDO

The data in this section reports the albedo comparisons measured for each asphalt slab. The albedo, or ratio of reflected radiation, for fresh asphalt is typically measured around 0.8 (Li, 2012). The three slabs measured, although similar in material and construction, measured slightly different values. This shows that samples tested for these materials should be conducted on multiple samples to validate measurements for a particular pavement type. The albedo measurements shown here are selected from the appropriate solar zenith as described in the Solar subsection within the Environmental Parameters section of this paper.

### July 31, 2015 – August 2, 2015

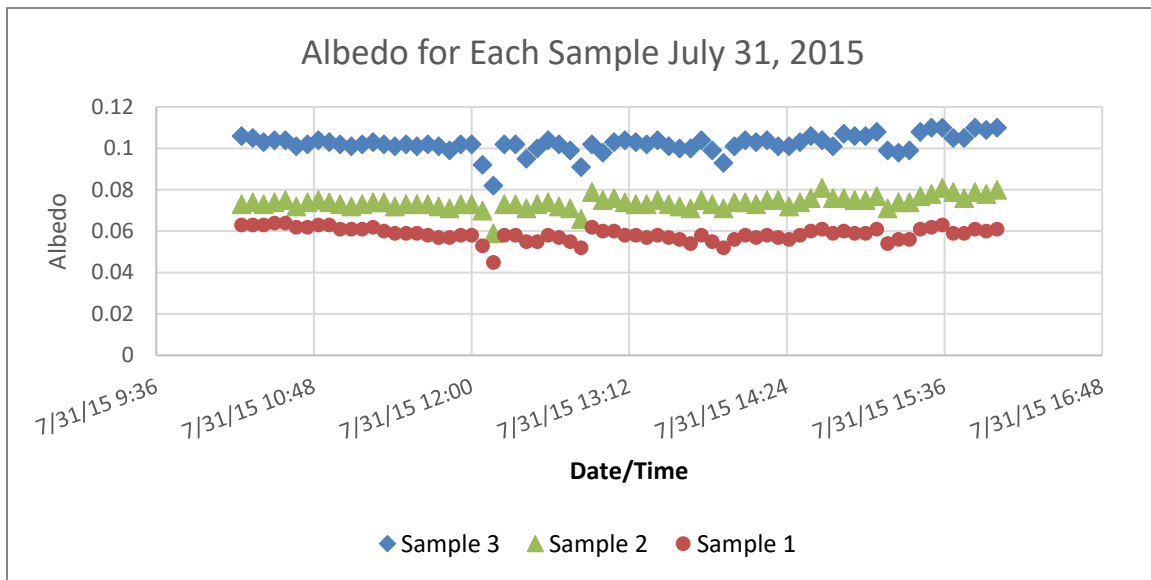


Figure 83: Comparison of 3 slabs albedo measurements for July 31, 2015

The albedo calculated for July 31, 2015 averaged 0.1 for sample 3, 0.073 for sample 2, and 0.054 for sample 1. The slight discrepancies throughout the test period indicate brief cloud cover, which is seen through each of the samples. The albedo remained relatively constant throughout the greater than 45° zenith period each day.

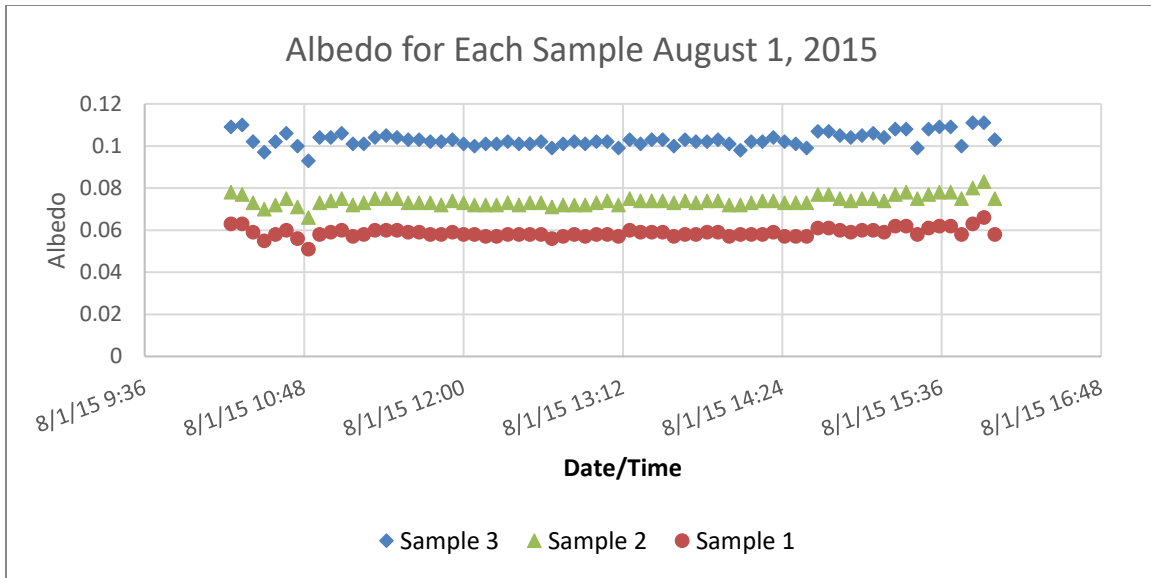


Figure 84: Comparison of 3 slabs albedo measurements for August 1, 2015

The albedo calculated for August 1, 2015 averaged 0.102 for sample 3, 0.072 for sample 2, and 0.057 for sample 1. The slight discrepancies throughout the test period indicate brief cloud cover, which is seen through each of the samples. The albedo remained relatively constant throughout the greater than 45° zenith period each day.

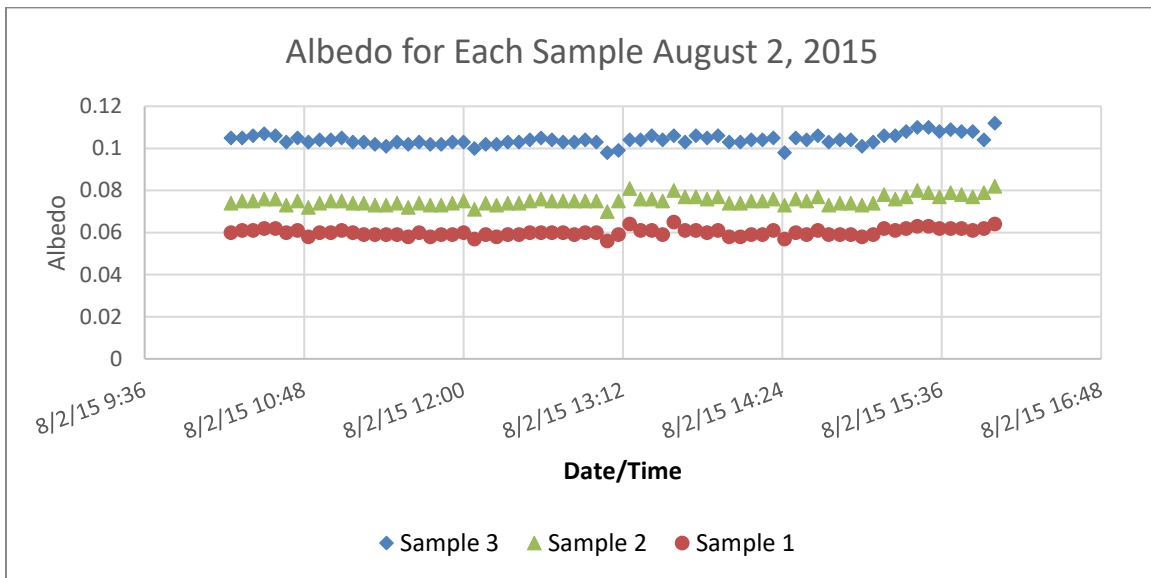


Figure 85: Comparison of 3 slabs albedo measurements for August 2, 2015

The albedo calculated for August 2, 2015 averaged 0.104 for sample 3, 0.075 for sample 2, and 0.06 for sample 1. The slight discrepancies throughout the test period indicate brief cloud cover, which is seen through each of the samples. The albedo remained relatively constant throughout the greater than 45° zenith period each day.

## January 4, 2016 – January 6, 2016

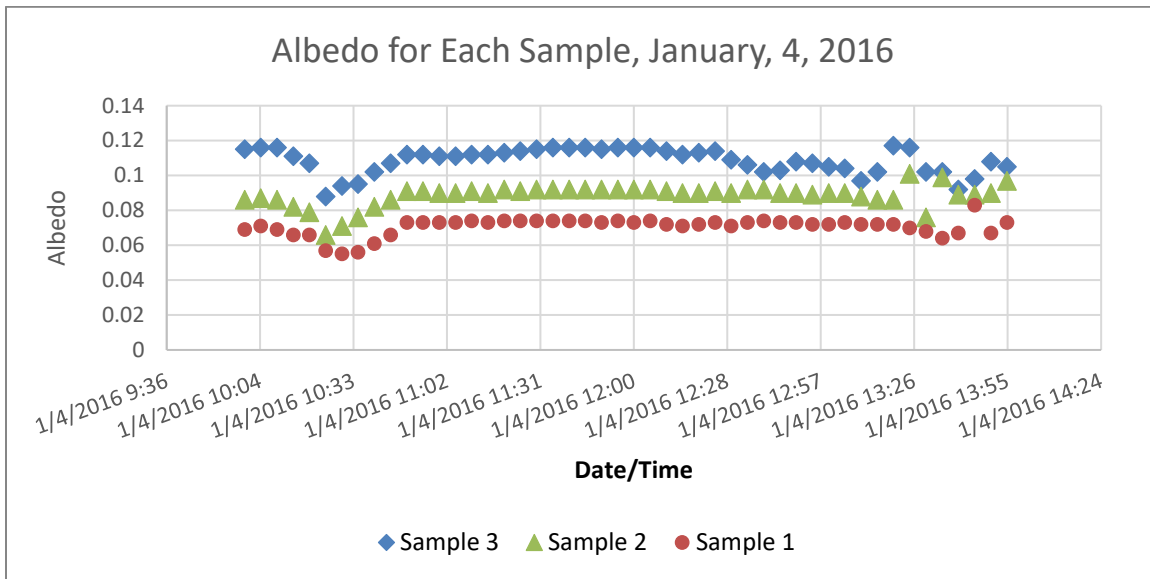


Figure 86: Comparison of 3 slabs albedo measurements for January 4, 2016

The albedo calculated for January 4, 2016 averaged 0.112 for sample 3, 0.092 for sample 2, and 0.073 for sample 1. The slight discrepancies throughout the test period indicate brief cloud cover, which is seen through each of the samples. The albedo remained relatively constant throughout the selected zenith period each day, since the zenith does not go above the recommended 45° angle.

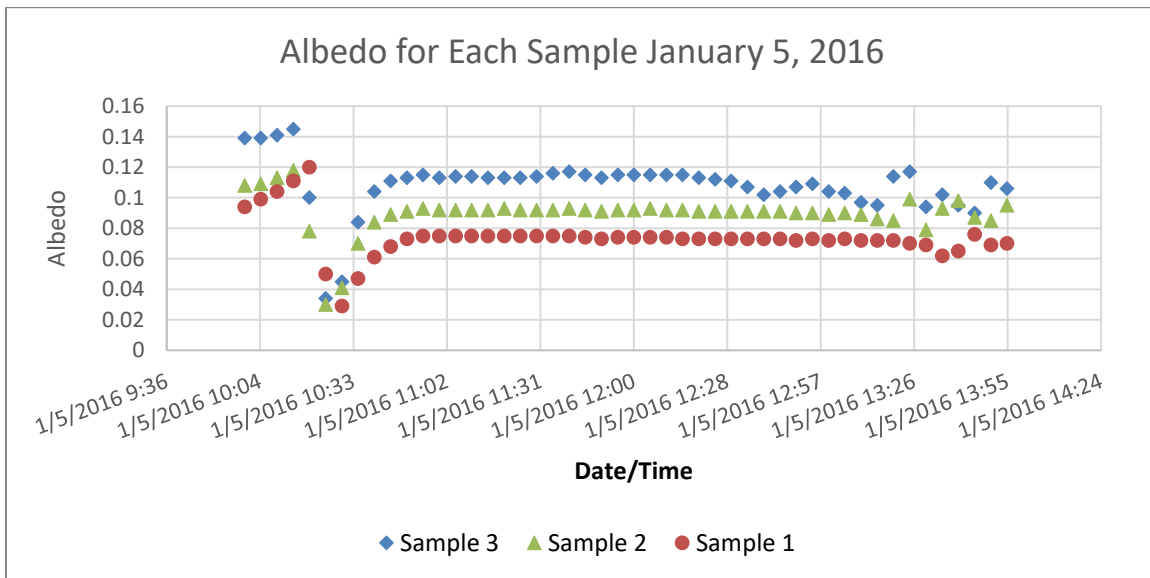


Figure 87: Comparison of 3 slabs albedo measurements for January 5, 2016

The albedo calculated for January 5, 2016 averaged 0.115 for sample 3, 0.092 for sample 2, and 0.074 for sample 1. The slight discrepancies throughout the test period indicate brief cloud cover, which is seen through each of the samples. The albedo remained relatively constant throughout the selected zenith

period each day, since the zenith does not go above the recommended 45° angle. There was significant cloud cover from 10:10 am through 10:40 am.

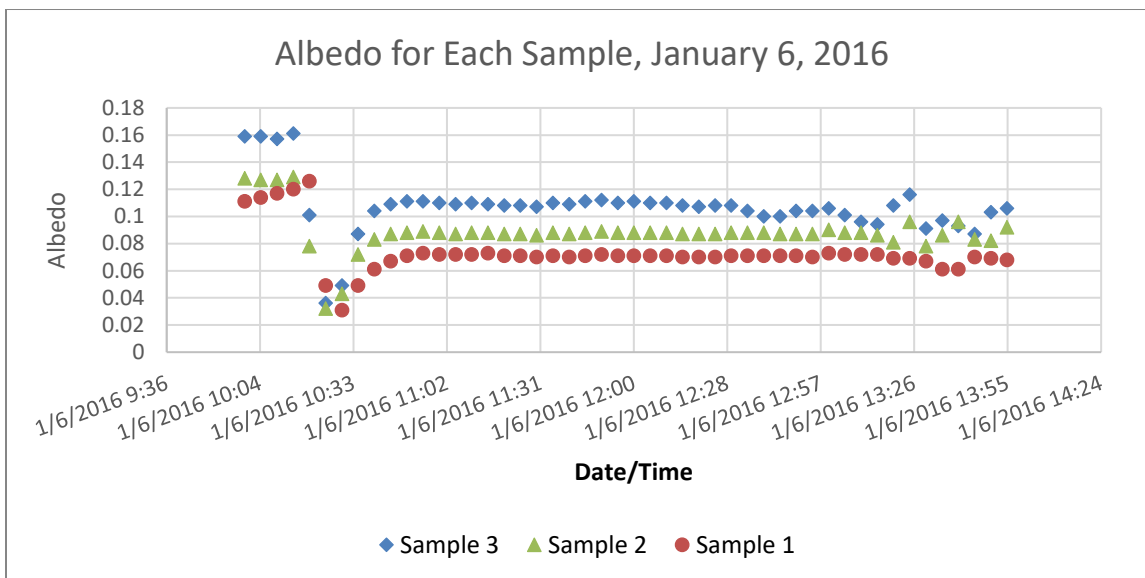


Figure 88: Comparison of 3 slabs albedo measurements for January 6, 2016

The albedo calculated for January 6, 2016 averaged 0.110 for sample 3, 0.087 for sample 2, and 0.072 for sample 1. The slight discrepancies throughout the test period indicate brief cloud cover, which is seen through each of the samples. The albedo remained relatively constant throughout the selected zenith period each day, since the zenith does not go above the recommended 45° angle.

## February 6 – February 8, 2016

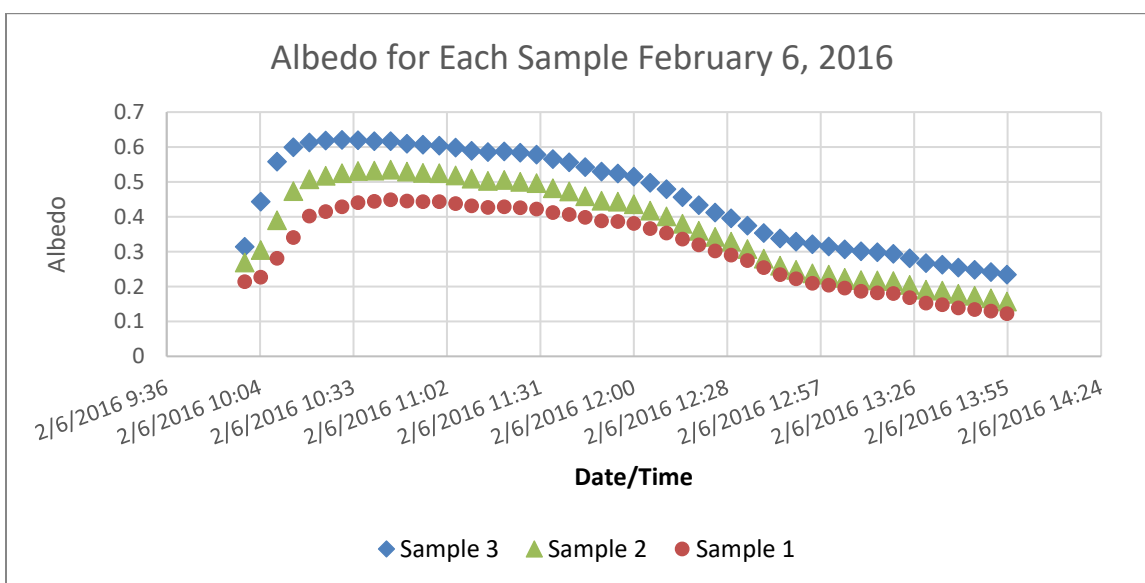


Figure 89: Comparison of 3 slabs albedo measurements for February 6, 2016

The albedo calculated for February 6, 2016 averaged 0.52 for sample 3, 0.45 for sample 2, and 0.381 for sample 1. The large discrepancy during this test period was a result of ice cover on the sample. Although the ice cover negates the validity of the data as a reportable metric, it was interesting to note here due to the effect it had on the asphalt slab.

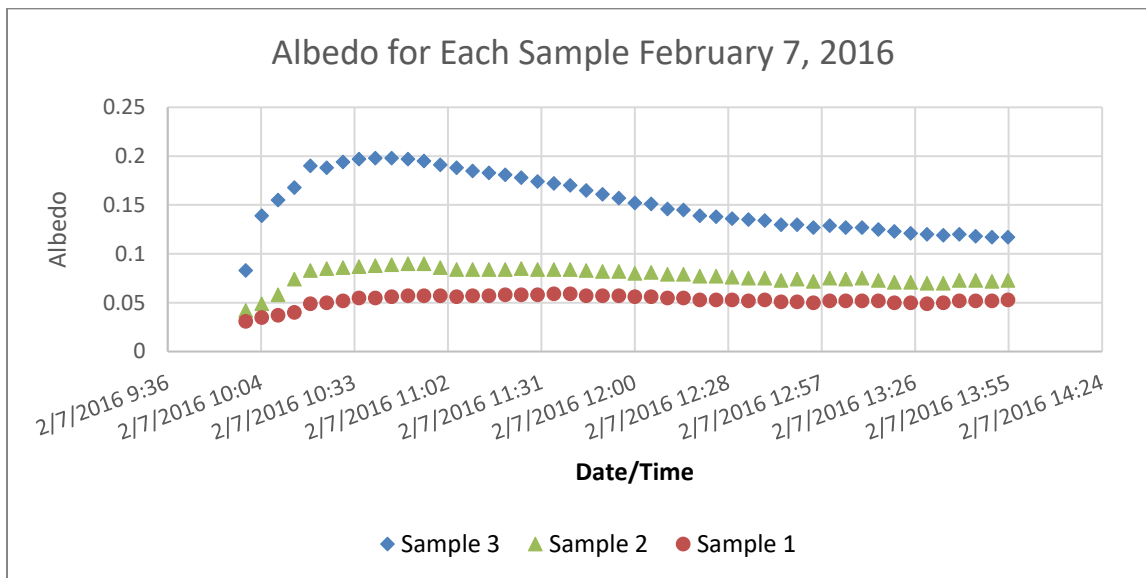


Figure 90: Comparison of 3 slabs albedo measurements for February 7, 2016

The albedo calculated for February 7, 2016 was still high from the day before, but was approaching standard levels by the end of the day. The albedo averaged 0.139 for sample 3, 0.08 for sample 2, and 0.058 for sample 1. The large discrepancy during this test period was a result of ice cover on the sample. Although the ice cover negates the validity of the data as a reportable metric, it was interesting to note here due to the effect it had on the asphalt slab.

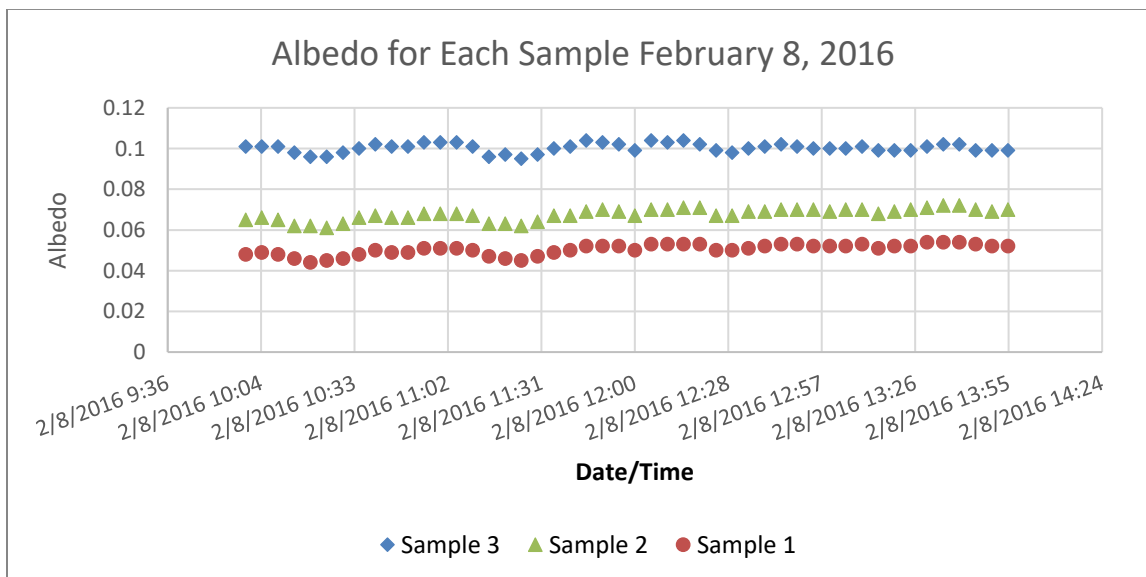


Figure 91: Comparison of 3 slabs albedo measurements for February 8, 2016

The albedo calculated for February 8, 2016 averaged 0.102 for sample 3, 0.067 for sample 2, and 0.052 for sample 1. The slight discrepancies throughout the test period indicate brief cloud cover, which is seen through each of the samples. The albedo remained relatively constant throughout the greater than 45° zenith period each day.

#### April 16, 2016 – April 18, 2016

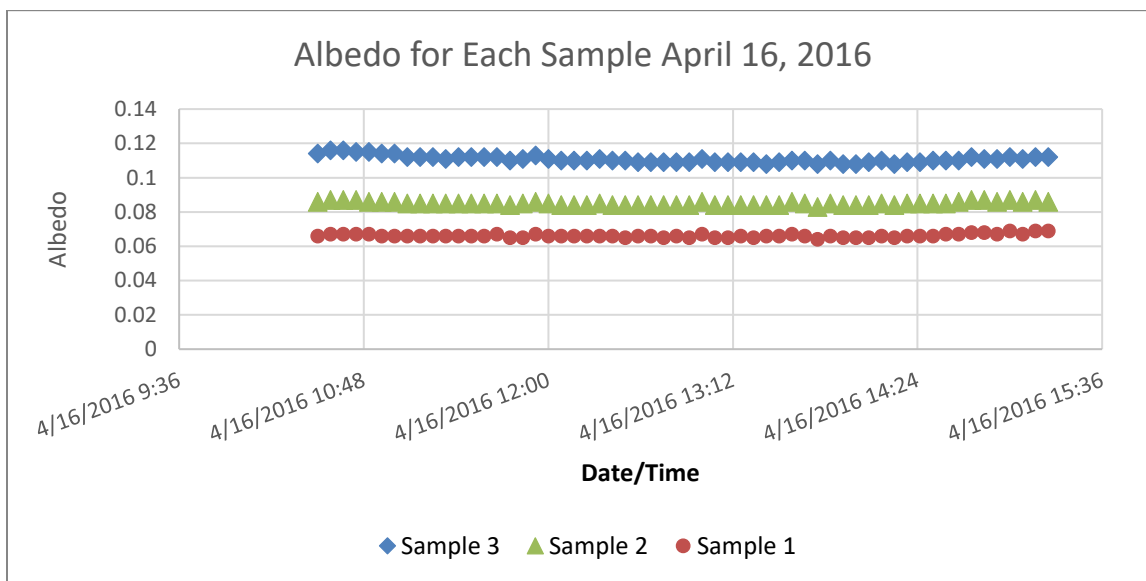


Figure 92: Comparison of 3 slabs albedo measurements for April 16, 2016

The albedo calculated for April 16, 2016 averaged 0.11 for sample 3, 0.084 for sample 2, and 0.065 for sample 1. The slight discrepancies throughout the test period indicate brief cloud cover, which is seen through each of the samples. The albedo remained relatively constant throughout the greater than 45° zenith period each day.

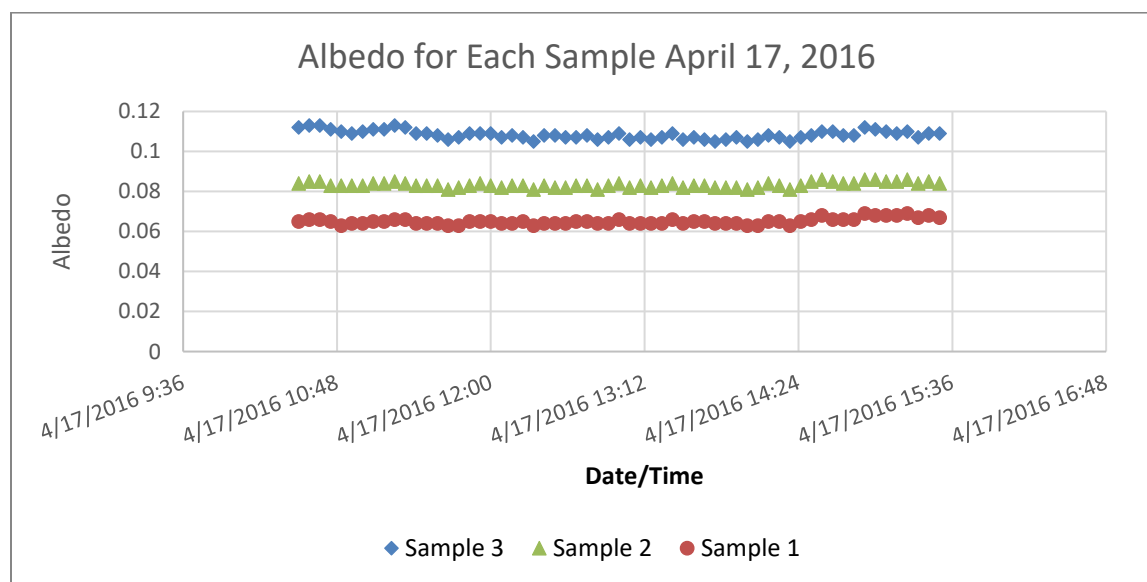


Figure 93: Comparison of 3 slabs albedo measurements for April 17, 2016

The albedo calculated for April 17, 2016 averaged 0.106 for sample 3, 0.081 for sample 2, and 0.064 for sample 1. The slight discrepancies throughout the test period indicate brief cloud cover, which is seen through each of the samples. The albedo remained relatively constant throughout the greater than 45° zenith period each day.

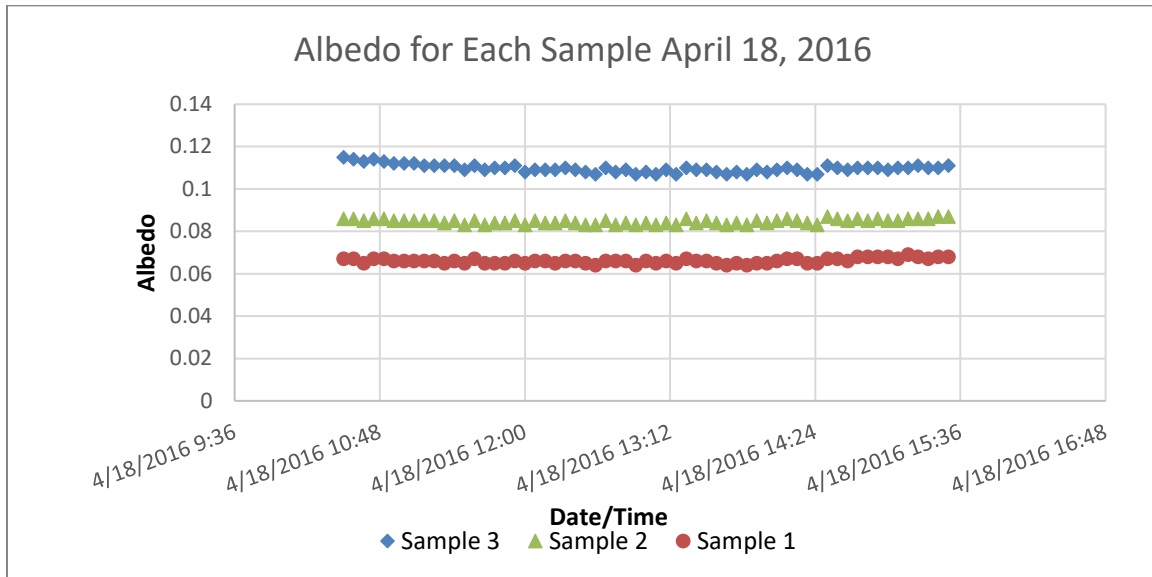


Figure 94: Comparison of 3 slabs albedo measurements for April 18, 2016

The albedo calculated for April 18, 2016 averaged 0.107 for sample 3, 0.083 for sample 2, and 0.065 for sample 1. The slight discrepancies throughout the test period indicate brief cloud cover, which is seen through each of the samples. The albedo remained relatively constant throughout the greater than 45° zenith period each day.



## SOLAR RADIATION

This section shows the solar irradiance and slab irradiance measurements conducted for each of the four test periods outlined in this paper. The equipment set up resulted in the measurement of solar insolation of the asphalt slabs near ground level ignoring daily atmospheric perturbations. As explained earlier in the Data Selection Process section of this paper, an effort was made to select data that was collected with maximum sun exposure, limited cloud cover, and as low humidity as possible. Other factors that can affect the amount of solar radiation that reaches the ground include dust and pollutants, which were not accounted for in this study. Since there is not a dataset available to calculate the offset for the atmospheric conditions for use in this report, the measurements are considered to be reminiscent of diffuse solar radiation. The spectral solar range for the Hukseflux net radiometers ranges from 285 to  $3000 \times 10^{-9} \text{m}$ , and the spectral longwave ranges from 4.5 to  $40 \times 10^{-6} \text{m}$ . The calibration records for these gauges can be found in Appendix B of this paper.

### July 31, 2015 – August 2, 2015

The shortwave solar radiation measured for sample 1, as shown in Figure 95, reached a high of 1187  $\text{W/m}^2$  on July 31, 2015, 1109  $\text{W/m}^2$  on August 1, 2015, and 1089  $\text{W/m}^2$  on August 2, 2015. The reflected shortwave radiation measured on sample 1 reached a high of 66.2  $\text{W/m}^2$  on July 31, 2015, 58.2  $\text{W/m}^2$  on August 1, 2015, and 63.9  $\text{W/m}^2$  on August 2, 2015.

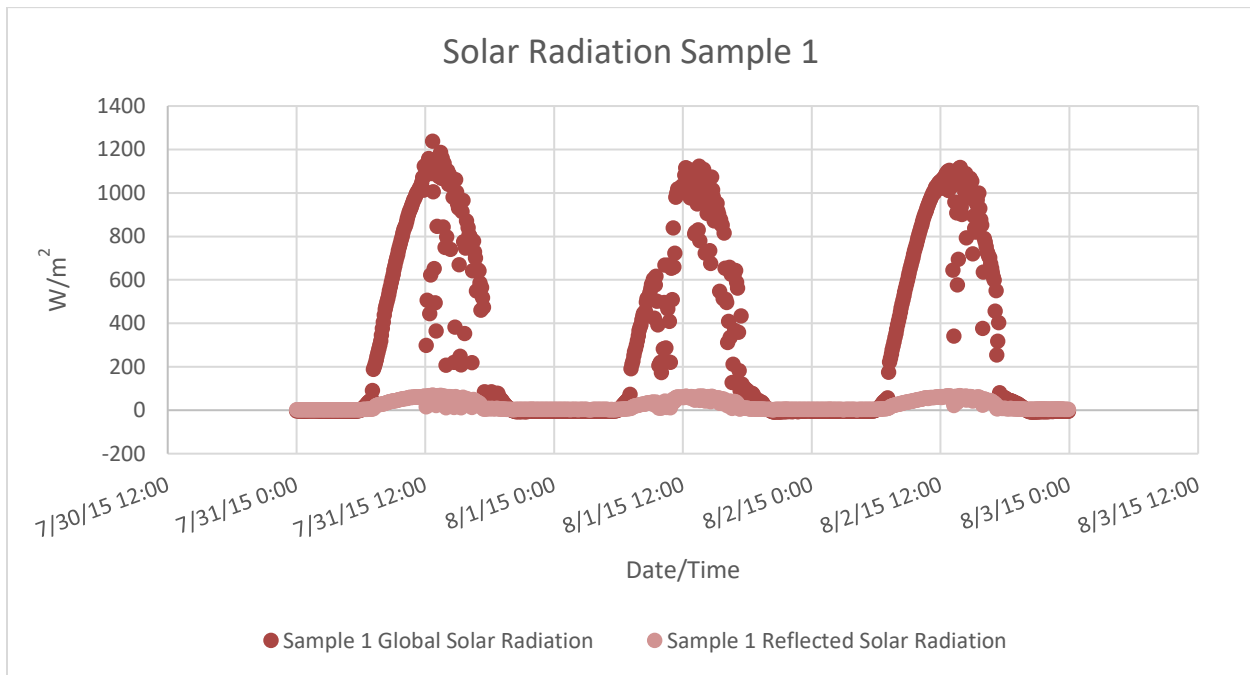
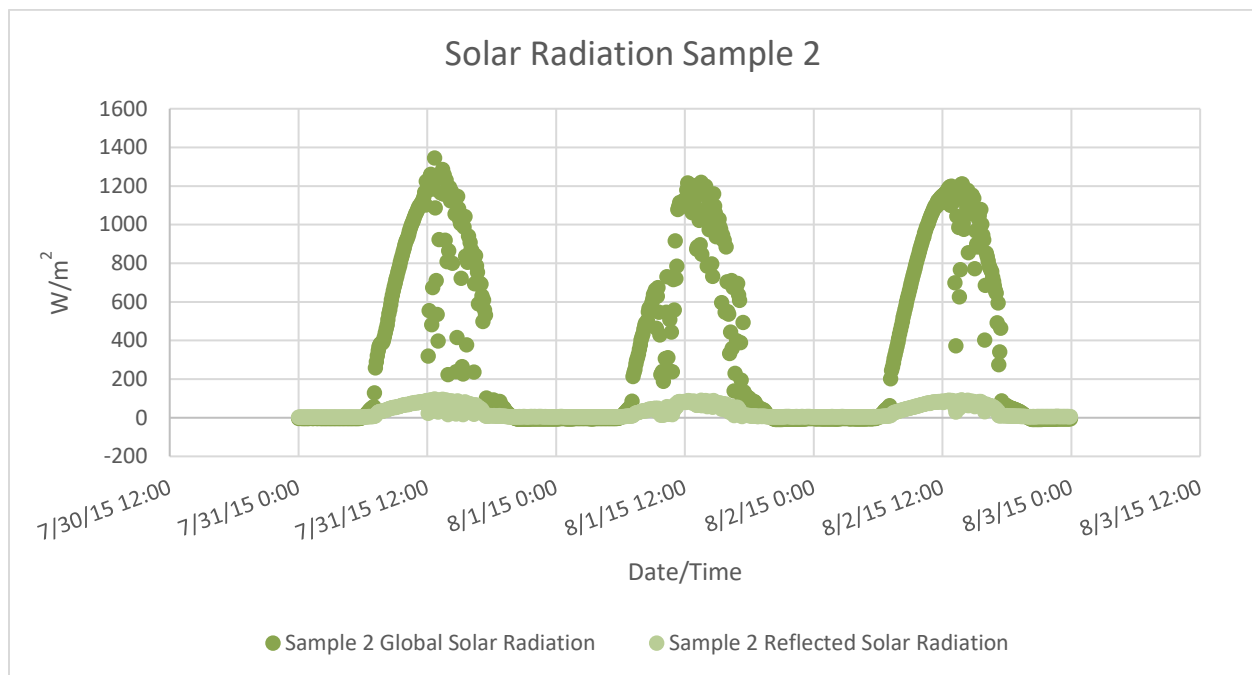


Figure 95: Solar radiation measured for sample 1 (slab 2) for testing period July 31, 2015 - August 2, 2015

The shortwave solar radiation measured for sample 2, as shown in Figure 96, reached a high of 1345  $\text{W/m}^2$  on July 31, 2015, 1200  $\text{W/m}^2$  on August 1, 2015, and 1178  $\text{W/m}^2$  on August 2, 2015. The reflected shortwave radiation measured on sample 2 reached a high of 91.8  $\text{W/m}^2$  on July 31, 2015, 80.9  $\text{W/m}^2$  on August 1, 2015, and 85.7  $\text{W/m}^2$  on August 2, 2015.



**Figure 96: Solar radiation measured for sample 2 (slab 3) for testing period July 31, 2015 - August 2, 2015**

The shortwave solar radiation measured for sample 3, as shown in Figure 97, reached a high of 1234  $W/m^2$  on July 31, 2015, 1105  $W/m^2$  on August 1, 2015, and 1112  $W/m^2$  on August 2, 2015. The reflected shortwave radiation measured on sample 3 reached a high of 118.9  $W/m^2$  on July 31, 2015, 91.6  $W/m^2$  on August 1, 2015, and 110.4  $W/m^2$  on August 2, 2015.

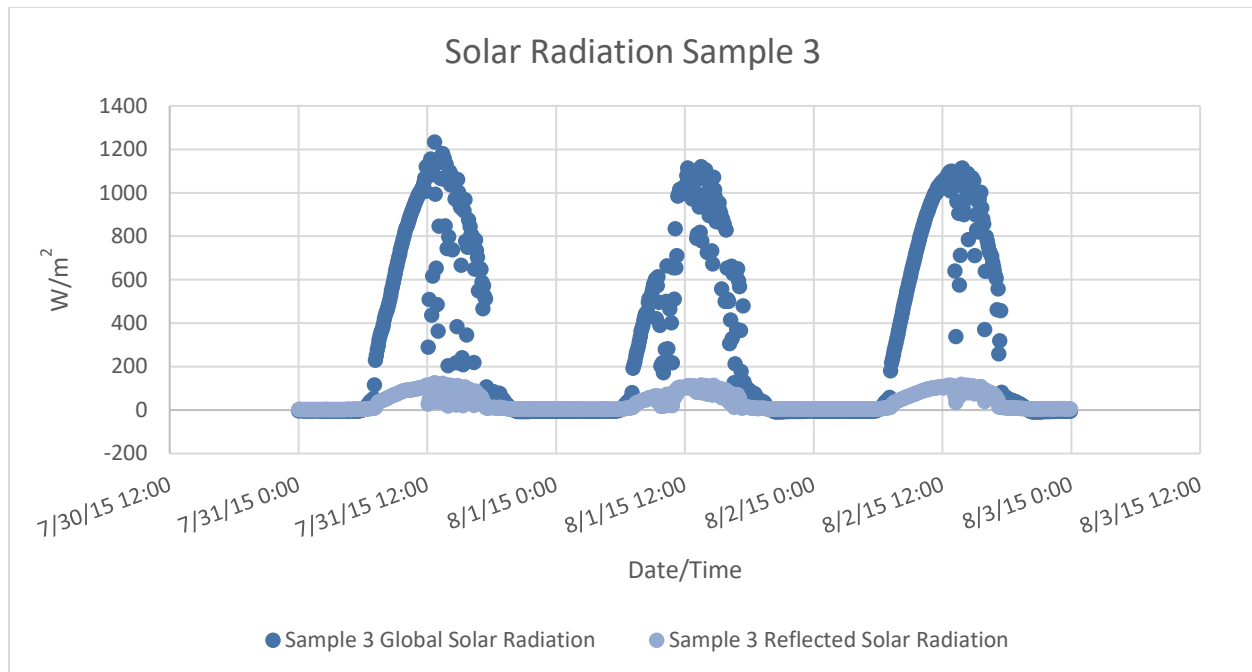


Figure 97: Solar radiation measured for sample 3 (slab 4) for testing period July 31, 2015 - August 2, 2015

The outgoing (upward) longwave radiation measured for sample 1, as shown in Figure 98, reached a high of 188.9 W/m<sup>2</sup> on July 31, 2015, 202.0 W/m<sup>2</sup> on August 1, 2015, and 231.7 W/m<sup>2</sup> on August 2, 2015. The incoming (downward) longwave radiation measured on sample 1 reached a high of -172.8 W/m<sup>2</sup> on July 31, 2015, -177.3 W/m<sup>2</sup> on August 1, 2015, and -199.1 W/m<sup>2</sup> on August 2, 2015.

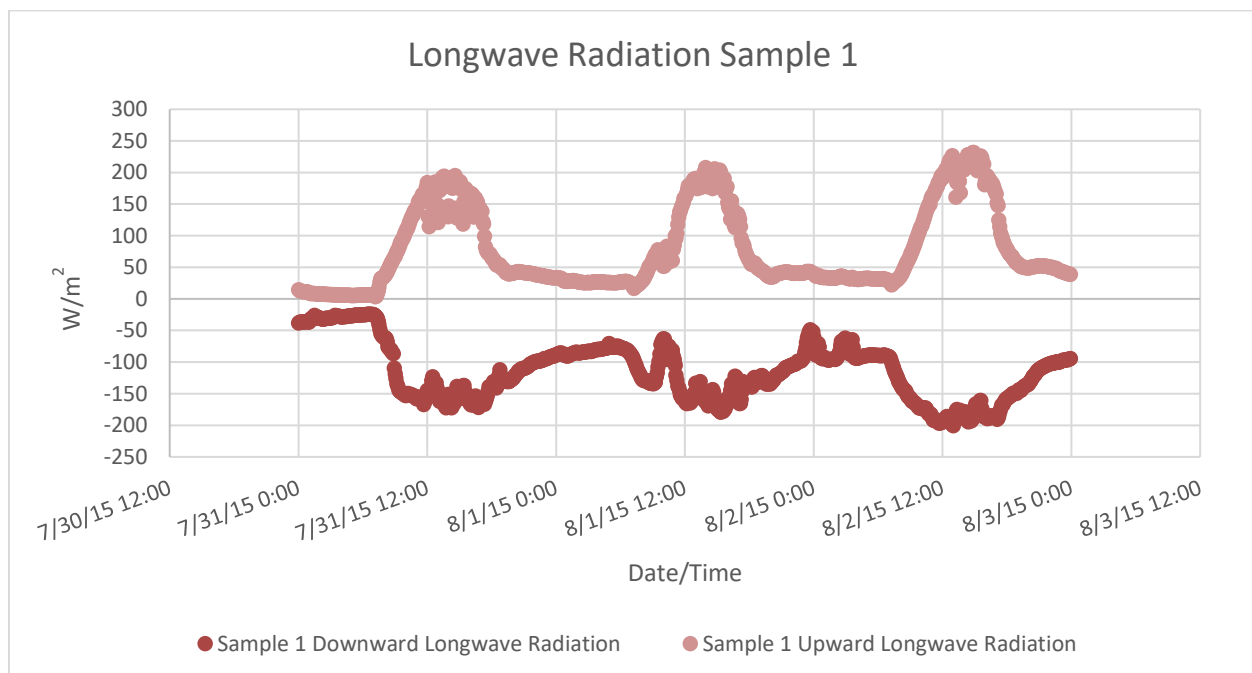


Figure 98: Infrared radiation measured for sample 1 (slab 2) for testing period July 31, 2015 - August 2, 2015

The outgoing (upward) longwave radiation measured for sample 1, as shown in Figure 99, reached a high of 177.2 W/m<sup>2</sup> on July 31, 2015, 175.9 W/m<sup>2</sup> on August 1, 2015, and 188.5 W/m<sup>2</sup> on August 2, 2015. The incoming (downward) longwave radiation measured on sample 1 reached a high of -167.0 W/m<sup>2</sup> on July 31, 2015, -171.2 W/m<sup>2</sup> on August 1, 2015, and -192.9 W/m<sup>2</sup> on August 2, 2015.

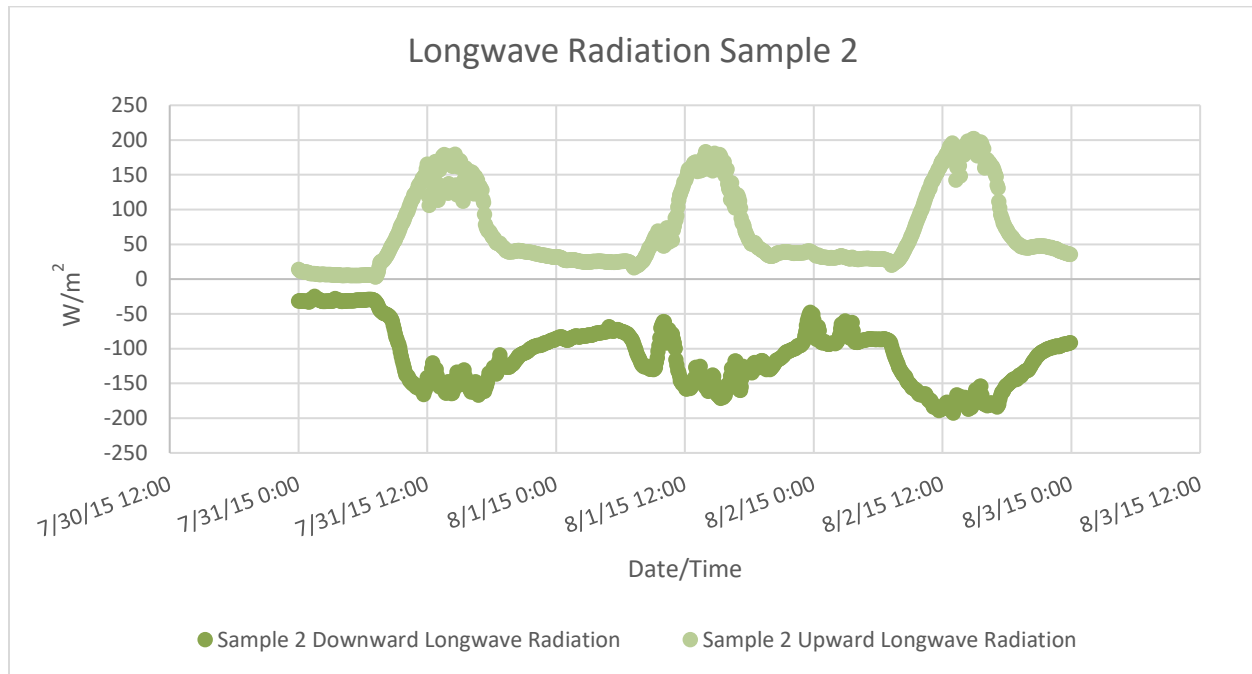


Figure 99: Infrared radiation measured for sample 2 (slab 3) for testing period July 31, 2015 - August 2, 2015

The outgoing (upward) longwave radiation measured for sample 3, as shown in Figure 100, reached a high of 185.9 W/m<sup>2</sup> on July 31, 2015, 193.1 W/m<sup>2</sup> on August 1, 2015, and 209.5 W/m<sup>2</sup> on August 2, 2015. The incoming (downward) longwave radiation measured on sample 3 reached a high of -172.9 W/m<sup>2</sup> on July 31, 2015, -178.8 W/m<sup>2</sup> on August 1, 2015, and -199.8 W/m<sup>2</sup> on August 2, 2015.

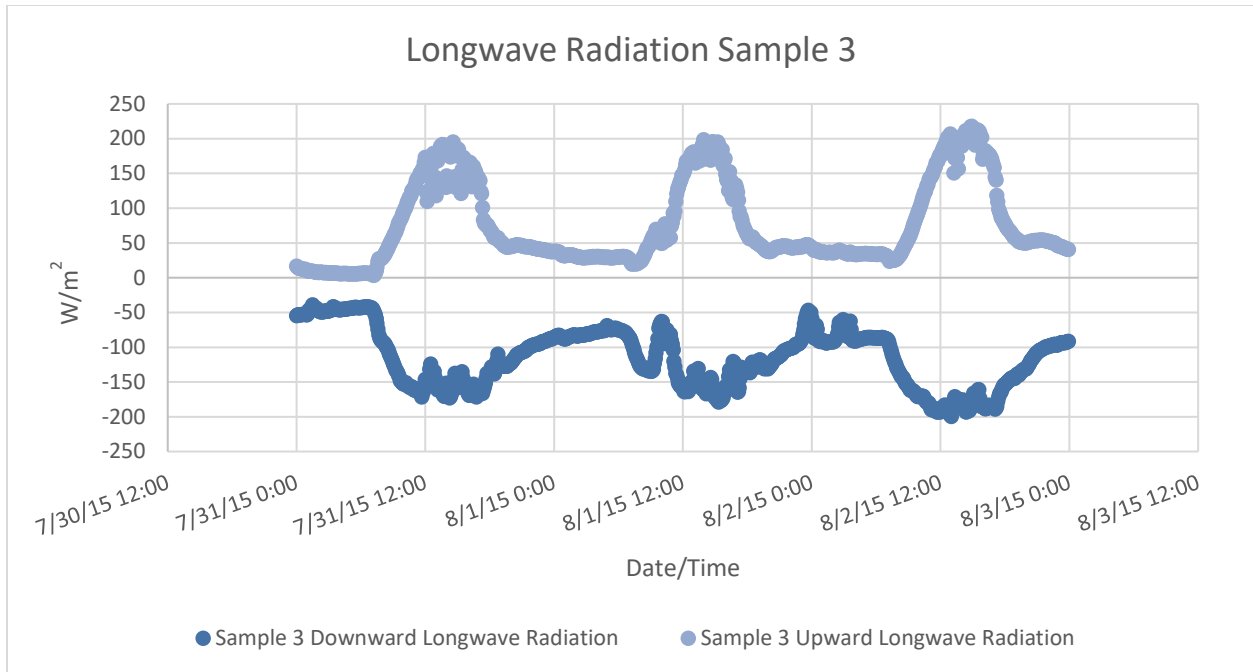


Figure 100: Infrared radiation measured for sample 3 (slab 4) for testing period July 31, 2015 - August 2, 2015

The net shortwave radiation ( $\text{SWup} - \text{SWdn}$ ) measured for sample 1, as shown in Figure 101, reached a high of 1168  $\text{W/m}^2$  on July 31, 2015, 1053  $\text{W/m}^2$  on August 1, 2015, and 1039  $\text{W/m}^2$  on August 2, 2015. The net longwave radiation ( $\text{LWup} - \text{LWdn}$ ) measured on sample 1 reached a high of -364.3  $\text{W/m}^2$  on July 31, 2015, -381.0  $\text{W/m}^2$  on August 1, 2015, and -417.6  $\text{W/m}^2$  on August 2, 2015.

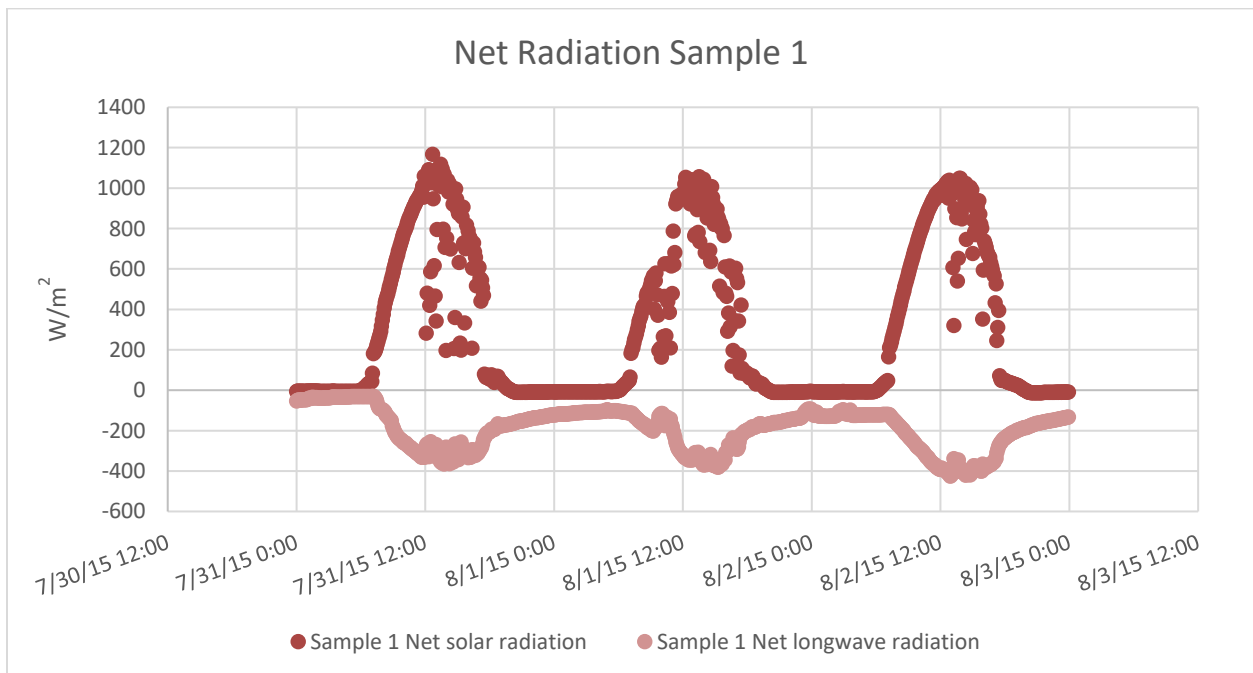
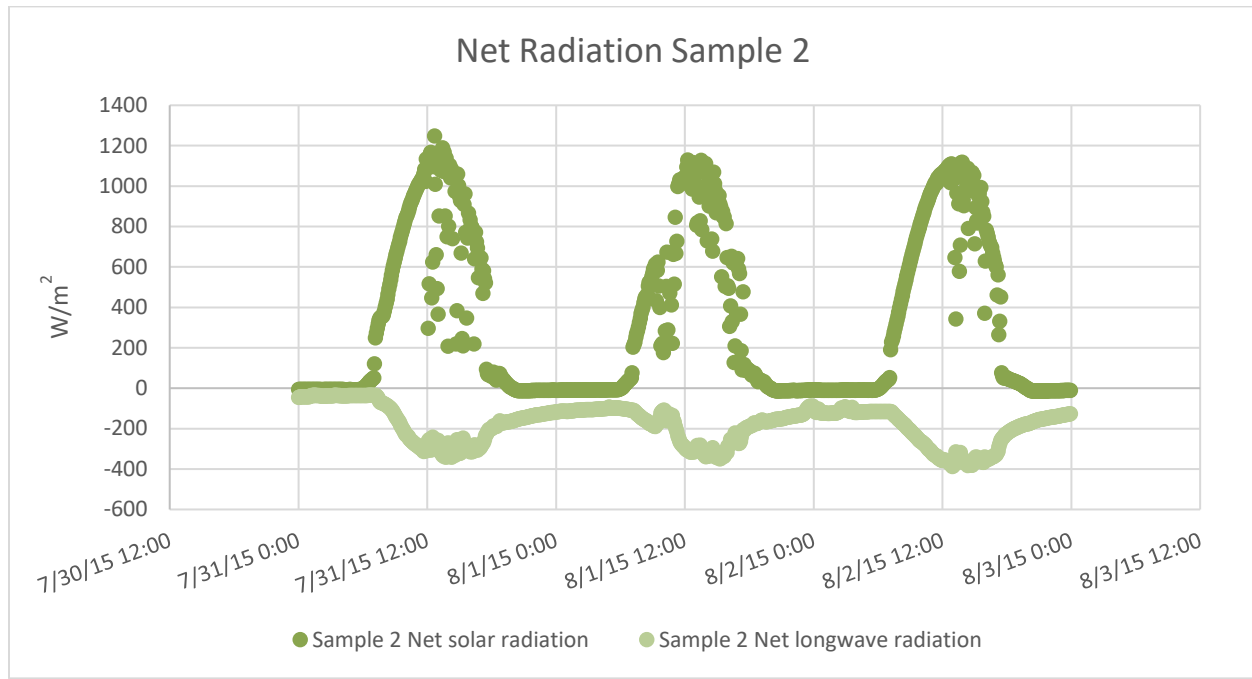


Figure 101: Net radiation measured for sample 1 (slab 2) for testing period July 31, 2015 - August 2, 2015

The net shortwave radiation (SWup – SWdn) measured for sample 2, as shown in Figure 102, reached a high of 1248 W/m<sup>2</sup> on July 31, 2015, 1124 W/m<sup>2</sup> on August 1, 2015, and 1119 W/m<sup>2</sup> on August 2, 2015. The net longwave radiation (LWup – LWdn) measured on sample 2 reached a high of -341.8 W/m<sup>2</sup> on July 31, 2015, -338.1 W/m<sup>2</sup> on August 1, 2015, and -379.3 W/m<sup>2</sup> on August 2, 2015.



**Figure 102: Net radiation measured for sample 2 (slab 3) for testing period July 31, 2015 - August 2, 2015**

The net shortwave radiation (SWup – SWdn) measured for sample 3, as shown in Figure 103, reached a high of 1108 W/m<sup>2</sup> on July 31, 2015, 1005 W/m<sup>2</sup> on August 1, 2015, and 974 W/m<sup>2</sup> on August 2, 2015. The net longwave radiation (LWup – LWdn) measured on sample 3 reached a high of -354.9 W/m<sup>2</sup> on July 31, 2015, -372.1 W/m<sup>2</sup> on August 1, 2015, and -400.2 W/m<sup>2</sup> on August 2, 2015.

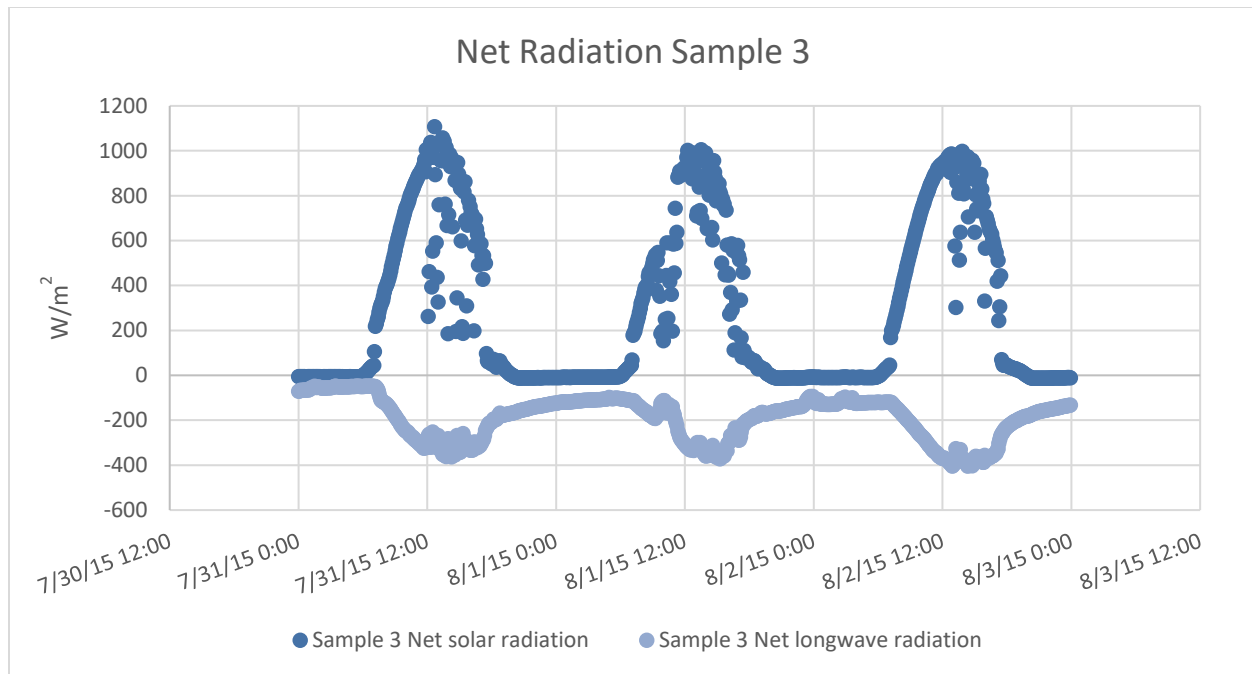
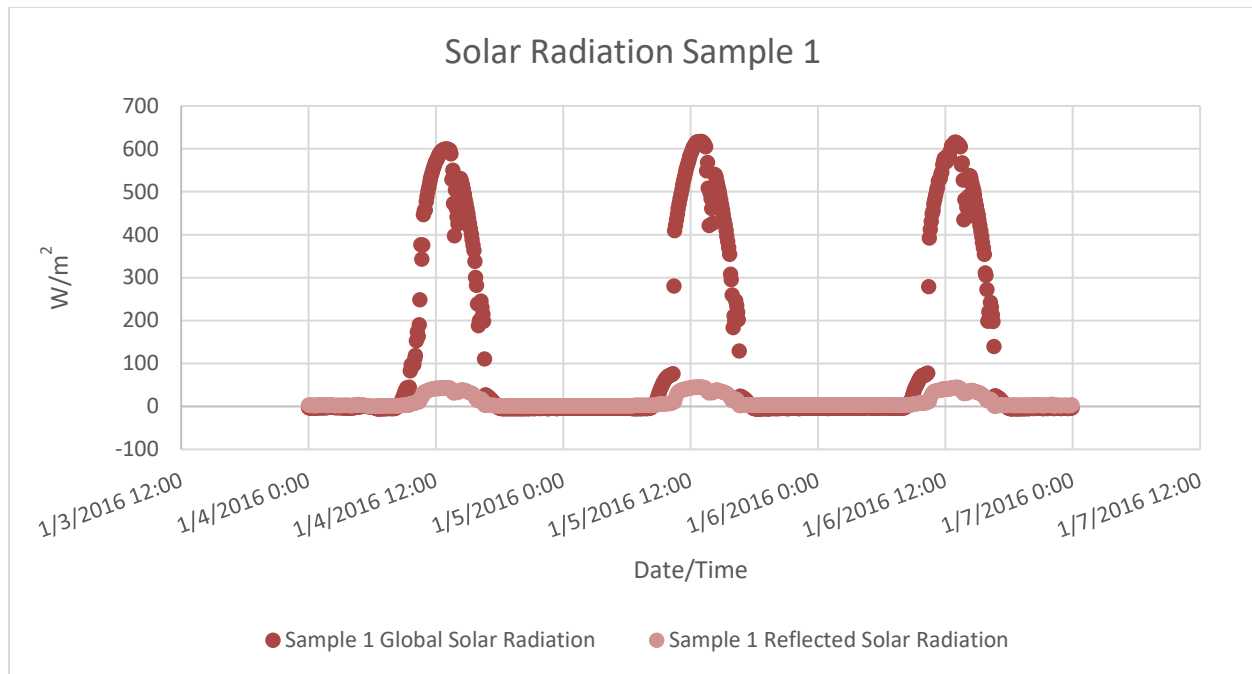


Figure 103: Net radiation measured for sample 3 (slab 4) for testing period July 31, 2015 - August 2, 2015

### January 4, 2016 – January 6, 2016

The shortwave solar radiation measured for sample 1, as shown in Figure 104, reached a high of 587.9 W/m² on January 4, 2016, 604.7 W/m² on January 5, 2016, and 607.8 W/m² on January 6, 2016. The reflected shortwave radiation measured on sample 1 reached a high of 43.0 W/m² on January 4, 2016, 44.9 W/m² on January 5, 2016, and 43.1 W/m² on January 6, 2016.



**Figure 104: Solar radiation measured for sample 1 (slab 2) for testing period January 31, 2016 - January 6, 2016**

The shortwave solar radiation measured for sample 2, as shown in Figure 105, reached a high of 630.2 W/m<sup>2</sup> on January 4, 2016, 644.3 W/m<sup>2</sup> on January 5, 2016, and 646.1 W/m<sup>2</sup> on January 6, 2016. The reflected shortwave radiation measured on sample 2 reached a high of 56.2 W/m<sup>2</sup> on January 4, 2016, 58.4 W/m<sup>2</sup> on January 5, 2016, and 56.4 W/m<sup>2</sup> on January 6, 2016.

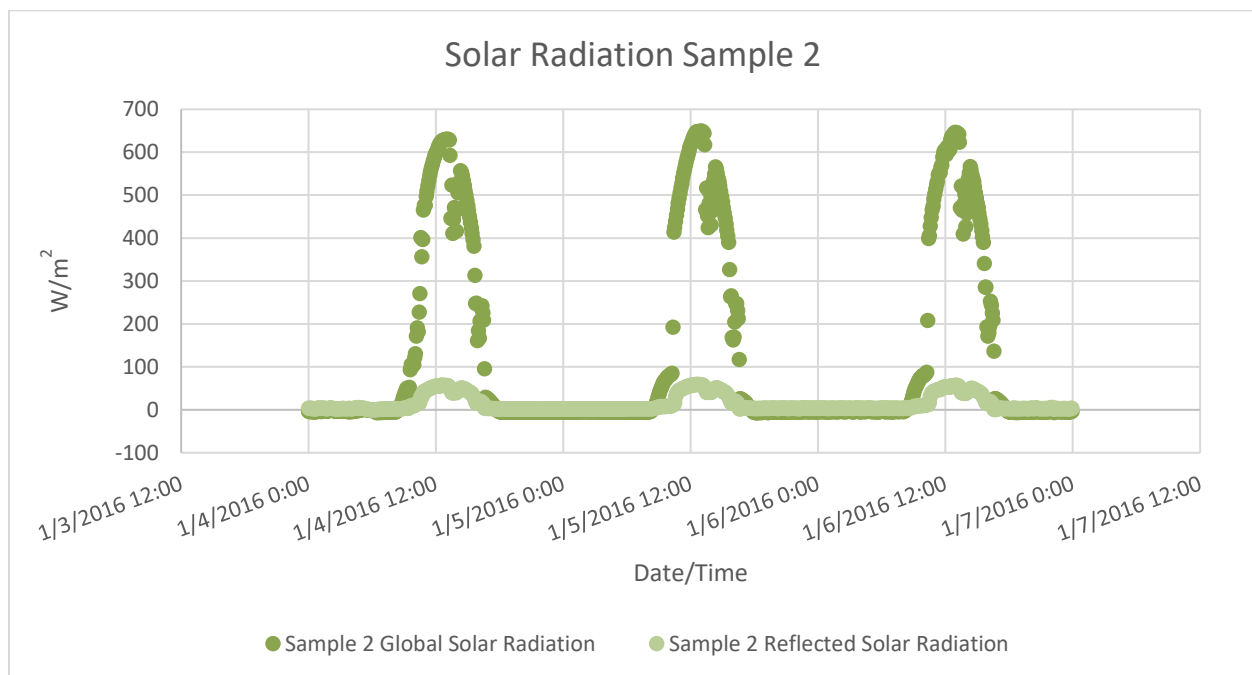


**Figure 105: Solar radiation measured for sample 2 (slab 3) for testing period January 31, 2016 - January 6, 2016**



The shortwave solar radiation measured for sample 3, as shown in Figure 106, reached a high of 575.2  $\text{W/m}^2$  on January 4, 2016, 597.1  $\text{W/m}^2$  on January 5, 2016, and 583.5  $\text{W/m}^2$  on January 6, 2016. The reflected shortwave radiation measured on sample 3 reached a high of 58.4  $\text{W/m}^2$  on January 4, 2016, 65.6  $\text{W/m}^2$  on January 5, 2016, and 58.4  $\text{W/m}^2$  on January 6, 2016.

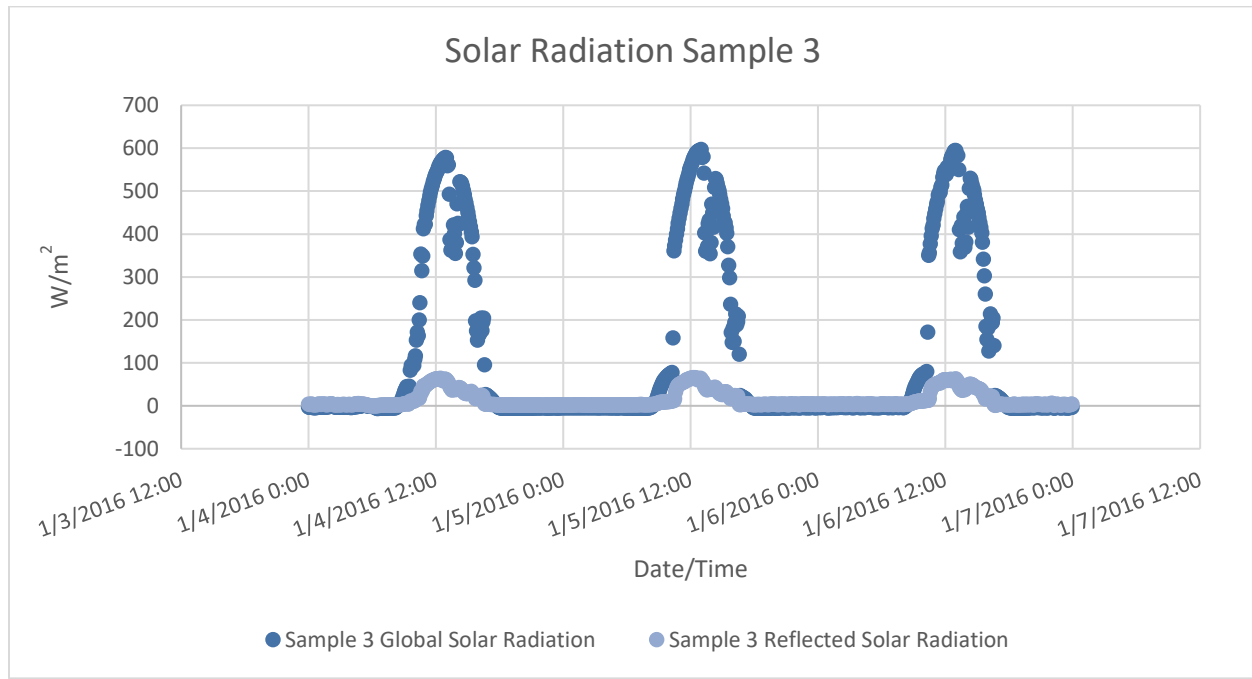


**Figure 106: Solar radiation measured for sample 3 (slab 4) for testing period January 31, 2016 - January 6, 2016**

The outgoing (upward) longwave radiation measured for sample 1, as shown in Figure 107, reached a high of 65.2  $\text{W/m}^2$  on January 4, 2016, 72.7  $\text{W/m}^2$  on January 5, 2016, and 50.1  $\text{W/m}^2$  on January 6, 2016. The incoming (downward) longwave radiation measured on sample 1 reached a high of -159.5  $\text{W/m}^2$  on January 4, 2016, -168.5  $\text{W/m}^2$  on January 5, 2016, and -183.7  $\text{W/m}^2$  on January 6, 2016.

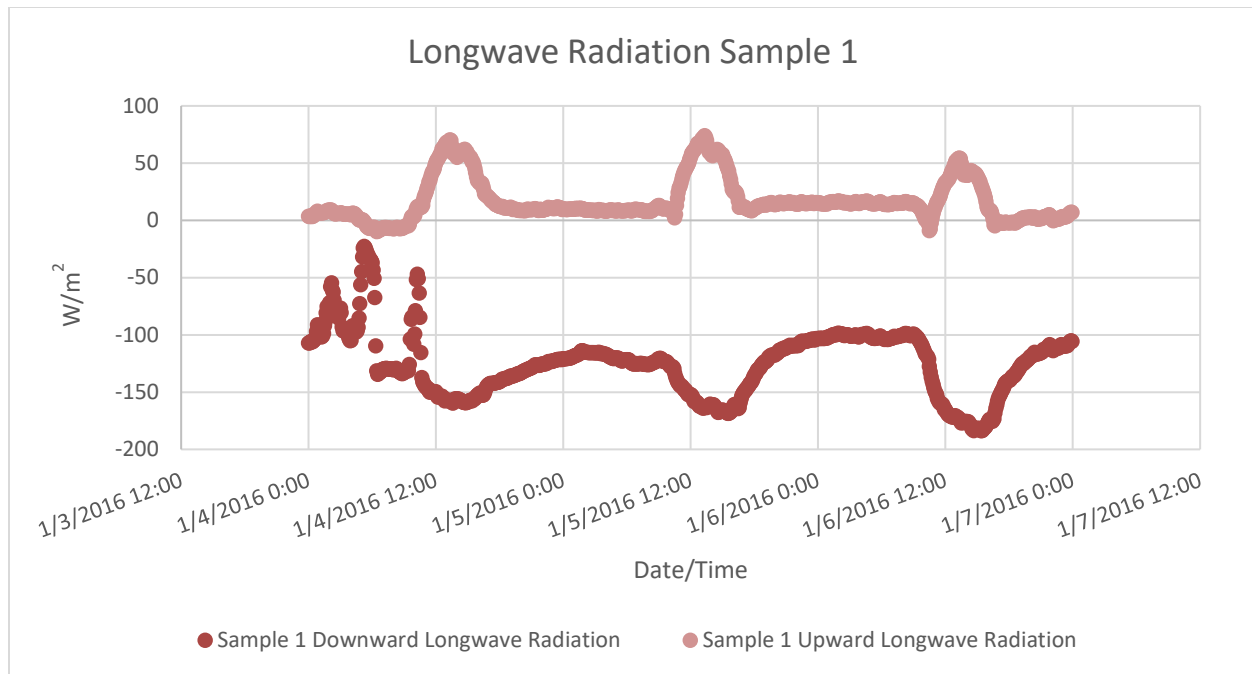


**Figure 107: Infrared radiation measured for sample 1 (slab 2) for testing period January 31, 2016 - January 6, 2016**

The outgoing (upward) longwave radiation measured for sample 2, as shown in Figure 108, reached a high of 54.6 W/m<sup>2</sup> on January 4, 2016, 56.2 W/m<sup>2</sup> on January 5, 2016, and 40.0 W/m<sup>2</sup> on January 6, 2016. The incoming (downward) longwave radiation measured on sample 2 reached a high of -154.5 W/m<sup>2</sup> on January 4, 2016, -163.6 W/m<sup>2</sup> on January 5, 2016, and -177.1 W/m<sup>2</sup> on January 6, 2016.

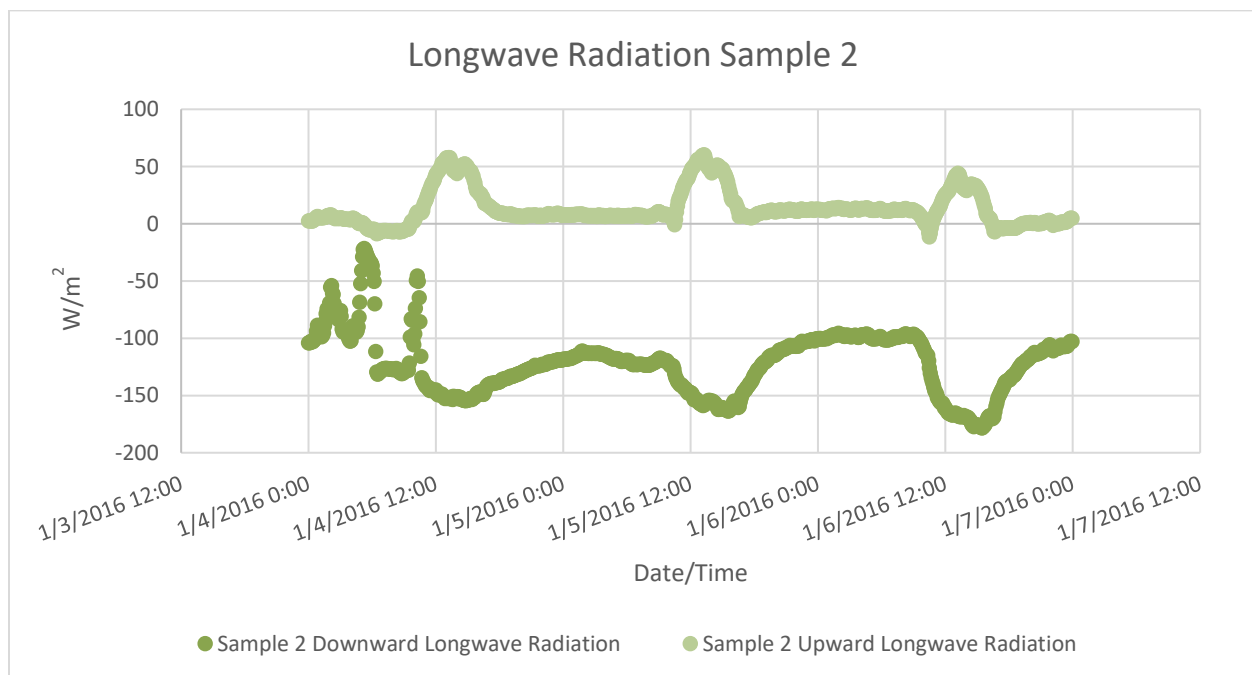


**Figure 108: Infrared radiation measured for sample 2 (slab 3) for testing period January 31, 2016 - January 6, 2016**

The outgoing (upward) longwave radiation measured for sample 3, as shown in Figure 109, reached a high of 53.6 W/m<sup>2</sup> on January 4, 2016, 50.8 W/m<sup>2</sup> on January 5, 2016, and 34.6 W/m<sup>2</sup> on January 6, 2016. The incoming (downward) longwave radiation measured on sample 3 reached a high of -151.1 W/m<sup>2</sup> on January 4, 2016, -159.8 W/m<sup>2</sup> on January 5, 2016, and -175.4 W/m<sup>2</sup> on January 6, 2016.

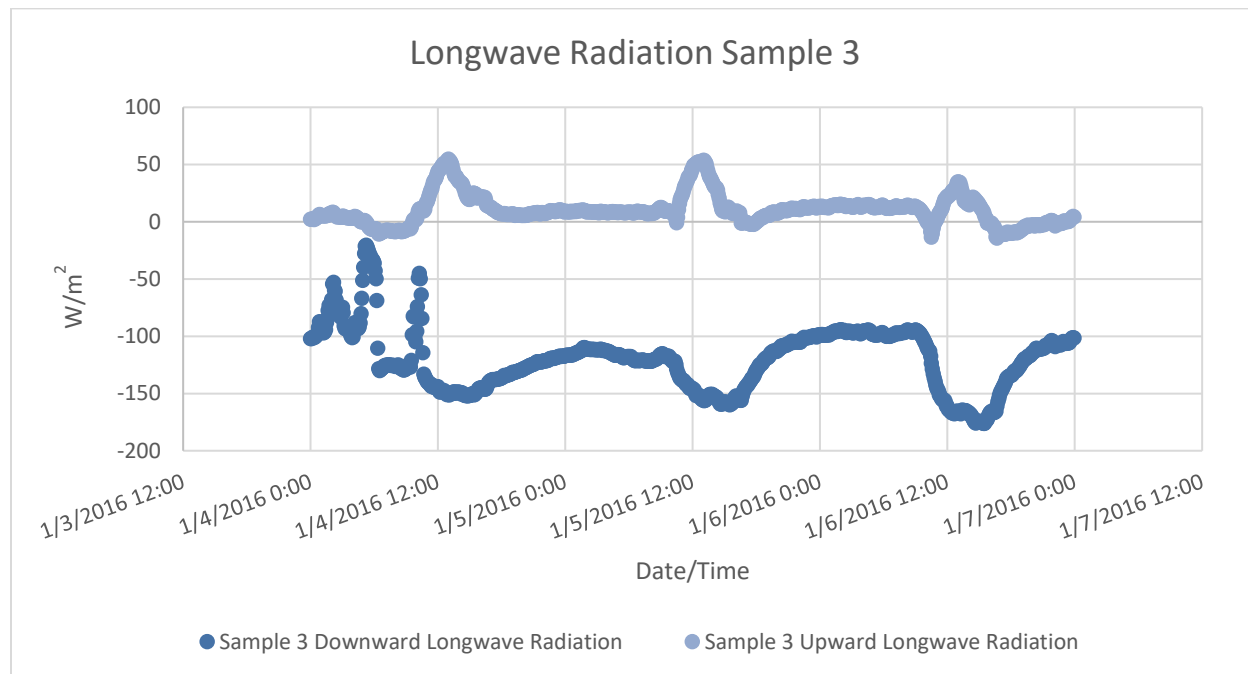


**Figure 109: Infrared radiation measured for sample 3 (slab 4) for testing period January 31, 2016 - January 6, 2016**

The net shortwave radiation (SWup – SWdn) measured for sample 1, as shown in Figure 110, reached a high of 556.1 W/m<sup>2</sup> on January 4, 2016, 566.2 W/m<sup>2</sup> on January 5, 2016, and 567.8 W/m<sup>2</sup> on January 6, 2016. The net longwave radiation (LWup – LWdn) measured on sample 1 reached a high of -226.3 W/m<sup>2</sup> on January 4, 2016, -235.7 W/m<sup>2</sup> on January 5, 2016, and -229.1 W/m<sup>2</sup> on January 6, 2016.

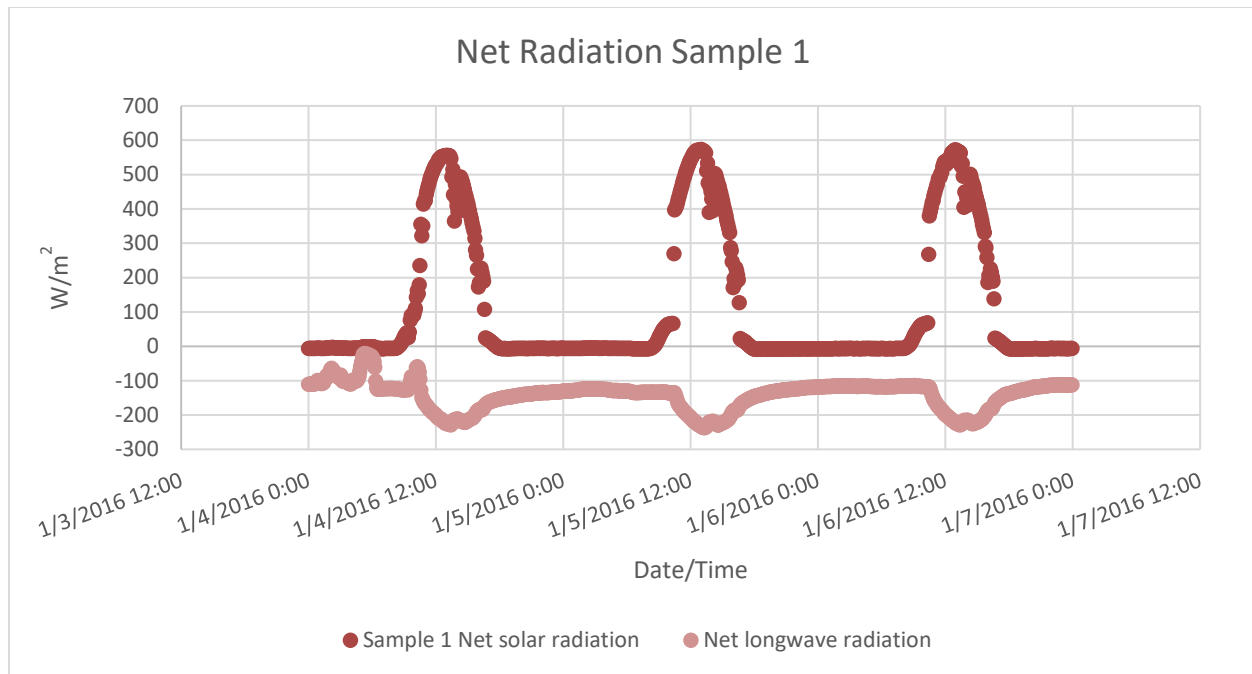


Figure 110: Net radiation measured for sample 1 (slab 2) for testing period January 31, 2016 - January 6, 2016

The net shortwave radiation (SWup – SWdn) measured for sample 2, as shown in Figure 111, reached a high of 574.6  $W/m^2$  on January 4, 2016, 565.0  $W/m^2$  on January 5, 2016, and 573.2  $W/m^2$  on January 6, 2016. The net longwave radiation (LWup – LWdn) measured on sample 2 reached a high of -210.1  $W/m^2$  on January 4, 2016, -217.7  $W/m^2$  on January 5, 2016, and -211.9  $W/m^2$  on January 6, 2016.

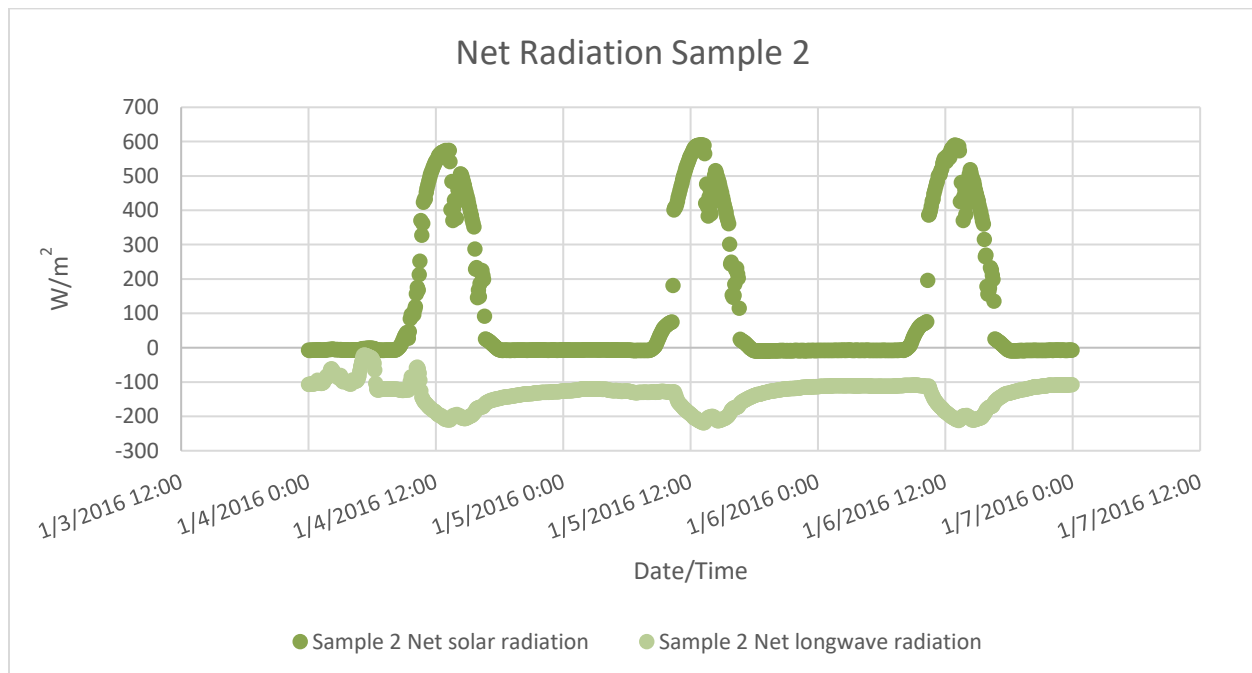


Figure 111: Net radiation measured for sample 2 (slab 3) for testing period January 31, 2016 - January 6, 2016

The net shortwave radiation (SWup – SWdn) measured for sample 3, as shown in Figure 112, reached a high of 506.9 W/m<sup>2</sup> on January 4, 2016, 523.5 W/m<sup>2</sup> on January 5, 2016, and 526.9 W/m<sup>2</sup> on January 6, 2016. The net longwave radiation (LWup – LWdn) measured on sample 3 reached a high of -204.3 W/m<sup>2</sup> on January 4, 2016, -207.0 W/m<sup>2</sup> on January 5, 2016, and -202.3 W/m<sup>2</sup> on January 6, 2016.

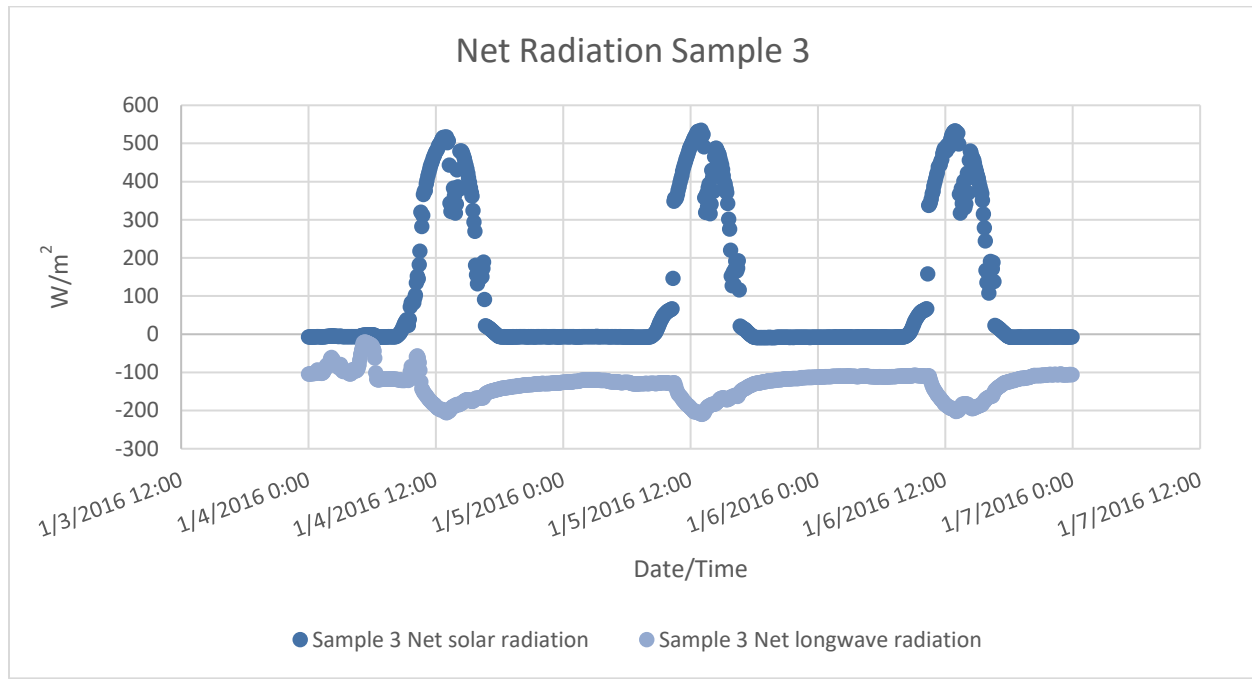
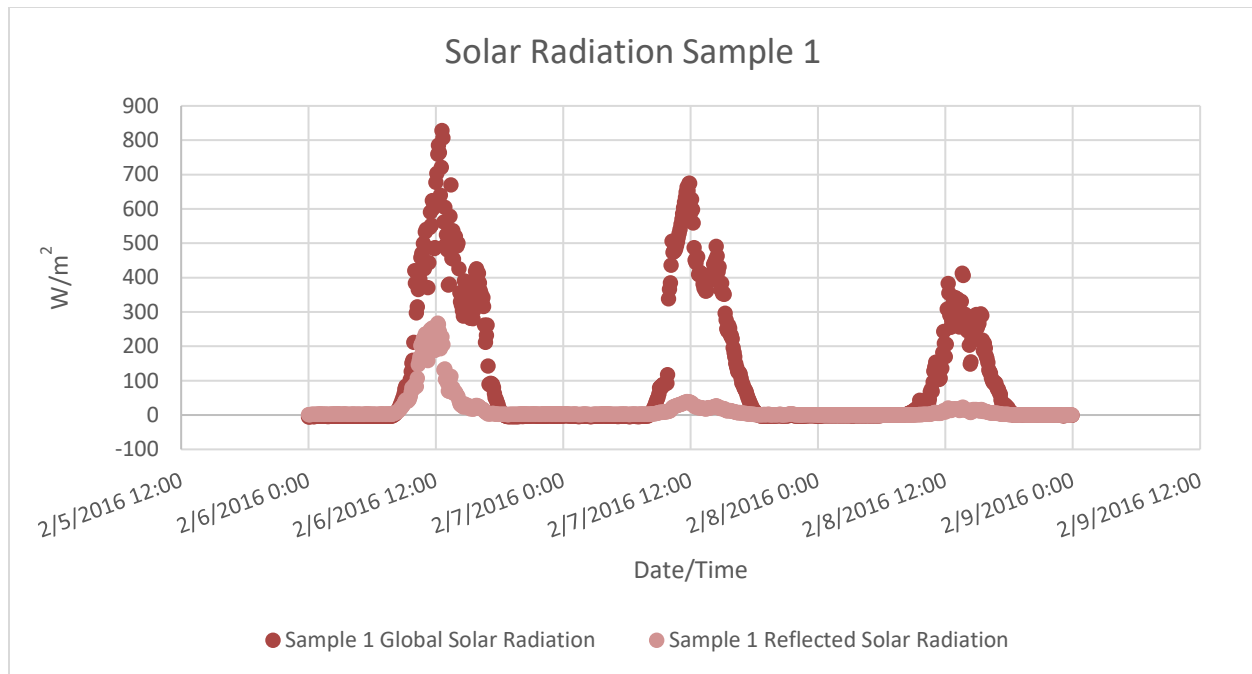


Figure 112: Net radiation measured for sample 3 (slab 4) for testing period January 31, 2016 - January 6, 2016

## February 6 – February 8, 2016

The shortwave solar radiation measured for sample 1, as shown in Figure 113, reached a high of 828.0 W/m<sup>2</sup> on February 6, 2016, 674.5 W/m<sup>2</sup> on February 7, 2016, and 406.2 W/m<sup>2</sup> on February 8, 2016. The reflected shortwave radiation measured on sample 1 reached a high of 267.9 W/m<sup>2</sup> on February 6, 2016, 32.8 W/m<sup>2</sup> on February 7, 2016, and 17.8 W/m<sup>2</sup> on February 8, 2016.



**Figure 113: Solar radiation measured for sample 1 (slab 2) for testing period February 6, 2016 - February 8, 2016**

The shortwave solar radiation measured for sample 2, as shown in Figure 114, reached a high of 876.0 W/m<sup>2</sup> on February 6, 2016, 712.4 W/m<sup>2</sup> on February 7, 2016, and 426.2 W/m<sup>2</sup> on February 8, 2016. The reflected shortwave radiation measured on sample 1 reached a high of 315.1 W/m<sup>2</sup> on February 6, 2016, 57.1 W/m<sup>2</sup> on February 7, 2016, and 26.1 W/m<sup>2</sup> on February 8, 2016.

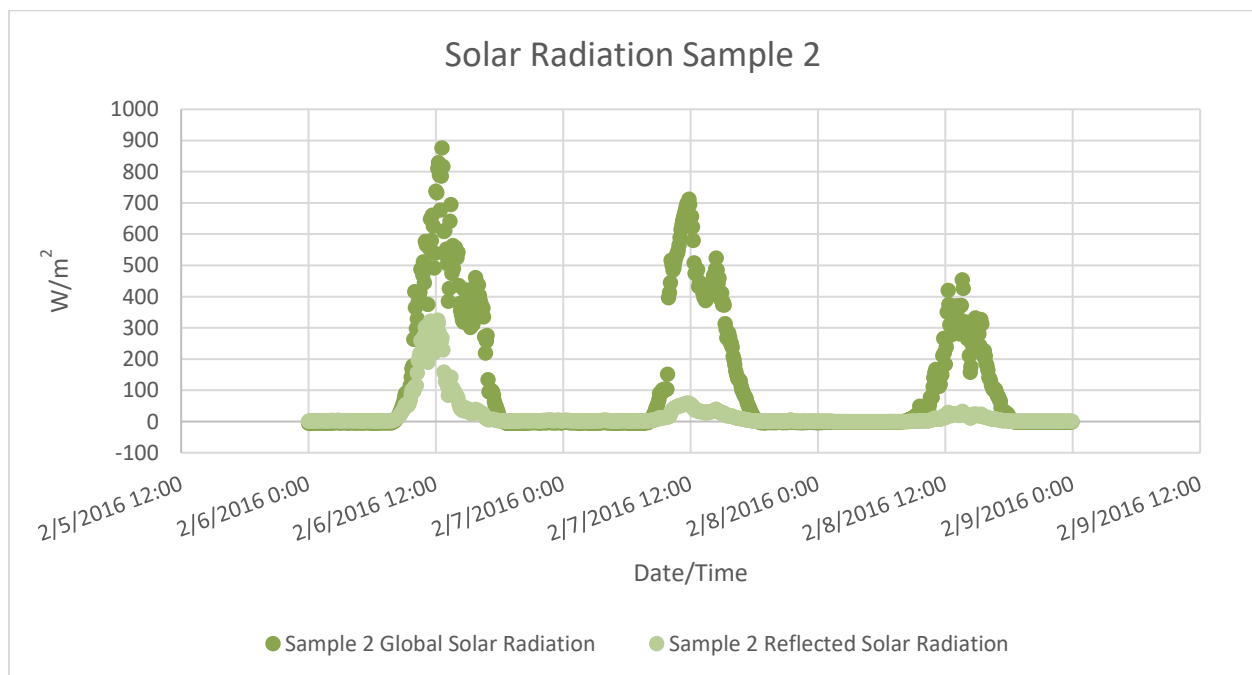


**Figure 114: Solar radiation measured for sample 2 (slab 3) for testing period February 6, 2016 - February 8, 2016**

The shortwave solar radiation measured for sample 3, as shown in Figure 115, reached a high of 803.0  $\text{W/m}^2$  on February 6, 2016, 633.6  $\text{W/m}^2$  on February 7, 2016, and 391.3  $\text{W/m}^2$  on February 8, 2016. The reflected shortwave radiation measured on sample 3 reached a high of 345.4  $\text{W/m}^2$  on February 6, 2016, 105.8  $\text{W/m}^2$  on February 7, 2016, and 39.82  $\text{W/m}^2$  on February 8, 2016.

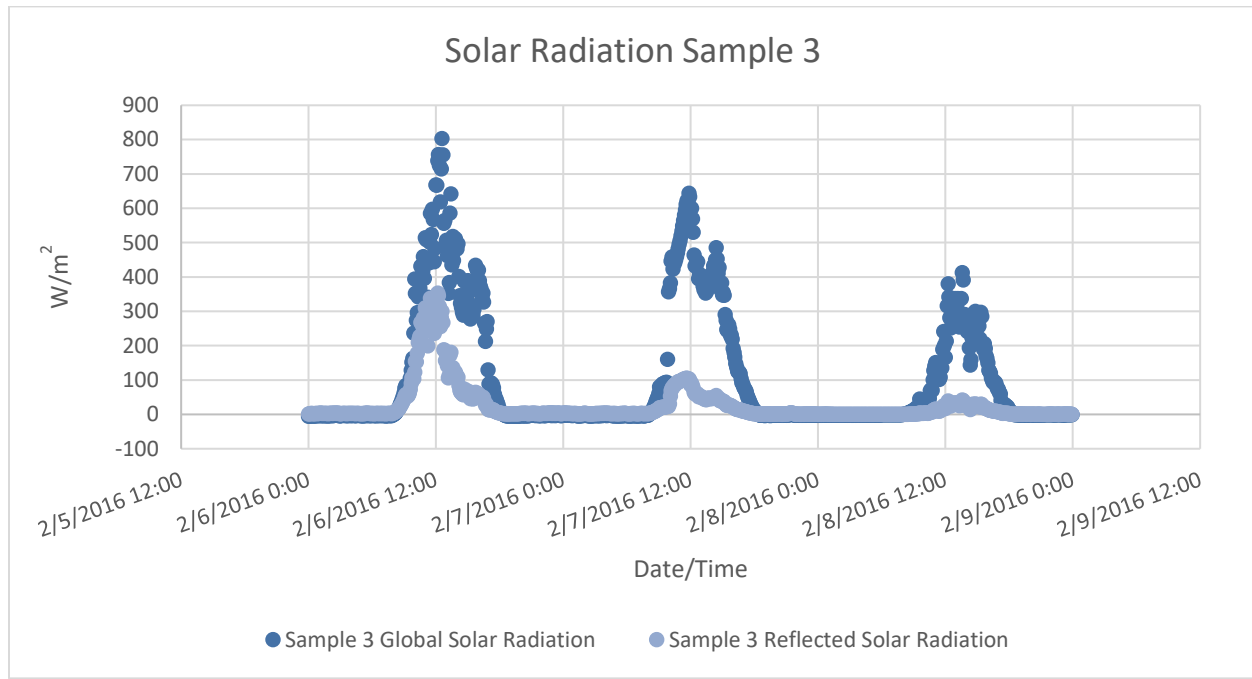


**Figure 115: Solar radiation measured for sample 3 (slab 4) for testing period February 6, 2016 - February 8, 2016**

The outgoing (upward) longwave radiation measured for sample 1, as shown in Figure 116, reached a high of 7.5  $\text{W/m}^2$  on February 6, 2016, 34.8  $\text{W/m}^2$  on February 7, 2016, and 43.1  $\text{W/m}^2$  on February 8, 2016. The incoming (downward) longwave radiation measured on sample 1 reached a high of -153.4  $\text{W/m}^2$  on February 6, 2016, -154.3  $\text{W/m}^2$  on February 7, 2016, and -52.4  $\text{W/m}^2$  on February 8, 2016.

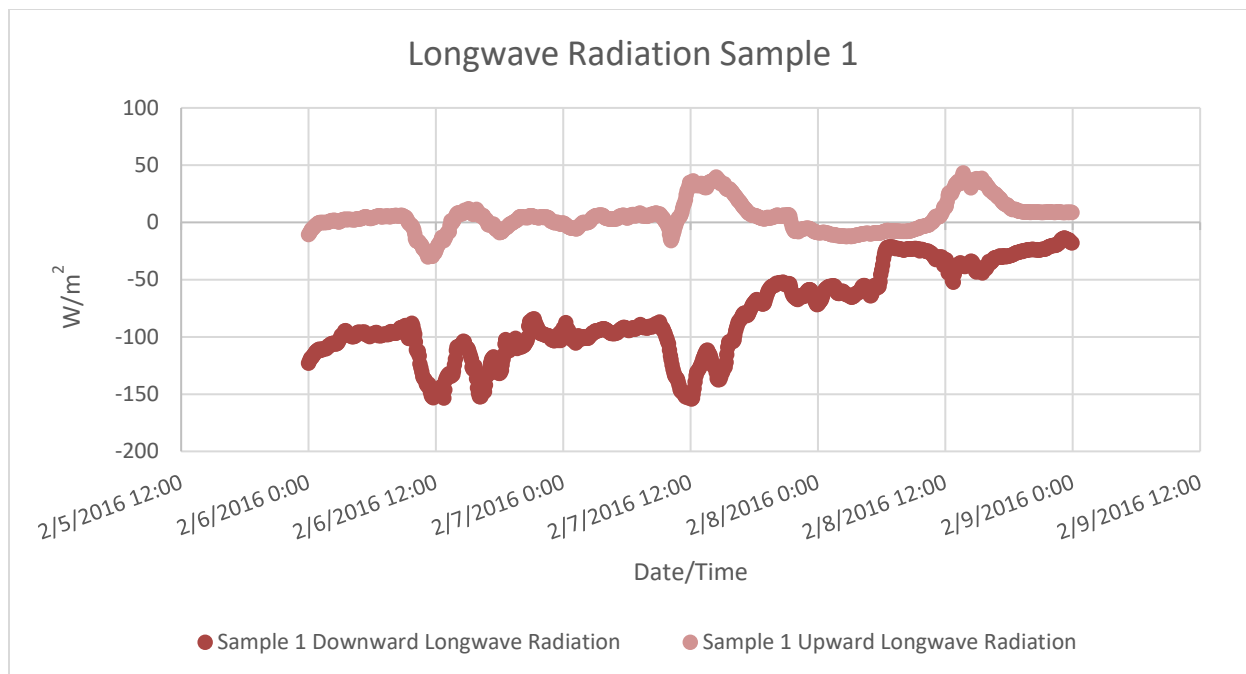


**Figure 116: Infrared radiation measured for sample 1 (slab 2) for testing period February 6, 2016 - February 8, 2016**

The outgoing (upward) longwave radiation measured for sample 2, as shown in Figure 117, reached a high of 9.1 W/m<sup>2</sup> on February 6, 2016, 28.3 W/m<sup>2</sup> on February 7, 2016, and 35.8 W/m<sup>2</sup> on February 8, 2016. The incoming (downward) longwave radiation measured on sample 2 reached a high of -150.2 W/m<sup>2</sup> on February 6, 2016, -151.1 W/m<sup>2</sup> on February 7, 2016, and -50.9 W/m<sup>2</sup> on February 8, 2016.

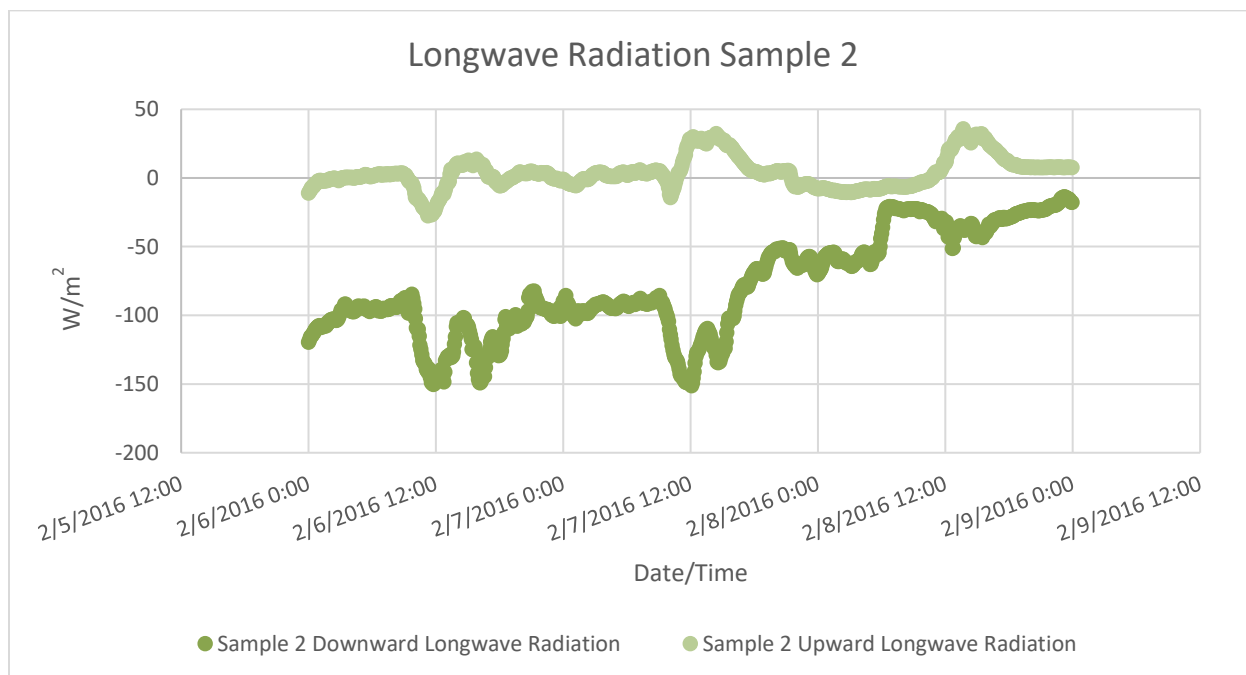


**Figure 117: Infrared radiation measured for sample 2 (slab 3) for testing period February 6, 2016 - February 8, 2016**



The outgoing (upward) longwave radiation measured for sample 3, as shown in Figure 118, reached a high of 1.5 W/m<sup>2</sup> on February 6, 2016, 24.2 W/m<sup>2</sup> on February 7, 2016, and 39.5 W/m<sup>2</sup> on February 8, 2016. The incoming (downward) longwave radiation measured on sample 3 reached a high of -152.3 W/m<sup>2</sup> on February 6, 2016, -153.3 W/m<sup>2</sup> on February 7, 2016, and -51.7 W/m<sup>2</sup> on February 8, 2016.

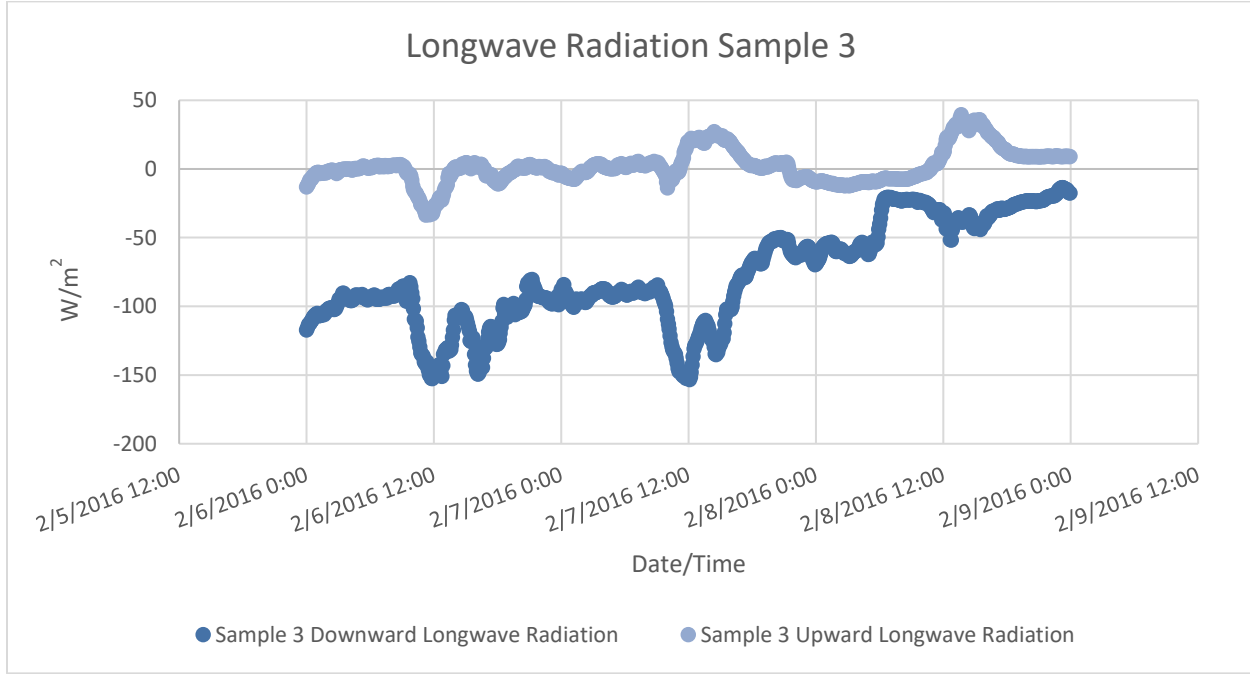


**Figure 118: Infrared radiation measured for sample 3 (slab 4) for testing period February 6, 2016 - February 8, 2016**

The net shortwave radiation (SWup – SWdn) measured for sample 1, as shown in Figure 119, reached a high of 600.6 W/m<sup>2</sup> on February 6, 2016, 616.1 W/m<sup>2</sup> on February 7, 2016, and 384.2 W/m<sup>2</sup> on February 8, 2016. The net longwave radiation (LWup – LWdn) measured on sample 1 reached a high of -159.6 W/m<sup>2</sup> on February 6, 2016, -189.1 W/m<sup>2</sup> on February 7, 2016, and -81.4 W/m<sup>2</sup> on February 8, 2016.

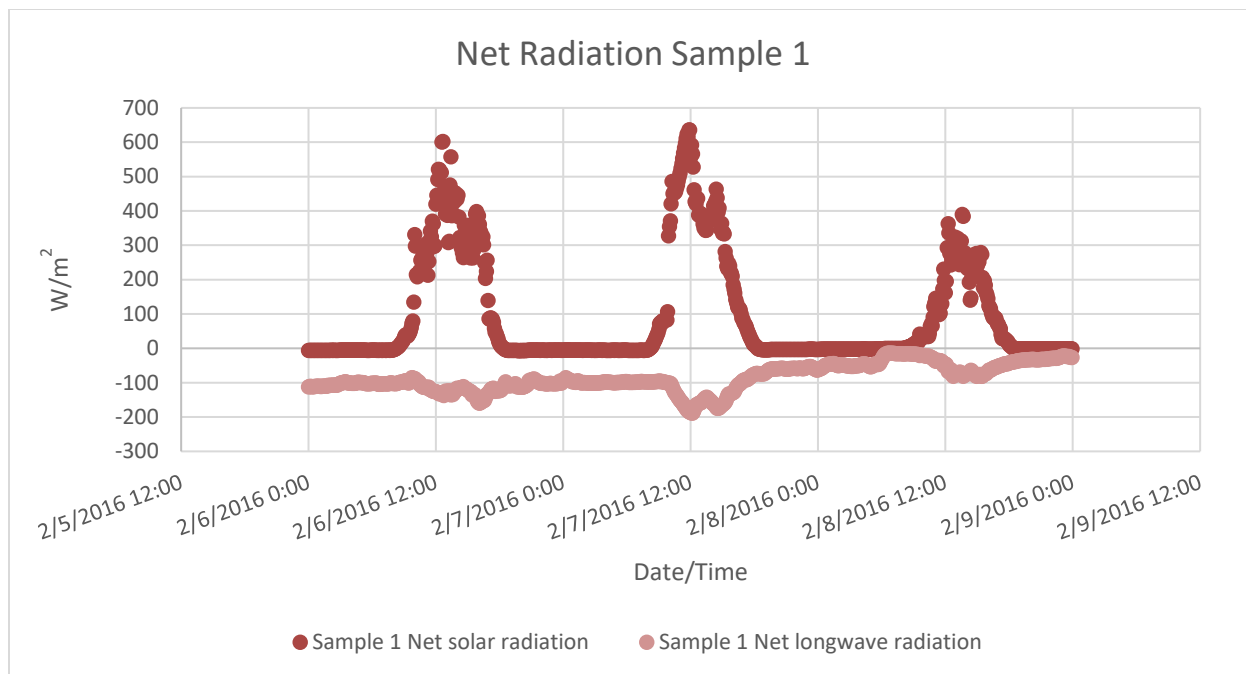


Figure 119: Net radiation measured for sample 1 (slab 2) for testing period February 6, 2016 - February 8, 2016

The net shortwave radiation (SWup – SWdn) measured for sample 2, as shown in Figure 120, reached a high of 607.2  $W/m^2$  on February 6, 2016, 653.5  $W/m^2$  on February 7, 2016, and 421.1  $W/m^2$  on February 8, 2016. The net longwave radiation (LWup – LWdn) measured on sample 2 reached a high of -159.8  $W/m^2$  on February 6, 2016, -179.4  $W/m^2$  on February 7, 2016, and -73.39  $W/m^2$  on February 8, 2016.

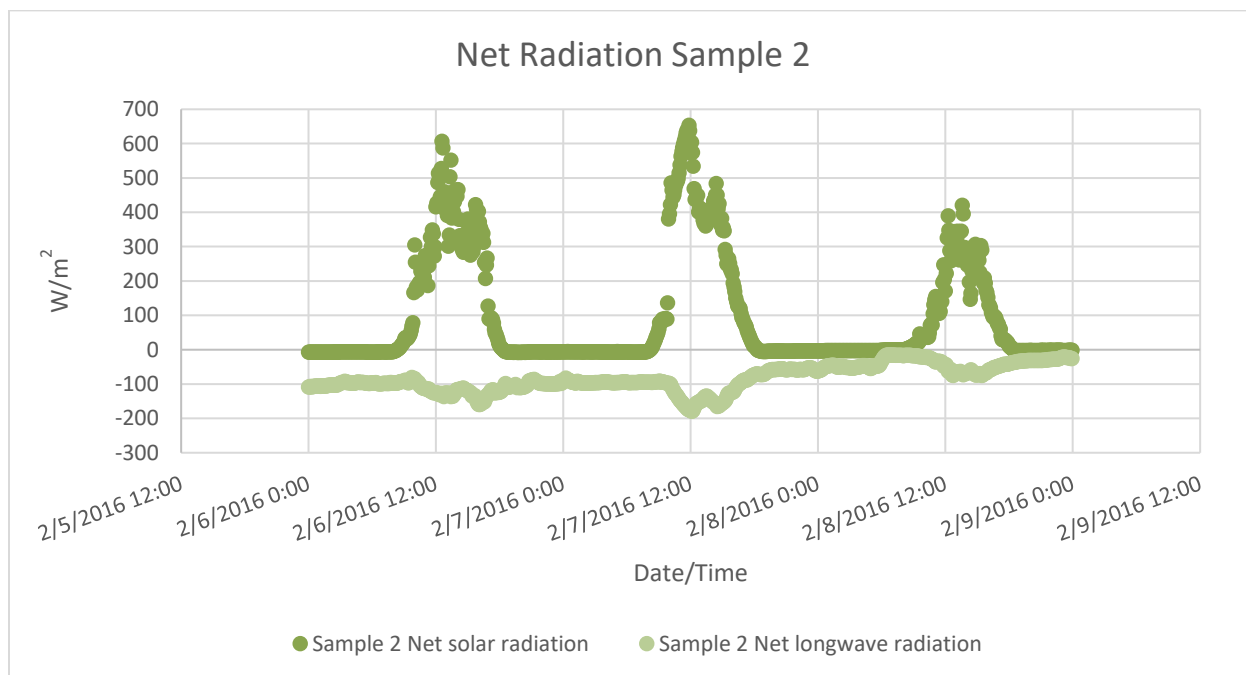


Figure 120: Net radiation measured for sample 2 (slab 3) for testing period February 6, 2016 - February 8, 2016

The net shortwave radiation (SWup – SWdn) measured for sample 3, as shown in Figure 121, reached a high of 461.3 W/m<sup>2</sup> on February 6, 2016, 534.2 W/m<sup>2</sup> on February 7, 2016, and 351.2 W/m<sup>2</sup> on February 8, 2016. The net longwave radiation (LWup – LWdn) measured on sample 3 reached a high of -150.1 W/m<sup>2</sup> on February 6, 2016, -169.4 W/m<sup>2</sup> on February 7, 2016, and -79.3 W/m<sup>2</sup> on February 8, 2016.

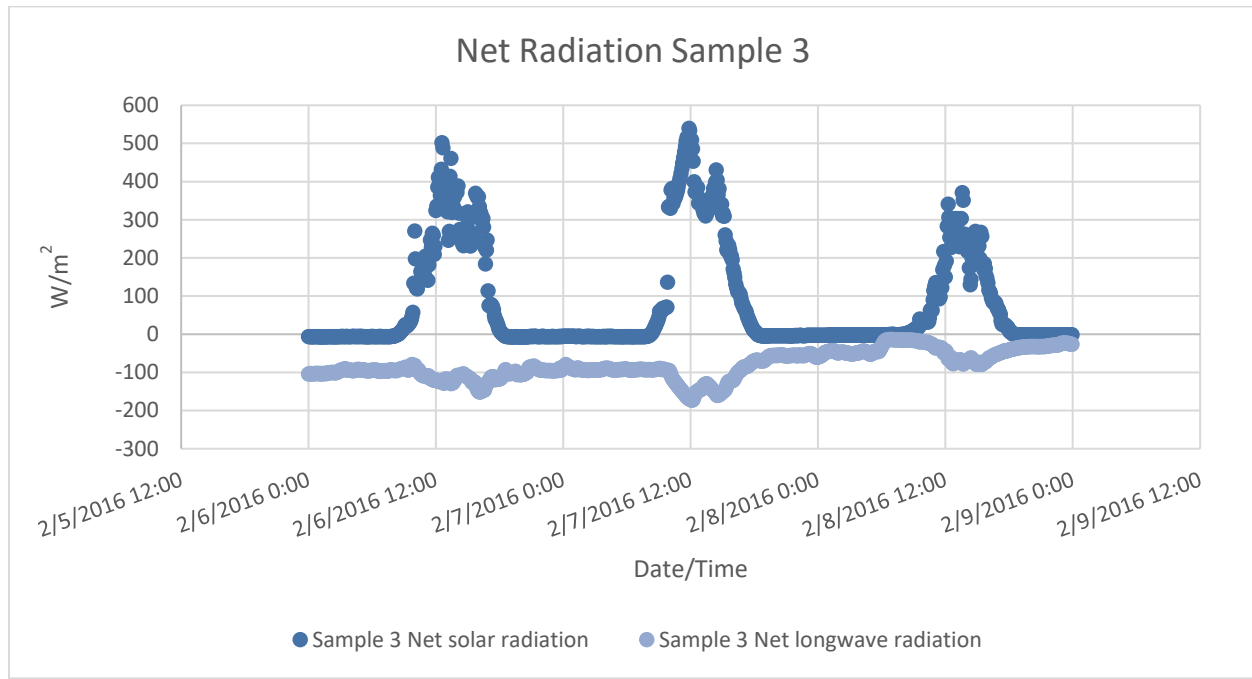
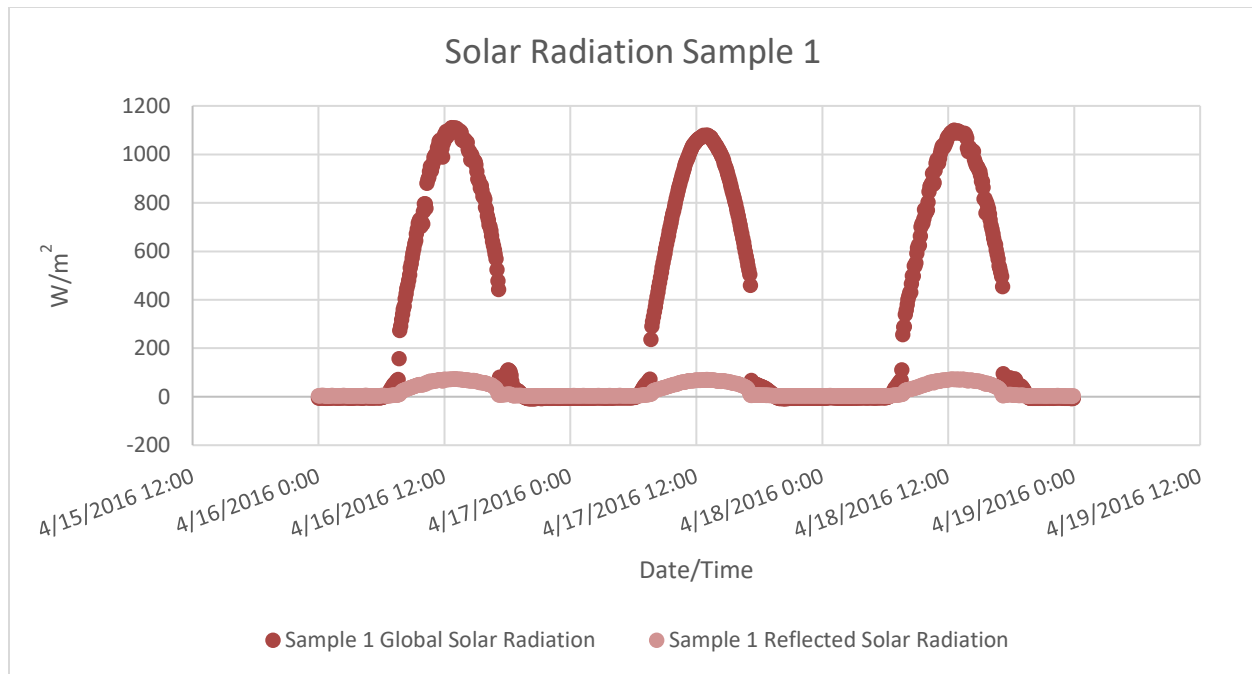


Figure 121: Net radiation measured for sample 3 (slab 4) for testing period February 6, 2016 - February 8, 2016

### April 16, 2016 – April 18, 2016

The shortwave solar radiation measured for sample 1, as shown in Figure 122, reached a high of 1111.0 W/m<sup>2</sup> on April 16, 2016, 1077.1 W/m<sup>2</sup> on April 17, 2016, and 1097.2 W/m<sup>2</sup> on April 18, 2016. The reflected shortwave radiation measured on sample 1 reached a high of 71.3 W/m<sup>2</sup> on April 16, 2016, 69.1 W/m<sup>2</sup> on April 17, 2016, and 71.1 W/m<sup>2</sup> on April 18, 2016.



**Figure 122: Solar radiation measured for sample 1 (slab 2) for testing period April 16, 2016 - April 18, 2016**

The shortwave solar radiation measured for sample 2, as shown in Figure 123, reached a high of 1186.0  $\text{W/m}^2$  on April 16, 2016, 1134  $\text{W/m}^2$  on April 17, 2016, and 1167  $\text{W/m}^2$  on April 18, 2016. The reflected shortwave radiation measured on sample 2 reached a high of 100.7  $\text{W/m}^2$  on April 16, 2016, 94.1  $\text{W/m}^2$  on April 17, 2016, and 97.6  $\text{W/m}^2$  on April 18, 2016.

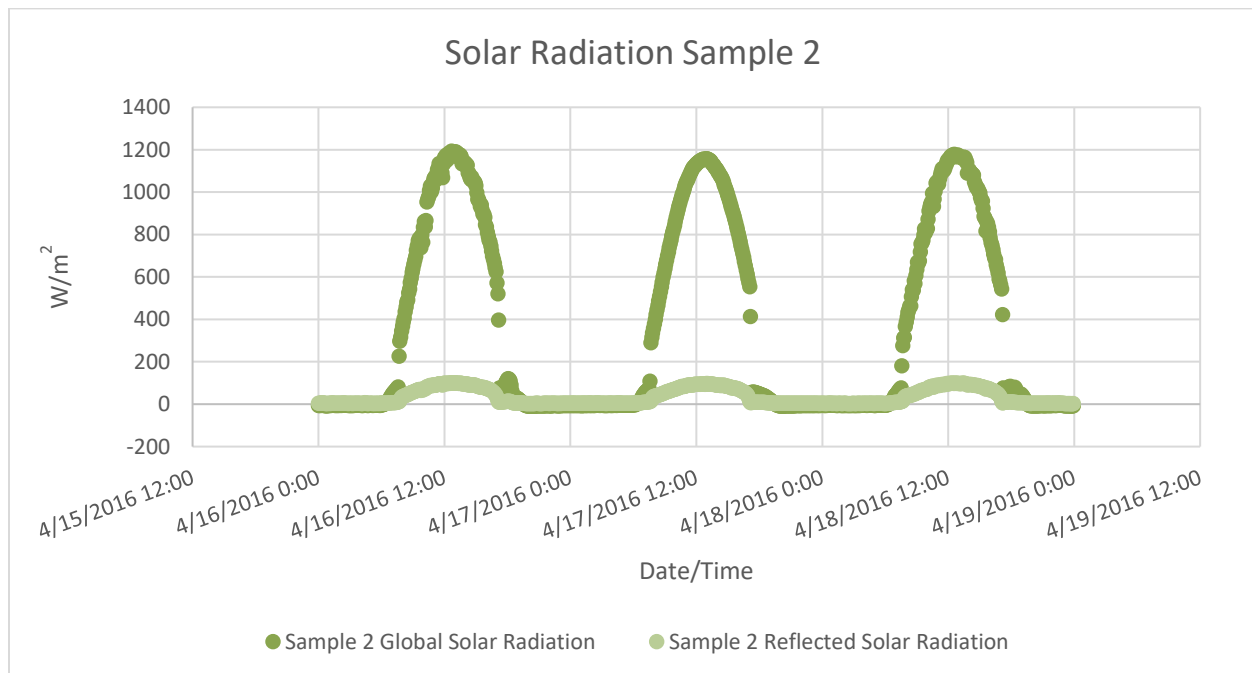


**Figure 123: Solar radiation measured for sample 2 (slab 3) for testing period April 16, 2016 - April 18, 2016**

The shortwave solar radiation measured for sample 3, as shown in Figure 124, reached a high of 1081.0 W/m<sup>2</sup> on April 16, 2016, 1063 W/m<sup>2</sup> on April 17, 2016, and 1079 W/m<sup>2</sup> on April 18, 2016. The reflected shortwave radiation measured on sample 3 reached a high of 119.3 W/m<sup>2</sup> on April 16, 2016, 105.6 W/m<sup>2</sup> on April 17, 2016, and 115.7 W/m<sup>2</sup> on April 18, 2016.

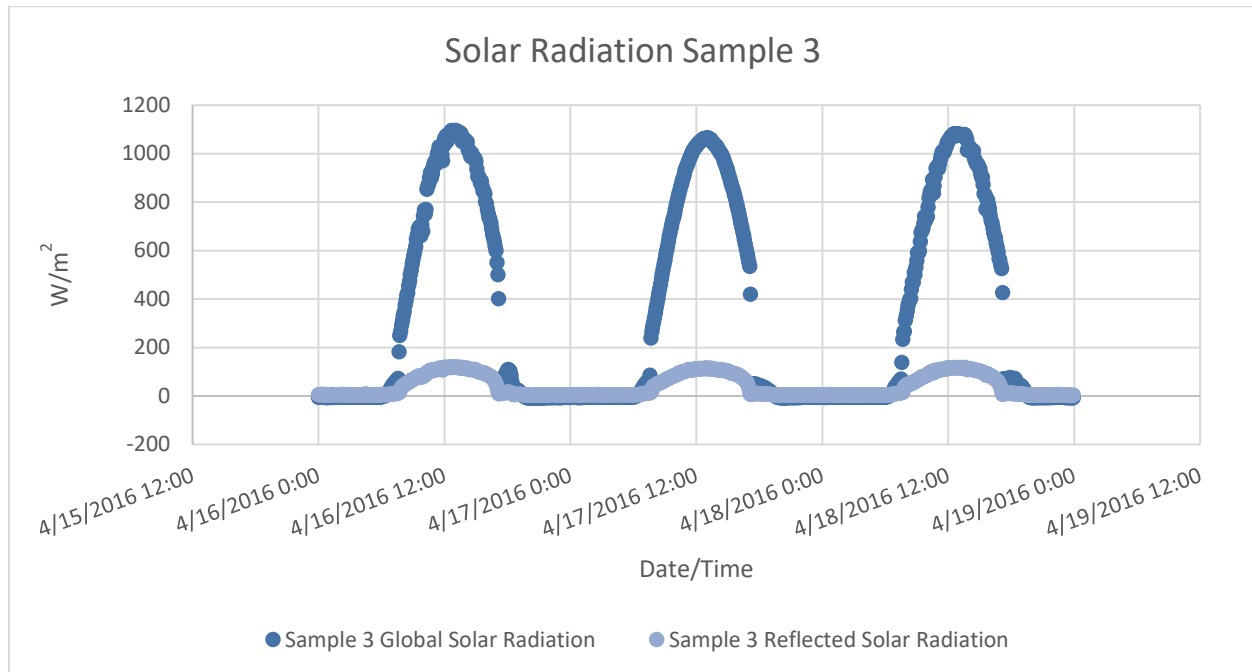


**Figure 124: Solar radiation measured for sample 3 (slab 4) for testing period April 16, 2016 - April 18, 2016**

The outgoing (upward) longwave radiation measured for sample 1, as shown in Figure 125, reached a high of 203.8 W/m<sup>2</sup> on April 16, 2016, 205.8 W/m<sup>2</sup> on April 17, 2016, and 199.5 W/m<sup>2</sup> on April 18, 2016. The incoming (downward) longwave radiation measured on sample 1 reached a high of -215.4 W/m<sup>2</sup> on April 16, 2016, -209.2 W/m<sup>2</sup> on April 17, 2016, and -232.0 W/m<sup>2</sup> on April 18, 2016.

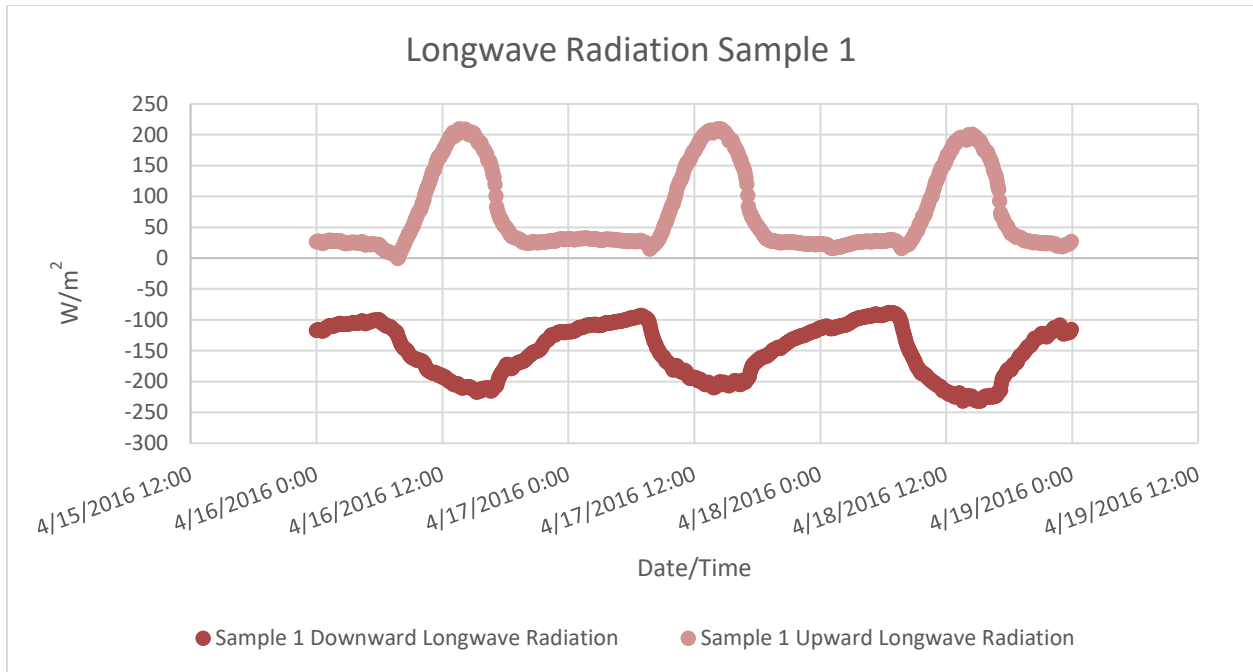


**Figure 125: Infrared radiation measured for sample 1 (slab 2) for testing period April 16, 2016 - April 18, 2016**

The outgoing (upward) longwave radiation measured for sample 2, as shown in Figure 126, reached a high of 172.0 W/m<sup>2</sup> on April 16, 2016, 171.0 W/m<sup>2</sup> on April 17, 2016, and 165.1 W/m<sup>2</sup> on April 18, 2016. The incoming (downward) longwave radiation measured on sample 2 reached a high of -210.5 W/m<sup>2</sup> on April 16, 2016, -203.5 W/m<sup>2</sup> on April 17, 2016, and -218.9 W/m<sup>2</sup> on April 18, 2016.

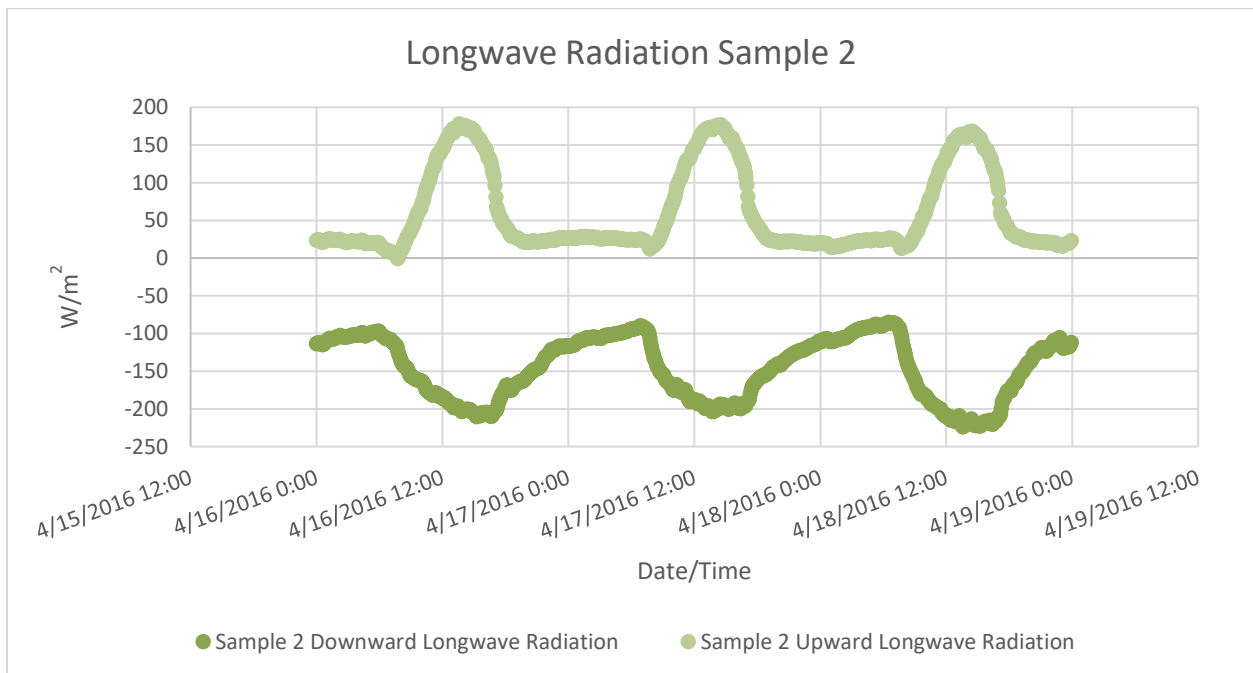


**Figure 126: Infrared radiation measured for sample 2 (slab 3) for testing period April 16, 2016 - April 18, 2016**

The outgoing (upward) longwave radiation measured for sample 3, as shown in Figure 127, reached a high of 191.0 W/m<sup>2</sup> on April 16, 2016, 190.1 W/m<sup>2</sup> on April 17, 2016, and 178.6 W/m<sup>2</sup> on April 18, 2016. The incoming (downward) longwave radiation measured on sample 3 reached a high of -211.7 W/m<sup>2</sup> on April 16, 2016, -208.8 W/m<sup>2</sup> on April 17, 2016, and -223.6 W/m<sup>2</sup> on April 18, 2016.

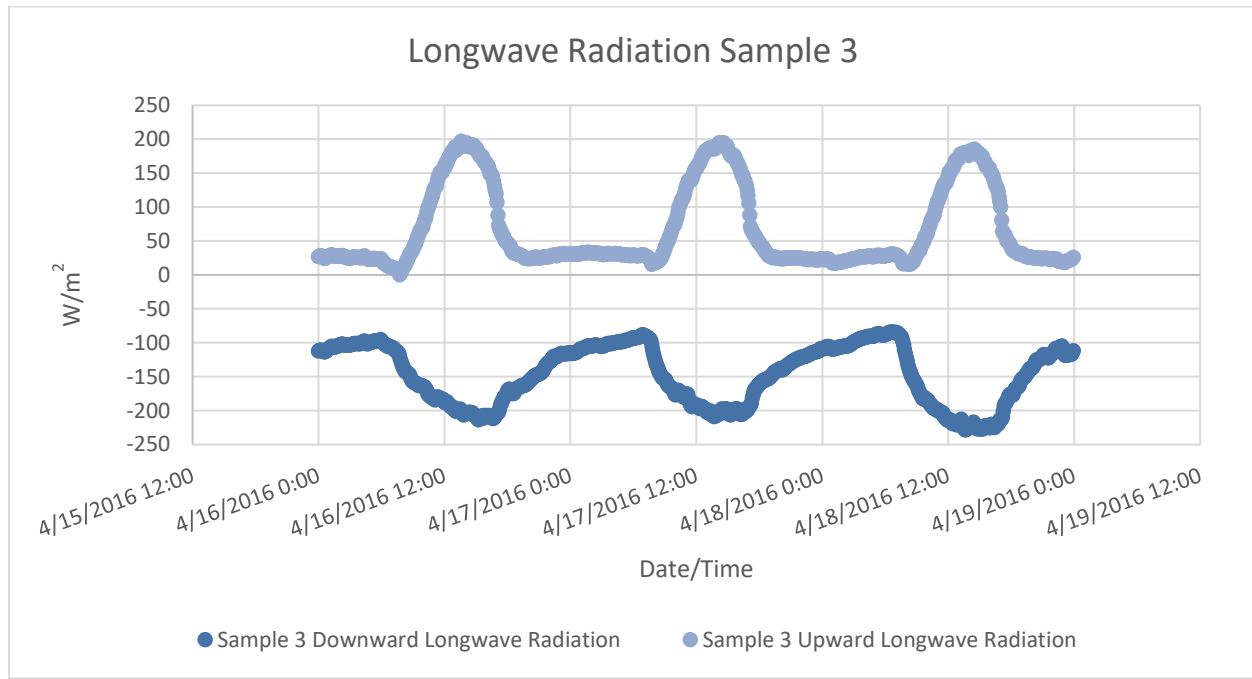


**Figure 127: Infrared radiation measured for sample 3 (slab 4) for testing period April 16, 2016 - April 18, 2016**

The net shortwave radiation (SWup – SWdn) measured for sample 1, as shown in Figure 128, reached a high of 1036 W/m<sup>2</sup> on April 16, 2016, 1002 W/m<sup>2</sup> on April 17, 2016, and 1013 W/m<sup>2</sup> on April 18, 2016. The net longwave radiation (LWup – LWdn) measured on sample 1 reached a high of -419.0 W/m<sup>2</sup> on April 16, 2016, -409.8 W/m<sup>2</sup> on April 17, 2016, and -426.8 W/m<sup>2</sup> on April 18, 2016.

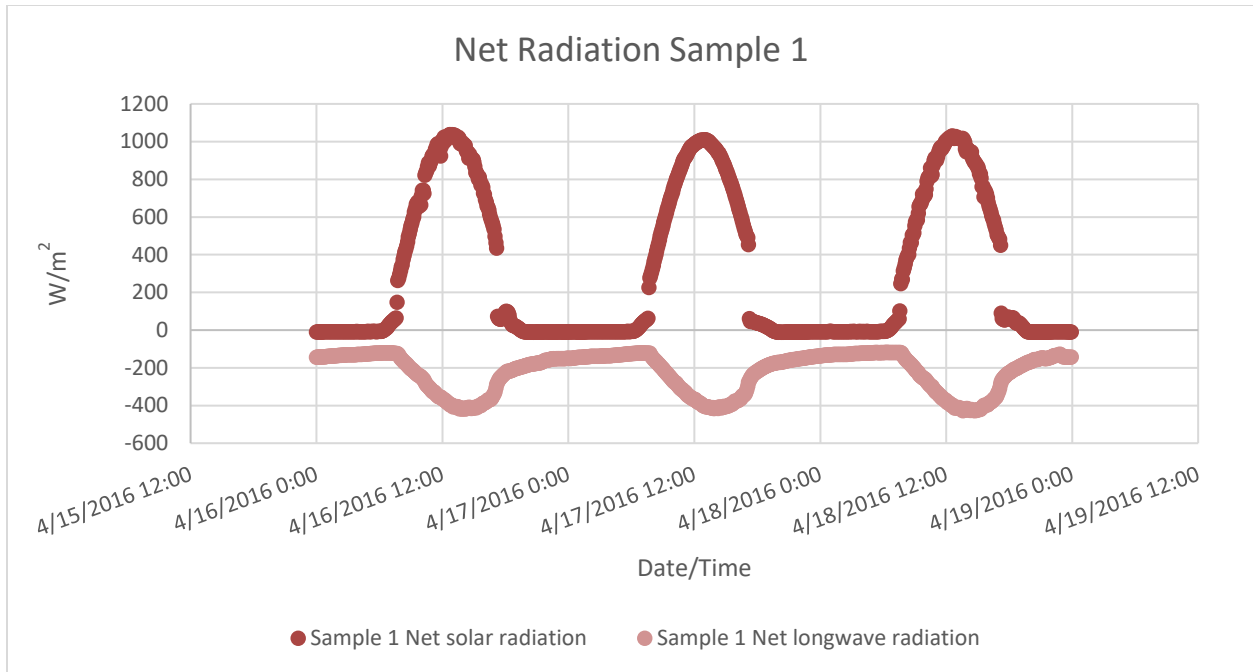


**Figure 128: Net radiation measured for sample 1 (slab 2) for testing period April 16, 2016 - April 18, 2016**

The net shortwave radiation (SWup – SWdn) measured for sample 2, as shown in Figure 129, reached a high of 1082  $\text{W/m}^2$  on April 16, 2016, 1056  $\text{W/m}^2$  on April 17, 2016, and 1063  $\text{W/m}^2$  on April 18, 2016. The net longwave radiation (LWup – LWdn) measured on sample 2 reached a high of -377.0  $\text{W/m}^2$  on April 16, 2016, -376.3  $\text{W/m}^2$  on April 17, 2016, and -387.0  $\text{W/m}^2$  on April 18, 2016.

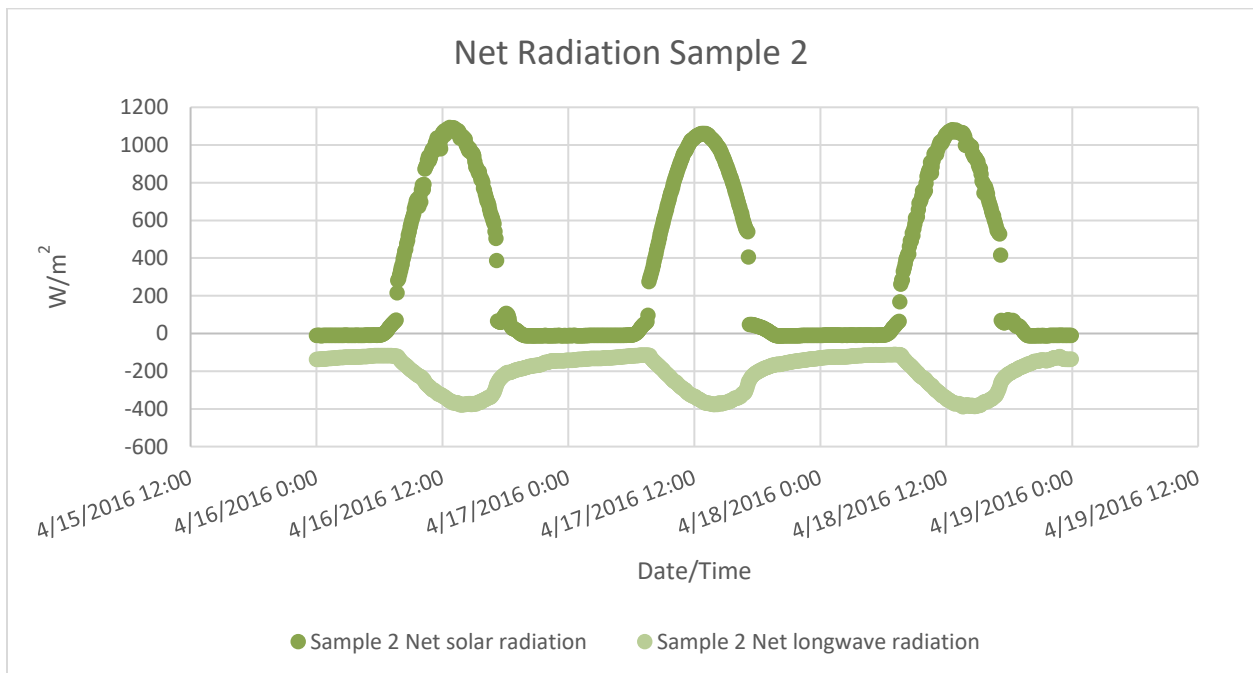


**Figure 129: Net radiation measured for sample 2 (slab 3) for testing period April 16, 2016 - April 18, 2016**



The net shortwave radiation (SWup – SWdn) measured for sample 3, as shown in Figure 130, reached a high of 962 W/m<sup>2</sup> on April 16, 2016, 949 W/m<sup>2</sup> on April 17, 2016, and 957 W/m<sup>2</sup> on April 18, 2016. The net longwave radiation (LWup – LWdn) measured on sample 3 reached a high of -397.5 W/m<sup>2</sup> on April 16, 2016, -393.0 W/m<sup>2</sup> on April 17, 2016, and -407.9 W/m<sup>2</sup> on April 18, 2016.

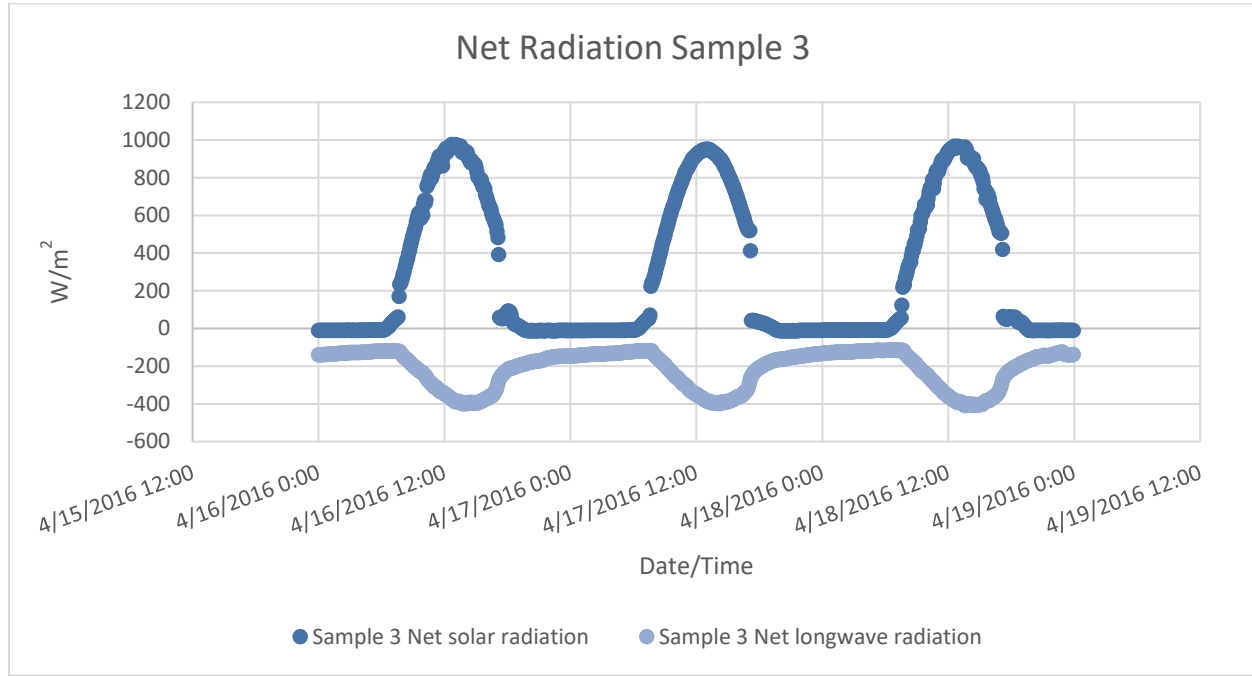


**Figure 130: Net radiation measured for sample 3 (slab 4) for testing period April 16, 2016 - April 18, 2016**

## CONCLUSIONS

### *THERMOCOUPLES*

The thermocouples utilized for this experiment were sufficient to provide sensible heat measurements for conditions inside each of the three asphalt slabs. There was good correlation between the measurements made when comparing one slab to another provided the environmental conditions and solar loading were similar. Since each of the slabs contained the same asphalt mix and each was compacted to approximately the same density, the good correlation between samples was expected. While the thermocouples provided sensible heat measurements, the flux from heating to cooling was unable to be calculated because two parameters were not explored within this experiment, namely the moisture content of the slabs and the moisture content of the surrounding soil. When asphalt density using a dense graded asphalt is below 6%, the mixture is associated with being impervious. The samples created for this experiment were above the 6% threshold. Furthermore, the thin film residual water due to dew or puddling of water on the surface would have an evaporation rate associated that was not captured throughout this experiment.

There was a significant difference between the slab temperature variability measured from the summer and winter months, as expected given the latitude and climate of New Jersey. Figure 131, below, shows the typical asphalt slab temperature dispersion from the top to bottom of the slab, which measured as high as a 12 degree difference from the top to bottom of the slab during the peak hours of April 16, 2016.

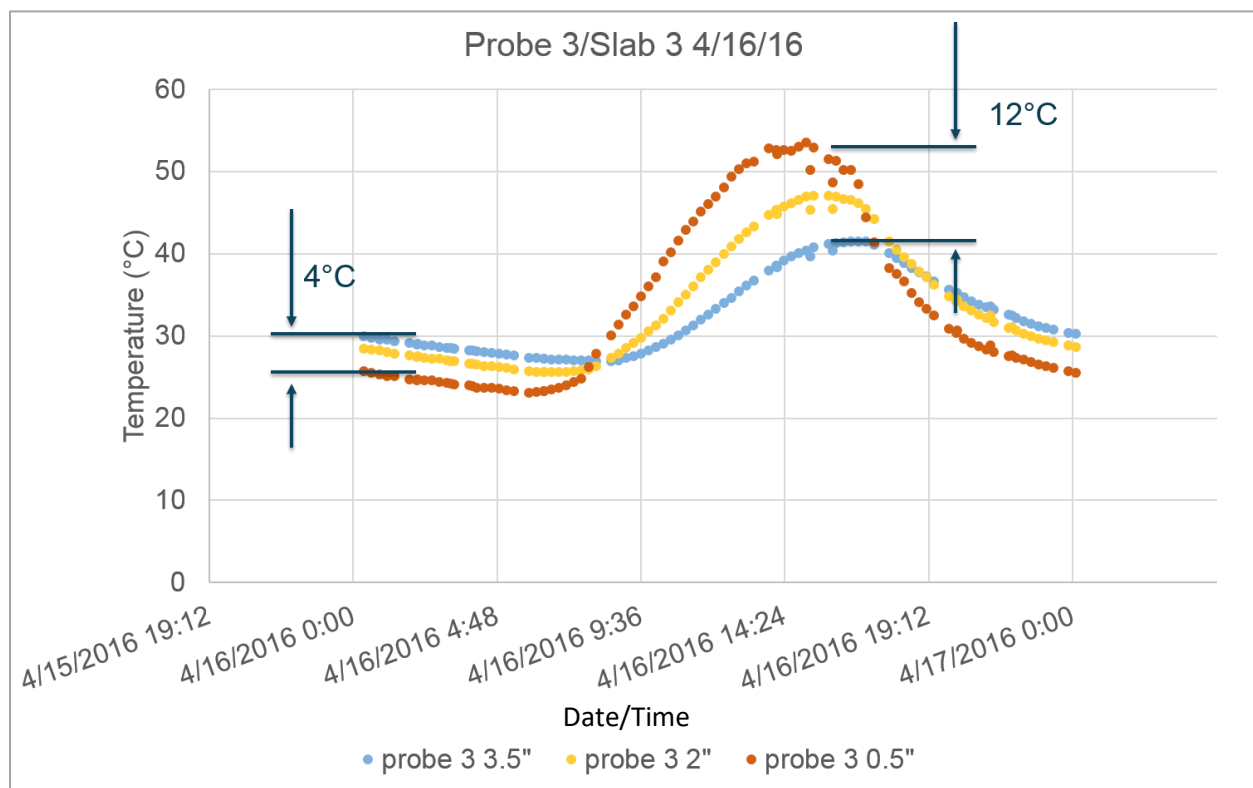


Figure 131: Reduced thermocouple measurements for the top, middle, and bottom of the slab for April 16, 2016

The nighttime difference from the top of the slab to the bottom of the slab on the same day was about 4°C, which signified that the solar radiation did play a critical role in increasing the slab temperature above ambient each day. Another important observation regarding the asphalt slab temperature, due to the surface being exposed to the majority of the solar loading, the top portion of the slab was significantly more variable than the bottom. Additionally, the surface both heated up and cooled down faster than the inner and bottom portions of the slab. The ambient temperature did play a role on the overall temperature of the asphalt slab. When evaluating the asphalt slab temperature compared to the ambient temperature, the first observation was that the slab temperatures were always typically higher than the ambient temperatures, with a more pronounced effect during the summer months.

During the winter months the slabs were closer to the ambient temperature. During the nighttime, as shown in Figure 132 below, the difference between the top and bottom of the asphalt slab was minimalized to less than 1°C (3°F). The cold ambient temperature coupled in addition to the lower solar input in the winter months caused the daily variability to be less from nighttime to day time. During the daytime in the winter, the difference in slab temperatures from the top of the sample to the bottom of the sample were also very low, measuring around 3°C (4.5°F).

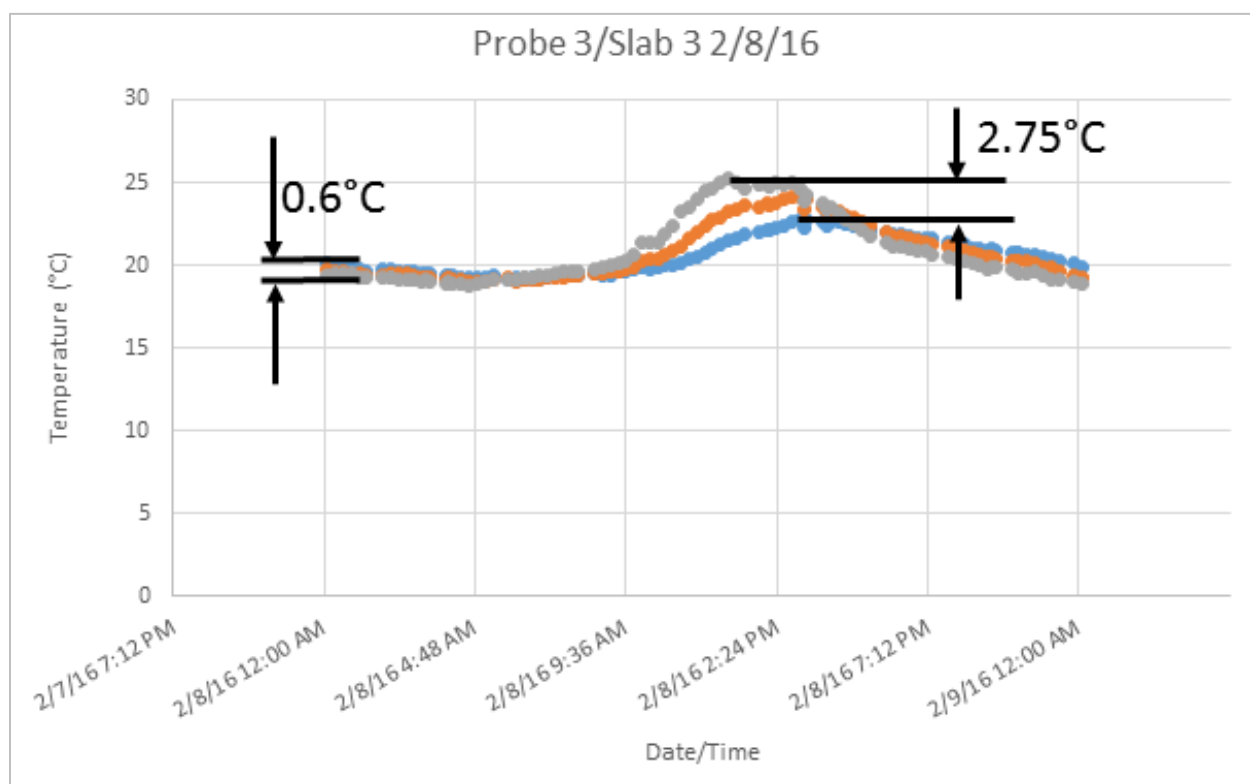


Figure 132: Reduced thermocouple measurements for the top, middle, and bottom of the slab for February 8, 2016

The difference in heat absorbed in the summer and winter months has some important implications including but not limited to the lower effect on the Urban Heat Island effect during the winter months

and not providing capable heat to melt snow and ice. From the aspect of asphalt binder grade functionality fitting in the NJ climate, the data suggests that the PG64-22v asphalt binder was not subjected to temperatures that exceeded either the high end or the low end of the binder temperature criteria. Although the high temperature criteria was satisfied, the slab temperatures in the spring, fall, and summer months were frequently over 50°C (122°F) within the top inch, which is important to consider when evaluating how the asphalt binder ages over an annual period in the field.

### ALBEDO

The albedo, or ratio of reflected light, was comparable to that of standard freshly mixed asphalt, averaging 0.08 between each of the three samples. Due slight differences in construction of the samples, the surfaces of each was not completely flat, which resulted in slightly different albedo values for each. The albedo of the asphalt slabs, while the sun was at its highest point in the day, was similar throughout the year, with the exception being when the slab surface was compromised. If there was a sheet of water or ice the change in surface properties would affect the measured albedo. An example of this is shown in Figure 133, where there was ice on the sample for the January 4-6 measurement period. The effect of the ice was pronounced and the result was evident by the errant data that spiked above the maximum threshold of reflectivity.

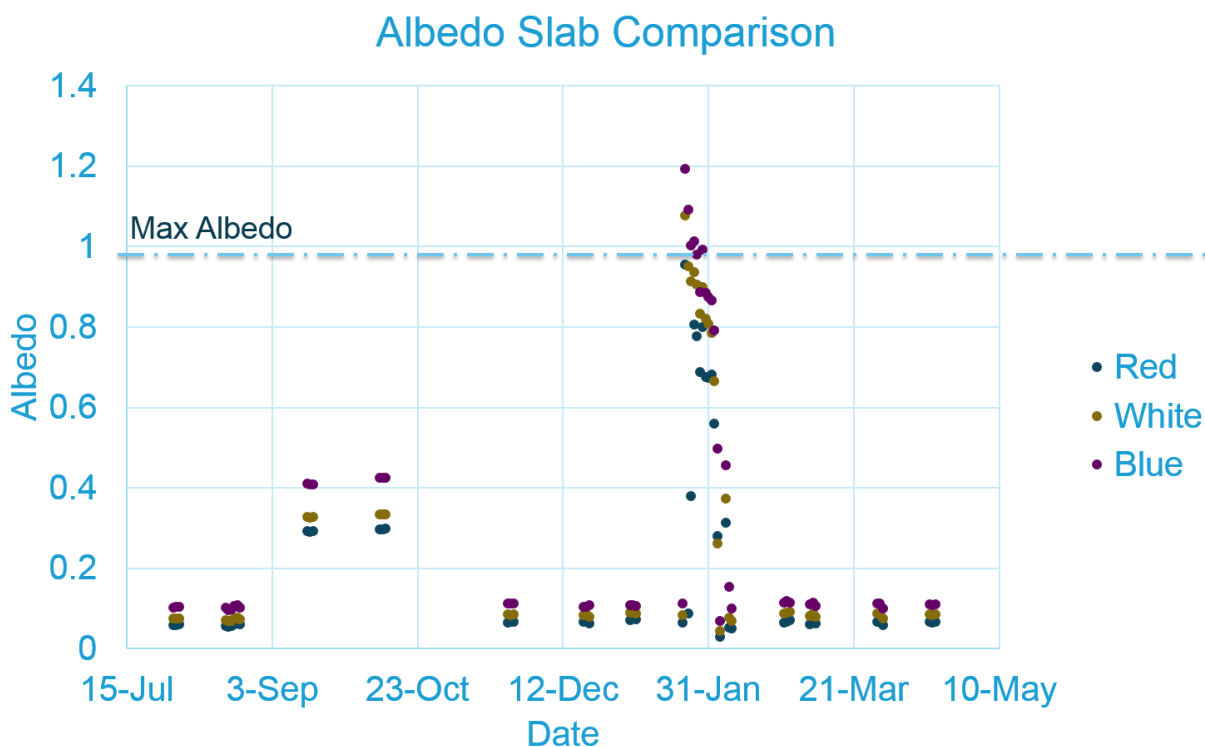


Figure 133: Annual albedo comparison across each of the three slabs

During that same period with high albedo, the asphalt slabs were still increasing and decreasing internal temperatures above ambient daily, which is counterintuitive as this author would have expected the internal temperature flux to decrease as the albedo increased. The data indicated that there is

additional factors controlling the internal heat of the slabs and that even as the reflectivity increased, the incoming solar energy still had a pronounced effect.

Although the superfluous albedo results shown here were interesting, the specification to measure albedo as denoted in ASTM E1918 (ASTM, 2015) would typically remove that data to create an even albedo comparison. With that metric applied to this dataset, the asphalt slabs were shown to remain at a consistent albedo throughout the year. Since the Traprock PG64-22v mix that was constructed for this project did not undergo any traffic wearing, this result was expected. The similarity between albedo for each of the three slabs over the year-long testing period, disregarding the February data, is shown in Figure 134 below.

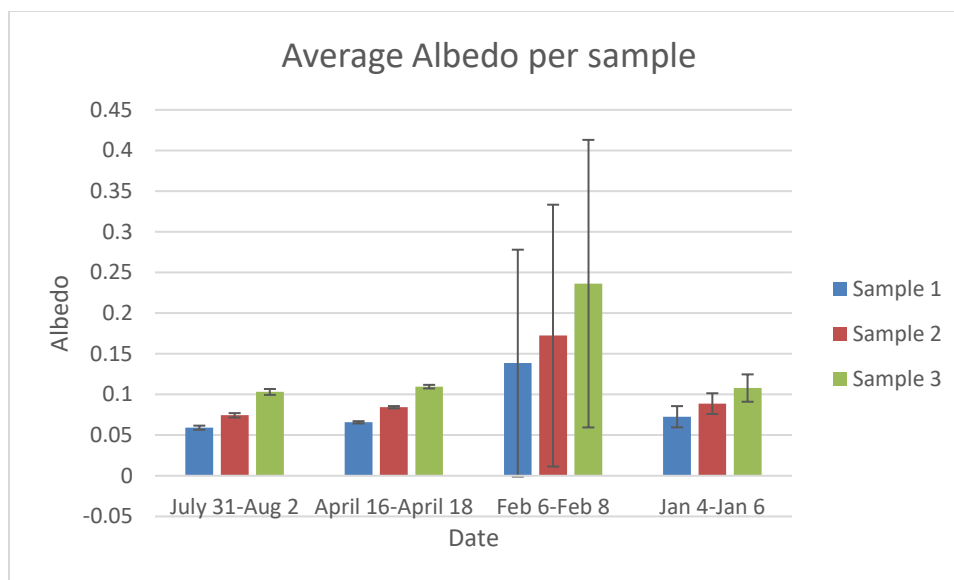


Figure 134: Average albedo values per sample

Figure 134 clearly shows that the albedo measured for the three slabs was consistent over the course of the year. Each slab had its own albedo, which supports one objective of this proposal, which was to suggest measuring multiple samples simultaneously to encourage statistical validation of the measurements for a particular asphalt (or Portland cement concrete) material. In this case, with only one mix that was prepared identically, in the same location, with the same environmental criteria, there were still notable differences in reflectivity from sample to sample. The differences can be attributed to variations in surface texture or differences in the alignment of near-surface aggregate.

### ***SOLAR RADIATION***

Measurements of solar radiation were conducted to show how much shortwave and longwave energy was being imparted on the asphalt samples throughout the year. The results confirmed that the incoming solar radiation was greatly affected by the azimuth of the sun due to seasonal variability at this latitude. The solar energy measured in the winter months was consistently half of the energy measured during the summer months. This difference was expected and has important implications for calculating local energy budgets for different transportation materials within this geographical region. The results

were shown as shortwave solar radiation, longwave radiation, net shortwave radiation (Incoming-outgoing), and net longwave radiation. The results shown below refer to the total net solar radiation which consists of the net shortwave average plus the net longwave average. Figure 135 shows the total net radiation for the July 31-Aug 2 testing period.

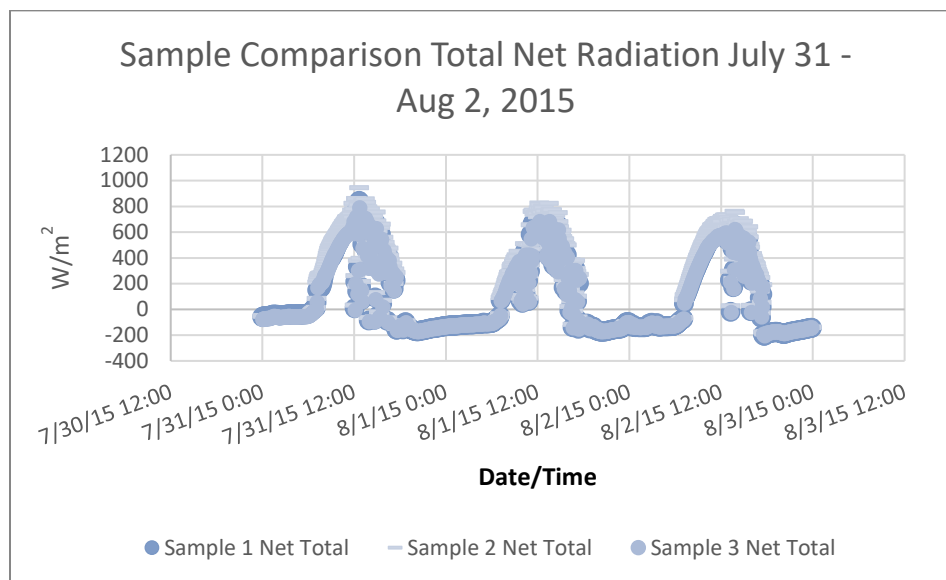


Figure 135: Sample comparison of the total net radiation measured for testing period July 31, 2015 – August 2, 2015

The total net radiation for the July 31 through August 2, 2015 shown in Figure 135 compares the differences between each of the asphalt slabs. The distinct diurnal pattern reflects the daytime and nighttime conditions exactly. The maximum incoming net total for the three day period was 800  $W/m^2$  and the maximum outgoing net total was -170  $W/m^2$ . There were direct similarities between the three samples, which confirmed that the three similar samples fundamentally absorbed and diffused the light energy to the same effect. Likely due to the maximum heat storage capacity of the asphalt blend, as the incoming energy increased during the day, the energy released throughout the night increased as well. The duration of incoming solar radiation was longer in the summer months as well, which supported the inclusion of additional solar energy that became transformed to heat energy, which then cooled overnight.

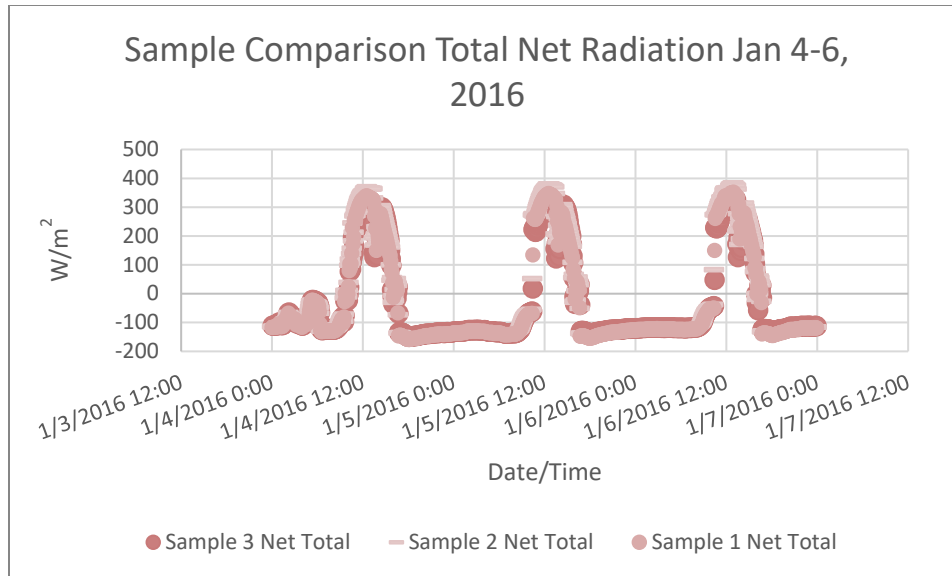


Figure 136: Sample comparison of the total net radiation measured for testing period January 4 2016 – January 6, 2016

Figure 136 shows the total net radiation for the January 4-6 measurement period. Within that period, the maximum total net incoming was  $390 \text{ W/m}^2$  and the maximum total net outgoing was  $-158.5 \text{ W/m}^2$ . There were slight differences between each of the three slabs, but the differences were not as pronounced as the natural variations that occurred due to presumable patchy cloud cover. The February net radiation comparison shown in Figure 137, shows that the winter months were fairly similar in both incoming and outgoing radiation.

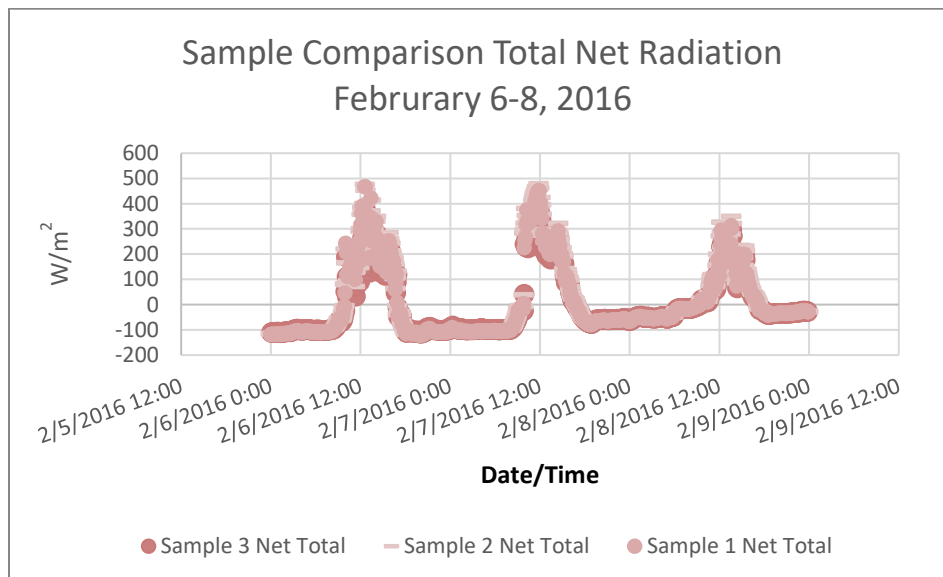


Figure 137: Sample comparison of the total net radiation measured for testing period February 6, 2016 – February 8, 2016

The net radiation for February measured a high of  $466 \text{ W/m}^2$  incoming and a maximum outgoing radiation of  $-117 \text{ W/m}^2$ . While the maximum incoming was higher than that of the January test period, the outgoing was lower than the January test period, which was likely due to the snow/ice cover found in that February test period. Based on the increased incoming radiation, the net radiation was expected

to increase as well, which did not prove to be the case within the February measurements. The peaked energy near mid-day showed that the short sunlight duration was the prominent deterministic factor driving energy absorption within the slab.

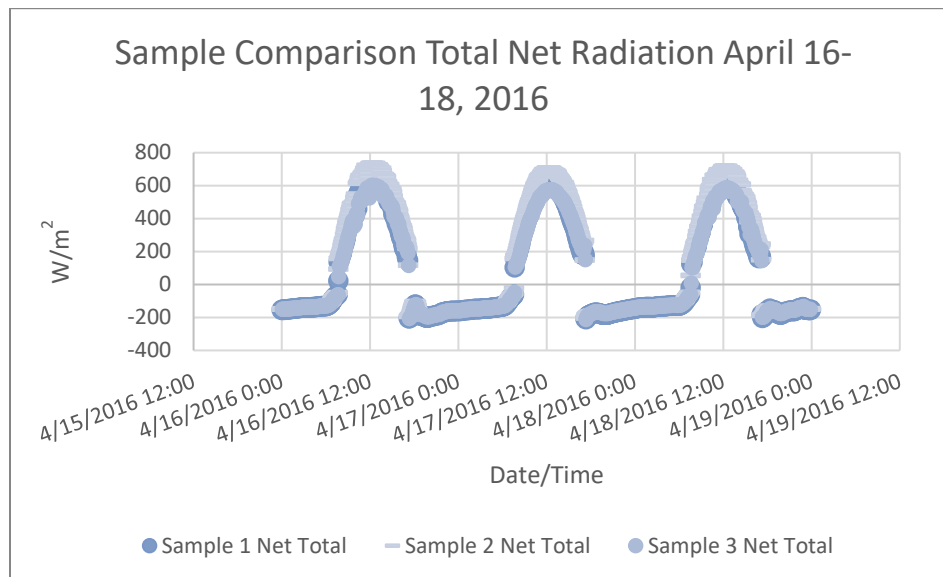


Figure 138: Sample comparison of the total net radiation measured for testing period April 16 2016 – April 18, 2016

Finally, Figure 138 shows the total net radiation for the April testing period. As expected, the net radiation was less than the summer months and more than the winter months. The maximum net incoming was 703.9 W/m<sup>2</sup> and the maximum outgoing net radiation was -206.4 W/m<sup>2</sup>. The slight upward trend of the outgoing radiation throughout the nighttime period exemplified the expected theoretical trend. Although that trend was not as apparent throughout the other testing periods, it was a consistent phenomenon where the rate of outgoing radiation increased as the magnitude of heat stored in the asphalt slab was higher.

The project provided a valuable insight into a few aspects that affect the impact of a particular transportation surfaces contribution to the urban heat island effect. By measuring the solar radiation and temperature simultaneously, it was possible to show the impact of the solar input on the internal slab temperatures. Due to seasonal variation, the impact of the solar radiation was more significant in the summer months than in the winter months. As expected, the freshly paved asphalt provided low albedo. As a non-trafficked surface that did not lose asphalt binder film thickness, it was notable that the albedo remained similar throughout the one year testing period. There were slight variations in albedo between the three asphalt slabs, which was also notable because they were comprised of the same mix and compacted using the same procedures. One of the major components required to measure the heat flux, which was not able to be calculated for this study, is the moisture content within the asphalt slabs. Water inside the slabs would provide different effects on the energy absorbed and stored depending on the state and volume. The data collected for the three slabs showed that it was possible to measure small samples of 1 square meter. Three samples were used to ensure the material being tested was being accurately portrayed. The three samples did show slight differences both in reflectivity as well as in absorption of solar radiation in the form of heat energy.



## RECOMMENDATIONS

This project highlighted the need for more research in this topic as the impact of infrastructure materials is increasingly being taken into account in both climatic evaluation models and life cycle impact models of infrastructure planning and design. Throughout the pavement material selection processes it is important to have sufficient and accurate data to predict the impact the construction of various materials will have on the local energy budgets and how that impact relates to the urban heat island effect. There are important implications regarding how radiative forcing affects the usability of a transportation surface for humans and animals alike. The more energy that is stored in a pavement throughout the daytime increases the amount of heat transposed to the environment throughout the nighttime periods.

If a surface is significantly hot before a rainstorm, the temperature of the runoff can be affected as it rapidly travels through the storm water system and into important streams and estuaries where breeding fish and amphibians can be negatively affected. Although data regarding this phenomenon is limited, it is suggested that research should be conducted to determine if particular pavements could be selected for sensitive environments to help reduce any impacts due to elevated water temperatures. Elevated surface temperatures can have major impacts on the local migration of species that cross roadways and others that use roadways as corridors.

As shown by Li, et. al., 2016, human behavior can be similarly affected by increased ground surface temperatures by conducting energetic studies regarding the sensitivity of average humans conducting different activities near surfaces that elevate local ambient temperatures.

The impact of different surface materials to potentially help reduce snow loading on roadways in cold climates is also an important factor to consider with transportation materials. More research should be conducted to determine if there are better mixes that can be utilized to melt snow and reduce ice loading. Since conventional transportation surface materials do not eliminate snow, the impact of salt, sand, and brine also need to be considered when evaluating these materials. Even if a transportation surface provides benefits in the reduction of solar forcing impacts, the same material may cause maintenance limitations that reduce the ability to clear road surface of snow and ice during the winter months.

Another important aspect that continued research in transportation surface solar radiation testing is the potential for energy harvesting utilizing thermo-metric methods. Due to the relatively high temperatures found near the surface of some transportation materials, there exists the potential to harness that solar energy by using the temperature differential between the paved surface and sub-surface soil to create useable energy.

One final implication and area of additional research resides in determining the in-service lifespan of the transportation surfaces due to aging, particularly with asphalt mixes, but also with pavement preservation materials and specialized epoxy mixes utilized to enhance skid resistance and reduce permeability over critical structures. Asphalt oxidizes more quickly at higher temperatures which can reduce the lifespan of an asphalt pavement. Darabi et. al., 2012, has also shown that there is a potential

for micro-crack self-healing throughout a portion of the lifecycle of an in-service asphalt pavement given the right circumstance. Both of these phenomenon require further study as both also provide useful insight to planners and design engineers alike.

Regarding the measurements and metrics evaluated for this study, it was determined that further research conducted in this area should consider including moisture content of the surface material being measured. Many of the feedback loops related to the impact of radiative forcing on a local energy budget are hysteretic and all are related to tensor properties of fluid dynamics and radiative forcing and cannot be properly modeled without the knowledge of the moisture content. Although this study was limited in the proximity of the environmental data utilized and did not evaluate moisture content, the sensible heat measurements clearly showed that there is differential radiative forcing due to solar radiation. This study also showed that due to the nature of the materials being evaluated, there is a high potential for differences in radiative forcing for different portions of the asphalt mat due to variations in construction and local aggregate arrangement.

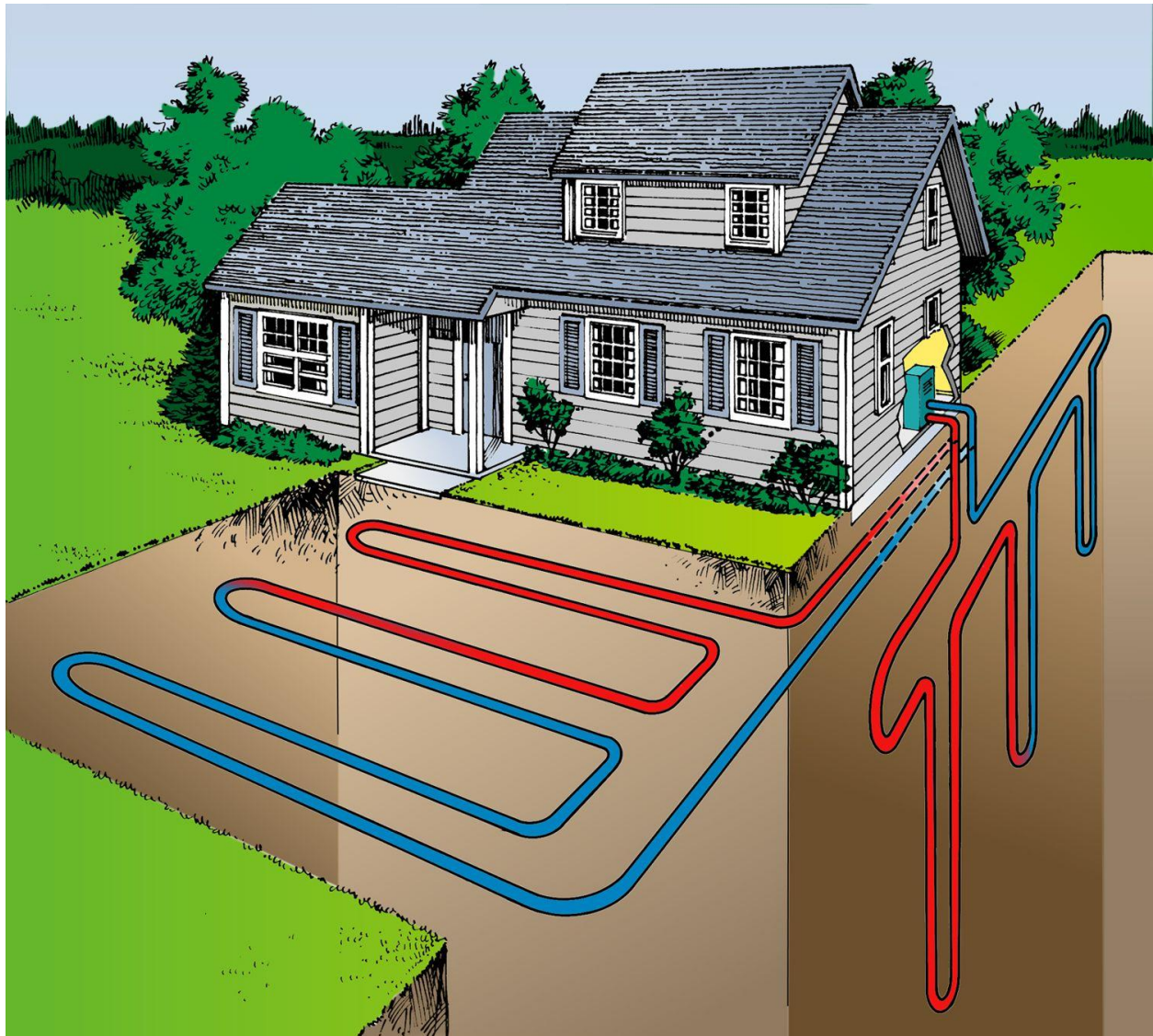
Further study should be conducted on alternative mixes, because the design of the structure and the aggregates utilized for the mix are integral in determining the maximum storage capacity of heat, the transference of heat, and the conversion of solar energy into heat. Given that the largest percentage of impervious transportation surfaces reside at the county and municipal level, it is important to evaluate materials typically utilized for those applications, such as cape seals, micro-surfaces, and various chip-seal pavements.

Based on the success of measuring 1 sq. m. samples that provided similar results for this study, the possibility to conduct future research using similar sample sizes provides an important opportunity for studying how in-service pavements behave near the end of their applicable service life. A 1 sq. m. sample can be easily removed from a pavement mat and shipped back to a laboratory for testing. It is still recommended to conduct measurements on at least two samples, whether laboratory or field produced to provide a verification check of the material due to the inherent variability of asphalt mixes.

## **CUSTOMER QUESTIONS AND ANSWERS**

Q1: Another interesting variable being proposed are geothermal systems for critical transportation infrastructure for future research to reduce winter maintenance and climate related pavement distress. Have you considered the effects of this technology?

A1 (a): I would suggest that a south eastern US (NC, SC, GA, AL, MS) solution using geothermal piping system similar to geothermal home heating



(<https://energync.org/geothermal-heat-pumps/>) would be quite possible. These systems are available in SOME locations in NJ but use is directly dependent on geological (geothermal) conditions ([https://www.nj.com/business/index.ssf/2009/03/homeowners\\_installing\\_geotherm.html](https://www.nj.com/business/index.ssf/2009/03/homeowners_installing_geotherm.html)). I believe these systems should be investigated for their snow-load-reduction but would also be interested in the aging effects on the asphalt. Could possibly work best if implemented in sub-base (thermal diffusion model would need to be developed to determine pipe locations under asphalt mixture) if that subbase were a rubberized concrete. Would need surrounding material to provide adequate subbase while also providing high thermal conductivity. This may affect asphalt base course thermal expansion (although this could be perceived as a benefit to reduce bottom up cracking with the correct asphalt binder in asphaltic healing models). A piping system such as this would be an inherently expensive design/build initially, then once the piping system is integrated into the asphalt surface the biggest issue becomes the inability to conduct

proper maintenance for various reasons: difficult to remove to pipeline; saw-cuts for utilities become extremely difficult (always an issue with this technology); traffic load/deformation concern for pipe bursts, and continual maintenance for the antifreeze system.

A1 (2): There have been several other studies suggesting the application of geothermal for de-icing has been utilized for bridge decks, highway, and asphalt pavements in the US and internationally. Efforts have been aimed towards feasibility, cost, lifecycle, and some implementation projects. I will send one reference with these comments, but if you are interested (and would like copies of any), some of my literature research along these lines include the following:

- i. Anand, P. Assessing the energy and financial viability of heated pavement systems for airports. *Iowa State University Digital Repository*. (2015).
- ii. Dehdezi, Pejman Keikhaei. Enhancing pavements for thermal applications. *Diss. University of Nottingham*. (2012).
- iii. Donnelly, Denis, E., Geothermal energy for highway snow and ice control. Summary Report No. CDH-DTP-R-81-13. *Colorado Department of Highways*. (1981).
- iv. Eugster, Walter J. "Road and bridge heating using geothermal energy. Overview and examples." *Proceedings European Geothermal Congress*. Vol. 2007. (2007).
- v. Mensah, Kwesi, and Jong Min Choi. "Review of technologies for snow melting systems." *Journal of Mechanical Science and Technology* 29.12: 5507-5521. (2015).
- vi. Pan, P., Wu, S., Xiao, Y., Liu, G. A review of hydronic asphalt pavement for energy harvesting and snow melting. *Renewable and Sustainable Energy Reviews*, 48, 624-634. (2015).
- vii. Veldkamp, et al. Corrosion in Dutch geothermal systems – Final Report TNO 2015 R10160. *Energy/Geological Survey of the Netherlands*. (2016).
- viii. Yildirim, N., and Hepbasli, A. (2015). Exergetic aspects of snow melting using a geothermal Heat Pump System. *Proceedings World Geothermal Congress 2015*. Melbourne, Australia, 19-25 April 2015.

Q2: Some studies are also looking into electromagnetic fibers to control pavement low temperatures for snow/ice removal and control. Have you considered the effects of this technology?

A2: Fibers can be used to increase the thermal conductivity of an asphalt surface. They have also been used for self-healing asphalt applications (best performance in SMA). Similar to any other asphalt additive, the effects would need to be verified by %material to determine if there would be an adverse effect to performance. It does not seem to work significantly well for heavy snow loads, but it could be beneficial to light snow loads. The latitude of usage in the US would be critical, NJ might fall into sufficient range, which would be another beneficial aspect to evaluate in an additional research effort. This application has the additional benefit of including additional recycled materials to an asphalt pavement.

Q3: It would be interesting to compare the results in your study to similar full depth porous asphalt mixture slabs. The asphalt industry has claimed that porous pavements create less of a heat island effect. Curious if any studies have compared dense graded asphalt vs. porous or if you have some

data from your study to comment. I don't believe this is just an air voids issue, but the presence of interconnected voids which may allow a greater propensity for cooling. Any comments or maybe some additional research?

A3 (a): There is a great deal of research going on in this area. Several studies have evaluated pervious asphalt already, but none have the missing link of measured moisture content that we had in the NJDOT Pervious Concrete for Sidewalk Use Project which can be found in Appendix A. Air-Voids do serve as a component to the thermal equilibrium of the local system but in several interconnected ways.

- ix. The air-voids can contain water (necessary to use phase change as mechanism for local cooling)
- x. Air can be a good insulator; but moving air can draw heat out of the system.
- xi. Interconnected voids allow more water to enter the pavement system, which can increase aggregate moisture storage (concrete), which is beneficial. In asphalt, if we consider the aggregates to be completely coated, the interconnected voids can act as a method to increase the amount of water entering the system.
- xii. The aggregate properties (thermal conductivity and specific heat) are critical.
- xiii. The surface color and texture are critical (% reflection/absorption).

A3 (b): Additional research is needed and strongly recommended here, as well as the comparison to other ground-surface materials (manmade and natural) to create references.

Q4: Full depth porous asphalt pavements would significantly reduce runoff and the negative environmental effects discussed in your recommendations. DEP does not provide credit for NJDOT's use of porous asphalt pavements and still considers these surfaces as impervious. This should be discussed in the conclusions and recommendations with a goal to get better support from DEP on these types of surfaces if they truly want to see increased use of these systems. What can be done to get DEP to support more widespread use?

A4 (a): Stormwater runoff was simply brought up in this project as an additional benefit that could be explored. This project was primarily focused on the thermal properties and measurement of local energy systems.

A4 (b): As part of the Pervious Concrete project, an infiltration study was conducted to show the different rates of stormwater runoff for impervious and pervious materials, which showed promising results. Generally, we design our pavements for significantly higher flow rate than is required, so it is possible that a less permeable mix could be created with increased strength/performance. Additional research to model surface flow, storage capacity, and infiltration would be required to prove to NJDEP the capabilities of these systems. The method to entice DEP approval would likely require the alteration of the runoff coefficients for these materials, which would need to take all of the inputs and outputs into account. I believe this would need to be evaluated as part of the EIS for a project to determine feasibility and with a robust enough study, could become more appealing to DEP. It is also likely that the DEP would be more apt

to consider the material as a useful BMP if it also required a project to consider a 100% retention/infiltration for all water flow of increased water as compared to natural or original condition, and this capability would be determined by the feasibility of the projects landscape, geology, hydrology as well as the appropriate use of infiltration basins, rain gardens, and other stormwater management BMPs.

## REFERENCES

1. Arnold Jr, C. L., & Gibbons, C. J. (1996). Impervious surface coverage: the emergence of a key environmental indicator. *Journal of the American planning Association*, 62(2), 243-258.
2. ASTM, 2015. ASTM E 1918-06: Standard test method for measuring solar reflectance of horizontal and low-sloped surfaces in the field. American Society for Testing and Materials. West Conshohocken, PA.
3. Hasse, J., & Lathrop, R. (2010). Changing Landscapes in the Garden State: Urban Growth and Open Space Loss in NJ, 1986 Thru 2007. *Geospatial Research Laboratory*, Rowan University.
4. Li, H. (2012). *Evaluation of cool pavement strategies for heat island mitigation*. (Doctoral dissertation, UC Davis).
5. Li, H., Harvey, J., & Kendall, A. (2013). Field measurement of albedo for different land cover materials and effects on thermal performance. *Building and Environment*, 59, 536-546.
6. Li, Hui, Yuan He, and John Harvey. "Human Thermal Comfort: Modeling the Impact of Different Cool Pavement Strategies." *Transportation Research Record: Journal of the Transportation Research Board* 2575 (2016): 92-102.
7. Darabi, Masoud K., Rashid K. Abu Al-Rub, and Dallas N. Little. "A continuum damage mechanics framework for modeling micro-damage healing." *International Journal of Solids and Structures* 49.3 (2012): 492-513.
8. Tran, N., Powell, B., Marks, H., West, R., & Kvasnak, A. (2009). Strategies for design and construction of high-reflectance asphalt pavements. *Transportation Research Record: Journal of the Transportation Research Board*, (2098), 124-130.
9. Xu, H. (2010). Analysis of impervious surface and its impact on urban heat environment using the normalized difference impervious surface Index (NDISI). *Photogrammetric Engineering & Remote Sensing*, 76(5), 557-565.
10. Yang, J., Wang, Z., & Kaloush, K. E. (2013). Unintended consequences: A research synthesis examining the use of reflective pavements to mitigate the urban heat island effect. Arizona State University National Center of Excellence for SMART Innovations (2014).

## **APPENDIX**

### ***APPENDIX A – NJDOT PERVIOUS CONCRETE FOR SIDEWALK USE TASK 3***

#### **Evaluation of the Energy Budget for Different Pervious Concrete Mixtures for Sidewalk Use**

##### **SubTask 3.1**

**Prepared by:**

**John Hencken, Co-PI  
Austin Taterka, Graduate Assistant**

**Rutgers University – CAIT  
100 Brett Rd.  
Piscataway, NJ 08854-8058  
<http://www.cait.rutgers.edu/>**



# Table of Contents

Table of Contents.....	149
Table of Figures.....	152
Objective.....	158
Test Description.....	160
Background of Energy Budget .....	160
Radiation (Shortwave, Longwave, Net) .....	160
Sensible Heat.....	161
Latent Heat.....	162
Ground Heat Flux .....	162
Total Energy Balance .....	162
Pervious Concrete.....	163
Benefits and Limitations .....	164
Site Description.....	164
Location .....	164
Site Setup .....	168
Field Sample Creation .....	188
Construction Environmental Conditions.....	197
Field Mix Aggregate Characterization .....	198
Soil Characterization.....	211
Equipment .....	212
Test Setup .....	212
Sensors.....	212
Anemometers and Weather Vane .....	213
Barometric Pressure .....	213
Tipping Bucket Rain Gauge.....	213
Ambient Temperature and Relative Humidity .....	214
Rotronic Hygroclip2 HC2S3.....	214
HMP45C .....	214
Net Radiometers.....	214

Kipp & Zonen CNR2 Net Radiometer .....	214
Kipp & Zonen CNR4 Net Radiometer .....	215
Hukseflux NR01 Net Radiometer.....	215
Load Cells.....	216
Load Cell Central Model SWCM-2.5K .....	216
Thermocouples.....	218
Campbell Scientific FW05 Type E Thermocouples.....	218
Omega Type K Thermocouples .....	219
Model 108 Temperature Probe .....	221
Time-Domain Reflectometers.....	224
Campbell Scientific CS616 .....	224
Campbell Scientific CS650 .....	225
Data Loggers and Multiplexers .....	228
Campbell Scientific CR10X Datalogger (1) .....	228
Campbell Scientific CR1000 Datalogger (3) .....	229
Campbell Scientific CR3000 Datalogger (2) .....	231
Campbell Scientific AM25T Thermocouple Multiplexer (1).....	233
Campbell Scientific AM16/32B Multiplexer (1) .....	233
Equipment Setup.....	234
Equipment Location and Orientation.....	239
Rooftop Weather Station.....	239
Ground Weather Station .....	240
Type-E Air Column Thermocouples .....	242
Slab Temperature Probes.....	243
Net Radiometers.....	244
Measurement Protocol .....	245
Data Derived from Outside Sources.....	261
Sky Condition Data .....	262
Zenith Data.....	263
Initial Data.....	264
Net Radiometers.....	264
Thermocouples.....	267

Type E.....	270
Type K.....	273
Rain Buckets .....	280
Barometric Pressure .....	281
Relative Humidity .....	282
Time-Domain Reflectometers.....	283
Anemometers.....	287
Load Cells.....	288
Density Determination .....	326
Final Analysis and Results.....	328
Mass H2O Slab .....	328
Volumetric Water Content Slab.....	329
Total Energy Budget .....	329
Sensible Heat Flux Calculations .....	329
Latent Heat Flux Calculations .....	331
Albedo .....	334
Conclusions.....	335
Future Research.....	337
Acknowledgements.....	339
References .....	340
A: NJDOT Section 606 - Sidewalks, Driveways, and Islands .....	341
B: NJDOT Section 903- Concrete.....	342
C: Soil Characterization: USDA .....	344
C1: Map .....	344
C2: USDA Soil Classification - Description .....	347
D: Tipping Bucket (2) & HMP45C - Wire Diagram .....	351
E: Wind (2) & Tipping Bucket (1) & Setra 278 - Wire Diagram .....	352
F: NR01 Green Ext. - Wire Diagram.....	353
G: NR01 Black Ext. - Wire Diagram .....	354
H: Rotronic Hygroclip2 HC2S3 and CNR4 - Wire Diagram .....	355
I: Load Cells - Wire Diagram .....	356
J: CNR2 & Young Wind (1) - Wire Diagram.....	357

K: COM - Wire Diagrams .....	358
L: CR3000 Thermo - Campbell DAQ Wire Diagram/Text .....	359
M: CR_AM25T Campbell Multiplexer Wire Diagram/Text .....	363
N: CR3000 Load Cell - Campbell DAQ Wire Diagram/Text .....	368
O: CR10X Weather - Campbell DAQ Wire Diagram/Text.....	374
P: CR1000 TDR - Campbell DAQ Wire Diagram/Text .....	376
Q: CR1000 Inside Temp - Campbell DAQ Wire Diagram/Text.....	378
R: CR1000 Inside Solar - Campbell DAQ Wire Diagram/Text .....	382

## Table of Figures

Figure 1: Net Surface Radiation Flux (Wallace & Hobbs 2006).....	161
Figure 2: The total energy balance .....	163
Figure 3: The Rutgers Asphalt Pavement Laboratory's location in New Jersey.....	165
Figure 4: The testing site.....	166
Figure 5: Proposed Test Slab Locations .....	167
Figure 6: Existing site layout prior to Pervious Concrete.....	168
Figure 7: Research Wall that was required to be re-sited .....	169
Figure 8: Bobcat E85 Excavator .....	170
Figure 9: Preparing to move wall footing .....	171
Figure 10: Moving the footing with the E85 Excavator .....	172
Figure 11: Rough foundations for pervious test samples, looking ESE.....	173
Figure 12: Rough foundations for pervious test samples, looking WNW.....	174
Figure 13: Bobcat E50 with 1ft (0.30m) bucket attachment .....	175
Figure 14: Auger attachment on Bobcat E50.....	176
Figure 15: Footing tubes in place inside rough foundations .....	177
Figure 16: Prepared subgrades for drainage with footing tubes exposed .....	178
Figure 17: Drainage Pipe with Wyle 'Y' .....	179
Figure 18: Non-woven geotextile fabric covering drainage pipe.....	180
Figure 19: Stockpile of ¾in (19mm) aggregate .....	181
Figure 20: Placing and compacting base course aggregate .....	182
Figure 21: Leveling the base course.....	183
Figure 22: Applying the final level of base course aggregate. Note the excessive dust in the aggregate.....	184
Figure 23: Testing the viability of the air bags .....	185
Figure 24: Layout of slab molds prior to geo-textile fabric.....	186
Figure 25: Verification of the final slab grade.....	187
Figure 26: Final layout of concrete molds prior to pouring .....	188
Figure 27: <i>Aggregate, water, admixtures and tools prepared to mix concrete slabs</i> .....	189
Figure 28: First batch pour of the pervious concrete sample awaiting final batch .....	190

Figure 29: Hand work and rodding to create concrete field samples.....	191
Figure 30: Preparing flexural, compressive, and permeability samples .....	192
Figure 31: Final field sample prior to curing .....	193
Figure 32: Wet curing samples .....	194
Figure 33: Prepared samples curing under plastic sheeting.....	195
Figure 34: Final layout of field slabs after curing procedure and prior to backfilling.....	196
Figure 35: Preparing aggregate for splitting .....	200
Figure 36: Quartering aggregate for sampling.....	201
Figure 37: Aggregate gradations compiled (0.45 Power) .....	205
Figure 38: Conceptual diagram showing equipment setup .....	212
Figure 39: Load Cell calibration curves .....	217
Figure 40: Type E Calibration Data.....	219
Figure 41: Type K Calibration Values .....	221
Figure 42: USP Calibrations.....	223
Figure 43: CS616 (6 inches) Calibration Curve .....	224
Figure 44: CS616 (9 inches) Calibration Curve .....	225
Figure 45: CS650 (3 inches) Calibration Curve .....	226
Figure 46: Dry TDR calibration sample, manifold is hanging on right after stemming from gravity fed bucket .....	227
Figure 47: Wet TDR calibration sample, manifold is hanging on right after stemming from gravity fed bucket .....	228
Figure 48: Laboratory setup to test individual equipment.....	235
Figure 49: Rough equipment siting plan .....	236
Figure 50: Preparing an Extension Line for Soldering .....	237
Figure 51: Insulation of signal extension wires.....	238
Figure 52: Rooftop weather station.....	239
Figure 53: Ground Weather Station, Left Foreground.....	241
Figure 54: Type-E close proximity air column thermocouples .....	242
Figure 55: <i>In-Slab temperature probe location</i> .....	244
Figure 56: Net Radiometer location.....	245
Figure 57: Final Sensor Layout by DAQ and Location .....	246
Figure 58: Outside equipment environmental containment box location .....	247
Figure 59: Almost completed wiring inside environmental containment boxes.....	248
Figure 60: In laboratory setup of additional DAQs and Multiplexer.....	249
Figure 61: Computer, power supply, and communications.....	250
Figure 62: Zenith Angles used for Albedo Calculations .....	264
Figure 63: Radiation for July 20 - July 22, 2017 at Slab 1.....	265
Figure 64: Radiation for July 20, 2017 at Slab 1.....	265
Figure 65: Net Radiation for July 20 - July 22, 2017 at Slab 1.....	266
Figure 66: Net Radiation for July 20 - July 22, 2017 at Slabs 1, 3, 4, 6, & 8 .....	266
Figure 67: Net Radiation for July 20 - July 22, 2017 at Slabs 1, 3, 4, 6, & 8 with Rain Bucket Readings on the Right Axis .....	267
Figure 68: Internal Slab Temperatures at 0.5 inches of embedment .....	268
Figure 69: Internal Slab Temperatures at 0.5 inches of embedment on July 20, 2017 .....	268

Figure 70: Internal Slab Temperatures at 0.5 inches of embedment on July 21, 2017 .....	269
Figure 71: Internal Slab Temperatures at 0.5 inches of embedment on July 22, 2017 .....	269
Figure 72: Under Slab Temperature at 4 inches Below Slab 3 on July 20, 2017 .....	270
Figure 73: Type E Temperatures at heights 25 cm, 13 cm, 6 cm, and 1 cm above Slab 4 .....	271
Figure 74: Type E Temperatures at heights 25 cm, 13 cm, 6 cm, and 1 cm above Slab 4 on July 20, 2017 .....	271
Figure 75: Ambient and Type E Temperatures at a height of 2 m and 25 cm above Slab 1 and Slab 4, respectively.....	272
Figure 76: Ambient Temperature at 2 m above Slab 1, Type E Temperature at 25 cm above Slab 4, Under Slab Temperature at 4" below Slab 4, and Soil T at a depth of 3" with Rain Bucket Data on the Right Axis.....	273
Figure 77: Slab 1 Internal, Under Slab, and Ambient Temperature Readings .....	274
Figure 78: Slab 2 Internal, Under Slab, and Ambient Temperature Readings .....	275
Figure 79: Slab 3 Internal, Under Slab, and Ambient Temperature Readings .....	276
Figure 80: Slab 4 Internal, Under Slab, and Ambient Temperature Readings .....	276
Figure 81: Slab 5 Internal, Under Slab, and Ambient Temperature Readings .....	277
Figure 82: Slab 6 Internal, Under Slab, and Ambient Temperature Readings .....	278
Figure 83: Slab 7 Internal, Under Slab, and Ambient Temperature Readings .....	279
Figure 84: Slab 8 Internal, Under Slab, and Ambient Temperature Readings .....	280
Figure 85: Rain Bucket Readings at the Roof Weather Station .....	281
Figure 86: Barometric Pressure Readings at the Roof Weather Station for July 20 - July 22, 2017 .....	282
Figure 87: Relative Humidity Readings at the Roof Weather Station for July 20 - July 22, 2017 .....	283
Figure 88: Soil VWC Unfiltered from 7/20-7/22 .....	284
Figure 89: Soil VWC 3" Filtered vs Unfiltered Measurement .....	285
Figure 90: Soil VWC 6" Filtered vs Unfiltered Measurement .....	286
Figure 91: Volumetric Water Content in Soil at a Depth of 3 and 6 inches with Rain Bucket Data on the Right Axis.....	287
Figure 92: Wind Speed at Roof Weather Station.....	287
Figure 93: Load Cell 1 Response vs Measured Rain Events .....	289
Figure 94: Load Cell 2 Response vs Measured Rain Events .....	290
Figure 95: Load Cell 3 vs Measured Rain Events.....	291
Figure 96: Load Cell 4 Response vs Measured Rain Events .....	292
Figure 97: Load Cell 5 Response vs Measured Rain Events .....	293
Figure 98: Load Cell 6 Response vs Measured Rain Events .....	294
Figure 99: Load Cell 7 Response vs Measured Rain Events .....	295
Figure 100: Load Cell 8 Response vs Measured Rain Events .....	296
Figure 101: Load Cell 9 Response vs Measured Rain Events .....	297
Figure 102: Load Cell 10 Response vs Measured Rain Events .....	298
Figure 103: Load Cell 11 Response vs Measured Rain Events .....	299
Figure 104: Load Cell 12 Response vs Measured Rain Events .....	300
Figure 105: Load Cell 13 Response vs Measured Rain Events .....	301
Figure 106: Load Cell 14 Response vs Measured Rain Events .....	302
Figure 107: Load Cell 15 Response vs Measured Rain Events .....	303
Figure 108: Load Cell 16 Response vs Measured Rain Events .....	304
Figure 109: Load Cell 1 Unfiltered vs Load Cell 1 Filtered .....	305
Figure 110: Load Cell 2 Unfiltered vs Load Cell 2 Filtered .....	305

Figure 111: Load Cell 3 Filtered vs Load Cell 3 Unfiltered .....	306
Figure 112: Load Cell 4 Filtered vs Load Cell 4 Unfiltered .....	306
Figure 113: Load Cell 5 Filtered vs Load Cell 5 Unfiltered .....	307
Figure 114: Load Cell 6 Filtered vs Load Cell 6 Unfiltered .....	307
Figure 115: Load Cell 7 Filtered vs Load Cell 7 Unfiltered .....	308
Figure 116: Load Cell 8 Filtered vs Load Cell 8 Unfiltered .....	308
Figure 117: Load Cell 9 Filtered vs Load Cell 9 Unfiltered .....	309
Figure 118: Load Cell 10 Filtered vs Load Cell 10 Unfiltered .....	309
Figure 119: Load Cell 11 Filtered vs Load Cell 11 Unfiltered .....	310
Figure 120: Load Cell 13 Filtered vs Load Cell 13 Unfiltered .....	310
Figure 121: Load Cell 14 Filtered vs Load Cell 14 Unfiltered .....	311
Figure 122: Load Cell 15 Filtered vs Load Cell 15 Unfiltered .....	311
Figure 123: Load Cell 16 Filtered vs Load Cell 16 Unfiltered .....	312
Figure 124: Slab 1 Mass Original vs Corrected.....	313
Figure 125: Slab 2 Mass Original vs Corrected.....	314
Figure 126: Slab 3 Mass Original vs Corrected.....	314
Figure 127: Slab 4 Mass Original vs Corrected.....	315
Figure 128: Slab 5 Mass Original vs Corrected.....	315
Figure 129: Slab 6 Mass Original vs Corrected.....	316
Figure 130: Slab 7 Mass Original vs Corrected.....	316
Figure 131: Slab 8 Mass Original vs Corrected.....	317
Figure 132: Slab 1 Mass vs Measured Rain events .....	317
Figure 133: Slab 2 Mass vs Measured Rain Events .....	318
Figure 134: Slab 3 Mass vs Measured Rain Events .....	318
Figure 135: Slab 4 Mass vs Measured Rain Events .....	319
Figure 136: Slab 5 Mass vs Measured Rain Events .....	319
Figure 137: Slab 6 Mass vs Measured Rain Events .....	320
Figure 138: Slab 7 Mass vs Measured Rain Events .....	321
Figure 139: Slab 8 Mass vs Measured Rain Events .....	321
Figure 140: Mass of Water in Slab 1 for July 20, 2017 through July 22, 2017 with Rain Bucket Readings on the Right Axis .....	322
Figure 141: Mass of Water in Slab 2 for July 20, 2017 through July 22, 2017 with Rain Bucket Readings on the Right Axis .....	322
Figure 142: Mass of Water in Slab 3 for July 20, 2017 through July 22, 2017 with Rain Bucket Readings on the Right Axis .....	323
Figure 143: Mass of Water in Slab 4 for July 20, 2017 through July 22, 2017 with Rain Bucket Readings on the Right Axis .....	323
Figure 144: Mass of Water in Slab 5 for July 20, 2017 through July 22, 2017 with Rain Bucket Readings on the Right Axis .....	324
Figure 145: Mass of Water in Slab 6 for July 20, 2017 through July 22, 2017 with Rain Bucket Readings on the Right Axis .....	324
Figure 146: Mass of Water in Slab 7 for July 20, 2017 through July 22, 2017 with Rain Bucket Readings on the Right Axis .....	325

Figure 147: Mass of Water in Slab 8 for July 20, 2017 through July 22, 2017 with Rain Bucket Readings on the Right Axis .....	325
Figure 148: The sensible heat flux for July 20 - 22, 2017 .....	330
Figure 149: The latent heat flux for July 20 - 22, 2017 .....	332
Figure 150: Calculated Albedo for each Pervious Mix Field Sample.....	334



# Table of Tables

Table 1: Base/Subgrade Threshold Materials .....	178
Table 2: Environmental parameters collected during construction .....	197
Table 3: Aggregates utilized for pervious concrete project .....	198
Table 4: Mass of source aggregates utilized .....	199
Table 5: Aggregate Specific Gravities.....	201
Table 6: Results from Ignition Oven Test.....	203
Table 7: Clayton #57 Gradation .....	205
Table 8: Weldon ½" Gradation .....	206
Table 9: Weldon ¾" gradation .....	207
Table 10: Weldon ¼" gradation .....	207
Table 11: NJ Gravel ¼" White Washed Gradation .....	209
Table 12: Weldon Concrete Sand .....	209
Table 13: Aggregate Moisture Content .....	210
Table 14: Load Cell calibration curve equations .....	217
Table 15: Calibration equations for Type-E Thermocouples .....	218
Table 16: Calibration equations for Type-E Thermocouples .....	219
Table 17: USP Calibration Equations.....	222
Table 18: CR1000 Datalogger Equipment used .....	231
Table 19: CR3000 Datalogger Equipment used .....	233
Table 20: Type E close proximity air column thermocouple heights .....	243
Table 21: In-slab thermocouple depth arrangement .....	243
Table 22: Field sample 1 sensors .....	250
Table 23: Field sample 2 sensors .....	252
Table 24: Field sample 3 sensors .....	253
Table 25: Field sample 4 sensors .....	254
Table 26: Field sample 5 sensors .....	256
Table 27: Field sample 6 sensors .....	257
Table 28: Field sample 7 sensors .....	258
Table 29: Field sample 8 sensors .....	259
Table 30: Sources of climatological data derived for regional locations Near the test site .....	262
Table 31: Sky conditions utilized for albedo calculations .....	262
Table 32: Load Cells utilized for Final Slab Mass.....	312
Table 33: The Sensible and Latent Heat Flux for Each Slab .....	332
Table 34: The energy budget and savings for each slab .....	334

# Objective

Due to concerns about Urban Heat Island effect and the desire for energy efficiency, different land cover types including natural, agricultural, and most building materials, such as roofing have been studied extensively (Yang, 2013). Major infrastructure components, such as concrete and asphalt road surfaces, parking lots, and sidewalks have more recently become a topic of interest (Li, 2013). Due to its dark color, asphalt is known to have a low albedo or low level of reflectivity, but the majority of albedo and solar radiation research conducted in the asphalt and concrete industry to date has highlighted freshly paved asphalt or concrete samples without accounting for changes in aged pavements, varying lift thickness, aggregate types, or structural parameters associated with widely varying asphalt mix designs. Standard concrete, on the other hand, is generally associated with higher reflectivity. The mix design parameters of either mix are known to affect the amount of light reflected, the amount of heat absorbed, the amount of heat retained, and the amount of heat expunged throughout the nighttime hours. Several studies have been completed to evaluate the benefits of more reflective surfaces, such as Portland Cement Concrete and chip seals using lightly colored aggregates (Li, 2013). Another recent study was conducted to determine if “cool” pavements provided any benefit to the environment (Li, 2012).

Unfortunately, urban heat island effect is not a problem that only New Jersey needs to be concerned with, but fortunately the issue has been gaining recognition around the country. The State of New Jersey currently holds over 39,000 miles of public roadways (of which 8410 lane miles (13534.58 km) are controlled by the state DOT), and 24 public use airports. As of 2007, the land cover of the state comprised of 800 sq. mi. of impervious surface which was increasing at a rate of 6.67 sq. mi. (1727.5 ha) per day (Hasse, 2010). This results in an 11% total impervious land cover as of 2007. Arnold and Gibbons (1996) showed that an increase of 10% in impervious surface area results in an increase of land surface temperature by 1-1.5 deg C, which was expanded upon by Xu in 2010 (Xu, 2010, Arnold, 1996). It should be noted that this relationship does not correlate with a linear scaling, but rather an exponential rate, resulting in a more rapid increase in temperature of urban areas than those of rural landscapes. Due to these NJ statistics, the need for research about the possibility of utilizing pervious surface instead of impervious surfaces, and how the design of each affects the albedo, and energy flux for asphalt and concrete pavements in New Jersey is paramount.

Albedo and solar radiation flux has been measured on asphalt and pavements utilizing two techniques, the solar spectrum reflectance measurement test, ASTM C1549, and the Pyranometer test method, ASTM E1918, the latter of which provides better measurements for pavement surfaces and gravel (Tran, 2009). Since the aggregates, mix designs, and climate are different from location to location, it is important to measure the solar radiation and albedo for state specific concrete parameters. This study was particularly designed to utilize a modified ASTM E1918 test with 3ft x 4ft (0.91m x 1.22m) sidewalk samples to evaluate candidate mix designs for pervious concrete mix applicable to NJ to determine how they affected the local energy budget.

The objective of Subtask 3.1 was to quantify how the different pervious concrete mixes compared to conventional concrete sidewalk with respect to the local energy budget determined for each slab.

## Test Description

To determine the effect that pervious concrete sidewalk mixes as compared to conventional concrete sidewalk mixes, an energy balance study was determined to be beneficial. Of the eleven mixes evaluated by structural Subtask 1.1, one conventional mix and three pervious mixes were selected for field evaluation. The field slabs were to be used for field aged structural analysis, field aged permeability, as well as the energy balance determination. 8 3ft x 4ft (0.91m x 1.22m) sidewalk samples were utilized as surrogates for a sidewalk slab to provide two slabs per mix for statistical evaluation, backup in case of slab cracking, and to provide extra material for structural evaluation. To provide the most realistic evaluation, the samples were constructed following the NJDOT specification Sections 606- Sidewalks, Driveways, and Islands, and 903- Concrete, which are shown in Appendix 1 and 2 respectively.

## Background of Energy Budget

### Radiation (Shortwave, Longwave, Net)

This section will describe what radiation is and how it works. Plus standard global radiation, how much is average absorption, reflection of clouds etc.

Surface radiation fluxes are governed by the rotation of the Earth, which causes diurnal cycle of the incoming radiation. Any given location on the Earth's surface will undergo a daily sunrise, solar noon, and sunset. Incoming solar radiation over all wavelengths in and near the visible spectrum that intersects the Earth's surface can be measured as incoming (downwards) shortwave radiation,  $R_{s\downarrow}$ . Some of the incoming shortwave radiation is reflected back up towards the atmosphere as shortwave radiation, which is measured as outgoing (upwards) shortwave radiation,  $R_{s\uparrow}$ . In addition, the atmosphere emits longwave radiation that intersects the Earth's surface, which is measured as incoming (downwards) longwave radiation,  $R_{L\downarrow}$ , and some of this radiation is reflected by the surface as outgoing (upwards) longwave radiation,  $R_{L\uparrow}$ . Consequently, the total (net) solar radiation flux,  $R_N$ , can be described by the following equation:

$$R_N = R_{s\downarrow} - R_{s\uparrow} + R_{L\downarrow} - R_{L\uparrow}$$

Solar radiation is measured by net radiometers. When weather is clear, the surface radiation flux varies with time as shown in Figure 1.

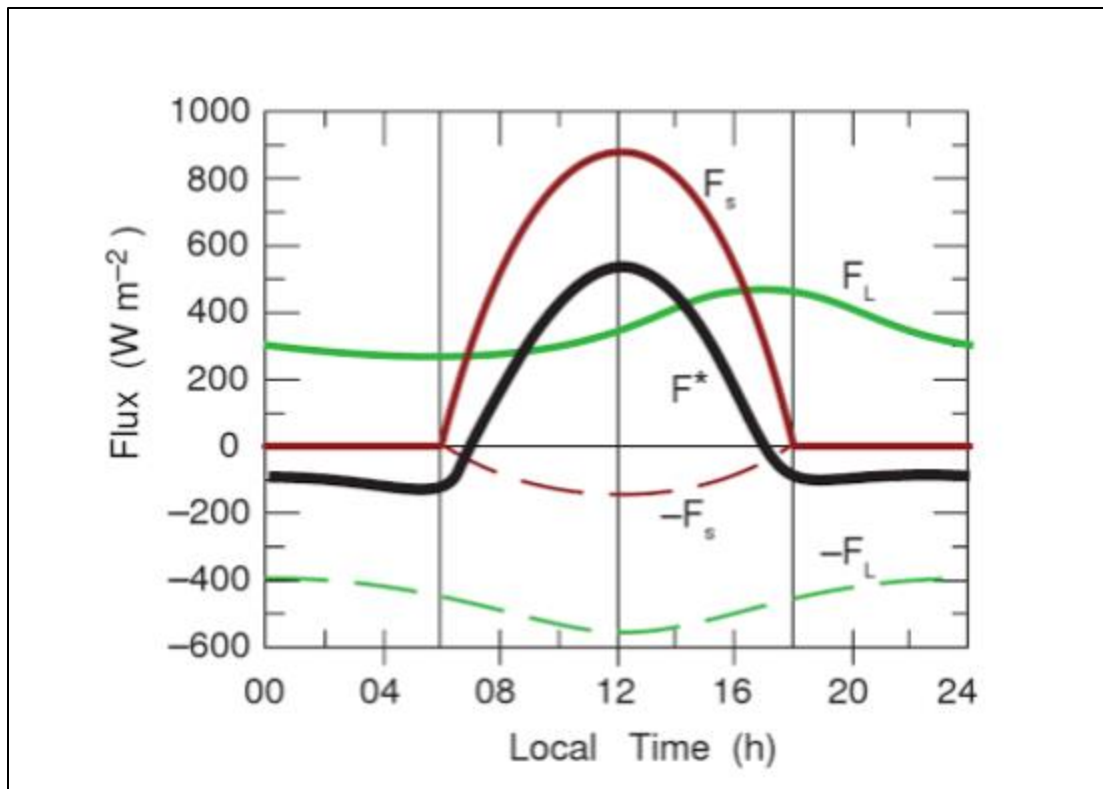


Figure 139: Net Surface Radiation Flux (Wallace & Hobbs 2006)

During the daytime, incoming solar radiation is proportional to the elevation of the sun and dependent on the time of day, latitude, and season. The reflected radiation is dependent on the composition of the surface and is typically reduced in amplitude. During the night, there is no shortwave radiation.

The net longwave surface radiation flux is nearly zero. However, the upward longwave radiation,  $R_{L\uparrow}$ , is modified slightly by the sensible heat flux. Because of the relatively small heat capacity of the surface, upward longwave radiation,  $R_{L\uparrow}$ , is nearly in phase with downward shortwave radiation,  $R_{s\downarrow}$ . Downwards longwave radiation,  $R_{L\downarrow}$ , is dependent on air temperature, which reaches its maximum just before sunset and its minimum just after sunrise.

At night, the net solar radiation,  $R_N$ , is nearly constant and slightly negative. During the daytime, net solar radiation at the surface is positive and reaches a maximum at solar noon. Positive net solar radiation indicates an input into the surface, which negative net solar radiation indicates output to the atmosphere (Wallace & Hobbs 2006).

## Sensible Heat

Sensible, latent, and ground heat fluxes must also be taken into account when establishing the surface energy balance. The sensible heat flux,  $Q_H$ , is the change in air temperature at the Earth's surface. It is measured by thin-gauge wire thermocouples (Type E) which are designed to not be

influenced by solar radiative fluxes. Atmospheric temperature can be multiplied by the Stefan-Boltzmann constant,  $\sigma$ , to find the sensible heat flux (Wallace & Hobbs 2006).

## Latent Heat

The latent heat flux,  $Q_E$ , is defined as the amount of radiation which induces a phase change of water from liquid to vapor. It is the product of the flux of water vapor and the latent heat of vaporization,  $H_e$ . For this project, the flux of water vapor was determined for each slab by quantifying the change in mass of the slabs during wetting and drying events (Wallace & Hobbs 2006).

## Ground Heat Flux

The ground heat flux,  $Q_G$ , is the amount of radiation which is transferred from the surface into the ground. It is defined as the product of the soil temperature and the Stefan-Boltzmann constant,  $\sigma$ . For this project, the ground flux was determined by measuring the soil temperature at a depth of three inches with a soil temperature probe on a time-domain reflectometer (TDR) (Wallace & Hobbs 2006).

## Total Energy Balance

The total energy balance can be determined by the following equation:

$$Q = RN - Q_H - Q_E - Q_G$$

In clear conditions, the total energy balance can be illustrated by Figure 2.

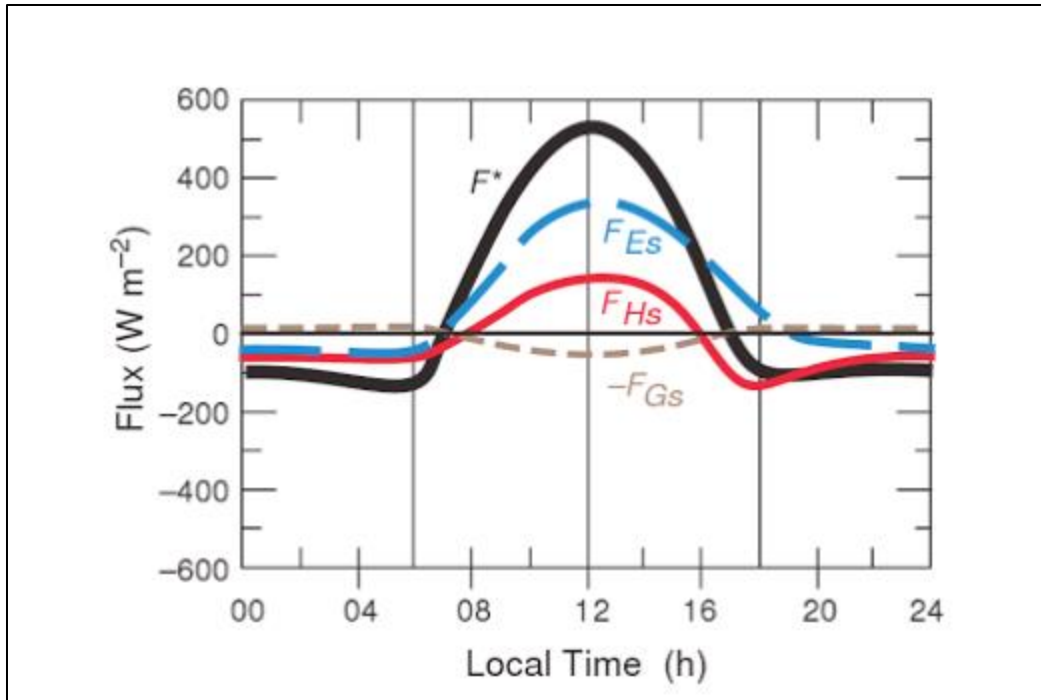


Figure 140: The total energy balance

If the surface conditions are moist, the majority of the daytime incoming solar radiation goes into evaporation. Conversely, when surface conditions are dry, incoming solar radiation goes into sensible heat flux.

The magnitude of the ground heat flux,  $Q_G$ , is approximately 10% of the net daytime radiation. This increases to 50% during the night (Wallace & Hobbs 2006).

## Pervious Concrete

Pervious concrete is a permeable material, often built with an underlying stone reservoir that temporarily stores surface runoff before it infiltrates into the subsoil. Unlike conventional concrete, pervious concrete allows storm water to infiltrate directly into the soil. There are various types of pervious surfaces, including pervious asphalt, pervious concrete and grass or permeable interlocking pavers. The focus of this study is on the use of pervious concrete for sidewalks. Until more information is determined related to its field performance, maintainability, constructability, and improved benefit over other approved storm water best management practices (BMPs), the inclusion of pervious concrete pavement into NJDOT projects needs to be carefully considered. This study is intended to provide general guidance on the design and applicability of pervious concrete systems for NJDOT sidewalk projects. The intent is to have consistent guidelines and standards, if a pervious pavement installation was ultimately chosen. A major concern related to pervious pavements is maintainability. When considering pervious concrete for storm water treatment, a project team should also evaluate the other approved BMPs and compare them to determine if pervious concrete would be considered the preferred BMP. Although, pervious concrete has seen growing use in the United States, there is still very limited practical experience

with this measure. According to the U.S. EPA, pervious pavement sites have had a high failure rate – approximately 75 percent. Failure has been attributed to poor design, inadequate construction techniques, and soils with low permeability, heavy vehicular traffic and poor maintenance. When using pervious concrete for sidewalks as BMP measure, its performance should be carefully monitored over the life of the development. With proper design and installation, pervious concrete for sidewalks can provide a cost-effective solution for storm water management in an environmentally friendly way. As a result, they are recognized as a best practice by the U.S. Environmental Protection Agency (EPA, 1999) and many state agencies (PDEP 2006, NJDEP 2016).

## Benefits and Limitations

There are several benefits for using pervious concrete in sidewalks. One of the most important benefits is its effectiveness for storm water management, improving water runoff quality, reducing storm water runoff, and restoring groundwater supplies. It can also filter contaminants thus improving water quality. Several studies have quantified high removal rates of total suspended solids (TSS), metals, oil and grease, as well as moderate removal rates for phosphorous, from using pervious concrete (Cahill et al. 2005; Roseen et al. 2012). They also can minimize the use of deicing chemicals and while they do not remove chlorides, the reduction of deicing chemicals use is an effective method for reducing chloride pollution (Roseen et al. 2014). However, pervious concrete has shown to clog with time without the proper periodic vacuuming, cleaning and maintenance. Pervious concrete can also ravel and fail if used in un-stabilized areas and not properly designed, constructed, and maintained. Pervious concrete construction also requires skilled labor and has higher initial costs. While pervious pavements have become popular in the area of storm water management, the true applicability in specific applications still needs further evaluation especially if there is potential for groundwater contamination. A site investigation is critical to evaluate whether pervious pavements are an appropriate BMP for a site. The site investigation should be conducted with appropriate staff to be able to consider hydrology and hydraulic design, soil permeability, pervious concrete thickness design, and environmental considerations and regulations.

## Site Description

### Location

The testing site was located at the Rutgers University Asphalt Pavement Laboratory, which is located at 93 Road 1, Piscataway, New Jersey. The laboratory is overseen by the Center for Advanced Infrastructure and Transportation. Figure 3 shows the laboratory's location in New Jersey. Figure 4 depicts the testing site location, which is in an open area outside of the laboratory that was selected due to project funding considerations. Figures 5 & 6 depict the arrangement and final location of the eight testing slabs.



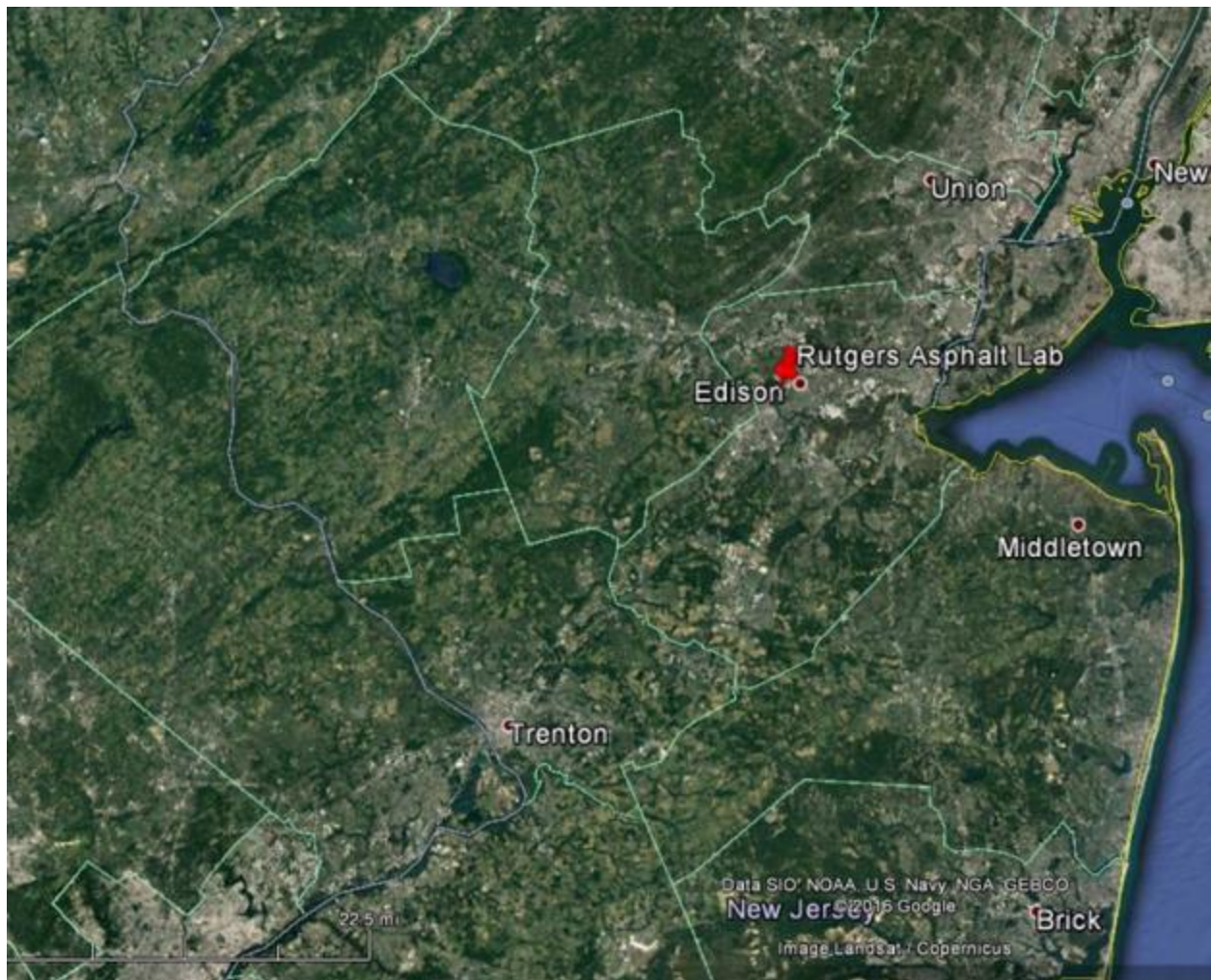


Figure 141: The Rutgers Asphalt Pavement Laboratory's location in New Jersey



Figure 142: The testing site

From the aerial view in Figure 4, it is easy to see how little room was available for locating the test slabs behind the laboratory. The ideal test area would be a wide open area non-influenced by buildings or trees with a completely open view of the sky, so the use of the space behind the lab provided an inherent problem to the project due to the variation in the angle of the sun that intrinsically would impart a direct effect on the quality of the measurements over an annual period.

In Figure 5, it is important to point out that there are a few constraints to the area that were required to design around. The two primary constraints were that there must remain a minimum of 12' fire lane access to both buildings. There was a currently existing set of shipping containers stored there that were unable to be moved as well as a concrete wall that was being utilized for a separate project. Before creating test slabs for the pervious concrete project, the concrete wall needed to be moved to allow for enough space. Since this wall contains multiple active research projects, it was determined that the wall must be re-erected in another location nearby rather than razing it.

The testing area used for this study is not ideal, but it was considered acceptable to provide relative results to compare values from sample to sample. The initial condition behind the lab was and remained a community area, so additional considerations were required to ensure the safety and accessibility to the area which also required mitigation as part of the project.



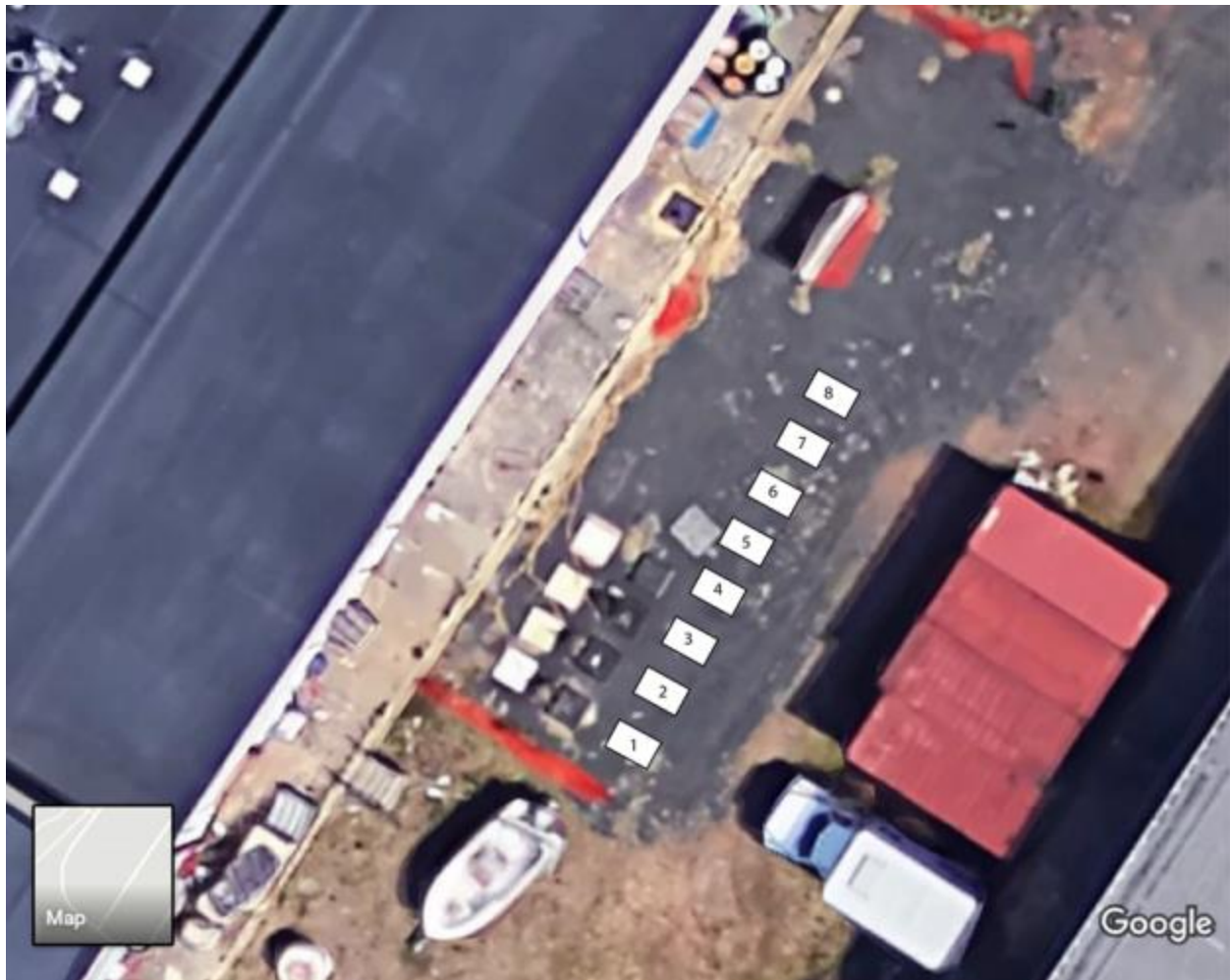


Figure 143: Proposed Test Slab Locations

After determining the area where the slabs would be placed, the site required significant amount of preparatory work to follow DOT sidewalk guidelines. The first step was to remove the existing asphalt and concrete slabs that were utilized for a previous study.

## Site Setup



**Figure 144: Existing site layout prior to Pervious Concrete**

As you can see in Figure 6 above, there were several asphalt and concrete samples as well as the wall and boat that were required to move prior to breaking ground for the new pervious concrete samples.

Figure 7 below shows the concrete wall that needed to be re-sited due to the excessive shadow it would cast over the slabs. By using 8 slabs, the wall was also physically located where two of the slabs were proposed to be built.





**Figure 145: Research Wall that was required to be re-sited**

To re-site the wall, the wall segments were removed individually and the footing was pulled using a Bobcat E85 excavator. The E85 was also utilized to rough out the foundations for the pervious concrete slabs.



Figure 146: Bobcat E85 Excavator





Figure 147: Preparing to move wall footing

To move the footing with the E85, 20,000 lbs. test nylon webbing was wrapped around the footing, centered and attached to a 20,000lb test line, outfitted with a clip to attach to the excavator. It was considered important to not damage the footing as it was to be reused.





Figure 148: Moving the footing with the E85 Excavator



The footing was moved to the alternate location on the far end of the test site and re-erected once balanced. Once the wall was relocated, the test slab foundations were roughed out with the E85 based on the proposed testing locations shown in Figure 5 above. Each foundation was roughed to approximately 4.5ft x 6ft (1.37m x 1.83m) to facilitate construction.



Figure 149: Rough foundations for pervious test samples, looking ESE



Figure 150: Rough foundations for pervious test samples, looking WNW

The roughed foundations were spaced 6ft (1.83m) apart from edge to edge to ensure enough space for sample creation, equipment wiring, and to reduce cross-slab test results contamination.

Although no practical sidewalk would require the use of footings, to ensure the load cells utilized to measure continuous slab mass would have a solid base, 1ft dia. x 2ft (0.30m dia. x 0.60m ) footings were installed. To prepare for footing installation, the centerline of each proposed sample locations were painted with white marking paint as shown in Figure 12 above. Round pre-made, widely available concrete molds were utilized. To conduct the more precise excavation and to drill holes for the footings, a Bobcat E50 with an auger attachment and a bucket attachment was utilized. The E50 is shown in Figure 13 below.





Figure 151: Bobcat E50 with 1ft (0.30m) bucket attachment

The auger attachment, shown in Figure 14 below, proved to be very useful to prepare the footing holes, but also caused a costly few day delay in construction when one of the hydraulic lines cracked at the fitting.



Figure 152: Auger attachment on Bobcat E50

Figure 14 above also shows the hard manual work required in addition to the auger. The footing tubes were all located on the South side of the sample plots, where the load cells were proposed to be located. There were two footings per each slab. After the footing tubes were installed, they were capped with buckets to prevent excess soil and water to fill as shown in Figure 15 below. After the footing tubes were installed and capped, they remained unfilled until the remainder of foundation heavy construction was completed.





Figure 153: Footing tubes in place inside rough foundations

After the footing tubes were in place, the drainage systems were the next item to be installed. Although most sidewalk sections do not have drainage systems, it was considered important given the location and purpose of the pervious sidewalk study. Drainage pipes required 4" stone surrounding the pipe. The piping system was designed where each slab had its own closed system that required pump out by lab personnel. This was done so that measurements could be taken using water that had flowed through the sample if desired. DOT pervious sidewalk guidelines suggested the use of non-woven geotextile fabric between the subgrade and the base level. Two of the slabs utilized no geotextile fabric between the subgrade, three of slab subgrades utilized 4mm plastic typical to standard concrete construction, and three of the slabs utilized non-woven geotextile fabric as stipulated by the NJDOT pervious design guidelines. The organization of subgrade threshold fabric choice is shown in Table 1 below.

Table 34: Base/Subgrade Threshold Materials

Slab #	Below Base/Subgrade Threshold	Drainage	Base Depth (inches)	Concrete Mix	Mix Design Basis
8	Plastic	Yes	6	Control	Clayton
7	None	Yes	6	Control	Clayton
6	Non-Woven Geotextile Fabric	Yes	6	PRC - 9	Silvi
5	Plastic	Yes	6	PRC - 9	Silvi
4	Non-Woven Geotextile Fabric	Yes	6	PRC - 7	-
3	Plastic	Yes	6	PRC - 7	-
2	Non-Woven Geotextile Fabric	Yes	6	PRC - 3	Clayton
1	None	Yes	6	PRC - 3	Clayton

The prepared foundations with subgrade prepared for drainage is shown in Figure 16 below.



Figure 154: Prepared subgrades for drainage with footing tubes exposed



One additional caveat with the drainage systems required a creative approach: Pre-made drainage piping does not have fittings. To alleviate this issue, the drainage systems were made from 4in (10.16cm) Schedule 40 PVC pipe arranged with two spurs created by a Wyle 'Y' and an upright to allow for access. The drainage pipe had holes drilled in the top prior to being covered by geotextile fabric. The uncovered drainage pipe is shown in Figure 17 below.



Figure 155: Drainage Pipe with Wyle 'Y'

Prior to installation the non-woven geotextile fabric was wrapped around the drainage pipe as shown in Figure 18 below.



**Figure 156: Non-woven geotextile fabric covering drainage pipe**

Once the drainage pipes were in place, 6" (0.15m) of  $\frac{3}{4}$ in (19mm) clean (washed) aggregate was utilized to create the base course of each slab. The donated aggregate was the only material dropped off by the supplier with a dump truck as shown in Figure 19 below.





**Figure 157: Stockpile of 3/4in (19mm) aggregate**

The stockpile utilized for this project is noteworthy because it was located directly on the ground. When placing the base course it became apparent that there was contamination from debris found on site. The authors would recommend that tarps or other containment devices should be utilized to protect the cleanliness of the base aggregate for use in pervious concrete and pervious asphalt applications. The foundations with base material being compacted is shown in Figure 20 below.



**Figure 158: Placing and compacting base course aggregate**

As shown in Figure 20 above, the base aggregate was compacted to ensure a solid base and proper level. DOT guidelines suggested an 86% compacted base course. The vibratory tamper shown in Figure 20 above, in conjunction with the small length and width of the foundations did not achieve the best results. A small sheepsfoot roller would be preferred for sidewalk applications.

Final grade was determined using line levels and verified with a handheld level as shown in Figure 21 below.





Figure 159: Leveling the base course

Final base course stone was added to the final level of the bottom of the concrete slab as shown below in Figure 22. Prior to pouring concrete, a final round of leveling was required to adjust any aggregate that had moved throughout the remainder of construction.

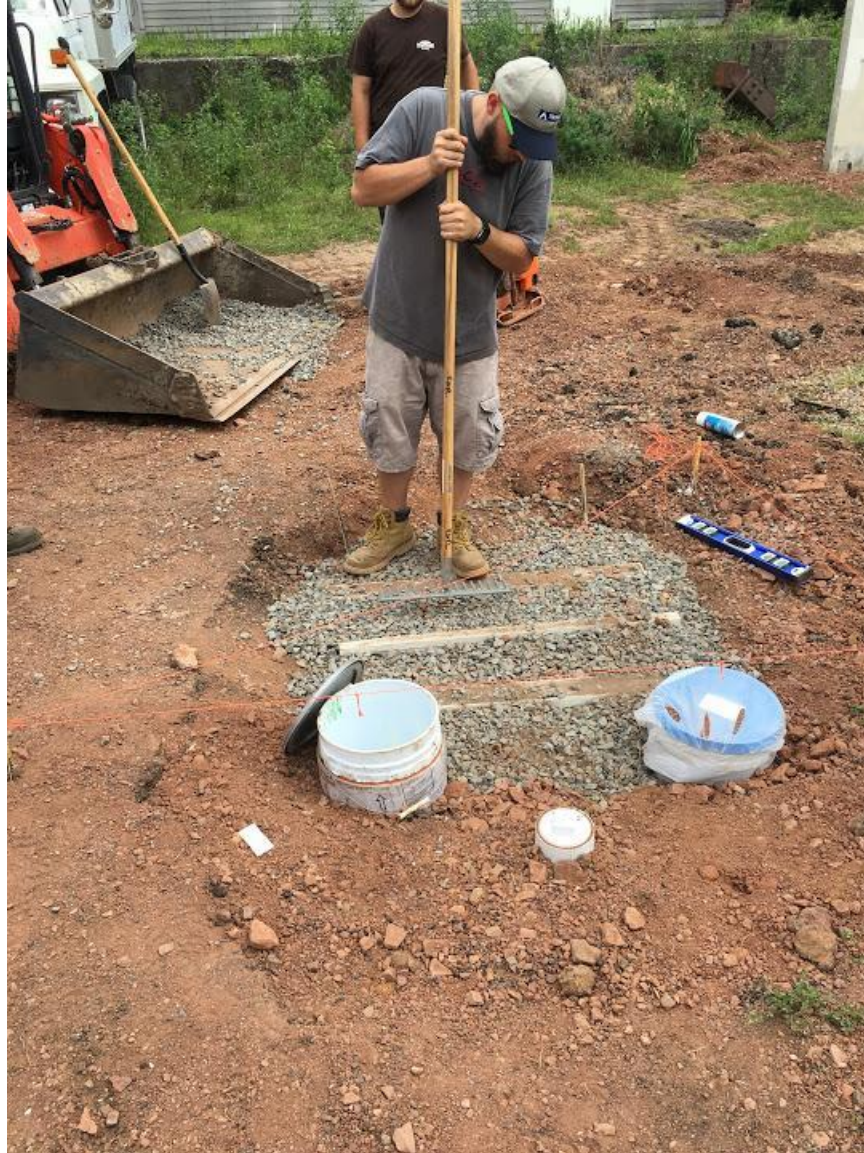


Figure 160: Applying the final level of base course aggregate. Note the excessive dust in the aggregate

After the base course was completed, 5000 psi consumer grade redi-mix was utilized to place the footings. The footings were covered with moist burlap and allowed to cure for two weeks prior to the construction of the slabs. The other important item to note in Figure 22 above is the use of spacers. Due to the concern of weak tensile strength of the pervious concrete mix which does not utilize mesh or rebar stabilization and the need to lift the slabs to outfit each with sensors, airbags were determined to be the best approach. The spacers (2x4 lumber) were utilized as a placeholder for the airbags. The airbags were created in the laboratory using donated firehose outfitted with caps and a Schrader valve to allow easy filling and deflating. The airbag viability was tested in the laboratory using a 5000lb (2267.9kg) sample as shown in Figure 23 below.





Figure 161: Testing the viability of the air bags

Each air bag was tested independently to ensure it would have the capability of lifting the test samples in the field. The ability to lift and lower the samples would prove critical in the ability to place the load cells and under slab temperature probes after the slabs cured.

After the two week curing period, frames and additional spacers were utilized to construct the slabs in place. Under normal construction conditions, there would be no need to utilize spacers under the slab during construction. They were required for the purpose of this project to ensure the bottom of the slab was flat. As with the subgrade threshold, geotextile fabric was required at the threshold. Each of the slabs utilized non-woven geo-textile fabric. The layout of the slab molds is shown in Figure 24 below prior to laying the geo-textile fabric.



Figure 162: Layout of slab molds prior to geo-textile fabric

Layout and level of the molds was meticulously controlled to ensure the South side corners of the slabs would rest atop the footings as shown in Figure 25 below.



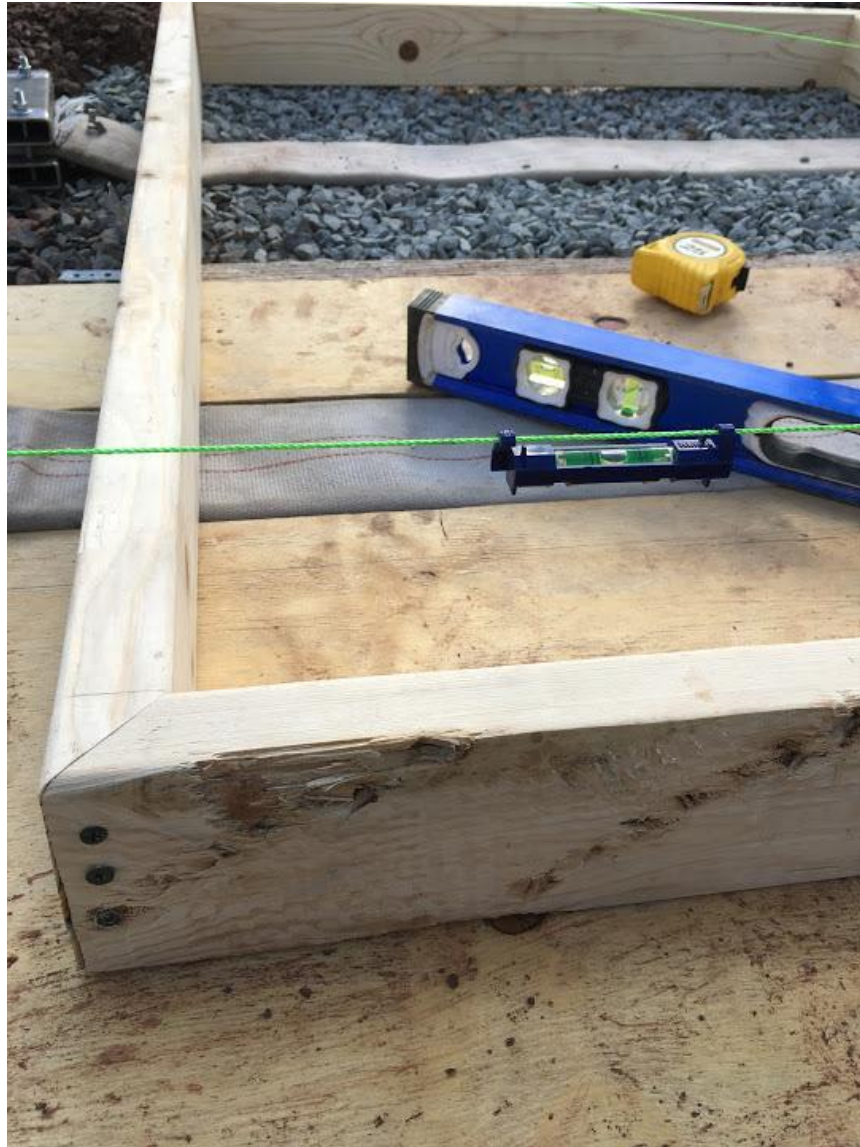


Figure 163: Verification of the final slab grade

Once the final level was ensured, the geotextile fabric was pinned under the mold as shown in Figure 26 below. The molds were held in place by strapping to ensure they held up throughout the remainder of the construction process.



Figure 164: Final layout of concrete molds prior to pouring

## Field Sample Creation

The aggregate utilized for this project was donated. The aggregate was picked up in 55 gallon ( $0.21\text{m}^3$ ) drums from the supplier and stockpiled in bins at the laboratory. Free water content of the aggregates was determined prior to construction following ACI 211.1-91 procedures. The results for the Aggregate moisture content prior to mixing is shown in the aggregate section below. Aggregates, water, and admixtures utilized for each mix was batched in separate 5 gal ( $0.02\text{m}^3$ ) buckets using a floor scale in the laboratory according to the mix designs determined by the structural design subtask 1.1. Everything required for slab construction was positioned to facilitate construction as shown in Figure 27 below.





**Figure 165:** Aggregate, water, admixtures and tools prepared to mix concrete slabs

Samples were mixed and placed on site to ensure the proportions of each mix remained as accurate to the mix design as possible. Due to the size of the available mixer, the slabs were poured in two mix batches. An example of the first batch poured awaiting a second batch is shown in figure 28.



Figure 166: First batch pour of the pervious concrete sample awaiting final batch

The mix was hand worked to fit the molds as shown in Figure 29 below.





Figure 167: Hand work and rodding to create concrete field samples

In addition to the field slabs, a set of conformance samples were created simultaneously to verify the mix met the design criteria. One 6in x 12in cylinder (15.2cm x 30.5cm) to test permeability, three 4in x 8in (10.2cm x 20.3 cm) cylinders to test compressive strength, and three 4in x 4in x 12in (10.2cm x 10.2cm x 20.3cm) flexural beam samples were created per field slab as shown in Figure 30 below. Samples were also taken to verify mix density.



Figure 168: Preparing flexural, compressive, and permeability samples

An example of a final field samples prior to curing is shown in Figure 31.





Figure 169: Final field sample prior to curing

Each slab and all field samples were covered with plastic and wet cured on site for two weeks. The slabs and samples were demolded after two days. To wet cure, each sample was wetted daily for at least 10 minutes per sample as shown in Figure 32. The finished test site with slabs and samples curing under plastic is shown in Figure 33 below.



Figure 170: Wet curing samples

Throughout the wet curing period, the slabs were covered with plastic, which can be seen in Figure 33.





**Figure 171: Prepared samples curing under plastic sheeting**

Finally, after the two week curing period the test samples are shown on the test site prior to backfilling. The backfilling of soil around the samples was required to wait until after the instrumentation was completed. The sample layout is shown in Figure 34 below.



Figure 172: Final layout of field slabs after curing procedure and prior to backfilling



## Construction Environmental Conditions

Throughout the mixing of the field slabs the environmental conditions were recorded. The conditions and mixing dates are shown in Table 2 below.

Table 35: Environmental parameters collected during construction

Environmental, Averages					
Slab ID	Date	Wind Speed (mph)	Temperature (°F)	Humidity	Barometric Pressure (inHg)
Slab 1	10/28/2016	2.0	54.07	47.35	30.07
Slab 2	10/28/2016	1.2	52.18	47.8	30.07
Slab 3	10/31/2016	0.5	71.73	26.07	30.10
Slab 4	11/2/2016	1.2	65.40	58.9	30.19
Slab 5	11/2/2016	1.4	71.65	64.6	30.17
Slab 6	11/2/2016	5.7	78.00	40.9	30.13
Slab 7	11/4/2016	1.0	71.35	64.4	30.08
Slab 8	11/4/2016	1.4	80.20	26.1	30.05

The ambient temperature during mixing and pouring of field concrete samples fluctuated from 52°F to 72°F (11.1°C to 22.2°C). Although it was late in the year and there was concern for approaching freezing temperatures during the curing procedure, the mixing and curing process was met with crisp, clear, and sunny days.

## Field Mix Aggregate Characterization

Several aggregate sizes were tested for structural evaluation of pervious concrete under subtask 1.1. The aggregates used for each mix are shown in Table 3 below. It is important to note that the main supplier, Weldon Industries Inc. does not routinely carry 1/4in. (6.4mm) aggregate but they utilized the plant's mix shaker to provide some for the purposes of this study.

Table 36: Aggregates utilized for pervious concrete project

Mix	NMAS (Nominal Maximum Aggregate Size)	Source
PRC-1	3/8	Weldon
PRC-2	3/8	Weldon
PRC-3	3/8	Weldon
PRC-4	3/8	Weldon
PRC-5	3/8	Weldon
PRC-6	3/8	Weldon
PRC-7	3/8	Weldon
PRC-8	3/8	Weldon
PRC-9	1/4	Weldon
PRC-10	1/2	NJ Gravel
PRC-11	1/4	NJ Gravel

The total quantity of aggregates picked up for the pervious concrete project weighed slightly over 12 tons. The breakdown of the sourced aggregate masses are shown in table 4 below.

Table 37: Mass of source aggregates utilized

Total Quantities of Aggregate Accumulated for Pervious Concrete Project Slab Creation (excluding structural laboratory mixes)				
Date	Stone Source	NMAS	Mass Drum lbs.	Total Daily Mass lbs.
6/8/2016	Weldon 3/8"	0.375"	654	654
7/1/2016	Weldon 1/4"	0.25"	705	705
7/1/2016	Weldon 3/8"	0.375"	690	2070
7/1/2016	Weldon 3/8"	0.375"	690	
7/1/2016	Weldon 3/8"	0.375"	690	
7/1/2016	Weldon Concrete Sand	Sand	672	672
7/29/2016	Weldon #57 (Tandem Delivery)	0.75"	12000	12000
10/19/2016	NJ Gravel and Sand Co. 1/4" (White Washed)	0.25"	636	1351
10/19/2016	NJ Gravel and Sand Co. 1/4" (White Washed)	0.25"	715	
10/21/2016	Weldon 1/4"	0.25"	621.5	1907
10/21/2016	Weldon 1/4"	0.25"	643.5	
10/21/2016	Weldon 1/4"	0.25"	642	
10/21/2016	Weldon 3/8"	0.375"	695.5	3181.5
10/21/2016	Weldon 3/8"	0.375"	597.5	
10/21/2016	Weldon 3/8"	0.375"	638	
10/21/2016	Weldon 3/8"	0.375"	621	
10/21/2016	Weldon 3/8"	0.375"	629.5	
11/1/2016	Weldon # 57	#57	602.5	1243
11/1/2016	Weldon # 57	#57	640.5	
11/1/2016	Weldon Concrete Sand	Sand	652	1315

11/1/2016	Weldon Concrete Sand	Sand	663	
			SUM	25098.5

The aggregates utilized for the field mixes were shoveled into 55 gallon (0.2m<sup>3</sup>) drums at the quarry, then returned to the lab to be split and quartered according to AASHTO T2 as shown in Figure 35 and Figure 36 below.



Figure 173: Preparing aggregate for splitting



Figure 174: Quartering aggregate for sampling

Specific gravity of fine aggregates and coarse aggregates were conducted using AASHTO T84 and AASHTO T85 respectively. The results for the aggregate specific gravities are shown in Table 5 below.

Table 38: Aggregate Specific Gravities

Average of No.57	Bulk SP.GR.	2.4859
	SSD SP.GR	2.5125
	APP.SP.GR	2.5534
	% Absorption	1.0785

Average of 1/2"	Bulk SP.GR.	2.11455
	SSD SP.GR	2.13475
	APP.SP.GR	2.1582
	% Absorption	0.958
Average of 3/8"	Bulk SP.GR.	2.2655
	SSD SP.GR	2.31785
	APP.SP.GR	2.387
	% Absorption	2.2
Average of 1/4"	Bulk SP.GR.	2.19305
	SSD SP.GR	2.2539
	APP.SP.GR	2.34135
	% Absorption	2.88875
Average of 1/4" white washed	Bulk SP.GR.	2.1275
	SSD SP.GR	2.1777
	APP.SP.GR	2.24005
	% Absorption	2.34975
Average of NAT Sand	Bulk SP.GR.	2.650245
	SSD SP.GR	2.661
	APP.SP.GR	2.6849
	% Absorption	0.46735
Concrete Sand	Bulk SP.GR.	2.6145
	SSD SP.GR	2.61456
	APP.SP.GR	2.6897
	% Absorption	1.068

The ignition oven test, AASHTO T308 was utilized on the aggregates to determine the amount of non-aggregate material found within the aggregate source.

Table 39: Results from Ignition Oven Test

Weldon 3/8"	Sample Weight(g)	1331
	Weight Loss(g)	21.7
	Percent Loss(%)	1.635
	Temp Comp(%)	0.225
	Calibrated Mass Loss (%)	1.405
NJ Gravel 1/4" white washed	Sample Weight(g)	1244
	Weight Loss(g)	5.5
	Percent Loss(%)	0.44
	Temp Comp(%)	0.24
	Calibrated Mass Loss (%)	0.1
NJ Gravel 1/2"	Sample Weight(g)	1829
	Weight Loss(g)	3
	Percent Loss(%)	0.17
	Temp Comp(%)	0.16
	Calibrated Mass Loss (%)	0.025
Weldon 1/4"	Sample Weight(g)	1833
	Weight Loss(g)	22.35
	Percent Loss(%)	1.305
	Temp Comp(%)	0.175
	Calibrated Mass Loss (%)	1.135
Clayton No.57 Likely supplied by Weldon	Sample Weight(g)	2684
	Weight Loss(g)	18.75



	Percent Loss(%)	0.695
	Temp Comp(%)	0.115
	Calibrated Mass Loss (%)	0.585
TrapRock Natural Sand	Sample Weight(g)	1528
	Weight Loss(g)	3.6
	Percent Loss(%)	0.25
	Temp Comp(%)	0.15
	Calibrated Mass Loss (%)	0.015
Weldon Concrete Sand	Sample Weight(g)	1443
	Weight Loss(g)	4.4
	Percent Loss(%)	0.305
	Temp Comp(%)	0.2
	Calibrated Mass Loss (%)	0.105

Aggregate gradations were conducted on each aggregate following AASHTO T27, Sieve Analysis of Fine and Coarse Aggregates. The compiled gradations are shown in Figure 37 below.

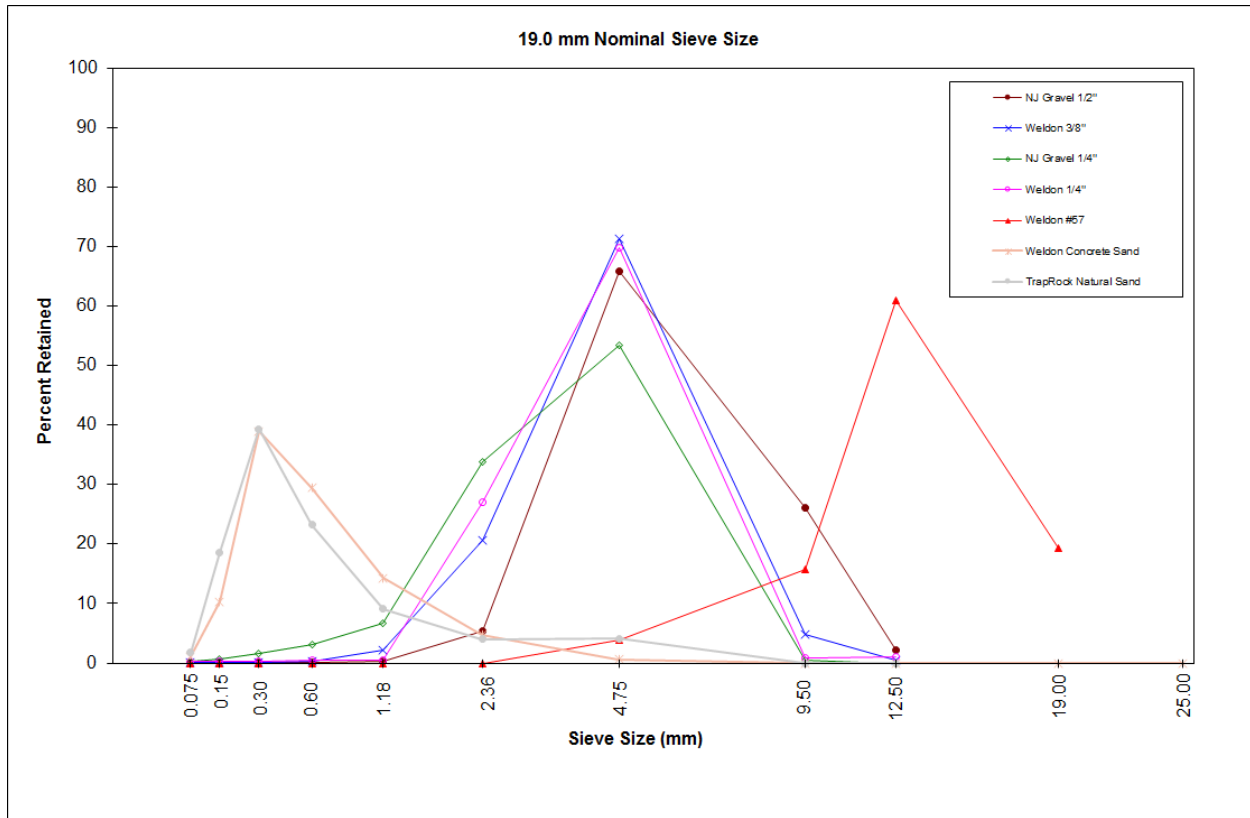


Figure 175: Aggregate gradations compiled (0.45 Power)

The aggregate gradations for Clayton #57 are shown in Table 7 below.

Table 40: Clayton #57 Gradation

Clayton #57				
Sieve	% Retained Sample 1	% Retained Sample 2	% Retained Sample 3	Average % Retained
50.0	0.00	0.00	0.00	0.00
37.5	0.00	0.00	0.00	0.00
25.0	19.42	43.46	23.95	28.94
19.0	60.89	41.69	58.20	53.59
12.5	15.74	12.00	14.85	14.20
9.5	3.88	2.83	2.93	3.21
4.75	0.02	0.01	0.02	0.02

2.36	0.01	0.00	0.01	0.01
1.18	0.01	0.00	0.01	0.01
0.60	0.00	0.00	0.00	0.00
0.30	0.00	0.00	0.00	0.00
0.150	0.02	0.00	0.01	0.01
0.075	0.00	0.00	0.01	0.00
Pan	0.00	0.00	0.00	0.00

The aggregate gradations for Weldon ½" are shown in Table 8 below.

Table 41: Weldon ½" Gradation

Weldon 1/2"				
Sieve	% Retained Sample 1	% Retained Sample 2	% Retained Sample 3	Average % Retained
50.0	0.00	0.00	0.00	0.00
37.5	0.00	0.00	0.00	0.00
25.0	0.00	0.00	0.00	0.00
19.0	0.00	0.00	0.00	0.00
12.5	1.91	2.17	2.08	2.06
9.5	30.75	28.72	26.10	28.52
4.75	61.29	63.70	65.82	63.61
2.36	5.45	4.85	5.35	5.22
1.18	0.30	0.28	0.32	0.30
0.60	0.09	0.08	0.09	0.09
0.30	0.07	0.08	0.07	0.07
0.150	0.06	0.05	0.06	0.06

0.075	0.07	0.05	0.08	0.07
Pan	0.01	0.02	0.01	0.02

The aggregate gradations for Weldon 3/8" are shown in Table 9 below.

Table 42: Weldon 3/8" gradation

Weldon 3/8"				
Sieve	% Retained Sample 1	% Retained Sample 2	% Retained Sample 3	Average % Retained
50	0.00	0.00	0.00	0.00
37.5	0.00	0.00	0.00	0.00
25	0.00	0.00	0.00	0.00
19	0.00	0.00	0.00	0.00
12.5	0.00	0.50	0.19	0.23
9.5	5.49	4.82	5.64	5.32
4.75	76.50	71.20	77.46	75.05
2.36	17.51	20.71	16.30	18.17
1.18	0.44	2.18	0.16	0.93
0.6	0.01	0.31	0.09	0.14
0.3	0.01	0.11	0.04	0.06
0.15	0.01	0.06	0.05	0.04
0.075	0.01	0.07	0.05	0.04
Pan	0.01	0.04	0.03	0.02

The aggregate gradations for Weldon 1/4" are shown in Table 10 below.

Table 43: Weldon 1/4" gradation

Weldon 1/4"
-------------

<b>Sieve</b>	<b>% Retained Sample 1</b>	<b>% Retained Sample 2</b>	<b>% Retained Sample 3</b>	<b>Average % Retained</b>
50	0.00	0.00	0.00	0.00
37.5	0.00	0.00	0.00	0.00
25	0.00	0.00	0.00	0.00
19	0.00	0.00	0.00	0.00
12.5	0.95	0.00	0.34	0.43
9.5	0.77	0.67	0.61	0.69
4.75	69.69	70.67	70.83	70.40
2.36	26.96	27.22	27.11	27.10
1.18	0.50	0.49	0.39	0.46
0.6	0.39	0.31	0.21	0.31
0.3	0.27	0.24	0.17	0.23
0.15	0.22	0.18	0.16	0.19
0.075	0.20	0.19	0.15	0.18
Pan	0.04	0.03	0.03	0.03

The aggregate gradations for NJ Gravel ¼” White Washed are shown in Table 11 below.

Table 44: NJ Gravel 1/4" White Washed Gradation

NJ Gravel 1/4" White Washed				
Sieve	% Retained Sample 1	% Retained Sample 2	% Retained Sample 3	Average % Retained
50.0	0.00	0.00	0.00	0.00
37.5	0.00	0.00	0.00	0.00
25.0	0.00	0.00	0.00	0.00
19.0	0.00	0.00	0.00	0.00
12.5	0.00	0.00	0.00	0.00
9.5	0.42	0.30	0.07	0.26
4.75	53.44	54.11	52.79	53.45
2.36	33.94	33.75	34.63	34.10
1.18	6.67	5.24	6.92	6.28
0.60	3.15	4.32	3.30	3.59
0.30	1.61	1.52	1.58	1.57
0.150	0.60	0.58	0.56	0.58
0.075	0.17	0.16	0.16	0.16
Pan	0.01	0.01	0.01	0.01

The aggregate gradations for Weldon Concrete Sand are shown in Table 12 below.

Table 45: Weldon Concrete Sand

Concrete Sand				
Sieve	% Retained Sample 1	% Retained Sample 2	% Retained Sample 3	Average % Retained
50	0.00	0.00	0.00	0.00
37.5	0.00	0.00	0.00	0.00

25	0.00	0.00	0.00	0.00
19	0.00	0.00	0.00	0.00
12.5	0.00	0.00	0.00	0.00
9.5	0.00	0.00	0.00	0.00
4.75	1.04	0.59	0.96	0.86
2.36	5.87	4.84	5.00	5.24
1.18	17.59	14.82	14.89	15.77
0.6	31.68	29.39	29.97	30.35
0.3	35.02	38.94	37.79	37.25
0.15	8.11	10.31	10.32	9.58
0.075	0.67	1.09	1.06	0.94
Pan	0.02	0.02	0.02	0.02

Aggregate Moisture Content during field sample preparation was determined by drying, ASTM Method C566.

**Table 46: Aggregate Moisture Content**

Date	Time	Aggregate	Sample #	Mass	Moisture Content, %
10/31/2016	8:20	Weldon 3/8	1	713	3.06
10/31/2016	11:00	Weldon 3/8	1	649.4	
10/31/2016	12:00	Weldon 3/8	1	694	
11/1/2016	8:00	Weldon 3/8	1	691.8	
10/31/2016	8:20	Weldon 3/8	2	1012.2	4.09
10/31/2016	11:00	Weldon 3/8	2	976.2	
10/31/2016	12:00	Weldon 3/8	2	975.3	
11/1/2016	8:00	Weldon 3/8	2	972.4	



10/31/2016	8:20	Weldon 3/8	3	954.9	3.96
10/31/2016	11:00	Weldon 3/8	3	927.7	
10/31/2016	12:00	Weldon 3/8	3	921.6	
11/1/2016	8:00	Weldon 3/8	3	918.5	
11/1/2016	19:30	Weldon 1/4	1	2654.9	3.44
11/2/2016	8:10	Weldon 1/4	1	2566.7	
11/1/2016	19:30	Weldon 1/4	2	2188.6	2.70
11/2/2016	8:10	Weldon 1/4	2	2131	
11/1/2016	19:30	Weldon 1/4	3	2268.3	3.50
11/2/2016	8:10	Weldon 1/4	3	2191.5	
11/3/2016	20:00	Concrete Sand	1	4471	2.92
11/4/2016	8:00	Concrete Sand	1	4344.3	
11/3/2016	20:00	Concrete Sand	2	2012	3.27
11/4/2016	8:00	Concrete Sand	2	1948.3	
11/3/2016	20:00	Weldon #57	1	4105.8	1.23
11/4/2016	8:00	Weldon #57	1	4056	
11/3/2016	20:00	Weldon #57	2	3951.2	1.23
11/4/2016	8:00	Weldon #57	2	3903.3	

## Soil Characterization

The soil found at the laboratory test site is predominantly shale, listed by the USDA as Klinesville-Urban land. The soil map provided by the USDA web soil survey can be found in Appendix 3. While the soil type, permeability, and structural capacity have a direct impact on the stormwater design, structural design, and mix selection for a given area, the location of this project was predetermined by availability of space and funding. Developing a knowledge of local soil parameters is strongly advised by the authors when considering the use of pervious concrete mix and how the underlying structure is designed based on the desired outcomes. Pervious structures can be built to either encourage local source-site infiltration, or they can be built with underlying drainage but each has its limitations.

# Equipment

## Test Setup

The test setup for this project consisted of a global sensor array to catch close proximity environmental conditions, as well as mix specific sensor arrays to capture data related to each slab specifically. Two weather-stations were utilized, one positioned on the roof of the laboratory and one positioned on the ground next to the field slabs. Each weather-station included barometric pressure, wind speed, wind direction, ambient temperature, relative humidity, and rainfall measurement equipment. Air column temperature, soil temperature, and soil moisture content was captured globally as well, where a single set of probes was outfitted near slab 4 and the data was utilized for each of the slabs measurements. Finally, each slab was outfitted with load cells to measure slab mass, a temperature probe at the bottom of the slab to measure the under slab temperature, four thermocouples to measure slab temperature, and a net radiometer above the slab to measure the incoming and outgoing solar radiation. The conceptual placement of equipment is shown in Figure 38 below. The detailed description of equipment is described throughout the remaining equipment sections below.

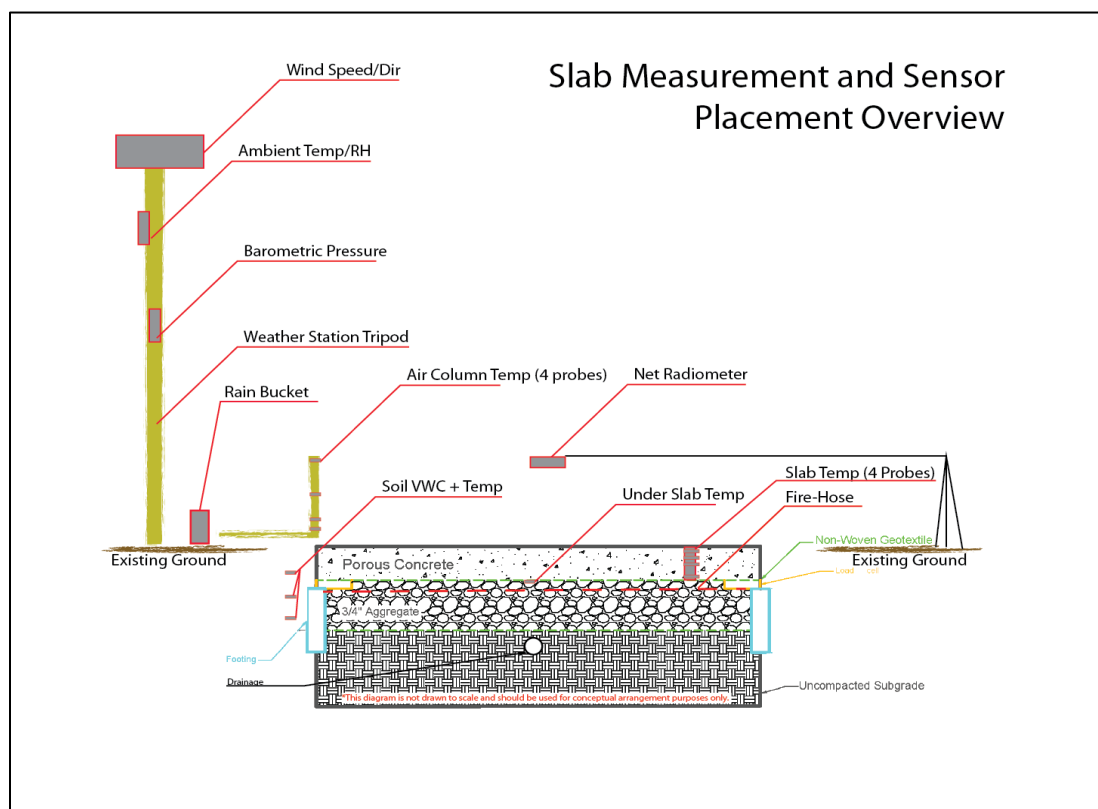


Figure 176: Conceptual diagram showing equipment setup

## Sensors

This section will discuss the sensors that were utilized for this project and brief notes about how they function, what they report, and the position they were placed at. There is a more detailed description of sensor layout in the Equipment Setup section of this paper.

## Anemometers and Weather Vane

To measure wind speed and direction, a 03001 R. M. Young Wind Sentry Set was used. This set includes a 03101 R. M. Young Wind Sentry Anemometer and a 03301 R. M. Young Wind Sentry Vane. Wind speed is measured with a three cup anemometer. Rotation of the cup wheel produces an AV sine wave voltage with frequency proportional to wind speed. Vane position is transmitted by a 10K ohm potentiometer. With a precision excitation voltage applied, the output voltage is proportional to wind direction.

Two 03001 R. M. Young Wind Sentry Sets were used at the site. One was installed at two meters above Slab 1. The second was installed at a height of 10 meters above the testing site on the roof of the adjacent laboratory, which was also two meters above the height of the roof.

## Barometric Pressure

Two Setra Model 278 Barometric Pressure Transducers were used at the site. One was installed at two meters above Slab 1. The second was installed at a height of 10 meters above the testing site on the roof of the adjacent laboratory, which was also two meters above the height of the roof. The Setra Model 278 has a SETRACERAM™ ceramic sensor and a small footprint and removable terminal block. The 278 has low power consumption and sleep mode feature. Under normal operation, this feature minimizes current draw when readings are not being taken.

The 278 utilizes a variable capacitance sensor that is made using ceramic material fused together with glass and gold to form the SETRACERAM™ pressure element. This stable material and design offers adequate thermal performance and low hysteresis. The ceramic sensor enables improved performance compared to other stainless steel sensors.

## Tipping Bucket Rain Gauge

To measure rainfall, two tipping bucket rain gauges were used. One of the rain gauges was sited at the location of Slab 2, while the other was sited 10 meters above the slabs on the roof of the laboratory. The Rain Collector II (US version), manufactured by Davis Instruments, was used at the ground location. The Texas Electronics TE525 was used at the roof location. The TE525 is an adaptation of the standard Weather Bureau tipping bucket rain gage. The sensor consists of a gold anodized aluminum collector funnel with a knife-edge that diverts the water to a tipping bucket mechanism. A magnet is attached to the tipping bucket, which actuates a magnetic switch on each tip of the bucket. The water drains out of the bottom of the housing. The tipping buckets were connected to an event counter on a data logger to measure accumulated rainfall.

## Ambient Temperature and Relative Humidity

### Rotronic Hygroclip2 HC2S3

To measure ambient temperature and relative humidity, a Rotronic Hygroclip2 HC2S3 Temperature and Relative Humidity Sensor was used. The sensor was sited two meters above the ground at the location of Slab 1. The HC2S3 is a rugged, accurate temperature/Relative Humidity probe that is ideal for long-term, unattended applications. It uses a Rotronic's IN1 capacitive sensor to measure relative humidity and a 100 ohm Platinum Resistance Temperature sensor to measure temperature. The HC2S3 comes with a polyethylene filter that protects its sensor from fine dust and particles and minimizes water absorption and retention.

The HC2S3 is a digital probe with linear voltage outputs for temperature and humidity and a UART serial interface. Its voltage signals can be measured with two single-ended or two differential inputs on the datalogger. The digital-to-analog converter used to generate the analog output signals has 16-bit resolution. The cable, which is manufactured by Campbell Scientific for the HC2S3, includes an internal voltage regulator that applies 3.3 V to the probe from a 5 to 24 V power source. Probes are polarity-protected by a keyed connector and diode in the connector interface provided with the Campbell Scientific cable.

### HMP45C

To measure ambient temperature and relative humidity on the roof (10 meters above the testing slabs), a HMP45C Temperature and Relative Humidity Probe was used. The HMP45C is a portable humidity and temperature indicator. Temperature is measured with a Platinum Resistance Temperature detector. Relative humidity is measured with the Vaisala HUMICAP® 180 humidity sensor which uses an operating principle based on the changes in the capacitance of the sensor as its thin polymer film absorbs water molecules.

## Net Radiometers

### Kipp & Zonen CNR2 Net Radiometer

One Kipp & Zonen CNR2 net radiometer was stationed above Slab 4 at a height of 15 cm. The CNR2 Net Radiometer is intended for the analysis of the radiation balance of shortwave and longwave infrared radiation. The most common application is the measurement of total net radiation at the earth's surface. The CNR2 design is such that both the upward facing and the downward facing instruments measure the energy that is received from the hemisphere. The short-wave sensor, or pyranometer, has a field of view of 180 degrees on the upper and 150 degrees on the lower detector. The long wave sensor, or pyrgeometer, has a field of view of 150 degrees on the upper and the lower detector. The output is expressed in Watts per square meter. The total spectral range that is measured is roughly from 0.3 to 40 micrometers. This spectral range covers both the solar radiation, 0.3 to 2.8 micrometers, and the far infrared radiation, 4.5 to 42 micrometers.

The design of the CNR2 is such that short-wave radiation and longwave radiation are measured separately. Short-wave radiation is measured by two pyranometers, one for measuring incoming short-wave radiation from the sky, and the other, which faces downward, for measuring the reflected shortwave radiation. The final result from these two pyranometers is net short-wave radiation. Long-wave radiation is measured by two pyrgeometers, one for measuring the long-wave radiation from the sky, the other from the soil surface. Net longwave radiation is a final result of measurements from those two detectors.

## Kipp & Zonen CNR4 Net Radiometer

One CNR4 net radiometer was stationed above Slab 1 at a height of 15 cm. The CNR4 is a research-grade net radiometer that measures the energy balance between incoming and outgoing radiation. The CNR4 Net Radiometer consists of a pyranometer pair, one facing upward, the other facing downward, and a pyrgeometer pair in a similar configuration. The pyranometer pair measures short-wave solar radiation, and the pyrgeometer pair measures long-wave far infrared radiation. The upper long-wave detector of CNR4 has a meniscus dome to ensure that water droplets roll off easily while improving the field of view to nearly 180°, compared with a 150° for a flat window. All four sensors are integrated directly into the instrument body, instead of separate modules mounted onto the housing.

Two temperature sensors, a thermistor and a Pt-100, are integrated with the CNR4 body. The temperature sensor is used to provide information to correct the infrared readings for the temperature of the instrument housing. Long-wave sensors were positioned close to each other and close to the temperature sensors to ensure that the temperatures of the measurement surfaces are the same and accurately known, improving the quality of the long-wave measurements. A completion resistor is located in the pigtail end of the thermistor cable to provide an easy interface with dataloggers for half-bridge measurement.

The CNR4 design has an integrated solar shield that reduces thermal effects on both the short-wave and the long-wave measurements. The cables are made from Santoprene jacket, which is intended for outdoor use, and is resistant to a variety of pollutants and UV-radiation. The mounting rod can be unscrewed for transport.

The CNR4 design is such that both the upward facing and the downward-facing instruments measure the energy that is received from the whole hemisphere (180° field of view). The output is expressed in W/m<sup>2</sup>. The total spectral range that is measured is roughly from 0.3 to 42 μm. This spectral range covers both the short-wave solar radiation, 0.3 to 2.8 μm, and the long-wave far infrared radiation, 4.5 to 42 μm. The gap between these two produces negligible errors.

## Hukseflux NR01 Net Radiometer

Three Hukseflux NR01 net radiometers were used in this experiment each of them was placed 15 cm above the center of Slabs 3, 6, & 8. The NR01 is a 4-component net-radiation sensor that is used for scientific-grade energy balance studies. The NR01 has separate measurements of

solar (shortwave) and Far Infrared (longwave) radiation. The NR01 serves to measure the four separate components of the surface radiation balance. Working completely passive, using thermopile sensors, the NR01 generates four small output voltages proportional to the incoming and outgoing shortwave and longwave fluxes. The sensor measures global solar radiation (shortwave in), reflected solar radiation (shortwave out), infrared emitted by the sky (longwave in), and infrared emitted by the ground surface (longwave out). From this, parameters such as shortwave albedo, sky temperature, ground surface temperature, and of course net-radiation (net value of all shortwave and longwave fluxes) can be calculated.

The shortwave sensors are also called pyranometers (type SR01), the long-wave sensors are called pyrgeometers (type IR01). Longwave radiation is mainly present in the 4,500 to 50,000 nm region, while the shortwave radiation is mainly present in the 300 to 3,000 nm region. For calculation of the sky- and surface temperatures, a Pt100 temperature sensor is included in the connection body of the pyrgeometers. In order to avoid deposition of dew, the pyrgeometers may be heated, using the heater that is included in the body of the sensor.

## Load Cells

### Load Cell Central Model SWCM-2.5K

Sixteen Load Cell Central Low Profile Shear Web Pancake Load Cells with 2,500 lbs. capacity were used to measure the change in weight of each slab. Two load cells were placed under the forward edge of each slab.

The SWCM load cell is designed for compression loads such as material testing, force calibration of presses, or nearly any force measurement application. The SWCM is constructed of a nickel-plated high alloy tool steel and fully potted to IP65 to protect from water and moisture damage. The standard output is 2 mV/V (for example, 20 milivolts full scale with 10V excitation) that was used with a Campbell Scientific datalogger to interface to a PC.

The load cells were calibrated using known masses to determine the linear relationship between the excitation voltages as compared to the load cell mass. The curves for which were then utilized to determine the conversion factors to utilize to convert from mV/V excitation to calculated mass. The calibration curves utilized for each load cell are shown in Figure 39 below.

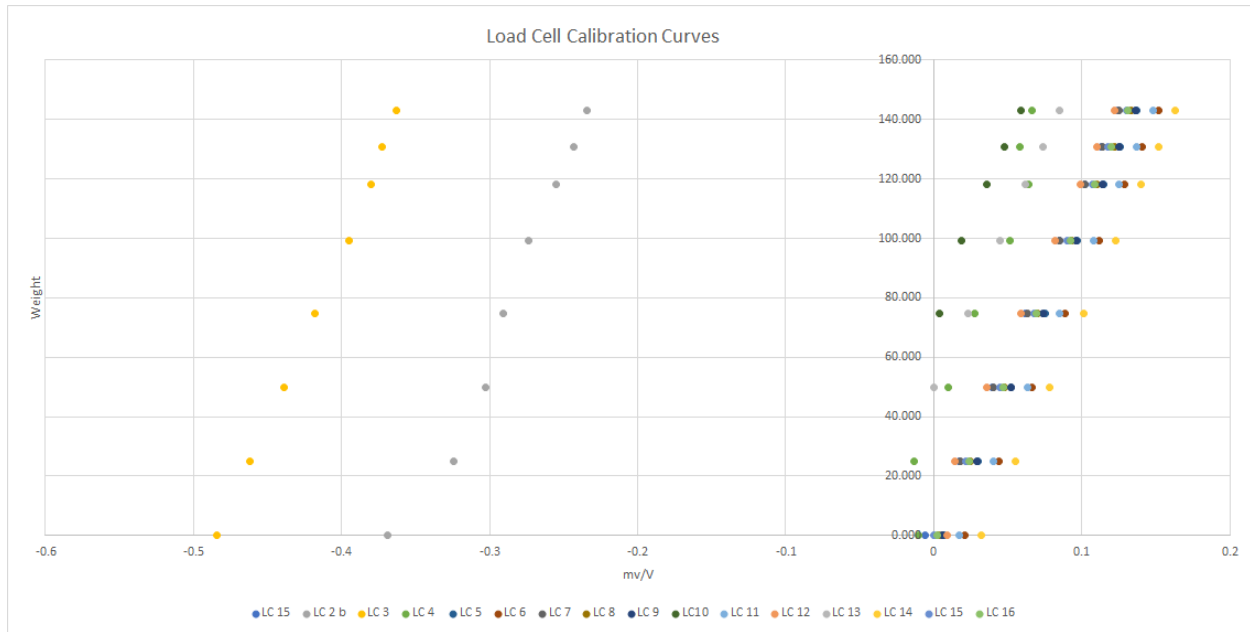


Figure 177: Load Cell calibration curves

The equations derived from each calibration curve to determine mass in lbs. from mV/V excitation measurements is shown in Table 14 below.

Table 47: Load Cell calibration curve equations

LC#	Calibrated load cell mass conversion equations	R2
1	$y = 1,096.4635051030x + 6.4286050366$	0.999988
2	$y = 1,130.0489954508x + 403.9975401068$	0.972087
3	$y = 1,172.3941690876x + 565.7615313302$	0.998139
4	$y = 1,533.7077502940x + 31.3061689795$	0.951075
5	$y = 1,100.3490005443x - 7.7931296328$	0.999961
6	$y = 1,091.8478623809x - 22.8094142437$	0.999964
7	$y = 1,153.0419165230x + 0.5373545456$	0.996347
8	$y = 1,098.8892712611x - 2.8688931945$	0.999953
9	$y = 1,102.2906506076x - 6.9837146123$	0.999944
10	$y = 1,217.0569130331x + 72.8281548850$	0.990885
11	$y = 1,093.7820460915x - 18.7533056298$	0.999968



12	$y = 1,179.9624307054x + 1.7772404476$	0.986936
13	$y = 1,100.2830481793x + 49.6546349542$	0.999926
14	$y = 1,094.1206054821x - 35.3324770927$	0.999958
15	$y = 1,102.5102062261x + 0.1652568343$	0.999954
16	$y = 1,106.2648398559x - 2.0429175736$	0.99997

## Thermocouples

### Campbell Scientific FW05 Type E Thermocouples

Four FW05 Type E thermocouple were used to measure the sensible heat above Slab 4 at heights of 1, 6, 13, and 25 cm. FW05 thermocouples measure atmospheric temperature gradients or fluctuations with research-grade accuracy. The FW05 has a 0.0005-inch diameter wire, which is the smallest offered by Campbell Scientific. The smallest gauge wire allows for the least amount of solar loading, but is the most fragile.

Type E thermocouples are comprised of a chromel wire and a constantan wire joined at a measurement junction. A voltage potential is generated when the measurement end of the thermocouple is at a different temperature than the reference end of the thermocouple. The magnitude of the voltage potential is related to the temperature difference. Therefore, temperature can be determined by measuring the differences in potential created at the junction of the two wires. A reference temperature measurement taken by the datalogger is required.

The calibration procedure utilized for the Type E Thermocouples was a cold water bath filled with ice which served as a reference temperature for 0 °C, an ambient temperature water bath, and a hot water bath. Due to the unlikely possibility that the local ambient temperature would reach 100 °C, it was determined to be more appropriate to use an upper end measurement near 50 °C. A minimum of three measurements were conducted in each water bath with each probe. A calibrated Fluke thermocouple was utilized as the reference temperature for verification. The calibrated linear equations to convert from measured signals to measurements in °C are shown in Table 15.

**Table 48: Calibration equations for Type-E Thermocouples**

Type E#	Calibrated Type-E Temp Conversion Equations	R <sup>2</sup>
1	$y = 1.009636x - 0.332600$	R <sup>2</sup> = 0.999879
2	$y = 1.001895x - 0.018552$	R <sup>2</sup> = 0.999303

3	$y = 1.002117x - 0.090031$	$R^2 = 0.999123$
4	$y = 1.021786x - 0.565473$	$R^2 = 0.999913$

The correction equations for the Type-E thermocouples were created using the following data shown in Figure 40.

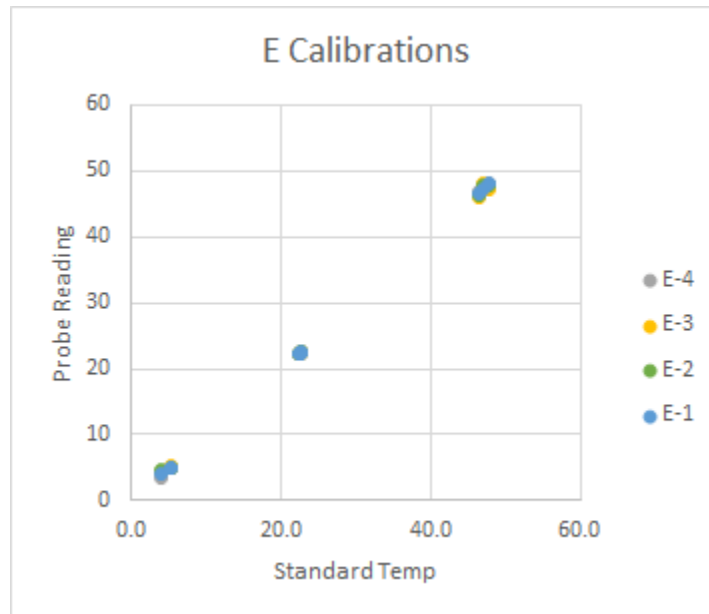


Figure 178: Type E Calibration Data

## Omega Type K Thermocouples

Within each testing slab, four Omega Type K thermocouples were inserted at depths of 0.5, 1, 2, and 3 inches. Type K thermocouples are comprised of a Nickel-Chromium wire and Nickel-Alumel wire joined at a measurement junction. A voltage potential is generated when the measurement end of the thermocouple is at a different temperature than the reference end of the thermocouple. The magnitude of the voltage potential is related to the temperature difference. Therefore, temperature can be determined by measuring the differences in potential created at the junction of the two wires. A reference temperature measurement taken by the datalogger is required.

The calibration procedure utilized for the Type K Thermocouples was a cold water bath filled with ice which served as a reference temperature for 0 °C, an ambient temperature water bath, and a hot water bath, which served as a reference temperature for 100 °C. A minimum of three measurements were conducted in each water bath with each probe. A calibrated Fluke thermocouple was utilized as the reference temperature for verification. The calibrated linear equations to convert from measured signals to measurements in °C are shown in Table 16.

Table 49: Calibration equations for Type-E Thermocouples

Type K#	Calibrated Type-E Temp Conversion Equations	R2
P1T1	$y = 1.005500x - 0.314837$	$R^2 = 0.999969$
P1T2	$y = 1.002437x - 0.230263$	$R^2 = 0.999968$
P1T3	$y = 1.005569x - 0.322829$	$R^2 = 0.999950$
P1T4	$y = 1.005312x - 0.331706$	$R^2 = 0.999975$
P2T1	$y = 0.962332x + 4.175593$	$R^2 = 0.939804$
P2T2	$y = 1.000912x - 0.225212$	$R^2 = 0.999934$
P2T3	$y = 1.005003x - 0.304028$	$R^2 = 0.999950$
P2T4	$y = 1.002564x - 0.275678$	$R^2 = 0.999948$
P3T1	$y = 1.003462x - 0.279078$	$R^2 = 0.999947$
P3T2	$y = 0.998059x - 0.102204$	$R^2 = 0.999907$
P3T3	$y = 1.002129x - 0.239608$	$R^2 = 0.999875$
P3T4	$y = 1.002345x - 0.129091$	$R^2 = 0.999915$
P4T1	$y = 0.998191x - 0.134919$	$R^2 = 0.999939$
P4T2	$y = 0.998497x - 0.078982$	$R^2 = 0.999968$
P4T3	$y = 1.000477x - 0.175865$	$R^2 = 0.999932$
P4T4	$y = 1.002195x - 0.146503$	$R^2 = 0.999970$
P5T1	$y = 0.999708x - 0.075069$	$R^2 = 0.999861$
P5T2	$y = 0.982611x + 0.124440$	$R^2 = 0.998628$
P5T3	$y = 0.873989x + 1.806175$	$R^2 = 0.997526$
P5T4	$y = 1.006567x - 0.203311$	$R^2 = 0.999985$
P6T1	$y = 0.971869x + 0.342415$	$R^2 = 0.998332$
P6T2	$y = 1.006529x - 0.233322$	$R^2 = 0.999987$
P6T3	$y = 0.941519x + 0.662340$	$R^2 = 0.996516$
P6T4	$y = 1.001791x + 0.255256$	$R^2 = 0.999905$

P7T1	$y = 1.007794x - 0.247807$	$R^2 = 0.999971$
P7T2	$y = 1.008290x - 0.278290$	$R^2 = 0.999985$
P7T3	$y = 1.010945x - 0.190096$	$R^2 = 0.999976$
P7T4	$y = 1.006813x - 0.123038$	$R^2 = 0.999984$
P8T1	$y = 1.005148x - 0.102156$	$R^2 = 0.999992$
P8T2	$y = 1.006337x - 0.146913$	$R^2 = 0.999998$
P8T3	$y = 1.000457x - 0.047267$	$R^2 = 0.999952$
P8T4	$y = 1.004421x - 0.138852$	$R^2 = 0.999984$

The correction equations for the Type-K thermocouples were created using the following data shown in Figure 41.

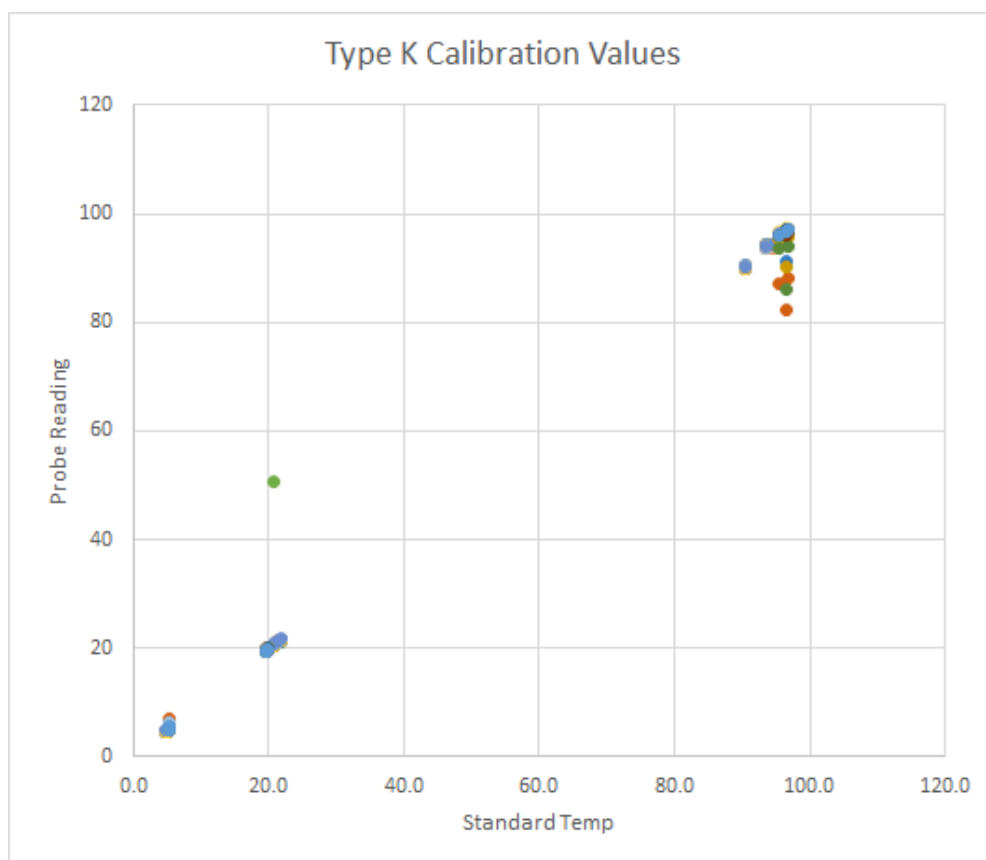


Figure 179: Type K Calibration Values

## Model 108 Temperature Probe

Beneath each of the eight testing slabs, one Model 108 temperature probe was inserted at depth of four inches below grade. The probe was placed in the middle of the slab at a depth of four inches below grade. The 108 Temperature Probe uses a thermistor to measure temperature in air, soil, and water. The sensor consists of a thermistor encapsulated in an epoxy-filled aluminum housing. This design allows the probe to be buried or submerged in water to 15 m (50 ft) or 21 psi. When measuring air temperature, a six-plate radiation shield is normally used to mount the 108 and limit solar radiation loading.

The calibration procedure utilized for the Type K Thermocouples was a cold water bath filled with ice which served as a reference temperature for 0 °C, an ambient temperature water bath, and a hot water bath, which served as a reference temperature for 100 °C. A minimum of three measurements were conducted in each water bath with each probe. A calibrated Fluke thermocouple was utilized as the reference temperature for verification. The calibrated linear equations to convert from measured signals to measurements in °C are shown in Table 17.

**Table 50: USP Calibration Equations**

<b>USP#</b>	<b>Calibrated USP Temp Conversion Equations</b>	<b>R2</b>
1	$y = 1.005934x - 1.049753$	$R^2 = 0.999719$
2	$y = 0.999792x - 0.732195$	$R^2 = 0.999792$
3	$y = 0.999573x - 0.788002$	$R^2 = 0.999783$
4	$y = 1.001435x - 0.998372$	$R^2 = 0.999640$
5	$y = 0.995723x - 0.902140$	$R^2 = 0.999668$
6	$y = 1.002499x - 0.906879$	$R^2 = 0.999742$
7	$y = 0.997937x - 0.715355$	$R^2 = 0.999709$
8	$y = 0.993726x + 0.168371$	$R^2 = 0.999944$

The correction equations for the Type-108 USP thermocouples were created using the following data shown in Figure 42.

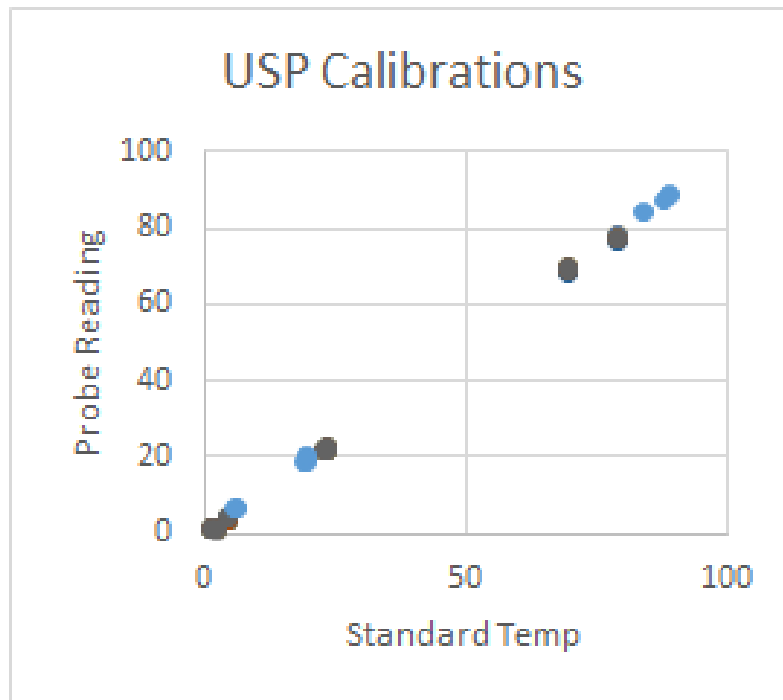


Figure 180: USP Calibrations

## Time-Domain Reflectometers

### Campbell Scientific CS616

Two CS650 was buried adjacent to Slab 4 at a depths of 6 and 9 inches below grade, respectively. The CS616 Water Content Reflectometer is designed to measure volumetric water content (VWC) of soils or other porous media. The water content information is derived from the probe sensitivity to the dielectric constant of the medium surrounding the probe rods.

The water content reflectometer consists of two stainless steel rods connected to a printed circuit board. A shielded four-conductor cable is connected to the circuit board to supply power, enable the probe, and monitor the pulse output. The circuit board is encapsulated in epoxy. High-speed electronic components on the circuit board are configured as a bistable multivibrator. The output of the multivibrator is connected to the probe rods which act as a waveguide. The travel time of the signal on the probe rods depends on the dielectric permittivity of the material surrounding the rods, and the dielectric permittivity depends on the water content. Therefore, the oscillation frequency of the multivibrator is dependent on the water content of the media being measured. Digital circuitry scales the multivibrator output to an appropriate frequency for measurement with a datalogger. The water content reflectometer output is essentially a square wave. The probe output period ranges from about 14 microseconds with rods in air to about 42 microseconds with the rods completely immersed in typical tap water. A calibration equation to convert period to volumetric water content.

The two CS616s were calibrated with known soil volumetric water contents to produce the calibration curves in Figures 43 & 44

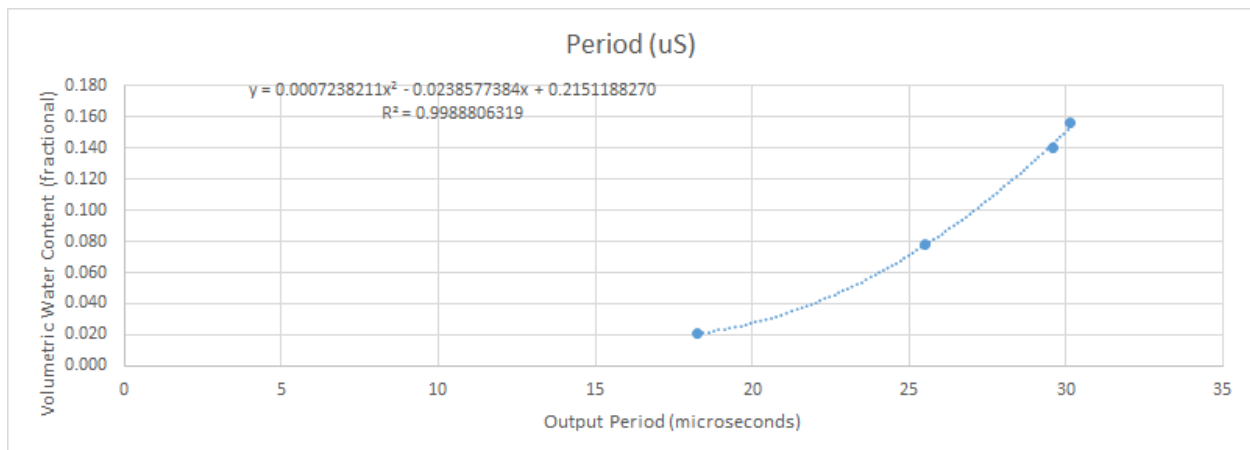


Figure 181: CS616 (6 inches) Calibration Curve



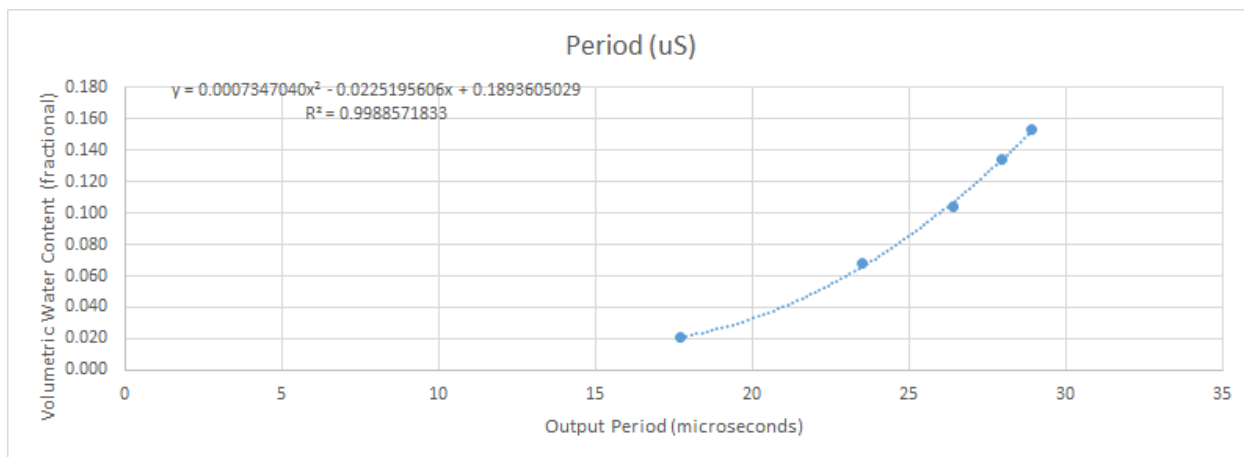


Figure 182: CS616 (9 inches) Calibration Curve

## Campbell Scientific CS650

One CS650 was buried adjacent to Slab 4 at a depth of 3 inches below grade. The CS650 is a multi-parameter smart sensor that monitors soil volumetric water content, bulk electrical conductivity, and temperature. The CS650 has 30 cm length rods. Volumetric water content information is derived from the probe's sensitivity to the dielectric permittivity of the medium surrounding the probe stainless-steel rods. The CS650 is configured as a water content reflectometer, with the two parallel rods forming an open-ended transmission line. A differential oscillator circuit is connected to the rods, with an oscillator state change triggered by the return of a reflected signal from one of the rods. The two-way travel time of the electromagnetic waves that are induced by the oscillator on the rod varies with changing dielectric permittivity. Water is the main contributor to the bulk dielectric permittivity of the soil or porous media, so the travel time of the reflected wave increases with increasing water content and decreases with decreasing water content, hence the name water content reflectometer. The average travel time of the reflected wave multiplied by a scaling factor of 128 is called the period average. Period average is reported in microseconds and is considered to be the raw output of a water content reflectometer.

Electrical conductivity is determined by exciting the rods with a known non-polarizing waveform and measuring the signal attenuation. Signal attenuation is reported as a dimensionless voltage ratio, which is the ratio of the excitation voltage to the measured voltage along the sensor rods when they are excited at a fixed 100 kHz frequency. Voltage ratio ranges from 1 in non-conductive media to about 17 in highly conductive media. Values greater than 17 are highly unstable and indicate that the soil conditions are outside of the specified operating range of the sensor.

Temperature is measured with a thermistor in contact with one of the rods. It is well known that transmission line oscillators used for water content measurements suffer from unwanted increases in oscillation period as increasing electrical conductivity causes transmission line signal attenuation. The CS650 handles this problem by making an electrical conductivity measurement and then correcting the oscillator period accordingly. On-board processing within the sensor head calculates electrical conductivity from the signal attenuation measurement and combines the

result with the oscillation period measurement to calculate the dielectric permittivity of the media and finally applies the Topp equation (Topp et al. 1980) to estimate volumetric water content.

Probe electronics are encapsulated in the rugged epoxy probe head. A five conductor cable including the drain or shield wire is used to provide power and ground as well as serial communication with the CS650. The CS650 is intended to communicate with SDI-12 recorders, including Campbell Scientific dataloggers. The orange Rx wire can be used to communicate by means of RS-232 Tx/Rx. The A200 USB-to-Serial Module allows RS-232 serial communication between a computer and the CS650 by means of Campbell Scientific's Device Configuration Utility (DevConfig) software.

The CS650 was calibrated with known soil volumetric water contents to produce the calibration curve in Figure 45.

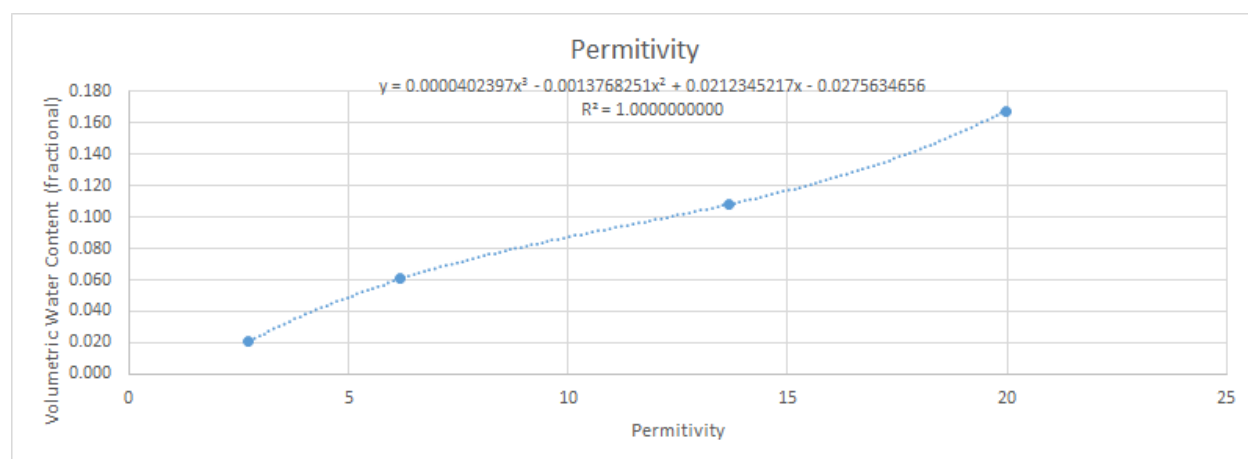


Figure 183: CS650 (3 inches) Calibration Curve

The calibration procedure for the CS650, as well as the CS616 TDR gauges was conducted using a probe housing that was filled with soil sampled from the site. The soil was sampled in accordance to ASSHTO T180, dried in an oven at 100°C for 24 hours and verified to have reached its dry equilibrium. Then the soil was shake-sifted over a #4 ASTM standard sieve and any particles passing the #4 sieve were retained. Best efforts were made to “compact” the soil around the probe in the probe housing. The probe housing was similar to a graduated cylinder which was outfitted with a 5-point manifold. The manifold allowed the gravity fed water source to be introduced to the soil sample from the bottom to ensure that the water-front moved evenly and proportionately to the soil rather than allowing the water to find its own path (of least resistance), which would likely follow the probe where the soil was disturbed to insert the probe and would then provide inherent error in the calibration. Change in mass of H<sub>2</sub>O determined the difference in moisture content, which was then related to the output from each gauge. Since the experiment required monitoring for small changes on a scale, the sensor wires were carefully oriented to ensure the wire mass, or change in wire mass, was not recorded. Figure 46 shows the dry sample prior to attaching the manifold.



Figure 184: Dry TDR calibration sample, manifold is hanging on right after stemming from gravity fed bucket

Figure 47 below shows the same sample after some water had been introduced.

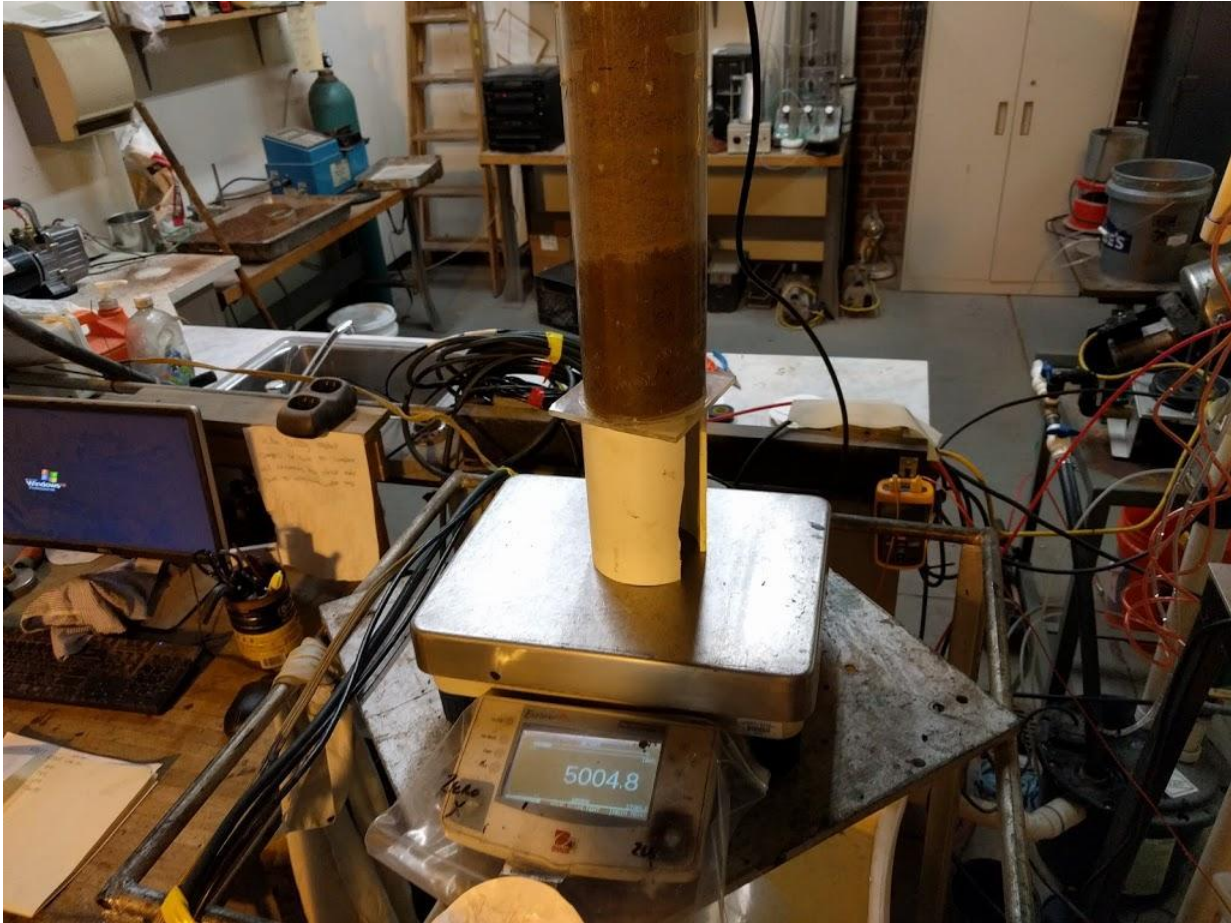


Figure 185: Wet TDR calibration sample, manifold is hanging on right after stemming from gravity fed bucket

## Data Loggers and Multiplexers

Six data loggers were utilized for this project. Descriptions of each are below.

### Campbell Scientific CR10X Datalogger (1)

The CR10X is a fully programmable datalogger/controller with non-volatile memory and a battery backed clock. The CR10X does not have an integral keyboard/display. The CR10X does not have an integral terminal strip. The power supply is external to the CR10X.

The CR10X Wiring Panel and CR10X datalogger make electrical contact through two D-type connectors. The Wiring Panel contains a 9-pin Serial I/O port used when communicating with the datalogger and provides terminals for connecting sensor, control, and power leads to the CR10X. It also provides transient protection and reverse polarity protection.



The CR10X datalogger received data from the following sensors:

- One (1) HMP45C
- One (1) 03001 R. M. Young Wind Sentry Set
- One (1) TE525
- One (1) Setra Model 278

## Campbell Scientific CR1000 Datalogger (3)

The CR1000 datalogger is one part of our data acquisition system. CPU, analog and digital measurements, analog and digital outputs, and memory usage are controlled by the operating system in conjunction with the user program and on-board clock. The user program is written in CRBasic, a programming language that includes data processing and analysis routines and a standard BASIC instruction set. Campbell Scientific datalogger support software facilitates program generation, editing, data retrieval, and real-time data monitoring. In addition to the CR1000 datalogger, suitable sensors and reliable telecommunications devices are required to complete a data acquisition system.

Sensors transduce phenomena into measurable electrical forms, outputting voltage, current, resistance, pulses, or state changes. The CR1000, sometimes with the assistance of various peripheral devices, can measure nearly all electronic sensors.

The CR1000 measures analog voltage and pulse signals, representing the magnitudes numerically. Numeric values are scaled to the units of measure, such as milliVolts and pulses, or user-specified engineering units, such as wind direction and wind speed. Measurements can be processed through calculations or statistical operations and stored in memory awaiting transfer to a PC via external storage or telecommunications.

Nearly all CR1000 functions depend on the internal clock. The operating system and the CRBasic user program use the clock for scheduling operations. The CRBasic program times functions through various instructions, but the method of timing is nearly always in the form of "time into an interval". For example, 6:00 AM is represented in CRBasic as "360 minutes into a 1440 minute interval", 1440 minutes being the length of a day and 360 minutes into that day corresponding to 6:00 AM.

0 minutes into an interval puts it at the "top" of that interval, i.e. at the beginning of the second, minute, hours, or day. For example, 0 minutes into a 1440 minute interval corresponds to Midnight. When an interval of a week is programmed, the week begins at Midnight on Monday morning.

The wiring panel of the CR1000 is the interface to many CR1000 functions. Hard-wired measurements require the physical connection of a sensor to an input channel and CRBasic programming to instruct the CR1000 how to make, process, and store the measurement

The CR1000 operates from a power supply with voltage ranging from 9.6 to 16 Vdc, and is internally protected against accidental polarity reversal.

Three CR1000 Dataloggers were used in this experiment. The following sensors, shown in Table 18, were input into the respective CR1000:

**Table 51: CR1000 Datalogger Equipment used**

<b>CR1000(I)</b>	<b>CR1000(II)</b>	<b>CR1000(III)</b>
Seven (7) Model 108s	One (1) CS650	One (1) Hukseflux NR01
Four (4) Type E Thermocouples	Two (2) CS616s	One (1) Kipp & Zonnen CNR2
One (1) 03001 R. M. Young Wind Sentry Set		

## Campbell Scientific CR3000 Datalogger (2)

The CR3000 can measure almost any sensor with an electrical response. The CR3000 measures electrical signals and converts the measurement to engineering units, performs calculations and reduces data to statistical values. Most applications do not require that every measurement be stored. Instead, individual measurements can be combined into statistical or computational summaries. The CR3000 will store data in memory to await transfer to the PC with an external storage devices or telecommunication device.

The CR3000 has a central-processing unit (CPU), analog and digital measurement inputs, analog and digital outputs, and memory. An operating system (firmware) coordinates the functions of these parts in conjunction with the on-board clock and the CRBasic application program.

The application program is written in CRBasic, which is a programming language that includes measurement, data processing, and analysis routines and the standard BASIC instruction set. For simpler applications, Short Cut, a user friendly program generator, can be used to write the program. For more demanding programs, use CRBasic Editor

The CR3000 wiring panel provides terminals for connecting sensors, power, and communication devices. Surge protection is incorporated internally in most wiring panel connectors. Terminal strips can be disconnected from the CR3000 wiring panel when necessary for maintenance or troubleshooting operations.

The CR3000 operates with power from 10 to 16 Vdc applied at the POWER IN terminals of the green connector on the face of the wiring panel, or at the power input receptacle on the underside of the CR3000 module, which is reserved for integrated power supplies. Power connects through the green POWER IN connector on the face of the CR3000. The positive power lead connects to 12V. The negative lead connects to G. The connection is internally reverse-polarity protected. The CR3000 is internally protected against accidental polarity reversal on the power inputs.

Two CR3000 Dataloggers were used in this experiment. The following sensors, shown in Table 19 below, were input into each CR3000:





Table 52: CR3000 Datalogger Equipment used

CR3000 (I)	CR3000 (II)
One (1) Kipp & Zonen CNR4	One (1) Huxeflux NR01
One (1) Huxeflux NR01	Eight (8) Omega Type K Thermocouples
One (1) Rain Collector II	One (1) AM25T Multiplexer 25 Omega Type K Thermocouples
One (1) Rotronic Hygroclip2 HC2S3	
One (1) AM16/32B Multiplexer 16 SWCM-2.5Ks	

### Campbell Scientific AM25T Thermocouple Multiplexer (1)

One AM25T was used to expand the ports of a CR3000 datalogger for input of 25 Omega Type K thermocouples. The AM25T multiplexer increases the number of channels for measuring thermocouples or voltage sensors with Campbell Scientific dataloggers. The AM25T is positioned between the sensors and the datalogger. The datalogger controls the AM25T's solid-state relays, sequentially connecting each sensor to the datalogger.

A maximum of 25 thermocouples (differential voltage measurement) can be multiplexed by an AM25T. Single-ended voltage measurements are not recommended. The AM25T must be used in a non-condensing environment. An enclosure is required for field use. In applications where one or two multiplexers are deployed in the field, the ENC12/14 can be used. The ENC16/18 can be used to house several multiplexers at the same site.

The AM25T is connected to the datalogger with eight insulated wires and a large ground wire. These wires are used to power and control the multiplexer, and connect the common analog inputs to the datalogger.

The AM25T is housed in an anodized aluminum case with a cover that will help reduce temperature gradients across the AM25T's terminal strips. The terminal strips that run the length of the AM25T are for sensor connections. All inputs are protected by spark gaps. All terminals accept stripped and tinned lead wires up to 1.5 mm (0.059 inches) in diameter. A strain-relief flange is located between the input terminals.

### Campbell Scientific AM16/32B Multiplexer (1)

One AM16/32B was used to expand the ports of a CR3000 datalogger for input of 16 Model SWCM-2.5k load cells. The primary function of the AM16/32B multiplexer is to increase the number of sensors that can be measured by CR6-series, CR800-series, CR1000, CR3000, and CR5000 dataloggers. The AM16/32B is positioned between the sensors and the datalogger.

Mechanical relays in the AM16/32B connect each of the sensor channels in turn to a common output destined for the datalogger. The user program advances the multiplexer through the sensor channels, making measurements and storing data. A slide switch located on the AM16/32B's top panel selects one of two modes of operation. In 2x32 mode, the multiplexer adds 32 terminal pairs. In 4x16 mode, it adds 16 terminal groups with four terminals each. The datalogger program is written according to the selected mode and the sensors to be measured.

The AM16/32B is intended for use in applications where more terminals are needed than the datalogger has available. Most commonly, the AM16/32B is used to multiplex analog sensor signals, although it can also be used to multiplex switched excitations, continuous analog outputs, or even certain pulse counting measurements (those that require only intermittent sampling). It is also possible to multiplex sensors of different, but compatible, types.

## Equipment Setup

The equipment/sensors were all wired in the laboratory. The first step in the procedure was to determine if each piece of equipment was functional. Each piece of equipment was connected to a datalogger separately and tested to verify it was functioning properly. The number of wires required to connect each to the datalogger was recorded. The total length of standard wire that came with each unit was recorded as well. Items that were broken were replaced or repaired as applicable. The majority of the repairs required cutting broken wire and soldering new wire to ensure proper connection. The second major repair was re-soldering terminal connections that had become loose. One of the Young Anemometers was missing a 6 pin plug, which was replaced with a new plug. The laboratory setup showing the test datalogger and equipment is shown in Figure 48 below.



**Figure 186: Laboratory setup to test individual equipment**

After each piece of equipment was tested, a wiring/data logger plan was developed to determine the applicable sensors that could be connected to each datalogger. Once the wiring plan was developed, a siting plan was developed for each of the six data loggers and two multiplexers. The rough siting plan was used to determine the required wire length that each of the pieces of equipment required to reach each field test slab. The rough siting plan is shown in Figure 49.

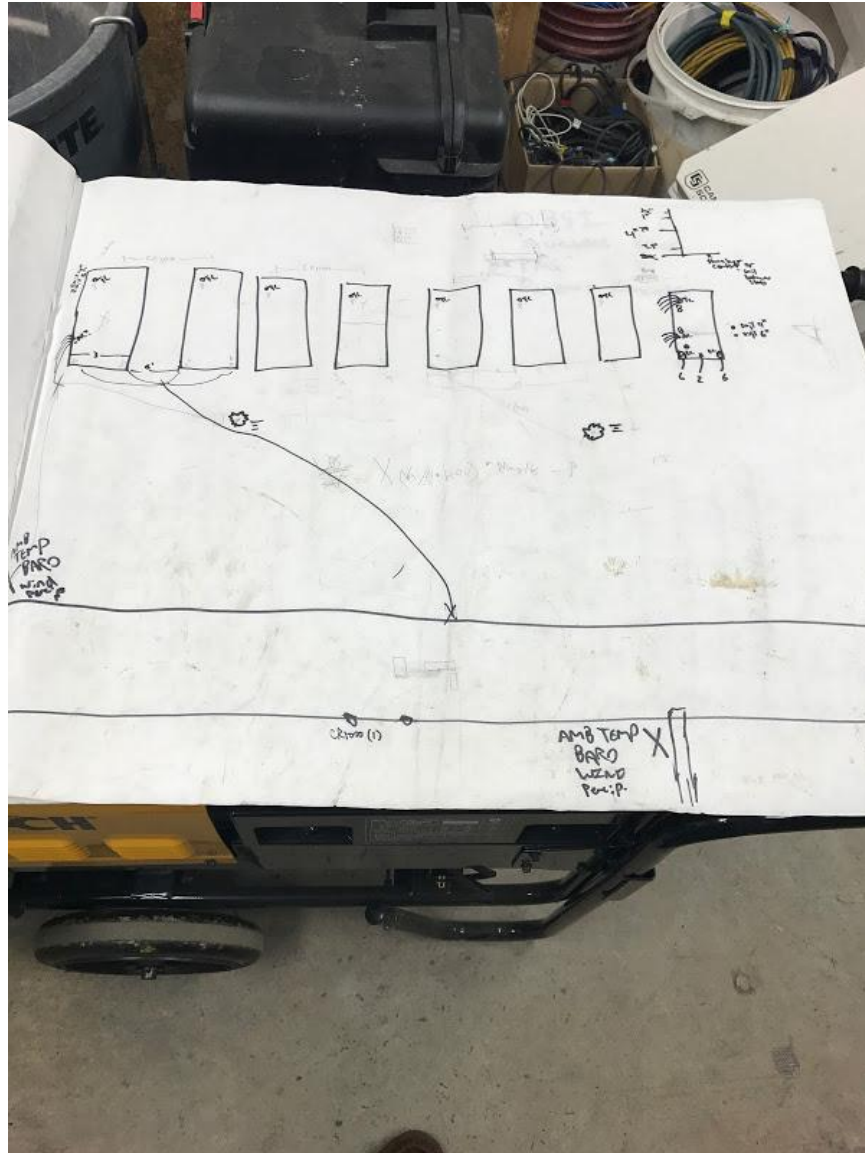
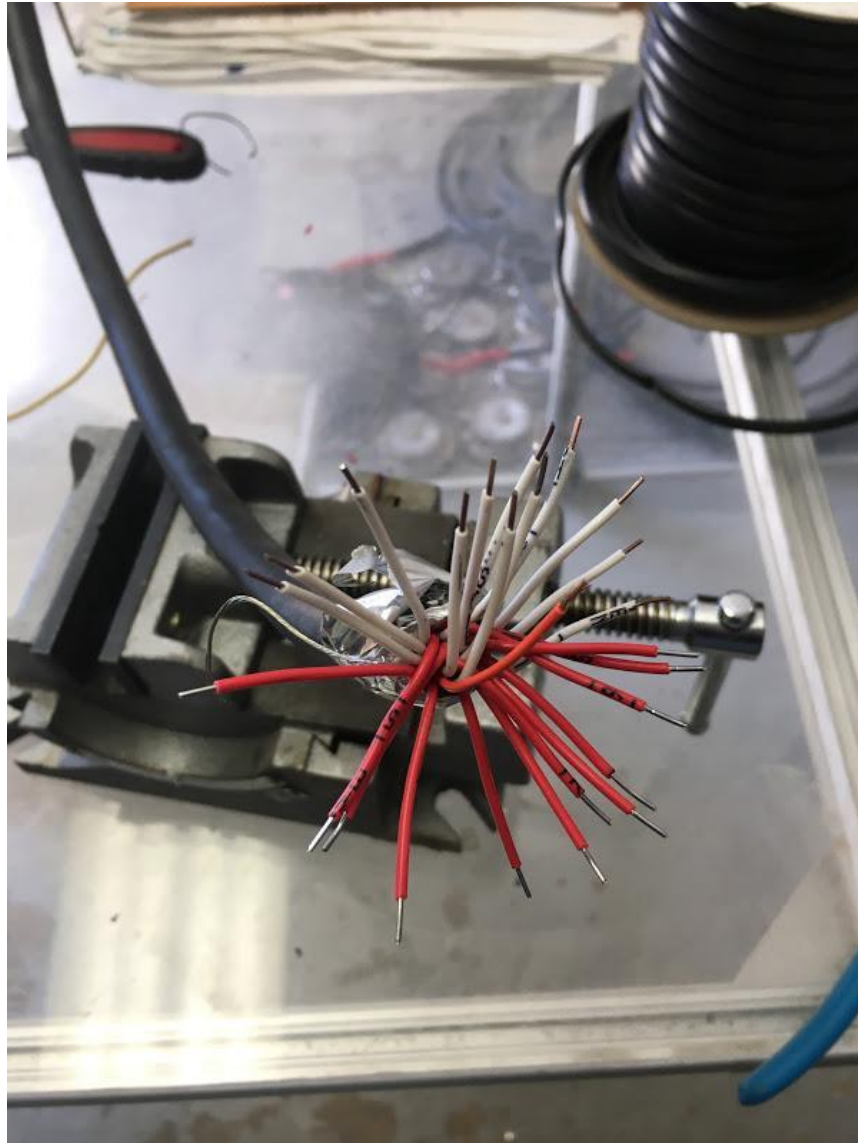


Figure 187: Rough equipment siting plan

The wiring for each piece of equipment was conducted as thoroughly as possible to alleviate any possible mechanical or electrical error within the sensors and measurements. All solder joints were coated with individual heat shrink tubing, then the entire line was covered in a larger heat shrink tubing. Finally an outside sheath was placed around the outside of the line to prevent water damage. Roughly 500 solder connections were made throughout repair, testing, and the extension of signal lines. An example of preparing a line for soldering is shown in Figure 50 below.



**Figure 188: Preparing an Extension Line for Soldering**

After the extension wire diagrams were finalized, the next step was to solder and protect the individual signal lines as shown in Figure 51 below.



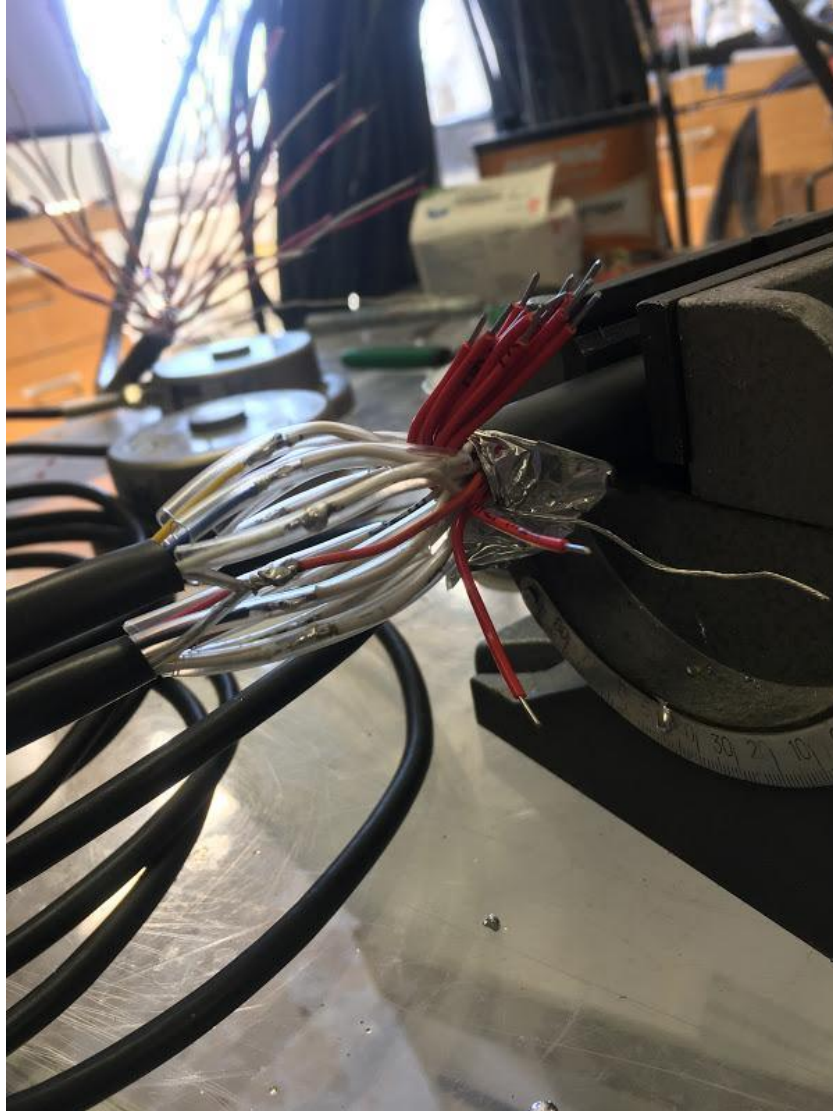


Figure 189: Insulation of signal extension wires

Due to budgetary constraints, the extension wires utilized for this project were limited to wire-on-hand. The load cell extension wires caused the majority of the load cell noise, as they utilized a 24 stranded JX extension wire, where four load cells all ran through the same line. Two load cells per line utilized the Iron wire while the remaining two utilized the Constantan wire. While evaluating the functionality of the load cells with this extension wire, there appeared to be no difference in the signals. When the extension wire was placed outside though, two sources of noise became overwhelming to the load cell signal; the number of wires over the signal distance caused excess noise within the line while the solar flux and heat caused noise along the distance of the line. The authors would recommend the use of single shielded, environmental grade line per sensor with the addition of a signal amplifier per line to ensure the environmental noise be kept to a minimum when evaluating such small loads over such a long time period. Aside from that extension wire issue, extreme care was taken to ensure that the final length of the signal wires matched within 6in (15.24cm).



The wiring diagrams for each Campbell datalogger as well as extension wires can be found in the appendix. The DAQ wiring and placement will be covered in the equipment orientation section of this paper.

## Equipment Location and Orientation

### Rooftop Weather Station

To provide local weather conditions, two weather stations were utilized. The first of which was placed at 33ft (10m). To accomplish this, the weather station was erected on the roof of the laboratory. The roof weather station assembly is shown in Figure 52.



Figure 190: Rooftop weather station

The rooftop weather station was not allowed to be connected to the building or roof in any way. Bolts were recessed on a double layer of  $\frac{3}{4}$ " (19mm) plywood to hold the tower while not scratching the roof. Pull tests were conducted on the ground to determine the appropriate ballast weight to withstand a 150 mph (67m/s) wind. The rooftop weather station was set up to measure wind speed and direction, precipitation, ambient temperature, relative humidity, and barometric pressure. It is customary to not conduct these measurements so close to the roof, but the data provided a valuable backup for the ground weather station data and was used for additional data verification.

## Ground Weather Station

The ground weather station was set-up very similarly to the roof weather station but in close proximity to the ground. This was considered important for this study since the pervious slabs were part of the ground and surface condition. The ground weather station is shown in Figure 53, in on the left of the foreground.



Figure 191: Ground Weather Station, Left Foreground



## Type-E Air Column Thermocouples

The Type-E air column thermocouples were located above slab 4. The data from the close-proximity air column thermocouples was utilized for each of the slabs. The holding bracket with thermocouples mounted is shown in Figure 54.



Figure 192: Type-E close proximity air column thermocouples

The four type E thermocouples were placed at logarithmically spaced intervals increasing in height from the surface of the slab. The heights of the type E thermocouples is shown in Table 20.

Table 53: Type E close proximity air column thermocouple heights

Thermocouple #	Height of Placement (inches)
E1	0.39
E2	2.36
E3	5.12
E4	9.84

## Slab Temperature Probes

The slab Temperature probes were located at the Northeast corner of each slab. Each probe had four type K thermocouples which were attached to a 0.9in (22.9mm) diameter silicone filled PVC pipe using electrical tape. Care was taken to ensure each thermocouple was lying flat against the PVC pipe and taped with the end of the thermocouple at the appropriate measurement depth. The measurement depths utilized for each in-slab temperature probe is shown in Table 21. The probe nomenclature was “P1T1” which signified Probe 1, thermocouple 1. Each slab had 4 thermocouples and one probe.

Table 54: In-slab thermocouple depth arrangement

Thermocouple #	Depth (inches)
PXT1	0.5
PXT2	1
PXT3	2
PXT4	3.5

The temperature probes were placed at 8 inches (20.32cm) from the corner of each slab. The placement of the in-slab temperature probes can be seen in Figure 55.



**Figure 193:** *In-Slab temperature probe location*

## Net Radiometers

The net radiometers utilized for this experiment were located at the center of each slab at a height of 18in (45.7cm) above the slab surface. The radiometers were held in place by tripods with extension booms to reduce the shadow effect the sensors would have on the surface. The sensors surface was made level with bubble levels and a handheld level if possible. The position of the net radiometer can be seen in Figure 56.





Figure 194: Net Radiometer location

## Measurement Protocol

The final layout of sensors per DAQ is shown in Figure 57. When arranging the equipment layout, there were several considerations that were required to mitigate. Each DAQ required power and communications to deliver data back to the main computer interface. Power cables were created to extend power to the two environmental containment boxes utilized. The sensors with the shortest extension wire were placed in the outside environmental containment boxes where the longest wire run measured approximately 40ft (12.2m) and the shortest run measured approximately 15ft (4.6m). The Campbell CX3000 Load Cell and AM16/32 multiplexer were located in the outside containment boxes, along with the CR1000 TDR DAQ. The second CR3000 utilized to measure type K thermocouples, the AM25T multiplexer, and two final CR1000s were mounted to a wall inside the laboratory near the main computer.



FINAL SENSOR LAYOUT			
CR3000(1)	BLUE	1 CNRH	net Radiometer
CR3000 Full trial (3)	DATA	1 NRO1	net Radiometer
outside	DATA-9P21	1 Rain Gauge	Generic Tipping Bucket
		1 AMB Temp/RH	
		1 AM 16/32	MUX
		↳ 16 Load cells	
CR1000 (1)	Black	7 thermometers	128L
(temp test 002)	DATA	4 "E" Thermocouples	Thin-wire Air column
outside		1 wind S/D	Young 03001
CR1000 (2)	DATA	2 TOR	616
outside		1 TOR	650
		(possibly add	3-4 Thermocouples for soil depth)
CR1000 (3)	DATA	1 NRO1	net radiometer
CR1000 Full trial (2)	DATA	1 CNR2	net radiometer
inside		1	
CR3000 (2)	DATA	1 NRO1	net Radiometer
CR3000 Full trial (3.5)	DATA	1 AM 25T	MUX
inside		↳ 25 "K" Thermocouples	slab sensible heat
		8 "K" Thermocouples	slab sensible heat
CR10X	DATA	1 AMB T/RH	HMP45C
CR10X Full trial (3)	DATA	1 wind S/D	Young 03001 (2)
inside		1 rain gauge	TB TES25
		1 Baro Pressure	CS100
		1	

Figure 195: Final Sensor Layout by DAQ and Location

The outside containment box location in comparison to the test slabs is shown in Figure 58.



Figure 196: Outside equipment environmental containment box location

The almost completed, wired data loggers inside the environmental containment box are shown in Figure 59 below.



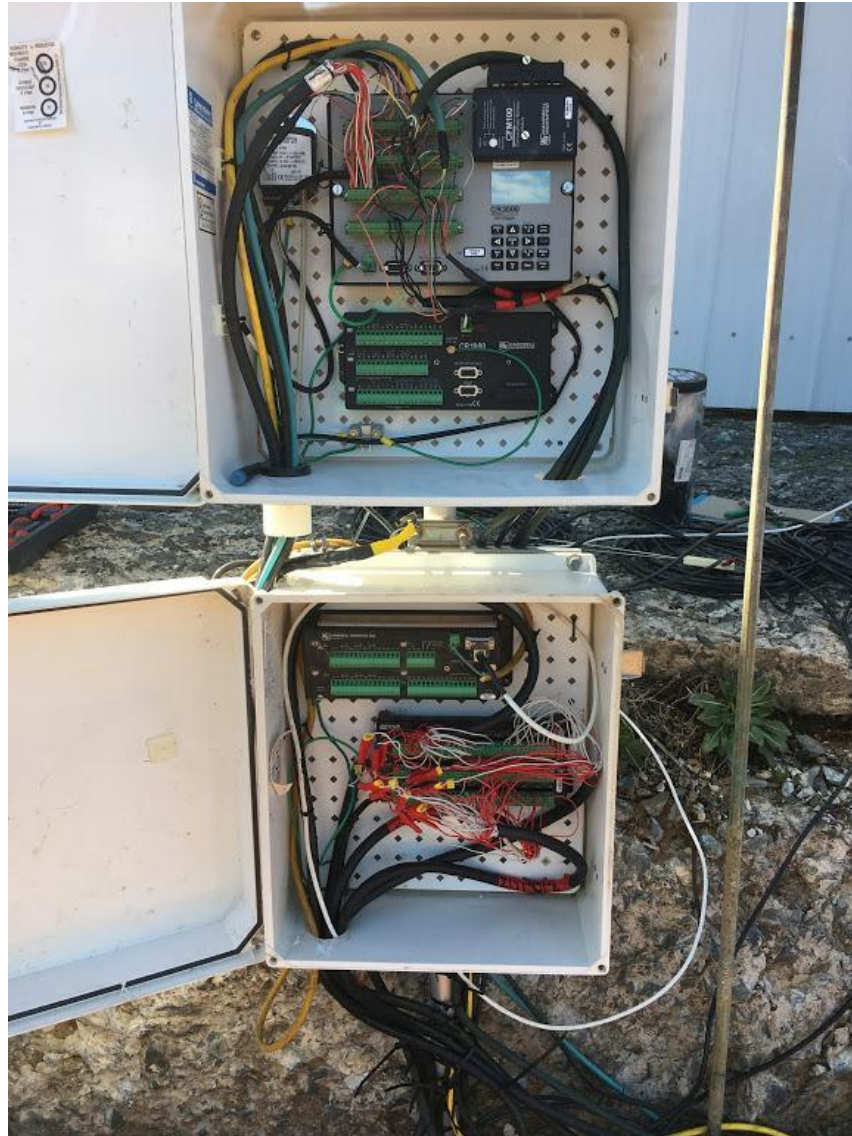


Figure 197: Almost completed wiring inside environmental containment boxes

The data loggers mounted inside the laboratory were mounted to a vibration resistant panel to ensure vibrations from the vibratory brick compactor on the adjacent wall would be dampened as well as to provide a separation from any moisture that might accumulate on the wall. The in-lab setup is shown in Figure 60.

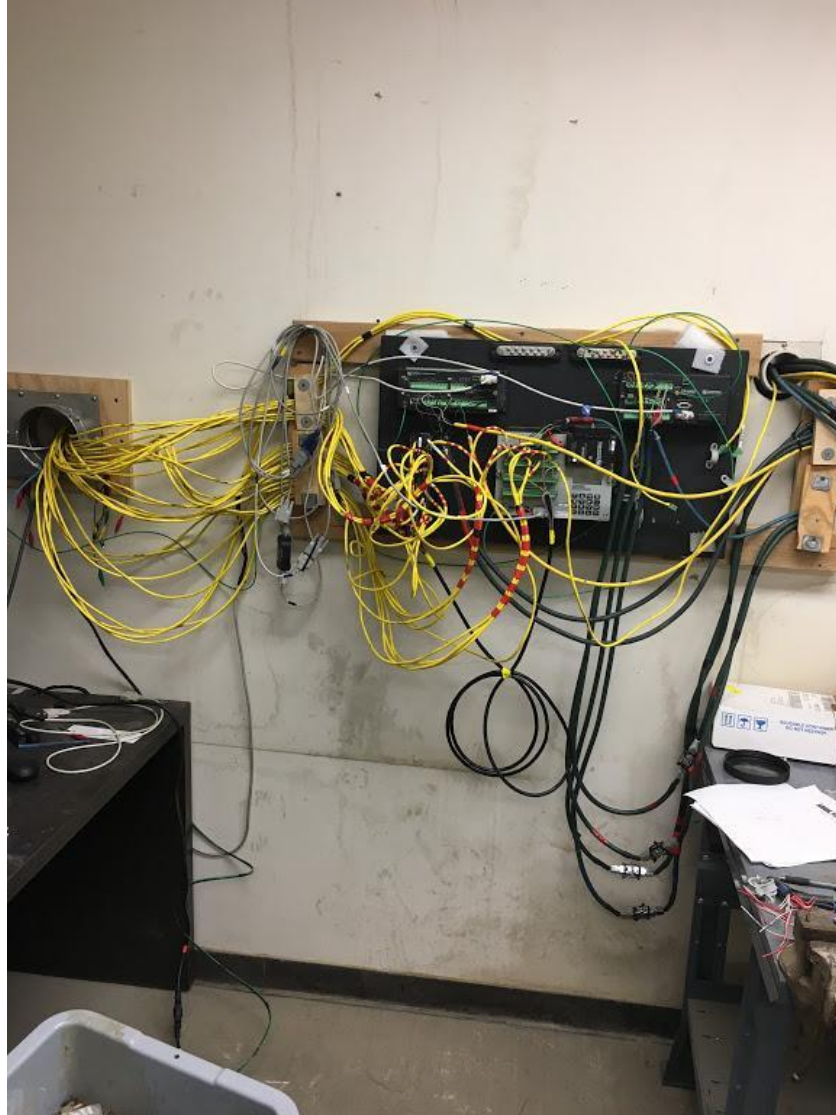


Figure 198: In laboratory setup of additional DAQs and Multiplexer

All of the power requirements for DAQs was handled by a dedicated Electro Industries Digi 360 regulated DC power supply, which was capped at 2 amps of output at 11.75 volts. The communications were supplied through USB to RS-232 adaptors into a standard Dell Computer which ran Windows 64-bit Professional. The power supply, computer, and connected communications can be seen in Figure 61. Due to the harsh laboratory conditions typically found where this computer was situated, it was determined to be necessary to add an additional cooling fan to ensure the computer would remain functional throughout the duration of the project.

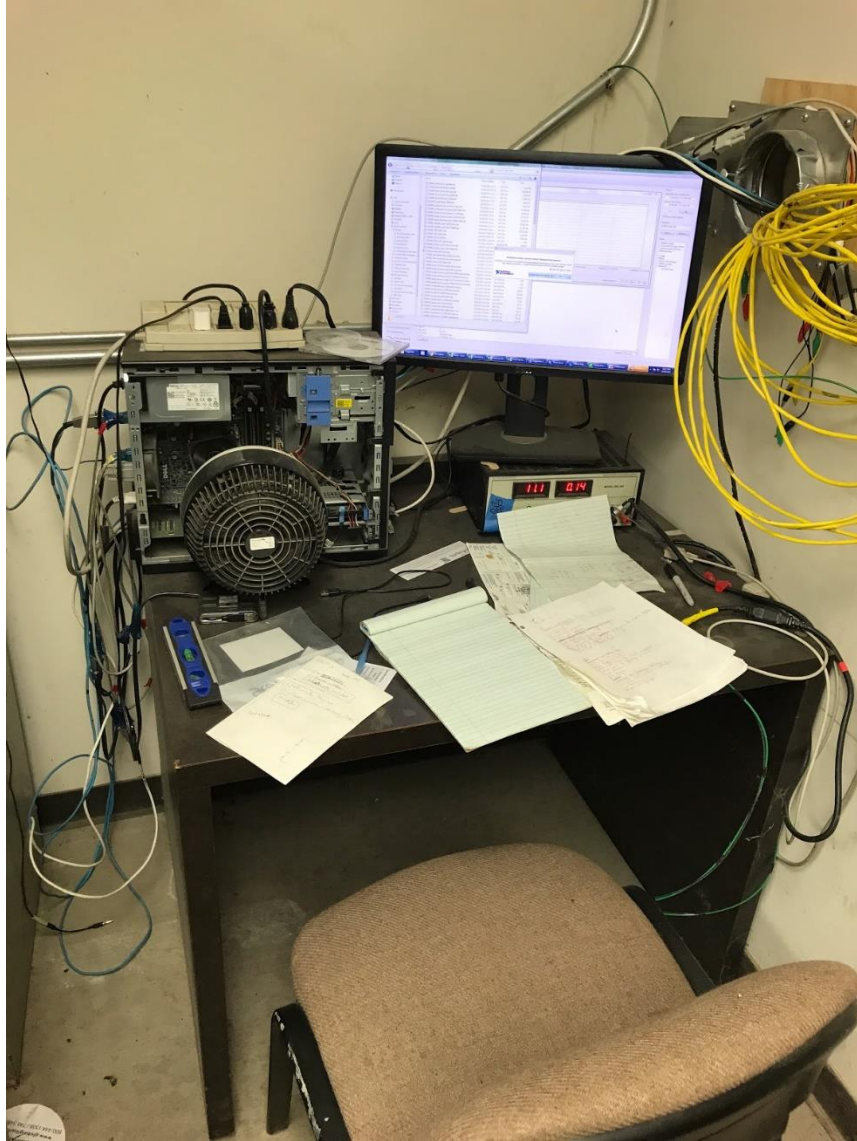


Figure 199: Computer, power supply, and communications

The final sensor layout as defined by field slab was determined once each piece of equipment was in place. The sensors associated with Field Slab 1 are shown in Table 22.

Table 55: Field sample 1 sensors

Slab 1			
Sensor ID	MatlabID	Units	Compile Sheet ID
USP1_COR_Avg	S1.USP	DegC	Temp_Blue_All
LoadCell(1)	S1.LC1	mV/V	CR3000 Outside Load Cells
LoadCell(2)	S1.LC2	mV/V	CR3000 Outside Load Cells

P1T1_COR	S1.ST1	Deg C	CR3000 Inside Thermocouples
P1T2_COR	S1.ST2	Deg C	CR3000 Inside Thermocouples
P1T3_COR	S1.ST3	Deg C	CR3000 Inside Thermocouples
P1T4_COR	S1.ST4	Deg C	CR3000 Inside Thermocouples
Sup	S1.SUP	W/m^2	CR3000 Outside Load Cells
SDn	S1.SDN	W/m^2	CR3000 Outside Load Cells
LUp	S1.LUP	W/m^2	CR3000 Outside Load Cells
LDn	S1.LDN	W/m^2	CR3000 Outside Load Cells
CNR4TC	-	Deg C	CR3000 Outside Load Cells
RsNet	S1.RSNET	W/m^2	CR3000 Outside Load Cells
RINet	S1.RLNET	W/m^2	CR3000 Outside Load Cells
Albedo	S1.A	W/m^2	CR3000 Outside Load Cells
Rn	S1.RN	W/m^2	CR3000 Outside Load Cells
LUpCo	S1.LUPCO	W/m^2	CR3000 Outside Load Cells
LDnCo	S1.LDNCO	W/m^2	CR3000 Outside Load Cells
Roof_AmbT_Avg	S1.AMB	DegC	CX10
Rf_RH_Sample	S1.RH	%	CX10
TB_Rain_Total	S1.RAIN	mm	CX10
NOAAP.RainEWR	S1.RAINEWR	mm	NOAAP
NOAAP.RainSOM	S1.RAINSOM	mm	NOAAP
WS_ms_Avg	S1.WS	m/s	Temp_Blue_All
WindDir	S1.WD	Deg	Temp_Blue_All
BP_mbar (GROUND)	S1.BP	in	CR3000 Outside Load Cells
3inVWC	S1.VWC3	m^3/m^3	TDR
Soil T	S1.SOILT3	degC	TDR

6inVW_2	S1.SOILT6	m <sup>3</sup> /m <sup>3</sup>	TDR
E1T1_COR_Avg	S1.E1	DegC	Temp_Blue_All
E1T2_COR_Avg	S1.E2	DegC	Temp_Blue_All
E1T3_COR_Avg	S1.E3	DegC	Temp_Blue_All
E1T4_COR_Avg	S1.E4	DegC	Temp_Blue_All

The sensors associated with field slab 2 are shown in Table 23.

Table 56: Field sample 2 sensors

Slab 2			
Sensor ID	Matlab ID	Units	Compile Sheet ID
USP2_COR_Avg	S2.USP	DegC	Temp_Blue_All
LoadCell(3)	S2.LC1	mV/V	CR3000 Outside Load Cells
LoadCell(4)	S2.LC2	mV/V	CR3000 Outside Load Cells
P2T1_COR	S2.ST1	Deg C	CR3000 Inside Thermocouples
P2T2_COR	S2.ST2	Deg C	CR3000 Inside Thermocouples
P2T3_COR	S2.ST3	Deg C	CR3000 Inside Thermocouples
P2T4_COR	S2.ST4	Deg C	CR3000 Inside Thermocouples
Roof_AmbT_Avg	S2.AMB	DegC	CX10
Rf_RH_Sample	S2.RH	%	CX10
TB_Rain_Total	S2.RAIN	mm	CX10
NOAAP.RainEWR	S2.RAINEWR	mm	NOAAP
NOAAP.RainSOM	S2.RAINSOM	mm	NOAAP
WS_ms_Avg	S2.WS	m/s	Temp_Blue_All
WindDir	S2.WD	deg	Temp_Blue_All
BP_mbar (GROUND)	S2.BP	in	CR3000 Outside Load Cells



3inVWC	S2.VWC3	mbar	TDR
Soil T	S2.SOILT3	degC	TDR
6inVW_2	S2.SOILT6	m <sup>3</sup> /m <sup>3</sup>	TDR
E1T1_COR_Avg	S2.E1	DegC	Temp_Blue_All
E1T2_COR_Avg	S2.E2	DegC	Temp_Blue_All
E1T3_COR_Avg	S2.E3	DegC	Temp_Blue_All
E1T4_COR_Avg	S2.E4	DegC	Temp_Blue_All

The sensors associated with field slab 3 are shown in Table 24.

Table 57: Field sample 3 sensors

Slab 3			
Sensor ID	Matlab ID	Units	Compile Sheet ID
USP3_COR_Avg	S3.USP	DegC	Temp_Blue_All
LoadCell(5)	S3.LC1	mV/V	CR3000 Outside Load Cells
LoadCell(6)	S3.LC2	mV/V	CR3000 Outside Load Cells
P3T1_COR	S3.ST1	Deg C	CR3000 Inside Thermocouples
P3T2_COR	S3.ST2	Deg C	CR3000 Inside Thermocouples
P3T3_COR	S3.ST3	Deg C	CR3000 Inside Thermocouples
P3T4_COR	S3.ST4	Deg C	CR3000 Inside Thermocouples
SR01Up	S3.SUP	W/m <sup>2</sup>	CR3000 Outside Load Cells
SR01Dn	S3.SDN	W/m <sup>2</sup>	CR3000 Outside Load Cells
IR01Up	S3.LUP	W/m <sup>2</sup>	CR3000 Outside Load Cells
IR01Dn	S3.LDN	W/m <sup>2</sup>	CR3000 Outside Load Cells
NR01TC	-	Deg C	CR3000 Outside Load Cells
NetRs	S3.RSNET	W/m <sup>2</sup>	CR3000 Outside Load Cells

NetRI	S3.RLNET	W/m <sup>2</sup>	CR3000 Outside Load Cells
Albedo_2	S3.A	W/m <sup>2</sup>	CR3000 Outside Load Cells
UpTot	S3.UpTot	W/m <sup>2</sup>	CR3000 Outside Load Cells
DnTot	S3.DnTot	W/m <sup>2</sup>	CR3000 Outside Load Cells
NetTot	S3.RN	W/m <sup>2</sup>	CR3000 Outside Load Cells
IR01UpCo	S3.LUPCO	W/m <sup>2</sup>	CR3000 Outside Load Cells
IR01DnCo	S3.LDNCO	W/m <sup>2</sup>	CR3000 Outside Load Cells
Roof_AmbT_Avg	S3.AMB	DegC	CX10
Rf_RH_Sample	S3.RH	%	CX10
TB_Rain_Total	S3.RAIN	mm	CX10
NOAAP.RainEWR	S3.RAINEWR	mm	NOAAP
NOAAP.RainSOM	S3.RAINSOM	mm	NOAAP
WS_ms_Avg	S3.WS	m/s	Temp_Blue_All
WindDir	S3.WD	deg	Temp_Blue_All
BP_mbar (GROUND)	S3.BP	in	CR3000 Outside Load Cells
3inVWC	S3.VWC3	mbar	TDR
Soil T	S3.SOILT3	degC	TDR
6inVW_2	S3.SOILT6	m <sup>3</sup> /m <sup>3</sup>	TDR
E1T1_COR_Avg	S3.E1	DegC	Temp_Blue_All
E1T2_COR_Avg	S3.E2	DegC	Temp_Blue_All
E1T3_COR_Avg	S3.E3	DegC	Temp_Blue_All
E1T4_COR_Avg	S3.E4	DegC	Temp_Blue_All

The sensors associated with field slab 4 are shown in Table 25.

Table 58: Field sample 4 sensors

Slab 4			
Sensor ID	Matlab ID	Units	Compile Sheet ID
USP4_COR_Avg	S4.USP	DegC	Temp_Blue_All
CNR2_NetSW_Avg	S4.RSNET	W/m^2	CR1000 Solar Inside
CNR2_NetLW_Avg	S4.RLNET	W/m^2	CR1000 Solar Inside
LoadCell(7)	S4.LC1	mV/V	CR3000 Outside Load Cells
LoadCell(8)	S4.LC2	mV/V	CR3000 Outside Load Cells
P4T1_COR	S4.ST1	Deg C	CR3000 Inside Thermocouples
P4T2_COR	S4.ST2	Deg C	CR3000 Inside Thermocouples
P4T3_COR	S4.ST3	Deg C	CR3000 Inside Thermocouples
P4T4_COR	S4.ST4	Deg C	CR3000 Inside Thermocouples
Roof_AmbT_Avg	S4.AMB	DegC	CX10
Rf_RH_Sample	S4.RH	%	CX10
TB_Rain_Total	S4.RAIN	mm	CX10
NOAAP.RainEWR	S4.RAINEWR	mm	NOAAP
NOAAP.RainSOM	S4.RAINSOM	mm	NOAAP
WS_ms_Avg	S4.WS	m/s	Temp_Blue_All
WindDir	S4.WD	deg	Temp_Blue_All
BP_mbar (GROUND)	S4.BP	in	CR3000 Outside Load Cells
3inVWC	S4.VWC3	m^3/m^3	TDR
Soil T	S4.SOILT	degC	TDR
6inVW_2	S4.SOILT6	m^3/m^3	TDR
E1T1_COR_Avg	S4.E1	DegC	Temp_Blue_All
E1T2_COR_Avg	S4.E2	DegC	Temp_Blue_All
E1T3_COR_Avg	S4.E3	DegC	Temp_Blue_All

E1T4_COR_Avg	S4.E4	DegC	Temp_Blue_All
--------------	-------	------	---------------

The sensors associated with field slab 5 are shown in Table 26.

Table 59: Field sample 5 sensors

Slab 5			
Sensor ID	Matlab ID	Units	Compile Sheet ID
USP5_COR_Avg	S5.USP	DegC	Temp_Blue_All
LoadCell(9)	S5.LC1	mV/V	CR3000 Outside Load Cells
LoadCell(10)	S5.LC2	mV/V	CR3000 Outside Load Cells
P5T1_COR	S5.ST1	Deg C	CR3000 Inside Thermocouples
P5T2_COR	S5.ST2	Deg C	CR3000 Inside Thermocouples
P5T3_COR	S5.ST3	Deg C	CR3000 Inside Thermocouples
P5T4_COR	S5.ST4	Deg C	CR3000 Inside Thermocouples
Roof_AmbT_Avg	S5.AMB	DegC	CX10
Rf_RH_Sample	S5.RH	%	CX10
TB_Rain_Total	S5.RAIN	mm	CX10
NOAAP.RainEWR	S5.RAINEWR	mm	NOAAP
NOAAP.RainSOM	S5.RAINSOM	mm	NOAAP
WS_ms_Avg	S5.WS	m/s	Temp_Blue_All
WindDir	S5.WD	deg	Temp_Blue_All
BP_mbar (GROUND)	S5.BP	in	CR3000 Outside Load Cells
3inVWC	S5.VWC3	m <sup>3</sup> /m <sup>3</sup>	TDR
Soil T	S5.SOILT	degC	TDR
6inVW_2	S5.SOILT6	m <sup>3</sup> /m <sup>3</sup>	TDR
E1T1_COR_Avg	S5.E1	DegC	Temp_Blue_All

E1T2_COR_Avg	S5.E2	DegC	Temp_Blue_All
E1T3_COR_Avg	S5.E3	DegC	Temp_Blue_All
E1T4_COR_Avg	S5.E4	DegC	Temp_Blue_All

The sensors associated with field slab 6 are shown in Table 27.

Table 60: Field sample 6 sensors

Slab 6			
Sensor ID	Matlab ID	Units	Compile Sheet ID
USP6_COR_Avg	S6.USP	DegC	Temp_Blue_All
LoadCell(11)	S6.LC1	mV/V	CR3000 Outside Load Cells
LoadCell(12)	S6.LC2	mV/V	CR3000 Outside Load Cells
P6T1_COR	S6.ST1	Deg C	CR3000 Inside Thermocouples
P6T2_COR	S6.ST2	Deg C	CR3000 Inside Thermocouples
P6T3_COR	S6.ST3	Deg C	CR3000 Inside Thermocouples
P6T4_COR	S6.ST4	Deg C	CR3000 Inside Thermocouples
Blue_SR01Up_Avg	S6.SUP	W/m <sup>2</sup>	CR1000 Solar Inside
Blue_SR01Dn_Avg	S6.SDN	W/m <sup>2</sup>	CR1000 Solar Inside
Blue_IR01Up_Avg	S6.LUP	W/m <sup>2</sup>	CR1000 Solar Inside
Blue_IR01Dn_Avg	S6.LDN	W/m <sup>2</sup>	CR1000 Solar Inside
Blue_NR01TC_Avg	-	DegC	CR1000 Solar Inside
Blue_NR01TK_Avg	-	K	CR1000 Solar Inside
Blue_NetRs_Avg	S6.RSNET	W/m <sup>2</sup>	CR1000 Solar Inside
Blue_NetRI_Avg	S6.RLNET	W/m <sup>2</sup>	CR1000 Solar Inside
Blue_Albedo_Avg	S6.A	W/m <sup>2</sup>	CR1000 Solar Inside
Blue_UpTot_Avg	S6.UpTot	W/m <sup>2</sup>	CR1000 Solar Inside

Blue_DnTot_Avg	S6.DnTot	W/m^2	CR1000 Solar Inside
Blue_NetTot_Avg	S6.RN	W/m^2	CR1000 Solar Inside
Blue_IR01UpCo_Avg	S6.LUPCO	W/m^2	CR1000 Solar Inside
Blue_IR01DnCo_Avg	S6.LDNCO	W/m^2	CR1000 Solar Inside
Roof_AmbT_Avg	S6.AMB	DegC	CX10
Rf_RH_Sample	S6.RH	%	CX10
TB_Rain_Total	S6.RAIN	mm	CX10
NOAAP.RainEWR	S6.RAINEWR	mm	NOAAP
NOAAP.RainSOM	S6.RAINSOM	mm	NOAAP
WS_ms_Avg	S6.WS	m/s	Temp_Blue_All
WindDir	S6.WD	deg	Temp_Blue_All
BP_mbar (GROUND)	S6.BP	in	CR3000 Outside Load Cells
3inVWC	S6.VWC3	m^3/m^3	TDR
Soil T	S6.SOILT3	degC	TDR
6inVW_2	S6.SOILT6	m^3/m^3	TDR
E1T1_COR_Avg	S6.E1	DegC	Temp_Blue_All
E1T2_COR_Avg	S6.E2	DegC	Temp_Blue_All
E1T3_COR_Avg	S6.E3	DegC	Temp_Blue_All
E1T4_COR_Avg	S6.E4	DegC	Temp_Blue_All

The sensors associated with field slab 7 are shown in Table 28.

Table 61: Field sample 7 sensors

Slab 7			
Sensor ID	Matlab ID	Units	Compile Sheet ID
USP7_COR_Avg	S7.USP	DegC	Temp_Blue_All

LoadCell(13)	S7.LC1	mV/V	CR3000 Outside Load Cells
LoadCell(14)	S7.LC2	mV/V	CR3000 Outside Load Cells
P7T1_COR	S7.ST1	Deg C	CR3000 Inside Thermocouples
P7T2_COR	S7.ST2	Deg C	CR3000 Inside Thermocouples
P7T3_COR	S7.ST3	Deg C	CR3000 Inside Thermocouples
P7T4_COR	S7.ST4	Deg C	CR3000 Inside Thermocouples
Roof_AmbT_Avg	S7.AMB	DegC	CX10
Rf_RH_Sample	S7.RH	%	CX10
TB_Rain_Total	S7.RAIN	mm	CX10
NOAAP.RainEWR	S7.RAINEWR	mm	NOAAP
NOAAP.RainSOM	S7.RAINSOM	mm	NOAAP
WS_ms_Avg	S7.WS	m/s	Temp_Blue_All
WindDir	S7.WD	deg	Temp_Blue_All
BP_mbar (GROUND)	S7.BP	in	CR3000 Outside Load Cells
3inVWC	S7.VWC3	m <sup>3</sup> /m <sup>3</sup>	TDR
Soil T	S7.SOILT3	degC	TDR
6inVW_2	S7.SOILT6	m <sup>3</sup> /m <sup>3</sup>	TDR
E1T1_COR_Avg	S7.E1	DegC	Temp_Blue_All
E1T2_COR_Avg	S7.E2	DegC	Temp_Blue_All
E1T3_COR_Avg	S7.E3	DegC	Temp_Blue_All
E1T4_COR_Avg	S7.E4	DegC	Temp_Blue_All

The sensors associated with field slab 8 are shown in Table 29.

Table 62: Field sample 8 sensors

<b>Slab 8</b>
---------------



<b>Sensor ID</b>	<b>Matlab ID</b>	<b>Units</b>	<b>Compile Sheet ID</b>
USP8_COR	S8.USP	Deg C	CR3000 Inside Thermocouples
LoadCell(15)	S8.LC1	mV/V	CR3000 Outside Load Cells
LoadCell(16)	S8.LC2	mV/V	CR3000 Outside Load Cells
P8T1_COR	S8.ST1	Deg C	CR3000 Inside Thermocouples
P8T2_COR	S8.ST2	Deg C	CR3000 Inside Thermocouples
P8T3_COR	S8.ST3	Deg C	CR3000 Inside Thermocouples
P8T4_COR	S8.ST4	Deg C	CR3000 Inside Thermocouples
Red_SR01Up	S8.SUP	W/m <sup>2</sup>	CR3000 Inside Thermocouples
Red_SR01Dn	S8.SDN	W/m <sup>2</sup>	CR3000 Inside Thermocouples
Red_IR01Up	S8.LUP	W/m <sup>2</sup>	CR3000 Inside Thermocouples
Red_IR01Dn	S8.LDN	W/m <sup>2</sup>	CR3000 Inside Thermocouples
Red_NR01TC	-	Deg C	CR3000 Inside Thermocouples
Red_NetRs	-	W/m <sup>2</sup>	CR3000 Inside Thermocouples
Red_NetRI	S8.RSNET	W/m <sup>2</sup>	CR3000 Inside Thermocouples
Red_Albedo	S8.RLNET	W/m <sup>2</sup>	CR3000 Inside Thermocouples
Red_UpTot	S8.A	W/m <sup>2</sup>	CR3000 Inside Thermocouples
Red_DnTot	S8.UpTot	W/m <sup>2</sup>	CR3000 Inside Thermocouples
Red_NetTot	S8.DnTot	W/m <sup>2</sup>	CR3000 Inside Thermocouples
Red_IR01UpCo	S8.RN	W/m <sup>2</sup>	CR3000 Inside Thermocouples
Red_IR01DnCo	S8.LUPCO	W/m <sup>2</sup>	CR3000 Inside Thermocouples
Roof_AmbT_Avg	S8.LDNCO	DegC	CX10
Rf_RH_Sample	S8.RH	%	CX10
TB_Rain_Total	S8.RAIN	mm	CX10
NOAAP.RainEWR	S8.RAINEWR	mm	NOAAP

NOAAP.RainSOM	S8.RAINSOM	mm	NOAAP
WS_ms_Avg	S8.WS	m/s	Temp_Blue_All
WindDir	S8.WD	deg	Temp_Blue_All
BP_mbar (GROUND)	S8.BP	in	CR3000 Outside Load Cells
3inVWC	S8.VWC3	m <sup>3</sup> /m <sup>3</sup>	TDR
Soil T	S8.SOILT3	degC	TDR
6inVW_2	S8.SOILT6	m <sup>3</sup> /m <sup>3</sup>	TDR
E1T1_COR_Avg	S6.E1	DegC	Temp_Blue_All
E1T2_COR_Avg	S6.E2	DegC	Temp_Blue_All
E1T3_COR_Avg	S6.E3	DegC	Temp_Blue_All
E1T4_COR_Avg	S6.E4	DegC	Temp_Blue_All

## Data Derived from Outside Sources

Although this project had several components of a local weather station, some additional information regarding the climatological information was required. The missing data was derived from government sponsored climatological databases. Based on the local availability, data was derived from the NCDC Quality Controlled Local Climatological Data. Each source provided slightly different datasets. Table 30 shows the information source, the location it was derived from, and the data that was provided by the dataset for each of the three locations.

## Sky Condition Data

Table 63: Sources of climatological data derived for regional locations Near the test site

Source	Location	Data Provided
NCDC Quality Controlled Local Climatological Data	Newark: Newark International Airport	Precipitation Snow/Ice(inches)
NCDC Quality Controlled Local Climatological Data	Somerville: Somerset Airport	Precipitation Snow/Ice(inches)
NCDC Quality Controlled Local Climatological Data	Somerville: Somerset Airport	Sky Conditions

The data that was derived from the NCDC Quality Controlled Local Climatological Data was downloaded from the website:

<http://www.ncdc.noaa.gov/qclcd/QCLCD?prior=N>

The dates that were determined to be sunny, as determined by the NCDC climatological data can be seen in Table 31, where the selected dates are shown in bold.

Table 64: Sky conditions utilized for albedo calculations

Date	Condition	Date	Condition
<b>7/18/2017</b>	<b>Clear</b>	8/5/2017	Cloudy
<b>7/19/2017</b>	<b>Clear</b>	<b>8/6/2017</b>	<b>Clear</b>
<b>7/20/2017</b>	<b>Clear</b>	8/7/2017	Rain
7/21/2017	Cloudy	8/8/2017	Overcast
7/22/2017	Rain	8/9/2017	Cloudy
7/23/2017	Cloudy	<b>8/10/2017</b>	<b>Clear</b>
7/24/2017	Rain	8/11/2017	Cloudy
7/25/2017	Cloudy	8/12/2017	Cloudy
7/26/2017	Cloudy	<b>8/13/2017</b>	<b>Clear</b>
7/27/2017	Cloudy	8/14/2017	Partly Cloudy

7/28/2017	Cloudy	8/15/2017	Cloudy
7/29/2017	Cloudy	8/16/2017	Partly Cloudy
<b>7/30/2017</b>	<b>Clear</b>	<b>8/17/2017</b>	<b>Clear</b>
<b>7/31/2017</b>	<b>Clear</b>	8/18/2017	Cloudy
<b>8/1/2017</b>	<b>Clear</b>	8/19/2017	Partly Cloudy
8/2/2017	Rain	<b>8/20/2017</b>	<b>Clear</b>
<b>8/3/2017</b>	<b>Clear</b>	8/21/2017	Partly Cloudy
8/4/2017	Cloudy	8/22/2017	Cloudy

## Zenith Data

One component of calculating albedo measurements requires the input of the zenith angle of the sun, which should be a minimum of 45 degrees from the highest elevation the sun will attain that day (5). The azimuth angle plays a less important role in the calculation, but is important when obstructions shade different test samples at different times throughout an annual period. The zenith and azimuth data was collected from solar topo online from the website:

<http://solartopo.com/solar-orbit.htm>

The zenith angle is important to normalize for measurements of albedo to ensure the incident angle of incoming solar radiation is reflecting in a similar manner across all test samples throughout time. It is also increasingly important in the space where this project was conducted, because of the close proximity of the buildings. A plot of the source zenith angles utilized for calculating albedo for this experiment is shown in Figure 62 below. Anecdotal evidence provided by the authors support the variation in the effect of the zenith and azimuth angles, where the sample sunrise, where the sunlight began to touch the samples, was approximately 6:30 AM in July. The sample sunset, or time at which the sunlight faded from direct contact with the samples was more angular and would begin with sample 4, then progress to 3 and finally 2. The sample sunset in July the sample sunset was close to 6 PM.

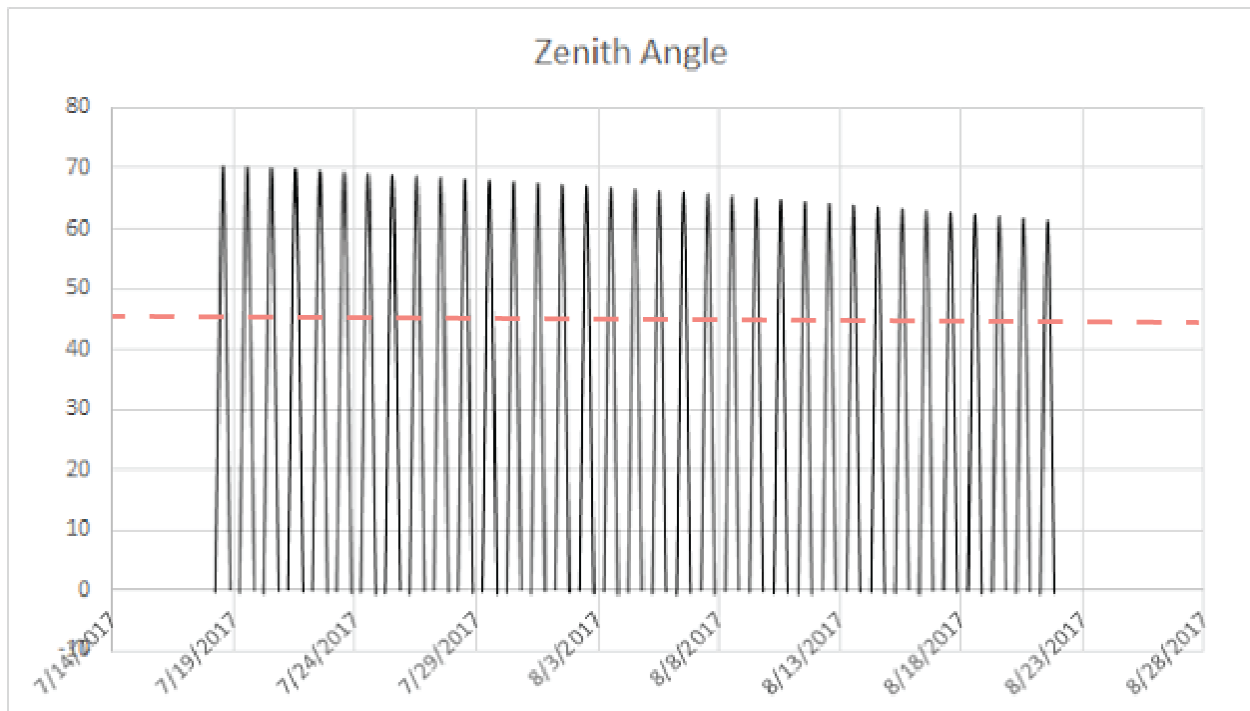


Figure 200: Zenith Angles used for Albedo Calculations

## Initial Data

### Net Radiometers

Figure 63 depicts the radiometer readings for July 20, 2017 through July 22, 2017. According to the NCDC, these days include a sunny day, a cloudy day, and a rainy day, respectively. The figure depicts the shortwave up, shortwave down, longwave up, longwave down, and net radiation readings.

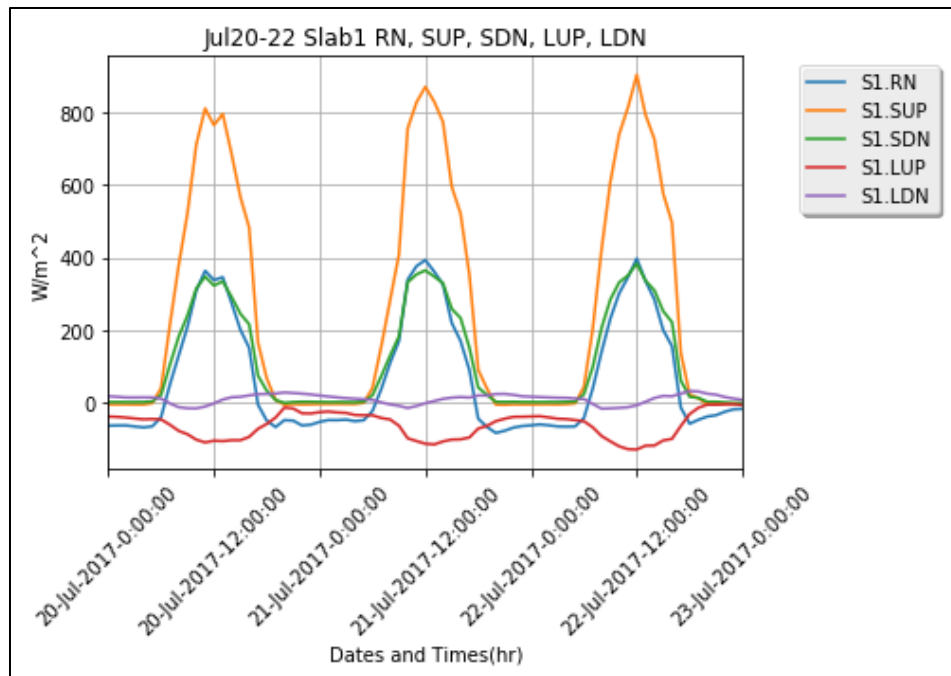


Figure 201: Radiation for July 20 - July 22, 2017 at Slab 1

Figure 64 depicts the radiometer readings for July 20, 2017 at slab 1. According to the NCDC, this was a sunny day. The figure depicts the shortwave up, shortwave down, longwave up, longwave down, and net radiation readings.

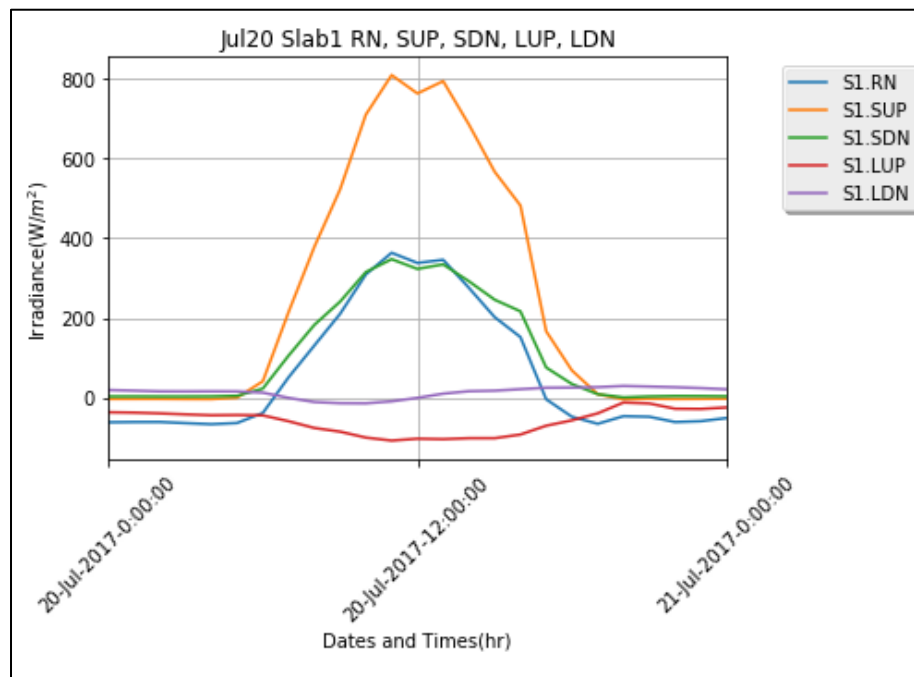


Figure 202: Radiation for July 20, 2017 at Slab 1

Figure 65 depicts the net radiometer readings for July 20, 2017 through July 22, 2017. According to the NCDC, these days include a sunny day, a cloudy day, and a rainy day, respectively.

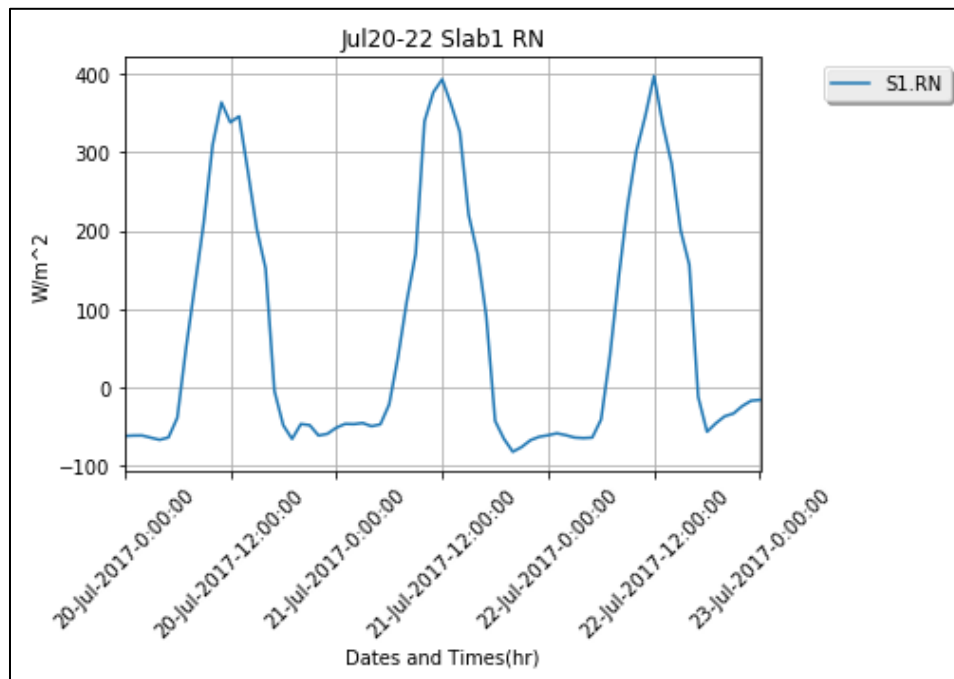


Figure 203: Net Radiation for July 20 - July 22, 2017 at Slab 1

Figure 66 depicts the net radiometer readings for July 20, 2017 through July 22, 2017 at Slabs 1, 3, 4, 6, and 8. According to the NCDC, these days include a sunny day, a cloudy day, and a rainy day, respectively. Note that Slab 1, which was constructed on conventional concrete evidenced the lowest net radiation, while Slab 6 and Slab 8 evidenced significantly higher net radiation.

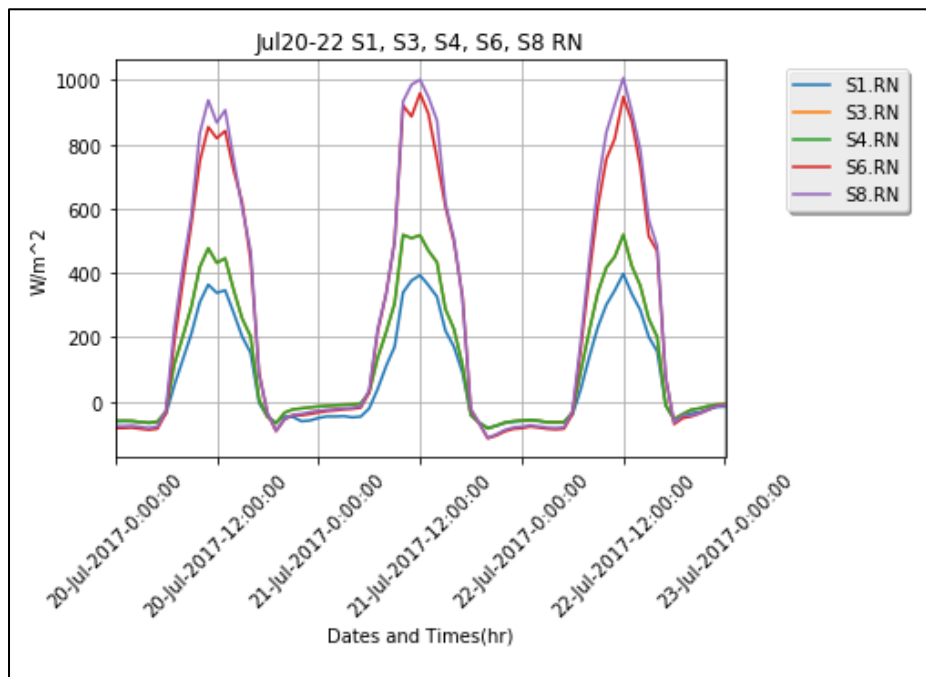


Figure 204: Net Radiation for July 20 - July 22, 2017 at Slabs 1, 3, 4, 6, & 8



Figure 67 depicts the net radiometer readings for July 20, 2017 through July 22, 2017 at Slabs 1, 3, 4, 6, and 8. According to the NCDC, these days include a sunny day, a cloudy day, and a rainy day, respectively. Rain bucket readings were added to the right axis.

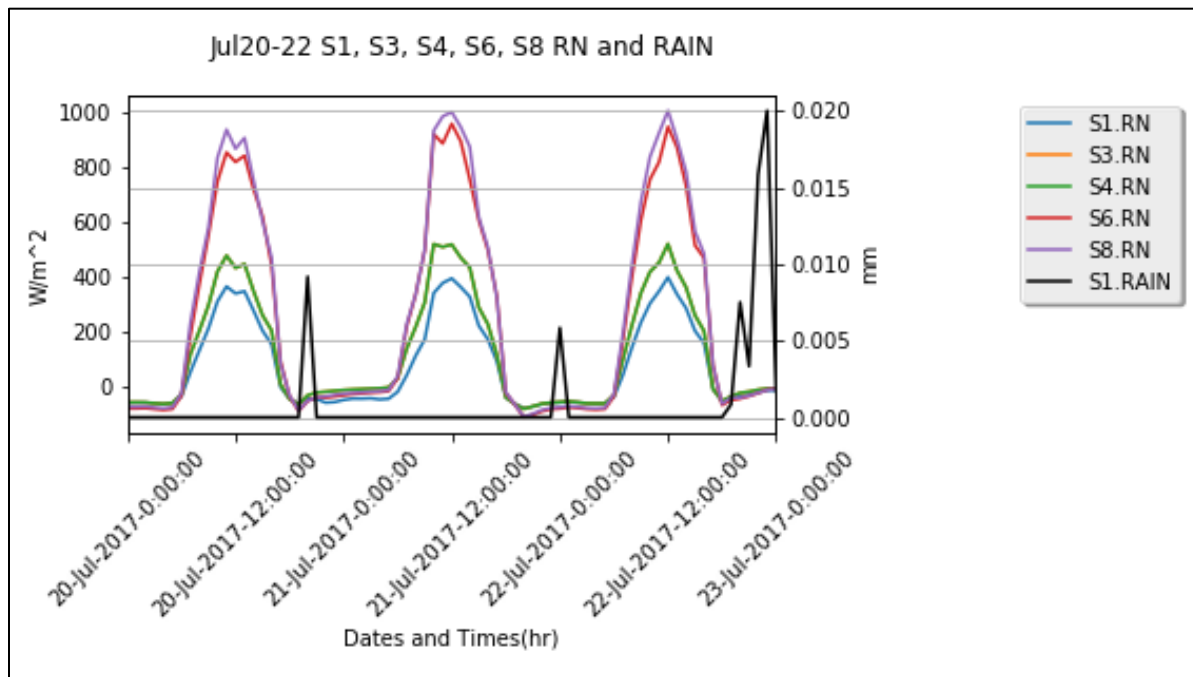


Figure 205: Net Radiation for July 20 - July 22, 2017 at Slabs 1, 3, 4, 6, & 8 with Rain Bucket Readings on the Right Axis

## Thermocouples

Figure 68 displays the internal slab temperatures of probe that were inserted at a depth of 0.5 inches from the slab surface. Note that Slab 4 underwent the greatest change in internal temperature. Also, our control slabs, Slab 1 and Slab 2 underwent the least change in internal temperature. Also, from Figure 66, Slabs 1 and 2 warmed and cool slower than the porous slabs.

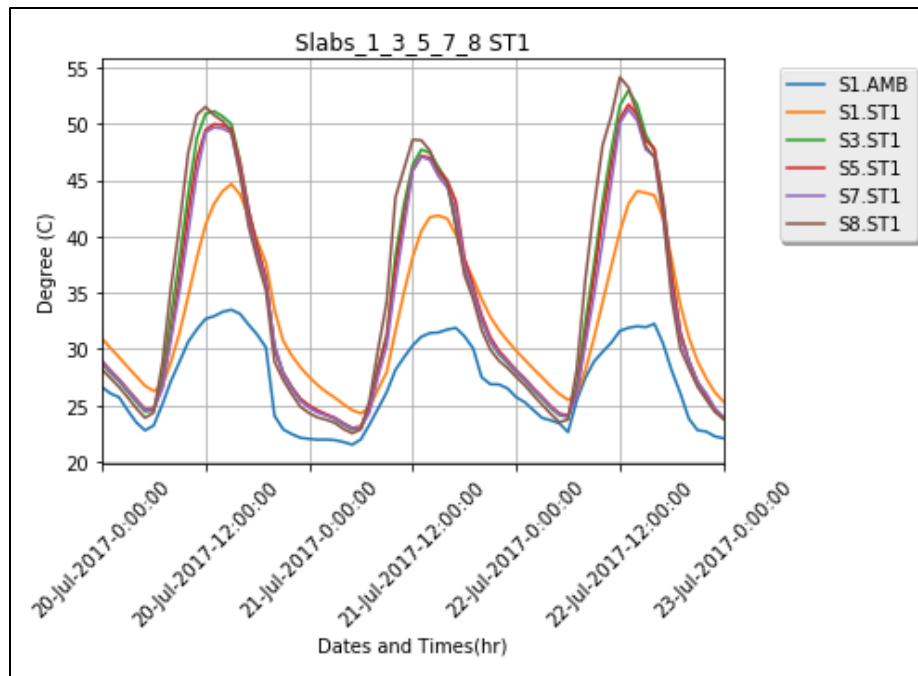


Figure 206: Internal Slab Temperatures at 0.5 inches of embedment

Figure 69 displays the internal slab temperatures of probe that were inserted at a depth of 0.5 inches from the slab surface on July 20, 2017. According to the NCDC, this was a sunny day.

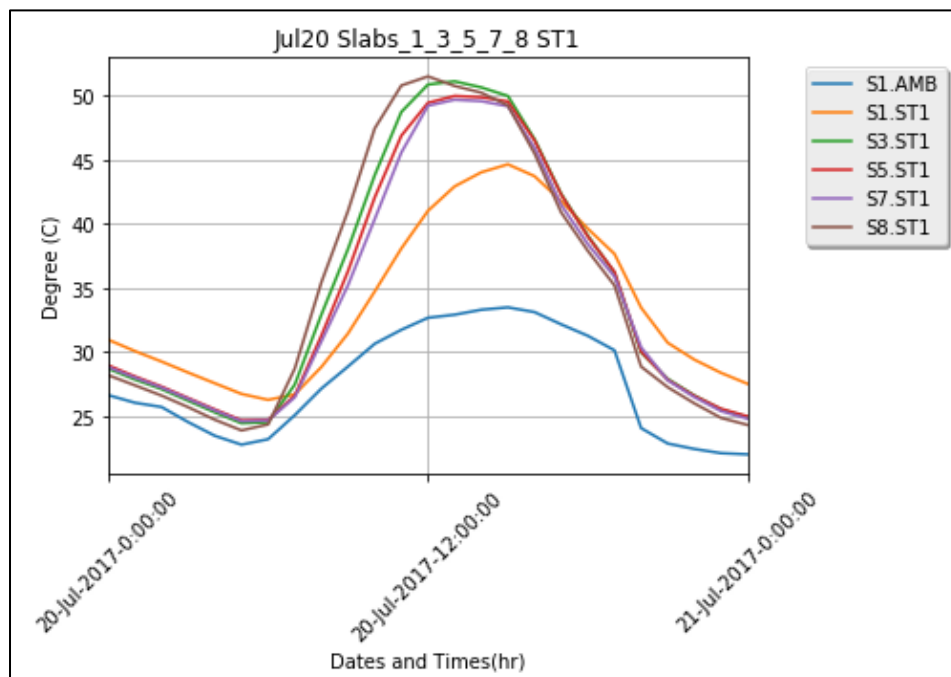


Figure 207: Internal Slab Temperatures at 0.5 inches of embedment on July 20, 2017

Figure 70 displays the internal slab temperatures of probe that were inserted at a depth of 0.5 inches from the slab surface on July 21, 2017. According to the NCDC, this was a cloudy day.

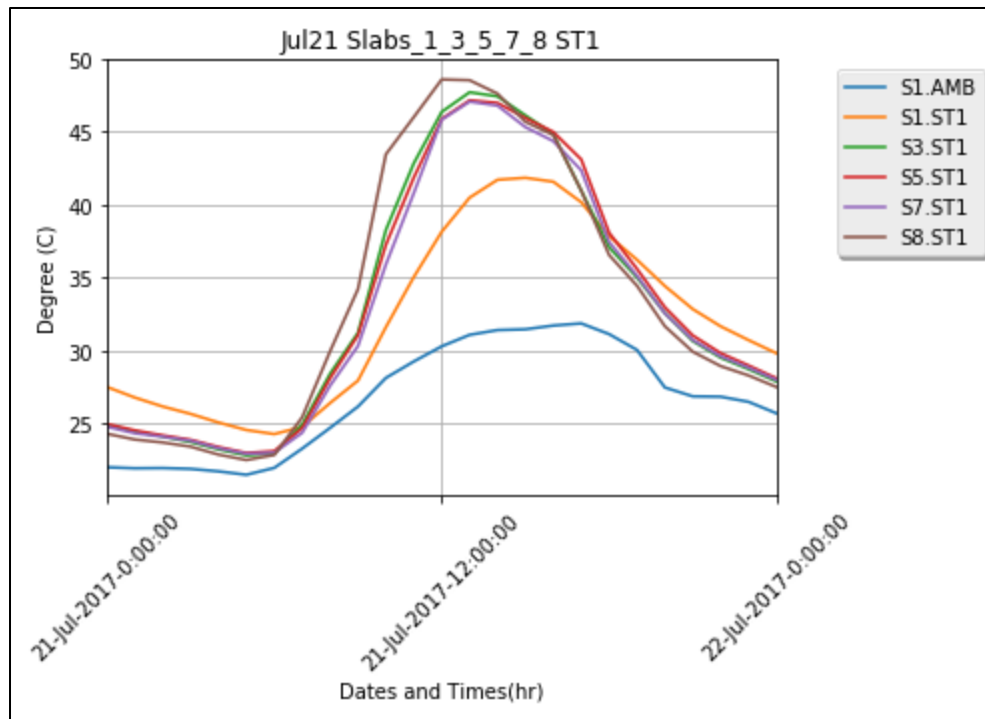


Figure 208: Internal Slab Temperatures at 0.5 inches of embedment on July 21, 2017

Figure 71 displays the internal slab temperatures of probe that were inserted at a depth of 0.5 inches from the slab surface on July 22, 2017. According to the NCDC, this was a rainy day.

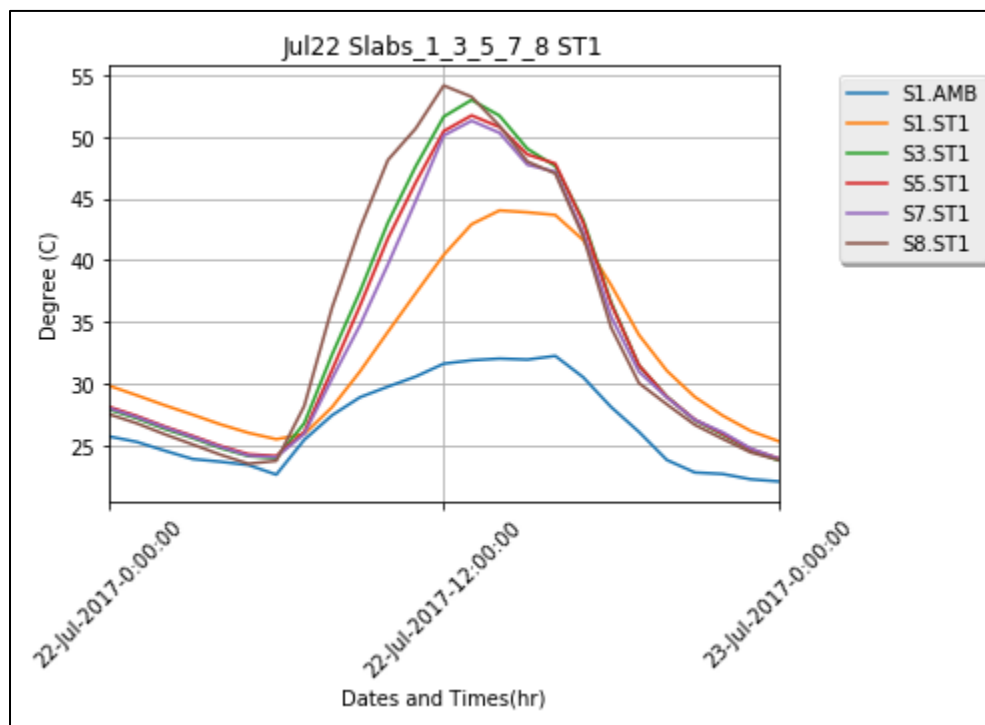


Figure 209: Internal Slab Temperatures at 0.5 inches of embedment on July 22, 2017

Figure 72 displays the under slab temperature of a probe that were positioned at a depth of 4 inches from the surface of Slab 3 on July 20, 2017. According to the NCDC, this was a sunny day. Note that the under slab temperature was greater than the ambient temperature and that the temperature fluctuations lagged of the under slab probe lagged behind the ambient temperature changes.

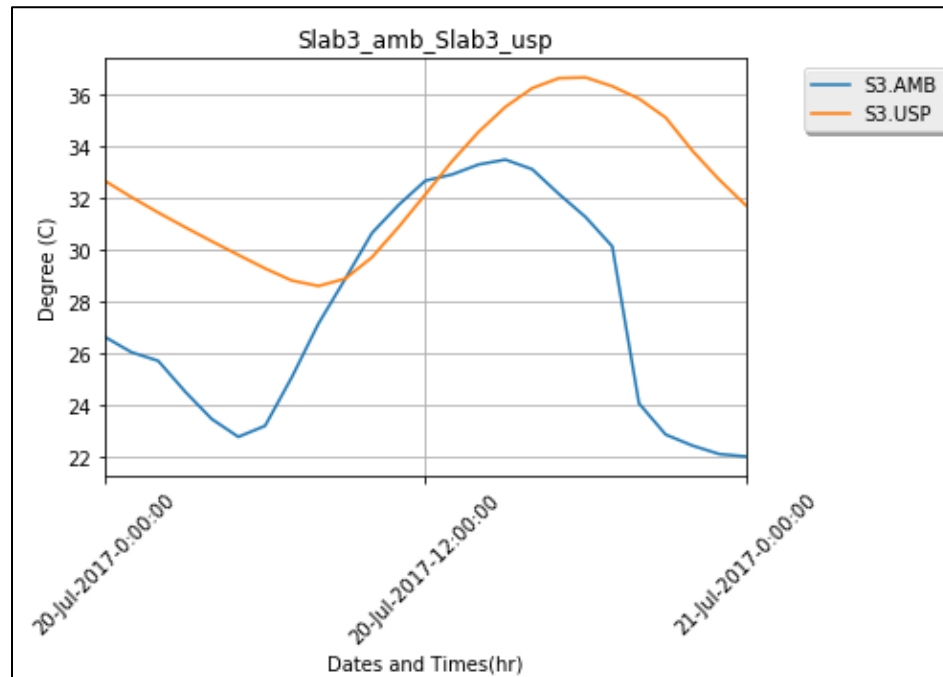


Figure 210: Under Slab Temperature at 4 inches Below Slab 3 on July 20, 2017

## Type E

Figure 73 depicts the temperature at elevations near the slab surface for July 20, 2017 through July 22, 2017. According to the NCDC, these days include a sunny day, a cloudy day, and a rainy day, respectively. The Type E thermocouple temperature readings were taken at a height of 25 cm, 13 cm, 6 cm, and 1 cm above Slab 4. Note that the temperature fluctuations became greater, the closer the probe was placed to the slab surface. This effect may be due to the influence of the slab on the sensible heat at elevations near the surface of the slab.

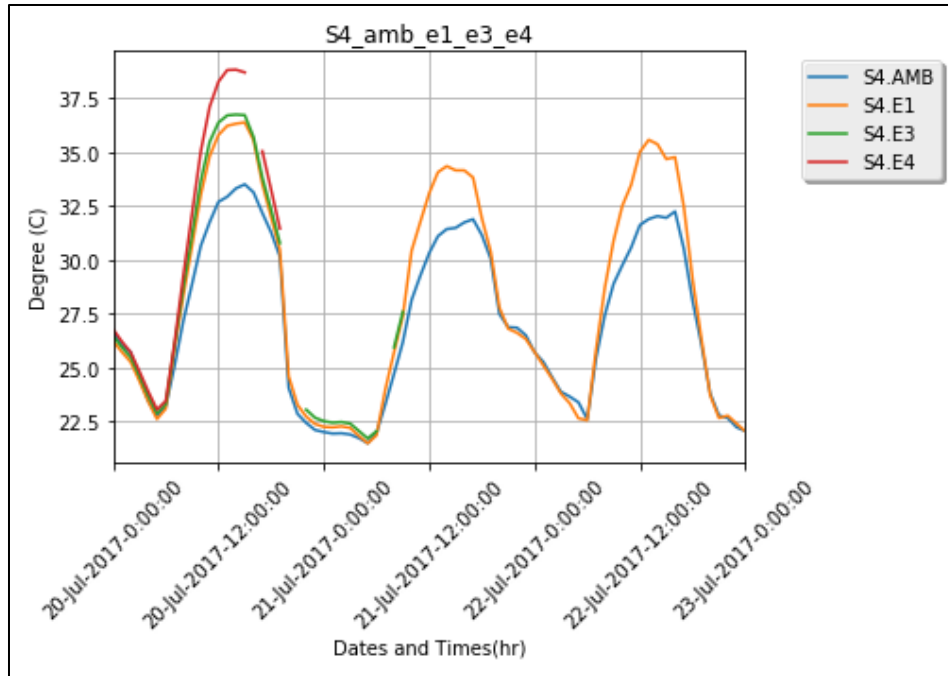


Figure 211: Type E Temperatures at heights 25 cm, 13 cm, 6 cm, and 1 cm above Slab 4

Figure 74 depicts the temperature at a elevations near the surface of Slab 4 for July 20, 2017. According to the NCDC, this was a sunny day. The Type E thermocouple temperature readings were taken at a height of 25 cm, 13 cm, 6 cm, and 1 cm above Slab 4. Note that the temperature fluctuations became greater, the closer the probe was placed to the slab surface. This effect may be due to the influence of the slab on the sensible heat at elevations near the surface of the slab.

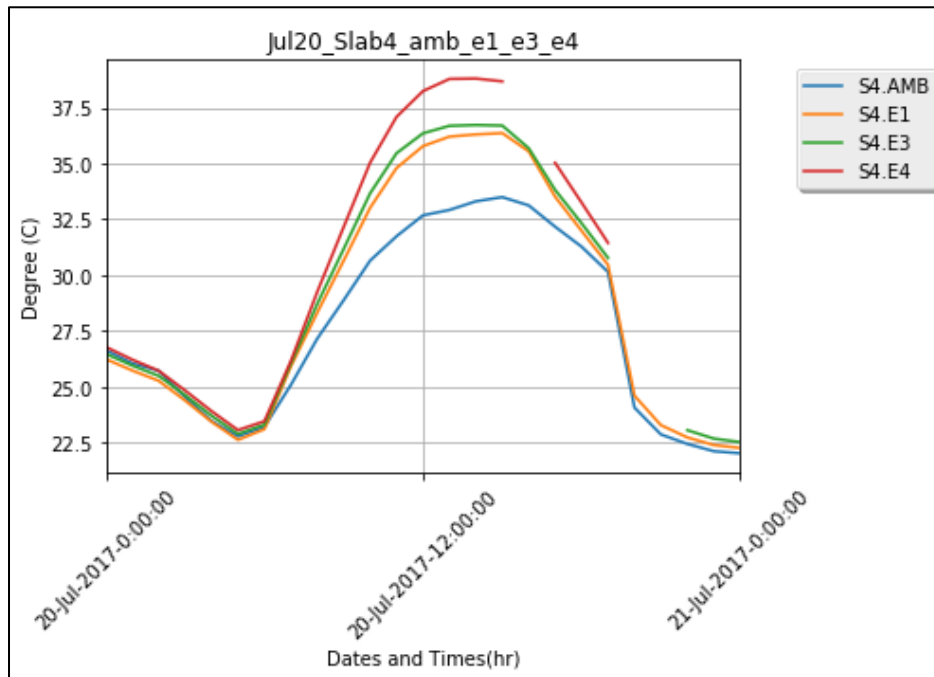


Figure 212: Type E Temperatures at heights 25 cm, 13 cm, 6 cm, and 1 cm above Slab 4 on July 20, 2017

Figure 75 depicts the ambient temperature readings as well as the temperature at a elevation near the slab surface for July 20, 2017 through July 22, 2017. According to the NCDC, these days include a sunny day, a cloudy day, and a rainy day, respectively. The ambient temperature was taken from a height of 2 meters above Slab 1 and the Type E thermocouple temperature reading was taken at a height of 25 cm above Slab 4. Note that the Type E probe underwent greater temperature fluctuations than the ambient temperature. This effect may be due to the influence of the slab on the sensible heat at elevations near the surface of the slab.

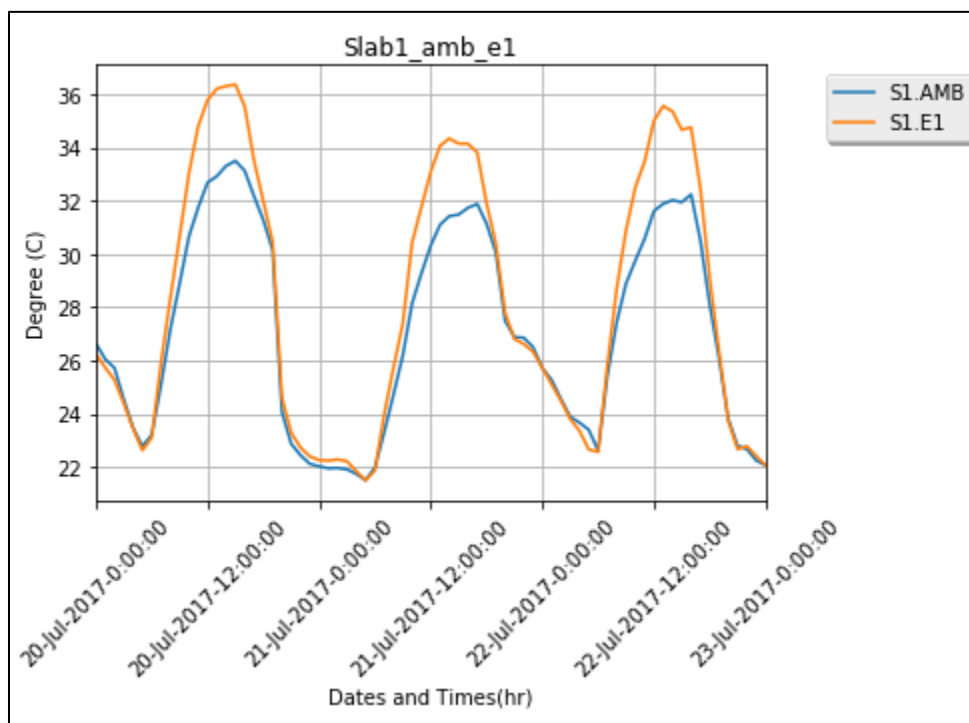


Figure 213: Ambient and Type E Temperatures at a height of 2 m and 25 cm above Slab 1 and Slab 4, respectively

Figure 75 depicts the ambient temperature at 2 m, the temperature at 25 cm above the slab surface, the temperature beneath the slab, and the soil temperature for July 20, 2017 through July 22, 2017. Rain bucket data is also displayed on the right axis. According to the NCDC, these days include a sunny day, a cloudy day, and a rainy day, respectively. The ambient temperature was taken from a height of 2 meters above Slab 1 and the Type E thermocouple temperature reading was taken at a height of 25 cm above Slab 4. The temperature under the slab was taken at 4 inches below the surface and the soil temperature was taken at a depth of 3 inches below the surface.

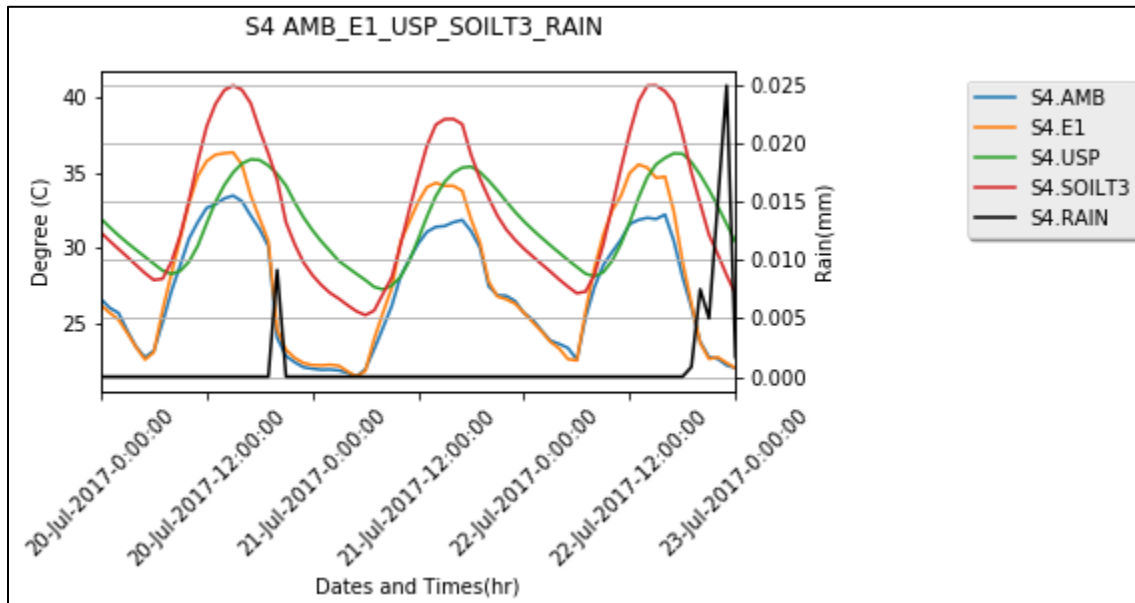


Figure 214: Ambient Temperature at 2 m above Slab 1, Type E Temperature at 25 cm above Slab 4, Under Slab Temperature at 4" below Slab 4, and Soil T at a depth of 3" with Rain Bucket Data on the Right Axis

## Type K

Figure 77 depicts the internal temperature readings for July 20, 2017 through July 22, 2017 at Slab 1. According to the NCDC, these days include a sunny day, a cloudy day, and a rainy day, respectively. Internal temperature readings were taken at slab depth of 0.5, 1, 2, and 3 inches, which corresponds with ST1, ST2, ST3, and ST4, respectively. A temperature reading from beneath the slab was taken at a depth of 4 inches and is depicted on the figure as USP. The ambient air temperature is also displayed on the graph as AMB.



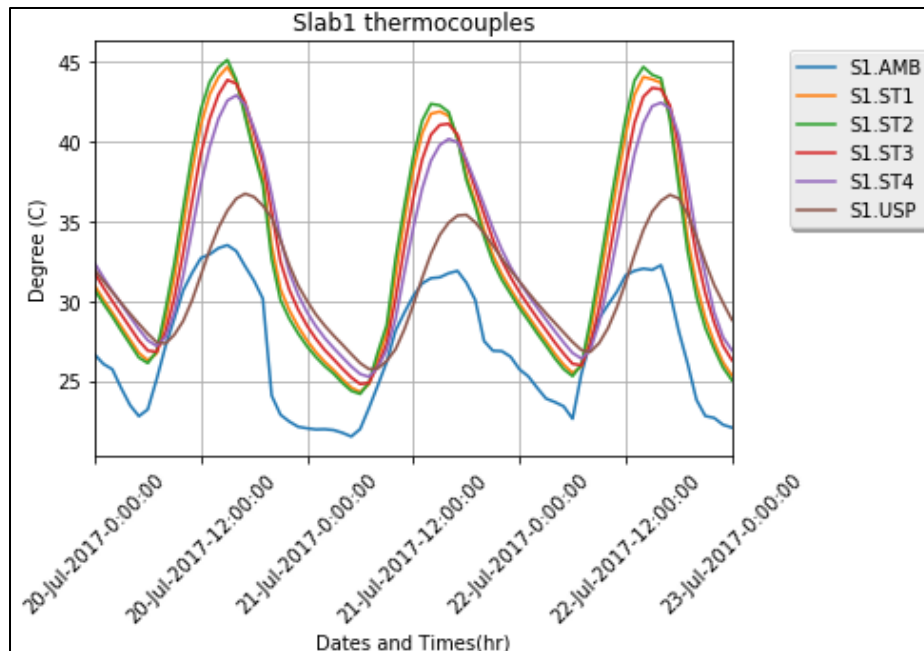


Figure 215: Slab 1 Internal, Under Slab, and Ambient Temperature Readings

Figure 78 depicts the internal temperature readings for July 20, 2017 through July 22, 2017 at Slab 2. According to the NCDC, these days include a sunny day, a cloudy day, and a rainy day, respectively. Internal temperature readings were taken at slab depth of 0.5, 1, 2, and 3 inches, which corresponds with ST1, ST2, ST3, and ST4, respectively. A temperature reading from beneath the slab was taken at a depth of 4 inches and is depicted on the figure as USP. The ambient air temperature is also displayed on the graph as AMB.

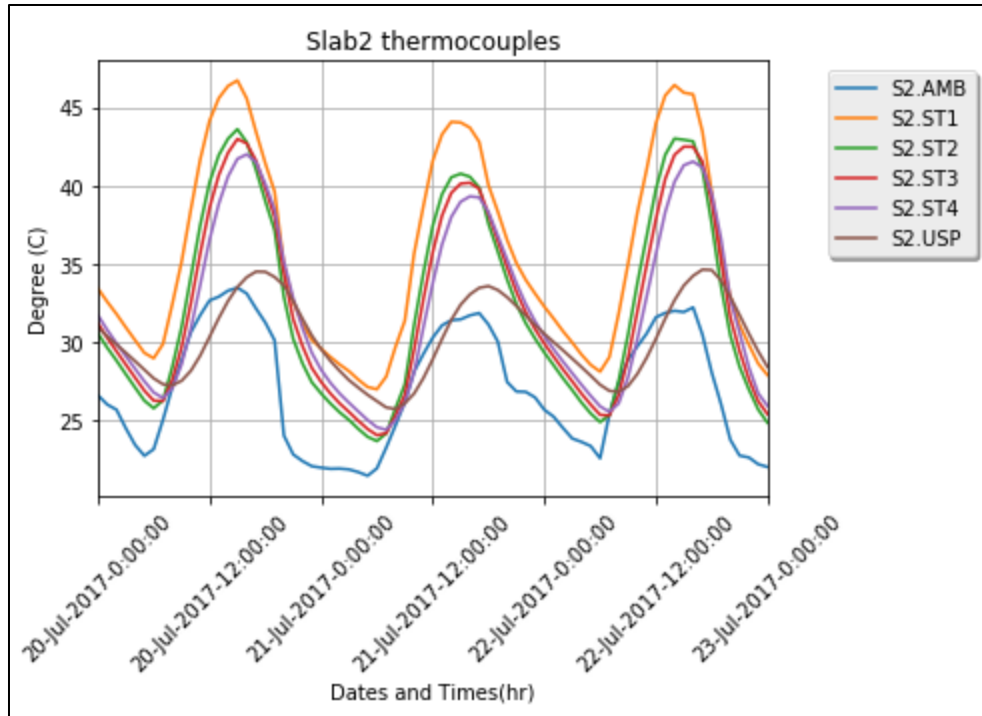


Figure 216: Slab 2 Internal, Under Slab, and Ambient Temperature Readings

Figure 79 depicts the internal temperature readings for July 20, 2017 through July 22, 2017 at Slab 3. According to the NCDC, these days include a sunny day, a cloudy day, and a rainy day, respectively. Internal temperature readings were taken at slab depth of 0.5, 1, 2, and 3 inches, which corresponds with ST1, ST2, ST3, and ST4, respectively. A temperature reading from beneath the slab was taken at a depth of 4 inches and is depicted on the figure as USP. The ambient air temperature is also displayed on the graph as AMB.

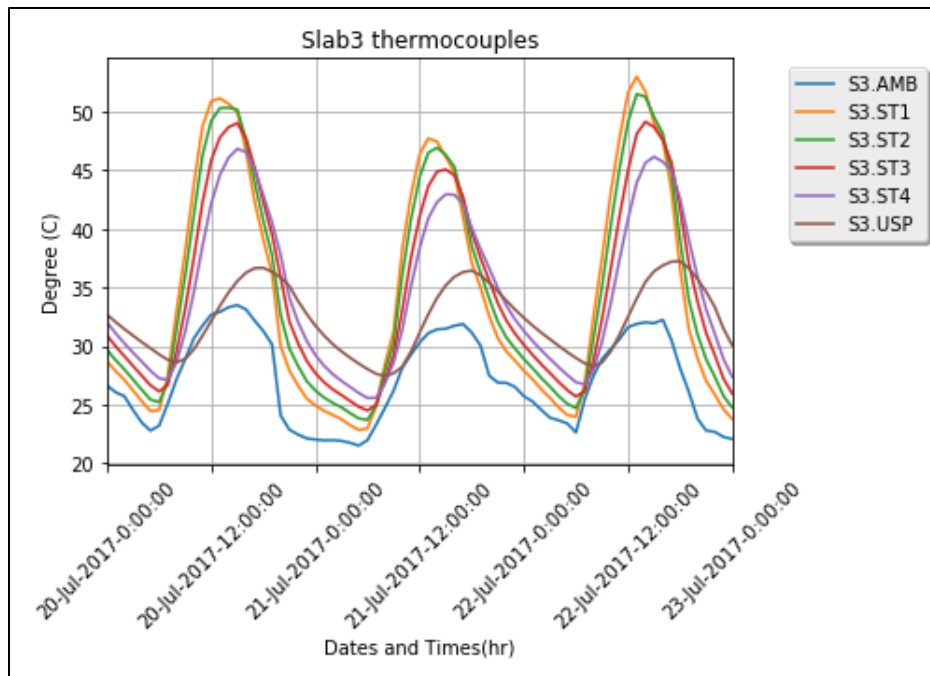


Figure 217: Slab 3 Internal, Under Slab, and Ambient Temperature Readings

Figure 80 depicts the internal temperature readings for July 20, 2017 through July 22, 2017 at Slab 4. According to the NCDC, these days include a sunny day, a cloudy day, and a rainy day, respectively. Internal temperature readings were taken at slab depth of 0.5, 1, 2, and 3 inches, which corresponds with ST1, ST2, ST3, and ST4, respectively. A temperature reading from beneath the slab was taken at a depth of 4 inches and is depicted on the figure as USP. The ambient air temperature is also displayed on the graph as AMB.

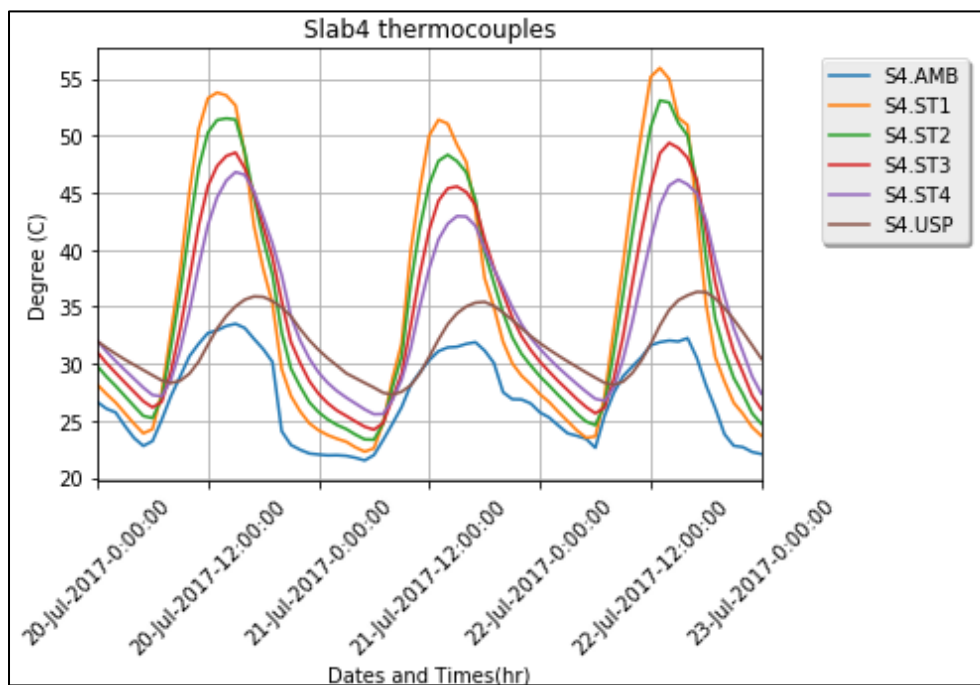


Figure 218: Slab 4 Internal, Under Slab, and Ambient Temperature Readings

Figure 81 depicts the internal temperature readings for July 20, 2017 through July 22, 2017 at Slab 5. According to the NCDC, these days include a sunny day, a cloudy day, and a rainy day, respectively. Internal temperature readings were taken at slab depth of 0.5, 1, 2, and 3 inches, which corresponds with ST1, ST2, ST3, and ST4, respectively. A temperature reading from beneath the slab was taken at a depth of 4 inches and is depicted on the figure as USP. The ambient air temperature is also displayed on the graph as AMB.

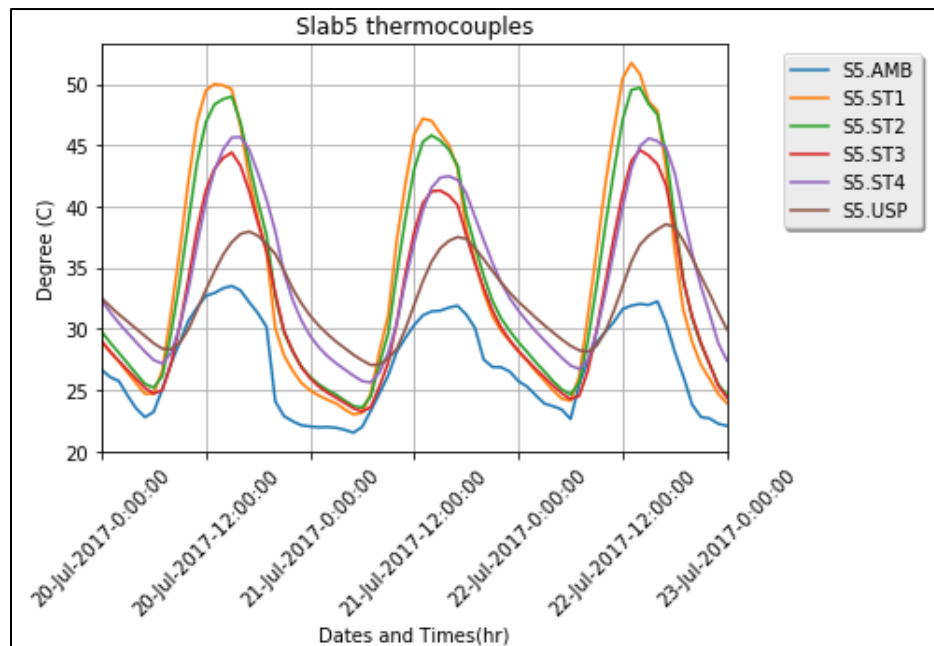


Figure 219: Slab 5 Internal, Under Slab, and Ambient Temperature Readings

Figure 82 depicts the internal temperature readings for July 20, 2017 through July 22, 2017 at Slab 6. According to the NCDC, these days include a sunny day, a cloudy day, and a rainy day, respectively. Internal temperature readings were taken at slab depth of 0.5, 1, 2, and 3 inches, which corresponds with ST1, ST2, ST3, and ST4, respectively. A temperature reading from beneath the slab was taken at a depth of 4 inches and is depicted on the figure as USP. The ambient air temperature is also displayed on the graph as AMB.

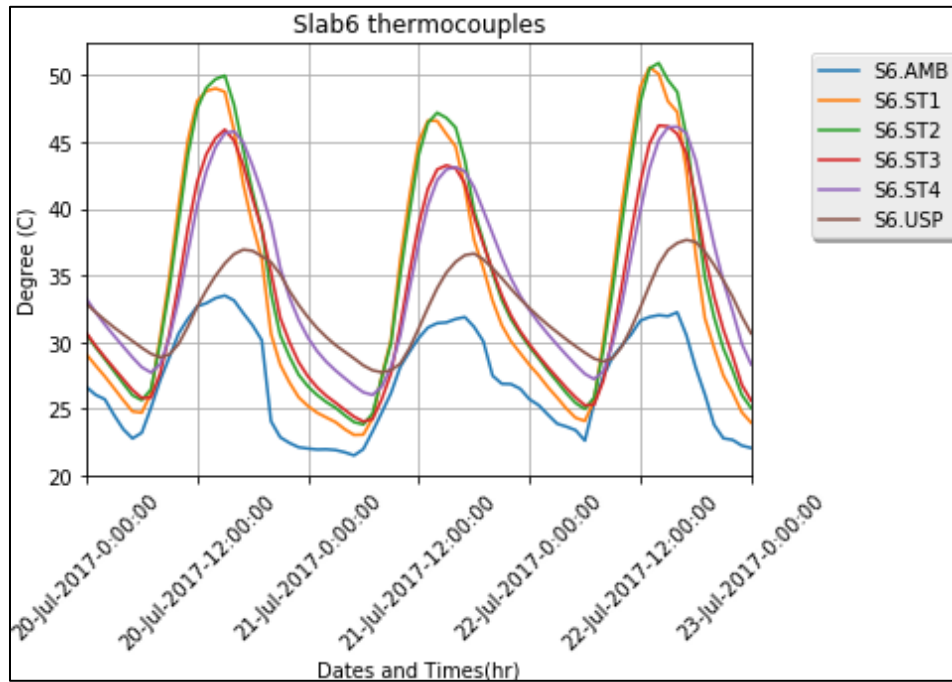


Figure 220: Slab 6 Internal, Under Slab, and Ambient Temperature Readings

Figure 83 depicts the internal temperature readings for July 20, 2017 through July 22, 2017 at Slab 7. According to the NCDC, these days include a sunny day, a cloudy day, and a rainy day, respectively. Internal temperature readings were taken at slab depth of 0.5, 1, 2, and 3 inches, which corresponds with ST1, ST2, ST3, and ST4, respectively. A temperature reading from beneath the slab was taken at a depth of 4 inches and is depicted on the figure as USP. The ambient air temperature is also displayed on the graph as AMB.

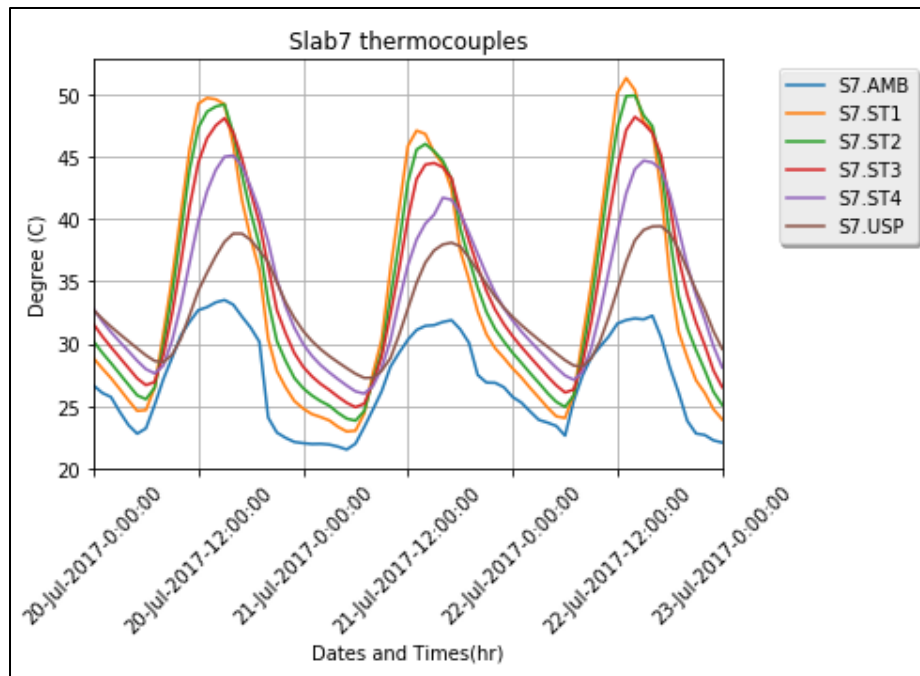


Figure 221: Slab 7 Internal, Under Slab, and Ambient Temperature Readings

Figure 84 depicts the internal temperature readings for July 20, 2017 through July 22, 2017 at Slab 8. According to the NCDC, these days include a sunny day, a cloudy day, and a rainy day, respectively. Internal temperature readings were taken at slab depth of 0.5, 1, 2, and 3 inches, which corresponds with ST1, ST2, ST3, and ST4, respectively. A temperature reading from beneath the slab was taken at a depth of 4 inches and is depicted on the figure as USP. The ambient air temperature is also displayed on the graph as AMB.

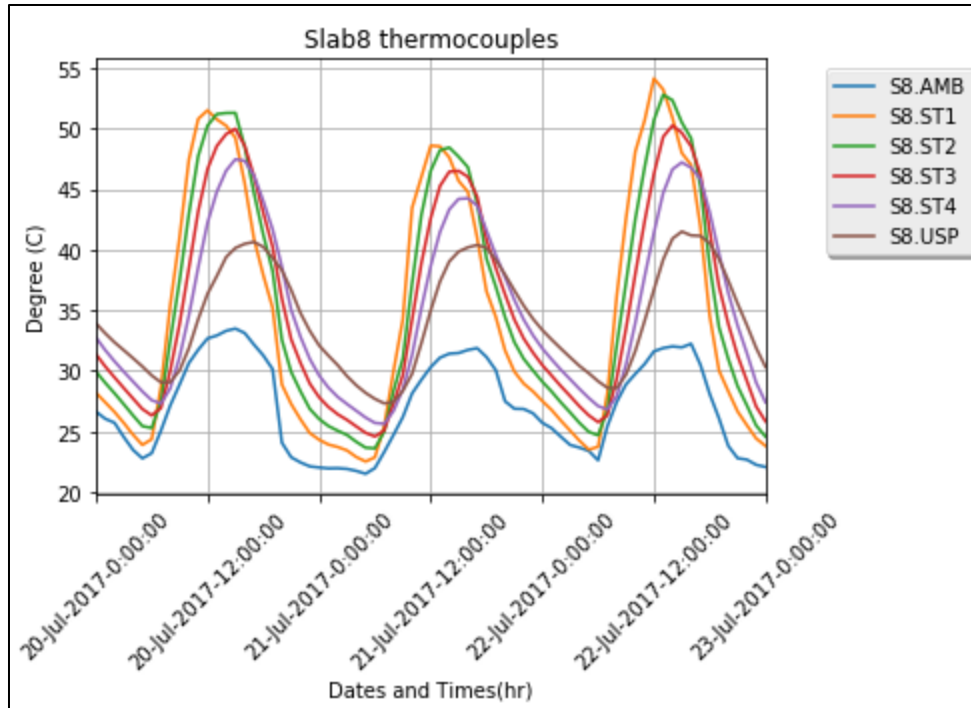


Figure 222: Slab 8 Internal, Under Slab, and Ambient Temperature Readings

## Rain Buckets

Figure 85 depicts the rain bucket readings at the roof weather station for July 20, 2017 through July 22, 2017. According to the NCDC, these days include a sunny day, a cloudy day, and a rainy day, respectively. The rain bucket provides a counter style measurement, so when there is no rain, there is no signal. When there is rain, the counter counts incrementally. The incremental counter is shown below.



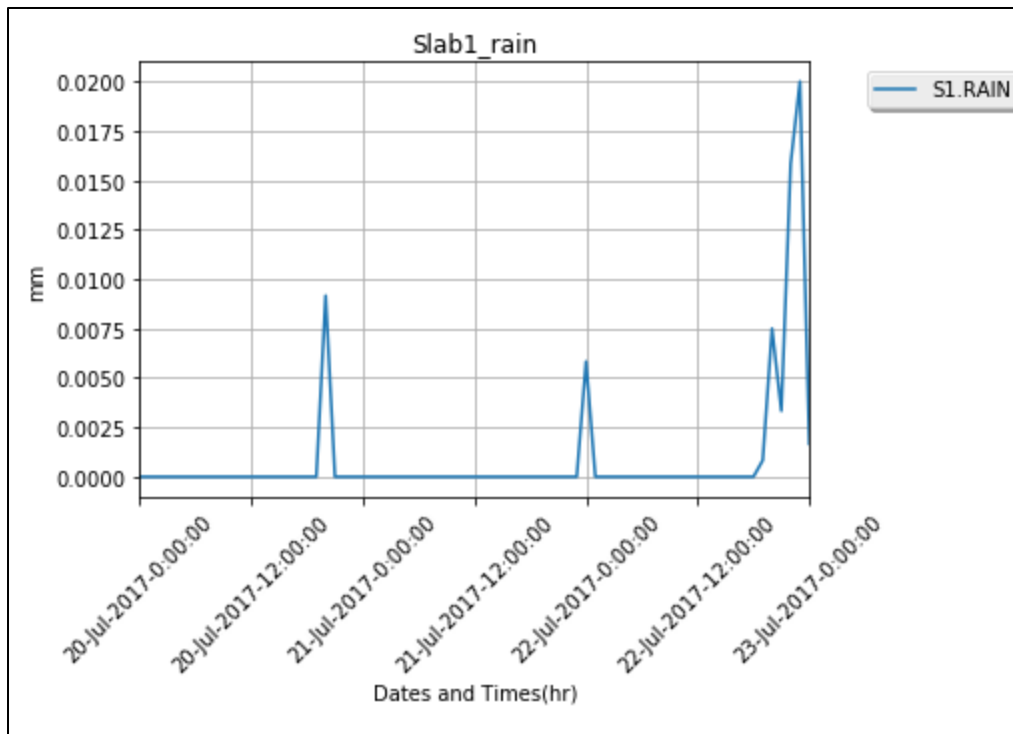


Figure 223: Rain Bucket Readings at the Roof Weather Station

## Barometric Pressure

Figure 86 depicts the barometric pressure readings at the roof weather station for July 20, 2017 through July 22, 2017. According to the NCDC, these days include a sunny day, a cloudy day, and a rainy day, respectively.

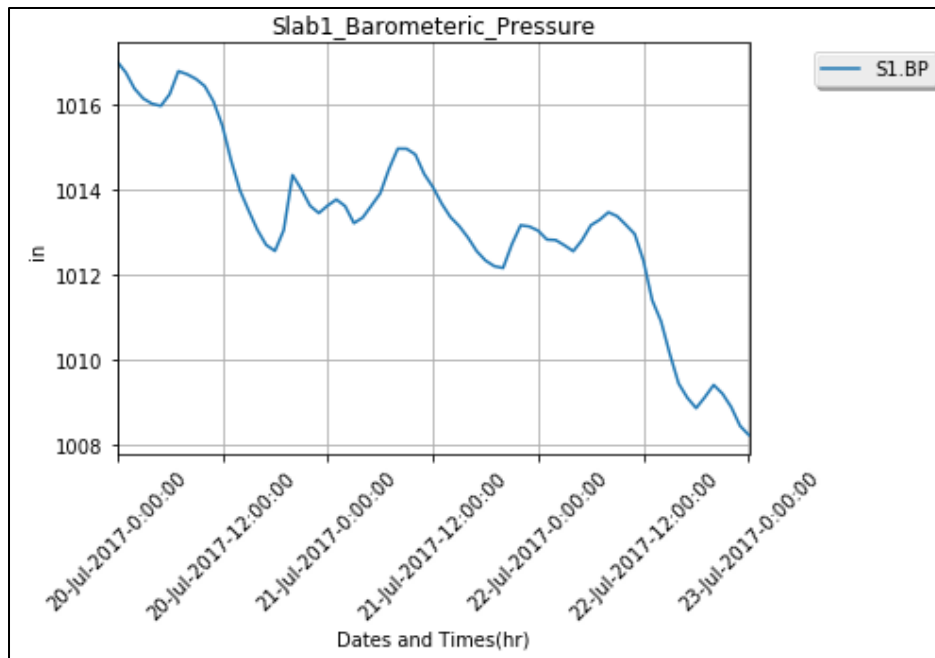


Figure 224: Barometric Pressure Readings at the Roof Weather Station for July 20 - July 22, 2017

## Relative Humidity

Figure 87 depicts the relative humidity readings at the roof weather station for July 20, 2017 through July 22, 2017. According to the NCDC, these days include a sunny day, a cloudy day, and a rainy day, respectively.

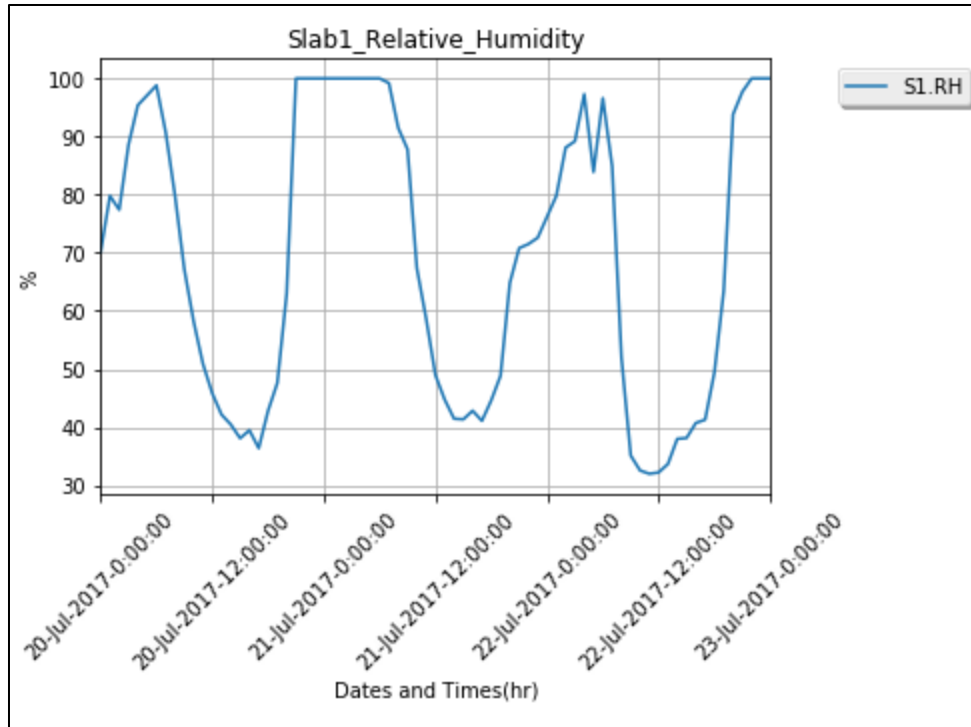


Figure 225: Relative Humidity Readings at the Roof Weather Station for July 20 - July 22, 2017

## Time-Domain Reflectometers

An example of the Time-Domain Reflectometer Data, shown in Figure 88 below, shows the soil volumetric water content shown from 7/20-7/22, which exemplifies a sunny day, a cloudy day, and a rainy day, clearly shows how the moisture content of the soil changed drastically once the rain event occurred.

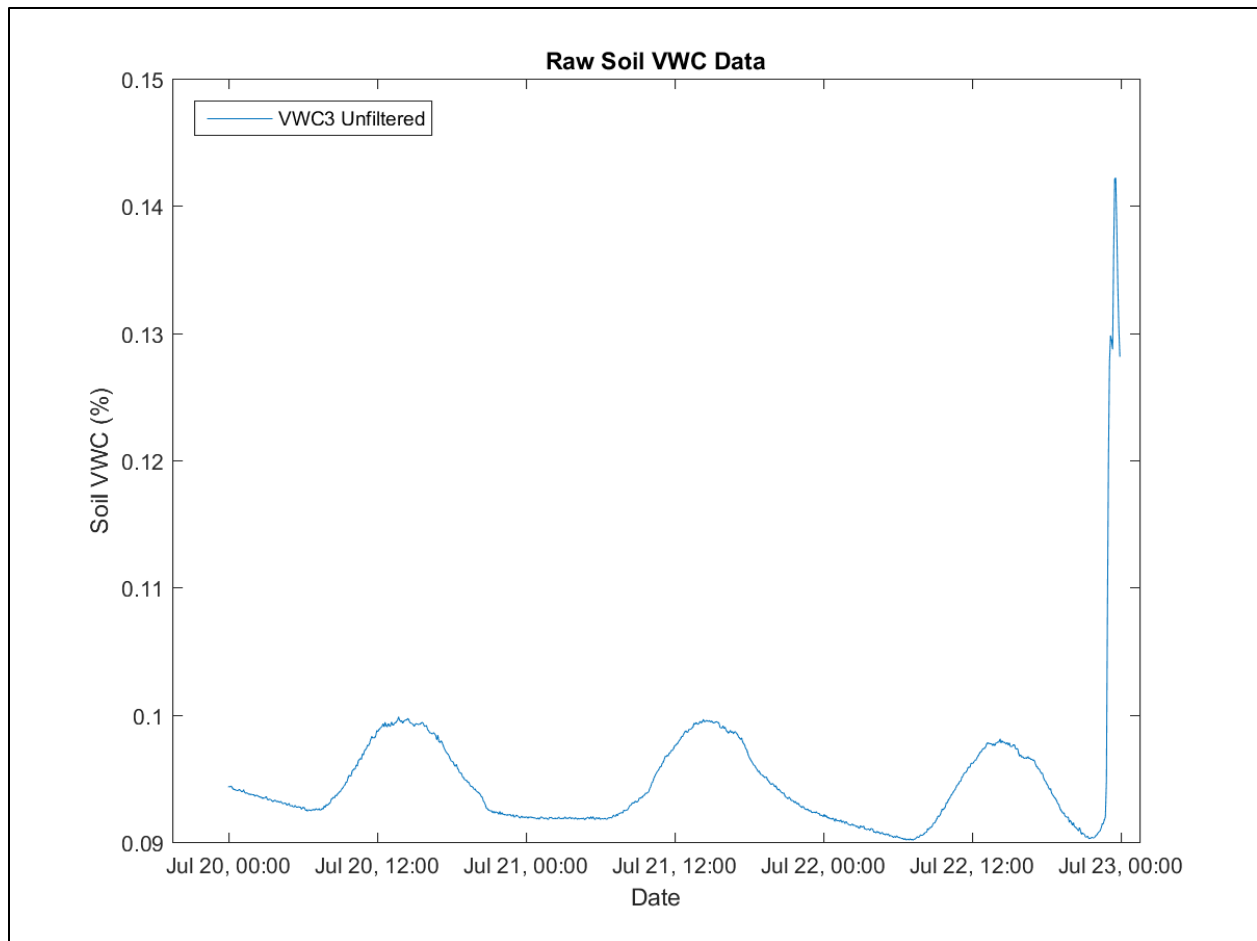


Figure 226: Soil VWC Unfiltered from 7/20-7/22

To filter the time-domain reflectometers for Soil Volumetric water content, first the signals were each taken separately, extended using the signal wavelet transformation (SWT) application in matlab. Since signal denoising was the intended goal, the extension method utilized was a right extension for SWT filtering. The signals were extended to the maximum extension offered, where the original signal length measured 12047 measurements and was extended to 16384 providing 6137 additional points for filtering analysis. Once each filter was sufficiently extended, the SWT denoising portion of the Wavelet application was utilized to transform each signal with a 14 part dB wavelet with 8 level decomposition. The thresholds were determined utilizing a soft medium penalization mode, with the sparsity dropped to the lowest level available for each signal. The thresholds for each filter were determined manually and independently for each load cell signal. Once the thresholds were determined, the filtered signal response was overlaid over the original time-domain reflectometer signal to show the goodness of fit. After the fit was confirmed to be sufficient, the improved filtered signals were cropped by 6137 points from the right to return the signals to original length. The filtered response of TDR 1 compared to the original signal is shown in Figure 89.

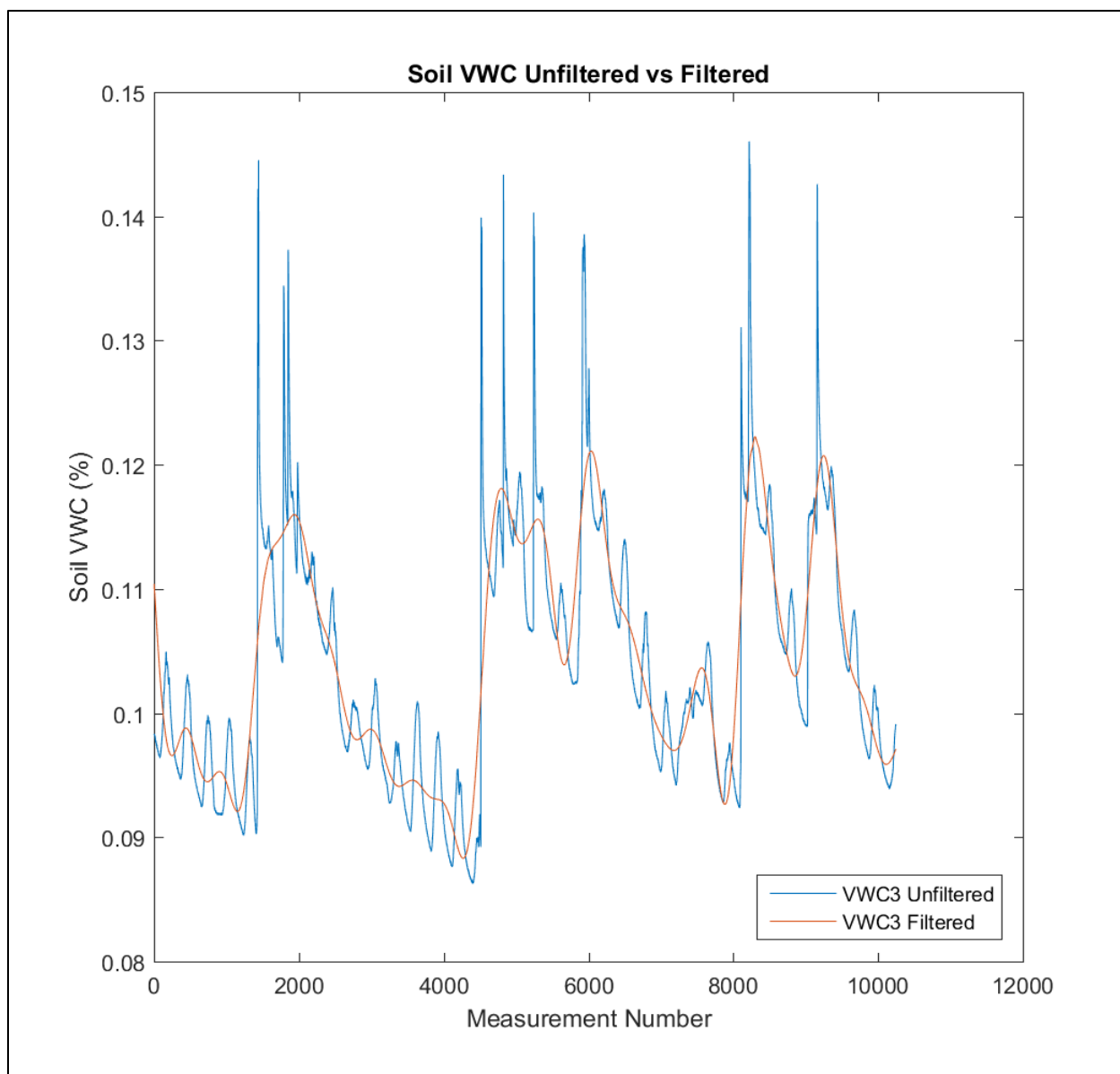


Figure 227: Soil VWC 3" Filtered vs Unfiltered Measurement

The filtered response of TDR 1 compared to the original signal is shown in Figure 90.

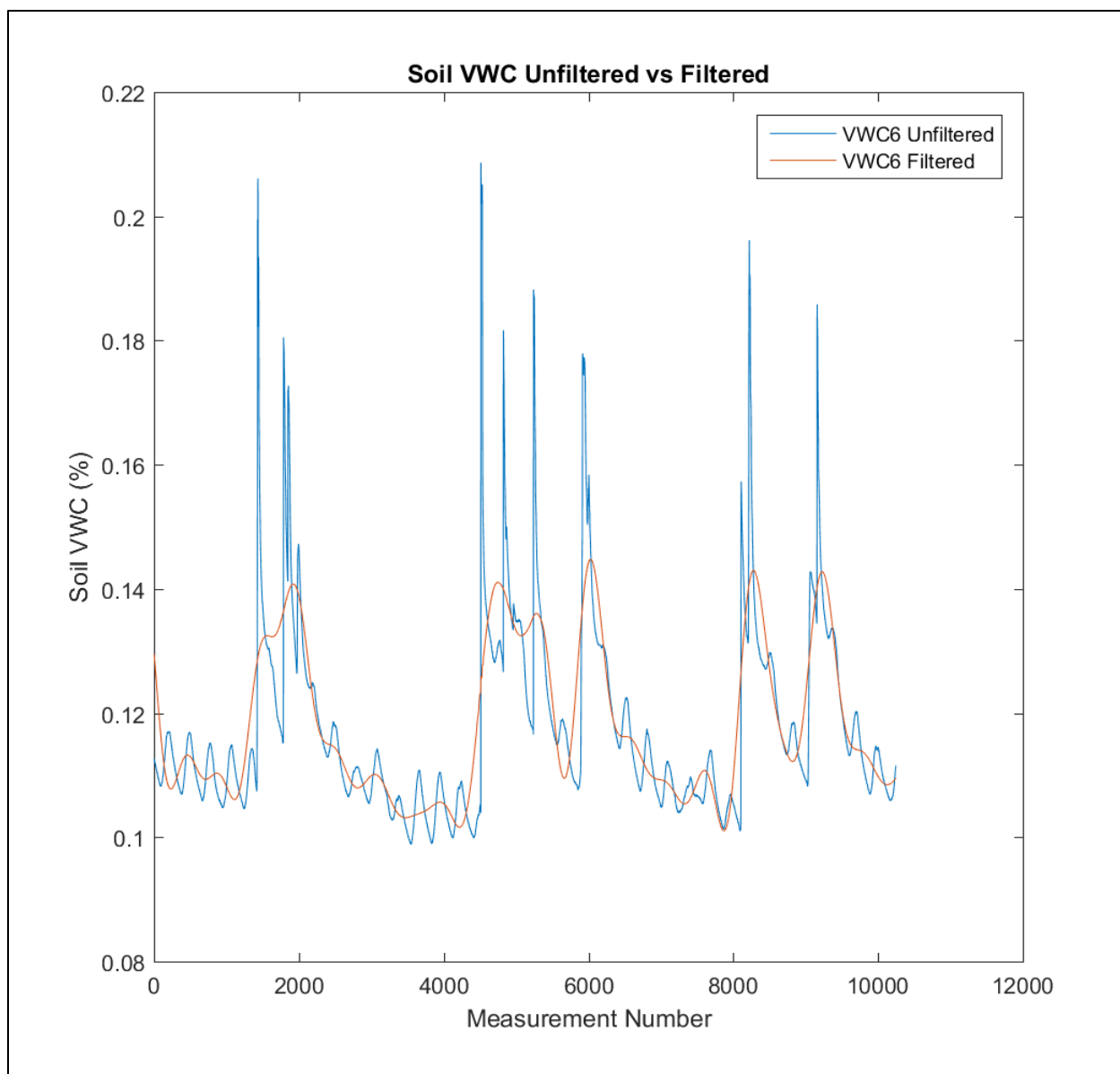


Figure 228: Soil VWC 6" Filtered vs Unfiltered Measurement

The final TDR reported no data for the duration of this measurement period.

Figure 91 displays the soil volumetric water content readings for July 20, 2017 through July 22, 2017. According to the NCDC, these days include a sunny day, a cloudy day, and a rainy day, respectively.

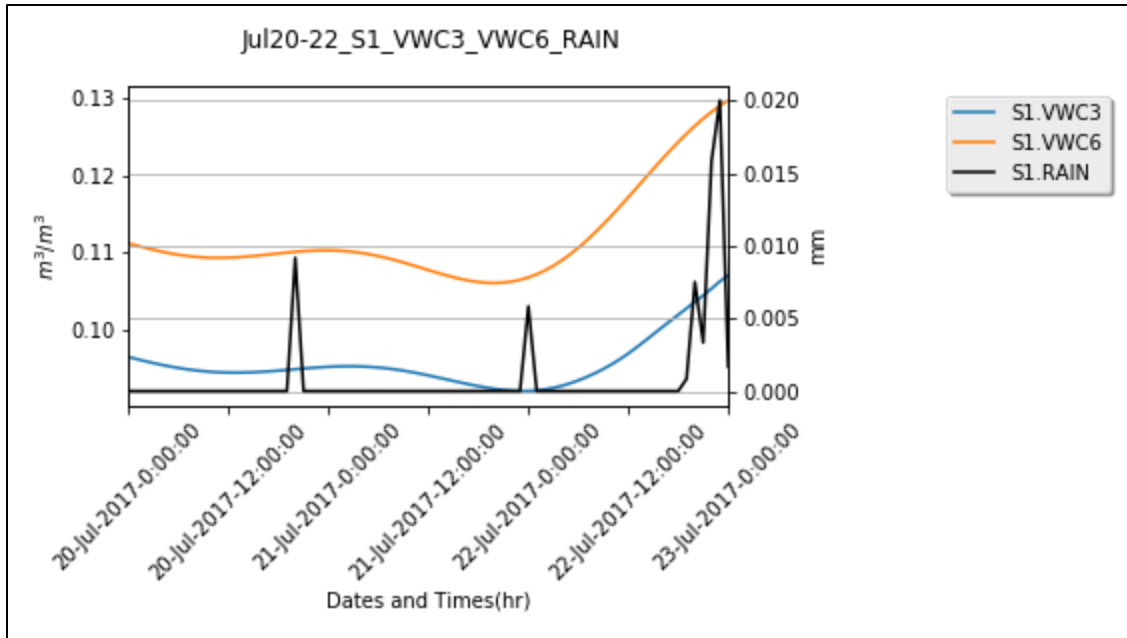


Figure 229: Volumetric Water Content in Soil at a Depth of 3 and 6 inches with Rain Bucket Data on the Right Axis

## Anemometers

Figure 92 displays the wind speed at the Roof Weather station for July 20, 2017 through July 22, 2017. According to the NCDC, these days include a sunny day, a cloudy day, and a rainy day, respectively.

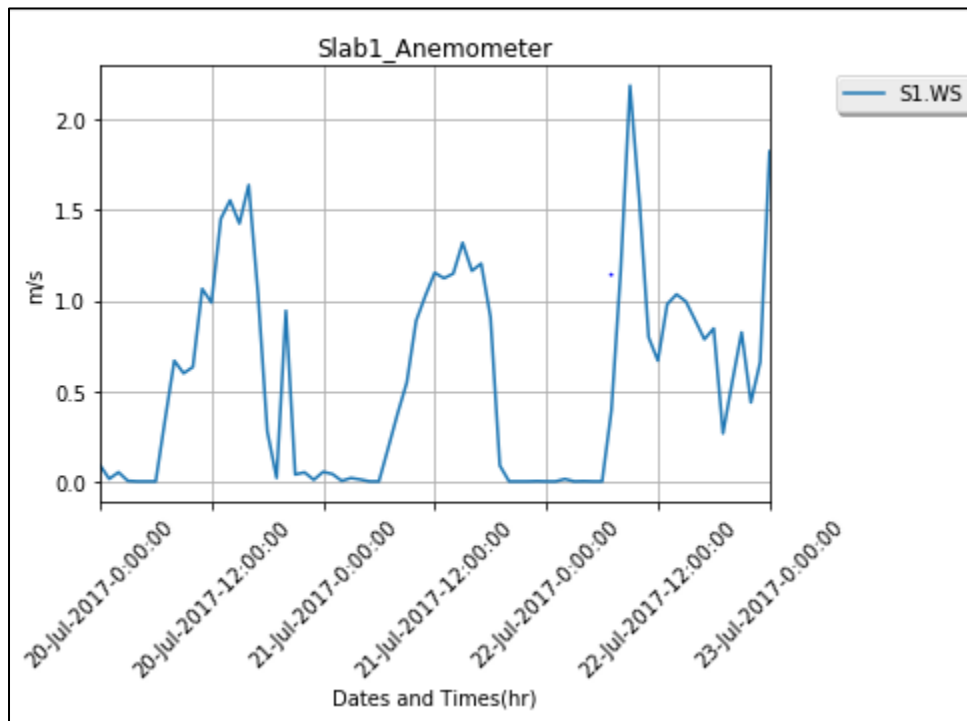


Figure 230: Wind Speed at Roof Weather Station



## Load Cells

The load cells utilized for this experiment posed the most complicated problems during data reduction. This is likely due to the extension wire utilized as well as the lack of signal amplifiers. The raw load cell results were extremely noisy and required a filtering procedure to be developed. The first step in the process was to examine the fit between the rain bucket data as compared to the load cell data. Each signal was compared to the rain bucket data to show the fit of the load cell response to the recorded rain events at the site. Only one rain bucket was available at the site due to equipment malfunction, so the results for that rain bucket compared to each load cell are shown below. Load Cell 1 vs Rain is shown in Figure 93 below with, the load cell response in lbs. on the left y-axis, rain bucket data in millimeter increments on the right y-axis, and measurement number (consecutive date) on the x-axis.

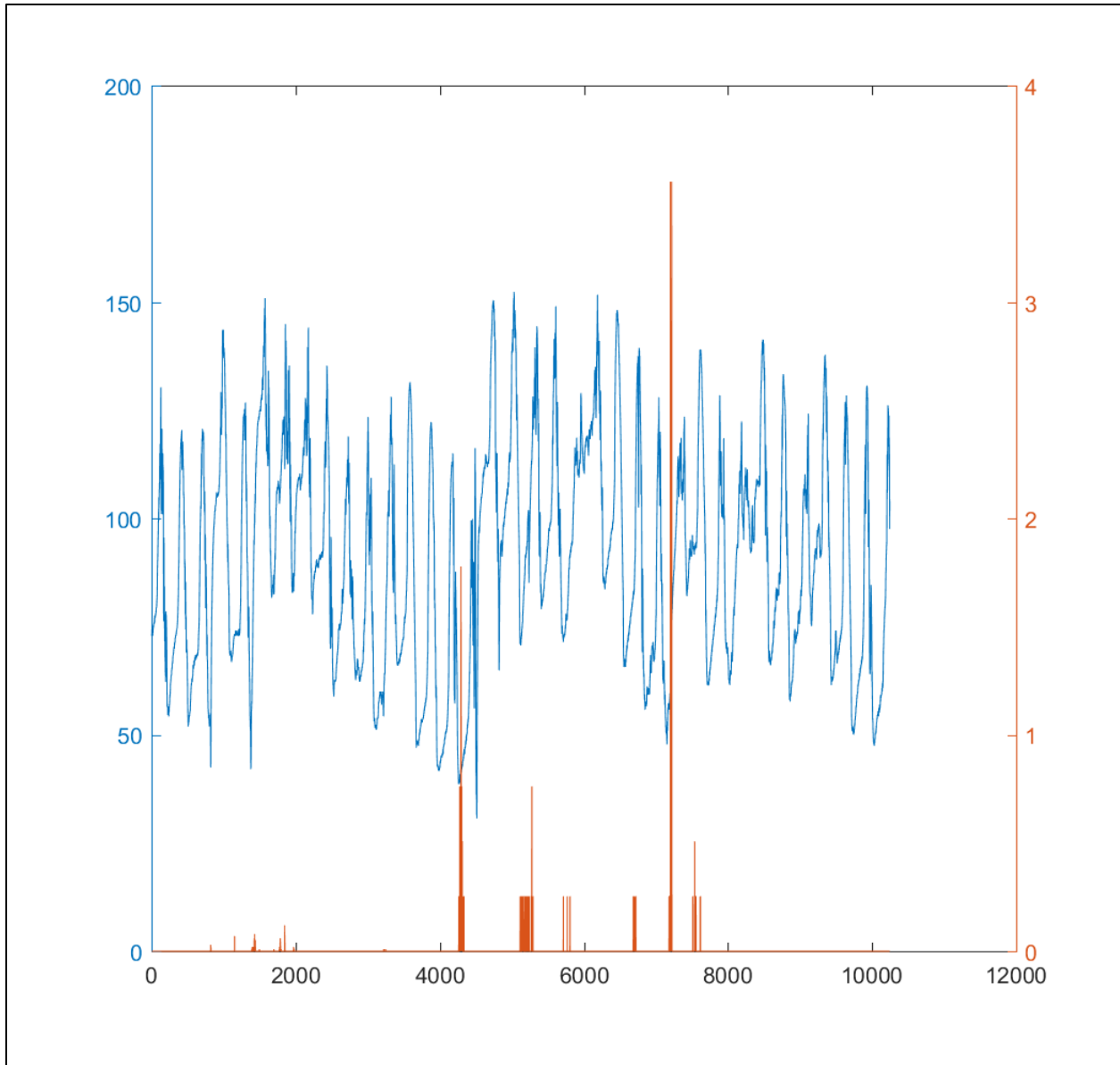


Figure 231: Load Cell 1 Response vs Measured Rain Events

Load Cell 2 vs Rain is shown in Figure 94 below with, the load cell response in lbs. on the left y-axis, rain bucket data in millimeter increments on the right y-axis, and measurement number (consecutive date) on the x-axis.

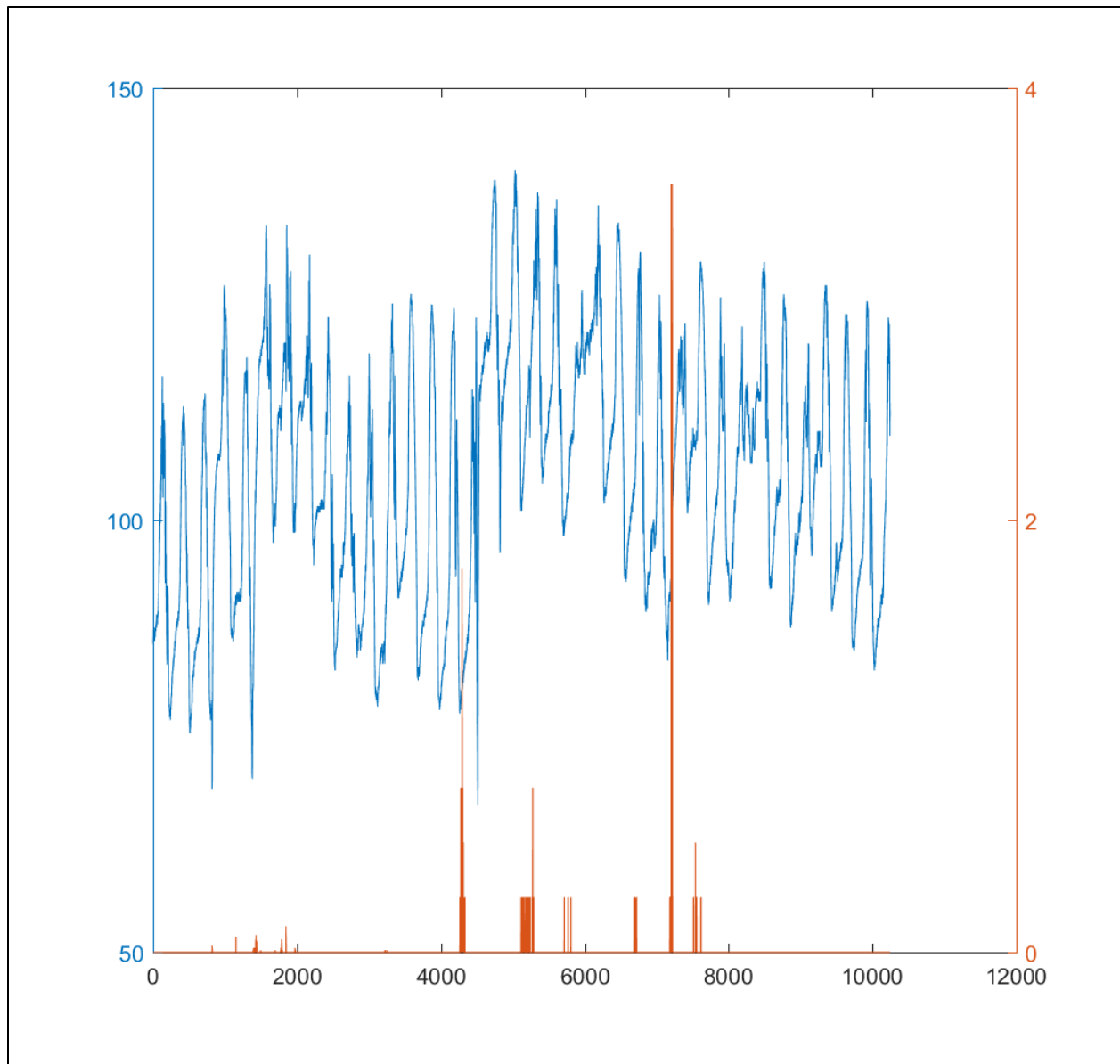


Figure 232: Load Cell 2 Response vs Measured Rain Events

Load Cell 3 vs Rain is shown in Figure 95 below with, the load cell response in lbs. on the left y-axis, rain bucket data in millimeter increments on the right y-axis, and measurement number (consecutive date) on the x-axis.

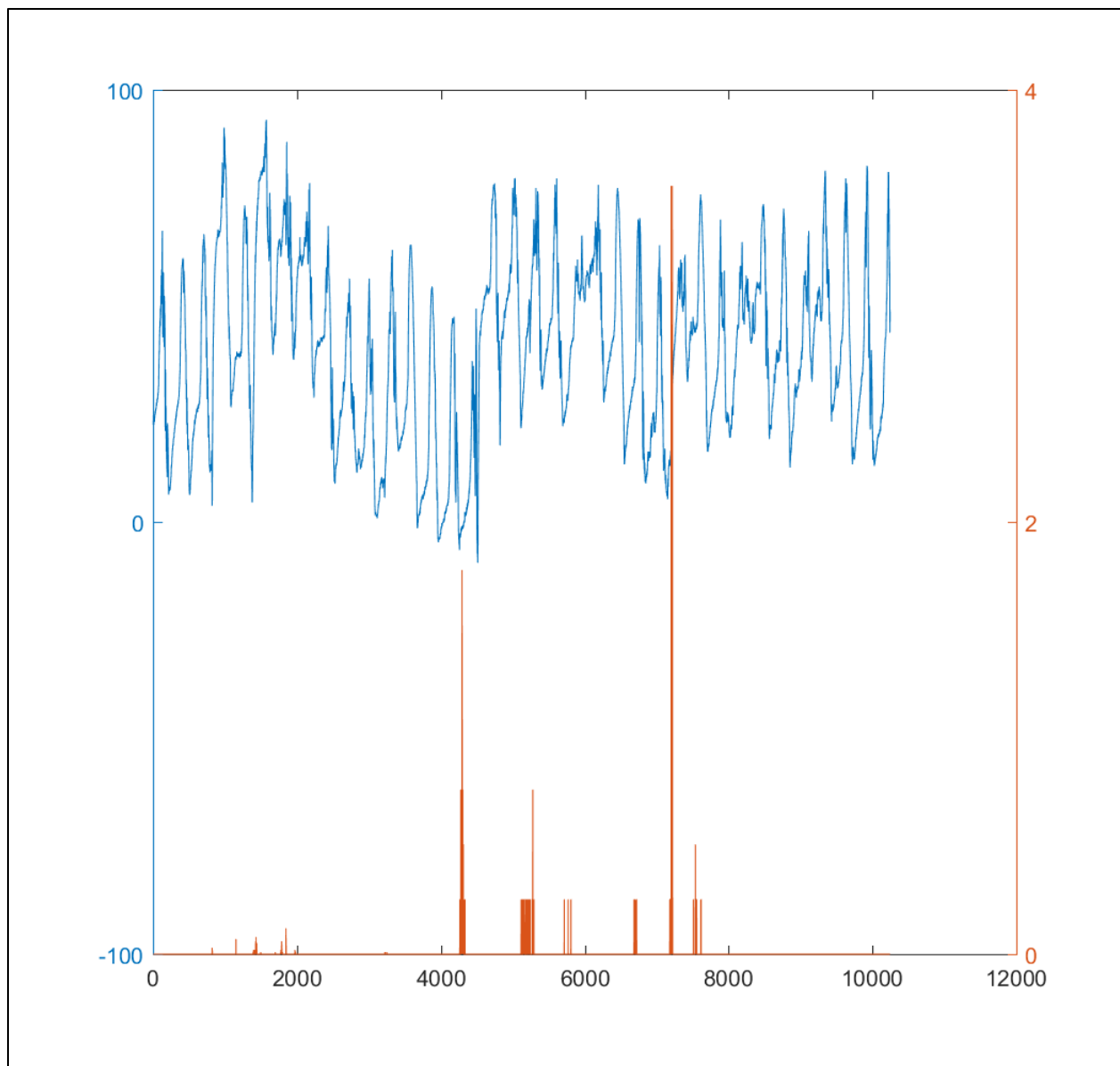


Figure 233: Load Cell 3 vs Measured Rain Events

Load Cell 4 vs Rain is shown in Figure 96 below with, the load cell response in lbs. on the left y-axis, rain bucket data in millimeter increments on the right y-axis, and measurement number (consecutive date) on the x-axis.

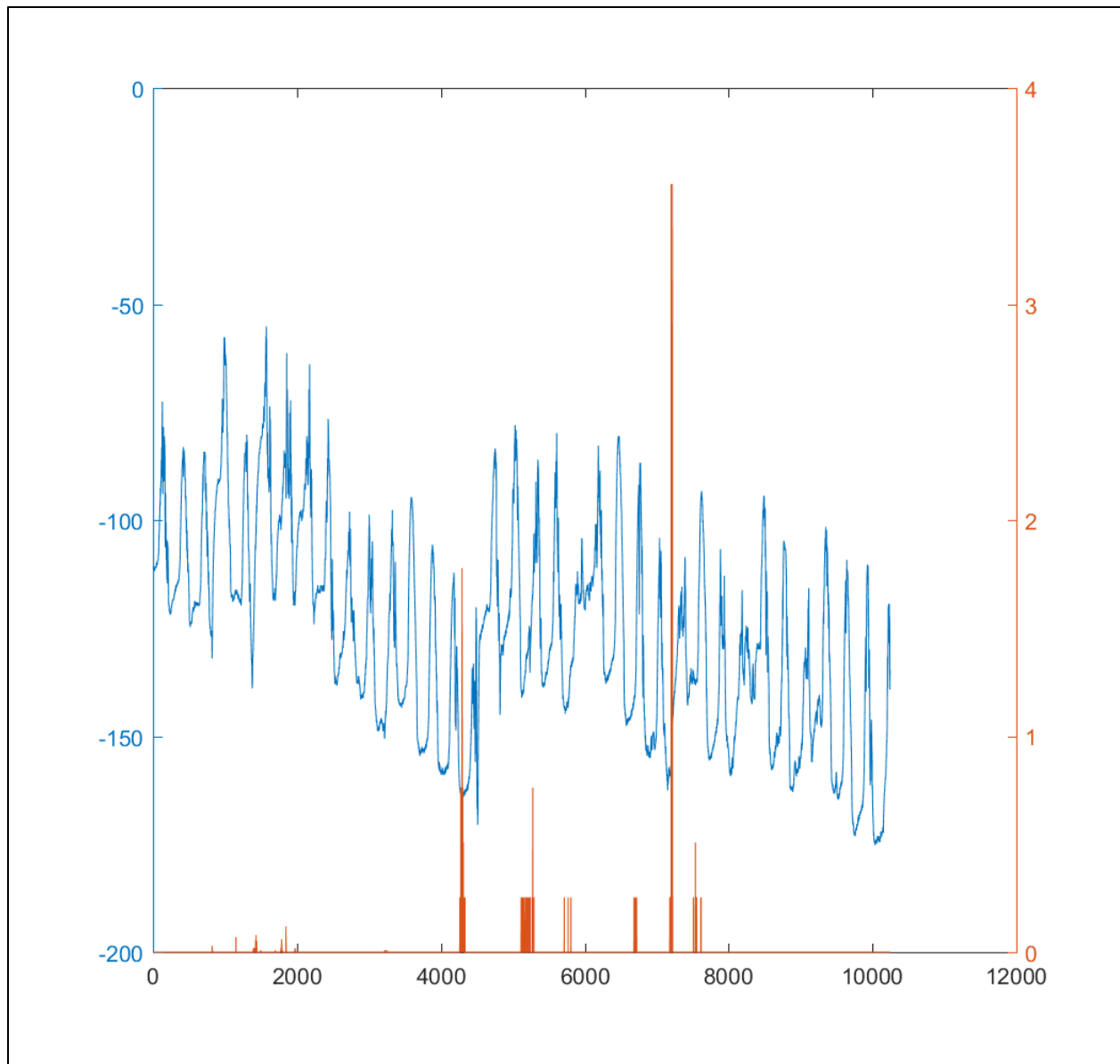


Figure 234: Load Cell 4 Response vs Measured Rain Events

Load Cell 5 vs Rain is shown in Figure 97 below with, the load cell response in lbs. on the left y-axis, rain bucket data in millimeter increments on the right y-axis, and measurement number (consecutive date) on the x-axis.

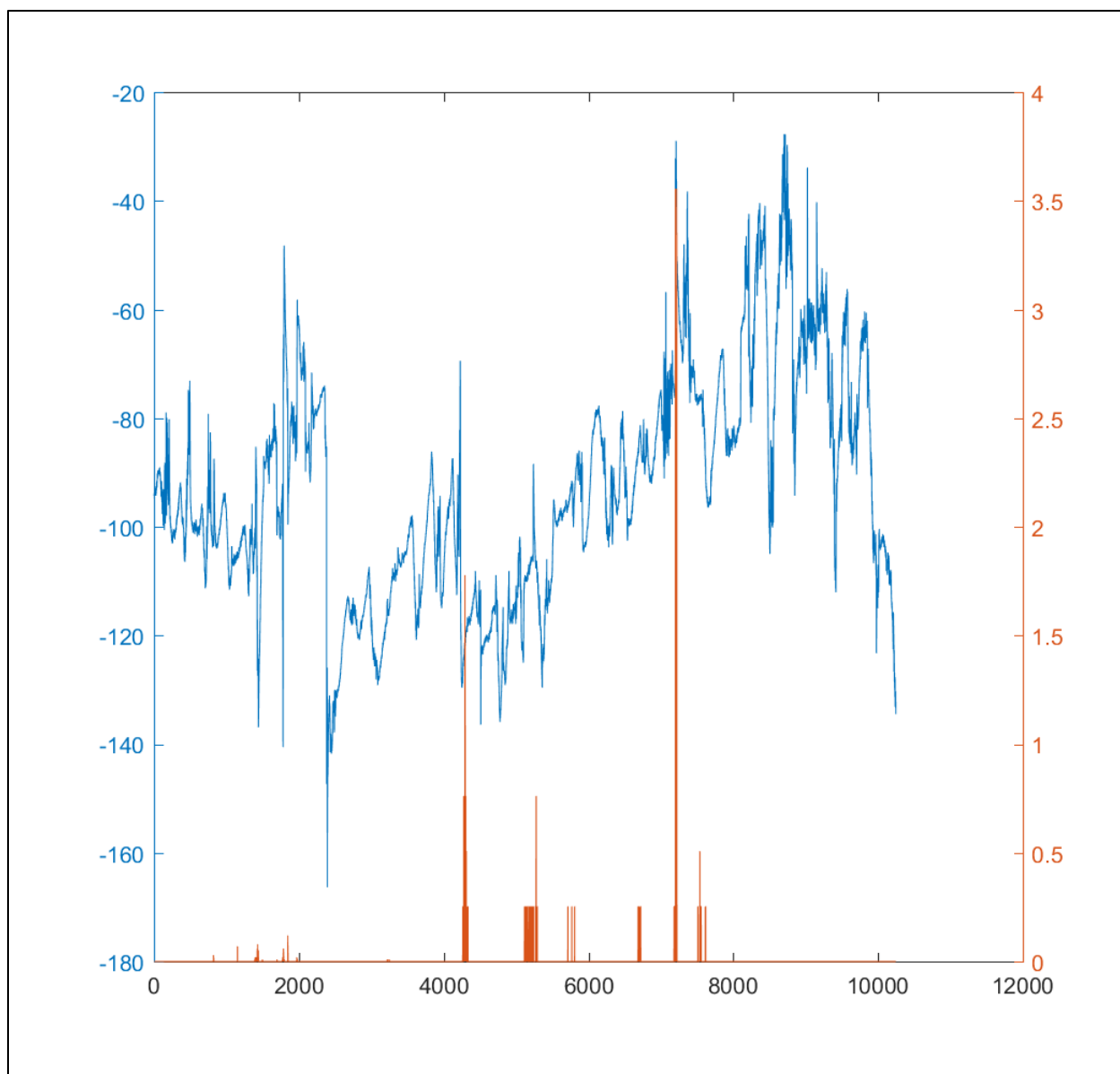


Figure 235: Load Cell 5 Response vs Measured Rain Events

Load Cell 6 vs Rain is shown in Figure 98 below with, the load cell response in lbs. on the left y-axis, rain bucket data in millimeter increments on the right y-axis, and measurement number (consecutive date) on the x-axis.

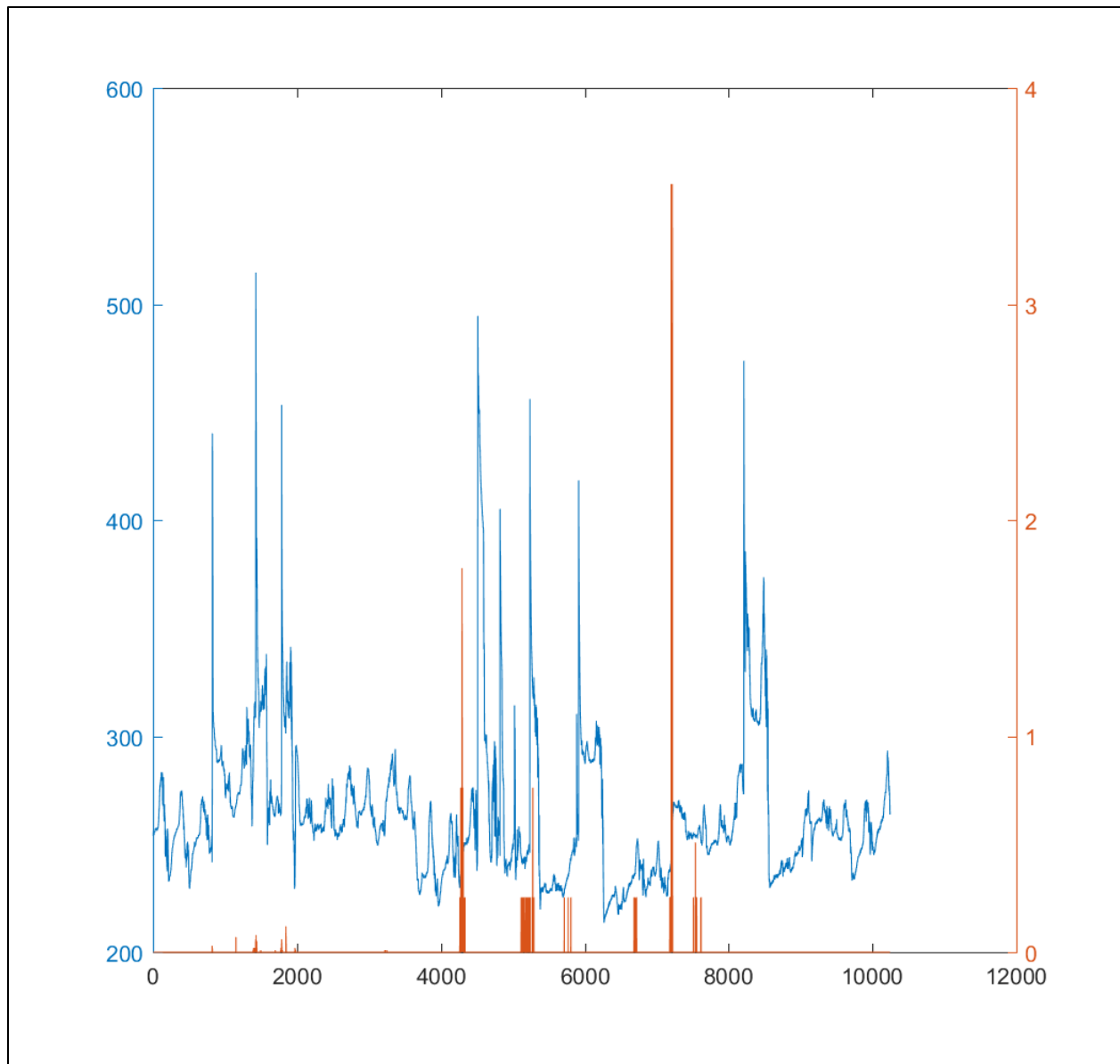


Figure 236: Load Cell 6 Response vs Measured Rain Events

Load Cell 7 vs Rain is shown in Figure 99 below with, the load cell response in lbs. on the left y-axis, rain bucket data in millimeter increments on the right y-axis, and measurement number (consecutive date) on the x-axis.



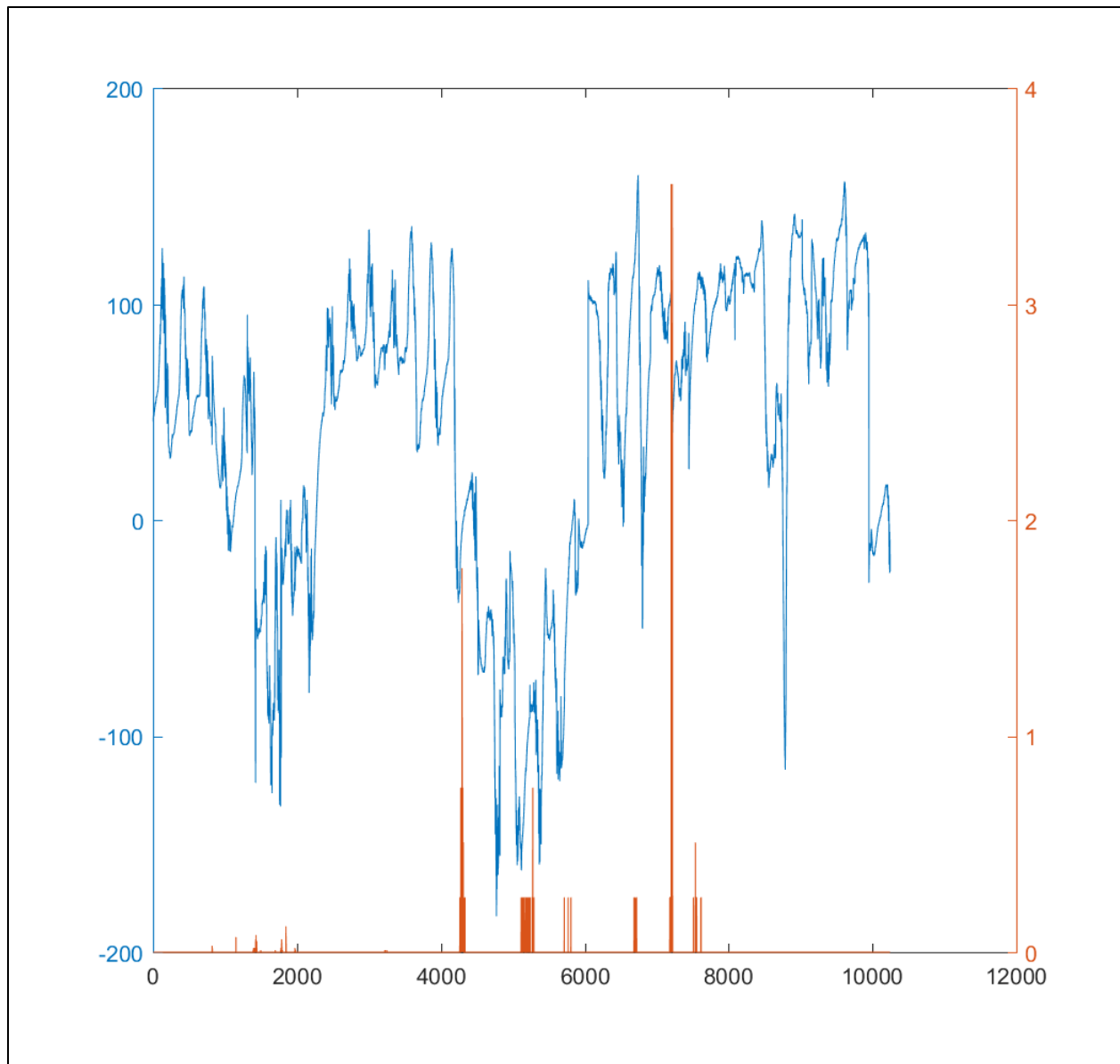


Figure 237: Load Cell 7 Response vs Measured Rain Events

Load Cell 8 vs Rain is shown in Figure 100 below with, the load cell response in lbs. on the left y-axis, rain bucket data in millimeter increments on the right y-axis, and measurement number (consecutive date) on the x-axis.

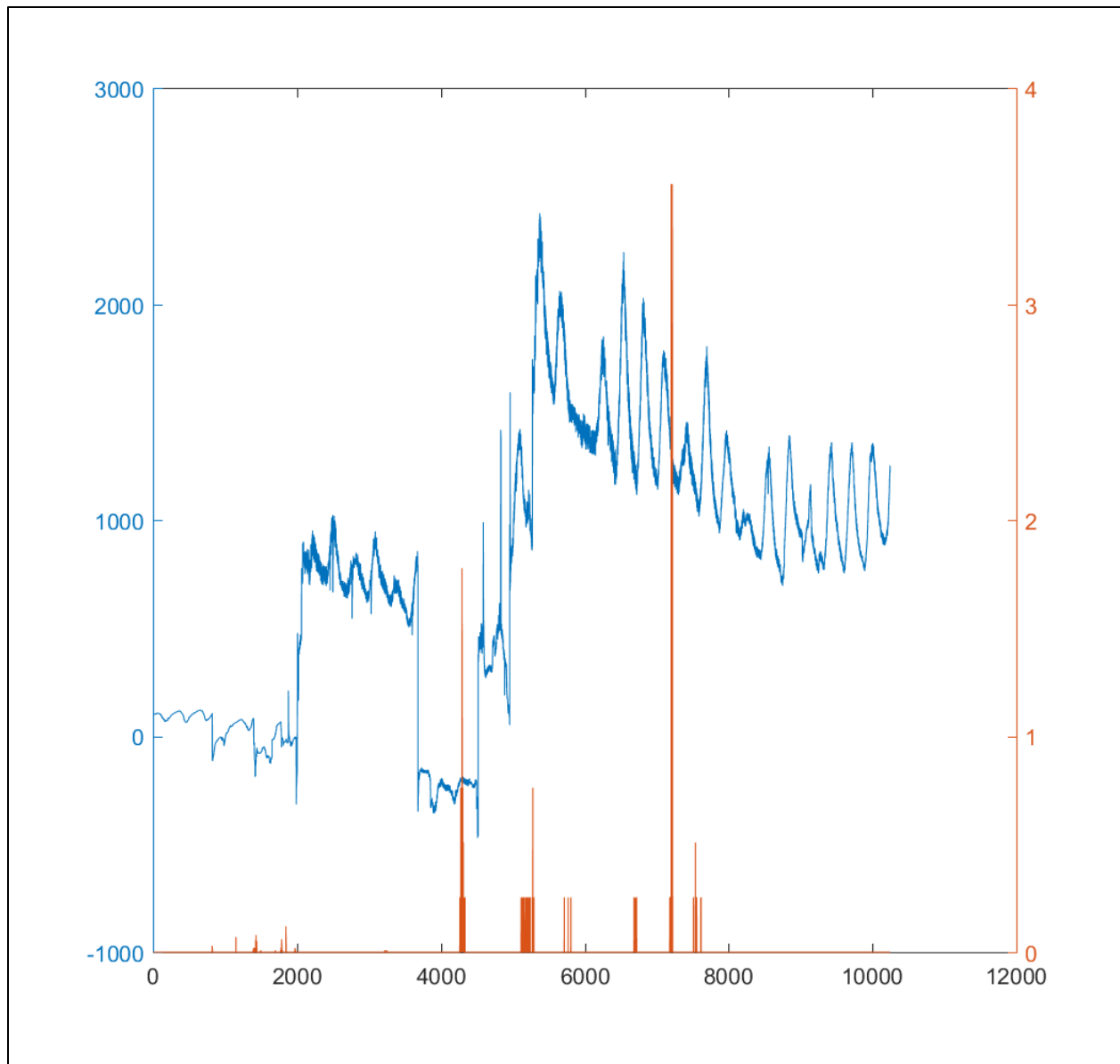


Figure 238: Load Cell 8 Response vs Measured Rain Events

Load Cell 9 vs Rain is shown in Figure 101 below with, the load cell response in lbs. on the left y-axis, rain bucket data in millimeter increments on the right y-axis, and measurement number (consecutive date) on the x-axis.

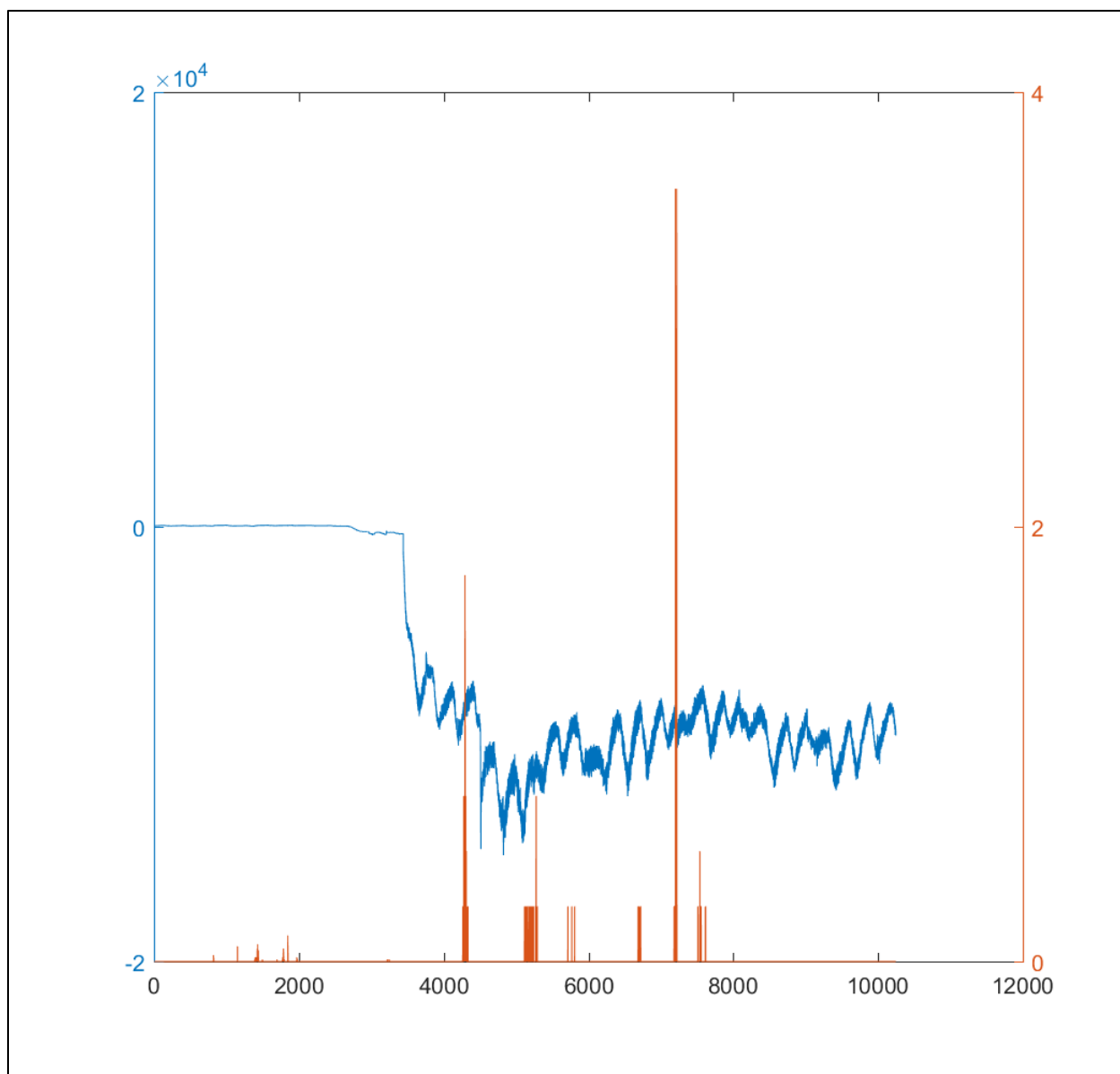


Figure 239: Load Cell 9 Response vs Measured Rain Events

Load Cell 10 vs Rain is shown in Figure 102 below with, the load cell response in lbs. on the left y-axis, rain bucket data in millimeter increments on the right y-axis, and measurement number (consecutive date) on the x-axis.

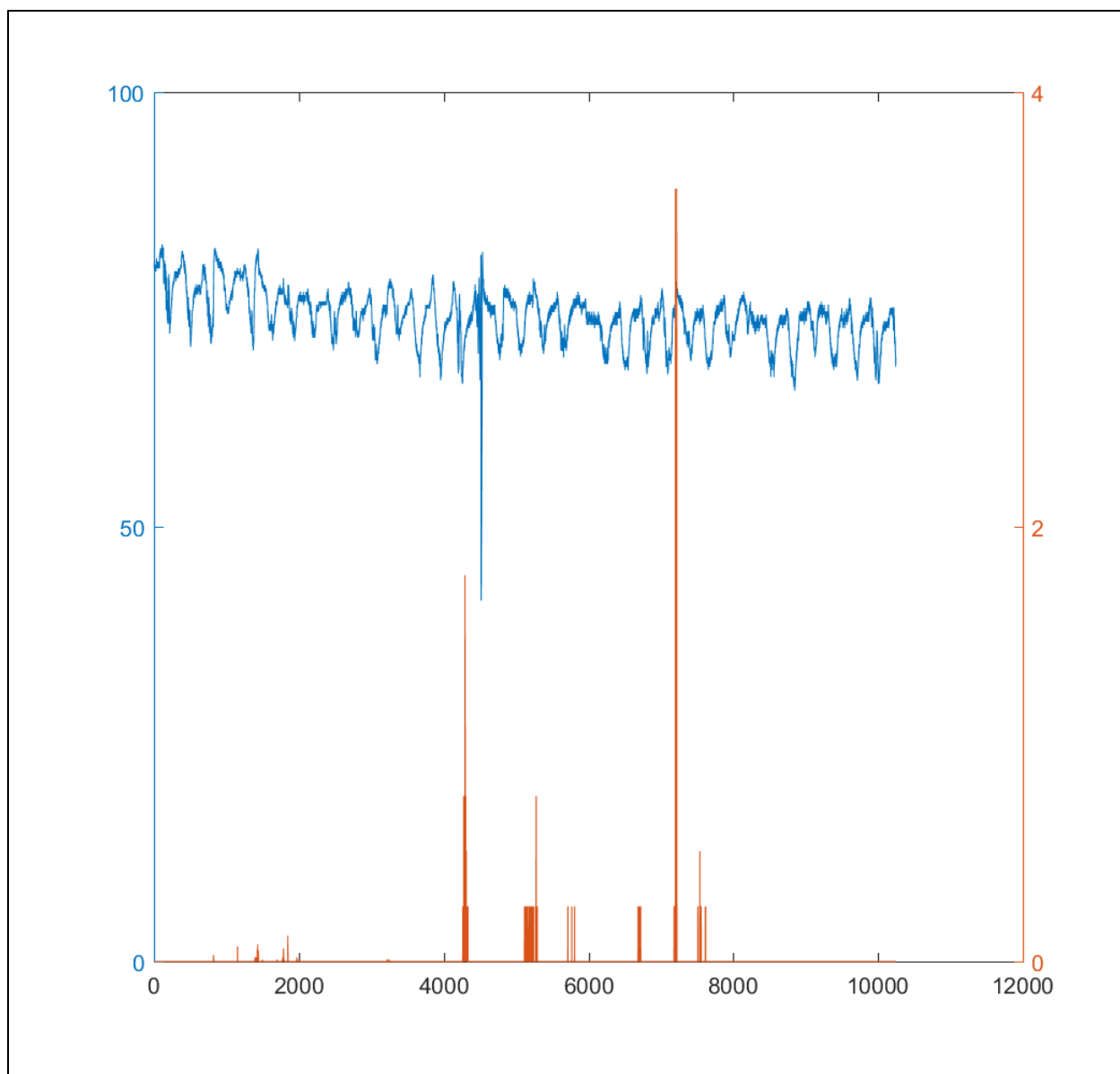


Figure 240: Load Cell 10 Response vs Measured Rain Events

Load Cell 11 vs Rain is shown in Figure 103 below with, the load cell response in lbs. on the left y-axis, rain bucket data in millimeter increments on the right y-axis, and measurement number (consecutive date) on the x-axis.

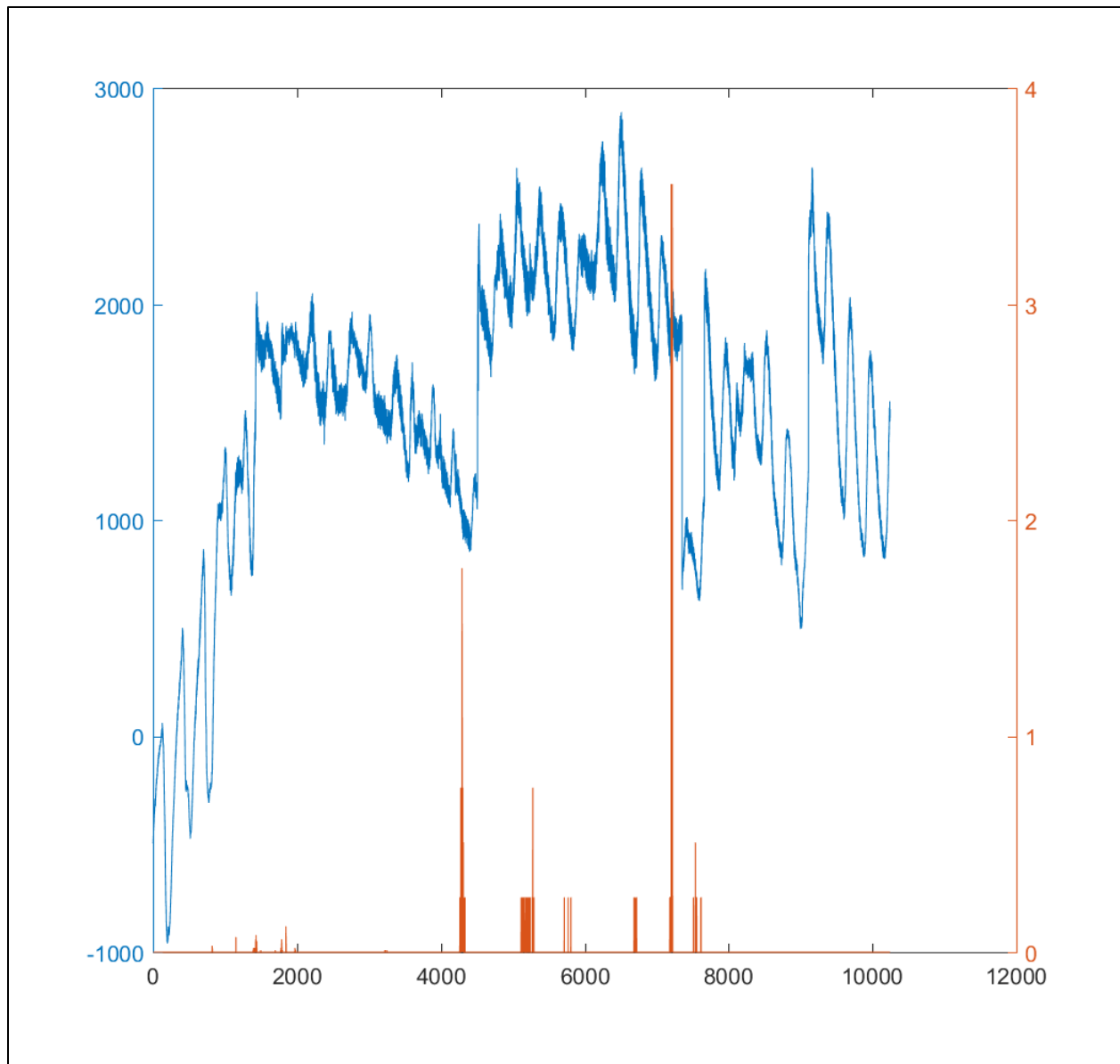


Figure 241: Load Cell 11 Response vs Measured Rain Events

Load Cell 12 vs Rain is shown in Figure 104 below with, the load cell response in lbs. on the left y-axis, rain bucket data in millimeter increments on the right y-axis, and measurement number (consecutive date) on the x-axis.

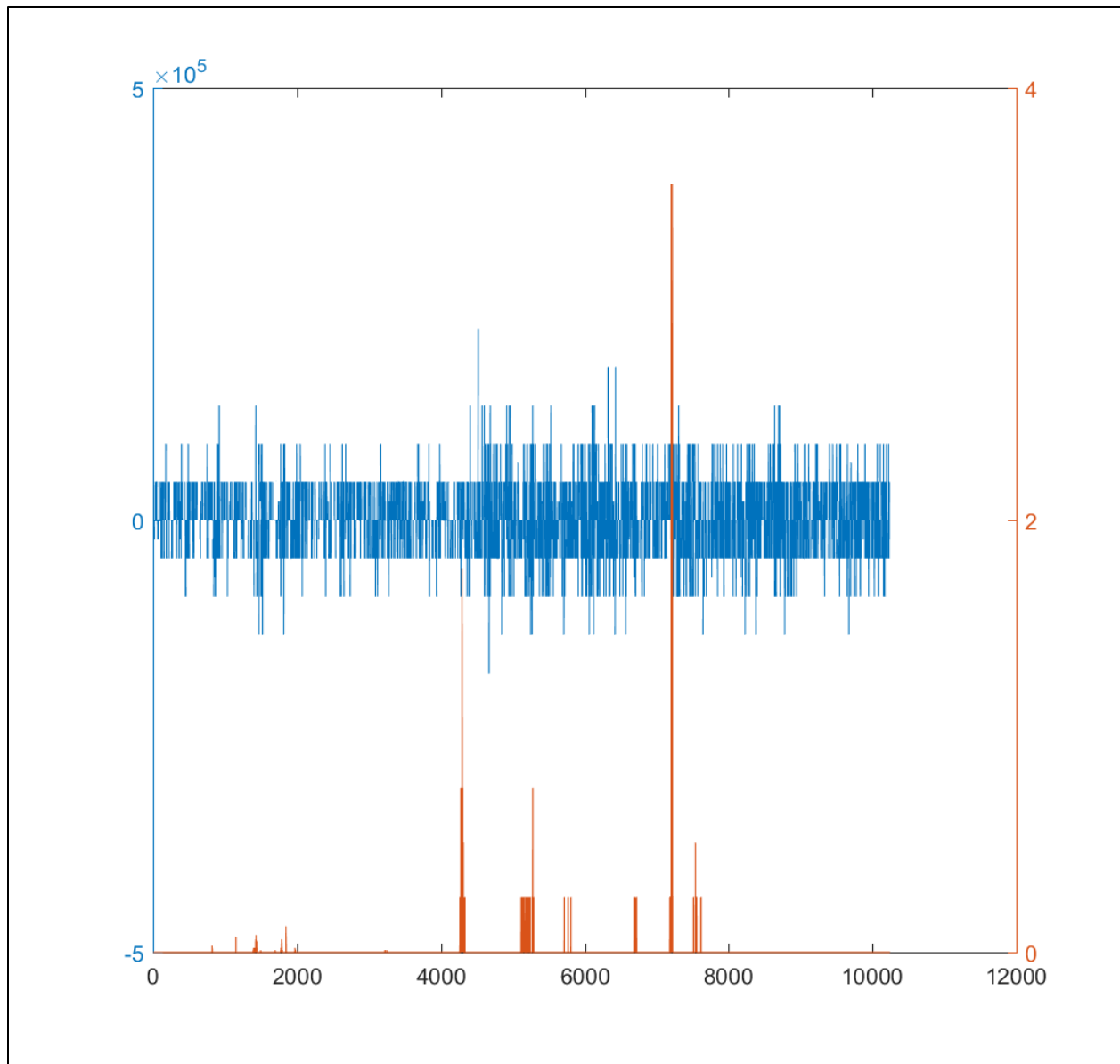


Figure 242: Load Cell 12 Response vs Measured Rain Events

Load Cell 12, as based on the results shown in Figure 104 above, was determined to be malfunctioning and was not able to be filtered or utilized for this experiment. Load Cell 13 vs Rain is shown in Figure 105 below with, the load cell response in lbs. on the left y-axis, rain bucket data in millimeter increments on the right y-axis, and measurement number (consecutive date) on the x-axis.

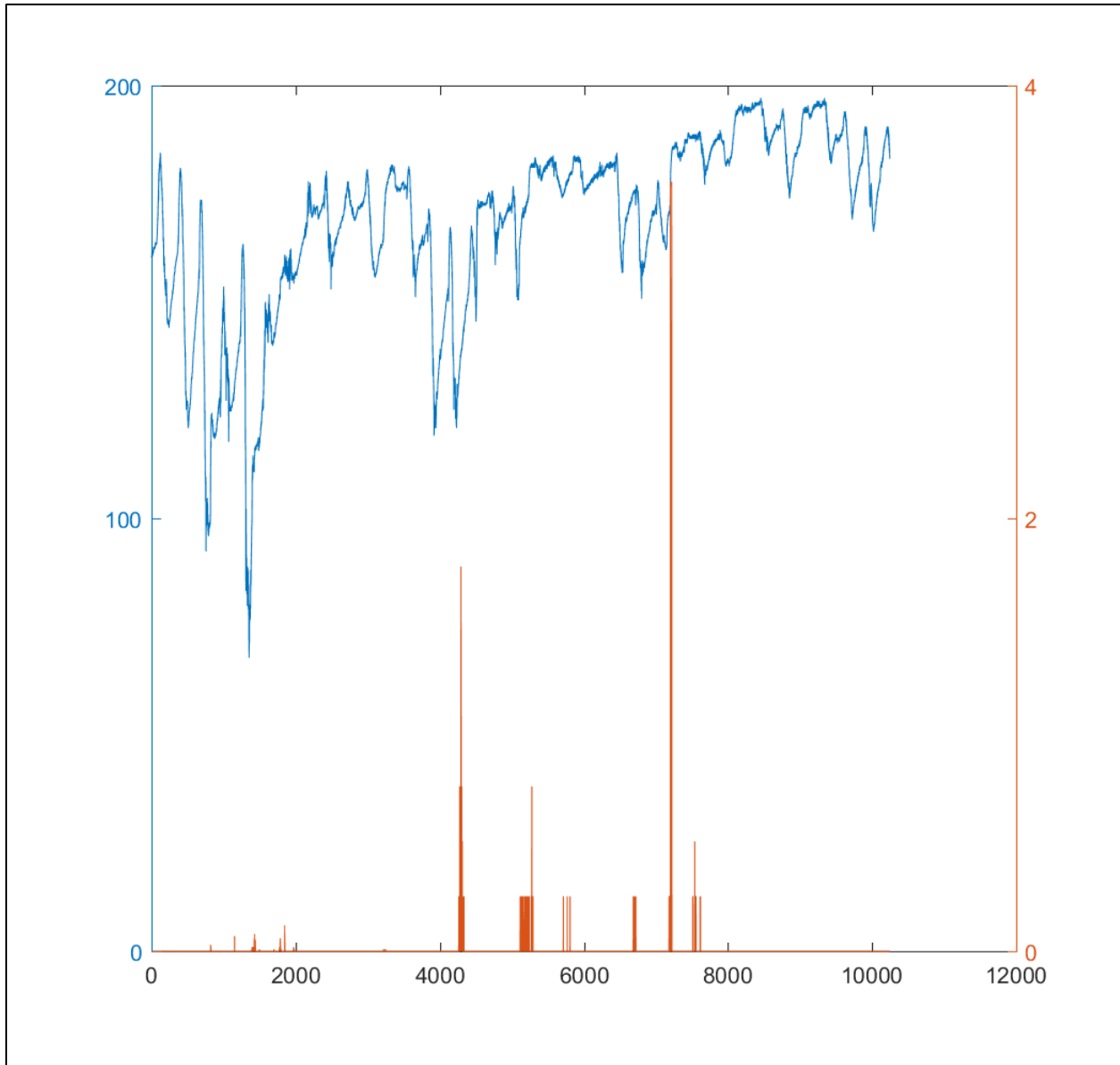


Figure 243: Load Cell 13 Response vs Measured Rain Events

Load Cell 14 vs Rain is shown in Figure 106 below with, the load cell response in lbs. on the left y-axis, rain bucket data in millimeter increments on the right y-axis, and measurement number (consecutive date) on the x-axis.



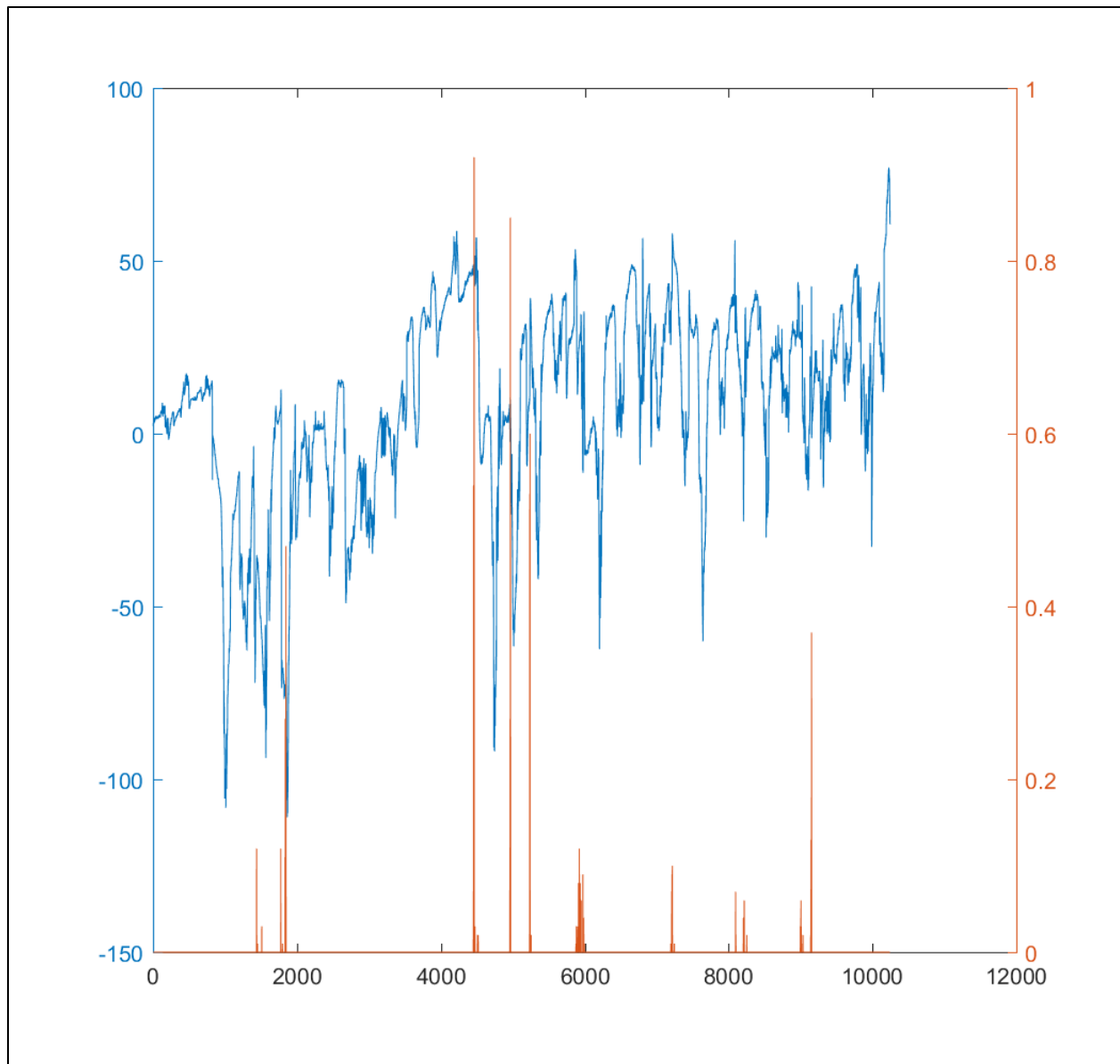


Figure 244: Load Cell 14 Response vs Measured Rain Events

Load Cell 15 vs Rain is shown in Figure 107 below with, the load cell response in lbs. on the left y-axis, rain bucket data in millimeter increments on the right y-axis, and measurement number (consecutive date) on the x-axis.

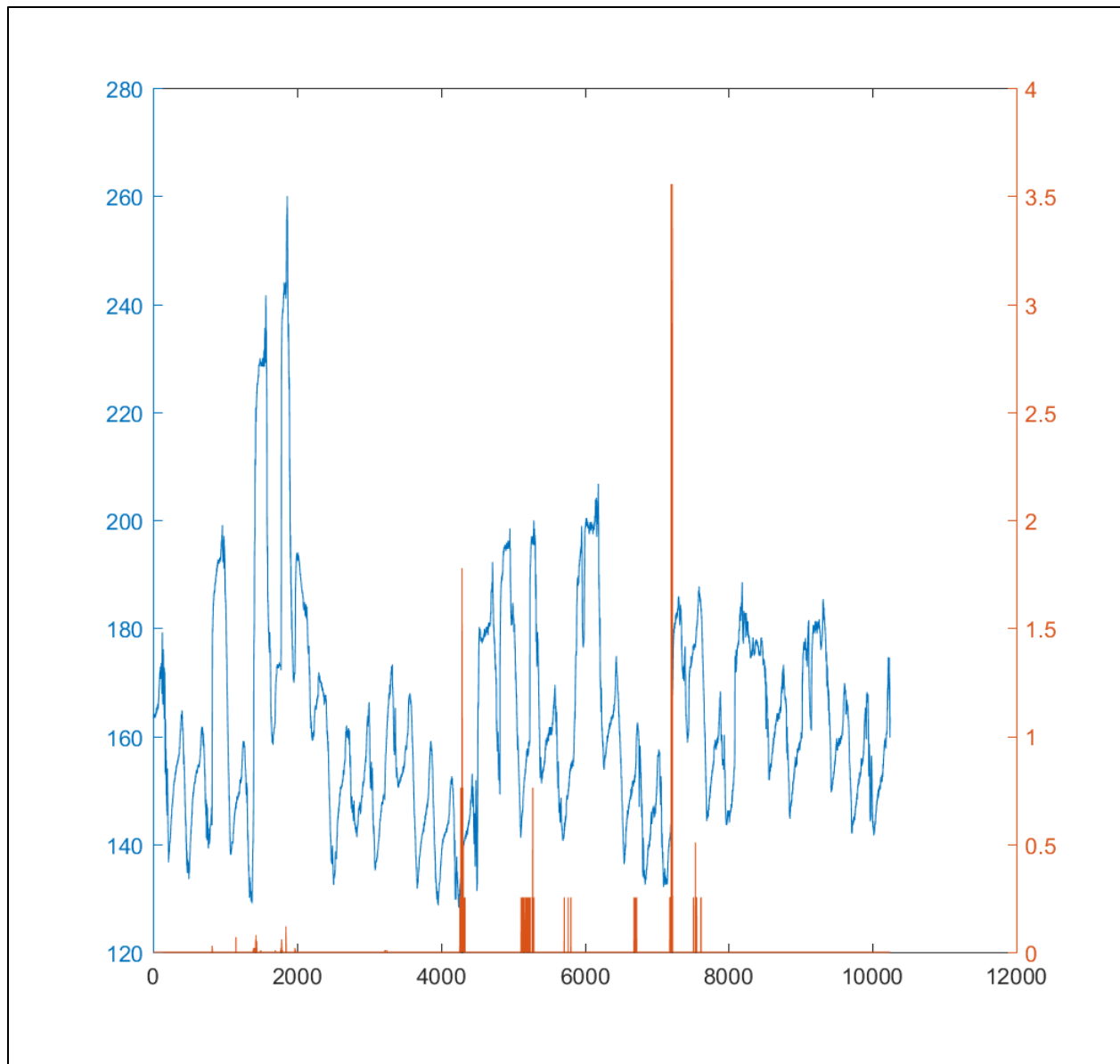


Figure 245: Load Cell 15 Response vs Measured Rain Events

Load Cell 16 vs Rain is shown in Figure 108 below with, the load cell response in lbs. on the left y-axis, rain bucket data in millimeter increments on the right y-axis, and measurement number (consecutive date) on the x-axis.

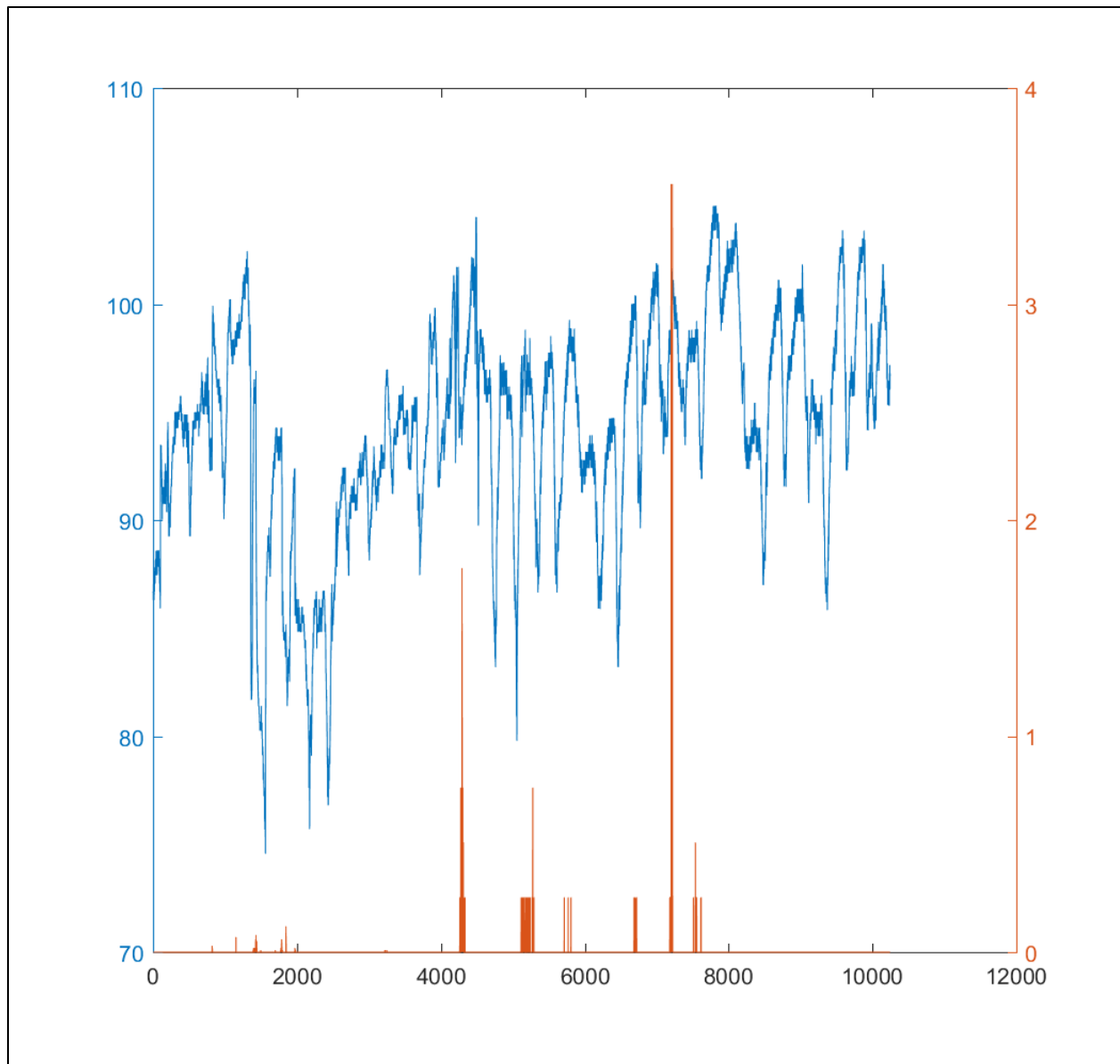


Figure 246: Load Cell 16 Response vs Measured Rain Events

To filter the load cells, first the signals were each taken separately, extended using the signal wavelet transformation (SWT) application in Matlab. Since signal denoising was the intended goal, the extension method utilized was a right extension for SWT filtering. The signals were extended to the maximum extension offered, where the original signal length measured 12047 measurements and was extended to 16384 providing 6137 additional points for filtering analysis. Once each filter was sufficiently extended, the SWT denoising portion of the Wavelet application was utilized to transform each signal with a 14 part dB wavelet with 8 level decomposition. The thresholds were determined utilizing a soft medium penalization mode, with the sparsity dropped to the lowest level available for each signal. The thresholds for each filter were determined manually and independently for each load cell signal. Once the thresholds were determined, the filtered signal response was overlaid over the original load cell signal to show the adequacy of fit. After the fit was confirmed to be sufficient, the improved filtered signals were cropped by 6137

points from the right to return the signals to original length. The filtered response of load cell 1 compared to the original signal is shown in Figure 109.

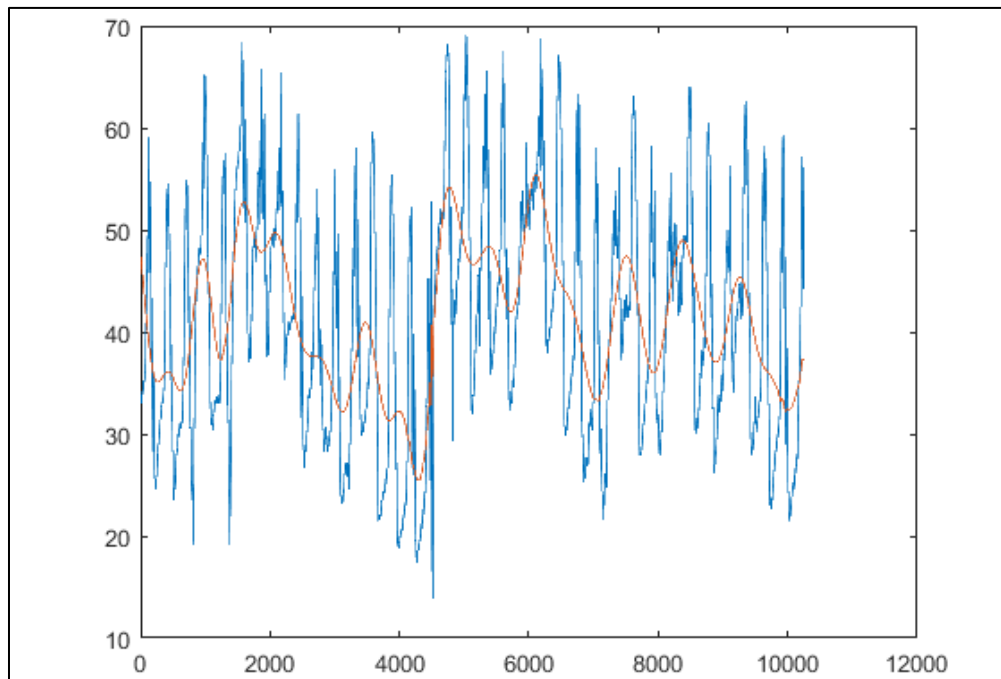


Figure 247: Load Cell 1 Unfiltered vs Load Cell 1 Filtered

The filtered response of load cell 2 compared to its original signal is shown in Figure 110.

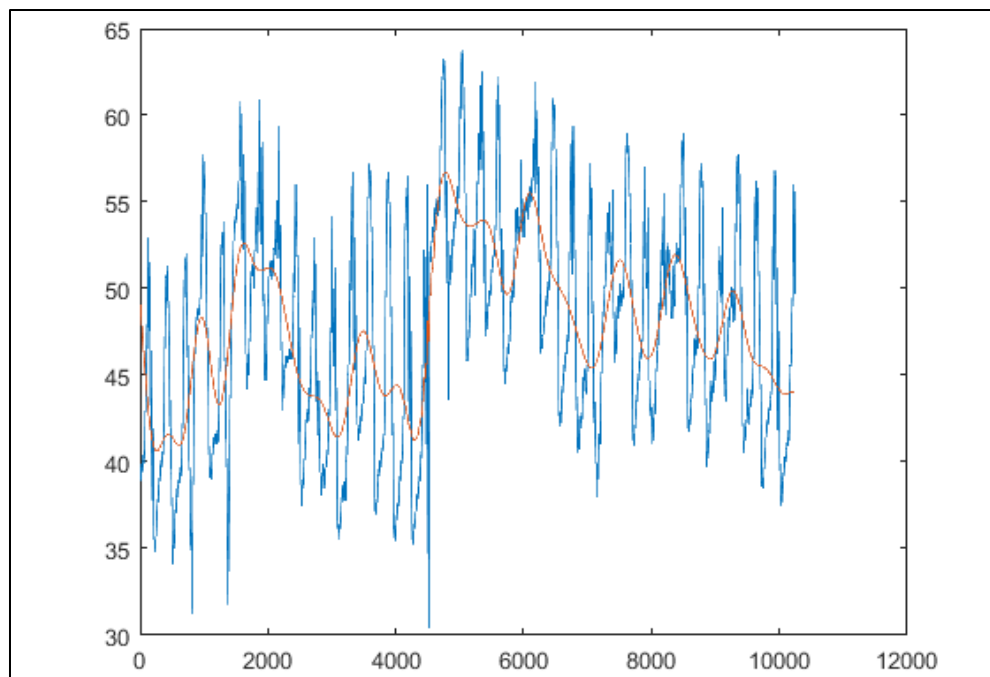


Figure 248: Load Cell 2 Unfiltered vs Load Cell 2 Filtered

The filtered response of load cell 3 compared to its original signal is shown in Figure 111.

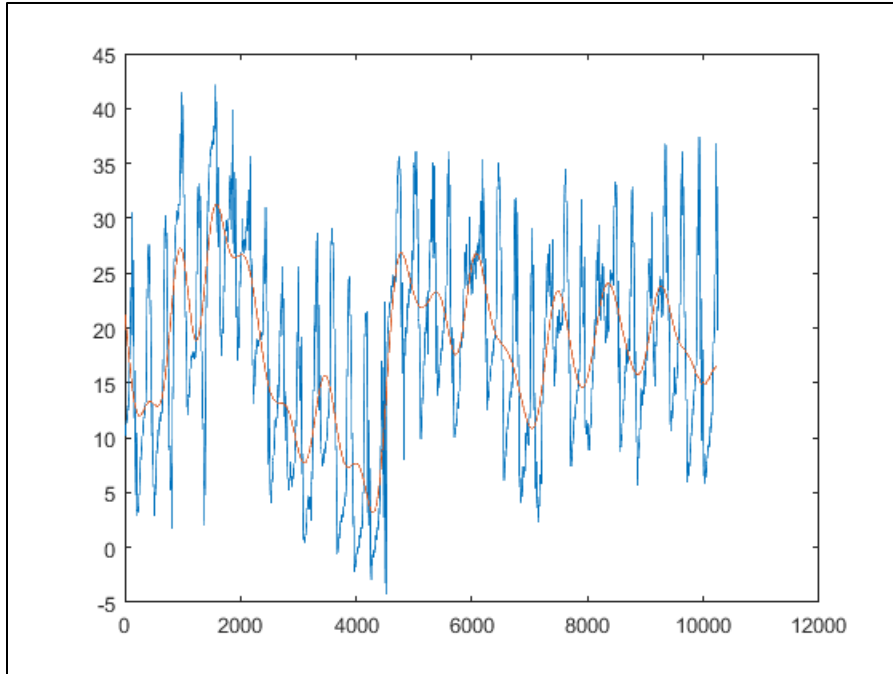


Figure 249: Load Cell 3 Filtered vs Load Cell 3 Unfiltered

The filtered response of load cell 4 compared to its original signal is shown in Figure 112.

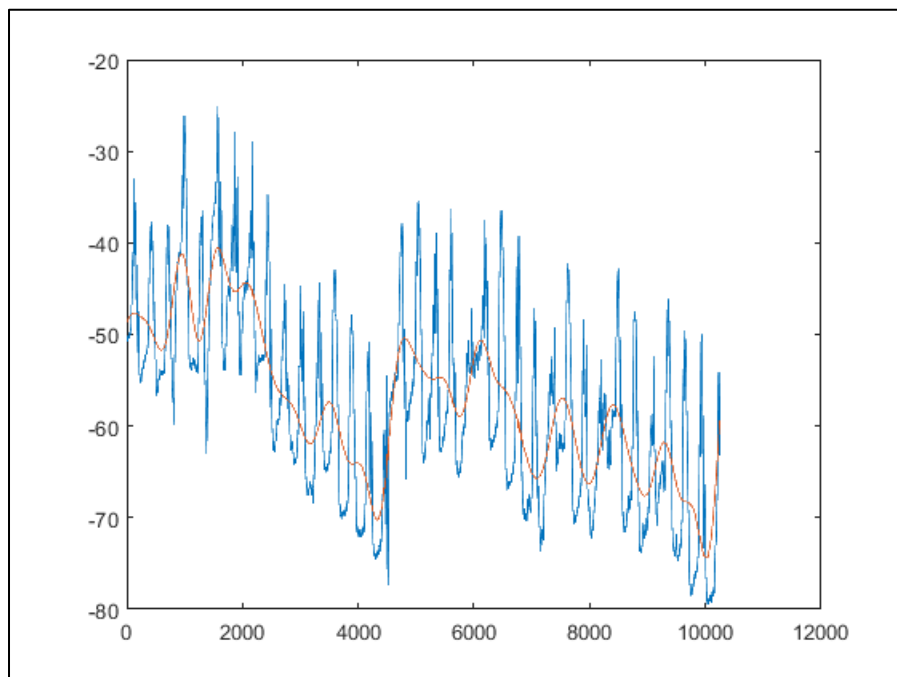


Figure 250: Load Cell 4 Filtered vs Load Cell 4 Unfiltered

The filtered response of load cell 5 compared to its original signal is shown in Figure 113.

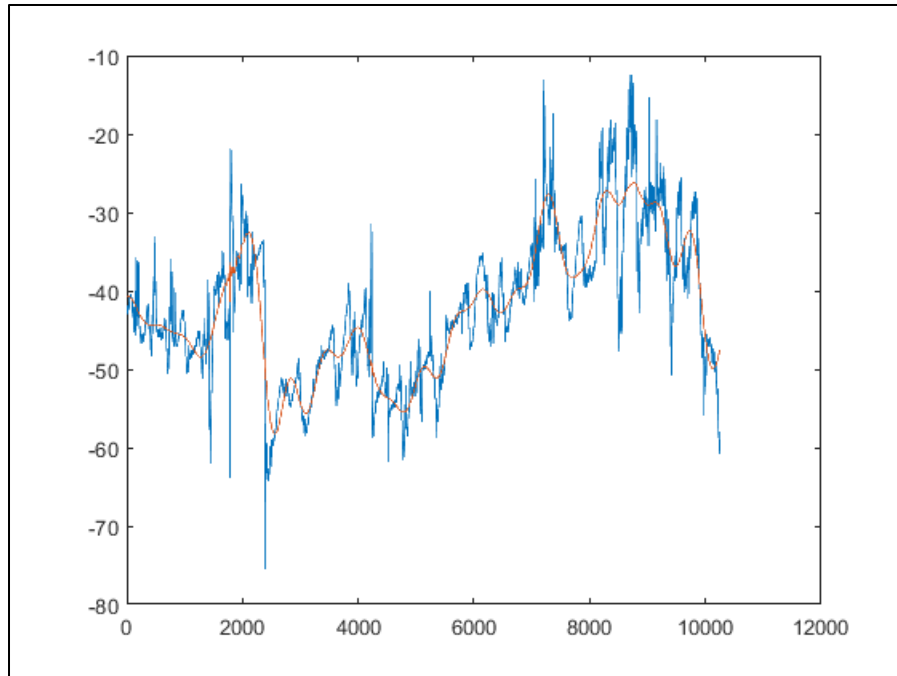


Figure 251: Load Cell 5 Filtered vs Load Cell 5 Unfiltered

The filtered response of load cell 6 compared to its original signal is shown in Figure 114.

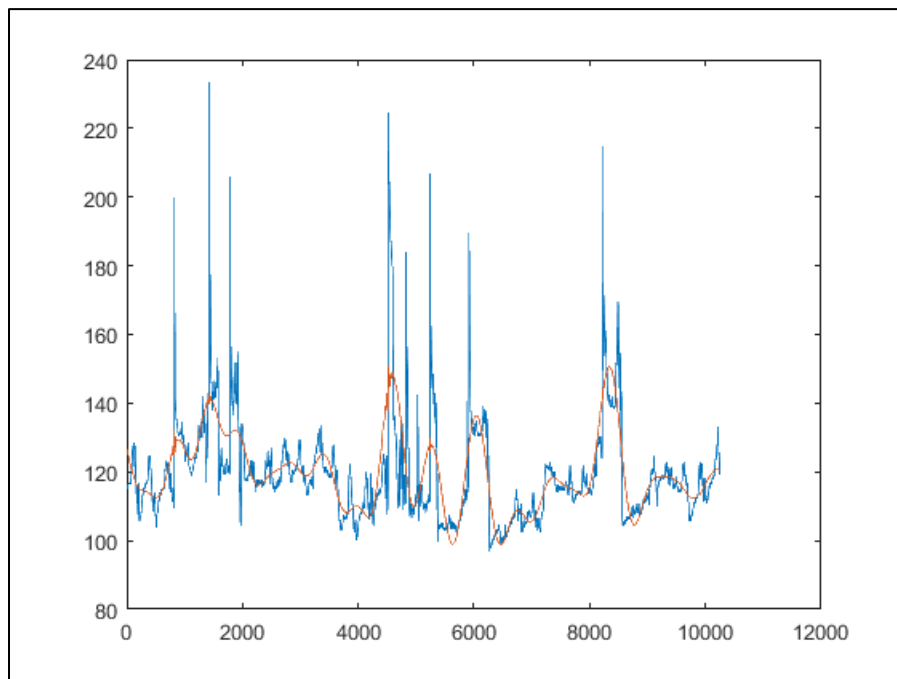


Figure 252: Load Cell 6 Filtered vs Load Cell 6 Unfiltered

The filtered response of load cell 7 compared to its original signal is shown in Figure 115.

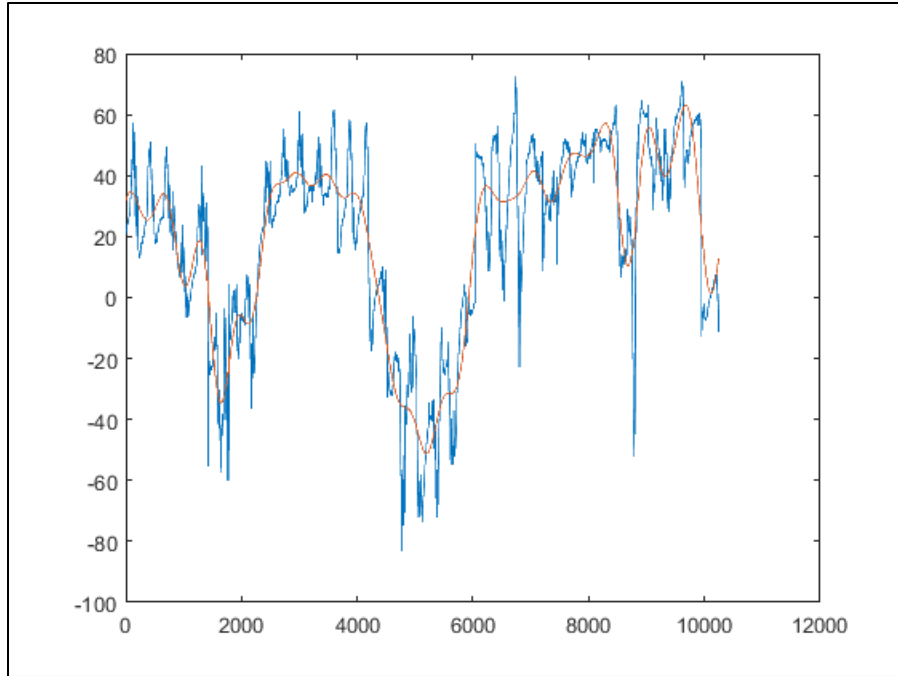


Figure 253: Load Cell 7 Filtered vs Load Cell 7 Unfiltered

The filtered response of load cell 8 compared to its original signal is shown in Figure 116.

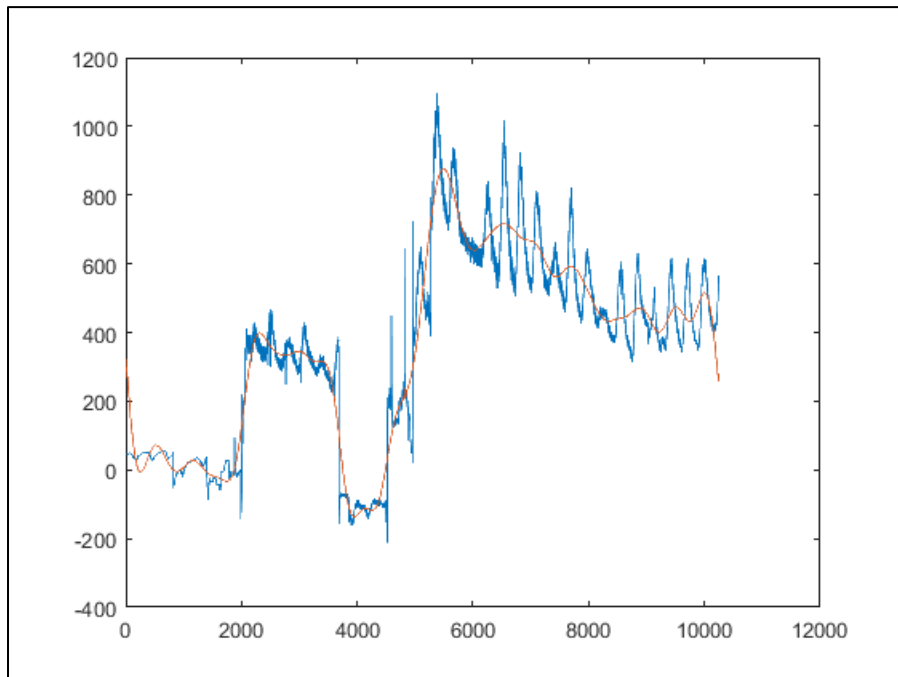


Figure 254: Load Cell 8 Filtered vs Load Cell 8 Unfiltered

The filtered response of load cell 9 compared to its original signal is shown in Figure 117.



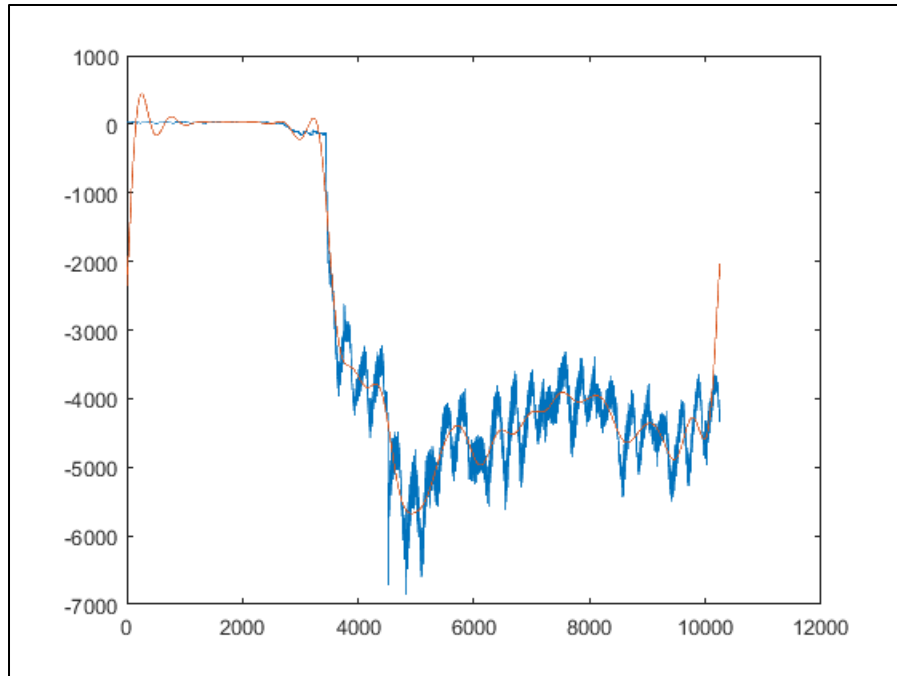


Figure 255: Load Cell 9 Filtered vs Load Cell 9 Unfiltered

The filtered response of load cell 10 compared to its original signal is shown in Figure 118.

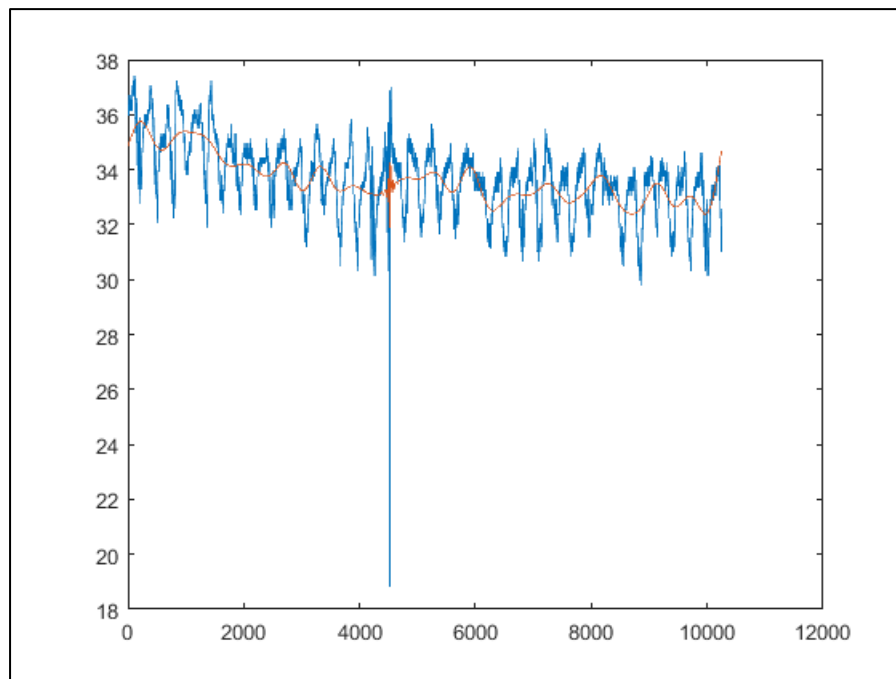


Figure 256: Load Cell 10 Filtered vs Load Cell 10 Unfiltered

The filtered response of load cell 11 compared to its original signal is shown in Figure 119.

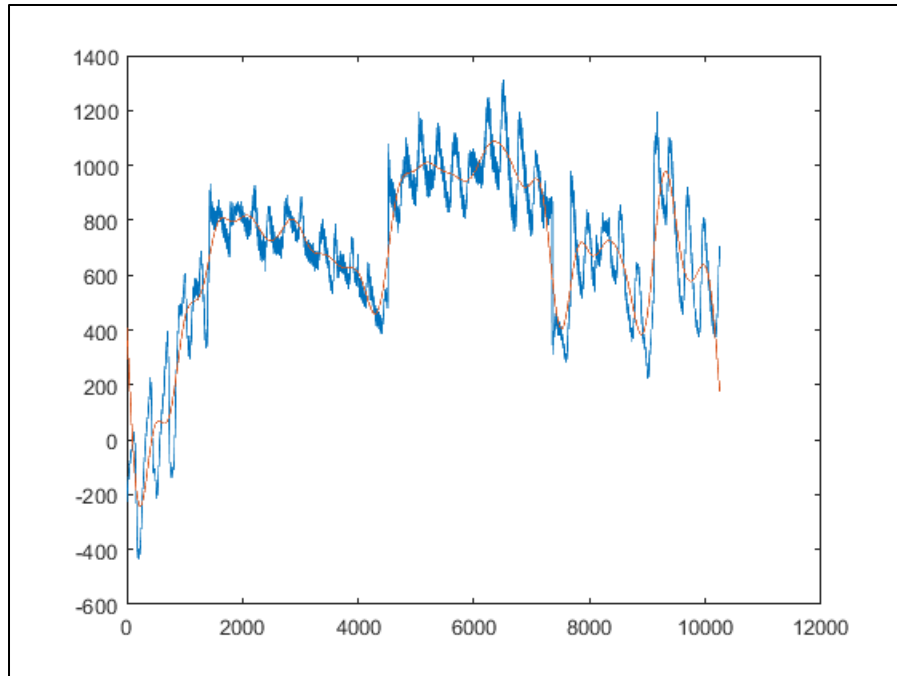


Figure 257: Load Cell 11 Filtered vs Load Cell 11 Unfiltered

The filtered response of load cell 12 is unavailable to show, because load cell 12 had an unidentifiable malfunction that resulted in no data. The filtered response of load cell 13 compared to its original signal is shown in Figure 120.

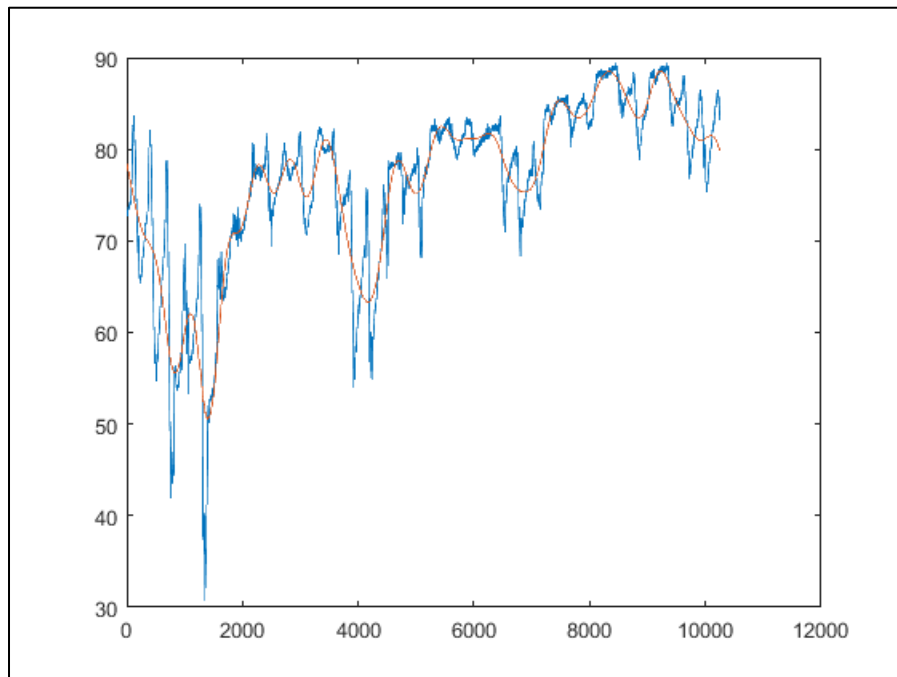


Figure 258: Load Cell 13 Filtered vs Load Cell 13 Unfiltered

The filtered response of load cell 14 compared to its original signal is shown in Figure 121.

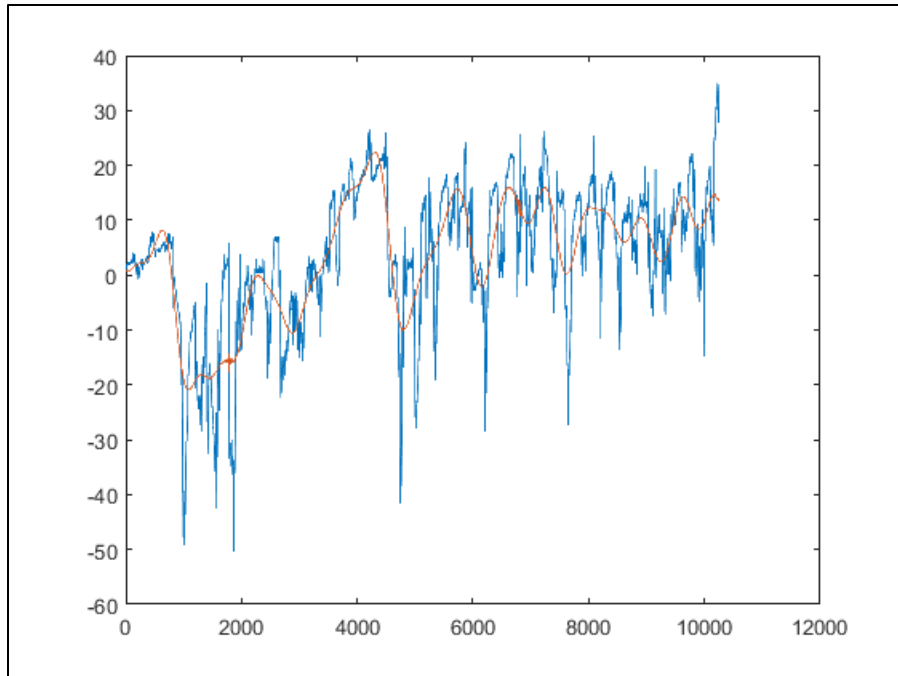


Figure 259: Load Cell 14 Filtered vs Load Cell 14 Unfiltered

The filtered response of load cell 15 compared to its original signal is shown in Figure 122.

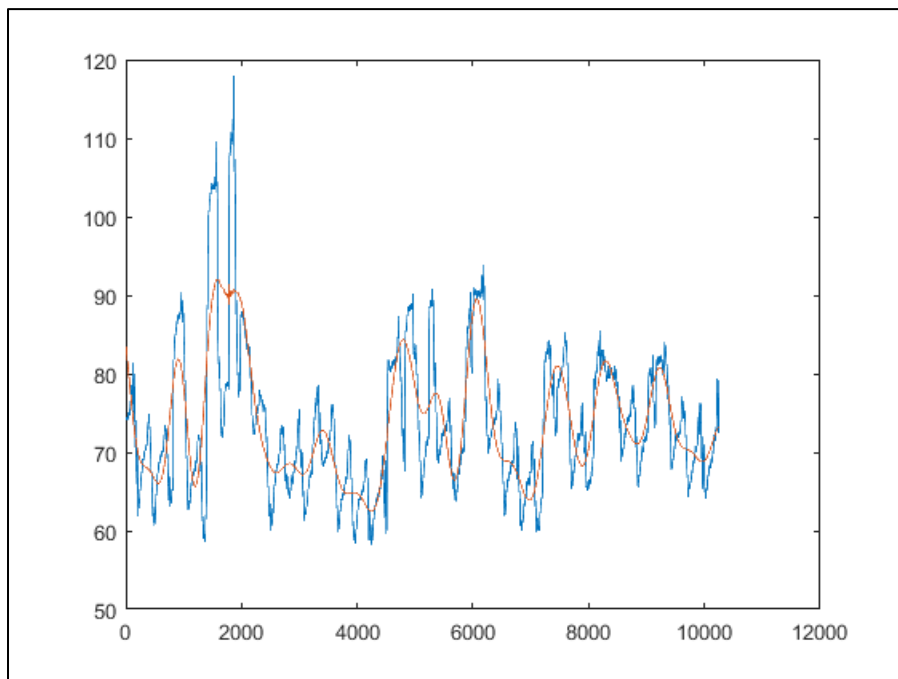


Figure 260: Load Cell 15 Filtered vs Load Cell 15 Unfiltered

The filtered response of load cell 16 compared to its original signal is shown in Figure 123.

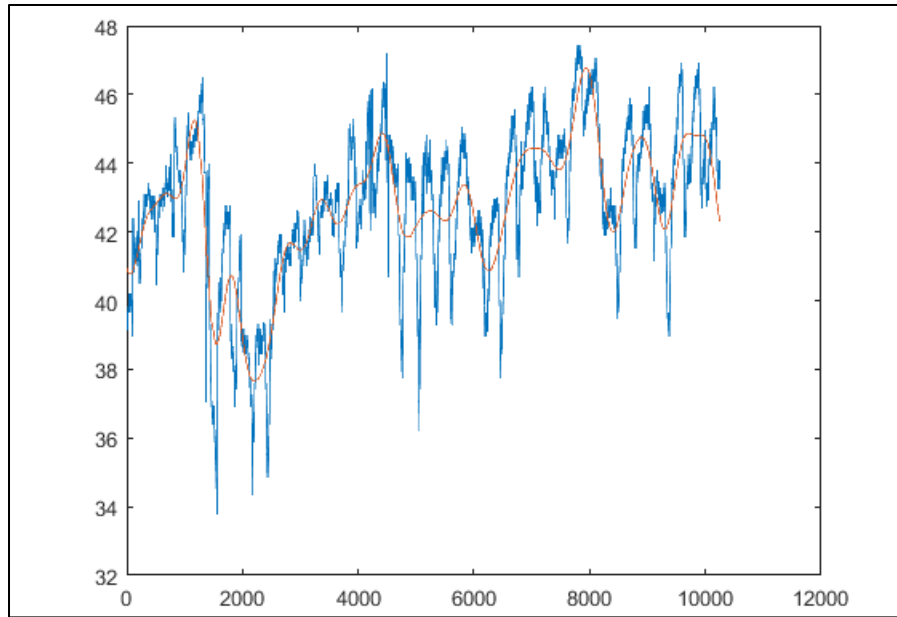


Figure 261: Load Cell 16 Filtered vs Load Cell 16 Unfiltered

After the load cell filtering procedure, the next step was to assign load cell values to slabs. Two load cells were used per slab in the sensor layout, but after evaluating the load cells compared to the measured rain events, it was clear that some of the load cells performed more closely to the expected response, where the mass increases after a rain event. The best signals were chosen to represent each slab. If both load cells were utilized for each slab, the average of each was utilized, otherwise the load cell with the better fit was chosen to represent that slabs mass for the purposes of this experiment. The result of this procedure determined that the mass of the slabs utilized from this point forth would be relative mass, which worked out well due to the poor quality of the load cell data and the poor fit determined by some of the load cells as shown above. The load cells utilized to derive slab mass for final calculations are shown in Table 32 below.

Table 65: Load Cells utilized for Final Slab Mass

Slab #	LC #(s)
1	1,2
2	3,4
3	6
4	7
5	10
6	11
7	13

8	15,16
---	-------

Once the load cells were assigned to slabs, the next objective was to limit the load cell response to meaningful levels. The minimum of each load cell was set respective to the dry mass of the measured sample. The maximum of each load cell was set respective to the maximum modified saturated surface dry value, which was found in Table 5, utilizing the procedure outlined in the density determination section of this report, by using the ratio of the (Dry Mass/Wet Mass)/(LCsigmin/LCsigmax). The corrected slab 1 mass as compared to the original filtered results are shown in Figure 124 below.

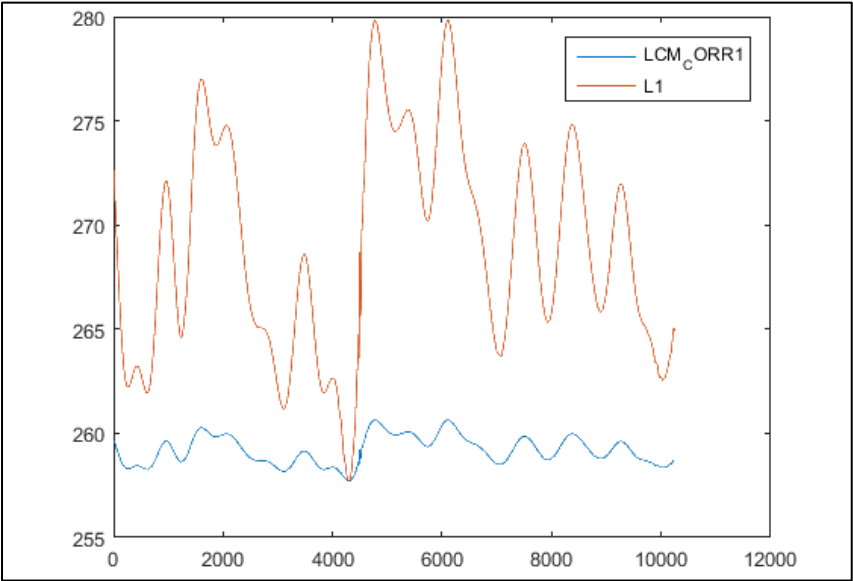


Figure 262: Slab 1 Mass Original vs Corrected

The corrected slab 2 mass as compared to the original filtered results are shown in Figure 125 below.

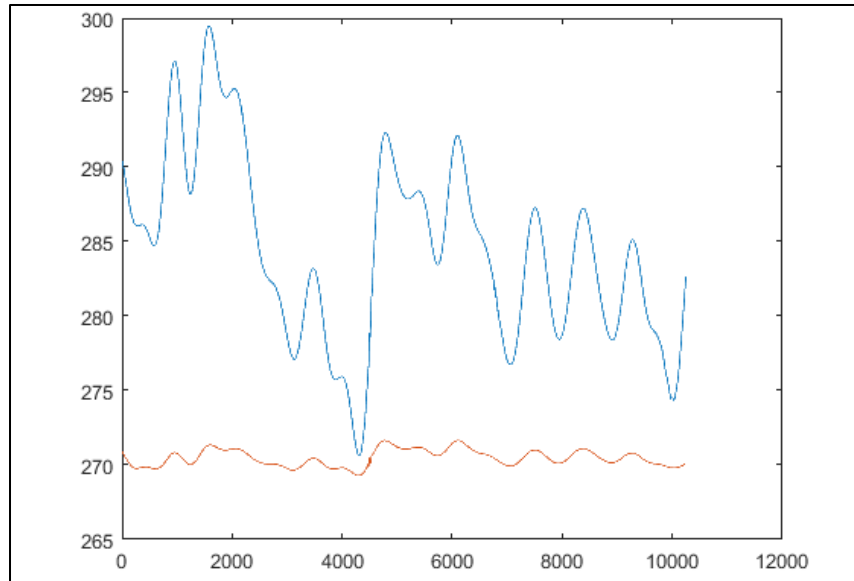


Figure 263: Slab 2 Mass Original vs Corrected

The corrected slab 3 mass as compared to the original filtered results are shown in Figure 126 below.

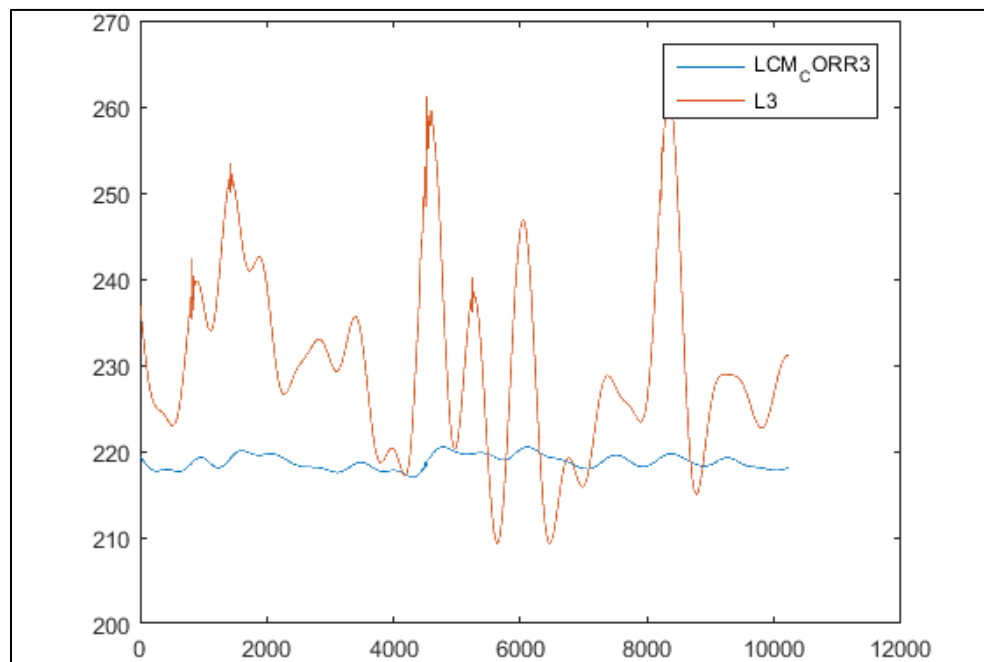


Figure 264: Slab 3 Mass Original vs Corrected

The corrected slab 4 mass as compared to the original filtered results are shown in Figure 127 below.

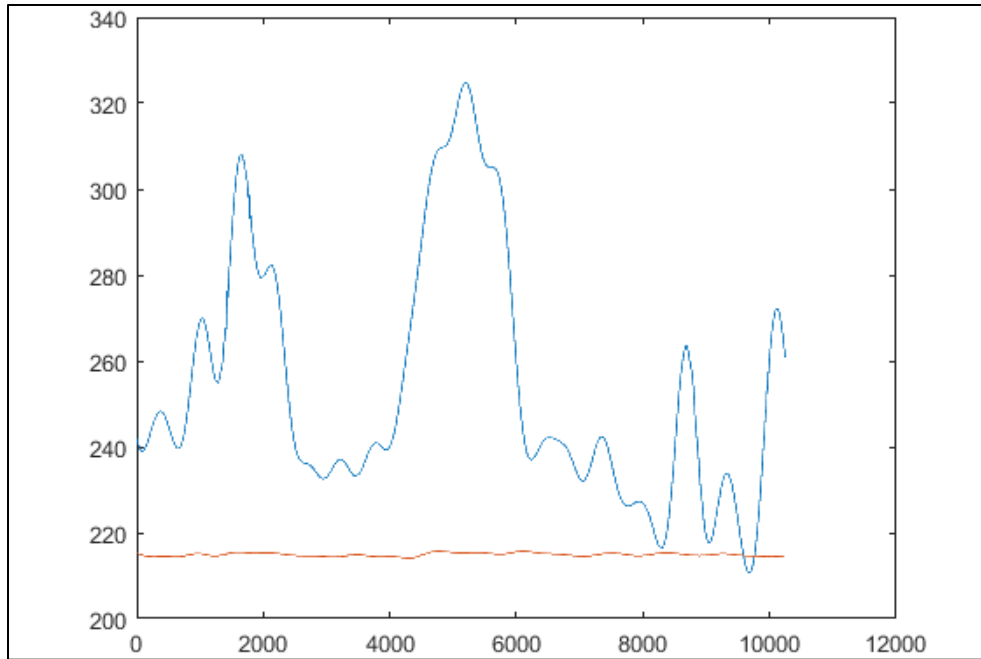


Figure 265: Slab 4 Mass Original vs Corrected

The corrected slab 5 mass as compared to the original filtered results are shown in Figure 128 below.

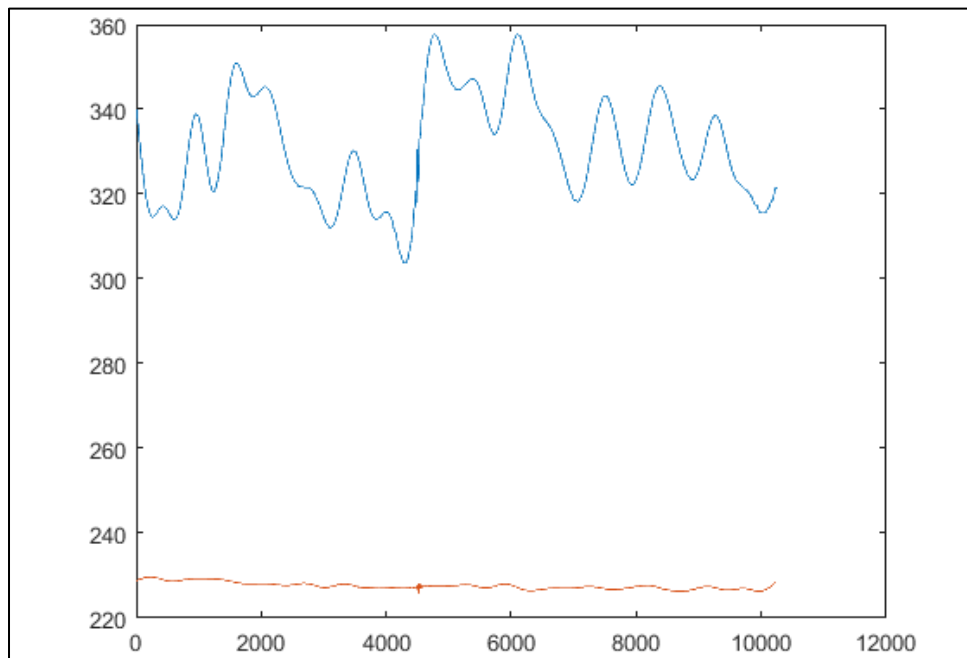


Figure 266: Slab 5 Mass Original vs Corrected

The corrected slab 6 mass as compared to the original filtered results are shown in Figure 129 below.



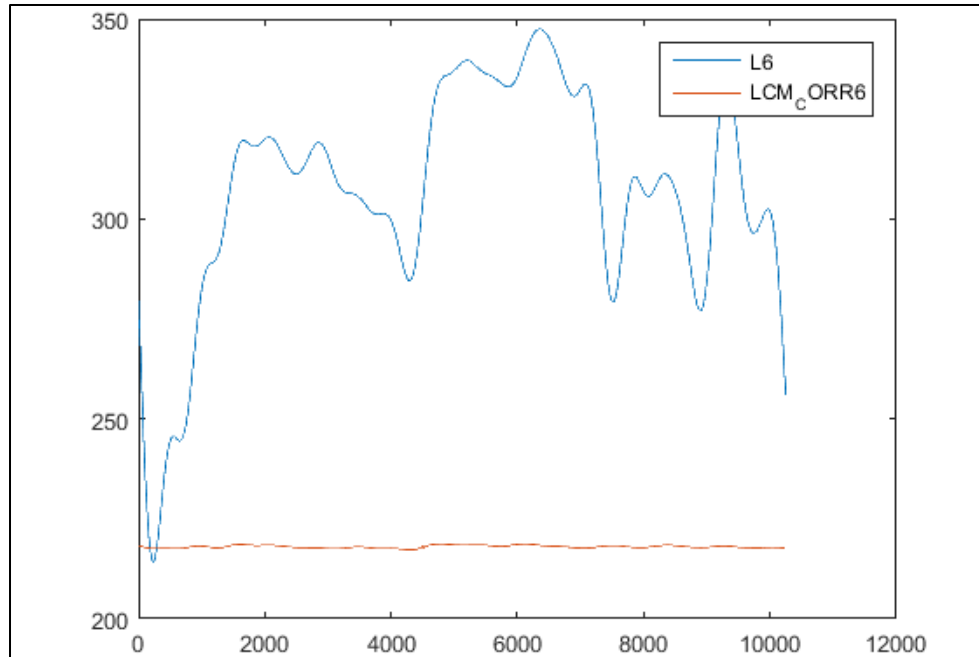


Figure 267: Slab 6 Mass Original vs Corrected

The corrected slab 7 mass as compared to the original filtered results are shown in Figure 130 below.

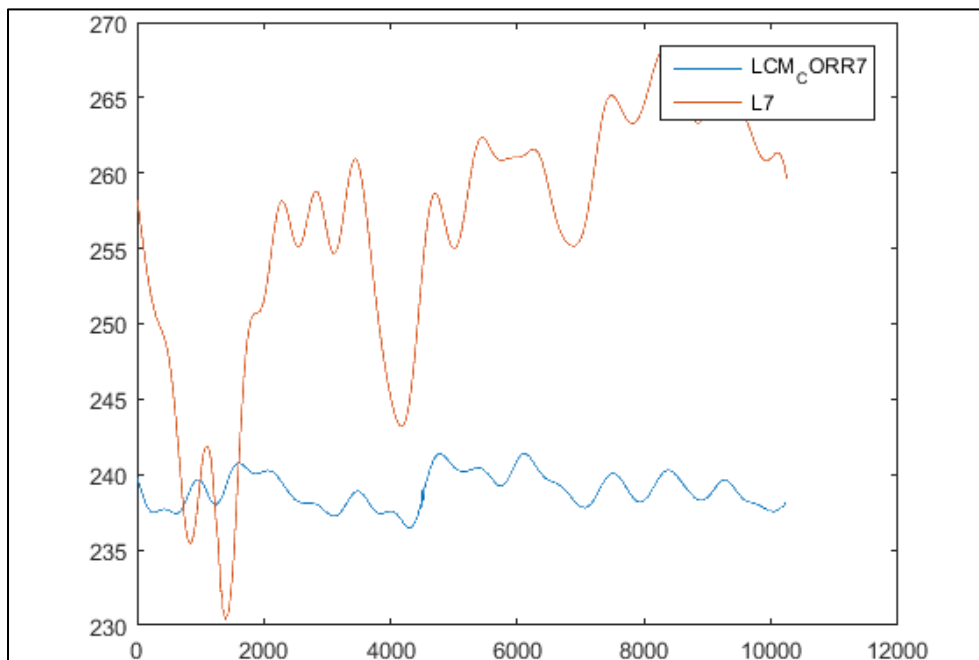


Figure 268: Slab 7 Mass Original vs Corrected

The corrected slab 8 mass as compared to the original filtered results are shown in Figure 131 below.

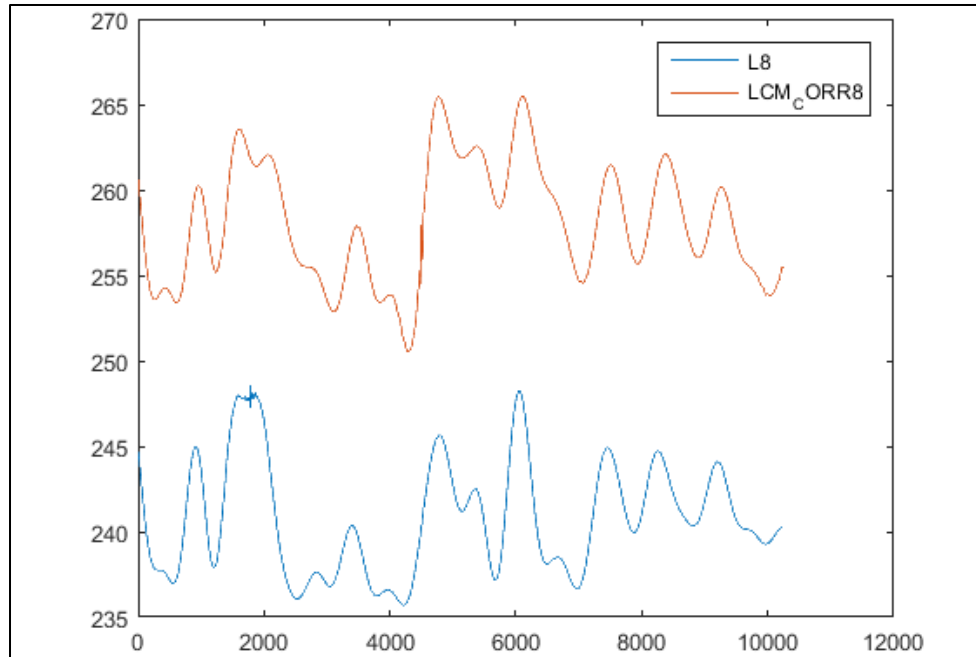


Figure 269: Slab 8 Mass Original vs Corrected

Once each corrected slab mass was determined, the fit as compared to the rain gauge was verified again. Slab 1 calculated mass vs rain event is shown in Figure 132 below.

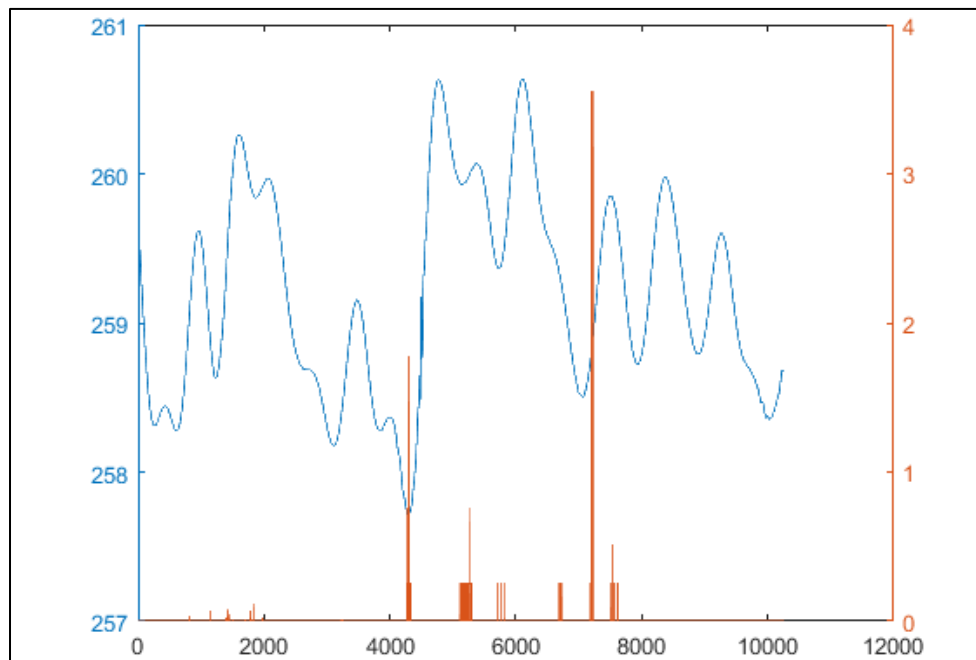


Figure 270: Slab 1 Mass vs Measured Rain events

Slab 2 calculated mass vs rain event is shown in Figure 133 below. The load cell response in lbs. on the left y-axis, rain bucket data in millimeter increments on the right y-axis, and measurement number (consecutive date) on the x-axis.

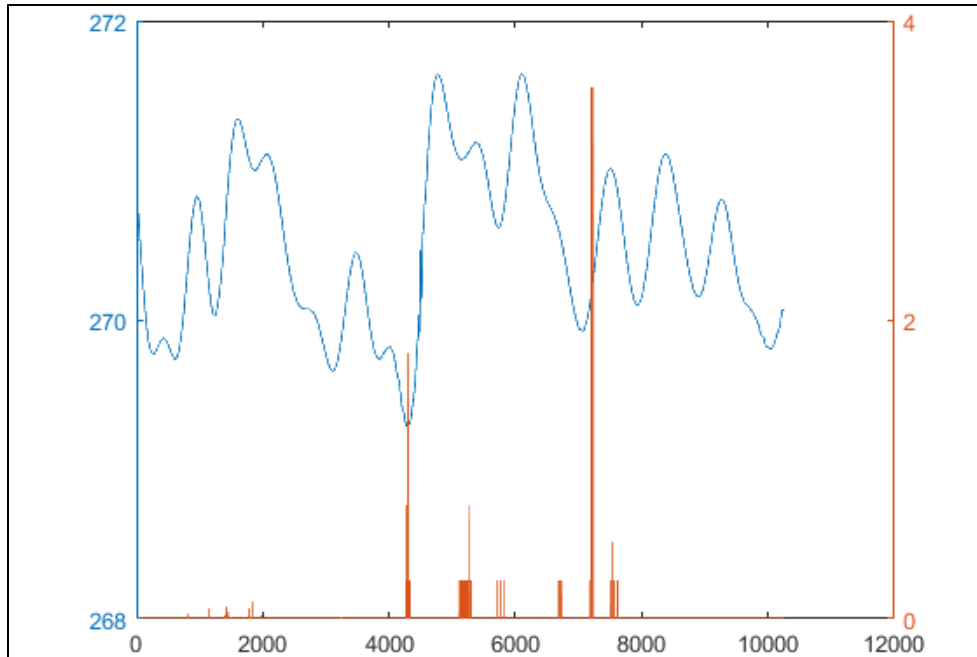


Figure 271: Slab 2 Mass vs Measured Rain Events

Slab 3 calculated mass vs rain event is shown in Figure 134 below. The load cell response in lbs. on the left y-axis, rain bucket data in millimeter increments on the right y-axis, and measurement number (consecutive date) on the x-axis.

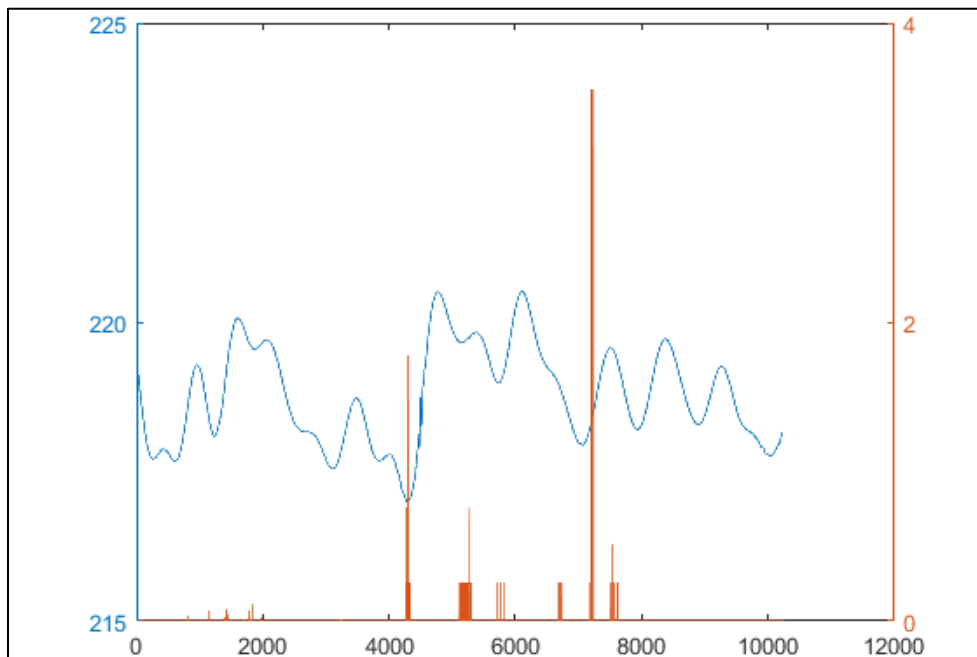


Figure 272: Slab 3 Mass vs Measured Rain Events

Slab 4 calculated mass vs rain event is shown in Figure 135 below. The load cell response in lbs. on the left y-axis, rain bucket data in millimeter increments on the right y-axis, and measurement number (consecutive date) on the x-axis.

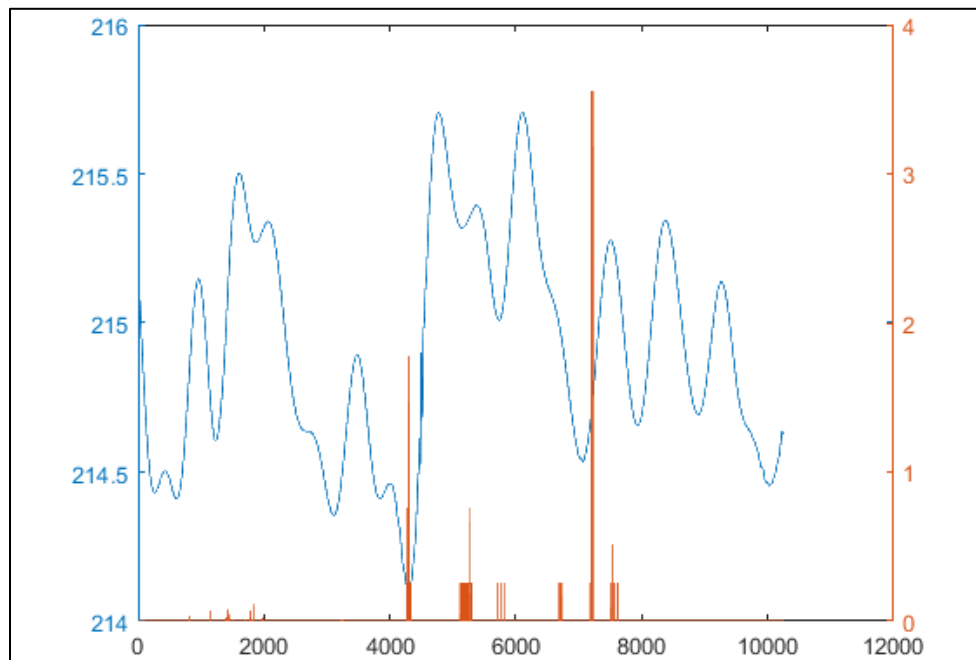


Figure 273: Slab 4 Mass vs Measured Rain Events

Slab 5 calculated mass vs rain event is shown in Figure 136 below. The load cell response in lbs. on the left y-axis, rain bucket data in millimeter increments on the right y-axis, and measurement number (consecutive date) on the x-axis.

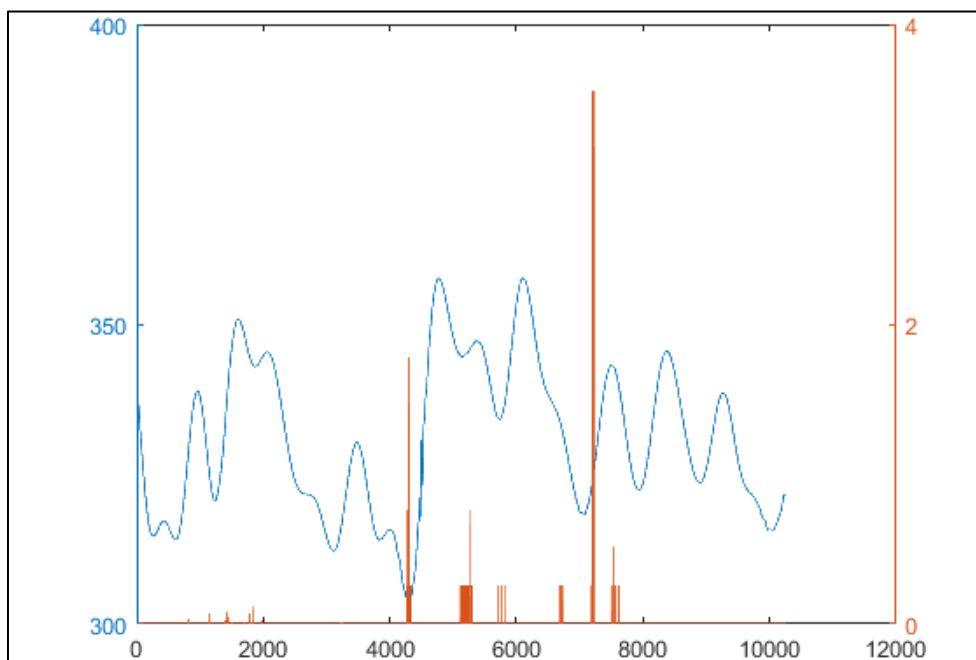


Figure 274: Slab 5 Mass vs Measured Rain Events

Slab 6 calculated mass vs rain event is shown in Figure 137 below. The load cell response in lbs. on the left y-axis, rain bucket data in millimeter increments on the right y-axis, and measurement number (consecutive date) on the x-axis.

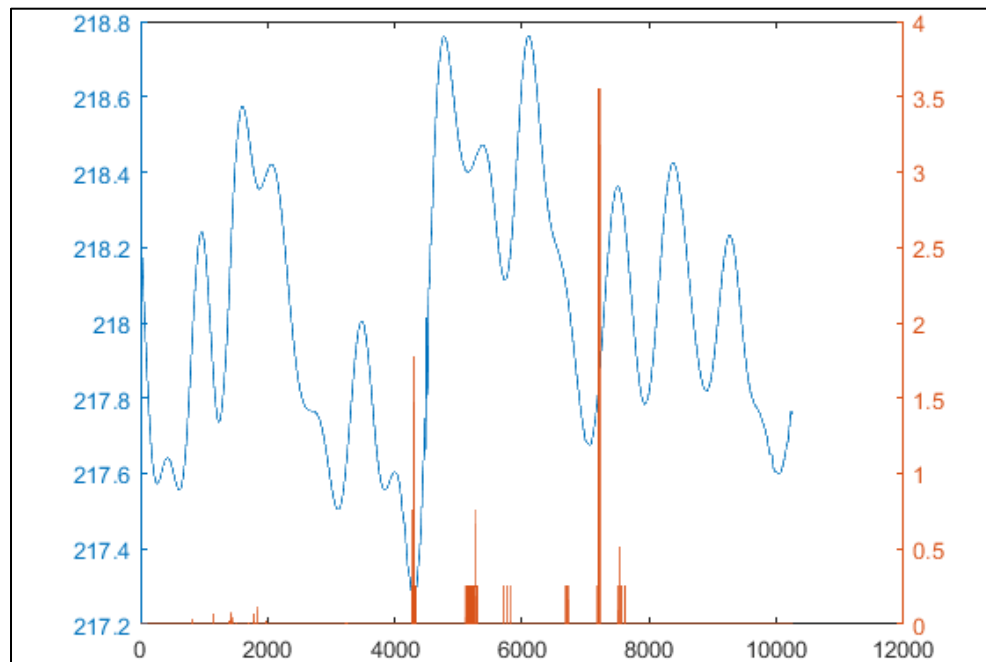


Figure 275: Slab 6 Mass vs Measured Rain Events

Slab 7 calculated mass vs rain event is shown in Figure 138 below. The load cell response in lbs. on the left y-axis, rain bucket data in millimeter increments on the right y-axis, and measurement number (consecutive date) on the x-axis.

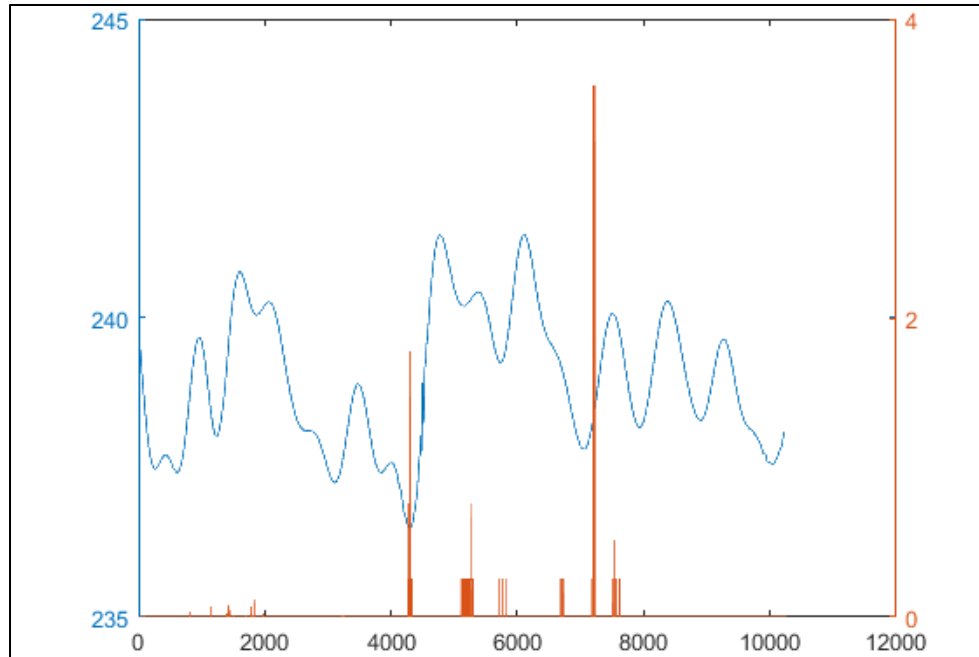


Figure 276: Slab 7 Mass vs Measured Rain Events

Slab 8 calculated mass vs rain event is shown in Figure 139 below. The load cell response in lbs. on the left y-axis, rain bucket data in millimeter increments on the right y-axis, and measurement number (consecutive date) on the x-axis.

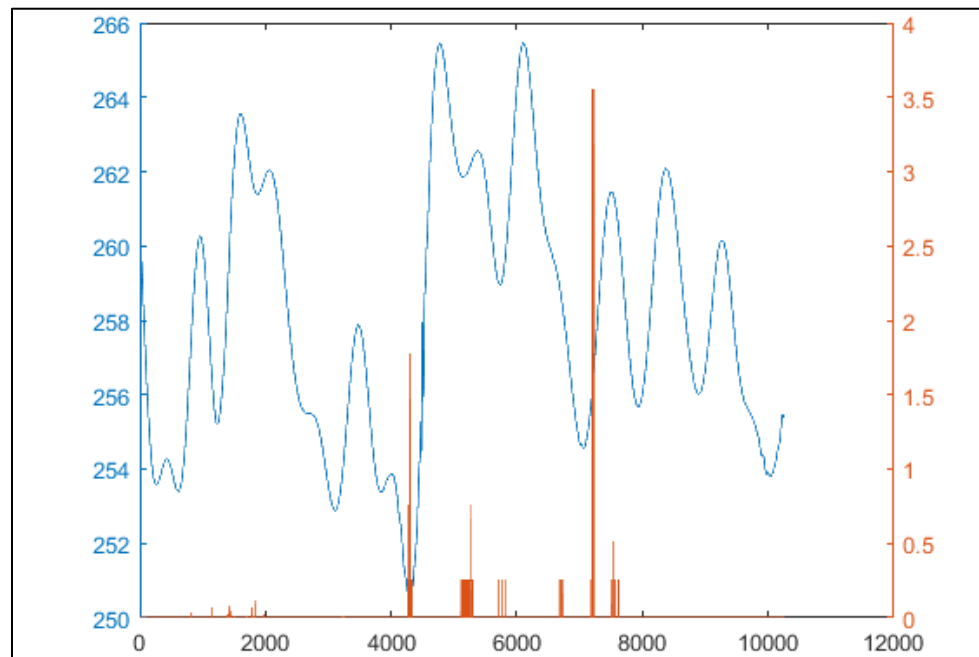


Figure 277: Slab 8 Mass vs Measured Rain Events

Figure 140 displays the mass of water in Slab 1 for July 20, 2017 through July 22, 2017. According to the NCDC, these days include a sunny day, a cloudy day, and a rainy day, respectively. The

load cell response in lbs. on the left y-axis, rain bucket data in millimeter increments on the right y-axis, and consecutive date on the x-axis.

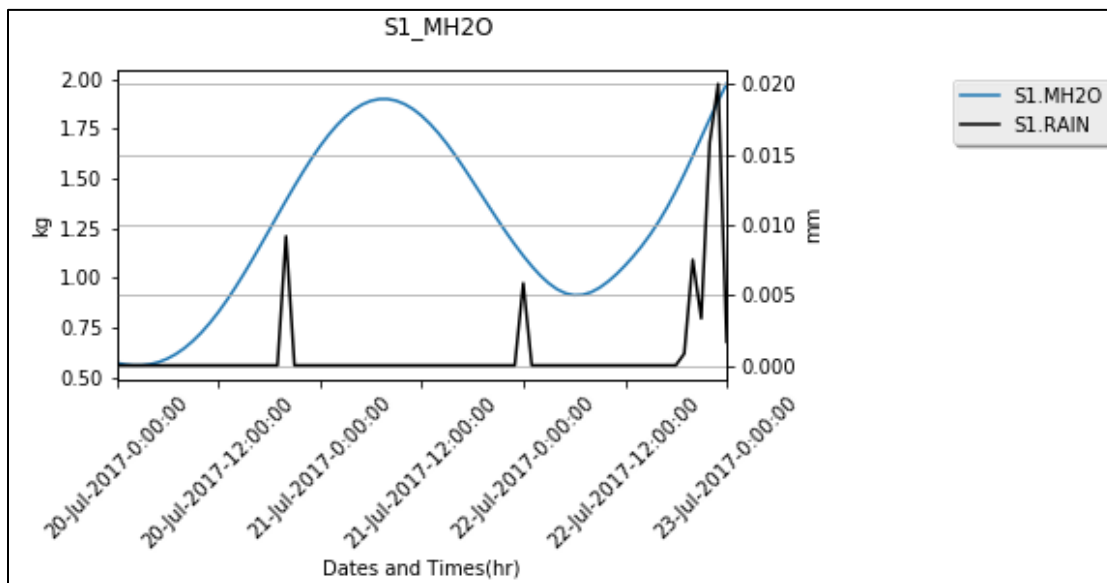


Figure 278: Mass of Water in Slab 1 for July 20, 2017 through July 22, 2017 with Rain Bucket Readings on the Right Axis

Figure 141 displays the mass of water in Slab 2 for July 20, 2017 through July 22, 2017. According to the NCDC, these days include a sunny day, a cloudy day, and a rainy day, respectively. The load cell response in lbs. on the left y-axis, rain bucket data in millimeter increments on the right y-axis, and consecutive date on the x-axis.

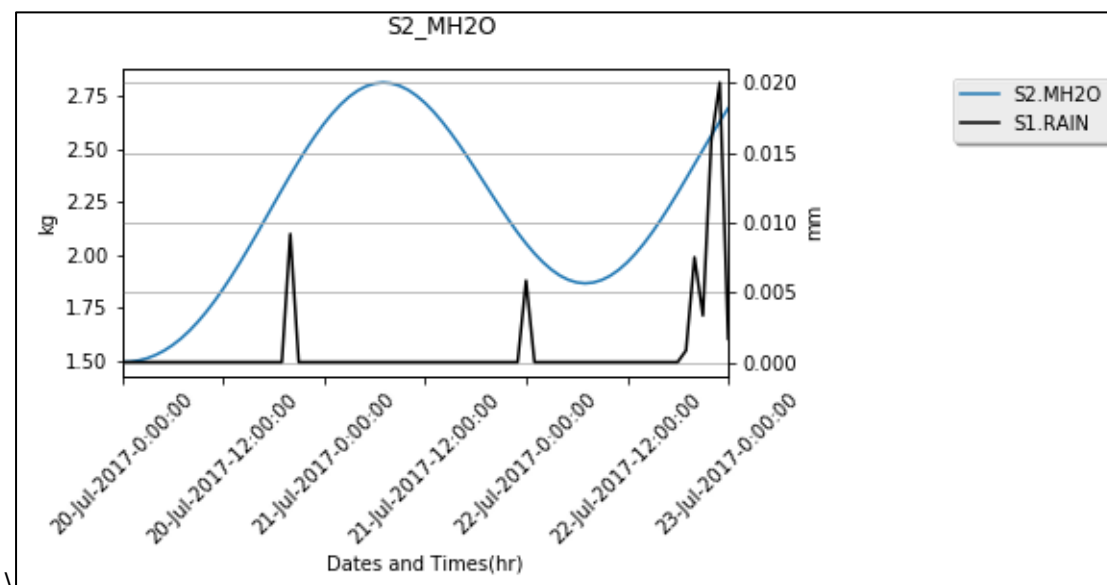


Figure 279: Mass of Water in Slab 2 for July 20, 2017 through July 22, 2017 with Rain Bucket Readings on the Right Axis

Figure 142 displays the mass of water in Slab 3 for July 20, 2017 through July 22, 2017. According to the NCDC, these days include a sunny day, a cloudy day, and a rainy day, respectively. The

load cell response in lbs. on the left y-axis, rain bucket data in millimeter increments on the right y-axis, and consecutive date on the x-axis.

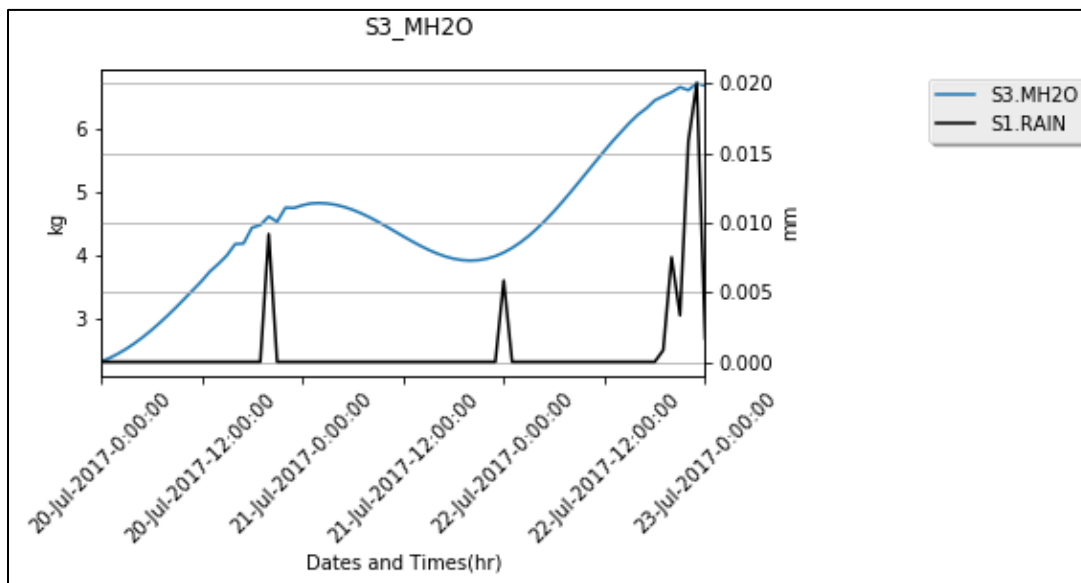


Figure 280: Mass of Water in Slab 3 for July 20, 2017 through July 22, 2017 with Rain Bucket Readings on the Right Axis

Figure 143 displays the mass of water in Slab 4 for July 20, 2017 through July 22, 2017. According to the NCDC, these days include a sunny day, a cloudy day, and a rainy day, respectively. The load cell response in lbs. on the left y-axis, rain bucket data in 0.01mm increments on the right y-axis, and consecutive date on the x-axis.

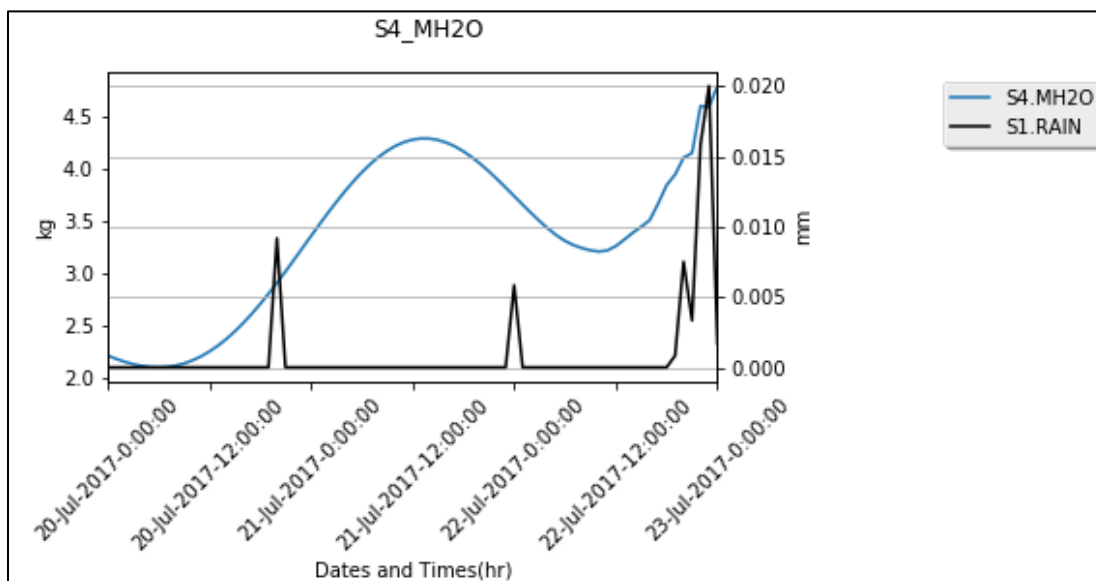


Figure 281: Mass of Water in Slab 4 for July 20, 2017 through July 22, 2017 with Rain Bucket Readings on the Right Axis

Figure 144 displays the mass of water in Slab 5 for July 20, 2017 through July 22, 2017. According to the NCDC, these days include a sunny day, a cloudy day, and a rainy day, respectively. The



load cell response in lbs. on the left y-axis, rain bucket data in millimeter increments on the right y-axis, and consecutive date on the x-axis.

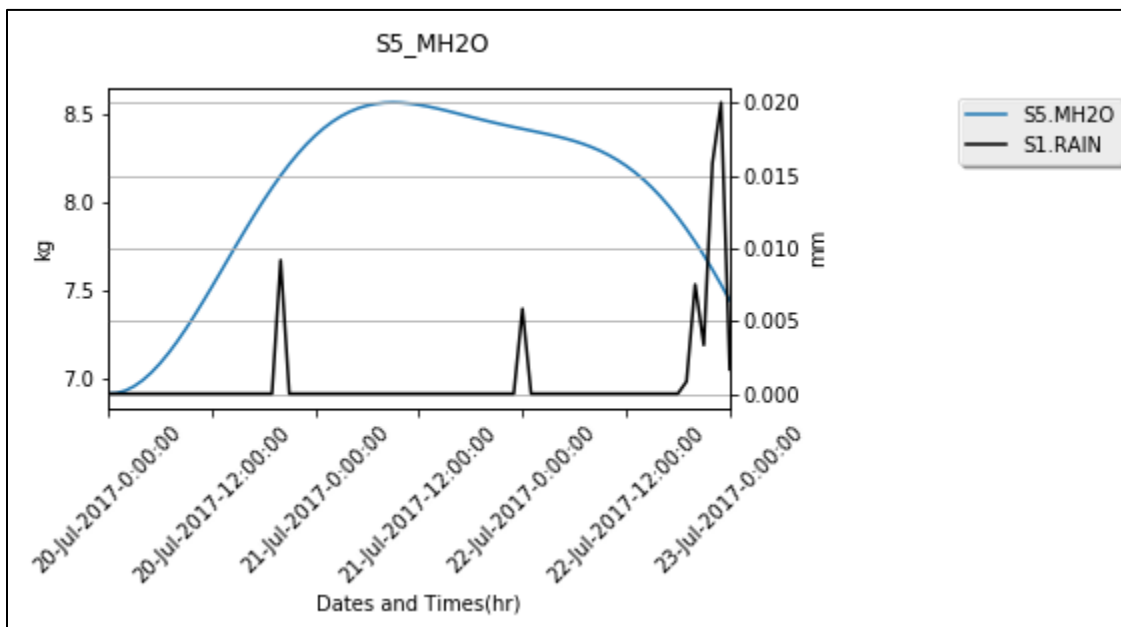


Figure 282: Mass of Water in Slab 5 for July 20, 2017 through July 22, 2017 with Rain Bucket Readings on the Right Axis

Figure 145 displays the mass of water in Slab 6 for July 20, 2017 through July 22, 2017. According to the NCDC, these days include a sunny day, a cloudy day, and a rainy day, respectively. Rain bucket readings are displayed on the right axis.

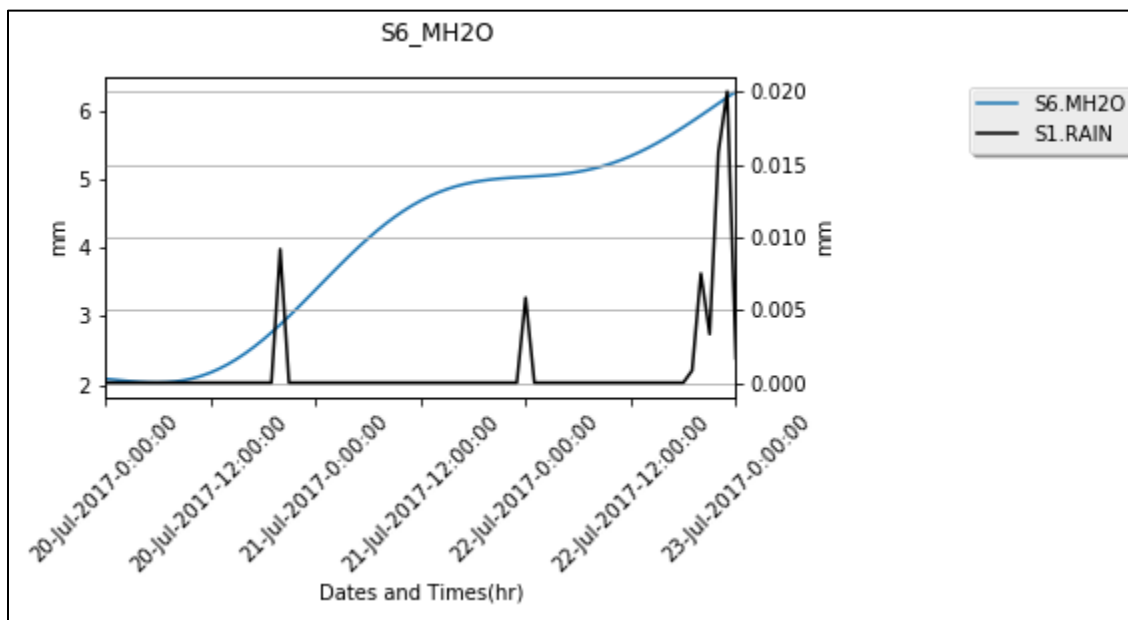


Figure 283: Mass of Water in Slab 6 for July 20, 2017 through July 22, 2017 with Rain Bucket Readings on the Right Axis

Figure 146 displays the mass of water in Slab 7 for July 20, 2017 through July 22, 2017. According to the NCDC, these days include a sunny day, a cloudy day, and a rainy day, respectively. The

load cell response in lbs. on the left y-axis, rain bucket data in millimeter increments on the right y-axis, and consecutive date on the x-axis.

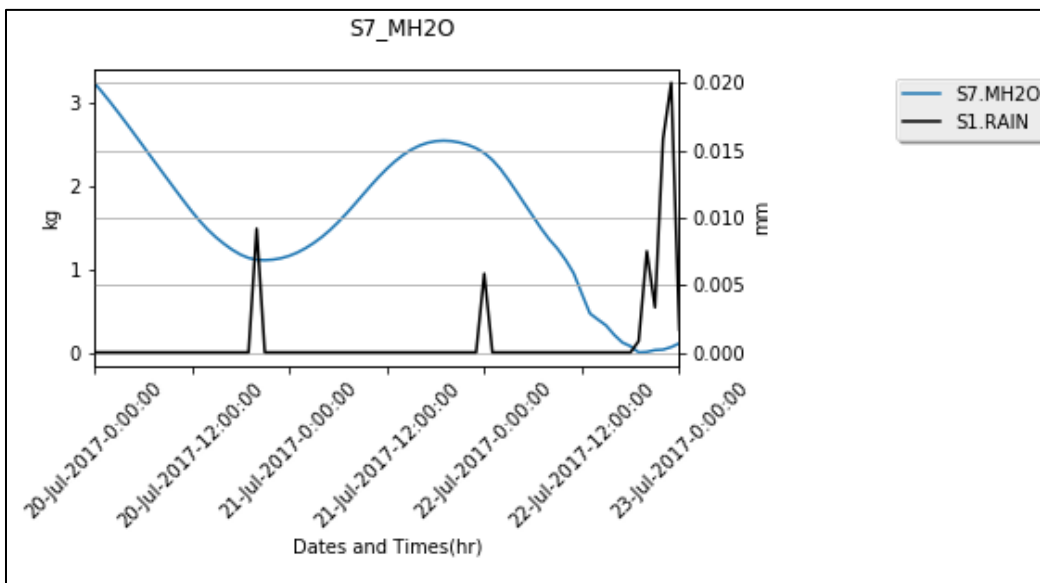


Figure 284: Mass of Water in Slab 7 for July 20, 2017 through July 22, 2017 with Rain Bucket Readings on the Right Axis

Figure 147 displays the mass of water in Slab 8 for July 20, 2017 through July 22, 2017. According to the NCDC, these days include a sunny day, a cloudy day, and a rainy day, respectively. The load cell response in lbs. on the left y-axis, rain bucket data in millimeter increments on the right y-axis, and consecutive date on the x-axis.

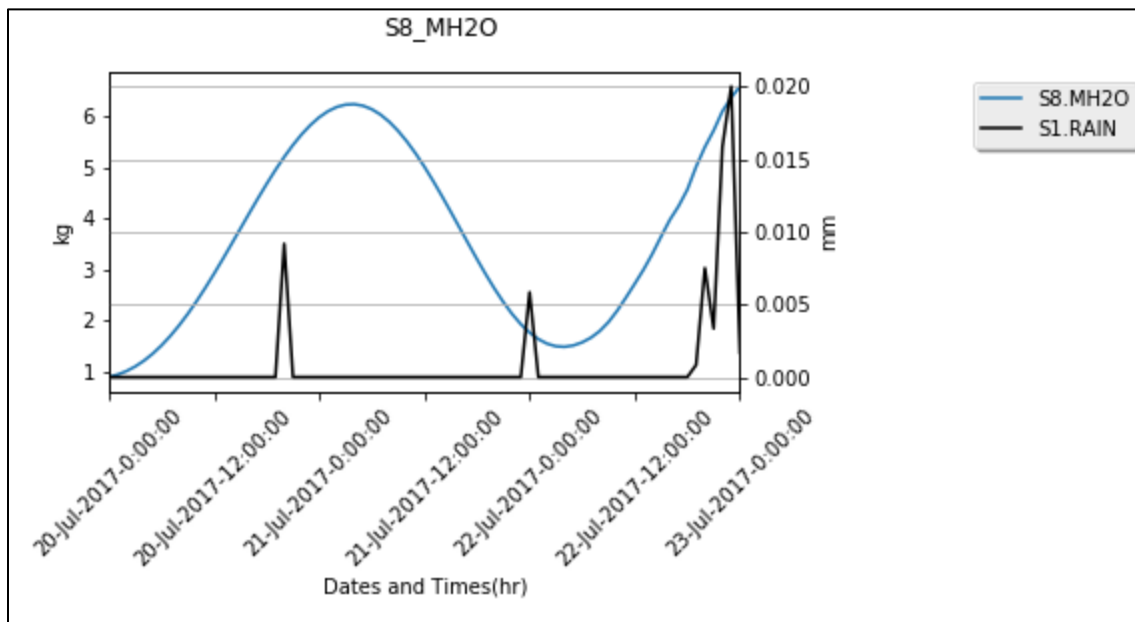


Figure 285: Mass of Water in Slab 8 for July 20, 2017 through July 22, 2017 with Rain Bucket Readings on the Right Axis

# Density Determination

Bulk Density, Apparent Specific Gravity, and the Theoretical Maximum Specific Gravity of the pervious mixes was determined in the laboratory using a modified Air-Void Percentage method (Using Core-Lok Bag Density ASTM D6752, ACI 211.1-91) which first required the technician to follow the following procedure. First the technician ensured the samples were dry. Then the technician would record the dry mass of the sample in air. Then the technician recorded the mass of the Cor-Lok bag before vacuum sealing the bag to the sample. The technician would then record the mass of the sample in bag after vacuum sealing to verify the mass of bag plus sample. The vacuum sealed sample would then be placed in a water bath on a balance hanger for four minutes to ensure there were no leaks in the bag. At this point, the technician would record the sealed buoyant mass. After pulling the sample from the water, the technician would dry the bag, verify the mass, and then cut off the bag. Very often the bag would leak, which would result in false measurements. Those measurements were disregarded, the samples were required to dry again, then that portion of the test could be repeated by the technician. Once the vacuum bag buoyant mass was determined, the sample would then be placed in a pycnometer mounted on a vibrating plate. The sample was placed under water in the pycnometer and vacuum was applied at 25 in Hg (635.00 mm Hg) for four minutes. During the four minute period, the vibrating table would be applied for three minutes. After the saturation process was completed, the entire pycnometer would be placed in the water bath before transferring the sample entirely underwater to the balance hanger. After a four minute normalization period, the fully saturated mass would be recorded.

Bulk Specific Gravity was calculated using the following equation:

$$\text{Bulk specific gravity } (G_{mb}) = A [B - E - (B - A) / F_t]$$

Where:

*A = mass of the dry sample in air before sealing*

*B = mass of the dry sealed sample*

*E = mass of the sealed sample in water*

*F<sub>t</sub> = apparent specific gravity of the plastic sealing material at 25 °C, when sealed, (provided by the manufacturer) (0.7)*

Apparent Specific Gravity was calculated using the following equation:

$$\text{Apparent specific gravity} = A [B - C - (B - A) / F_{t1}]$$

Where:

*C = mass of the unsealed sample in water (total saturation)*

*F<sub>t1</sub> = apparent specific gravity of plastic sealing material at 25 °C, when opened underwater, (still need to get this number (assumed F<sub>t</sub> for the time being)*



The Bulk Specific Gravity and Apparent Specific gravity were corrected for water bath water density at various measurement temperatures based on the following equation:

$$\rho_{H_2O} = 2 \times 10^{-5} x^3 - 6.3 \times 10^{-3} x^2 + 2.69 \times 10^{-2} x + 1000$$

The Theoretical Maximum Specific Gravity was calculated using the following equation:

Theoretical maximum specific gravity =

$$G_{MM} = A / (A - C)$$

This was then utilized to determine the Effective AV percentage based on the following equation:

$$\text{Effective Air-Void Content (\%)} = 100 * (1 - G_{mB}/G_{MM})$$

Once the Apparent Specific Gravity, Bulk Specific Gravity, and Maximum Specific Gravity was determined, it was necessary to conduct a separate test to determine the Maximum Effective Moisture Content. Since the air voids could only fill if the sample were overtopped, the Effective water content metric was designed to represent the maximum amount of water that the sample could hold in service, by following the following procedure: Dry samples were fully submerged in the water bath for less than 1 minute. After that, the sample would be placed on an open-aired wire rack for four minutes, or effectively once the dripping stopped. The mass was recorded at that point and the following equation was utilized to determine the Modified Saturated Surface Dry measurement or Maximum Effective Moisture Content:

$$\text{Max Effective Water (\%)} = \frac{\text{Mass of Stored water}}{\text{Dry Mass of Sample}}$$

## Final Analysis and Results

### Mass H2O Slab

After the load cell filtering procedure was completed and the load cell signals were averaged as shown in Table 32, the load cell data was adjusted so that the minimum signal was set to the minimum mass of the dry sample. The dry mass of the sample was determined by the following equation:

$$\text{SlabMassDry} = (\text{Slab } G_{SB} * 1000) * \text{Slab Volume}$$

The maximum of the load cell signal was set to the maximum effective water content for each mix independently using the following equation:

$$MaxWetMass = ((SlabMassDry * (\%SSDm/100)) + SlabMassDry)$$

The correction curve was determined using the following equation:

$$LC\_CORR = (Drymass/wetmass) / (LCsigmin/LCsigmax)$$

The density of the slab water was corrected for temperature using the following equation:

$$H2O\_CORR = ((0.00002 * ST1\_A^3) - (0.0063 * ST1\_A^2) + (0.0269 * ST1\_A) + 1000)$$

Finally the MH2O was determined using the following equation:

$$MH2O = CorrectedLCMass - SlabMassDry$$

Where: LCMASSCORR is the wet mass of the slab and SM.DS is the dry mass of the same slab.

## Volumetric Water Content Slab

Once the mass of H2O for each slab was determined, the volumetric water content was determined using the following equation:

$$Slab \%VWC = (MassH2O/Sl\_H2O\_Corr/SlabVol*100)$$

Where MassH2O was the mass of water per slab, H2O\_Corr was the density correction factor, and SlabVol was the total slab volume.

## Total Energy Budget

As stated in the introduction, the net radiation equation is as follows:

$$dE/dt = R_{long} + R_{short} + Le + G + H$$

Where dE/dt is the change in energy over time of the system, R<sub>long</sub> is the net longwave radiation, R<sub>short</sub> is the net shortwave radiation, Le is the latent heat flux, G is the ground heat flux, and H is the sensible heat flux. R<sub>long</sub> and R<sub>short</sub> are both directly measured by the net radiometers. The ground heat flux is assumed to be zero over the measuring window.

## Sensible Heat Flux Calculations

The sensible heat flux is determined with the follow equation:

$$H = -\rho C_p (T_a - T_s) r_H$$

Where the air density in  $\text{kgm}^3$ ,  $C_p$  is the specific heat of air taken as  $1005 \text{ kgm}^2/\text{Ks}^2$ ,  $T_a$  is the ambient air temperature in deg C,  $T_s$  is the temperature of the air near the surface of the slab, and  $r_H$  is the roughness coefficient taken as 100. The roughness coefficient ranges from 20 to 100 depending on surface conditions. Due to the nature of the testing site, with two buildings and high grass surrounding, 100 was chosen as the roughness coefficient.

For this experiment, we took the ambient air temperature from the roof weather station at a height of approximately 7 m. The air temperature near the surface of the slab was taken at a height of 25 cm above Slab 4.

Moist air density was determined with the following equation:

$$\rho_{air} = BP * R_d * T_a$$

Where BP is the barometric pressure in Pa and  $R_d$  is the specific gas constant of dry air. Barometric pressure was taken at a height 1 m. The specific gas constant for dry air was  $287.058 \text{ JkgK}$ .

A graph of the sensible heat flux is presented in Figure 148.

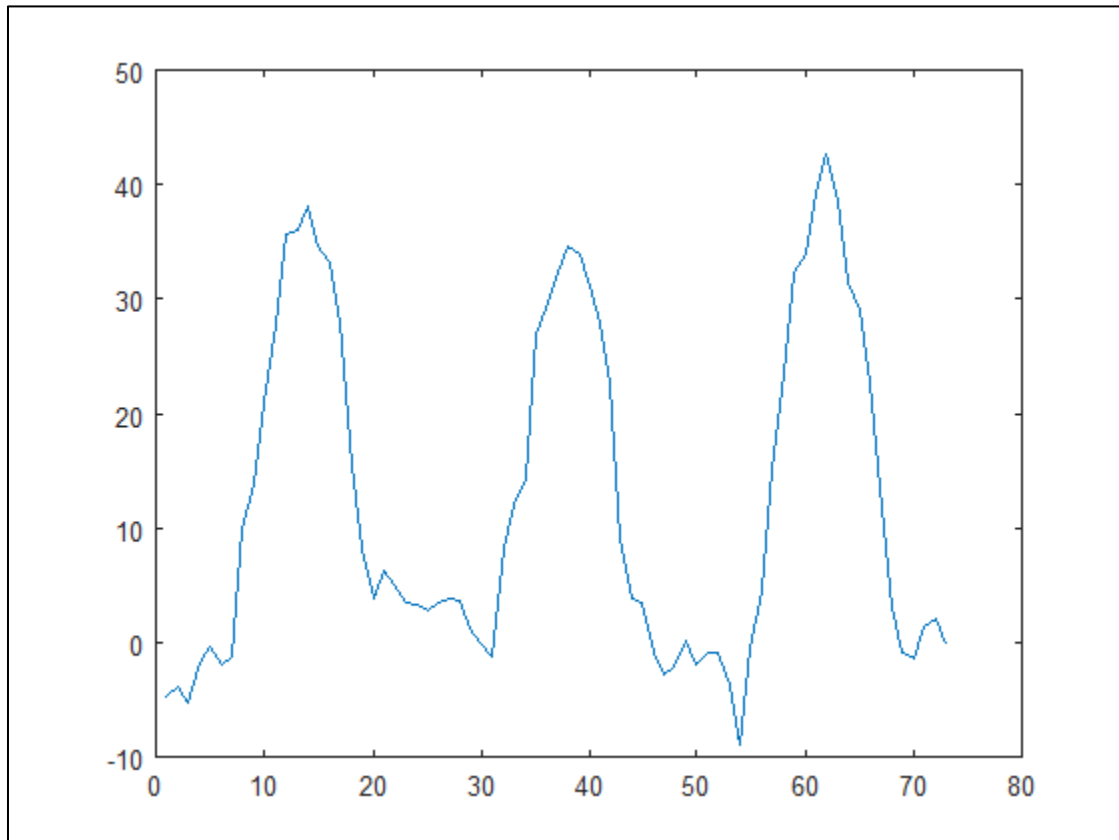


Figure 286: The sensible heat flux for July 20 - 22, 2017

Integration of the curves resulted in a sensible heat flux of 917 W/m<sup>2</sup>.

## Latent Heat Flux Calculations

The latent heat flux was determined with the following equations:

$$Le = \rho_{air} He Ce U (q_s - q_a)$$

Where  $\rho_{air}$  is the air density in gcm, He is the latent heat of vaporization for water taken as 2500 Jkg, Ce is the bulk transfer coefficient for moisture taken as 0.001, U is wind speed in ms,  $q_s$  is the specific humidity at the slab-surface interface in gkg, and  $q_a$  is the specific humidity of the air column.

To determine the specific humidity of the air ( $q_a$ ) column the following equations were used:

$$q_a = w / (w + 1)$$

$$W = e R_d R_v (BP - e)$$

$$e = RH^* e_s$$

$$e_s(T) = e_{s0} [ (L_v(T) R_v (1/T_0 - 1/T) ]$$

To determine the specific humidity of the slab-surface interface ( $q_s$ ), RH in the above equation was assumed to be the %VWC<sub>slab</sub>

Where  $R_v$  is the specific gas constant of water vapor taken as 461.295 JkgK,  $L_v(T)$  is the specific enthalpy of vaporization for water JkgK, RH is the relative humidity of the air,  $T_0$  is a reference temperature set to 273.15 K (0 deg C), T is the average slab temperature, and  $e_s(T)$  is the saturation vapor pressure at reference temperature,  $T_0$ .

The specific enthalpy of vaporization for water was determined by using the following relationship:

$$L_v(T) = 4185.8845661367T + 141.019219569016$$

The air density, a, was determined by first calculating the saturated vapor pressure,  $P_{sat}$ , and partial vapor pressure for the air,  $P_v$ . The following equation was used to determine saturated vapor pressure for air:

$$P_{sat} = 6.1078107.5Ts237.3 + Ts$$

And



$$P_v = P_{sat}RH$$

Where RH is the relative humidity measured at the roof weather station at approximately 7 m above the testing slabs.

The density of the moist air in the slab was found using the following equation:

$$\rho_{air} = 1.2929 * (T_0 T_s + T_0) (BP - (0.3873 * P_v) * 1.013e5)$$

The latent heat flux was determined for each of the testing slabs. Figure 149 presents the curves for latent heat flux for the testing dates of July 20 - 22, 2017. Slabs 2, 5, and 7 were excluded because of unexpected trends in the data.

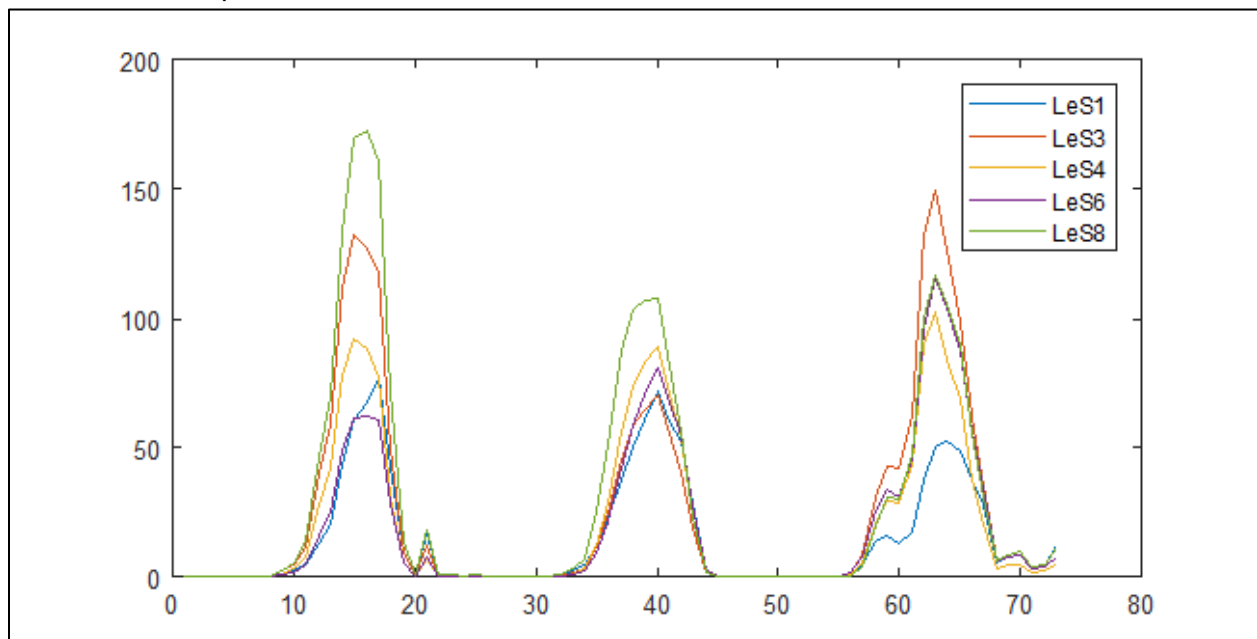


Figure 287: The latent heat flux for July 20 - 22, 2017

Table 33 displays the values found after integrating the curves, which can be compared to the sensible heat flux.

Table 66: The Sensible and Latent Heat Flux for Each Slab

Slab ID	Heat Flux (W/m2)
Sensible Heat Flux	917
Slab 1	1111
Slab 3	1888
Slab 4	1495

Slab 6	1420
Slab 8	2196

The energy flux savings for each slab can be calculated by dividing the latent heat flux for each slab by the sensible heat flux. Table 34 displays the energy budget savings for each slab.

Table 67: The energy budget and savings for each slab

Slab ID	Mix ID	Heat Flux (W/m <sup>2</sup> )	% Benefit vs PRC
Slab 1	PRC	1.212	0
Slab 3	PRC9	2.059	52%
Slab 4	PRC9	1.631	29%
Slab 6	PRC7	1.549	24%
Slab 8	PRC3	2.395	66%

## Albedo

The calculated albedo for this project ranged from 0.42 for PRC-C as the most reflective, while PRC-9 had a measured albedo of 0.18, PRC-7 had a measured albedo of 0.24, and PRC-3 had a measured albedo of 0.19. The calculated albedo for each slab with standard deviation is plotted in Figure 150.

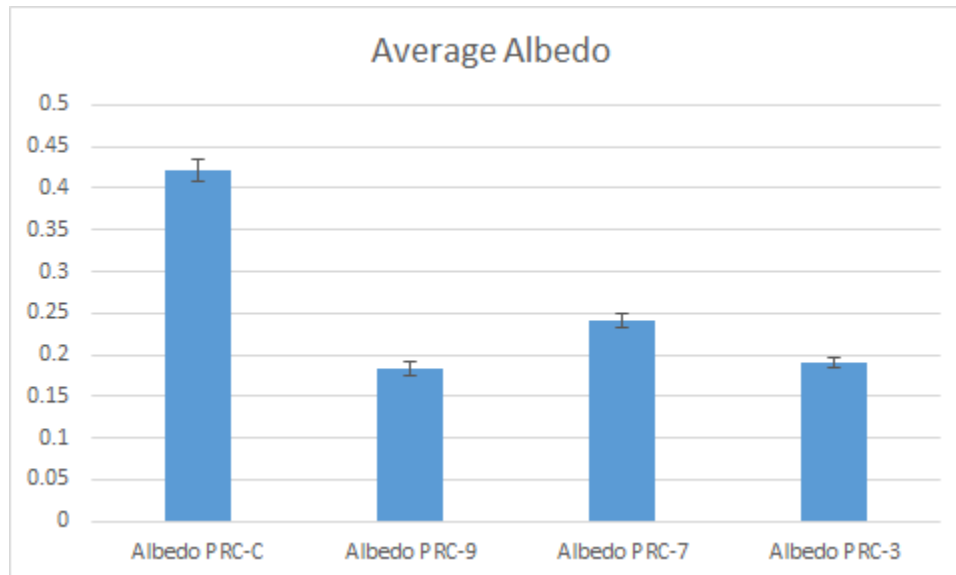


Figure 288: Calculated Albedo for each Pervious Mix Field Sample

# Conclusions

Pervious concrete is a material that has been explored by materials and environmental engineers for several years as an optional surface treatment that can be used to provide particular benefits to reduce storm water runoff and encourage site infiltration. Frequently, this material is suggested to provide additional benefits such as filtering storm water runoff and providing a dry surface during rain events for constituents to enjoy the use of which on high speed vehicular traffic situations correlates to reduced splash and spray. Pervious concrete is typically not used for major load bearing applications, but is mostly limited to sidewalk and other light duty use.

Pervious concrete has some inherent flaws, such as a high propensity to ravel, reduced tensile strength, lower compressive strength as compared to conventional concrete, reduced workability, increased training efforts and increased design costs, and higher costs to implement and maintain. Given these inherent flaws, there are still particular situations where pervious concrete provides additional benefits that can encourage use. When a project is adequate and well-constructed, the benefits can be worth the effort. As a material with benefits aside from simple loading and longevity, environmental benefits need to be quantified to show the true benefit of the material. The important environmental/other benefits that should be quantified for pervious transportation materials should include the increase in good public perception for a department utilizing these materials, reduction of storm water flow, and the effect of the material on the local energy budget.

As with most environmental benefits, quantifying the benefit of a material utilized in the environment presents significant challenges for modeling. Previous studies of pervious concrete has leveraged the results of albedo measured for each material as a method to quantify benefit (5, 6, 11), which although important and easy to measure, does not always directly relate to energy reduction benefits from a particular material. Albedo measurements are also made inaccurate by the use of a single pyranometer, which cannot capture light reflected at oblique angles (measured albedo can be lower due to increasing the number of reflected angles). While it is true that if more light is reflected, less energy will be transferred to that material, it was determined for the purpose of this study to measure the impact of different material choices on localized energy budgets to rank materials based on the reduction in energy transferred to the material vs energy transferred to the phase change of water (i.e. evaporation).

Natural systems, including those with biotic growth, include the process of evapotranspiration where plants utilize energy to conduct work on water as part of photosynthesis. This process increases the local residence time of storm water and groundwater as well as providing a localized cooling effect as the temperature increases, more moisture is retained to ensure the plants viability. Anthropogenic materials utilized for pavements do not provide this water retaining/evapotranspiration benefit, but the assumption made for study in this paper was as follows:

Following the assumption that as materials in the environment heat up, that stored heat impacts the local thermal equilibrium negatively (increase in temperature), which leads to an increase in the urban heat island effect (UHI), if water was able to infiltrate and remain in the pavement material for a period of time after a storm event, that water would be required to undergo a phase change to evaporate before that pavement would increase in temperature. Quantifying the amount of energy utilized to conduct the phase change as opposed to heating the material then provides the benefit the local environment is receiving as compared to a conventional pavement type.

Quantifying local energy budgets is not a new field of research, but when evaluating pavement materials is still relatively in its infancy as compared to research conducted over the sea, jungles, polar ice caps, and the architectural building industry. Benefits found with architectural building can be easily quantified into dollars and cents to show reduced energy savings for winter/summer use, to quantify benefit of different surface materials utilized, and the impacts of different insulation materials. Benefits found for pavement materials are more generally unrecognized by the general public and are typically associated with longevity, construction costs, and turnaround speed for construction; this research helps to quantify additional benefit not typically associated with pavement materials and begins to show how it can impact the greater population.

As explained throughout this report, to determine the energy budget for pavement materials required several test slabs to be constructed to provide in-situ measurements including solar loading and temperature differentials throughout time throughout the pavements, air, and ground. After working through the many moving parts associated with an in-situ implementation such as this, with efforts to provide statistical repeatability and increase accuracy where possible, it was determined that the methodology utilized was the correct approach. The most important and most difficult aspect of this research was the measurement of the water content of each slab. Capacitance and resistance measurement are associated with an inherent flaw where moisture can be locally touching one of the sensors in an air-void and the measured values are then reported inaccurately. Ground-penetrating radar could provide an acceptably accurate measure of water content, but is very time consuming and provides “spot check” measurements, which would be too low of resolution for determining the energy budgets appropriately. This was the metric that made this project stand apart from past studies, where the moisture content was determined by change in mass. Following this methodology also proved to be the most difficult to set up and there were several pitfalls determined within the load cell section of this report; by following a similar methodology but using better load cells, better extension wires and better control mechanisms one would be able to provide a more accurate quantification of the benefit of pervious materials.

As a result of this project, it was determined that pervious concrete materials, as related to conventional concrete materials, provided a reduction in the local energy budget ranging from 24%-66% depending on material. The overall surface color of each mix, whether or not fly ash

was present, and the aggregate size were the major differences between the mixes studied for this project. The aggregate geology utilized were similarly sourced and had similar thermal properties aside from gradation and maximum aggregate sizes. At the time of writing this final report, the authors concluded that one of the major drivers of the quantified benefit related to the mix porosity and the ability to retain some of the water through absorption (aggregate and cement paste), adhesion and capillary forcing. This creates an unfortunate conundrum where the environmental benefit curve (reduction of UHI with increased moisture content) would have a practical limit determined by the materials susceptibility to raveling and cracking potential as a function of slab moisture, which would need to be optimized. Additional benefits can also potentially be found by changing the aggregate geology or the color of the mix, either by aggregate/pozzolanic material selection or the impregnation of artificial color.

While the solar benefits determined in this subtask of this pervious concrete project were not included in the life cycle assessment of the material, the next logical step would be to include the benefit over time to quantify the perceived benefit over time and to paint the pervious materials in a better light. While pervious materials are lacking in the strength and are prone to raveling, there are other benefits that set them aside from conventional concretes. These long term benefits to the environment must be quantified to show the true benefits of the pervious materials ability to functionally reduce local impacts to the urban heat island effect. As with many best management practices utilized to reduce urban heat island effect, using a pervious pavement is not a grand all-encompassing solution, but one of many pieces of a puzzle. The more of these best management practices that can be utilized on a project by project basis increases the overall chance of making a beneficial impact on the urban environment and begin to reduce the anthropogenic impacts on the local natural environment.

## Future Research

Although this study of pervious materials was a fairly robust study, due to time constraints the measurement period was only effective between July 18, 2017 and August 22, 2017. It would be preferential to take measurements throughout each season to help create a better annual model. Additional research should be considered for additional pervious concrete mixes with different source aggregates of different color and size. Comparisons between conventional asphalt and concrete mixtures compared to pervious asphalt and concrete mixtures should be conducted. An on-site cloud meter, such as a passive cloud cover detector would help determine sky conditions better than deriving data from offsite. The load cell mass measurement to determine slab mass was a step in the correct direction, because all other methods of determining slab moisture content or mass of water held within the slab are fundamentally flawed, but to increase the accuracy and precision of the slab mass calculations, additional research utilizing signal amplifiers and single-shielded extension wire should be utilized. Another approach to studying the energy budget of surface materials would be to experiment inside a controlled chamber to ensure the desired environmental conditions. Better research to determine specific heat and thermal conductivity of both pervious mix, conventional mix, source aggregates, and cementitious material should be conducted as well.



# Acknowledgements

The authors would like to acknowledge several people for their dedicated help throughout this project. First, We would like to acknowledge Ricardo Arocha from Weldon Industries Inc. for providing critical mix design information, industry insight, and donating 12 tons of aggregate to make the foundations and slabs for this project. We would like to thank Frank Moon for allowing us to borrow a Campbell AM16/32 multiplexer for use on this project. Brandon Banham, from Campbell Scientific Inc. was also an instrumental help to the project by preparing a new wire diagram and initial program to measure the load cell response. He also helped troubleshoot load cell signal issues and rewrote the measurement program several times. We would like to thank Thomas Bennert for the use of his laboratory space and aggregate testing equipment throughout the project.

Seven graduate students assisted in various ways: We would like to acknowledge Helen He and Scott Buxbaum for assistance throughout the slab construction phase of the project. Helen and Scott also conducted the mixing for the structural component of the project and their familiarity with the pervious mixes led to the field samples success. Salah Hameed helped with aggregate sourcing, while Alaa Abd Ali helped construct the field samples and helped calibrate the load cells. Lauren Iacobucci helped with the Campbell program for the load cell and load cell multiplexer. Michael Tulanowski helped creating thermocouples and wiring equipment, immensely throughout both the foundation construction and slab construction processes, mold construction, and theoretical discussion. Edwin Haas helped determine equipment functionality and with theoretical discussion throughout the entire project.

Seven undergraduate students also helped significantly throughout the project. The authors would like to thank Muneshwar Sharma for help with foundation construction and aggregate testing. Mr. Sharma also completed a special problems class evaluating aggregate for this project. Taylor Niles proved instrumental throughout the foundation construction process. He also completed a special problem class where he helped create the constant head permeability test apparatus and procedure, as well as testing the hydraulic conductivity of the first round of pervious concrete samples. Jessie Feng helped prepare the admixtures and field mix conformance samples. Lyra Saranglao and Jane Peterken helped conduct hydraulic conductivity testing throughout this project to provide falling head results as well as conducting the density testing on the field and laboratory samples. Matthew Anderson helped reduce and analyze the final dataset. Finally Robert Jarrett helped throughout the foundation construction process as well as conducting the hydraulic conductivity and final structural sample preparation.



# References

1. Arnold Jr, C. L., & Gibbons, C. J. (1996). *Impervious surface coverage: the emergence of a key environmental indicator*. Journal of the American planning Association, 62(2), 243-258.
2. Cahill et al. (2005)
3. EPA (1999)
4. Hasse (2010)
5. Li, H. (2012). *Evaluation of cool pavement strategies for heat island mitigation*. University of California, Davis.
6. Li (2013)
7. NJDEP (2016)
8. PDEP (2006)
9. Roseen et al. 2012
10. Roseen et al. 2014
11. Tran, N., Powell, B., Marks, H., West, R., & Kvasnak, A. (2009). Strategies for design and construction of high-reflectance asphalt pavements. Transportation Research Record: Journal of the Transportation Research Board, (2098), 124-130.
12. Wallace, J. M., & Hobbs, P. V. (2006). *Atmospheric science: an introductory survey* (Vol. 92). Academic press.
13. Wang, J., & Bras, R. L. (1998). *A new method for estimation of sensible heat flux from air temperature*. Water resources research, 34(9), 2281-2288.
14. Xu (2010)
15. Yang (2013)

# Appendix

## A: NJDOT Section 606 - Sidewalks, Driveways, and Islands

### SECTION 606-SIDEWALKS, DRIVEWAYS, AND ISLANDS

#### 606.02.01 Materials

THE FOLLOWING IS ADDED TO LIST OF MATERIALS

Pervious Concrete.....	903.11
Coarse Aggregate (No. 57).....	901.03
Non-woven geotextile .....	919.01
White Polyethylene Sheeting.....	903.10

#### 606.03 CONSTRUCTION

THE FOLLOWING SUBPART IS ADDED:

##### 606.03.04 Pervious Concrete Sidewalk

- A. **Subgrade Preparation.** Construct subgrade to ensure that the required sidewalk thickness is obtained at all locations. Ensure the subgrade is compacted by a mechanical vibratory compactor to a maximum density of  $92\% \pm 2\%$  of a maximum dry density as established by ASTM D 1557. . Ensure the prepared subgrade is not disturbed prior to construction. Scarify, regrade and recompact disturbed subgrade prior to concrete placement.
- B. **Aggregate Base Course.** Prior to placing the aggregate base course, place the non-woven geotextile on top of the prepared subgrade. Ensure the geotextile is wrapped around the side and over the top of the aggregate base course extending a minimum of 6-inches from the edge of the top. Place the aggregate base course to a thickness as shown in the Plans. Ensure that required sidewalk thickness is achieved at all locations.
- C. **Forms.** Ensure that the forms are thoroughly cleaned and treated with a material that will prevent adherence of the concrete to the forms without discoloring the concrete prior to each use of the forms.
- D. **Expansion Joints.** Construct ½-inch wide expansion joints, placed at intervals of approximately 20 feet, with preformed joint filler. Ensure that the expansion joint material extends to the full depth of the concrete.
- E. **Placing Concrete and Finishing.** Obtain RE approval of formwork and joint placement before placing concrete. Place concrete according to the limitations specified in 504.03.02.C. Ensure the placement of pervious concrete also is in accordance with ACI 522.1. Do not use steel trowels or power finishing equipment. Finish the sidewalk to the elevation and thickness specified in Plans.
- F. **Curing.** Place polyethylene sheeting on the finished surface within 20 minutes of concrete discharge. Completely cover the sidewalk surface with polyethylene sheeting. Cut sheeting to a minimum of full placement width. Secure polyethylene sheeting without using dirt. Cure sidewalk for a minimum of 7 uninterrupted days.

#### 606.04 MEASUREMENT AND PAYMENT

THE FOLLOWING IS ADDED:

<i>Item</i>	<i>Pay Unit</i>
PERVIOUS CONCRETE SIDEWALK	SY

## B: NJDOT Section 903- Concrete

### SECTION 903 – CONCRETE

#### 903.03.05 Control and Acceptance Testing Requirements

##### E. Acceptance Testing for Strength for Pay-Adjustment Items.

No concrete Items are subject to pay adjustment..

##### F. Acceptance Testing for Strength for Non-Pay-Adjustment Items.

THE FIFTH PARAGRAPH IS CHANGED TO:

If cores are taken, the Department will use the core results to determine the final disposition of the lot. If, based on the core results, the lot is determined to be at a quality level of  $PD < 75$ , the Department will compute the pay-adjustment as specified in 903.03.05.E. The Department will not award positive pay adjustment for non-pay-adjustment Items. If the lot is confirmed to be at a quality level of  $PD \geq 75$ , the ME will reject the lot and the RE may do one of the following:

1. Require the Contractor to remove and replace the defective lot
2. Allow the Contractor to leave the defective lot in place and receive a PPA computed by Equation 2.
3. Allow the Contractor to submit a plan, for approval, for corrective action.

THE FOLLOWING SUBSECTION IS ADDED:

#### 903.11 PERVIOUS CONCRETE

##### 903.11.01 Composition

Compose pervious concrete of cement, coarse aggregate, admixtures, and water. Provide materials as specified:

1. Cement: Portland Cement Type I or II conforming to ASTM C 150 or Portland Cement Type IP or IS conforming to ASTM C 595.
2. Aggregate (Pervious Mixture): Use Florida Department of Transportation (FDOT) No. 8 coarse aggregate (3/8" to No. 16) per ASTM C 33 or No. 89 coarse aggregate (3/8" to No. 50) per ASTM D 448. If other gradation of aggregate is to be used, submit data on proposed material to Owner or Agent for approval.
3. Aggregate (Reservoir): No. 2 (2 1/2" to 1 1/2") and No. 57 coarse aggregate (1" to No. 4) per ASTM C 33.
4. Admixtures: Type A Water Reducing Admixtures – ASTM C 494.  
Type B Retarding – ASTM C 494.  
Type D Water Reducing/Retarding – ASTM C 494.

Also, a hydration stabilizer can be utilized and is recommended in the design and production of pervious concrete. This stabilizer suspends cement hydration by forming a protective barrier around the cementitious particles, which delays the particles from achieving initial set. The admixture's primary function should be as a hydration stabilizer; however, it must also meet the requirements of ASTM C 494 Type B Retarding or Type D Water Reducing/Retarding admixtures.

5. Water: Potable or shall comply with Section 919.08.
6. Non-Woven Geotextile Filter Fabric: Geotextile fabric shall be as specified in 919.01 based on application and installation conditions. Verify compatibility between geotextile and adjacent soils for filtration, clogging and permeability and follow manufacturer recommendations for use as subsurface drainage layer between subgrade soils and the aggregate reservoir layer.

##### 903.11.02 Mix Design and Verification

Design at least 1 mix to equal or exceed the verification strengths and other required properties. At least 20 days prior to the start of pervious concrete placement, submit each mix design on concrete mix design forms provided by the ME. Identify the sources of materials and test data on the forms.

ROUTE 9 NORTHFIELD SIDEWALK REPLACEMENT  
CONTRACT NO. 037048027

Page 46 of 53

- A. **Cement Content:** For pavements subjected to vehicular traffic loading, the total cementitious material shall not be less than five hundred fifty (550) pounds per cubic yard.
- B. **Aggregate Content:** The volume of aggregate per cubic yard shall be equal to twenty seven (27) cubic feet when calculated as a function of the unit weight determined in accordance with ASTM C 29 jigging procedure.
- C. **Admixtures:** Admixtures shall be used in accordance with the manufacturer's instructions and recommendations.
- D. **Mix Water:** Mix water shall be such that the cement paste displays a wet metallic sheen without causing the paste to flow from the aggregate. (Mix water yielding a cement paste with a dull-dry appearance has insufficient water for hydration.)
  - Insufficient water results in inconsistency in the mix and poor bond strength.
  - High water content results in the paste sealing the void system primarily at the bottom and poor surface bond.

#### **903.11.03 Mixing for Central Plant and Transit Mixing**

Conform to the requirements of 903.03.03. Truck mixers shall be operated at the speed designated by the manufacturer for seventy-five (75) to one hundred (100) revolutions of the drum. Use the pervious concrete mixture within one (1) hour of the introduction of the mix water, unless otherwise approved by the RE. This time can be increased to ninety (90) minutes when using an extended set control admixture in accordance with an approved mix design.

#### **903.11.04 Mixing on the Project**

Conform to the requirements of 903.03.04. Use the pervious concrete mixture within one (1) hour of the introduction of the mix water, unless otherwise approved by the RE. This time can be increased to ninety (90) minutes when using an extended set control admixture in accordance with an approved mix design.

#### **903.11.05 Control and Acceptance Testing Requirements**

- A. Fresh Density:
  - 1. Determine density using a minimum 0.25 ft<sup>3</sup> cylindrical metal measure. Fill and compact the measure in accordance with ASTM C 1688.
  - 2. Fresh density shall be within  $\pm 5$  pcf of the designed density
- B. In-Place Infiltration:
  - 1. Determine the in-place infiltration in accordance with ASTM C 1701.
- C. Core holes left from samples taken shall be filled with pervious, conventional concrete or pre-blended grout.

## **SECTION 904 – PRECAST AND PRESTRESSED CONCRETE**

#### **904.01.02 Fabrication**

THE ENTIRE SUBPART IS CHANGED TO:

Fabricate precast concrete at a plant as specified in 1011.01 and listed on the QPL.

- 1. **Placing Reinforcement Steel.** Before placing the concrete, place reinforcement steel in position as shown on the approved working drawings and as specified in 504.03.01. Firmly tie the reinforcement to prevent displacement during placing of the concrete.
- 2. **Placing Concrete.** Place concrete as specified in 504.03.02.D and 504.03.02.E. Before placing concrete,

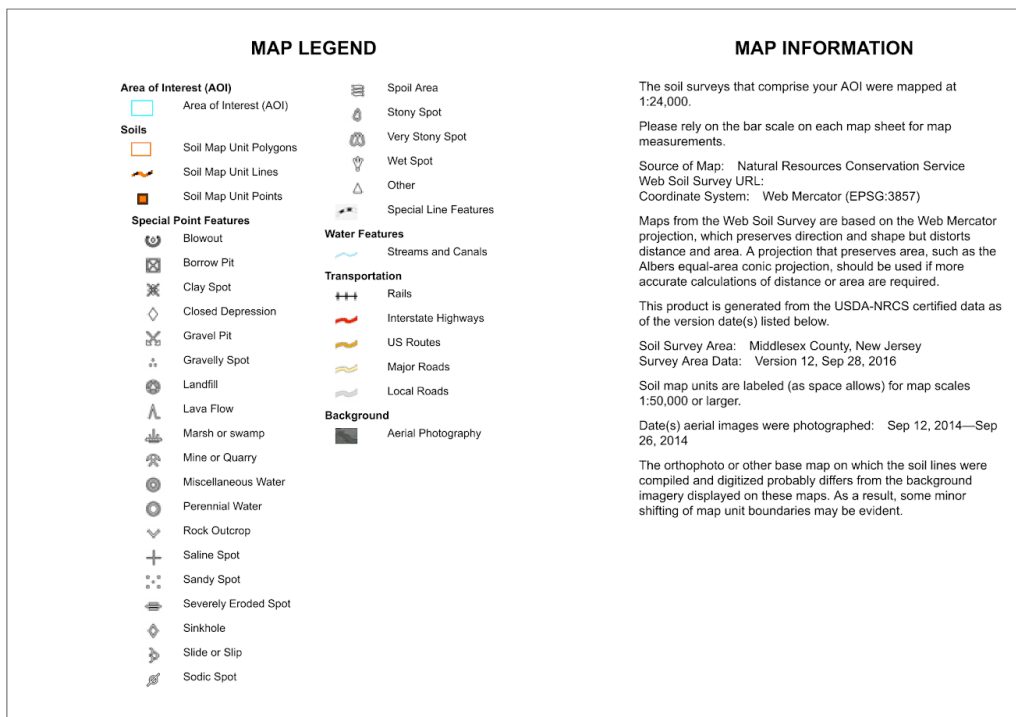
ROUTE 9 NORTHFIELD SIDEWALK REPLACEMENT  
CONTRACT NO. 037048027

Page 47 of 53

## C: Soil Characterization: USDA

### C1: Map





## Map Unit Legend

Map Unit Symbol	Map Unit Name	Acres in AOI	Percent of AOI
KkoB	Klinesville channery loam, 2 to 6 percent slopes	295.9	21.1%
KkoC	Klinesville channery loam, 6 to 12 percent slopes	103.9	7.4%
KkoE	Klinesville channery loam, 18 to 35 percent slopes	56.8	4.0%
KkuB	Klinesville-Urban land complex, 0 to 6 percent slopes	618.0	44.0%
LbuB	Lansdowne-Urban land complex, 0 to 6 percent slopes	8.4	0.6%
LbxA6	Lansdowne moderately deep variant silt loam, 0 to 2 percent slopes	18.0	1.3%
RehA	Reaville silt loam, 0 to 2 percent slopes	62.3	4.4%
RemB	Reaville-Urban land complex, 0 to 6 percent slopes	31.3	2.2%
RorAt	Rowland silt loam, 0 to 2 percent slopes, frequently flooded	94.7	6.7%
UdbB	Udorthents, bedrock substratum, 0 to 8 percent slopes	12.7	0.9%
UR	Urban land	57.7	4.1%
WATER	Water	44.5	3.2%
<b>Totals for Area of Interest</b>		<b>1,404.1</b>	<b>100.0%</b>



## C2: USDA Soil Classification - Description

Map Unit Description: Klainesville-Urban land complex, 0 to 6 percent slopes---Middlesex County, New Jersey

Lab Soil Conditions

### Map Unit Description

The map units delineated on the detailed soil maps in a soil survey represent the soils or miscellaneous areas in the survey area. The map unit descriptions in this report, along with the maps, can be used to determine the composition and properties of a unit.

A map unit delineation on a soil map represents an area dominated by one or more major kinds of soil or miscellaneous areas. A map unit is identified and named according to the taxonomic classification of the dominant soils. Within a taxonomic class there are precisely defined limits for the properties of the soils. On the landscape, however, the soils are natural phenomena, and they have the characteristic variability of all natural phenomena. Thus, the range of some observed properties may extend beyond the limits defined for a taxonomic class. Areas of soils of a single taxonomic class rarely, if ever, can be mapped without including areas of other taxonomic classes. Consequently, every map unit is made up of the soils or miscellaneous areas for which it is named and some minor components that belong to taxonomic classes other than those of the major soils.

Most minor soils have properties similar to those of the dominant soil or soils in the map unit, and thus they do not affect use and management. These are called noncontrasting, or similar, components. They may or may not be mentioned in a particular map unit description. Other minor components, however, have properties and behavioral characteristics divergent enough to affect use or to require different management. These are called contrasting, or dissimilar, components. They generally are in small areas and could not be mapped separately because of the scale used. Some small areas of strongly contrasting soils or miscellaneous areas are identified by a special symbol on the maps. If included in the database for a given area, the contrasting minor components are identified in the map unit descriptions along with some characteristics of each. A few areas of minor components may not have been observed, and consequently they are not mentioned in the descriptions, especially where the pattern was so complex that it was impractical to make enough observations to identify all the soils and miscellaneous areas on the landscape.

The presence of minor components in a map unit in no way diminishes the usefulness or accuracy of the data. The objective of mapping is not to delineate pure taxonomic classes but rather to separate the landscape into landforms or landform segments that have similar use and management requirements. The delineation of such segments on the map provides sufficient information for the development of resource plans. If intensive use of small areas is planned, however, onsite investigation is needed to define and locate the soils and miscellaneous areas.

An identifying symbol precedes the map unit name in the map unit descriptions. Each description includes general facts about the unit and gives important soil properties and qualities.



Soils that have profiles that are almost alike make up a *soil series*. All the soils of a series have major horizons that are similar in composition, thickness, and arrangement. Soils of a given series can differ in texture of the surface layer, slope, stoniness, salinity, degree of erosion, and other characteristics that affect their use. On the basis of such differences, a soil series is divided into *soil phases*. Most of the areas shown on the detailed soil maps are phases of soil series. The name of a soil phase commonly indicates a feature that affects use or management. For example, Alpha silt loam, 0 to 2 percent slopes, is a phase of the Alpha series.

Some map units are made up of two or more major soils or miscellaneous areas. These map units are complexes, associations, or undifferentiated groups.

A *complex* consists of two or more soils or miscellaneous areas in such an intricate pattern or in such small areas that they cannot be shown separately on the maps. The pattern and proportion of the soils or miscellaneous areas are somewhat similar in all areas. Alpha-Beta complex, 0 to 6 percent slopes, is an example.

An *association* is made up of two or more geographically associated soils or miscellaneous areas that are shown as one unit on the maps. Because of present or anticipated uses of the map units in the survey area, it was not considered practical or necessary to map the soils or miscellaneous areas separately. The pattern and relative proportion of the soils or miscellaneous areas are somewhat similar. Alpha-Beta association, 0 to 2 percent slopes, is an example.

An *undifferentiated group* is made up of two or more soils or miscellaneous areas that could be mapped individually but are mapped as one unit because similar interpretations can be made for use and management. The pattern and proportion of the soils or miscellaneous areas in a mapped area are not uniform. An area can be made up of only one of the major soils or miscellaneous areas, or it can be made up of all of them. Alpha and Beta soils, 0 to 2 percent slopes, is an example.

Some surveys include *miscellaneous areas*. Such areas have little or no soil material and support little or no vegetation. Rock outcrop is an example.

Additional information about the map units described in this report is available in other soil reports, which give properties of the soils and the limitations, capabilities, and potentials for many uses. Also, the narratives that accompany the soil reports define some of the properties included in the map unit descriptions.

## Middlesex County, New Jersey

### KkuB—Klinesville-Urban land complex, 0 to 6 percent slopes

#### Map Unit Setting

*National map unit symbol:* 1kv6x

*Elevation:* 250 to 1,300 feet

*Mean annual precipitation:* 28 to 59 inches

*Mean annual air temperature:* 46 to 79 degrees F

*Frost-free period:* 161 to 231 days

*Farmland classification:* Not prime farmland

#### Map Unit Composition

*Klinesville and similar soils:* 45 percent

*Urban land:* 35 percent

*Minor components: 20 percent  
Estimates are based on observations, descriptions, and transects of the  
mapunit.*

#### **Description of Klinesville**

##### **Setting**

*Landform: Hills  
Landform position (two-dimensional): Shoulder  
Down-slope shape: Linear  
Across-slope shape: Convex  
Parent material: Fine-loamy residuum weathered from shale*

##### **Typical profile**

*A - 0 to 8 inches: channery loam  
B - 8 to 12 inches: channery silt loam  
R - 12 to 80 inches: weathered bedrock*

##### **Properties and qualities**

*Slope: 0 to 5 percent  
Depth to restrictive feature: 10 to 20 inches to lithic bedrock  
Natural drainage class: Somewhat excessively drained  
Runoff class: Low  
Capacity of the most limiting layer to transmit water (Ksat): High (2.00  
to 6.00 in/hr)  
Depth to water table: More than 80 inches  
Frequency of flooding: None  
Frequency of ponding: None  
Available water storage in profile: Very low (about 1.1 inches)*

##### **Interpretive groups**

*Land capability classification (irrigated): None specified  
Land capability classification (nonirrigated): 3e  
Hydrologic Soil Group: D*

#### **Description of Urban Land**

##### **Setting**

*Landform: Hills  
Down-slope shape: Linear, convex  
Across-slope shape: Linear  
Parent material: Surface covered by pavement, concrete, buildings,  
and other structures underlain by disturbed and natural soil  
material*

##### **Typical profile**

*C - 0 to 6 inches: variable*

##### **Interpretive groups**

*Land capability classification (irrigated): None specified  
Land capability classification (nonirrigated): 8s*

### Minor Components

#### Reaville

*Percent of map unit:* 10 percent

*Landform:* Interfluves

*Down-slope shape:* Convex

*Across-slope shape:* Linear

#### Penn

*Percent of map unit:* 10 percent

*Landform:* Hills

*Landform position (two-dimensional):* Backslope

*Landform position (three-dimensional):* Interfluve

*Down-slope shape:* Linear

*Across-slope shape:* Convex

### Data Source Information

Soil Survey Area: Middlesex County, New Jersey

Survey Area Data: Version 11, Sep 17, 2015

## D: Tipping Bucket (2) & HMP45C - Wire Diagram

3/10/17

Find wire diagram for extension  
of tipping ram bucket 2 (black one)

<u>RB</u>	<u>ext blue</u>
(Pulse) Black/RED	Red
( $\frac{1}{2}$ ) yellow/green	green

3/10/17

Find wire diagrams for HMP45C

HMP45C

yellow	1
Blue	2
Red	3
clear	4
White	5
Black	6

3/11/17

Find wire diagram for CS650

<u>CS650</u>	<u>ext (Green)</u>
Red	1
Green	2
orange	3
black	4
clear	5



# E: Wind (2) & Tipping Bucket (1) & Setra 278 - Wire Diagram

3/10/17

Final wire diagram wind-dir + speed Z  
combined to blue 49' extension wire

	Dir Z	ext (blue)
Dir	Black	Black
	White	White
	Red	Red
	Shield	Green
Speed	White	Orange
	Black	Blue
	Shield	Comb. shield (bare)

3/10/17

Final wire diagram baro pressure 1 and  
tx tipping bucket (roof)

Setra	ext green
Blue	1
Red	2
Green	3
Black	4
Yellow	5
Clear	6

Tx	ext green
White	7
Clear	Green + yellow
Black	8 + yellow

# F: NR01 Green Ext. - Wire Diagram

3/9/17 Final wire diagram 75' green to Campbell CR1000  
From 2015 use!

CR300	NR01	CR1000	GREEN WSR6
9H	Red Pyr (1)	1H	7
9L	Blue 1	2L	2 + $\frac{1}{2}$
10H	White 1	2H	4
10L	Green 1	2L	5 + $\frac{1}{2}$
11H	Brown 1	3H	6
11L	Yellow 1	3L	1 + $\frac{1}{2}$
12H	Purple 1	4H	3
12L	Grey 1	4L	8 + $\frac{1}{2}$
$\frac{1}{2}$	Shield 1 $\frac{1}{2}$	$\frac{1}{2}$	Green + Yellow
13H	White 2	Jumper	black Vx1 (3 prongs in DICK 5)
13L	Green 2	Jumper	7 #2
IX1	red 2	Jumper	2
IXR	blue 2	6H	4
$\frac{1}{2}$	Shield 2 $\frac{1}{2}$	6L	5 + $\frac{1}{2}$

Cable 1



# G: NR01 Black Ext. - Wire Diagram

3/13/17 Find wire diagram NR01 to black ext.

NR01		Ext Black	
cable 1 / Red   Blue white green Brown yellow Purple Gray clear	Red	Red	1
	Blue	Blue	2
	white	white	3
	green	green	4
	Brown	dr Brown	5
	yellow	yellow	6
	Purple	purple	7
	Gray	gray	8
	clear	tan	
cable 2   white green Red blue shield	white	white	(yellow ext)
	green	green	
	Red	Red	
	blue	black	
	shield	shield	

# H: Rotronic Hygroclip2 HC2S3 and CNR4 - Wire Diagram

3/11/17	Find wire diagram HC2S3/CP	
	HC2S3	ext./green
	Brown	1
	white	2
	green	3
	clear	4
	yellow	5
	gray	6
3/13/17	Find wire diagram CNR4	
	CNR4	ext./black wire
	solar/red	Red
	solar/blue	Blue
	solar/white	white
	solar/black	Black
	solar/gray	gray
	solar/yellow	Yellow
	solar/brown	dr brown
	solar/green	green
	solar/clear	tan
	Temp/white	Pink
	Temp/clear	tan
	Temp/black	purple
	Temp/red	ORANGE



# I: Load Cells - Wire Diagram

3/8/17  
Final wire

for off hat wire cuttings

Find wire diagram  
load cells 3/7/17

	1-JX	2-JX	3-JX	4-JX
Red	1R	7R	1W	7W
Brown	2R	8R	2W	8W
Black	3R	10R	3W	9W
Yellow	4R	9R	4W	10W
Blue	5R	11R	5W	11W
White	6R	12R	6W	12W
Shield	ORANGE	ORANGE	SH	SH

---

Red	1W	7W	1R	7R
Brown	2W	8W	2R	8R
Black	3W	9W	3R	9R
Yellow	4W	10W	4R	10R
Blue	5W	11W	5R	11R
White	6W	12W	6R	12R
Shield	orange	orange	Shield	Shield

---

Red	1R	7R	1W	7W
Brown	2R	8R	2W	8W
Black	3R	9R	3W	9W
Yellow	4R	10R	4W	10W
Blue	5R	11R	5W	11W
White	6R	12R	6W	12W
Shield	ORANGE	ORANGE	Shield	Shield

---

Red	1W	7W	1R	7R
Brown	2W	8W	2R	8R
Black	3W	9W	3R	9R
Yellow	4W	10W	4R	10R
Blue	5W	11W	5R	11R
White	6W	12W	6R	12R
Shield	orange	orange	Shield	Shield

## J: CNR2 & Young Wind (1) - Wire Diagram

3/9/17

Final wire Diagram CNR4 extension  
original wire 20'  
ext 70'

CNR4	Ext wire
BLUE	BLUE
Black	Black (20GA)
white	white
Brown	orange
Green	shield
—	red
—	Blk/wht (coax)
—	Blk (coax)

---

Final wire diagram ext. wind dir 1 (yellow ext)

Dir 1	Yellow ext wire
Red	Red
Black	Black
white	white
shield	green

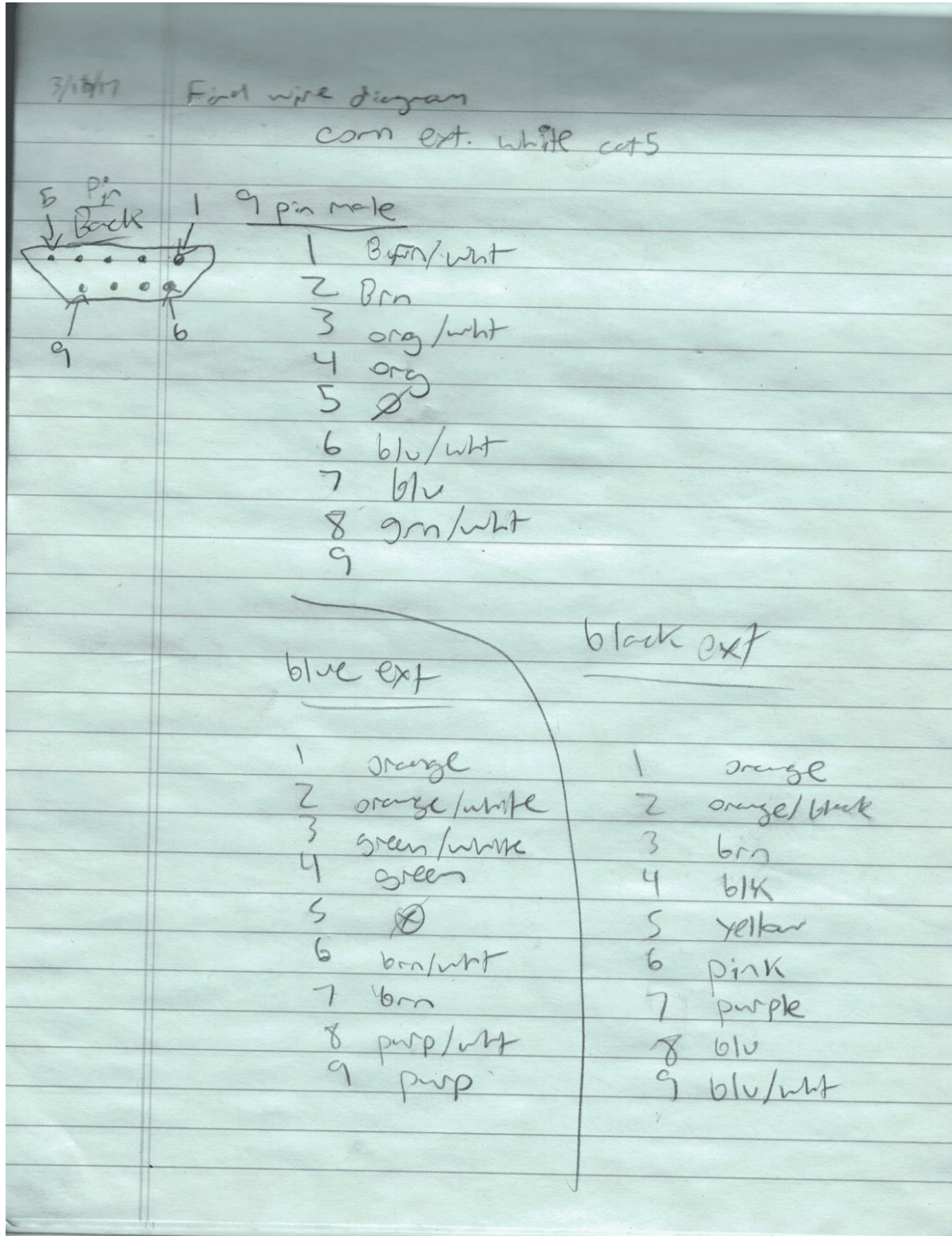
---

Final diagram ext. wind speed 1 (yellow ext)

	Speed 1	Yellow ext
(power)	red	black
(shield)	green	green



# K: COM - Wire Diagrams



# L: CR3000 Thermo - Campbell DAQ Wire Diagram/Text

CR3000 Wiring Diagram for cr3000fulltrial3.5.scw

NR01 - Red_SR01Up, Red_SR01Dn, Red_IR01Up, Red...	CR3000
Cable 1 Pyranometer Up Sig, Red	1H
Cable 1 Pyranometer Up Ref, Blue	1L
Cable 1 Pyranometer Down Sig, White	2H
Cable 1 Pyranometer Down Ref, Green	2L
Cable 1 Pyrgeometer Up Sig, Brown	3H
Cable 1 Pyrgeometer Up Ref, Yellow	3L
Cable 1 Pyrgeometer Down Sig, Purple	4H
Cable 1 Pyrgeometer Down Ref, Grey	4L
Cable 2 PT100 Signal, White	5H
Cable 2 PT100 Signal Ref, Green	5L
Shield, Clear	$\frac{1}{\equiv}$ (Ground)
Shield, Clear	$\frac{1}{\equiv}$ (Ground)
Cable 2 Current Excite, Red	IX1
Cable 2 Current Return, Blue	IXR
	1L
	$\frac{1}{\equiv}$ (Ground)
Jumper	2L
	$\frac{1}{\equiv}$ (Ground)
Jumper	3L
	$\frac{1}{\equiv}$ (Ground)
Jumper	4L
	$\frac{1}{\equiv}$ (Ground)
Jumper	
AM25T	CR3000
HI	6H
LO	6L
+12	12V
CLK	C1
RES	C2
Ground	G
AG	$\frac{1}{\equiv}$ (Ground)
EX	VX1
Type K TC (1) - P7T2	CR3000
Yellow	7H
Red	7L
Type K TC (2) - P7T3	CR3000
Yellow	8H
Red	8L
Type K TC (3) - P7T4	CR3000
Yellow	9H
Red	9L

Page 1

**Type K TC (4) - P8T1** **CR3000**

Yellow	10H
Red	10L

**Type K TC (5) - P8T2** **CR3000**

Yellow	11H
Red	11L

**Type K TC (6) - P8T3** **CR3000**

Yellow	12H
Red	12L

**Type K TC (7) - P8T4** **CR3000**

Yellow	13H
Red	13L

**Type K TC (8) - USP8** **CR3000**

Yellow	14H
Red	14L

CR3000		Attached Sens	
Terminal	Wire/Terminal	Name	Measurements
1H	Cable 1 Pyranometer Up Sig, Red	NR01	Red_SR01Up, Red_SR01Dn, Red_IR01Up, Red_IR01
1L	Cable 1 Pyranometer Up Ref, Blue	NR01	Red_SR01Up, Red_SR01Dn, Red_IR01Up, Red_IR01
	Jumper to Ground	NR01	Red_SR01Up, Red_SR01Dn, Red_IR01Up, Red_IR01
$\frac{\perp}{\perp}$ (Ground)	Jumper to 1L	NR01	Red_SR01Up, Red_SR01Dn, Red_IR01Up, Red_IR01
2H	Cable 1 Pyranometer Down Sig, White	NR01	Red_SR01Up, Red_SR01Dn, Red_IR01Up, Red_IR01
2L	Cable 1 Pyranometer Down Ref, Green	NR01	Red_SR01Up, Red_SR01Dn, Red_IR01Up, Red_IR01
	Jumper to Ground	NR01	Red_SR01Up, Red_SR01Dn, Red_IR01Up, Red_IR01
$\frac{\perp}{\perp}$ (Ground)	Jumper to 2L	NR01	Red_SR01Up, Red_SR01Dn, Red_IR01Up, Red_IR01
3H	Cable 1 Pyrgeometer Up Sig, Brown	NR01	Red_SR01Up, Red_SR01Dn, Red_IR01Up, Red_IR01
3L	Cable 1 Pyrgeometer Up Ref, Yellow	NR01	Red_SR01Up, Red_SR01Dn, Red_IR01Up, Red_IR01
	Jumper to Ground	NR01	Red_SR01Up, Red_SR01Dn, Red_IR01Up, Red_IR01
$\frac{\perp}{\perp}$ (Ground)	Jumper to 3L	NR01	Red_SR01Up, Red_SR01Dn, Red_IR01Up, Red_IR01
4H	Cable 1 Pyrgeometer Down Sig, Purple	NR01	Red_SR01Up, Red_SR01Dn, Red_IR01Up, Red_IR01
4L	Cable 1 Pyrgeometer Down Ref, Grey	NR01	Red_SR01Up, Red_SR01Dn, Red_IR01Up, Red_IR01
	Jumper to Ground	NR01	Red_SR01Up, Red_SR01Dn, Red_IR01Up, Red_IR01
$\frac{\perp}{\perp}$ (Ground)	Jumper to 4L	NR01	Red_SR01Up, Red_SR01Dn, Red_IR01Up, Red_IR01
5H	Cable 2 PT100 Signal, White	NR01	Red_SR01Up, Red_SR01Dn, Red_IR01Up, Red_IR01
5L	Cable 2 PT100 Signal Ref, Green	NR01	Red_SR01Up, Red_SR01Dn, Red_IR01Up, Red_IR01
$\frac{\perp}{\perp}$ (Ground)	Shield, Clear	NR01	Red_SR01Up, Red_SR01Dn, Red_IR01Up, Red_IR01
	Shield, Clear	NR01	Red_SR01Up, Red_SR01Dn, Red_IR01Up, Red_IR01
	AG	AM25T	
6H	HI	AM25T	
6L	LO	AM25T	
$\frac{\perp}{\perp}$ (Ground)			
7H	Yellow	Type K TC (1)	P7T2
7L	Red	Type K TC (1)	P7T2
$\frac{\perp}{\perp}$ (Ground)			
8H	Yellow	Type K TC (2)	P7T3
8L	Red	Type K TC (2)	P7T3
$\frac{\perp}{\perp}$ (Ground)			
9H	Yellow	Type K TC (3)	P7T4
9L	Red	Type K TC (3)	P7T4
$\frac{\perp}{\perp}$ (Ground)			
10H	Yellow	Type K TC (4)	P8T1
10L	Red	Type K TC (4)	P8T1
$\frac{\perp}{\perp}$ (Ground)			
11H	Yellow	Type K TC (5)	P8T2
11L	Red	Type K TC (5)	P8T2
$\frac{\perp}{\perp}$ (Ground)			
12H	Yellow	Type K TC (6)	P8T3
12L	Red	Type K TC (6)	P8T3
$\frac{\perp}{\perp}$ (Ground)			
13H	Yellow	Type K TC (7)	P8T4
13L	Red	Type K TC (7)	P8T4
$\frac{\perp}{\perp}$ (Ground)			
14H	Yellow	Type K TC (8)	USP8
14L	Red	Type K TC (8)	USP8
$\frac{\perp}{\perp}$ (Ground)			
VX1	EX	AM25T	
VX2			
$\frac{\perp}{\perp}$ (Ground)			
VX3			
VX4			
$\frac{\perp}{\perp}$ (Ground)			
CA01			
CA02			
$\frac{\perp}{\perp}$ (Ground)			
IX1	Cable 2 Current Excite, Red	NR01	Red_SR01Up, Red_SR01Dn, Red_IR01Up, Red_IR01
IX2			
IX3			
IXR	Cable 2 Current Return, Blue	NR01	Red_SR01Up, Red_SR01Dn, Red_IR01Up, Red_IR01
$\frac{\perp}{\perp}$ (Ground)			
P1			
$\frac{\perp}{\perp}$ (Ground)			

Terminal	Wire/Terminal	Name	Measurements
P2			
$\perp$	(Ground)		
P3			
$\perp$	(Ground)		
P4			
C1	CLK	AM25T	
C2	RES	AM25T	
C3			
C4			
G	$\perp$ (Ground)	AM25T	
C5			
C6			
C7			
C8			
G			
5V			
G			
SW12V-1			
SW12V-2			
G			
12V	+12	AM25T	
12V			
G			
SDM-C1			
SDM-C2			
SDM-C3			

# M: CR\_AM25T Campbell Multiplexer Wire Diagram/Text

AM25T Wiring Diagram for cr3000fulltrial3.5.scw

Type K TC (1) - P1T1	AM25T
Blue	1H
Red	1L
Type K TC (2) - P1T2	AM25T
Blue	2H
Red	2L
Type K TC (3) - P1T3	AM25T
Blue	3H
Red	3L
Type K TC (4) - P1T4	AM25T
Blue	4H
Red	4L
Type K TC (5) - P2T1	AM25T
Blue	5H
Red	5L
Type K TC (6) - P2T2	AM25T
Blue	6H
Red	6L
Type K TC (7) - P2T3	AM25T
Blue	7H
Red	7L
Type K TC (8) - P2T4	AM25T
Blue	8H
Red	8L
Type K TC (9) - P3T1	AM25T
Blue	9H
Red	9L
Type K TC (10) - P3T2	AM25T
Blue	10H
Red	10L
Type K TC (11) - P3T3	AM25T
Blue	11H
Red	11L
Type K TC (12) - P3T4	AM25T
Blue	12H
Red	12L

Page 1



<b>Type K TC (13) - P4T1</b>	<b>AM25T</b>
Blue	13H
Red	13L
<b>Type K TC (14) - P4T2</b>	<b>AM25T</b>
Blue	14H
Red	14L
<b>Type K TC (15) - P4T3</b>	<b>AM25T</b>
Blue	15H
Red	15L
<b>Type K TC (16) - P4T4</b>	<b>AM25T</b>
Blue	16H
Red	16L
<b>Type K TC (17) - P5T1</b>	<b>AM25T</b>
Blue	17H
Red	17L
<b>Type K TC (18) - P5T2</b>	<b>AM25T</b>
Blue	18H
Red	18L
<b>Type K TC (19) - P5T3</b>	<b>AM25T</b>
Blue	19H
Red	19L
<b>Type K TC (20) - P5T4</b>	<b>AM25T</b>
Blue	20H
Red	20L
<b>Type K TC (21) - P6T1</b>	<b>AM25T</b>
Blue	21H
Red	21L
<b>Type K TC (22) - P6T2</b>	<b>AM25T</b>
Blue	22H
Red	22L
<b>Type K TC (23) - P6T3</b>	<b>AM25T</b>
Blue	23H
Red	23L
<b>Type K TC (24) - P6T4</b>	<b>AM25T</b>
Blue	24H
Red	24L

Type K TC (25) - P7T1	AM25T
Blue	25H
Red	25L

AM25T		Attached Sensor/Device	
Terminal	Wire/Terminal	Name	Measurements
+12	12V	CR3000	
$\perp$ (Ground)	G	CR3000	
CLK	C1	CR3000	
RES	C2	CR3000	
EX	VX1	CR3000	
AG	$\perp$ (Ground)	CR3000	
HI	6H	CR3000	
LO	6L	CR3000	
$\perp$ (Ground)	G	CR3000	
1H	Blue	Type K TC (1)	P1T1
1L	Red	Type K TC (1)	P1T1
$\perp$ (Ground)	G	CR3000	
2H	Blue	Type K TC (2)	P1T2
2L	Red	Type K TC (2)	P1T2
$\perp$ (Ground)	G	CR3000	
3H	Blue	Type K TC (3)	P1T3
3L	Red	Type K TC (3)	P1T3
$\perp$ (Ground)	G	CR3000	
4H	Blue	Type K TC (4)	P1T4
4L	Red	Type K TC (4)	P1T4
$\perp$ (Ground)	G	CR3000	
5H	Blue	Type K TC (5)	P2T1
5L	Red	Type K TC (5)	P2T1
$\perp$ (Ground)	G	CR3000	
6H	Blue	Type K TC (6)	P2T2
6L	Red	Type K TC (6)	P2T2
$\perp$ (Ground)	G	CR3000	
7H	Blue	Type K TC (7)	P2T3
7L	Red	Type K TC (7)	P2T3
$\perp$ (Ground)	G	CR3000	
8H	Blue	Type K TC (8)	P2T4
8L	Red	Type K TC (8)	P2T4
$\perp$ (Ground)	G	CR3000	
9H	Blue	Type K TC (9)	P3T1
9L	Red	Type K TC (9)	P3T1
$\perp$ (Ground)	G	CR3000	
10H	Blue	Type K TC (10)	P3T2
10L	Red	Type K TC (10)	P3T2
$\perp$ (Ground)	G	CR3000	
11H	Blue	Type K TC (11)	P3T3
11L	Red	Type K TC (11)	P3T3
$\perp$ (Ground)	G	CR3000	
12H	Blue	Type K TC (12)	P3T4
12L	Red	Type K TC (12)	P3T4
$\perp$ (Ground)	G	CR3000	
13H	Blue	Type K TC (13)	P4T1
13L	Red	Type K TC (13)	P4T1
$\perp$ (Ground)	G	CR3000	
14H	Blue	Type K TC (14)	P4T2
14L	Red	Type K TC (14)	P4T2
$\perp$ (Ground)	G	CR3000	
15H	Blue	Type K TC (15)	P4T3
15L	Red	Type K TC (15)	P4T3
$\perp$ (Ground)	G	CR3000	
16H	Blue	Type K TC (16)	P4T4
16L	Red	Type K TC (16)	P4T4
$\perp$ (Ground)	G	CR3000	
17H	Blue	Type K TC (17)	P5T1
17L	Red	Type K TC (17)	P5T1
$\perp$ (Ground)	G	CR3000	
18H	Blue	Type K TC (18)	P5T2
18L	Red	Type K TC (18)	P5T2
$\perp$ (Ground)	G	CR3000	
19H	Blue	Type K TC (19)	P5T3
19L	Red	Type K TC (19)	P5T3
$\perp$ (Ground)	G	CR3000	

Terminal	Wire/Terminal	Name	Measurements
20H	Blue	Type K TC (20)	P5T4
20L	Red	Type K TC (20)	P5T4
$\frac{\perp}{=}$ (Ground)	G	CR3000	
21H	Blue	Type K TC (21)	P6T1
21L	Red	Type K TC (21)	P6T1
$\frac{\perp}{=}$ (Ground)	G	CR3000	
22H	Blue	Type K TC (22)	P6T2
22L	Red	Type K TC (22)	P6T2
$\frac{\perp}{=}$ (Ground)	G	CR3000	
23H	Blue	Type K TC (23)	P6T3
23L	Red	Type K TC (23)	P6T3
$\frac{\perp}{=}$ (Ground)	G	CR3000	
24H	Blue	Type K TC (24)	P6T4
24L	Red	Type K TC (24)	P6T4
$\frac{\perp}{=}$ (Ground)	G	CR3000	
25H	Blue	Type K TC (25)	P7T1
25L	Red	Type K TC (25)	P7T1
$\frac{\perp}{=}$ (Ground)	G	CR3000	

# N: CR3000 Load Cell - Campbell DAQ Wire Diagram/Text

CR3000 Wiring Diagram for cr3000fulltrial3.scw

CNR4 - SUp, SDn, LUp, LDn, SUpMult, SDnMult, LUpM...	CR3000
SOLAR, Red	1H
SOLAR, Blue	1L
SOLAR, White	2H
SOLAR, Black	2L
SOLAR, Grey	3H
SOLAR, Yellow	3L
SOLAR, Brown	4H
SOLAR, Green	4L
TEMP, White	5H
TEMP, Clear	⏏ (Ground)
SOLAR, Clear	⏏ (Ground)
TEMP, Black	⏏ (Ground)
TEMP, Red	VX1
	1L
	⏏ (Ground)
Jumper	2L
	⏏ (Ground)
Jumper	3L
	⏏ (Ground)
Jumper	4L
	⏏ (Ground)
Jumper	

<b>NR01 - SR01Up, SR01Dn, IR01Up, IR01Dn, NR01TC, ...</b>		<b>CR3000</b>
Cable 1 Pyranometer Up Sig, Red		6H
Cable 1 Pyranometer Up Ref, Blue		6L
Cable 1 Pyranometer Down Sig, White		7H
Cable 1 Pyranometer Down Ref, Green		7L
Cable 1 Pyrgeometer Up Sig, Brown		8H
Cable 1 Pyrgeometer Up Ref, Yellow		8L
Cable 1 Pyrgeometer Down Sig, Purple		9H
Cable 1 Pyrgeometer Down Ref, Grey		9L
Cable 2 PT100 Signal, White		10H
Cable 2 PT100 Signal Ref, Green		10L
Shield, Clear		$\frac{1}{\text{---}}$ (Ground)
Shield, Clear		$\frac{1}{\text{---}}$ (Ground)
Cable 2 Current Excite, Red		IX1
Cable 2 Current Return, Blue		IXR
		6L
		$\frac{1}{\text{---}}$ (Ground)
Jumper		7L
		$\frac{1}{\text{---}}$ (Ground)
Jumper		8L
		$\frac{1}{\text{---}}$ (Ground)
Jumper		9L
		$\frac{1}{\text{---}}$ (Ground)
Jumper		
<b>Generic TB - Rain_mm</b>		<b>CR3000</b>
Ground		$\frac{1}{\text{---}}$ (Ground)
Shield		$\frac{1}{\text{---}}$ (Ground)
Signal		P1
<b>CS650/655 (VWC, EC, T, P, PA, and VR) - VWC, EC, T,...</b>		<b>CR3000</b>
Red		12V
Green		C7
Orange		G
Black		G
Clear		G
<b>CS616 (1) - VW, PA_uS</b>		<b>CR3000</b>
Green		5L
Red		12V
Orange		C1
Black		G
Clear		$\frac{1}{\text{---}}$ (Ground)

**CS616 (2) - VW\_2, PA\_uS\_2**

**CR3000**

Green	11H
Red	12V
Orange	C2
Black	G
Clear	$\frac{1}{\equiv}$ (Ground)

**CS100 - BP\_mbar**

**CR3000**

Blue	11L
Red	12V
Green	C8
Black	G
Yellow	$\frac{1}{\equiv}$ (Ground)
Clear	$\frac{1}{\equiv}$ (Ground)

**HC2S3 (CP) - AirTC, RH**

**CR3000**

Brown	12H
White	12L
Green	12V
Clear	$\frac{1}{\equiv}$ (Ground)
Yellow	$\frac{1}{\equiv}$ (Ground)
Gray	$\frac{1}{\equiv}$ (Ground)

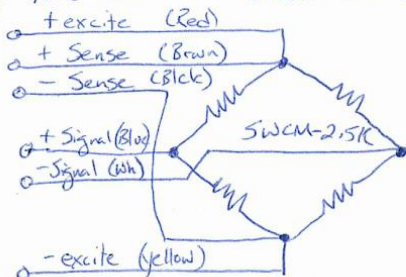
John Hencken  
Rutgers University

CR3000 / AM16/32B / 16 load cells

2/23/17

16 6W Full Bridge load cells

(load cell central model # SWCM-2.5K)



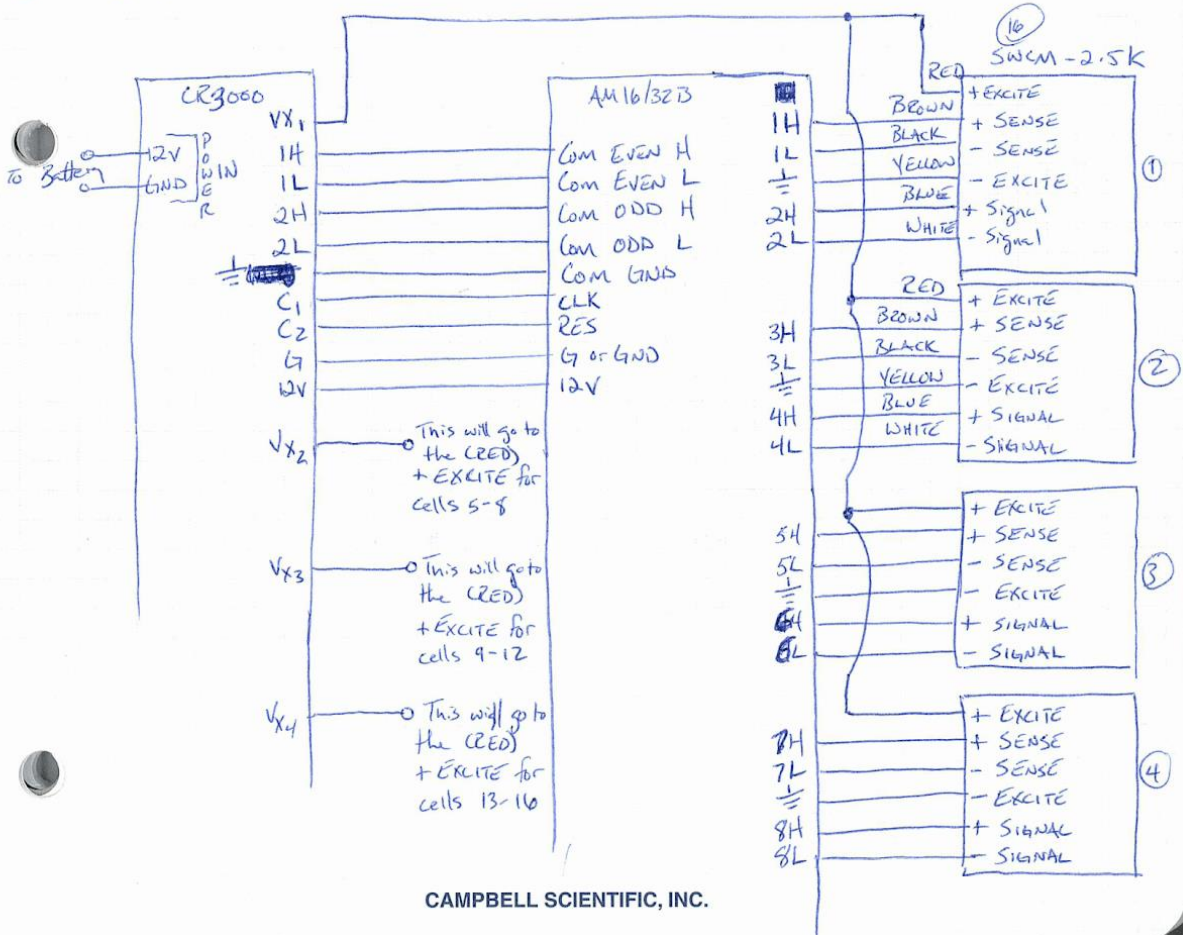
+ excite	Red
- excite	Yellow
+ Signal	Blue
- Signal	White
+ Sense	Brown
- Sense	Black

CR3000 Vx 1-4

Range  $\pm 5$  Vdc  
Current Source/Sink  $\pm 50$  mA

2.0 mV/V for 10 Vexcit  
2.0 mV/V for 5 Vexcit

so if the input impedance of these load cells is 700 $\Omega$  then one excitation could source  $\approx 7$  load cells at a time - I worry about sensor warming - recommend doing 4 at a time





CR3000		Attached Sensor/Device	
Terminal	Wire/Terminal	Name	Measurements
1H	SOLAR, Red	CNR4	Sup, SdN, LUp, LDn, SupMult, SdNMult, LUpMult, LDnMult, CNR4TC, CNR4TK, RsNet, RiNet, Albedo, Rn, LUpCo, LDnCo
1L	SOLAR, Blue	CNR4	Sup, SdN, LUp, LDn, SupMult, SdNMult, LUpMult, LDnMult, CNR4TC, CNR4TK, RsNet, RiNet, Albedo, Rn, LUpCo, LDnCo
$\frac{+}{-}$ (Ground)	Jumper to Ground	CNR4	Sup, SdN, LUp, LDn, SupMult, SdNMult, LUpMult, LDnMult, CNR4TC, CNR4TK, RsNet, RiNet, Albedo, Rn, LUpCo, LDnCo
2H	SOLAR, White	CNR4	Sup, SdN, LUp, LDn, SupMult, SdNMult, LUpMult, LDnMult, CNR4TC, CNR4TK, RsNet, RiNet, Albedo, Rn, LUpCo, LDnCo
2L	SOLAR, Black	CNR4	Sup, SdN, LUp, LDn, SupMult, SdNMult, LUpMult, LDnMult, CNR4TC, CNR4TK, RsNet, RiNet, Albedo, Rn, LUpCo, LDnCo
$\frac{+}{-}$ (Ground)	Jumper to Ground	CNR4	Sup, SdN, LUp, LDn, SupMult, SdNMult, LUpMult, LDnMult, CNR4TC, CNR4TK, RsNet, RiNet, Albedo, Rn, LUpCo, LDnCo
3H	SOLAR, Grey	CNR4	Sup, SdN, LUp, LDn, SupMult, SdNMult, LUpMult, LDnMult, CNR4TC, CNR4TK, RsNet, RiNet, Albedo, Rn, LUpCo, LDnCo
4H	SOLAR, Brown	CNR4	Sup, SdN, LUp, LDn, SupMult, SdNMult, LUpMult, LDnMult, CNR4TC, CNR4TK, RsNet, RiNet, Albedo, Rn, LUpCo, LDnCo
4L	SOLAR, Green	CNR4	Sup, SdN, LUp, LDn, SupMult, SdNMult, LUpMult, LDnMult, CNR4TC, CNR4TK, RsNet, RiNet, Albedo, Rn, LUpCo, LDnCo
$\frac{+}{-}$ (Ground)	Jumper to Ground	CNR4	Sup, SdN, LUp, LDn, SupMult, SdNMult, LUpMult, LDnMult, CNR4TC, CNR4TK, RsNet, RiNet, Albedo, Rn, LUpCo, LDnCo
5H	TEMP, White	CNR4	Sup, SdN, LUp, LDn, SupMult, SdNMult, LUpMult, LDnMult, CNR4TC, CNR4TK, RsNet, RiNet, Albedo, Rn, LUpCo, LDnCo
5L	Green	CS616 (1)	VW, PA_uS
$\frac{+}{-}$ (Ground)	TEMP, Black	CNR4	Sup, SdN, LUp, LDn, SupMult, SdNMult, LUpMult, LDnMult, CNR4TC, CNR4TK, RsNet, RiNet, Albedo, Rn, LUpCo, LDnCo
6H	Cable 1 Pyranometer Up Sig, Red	NR01	SR01Up, SR01Dn, IR01Up, IR01Dn, NR01TC, NR01TK, NetRs, NetRI, Albedo_2, UpTot, DnTot, NetTot, IR01UpCo, IR01DnCo
6L	Cable 1 Pyranometer Up Ref, Blue	NR01	SR01Up, SR01Dn, IR01Up, IR01Dn, NR01TC, NR01TK, NetRs, NetRI, Albedo_2, UpTot, DnTot, NetTot, IR01UpCo, IR01DnCo
$\frac{+}{-}$ (Ground)	Jumper to Ground	NR01	SR01Up, SR01Dn, IR01Up, IR01Dn, NR01TC, NR01TK, NetRs, NetRI, Albedo_2, UpTot, DnTot, NetTot, IR01UpCo, IR01DnCo
	SOLAR, Clear	CNR4	Sup, SdN, LUp, LDn, SupMult, SdNMult, LUpMult, LDnMult, CNR4TC, CNR4TK, RsNet, RiNet, Albedo, Rn, LUpCo, LDnCo
	TEMP, Clear	CNR4	Sup, SdN, LUp, LDn, SupMult, SdNMult, LUpMult, LDnMult, CNR4TC, CNR4TK, RsNet, RiNet, Albedo, Rn, LUpCo, LDnCo
	Jumper to 6L	NR01	SR01Up, SR01Dn, IR01Up, IR01Dn, NR01TC, NR01TK, NetRs, NetRI, Albedo_2, UpTot, DnTot, NetTot, IR01UpCo, IR01DnCo
7H	Cable 1 Pyranometer Down Sig, White	NR01	SR01Up, SR01Dn, IR01Up, IR01Dn, NR01TC, NR01TK, NetRs, NetRI, Albedo_2, UpTot, DnTot, NetTot, IR01UpCo, IR01DnCo
7L	Cable 1 Pyranometer Down Ref, Green	NR01	SR01Up, SR01Dn, IR01Up, IR01Dn, NR01TC, NR01TK, NetRs, NetRI, Albedo_2, UpTot, DnTot, NetTot, IR01UpCo, IR01DnCo
$\frac{+}{-}$ (Ground)	Jumper to Ground	NR01	SR01Up, SR01Dn, IR01Up, IR01Dn, NR01TC, NR01TK, NetRs, NetRI, Albedo_2, UpTot, DnTot, NetTot, IR01UpCo, IR01DnCo

8H	Cable 1 Pyrgeometer Up Sig, Brown	NR01	SR01Up, SR01Dn, IR01Up, IR01Dn, NR01TC, NR01TK, NetRs, NetRI, Albedo_2, UpTot, DnTot, NetTot, IR01UpCo, IR01DnCo
8L	Cable 1 Pyrgeometer Up Ref, Yellow	NR01	SR01Up, SR01Dn, IR01Up, IR01Dn, NR01TC, NR01TK, NetRs, NetRI, Albedo_2, UpTot, DnTot, NetTot, IR01UpCo, IR01DnCo
$\frac{+}{-}$ (Ground)	Jumper to Ground	NR01	SR01Up, SR01Dn, IR01Up, IR01Dn, NR01TC, NR01TK, NetRs, NetRI, Albedo_2, UpTot, DnTot, NetTot, IR01UpCo, IR01DnCo
9H	Cable 1 Pyrgeometer Down Sig, Purple	NR01	SR01Up, SR01Dn, IR01Up, IR01Dn, NR01TC, NR01TK, NetRs, NetRI, Albedo_2, UpTot, DnTot, NetTot, IR01UpCo, IR01DnCo
9L	Cable 1 Pyrgeometer Down Ref, Grey	NR01	SR01Up, SR01Dn, IR01Up, IR01Dn, NR01TC, NR01TK, NetRs, NetRI, Albedo_2, UpTot, DnTot, NetTot, IR01UpCo, IR01DnCo
$\frac{+}{-}$ (Ground)	Jumper to Ground	NR01	SR01Up, SR01Dn, IR01Up, IR01Dn, NR01TC, NR01TK, NetRs, NetRI, Albedo_2, UpTot, DnTot, NetTot, IR01UpCo, IR01DnCo
10H	Cable 2 PT100 Signal, White	NR01	SR01Up, SR01Dn, IR01Up, IR01Dn, NR01TC, NR01TK, NetRs, NetRI, Albedo_2, UpTot, DnTot, NetTot, IR01UpCo, IR01DnCo
10L	Cable 2 PT100 Signal Ref, Green	NR01	SR01Up, SR01Dn, IR01Up, IR01Dn, NR01TC, NR01TK, NetRs, NetRI, Albedo_2, UpTot, DnTot, NetTot, IR01UpCo, IR01DnCo
$\frac{+}{-}$ (Ground)	Shield, Clear	NR01	SR01Up, SR01Dn, IR01Up, IR01Dn, NR01TC, NR01TK, NetRs, NetRI, Albedo_2, UpTot, DnTot, NetTot, IR01UpCo, IR01DnCo
	Shield, Clear	NR01	SR01Up, SR01Dn, IR01Up, IR01Dn, NR01TC, NR01TK, NetRs, NetRI, Albedo_2, UpTot, DnTot, NetTot, IR01UpCo, IR01DnCo
	Ground	Generic TB	Rain_mm
	Ground	Generic TB	Rain_mm
11H	Green	CS616 (2)	VW_2, PA_uS_2
11L	Blue	CS100	BP_mbar
$\frac{+}{-}$ (Ground)	Clear	CS616 (1)	VW, PA_uS
	Clear	CS616 (2)	VW_2, PA_uS_2
	Yellow	CS100	BP_mbar
	Clear	CS100	BP_mbar
12H	Brown	HC253 (CP)	AirTC, RH
12L	White	HC253 (CP)	AirTC, RH
$\frac{+}{-}$ (Ground)	Yellow	HC253 (CP)	AirTC, RH
	Gray	HC253 (CP)	AirTC, RH
	Clear	HC253 (CP)	AirTC, RH

Page 1

CR3000 Wiring Text for cr3000fulltrial3.scw

Terminal	Wire/Terminal	Name	Measurements
13L	AM 16/32 COM EVEN L (13L)		
$\frac{+}{-}$ (Ground)			
14H	AM 16/32 COM ODD H (14H)		
14L	AM 16/32 COM ODD L (14L)		
$\frac{+}{-}$ (Ground)	AM 16/32 COM GROUND		
VX1	TEMP, Red	CNR4	Sup, SdN, LUp, LDn, SupMult, SdNMult, LUpMult, LDnMult, CNR4TC, CNR4TK, RsNet, RiNet, Albedo, Rn, LUpCo, LDnCo
VX2			
$\frac{+}{-}$ (Ground)			
VX3			
VX4			
$\frac{+}{-}$ (Ground)			
CA01			
CA02			
$\frac{+}{-}$ (Ground)			
IX1	Cable 2 Current Excite, Red	NR01	SR01Up, SR01Dn, IR01Up, IR01Dn, NR01TC, NR01TK, NetRs, NetRI, Albedo_2, UpTot, DnTot, NetTot, IR01UpCo, IR01DnCo
IX2			
IX3			
IXR	Cable 2 Current Return, Blue	NR01	SR01Up, SR01Dn, IR01Up, IR01Dn, NR01TC, NR01TK, NetRs, NetRI, Albedo_2, UpTot, DnTot, NetTot, IR01UpCo, IR01DnCo
$\frac{+}{-}$ (Ground)			
P1	Signal	Generic TB	Rain_mm
$\frac{+}{-}$ (Ground)			
P2			
$\frac{+}{-}$ (Ground)			
P3			
$\frac{+}{-}$ (Ground)			
P4			
C1	Orange	CS616 (1)	VW, PA_uS
C2	Orange	CS616 (2)	VW_2, PA_uS_2
C3			
C4			
G	Black	CS650/655 (VWC, EC, T, P, PA, and VR)	VWC, EC, T, P, PA, VR
	Clear	CS650/655 (VWC, EC, T, P, PA, and VR)	VWC, EC, T, P, PA, VR
	Orange	CS650/655 (VWC, EC, T, P, PA, and VR)	VWC, EC, T, P, PA, VR
	Black	CS616 (1)	VW, PA_uS
	Black	CS616 (2)	VW_2, PA_uS_2
C5			
C6			
C7	Green	CS650/655 (VWC, EC, T, P, PA, and VR)	VWC, EC, T, P, PA, VR
C8	Green	CS100	BP_mbar
G	Black	CS100	BP_mbar
SV			
G	AM 16/32 G (G)		
SW12V-1			
SW12V-2			
G			
12V	Red	CS650/655 (VWC, EC, T, P, PA, and VR)	VWC, EC, T, P, PA, VR
	Red	CS616 (1)	VW, PA_uS
	Red	CS616 (2)	VW_2, PA_uS_2
	Red	CS100	BP_mbar
	Green	HC253 (CP)	AirTC, RH
12V	AM 16/32 12V (12V)		
G			
SDM-C1			
SDM-C2			

Page 2

Terminal	Wire/Terminal	Name	Measurements
----------	---------------	------	--------------

SDM-C3

# O: CR10X Weather - Campbell DAQ Wire Diagram/Text

CR10X Wiring Diagram for cr10xtrial3.scw

<b>HMP45C (6WCP) - Roof_AirT, Roof_RH</b>	<b>CR10X</b>
Yellow	1H
Blue	1L
Red	12V
Black	AG
White	AG
Clear	G

<b>CS100 - BP_mbar</b>	<b>CR10X</b>
Blue	2H
Red	12V
Yellow	AG
Green	C1
Clear	G
Black	G

<b>TE525/TE525WS - RoofTB_in</b>	<b>CR10X</b>
White	G
Clear	G
Black	P1

<b>03001 - Roof_WS_m, Roof_Wind</b>	<b>CR10X</b>
Vane, Red	2L
Vane, White	AG
Vane, Black	E1
Anemometer, White	G
Vane, Clear	G
Anemometer, Clear	G
Anemometer, Black	P2

CR10X		Attached Sensor/Device	
Terminal	Wire/Terminal	Name	Measurements
G	Clear	HMP45C (6WCP)	Roof_AirT, Roof_RH
	Clear	CS100	BP_mbar
	Black	CS100	BP_mbar
	Clear	TE525/TE525WS	RoofTB_in
G	White	TE525/TE525WS	RoofTB_in
	Anemometer, White	03001	Roof_WS_m, Roof_Wind
	Anemometer, Clear	03001	Roof_WS_m, Roof_Wind
	Vane, Clear	03001	Roof_WS_m, Roof_Wind
1H	Yellow	HMP45C (6WCP)	Roof_AirT, Roof_RH
1L	Blue	HMP45C (6WCP)	Roof_AirT, Roof_RH
AG	White	HMP45C (6WCP)	Roof_AirT, Roof_RH
	Black	HMP45C (6WCP)	Roof_AirT, Roof_RH
	Yellow	CS100	BP_mbar
	Vane, White	03001	Roof_WS_m, Roof_Wind
2H	Blue	CS100	BP_mbar
2L	Vane, Red	03001	Roof_WS_m, Roof_Wind
AG			
3H			
3L			
AG			
E1	Vane, Black	03001	Roof_WS_m, Roof_Wind
AG			
E2			
G			
G			
G			
4H			
4L			
AG			
5H			
5L			
AG			
6H			
6L			
AG			
E3			
AG			
G			
G			
P1	Black	TE525/TE525WS	RoofTB_in
G			
P2	Anemometer, Black	03001	Roof_WS_m, Roof_Wind
G			
C8			
C7			
C6			
C5			
C4			
C3			
C2			
C1	Green	CS100	BP_mbar
G			
12V	Red	HMP45C (6WCP)	Roof_AirT, Roof_RH
	Red	CS100	BP_mbar
12V			
5V			
5V			
G			
SW 12V CTRL			
SW 12V			
G			

# P: CR1000 TDR - Campbell DAQ Wire Diagram/Text

CR1000 Wiring Diagram for 2017.05.24 - CR1000 TDRs and HC2S3 DIFF.SCW

## CS650/655 (VWC, EC, T, P, PA, and VR) - VWC\_1, EC,... CR1000

Red	12V
Green	C7
Orange	G
Black	G
Clear	G

## CS616 (1) - VW\_3, PA\_uS\_3 CR1000

Green	1H
Red	12V
Orange	C1
Black	G
Clear	$\perp$ (Ground)

## CS616 (2) - VW\_2, PA\_uS\_2 CR1000

Green	1L
Red	12V
Orange	C2
Black	G
Clear	$\perp$ (Ground)

## HC2S3 (PS) - AirTC, RH CR1000

Brown	2H
White	2L
Clear	$\perp$ (Ground)
Grey	$\perp$ (Ground)
Yellow	$\perp$ (Ground)
Green	SW-12

CR1000		Attached Sensor/Device	
Terminal	Wire/Terminal	Name	Measurements
1H	Green	CS616 (1)	VW_3, PA_uS_3
1L	Green	CS616 (2)	VW_2, PA_uS_2
⏏ (Ground)	Clear	CS616 (1)	VW_3, PA_uS_3
	Clear	CS616 (2)	VW_2, PA_uS_2
	Yellow	HC2S3 (PS)	AirTC, RH
	Grey	HC2S3 (PS)	AirTC, RH
2H	Brown	HC2S3 (PS)	AirTC, RH
2L	White	HC2S3 (PS)	AirTC, RH
⏏ (Ground)	Clear	HC2S3 (PS)	AirTC, RH
3H			
3L			
⏏ (Ground)			
4H			
4L			
⏏ (Ground)			
VX1 or EX1			
⏏ (Ground)			
P1			
⏏ (Ground)			
P2			
⏏ (Ground)			
5H			
5L			
⏏ (Ground)			
6H			
6L			
⏏ (Ground)			
7H			
7L			
⏏ (Ground)			
8H			
8L			
⏏ (Ground)			
VX2 or EX2			
⏏ (Ground)			
VX3 or EX3			
G	Black	CS650/655 (VWC, EC, T, P, PA, and VR)	VWC_1, EC, T, P, PA, VR
	Clear	CS650/655 (VWC, EC, T, P, PA, and VR)	VWC_1, EC, T, P, PA, VR
	Orange	CS650/655 (VWC, EC, T, P, PA, and VR)	VWC_1, EC, T, P, PA, VR
	Black	CS616 (1)	VW_3, PA_uS_3
	Black	CS616 (2)	VW_2, PA_uS_2
5V			
G			
SW-12	Green	HC2S3 (PS)	AirTC, RH
G			
12V	Red	CS650/655 (VWC, EC, T, P, PA, and VR)	VWC_1, EC, T, P, PA, VR
	Red	CS616 (1)	VW_3, PA_uS_3
	Red	CS616 (2)	VW_2, PA_uS_2
12V			
G			
C1	Orange	CS616 (1)	VW_3, PA_uS_3
C2	Orange	CS616 (2)	VW_2, PA_uS_2
C3			
C4			
G			
C5			
C6			
C7	Green	CS650/655 (VWC, EC, T, P, PA, and VR)	VWC_1, EC, T, P, PA, VR
C8			
G			

# Q: CR1000 Inside Temp - Campbell DAQ Wire Diagram/Text

CR1000 Wiring Diagram for temptest002.scw

## 108 (1) - USP1

## CR1000

Red	1H
Clear	$\frac{1}{\text{---}}$ (Ground)
Purple	$\frac{1}{\text{---}}$ (Ground)
Black	VX1 or EX1

## 108 (2) - USP2

## CR1000

Red	1L
Clear	$\frac{1}{\text{---}}$ (Ground)
Purple	$\frac{1}{\text{---}}$ (Ground)
Black	VX1 or EX1

## 108 (3) - USP3

## CR1000

Red	2H
Clear	$\frac{1}{\text{---}}$ (Ground)
Purple	$\frac{1}{\text{---}}$ (Ground)
Black	VX1 or EX1

## 108 (4) - USP4

## CR1000

Red	2L
Clear	$\frac{1}{\text{---}}$ (Ground)
Purple	$\frac{1}{\text{---}}$ (Ground)
Black	VX1 or EX1

## 108 (5) - USP5

## CR1000

Red	3H
Clear	$\frac{1}{\text{---}}$ (Ground)
Purple	$\frac{1}{\text{---}}$ (Ground)
Black	VX2 or EX2

## 108 (6) - USP6

## CR1000

Red	3L
Clear	$\frac{1}{\text{---}}$ (Ground)
Purple	$\frac{1}{\text{---}}$ (Ground)
Black	VX2 or EX2

## 108 (7) - USP7

## CR1000

Red	4H
Clear	$\frac{1}{\text{---}}$ (Ground)
Purple	$\frac{1}{\text{---}}$ (Ground)
Black	VX2 or EX2

## Type E TC (1) - E1T1

## CR1000

Purple	5H
Red	5L

**Type E TC (2) - E1T2**

**CR1000**

Purple	6H
Red	6L

**Type E TC (3) - E1T3**

**CR1000**

Purple	7H
Red	7L

**Type E TC (4) - E1T4**

**CR1000**

Purple	8H
Red	8L

**03001 - WS\_ms, WindDir**

**CR1000**

Vane, Red	4L
Vane, Clear	$\frac{1}{\text{---}}$ (Ground)
Vane, White	$\frac{1}{\text{---}}$ (Ground)
Anemometer, White	$\frac{1}{\text{---}}$ (Ground)
Anemometer, Clear	$\frac{1}{\text{---}}$ (Ground)
Anemometer, Black	P1
Vane, Black	VX3 or EX3



CR1000		Attached Sensor/Device	
Terminal	Wire/Terminal	Name	Measurements
1H	Red	108 (1)	USP1
1L	Red	108 (2)	USP2
⏏ (Ground)	Purple	108 (1)	USP1
	Clear	108 (1)	USP1
	Purple	108 (2)	USP2
	Clear	108 (2)	USP2
2H	Red	108 (3)	USP3
2L	Red	108 (4)	USP4
⏏ (Ground)	Purple	108 (3)	USP3
	Clear	108 (3)	USP3
	Purple	108 (4)	USP4
	Clear	108 (4)	USP4
3H	Red	108 (5)	USP5
3L	Red	108 (6)	USP6
⏏ (Ground)	Purple	108 (5)	USP5
	Clear	108 (5)	USP5
	Purple	108 (6)	USP6
	Clear	108 (6)	USP6
4H	Red	108 (7)	USP7
4L	Vane, Red	03001	WS_ms, WindDir
⏏ (Ground)	Purple	108 (7)	USP7
	Clear	108 (7)	USP7
	Anemometer, White	03001	WS_ms, WindDir
	Anemometer, Clear	03001	WS_ms, WindDir
VX1 or EX1	Black	108 (1)	USP1
	Black	108 (2)	USP2
	Black	108 (3)	USP3
	Black	108 (4)	USP4
⏏ (Ground)	Vane, Clear	03001	WS_ms, WindDir
	Vane, White	03001	WS_ms, WindDir
P1	Anemometer, Black	03001	WS_ms, WindDir
⏏ (Ground)			
P2			
⏏ (Ground)			
5H	Purple	Type E TC (1)	E1T1
5L	Red	Type E TC (1)	E1T1
⏏ (Ground)			
6H	Purple	Type E TC (2)	E1T2
6L	Red	Type E TC (2)	E1T2
⏏ (Ground)			
7H	Purple	Type E TC (3)	E1T3
7L	Red	Type E TC (3)	E1T3
⏏ (Ground)			
8H	Purple	Type E TC (4)	E1T4
8L	Red	Type E TC (4)	E1T4
⏏ (Ground)			
VX2 or EX2	Black	108 (5)	USP5
	Black	108 (6)	USP6
	Black	108 (7)	USP7
⏏ (Ground)			
VX3 or EX3	Vane, Black	03001	WS_ms, WindDir
G			
5V			
G			
SW-12			
G			
12V			
12V			
G			
C1			
C2			
C3			
C4			
G			

Terminal	Wire/Terminal	Name	Measurements
C5			
C6			
C7			
C8			
G			

# R: CR1000 Inside Solar - Campbell DAQ Wire Diagram/Text


CR1000 Wiring Diagram for cr1000fulltrial2.scw

NR01 - Blue_SR01Up, Blue_SR01Dn, Blue_IR01Up, Bl...		CR1000
Cable 1 Pyranometer Up Sig, Red		1H
Cable 1 Pyranometer Up Ref, Blue		1L
Cable 1 Pyranometer Down Sig, White		2H
Cable 1 Pyranometer Down Ref, Green		2L
Cable 1 Pyrgeometer Up Sig, Brown		3H
Cable 1 Pyrgeometer Up Ref, Yellow		3L
Cable 1 Pyrgeometer Down Sig, Purple		4H
Cable 1 Pyrgeometer Down Ref, Grey		4L
Cable 2 PT100 Signal, White		6H
Cable 2 PT100 Signal Ref, Green		6L
Shield, Clear		$\frac{1}{\equiv}$ (Ground)
Shield, Clear		$\frac{1}{\equiv}$ (Ground)
<b>4WPB100</b>		
Cable 2 Current Excite, Red	L	
Cable 2 Current Return, Blue	G	
Black		VX1 or EX1
HI pin		5H
LO pin		5L
GND pin		$\frac{1}{\equiv}$ (Ground)
		1L
		$\frac{1}{\equiv}$ (Ground)
Jumper		2L
		$\frac{1}{\equiv}$ (Ground)
Jumper		3L
		$\frac{1}{\equiv}$ (Ground)
Jumper		4L
		$\frac{1}{\equiv}$ (Ground)
Jumper		$\frac{1}{\equiv}$ (Ground)
CNR2 - CNR2_NetSW, CNR2_NetLW, CNR2_NetRad		CR1000
White		7H
Blue		7L
Brown		8H
Black		8L
Clear		$\frac{1}{\equiv}$ (Ground)

CR1000		Attached Sensor	
Terminal	Wire/Terminal	Name	Measurements
1H	Cable 1 Pyranometer Up Sig, Red	NR01	Blue_SR01Up, Blue_SR01Dn, Blue_IR01Up, Blue_IR01Dn
1L	Cable 1 Pyranometer Up Ref, Blue	NR01	Blue_SR01Up, Blue_SR01Dn, Blue_IR01Up, Blue_IR01Dn
$\frac{1}{2}$ (Ground)	Jumper to 1L	NR01	Blue_SR01Up, Blue_SR01Dn, Blue_IR01Up, Blue_IR01Dn
2H	Cable 1 Pyranometer Down Sig, White	NR01	Blue_SR01Up, Blue_SR01Dn, Blue_IR01Up, Blue_IR01Dn
2L	Cable 1 Pyranometer Down Ref, Green	NR01	Blue_SR01Up, Blue_SR01Dn, Blue_IR01Up, Blue_IR01Dn
$\frac{1}{2}$ (Ground)	Jumper to 2L	NR01	Blue_SR01Up, Blue_SR01Dn, Blue_IR01Up, Blue_IR01Dn
3H	Cable 1 Pyrgeometer Up Sig, Brown	NR01	Blue_SR01Up, Blue_SR01Dn, Blue_IR01Up, Blue_IR01Dn
3L	Cable 1 Pyrgeometer Up Ref, Yellow	NR01	Blue_SR01Up, Blue_SR01Dn, Blue_IR01Up, Blue_IR01Dn
$\frac{1}{2}$ (Ground)	Jumper to 3L	NR01	Blue_SR01Up, Blue_SR01Dn, Blue_IR01Up, Blue_IR01Dn
4H	Cable 1 Pyrgeometer Down Sig, Purple	NR01	Blue_SR01Up, Blue_SR01Dn, Blue_IR01Up, Blue_IR01Dn
4L	Cable 1 Pyrgeometer Down Ref, Grey	NR01	Blue_SR01Up, Blue_SR01Dn, Blue_IR01Up, Blue_IR01Dn
$\frac{1}{2}$ (Ground)	Jumper to 4L	NR01	Blue_SR01Up, Blue_SR01Dn, Blue_IR01Up, Blue_IR01Dn
VX1 or EX1	Black	4WPB100	Blue_SR01Up, Blue_SR01Dn, Blue_IR01Up, Blue_IR01Dn
$\frac{1}{2}$ (Ground)	Shield, Clear	NR01	Blue_SR01Up, Blue_SR01Dn, Blue_IR01Up, Blue_IR01Dn
	Shield, Clear	NR01	Blue_SR01Up, Blue_SR01Dn, Blue_IR01Up, Blue_IR01Dn
	Clear	CNR2	CNR2_NetSW, CNR2_NetLW, CNR2_NetRad
P1			
$\frac{1}{2}$ (Ground)			
P2			
$\frac{1}{2}$ (Ground)			
5H	HI pin	4WPB100	Blue_SR01Up, Blue_SR01Dn, Blue_IR01Up, Blue_IR01Dn
5L	LO pin	4WPB100	Blue_SR01Up, Blue_SR01Dn, Blue_IR01Up, Blue_IR01Dn
$\frac{1}{2}$ (Ground)	GND pin	4WPB100	Blue_SR01Up, Blue_SR01Dn, Blue_IR01Up, Blue_IR01Dn
6H	Cable 2 PT100 Signal, White	NR01	Blue_SR01Up, Blue_SR01Dn, Blue_IR01Up, Blue_IR01Dn
6L	Cable 2 PT100 Signal Ref, Green	NR01	Blue_SR01Up, Blue_SR01Dn, Blue_IR01Up, Blue_IR01Dn
$\frac{1}{2}$ (Ground)			
7H	White	CNR2	CNR2_NetSW, CNR2_NetLW, CNR2_NetRad
7L	Blue	CNR2	CNR2_NetSW, CNR2_NetLW, CNR2_NetRad
$\frac{1}{2}$ (Ground)			
8H	Brown	CNR2	CNR2_NetSW, CNR2_NetLW, CNR2_NetRad
8L	Black	CNR2	CNR2_NetSW, CNR2_NetLW, CNR2_NetRad
$\frac{1}{2}$ (Ground)			
VX2 or EX2			
$\frac{1}{2}$ (Ground)			
VX3 or EX3			
G			
5V			
G			
SW-12			
G			
12V			
12V			
G			
C1			
C2			
C3			
C4			
G			
C5			
C6			
C7			
C8			
G			

4WPB100		Attached Sensor	
Terminal	Wire/Terminal	Name	Measurements
L	Cable 2 Current Excite, Red	NR01	
G	Cable 2 Current Return, Blue	NR01	
Black	VX1 or EX1	CR1000	

CR1000 Wiring Text for cr1000fulltrial2.scw

Terminal	Wire/Terminal	Name	Measurements
HI pin	5H	CR1000	
LO pin	5L	CR1000	
GND pin	 (Ground)	CR1000	

## APPENDIX B - HUKSEFLUX NET RADIOMETERS

Probe 1945



Hukseflux Thermal Sensors B.V.  
www.hukseflux.com  
info@hukseflux.com

### Product certificate

Pages: 1  
Release date: 22-12-2014

Product code **NR01-05**  
Product identification **serial number 2347**  
Product type 4-component net-radiation sensor  
Measurand net radiation

#### Product specifications

1:	functional test	<b>passed</b>
2:	cable length	<b>5 m</b>

Person authorising acceptance and release of product: **Date:**  
W.J.B. Focke 22-12-2014

#### Calibration results

Component	SR01 ↓	SR01 ↑	IR01 ↓	IR01 ↑
Position	1	2	3	4
Serial number	<b>3928</b>	<b>3929</b>	<b>3875</b>	<b>3876</b>
Sensitivity	<b><math>19.09 \times 10^{-6}</math></b>	<b><math>19.47 \times 10^{-6}</math></b>	<b><math>12.63 \times 10^{-6}</math></b>	<b><math>11.47 \times 10^{-6}</math></b>
Uncertainty*	$\pm 0.23 \times 10^{-6}$	$\pm 0.24 \times 10^{-6}$	$\pm 0.67 \times 10^{-6}$	$\pm 0.61 \times 10^{-6}$
Calibration date	12-12-2014	12-12-2014	05-12-2014	05-12-2014
Resistance	70.3	65.6	195.6	169.9

With Sensitivity in V/(W/m<sup>2</sup>), Uncertainty in V/(W/m<sup>2</sup>), Resistance in Ω

\* the number following the ± symbol is the expanded uncertainty with a coverage factor  $k = 2$ , and defines an interval estimated to have a level of confidence of 95 percent

Table 0.1 connections **Cable 1**

PCB04	WIRE	
1	Blue	SR01 ↓ [-]
2	Red	SR01 ↓ [+]
3	Yellow	IR01 ↓ [-]
4	Brown	IR01 ↓ [+]
5	Grey	IR01 ↑ [-]
6	Pink	IR01 ↑ [+]
7	Green	SR01 ↑ [-]
8	White	SR01 ↑ [+]
11	Black	shield

Table 0.2 connections **Cable 2**

PCB05	WIRE	
1	Brown	heater
2	Red	Pt100 [+]
3	White	Pt100 [-]
4	Blue	Pt100 [-]
5	Green	Pt100 [-]
6	Yellow	heater
	Pink	not connected
	Grey	not connected
10	Black	shield

The Pt100 is a single four-wire resistance temperature detector measuring instrument body temperature.

SR01 calibration procedure according to ISO 9847. Traceability of calibration is to the WRR (World Radiometric Reference) maintained at the World Radiation Center in Davos, Switzerland.

IR01 calibration procedure according to Hukseflux IROC2. Traceability of calibration is to the WISG (World Infrared Standard Group) operated at the Infrared Radiometry Section of the World Radiation Center in Davos, Switzerland.

Please consult the user manual for detailed measurement functions and product set up, operation and maintenance instructions.

NR01 product certificate

page 1/1

Probe 2346

## Product certificate

Pages: 1  
Release date: 22-12-2014

Product code **NR01-05**  
Product identification **serial number 2346**  
Product type **4-component net-radiation sensor**  
Measurand **net radiation**

### Product specifications

1:	functional test	<b>passed</b>
2:	cable length	<b>5 m</b>

Person authorising acceptance and release of product: **Date:**  
W.J.B. Fokke **22-12-2014**

### Calibration results

Component	SR01 ↓	SR01 ↑	IR01 ↓	IR01 ↑
Position	1	2	3	4
Serial number	<b>3926</b>	<b>3927</b>	<b>3873</b>	<b>3874</b>
Sensitivity	<b><math>17.43 \times 10^{-6}</math></b>	<b><math>19.70 \times 10^{-6}</math></b>	<b><math>13.15 \times 10^{-6}</math></b>	<b><math>13.32 \times 10^{-6}</math></b>
Uncertainty*	$\pm 0.21 \times 10^{-6}$	$\pm 0.24 \times 10^{-6}$	$\pm 0.70 \times 10^{-6}$	$\pm 0.71 \times 10^{-6}$
Calibration date	13-11-2014	13-11-2014	05-12-2014	05-12-2014
Resistance	64.3	66.1	190.0	211.7

With Sensitivity in  $V/(W/m^2)$ , Uncertainty in  $V/(W/m^2)$ , Resistance in  $\Omega$

\* the number following the  $\pm$  symbol is the expanded uncertainty with a coverage factor  $k = 2$ , and defines an interval estimated to have a level of confidence of 95 percent

**Table 0.1 connections Cable 1**

PCB04	WIRE	
1	Blue	SR01 ↓ [-]
2	Red	SR01 ↑ [+]
3	Yellow	IR01 ↓ [-]
4	Brown	IR01 ↑ [+]
5	Grey	IR01 * [-]
6	Pink	IR01 * [+]
7	Green	SR01 * [-]
8	White	SR01 * [+]
11	Black	shield

**Table 0.2 connections Cable 2**

PCB05	WIRE	
1	Brown	heater
2	Red	Pt100 [+]
3	White	Pt100 [+]
4	Blue	Pt100 [-]
5	Green	Pt100 [-]
6	Yellow	heater
	Pink	not connected
	Grey	not connected
10	Black	shield

The Pt100 is a single four-wire resistance temperature detector measuring instrument body temperature.

SR01 calibration procedure according to ISO 9847. Traceability of calibration is to the WRR (World Radiometric Reference) maintained at the World Radiation Center in Davos, Switzerland.

IR01 calibration procedure according to Hukseflux IRC02. Traceability of calibration is to the WISG (World Infrared Standard Group) operated at the Infrared Radiometry Section of the World Radiation Center in Davos, Switzerland.

Please consult the user manual for detailed measurement functions and product set up, operation and maintenance instructions.



Hukseflux Thermal Sensors B.V.  
www.hukseflux.com  
info@hukseflux.com

## Product certificate

Pages: 1  
Release date: 22-12-2014

Product code **NR01-05**  
Product Identification **serial number 2347**  
Product type 4-component net-radiation sensor  
Measurand net radiation

### Product specifications

1:	functional test	<b>passed</b>
2:	cable length	<b>5 m</b>

Person authorising acceptance and release of product: W.J.B. Focke

Date: 22-12-2014

### Calibration results

Component	SR01 ↓	SR01 ↑	IR01 ↓	IR01 ↑
Position	1	2	3	4
Serial number	<b>3928</b>	<b>3929</b>	<b>3875</b>	<b>3876</b>
Sensitivity	<b><math>19.09 \times 10^{-6}</math></b>	<b><math>19.47 \times 10^{-6}</math></b>	<b><math>12.63 \times 10^{-6}</math></b>	<b><math>11.47 \times 10^{-6}</math></b>
Uncertainty*	$\pm 0.23 \times 10^{-6}$	$\pm 0.24 \times 10^{-6}$	$\pm 0.67 \times 10^{-6}$	$\pm 0.61 \times 10^{-6}$
Calibration date	12-12-2014	12-12-2014	05-12-2014	05-12-2014
Resistance	70.3	65.6	195.6	169.9

With Sensitivity in  $V/(W/m^2)$ , Uncertainty in  $V/(W/m^2)$ , Resistance in  $\Omega$

\* the number following the  $\pm$  symbol is the expanded uncertainty with a coverage factor  $k = 2$ , and defines an interval estimated to have a level of confidence of 95 percent.

Table 0.1 connections **Cable 1**

PCB04	WIRE	
1	Blue	SR01 ↓ [-]
2	Red	SR01 ↓ [+]
3	Yellow	IR01 ↓ [-]
4	Brown	IR01 ↓ [+]
5	Grey	TR01 ↑ [-]
6	Pink	IR01 ↑ [+]
7	Green	SR01 ↑ [-]
8	White	SR01 ↑ [+]
11	Black	shield

Table 0.2 connections **Cable 2**

PCB05	WIRE	
1	Brown	heater
2	Red	Pt100 [+]
3	White	Pt100 [-]
4	Blue	Pt100 [-]
5	Green	Pt100 [-]
6	Yellow	heater
	Pink	not connected
	Grey	not connected
10	Black	shield

The Pt100 is a single four-wire resistance temperature detector measuring instrument body temperature.

SR01 calibration procedure according to ISO 9847. Traceability of calibration is to the WRR (World Radiometric Reference) maintained at the World Radiation Center in Davos, Switzerland.

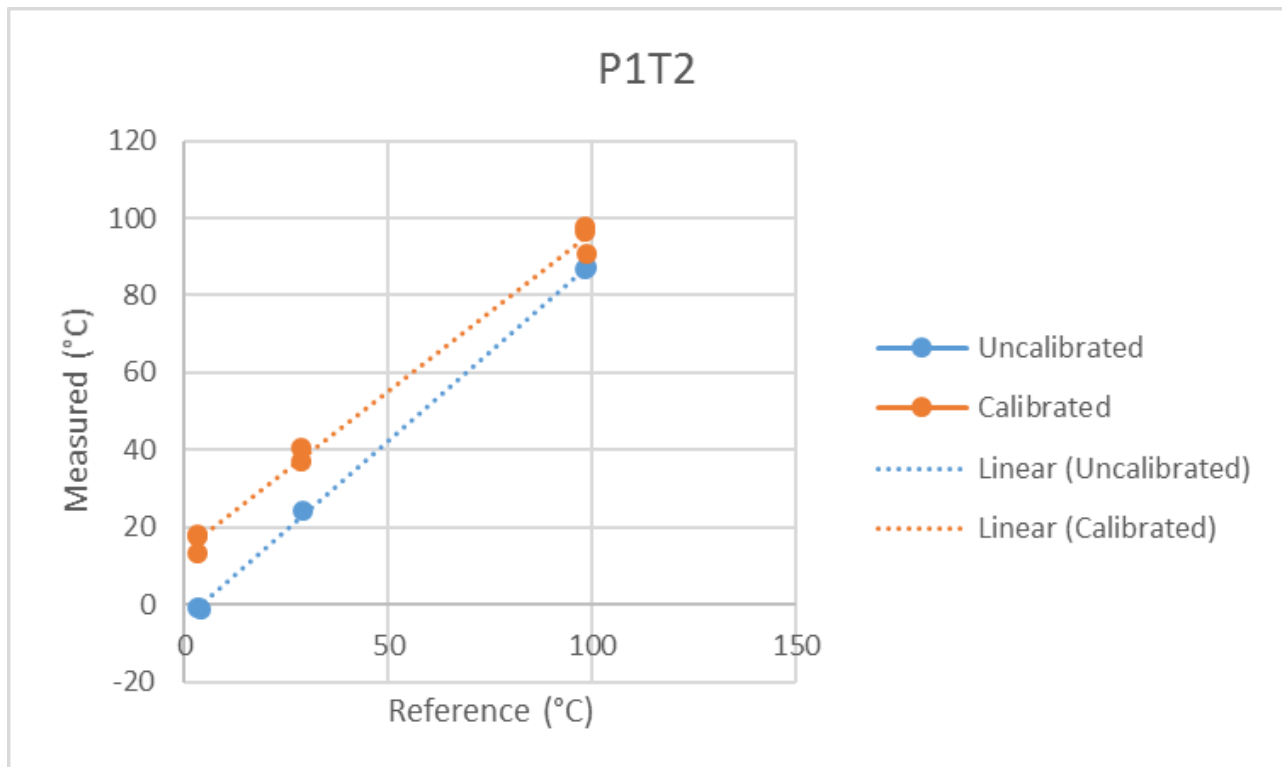
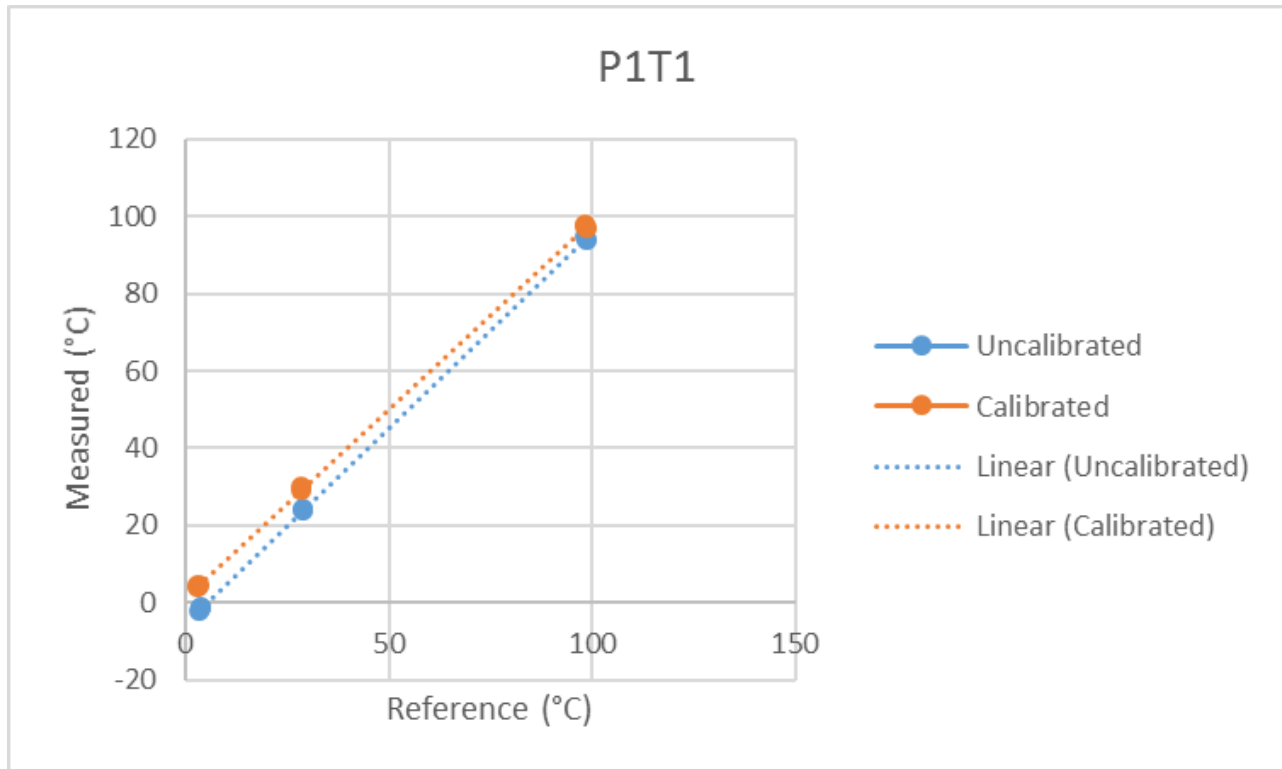
IR01 calibration procedure according to Hukseflux IROC2. Traceability of calibration is to the WISG (World Infrared Standard Group) operated at the Infrared Radiometry Section of the World Radiation Center in Davos, Switzerland.

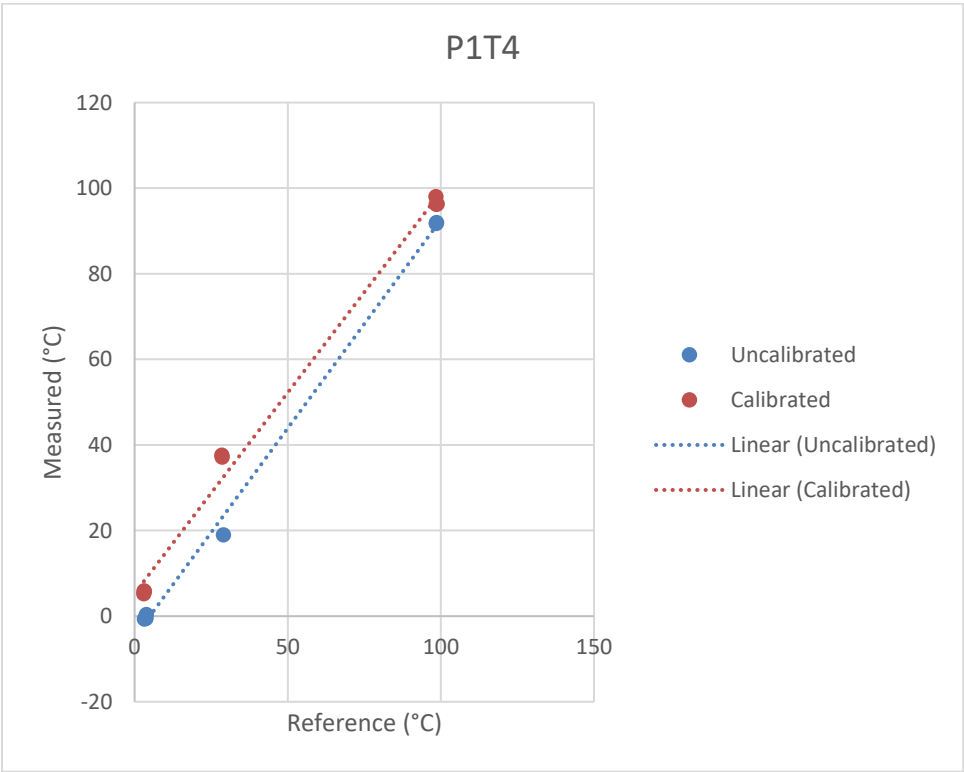
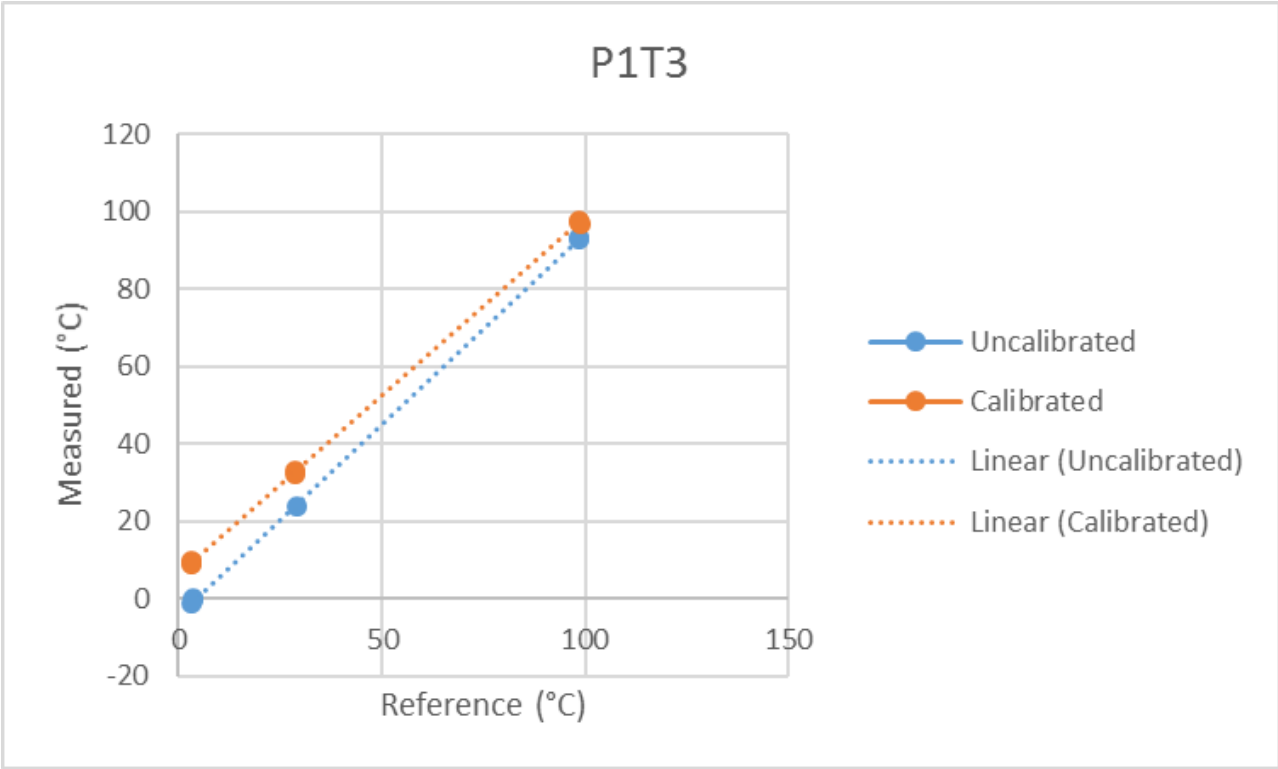
Please consult the user manual for detailed measurement functions and product set up, operation and maintenance instructions.

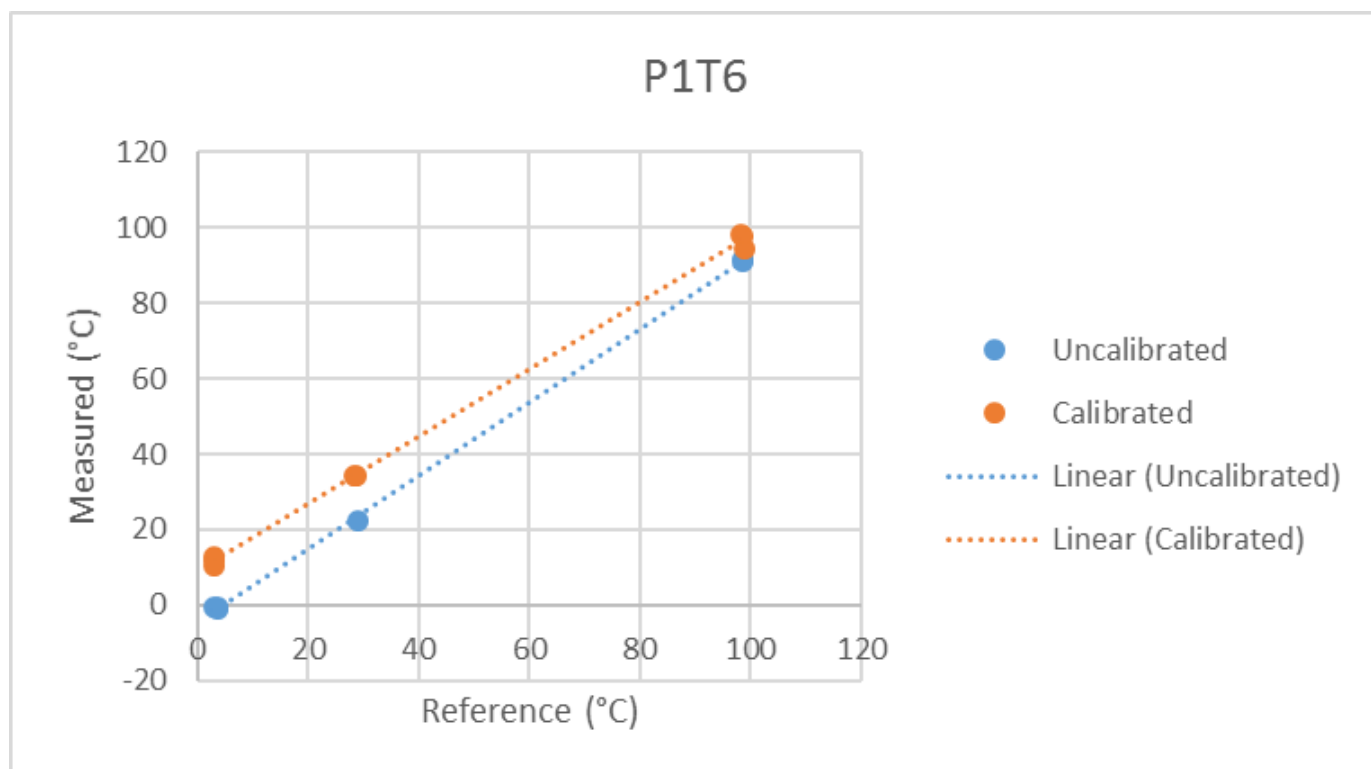
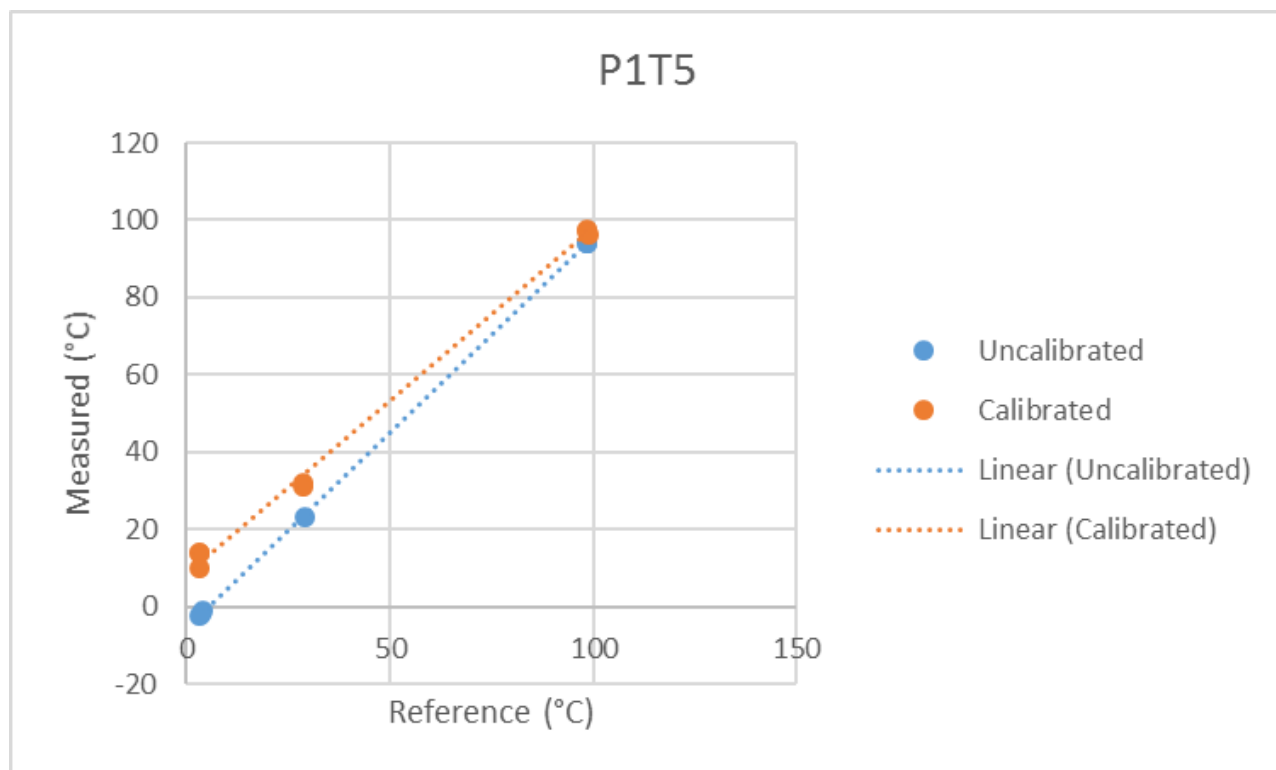


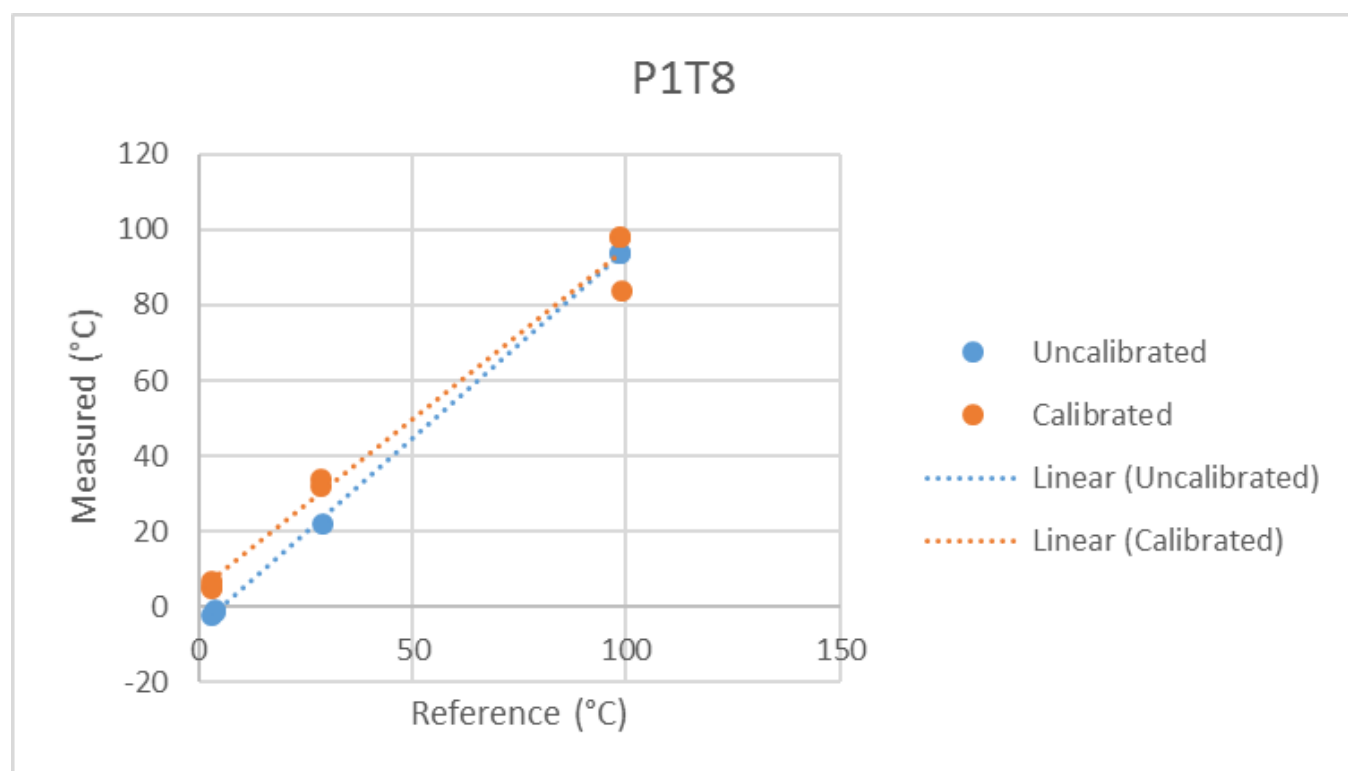
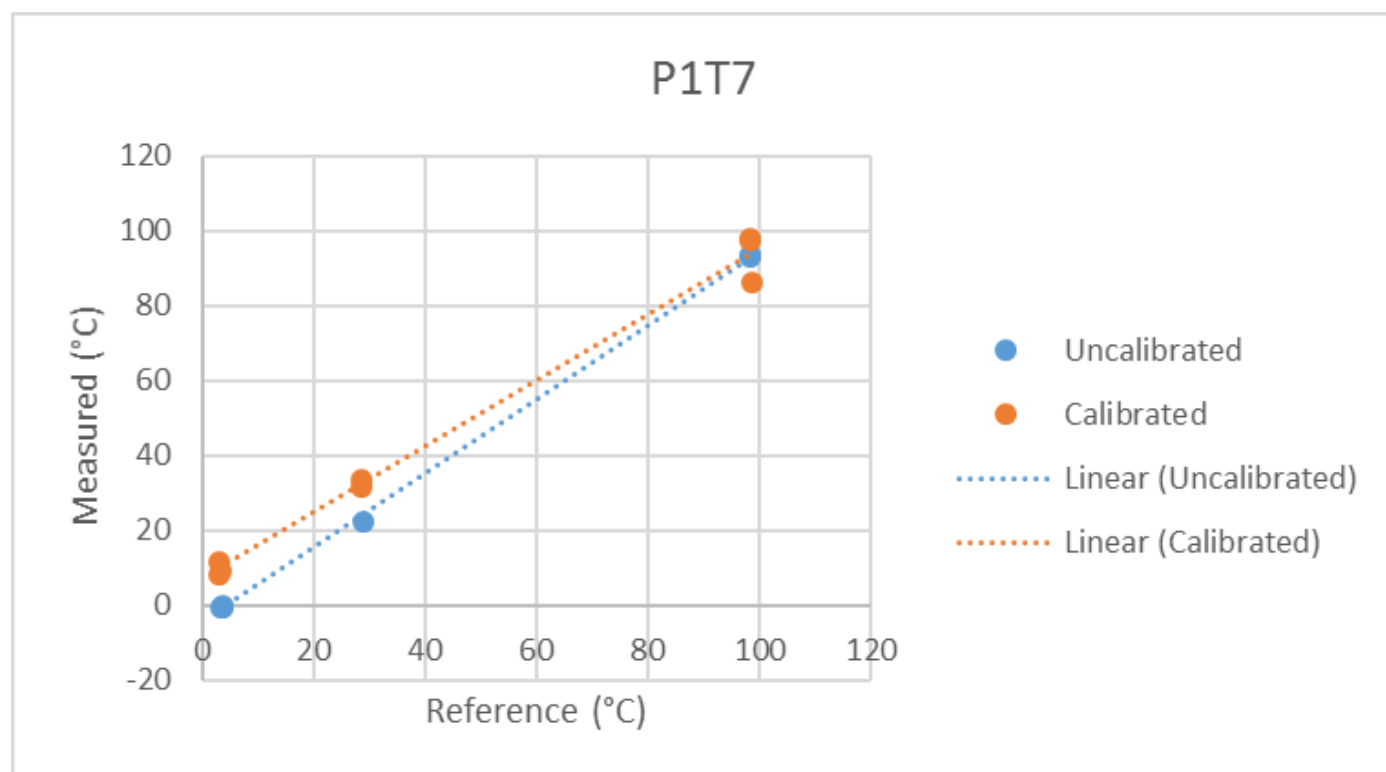
## APPENDIX C - THERMOCOUPLES

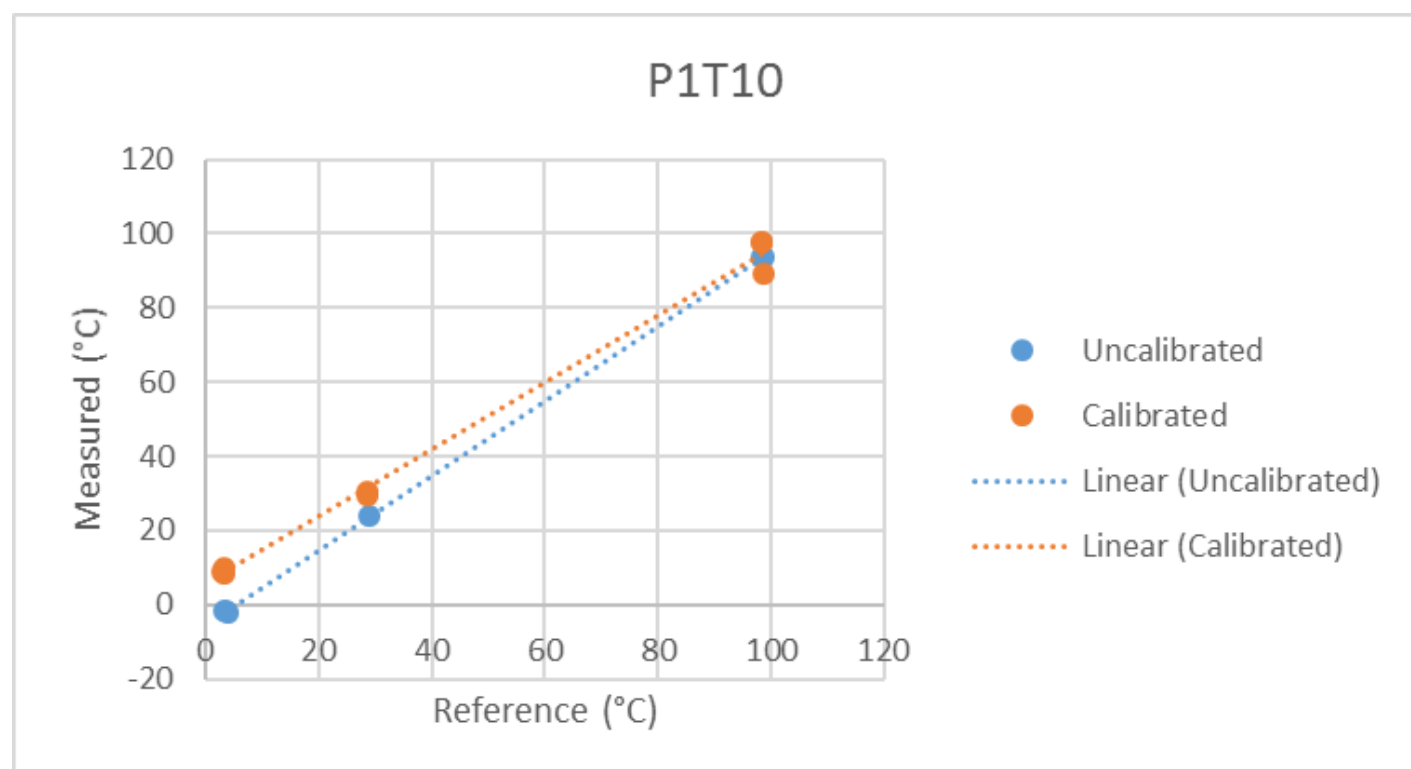
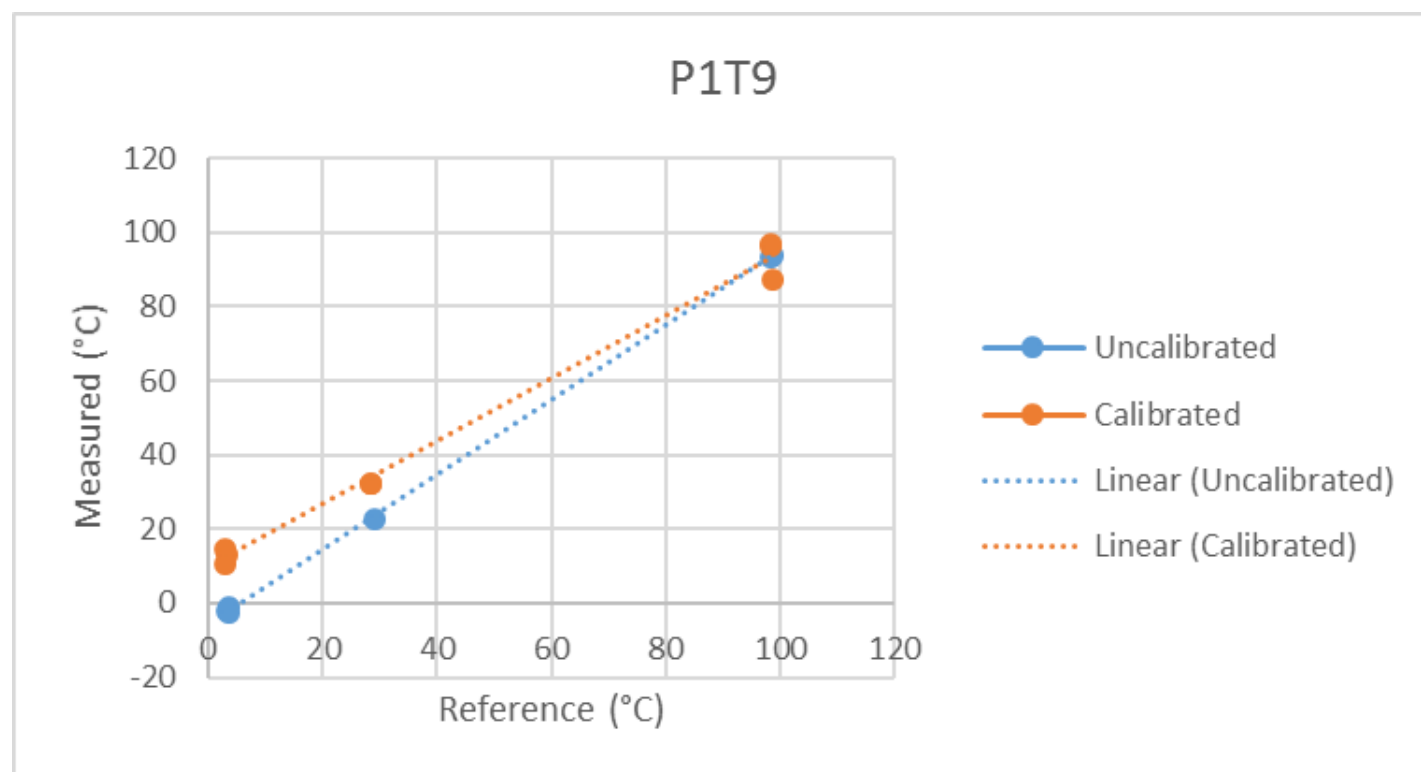
Probe 1



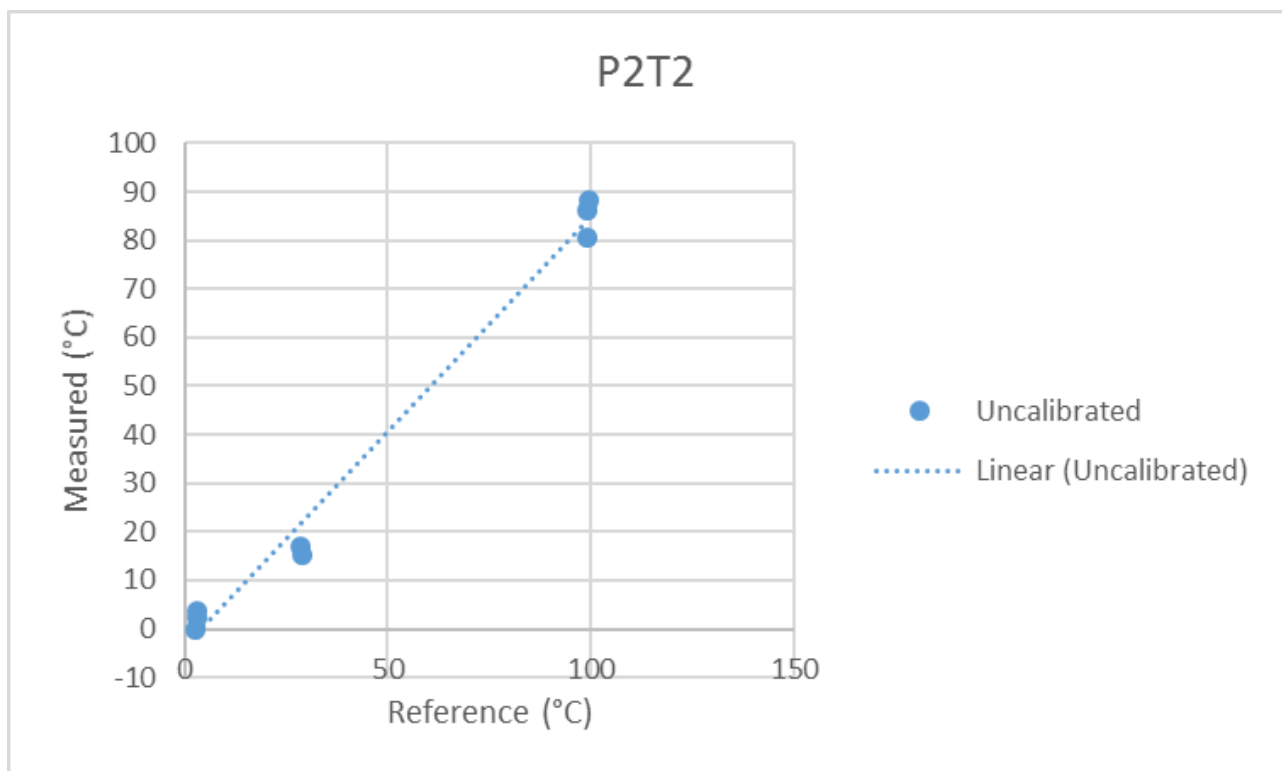
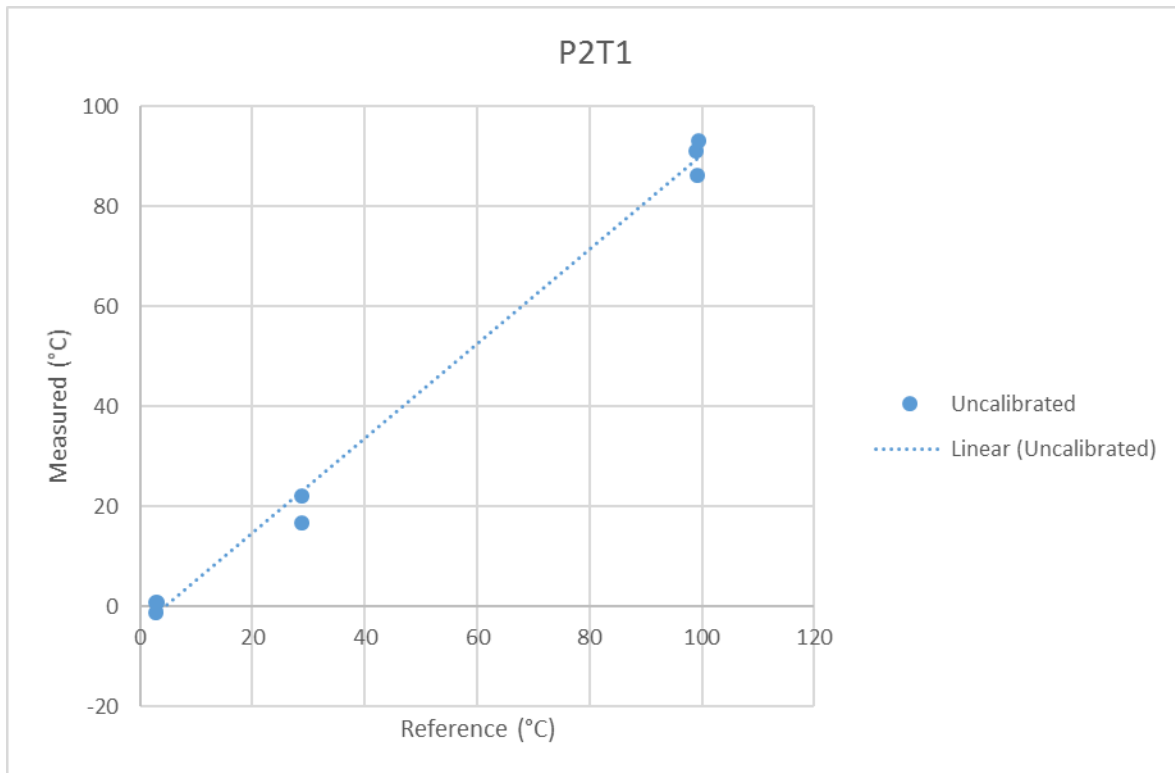


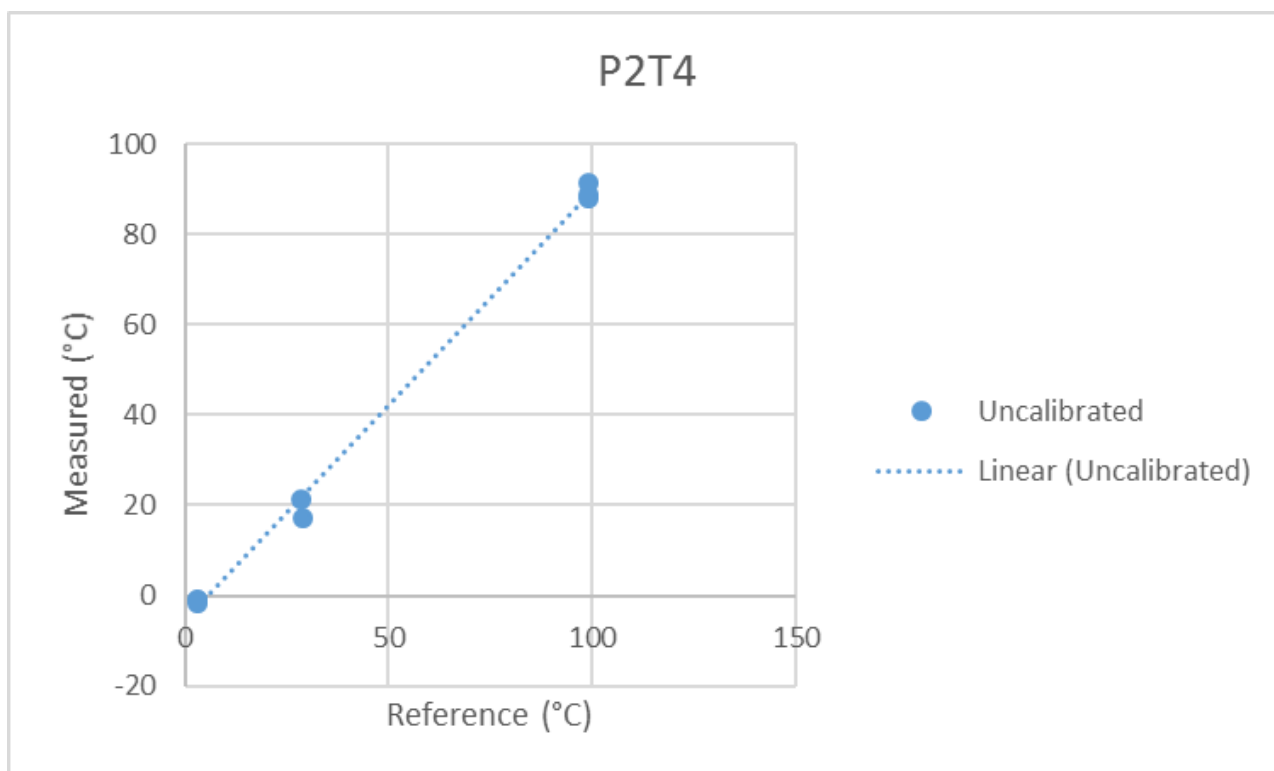
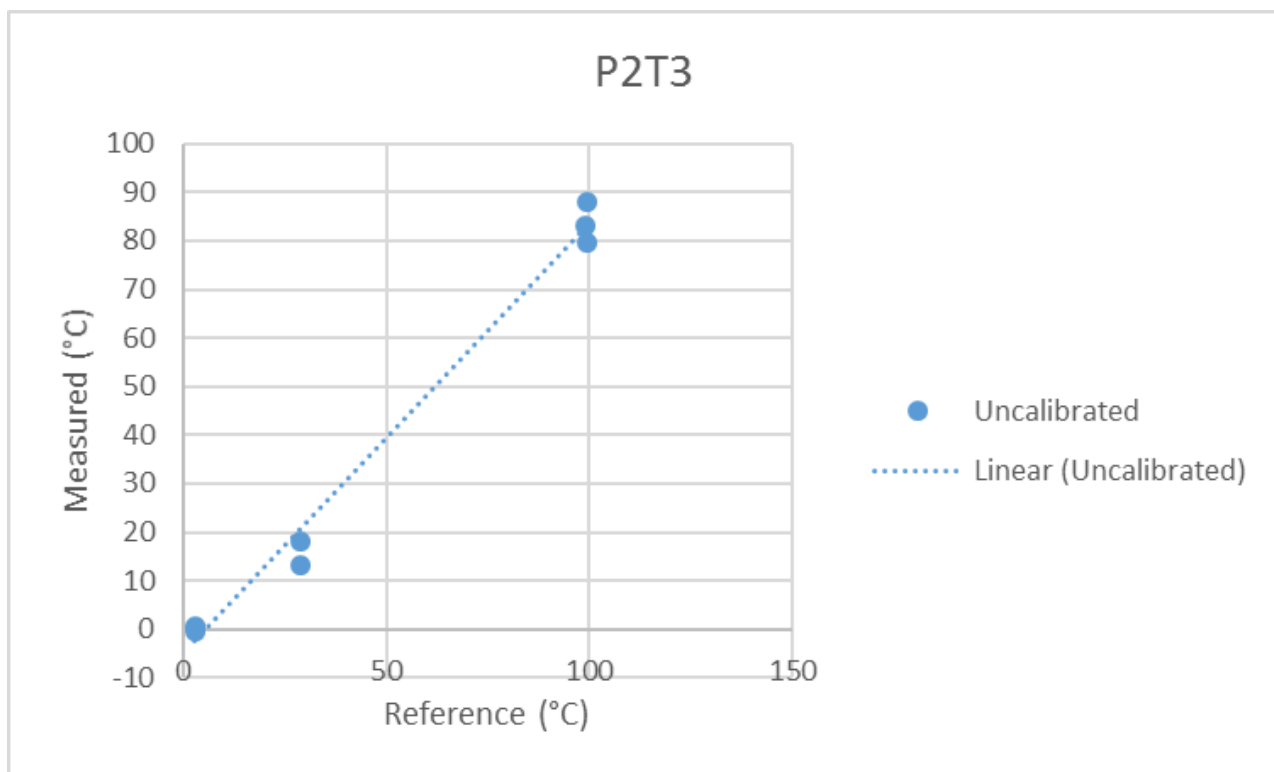


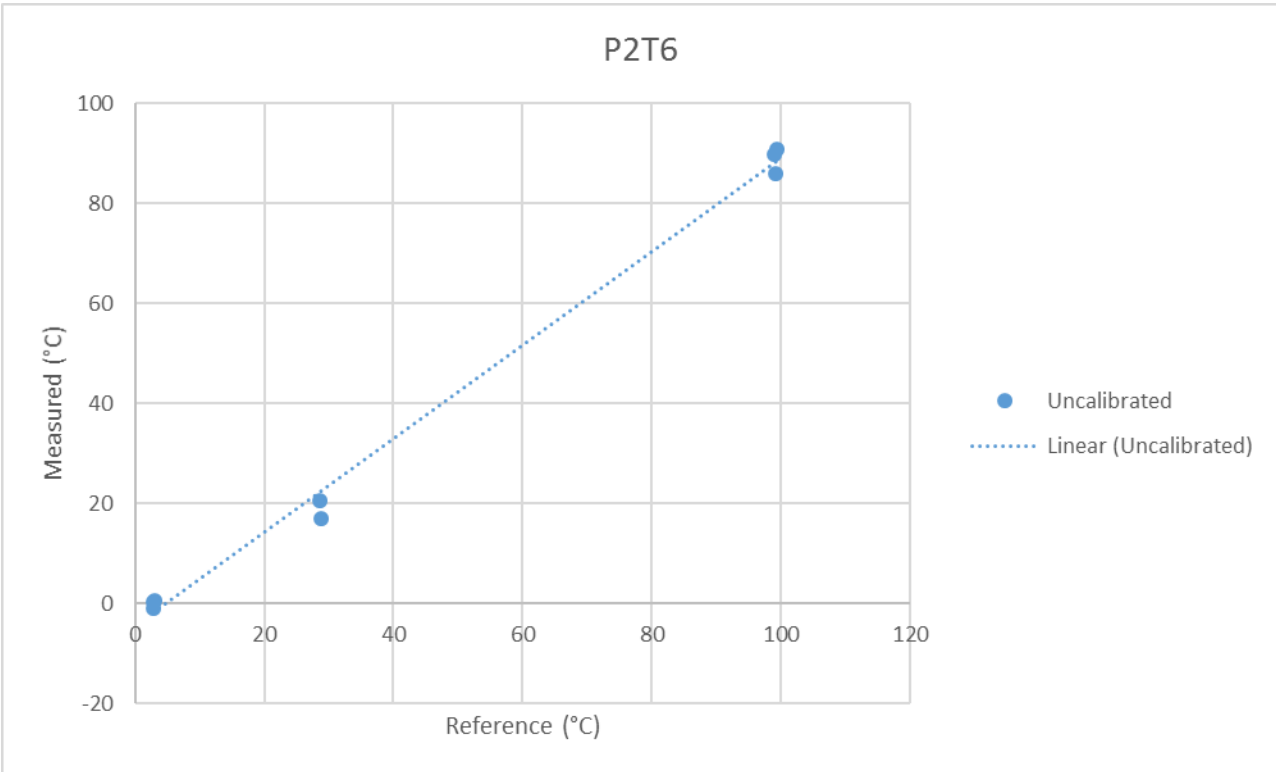
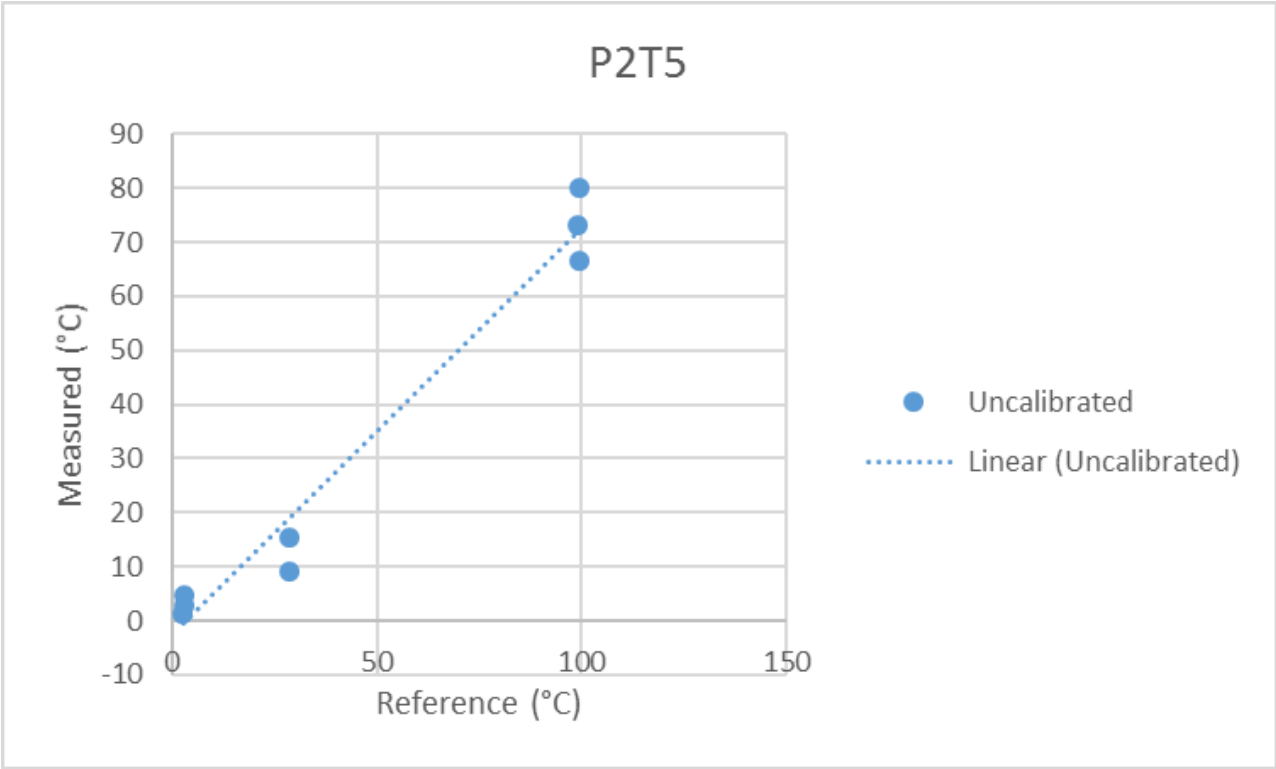




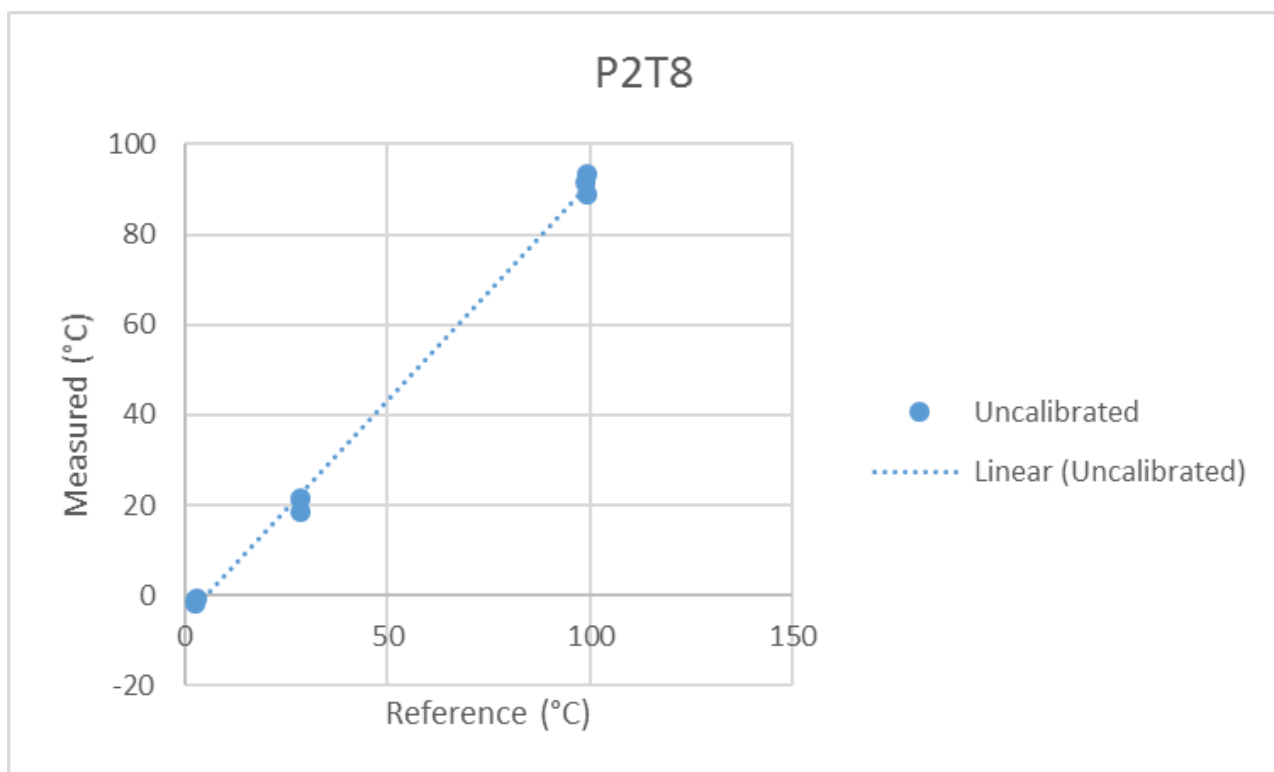
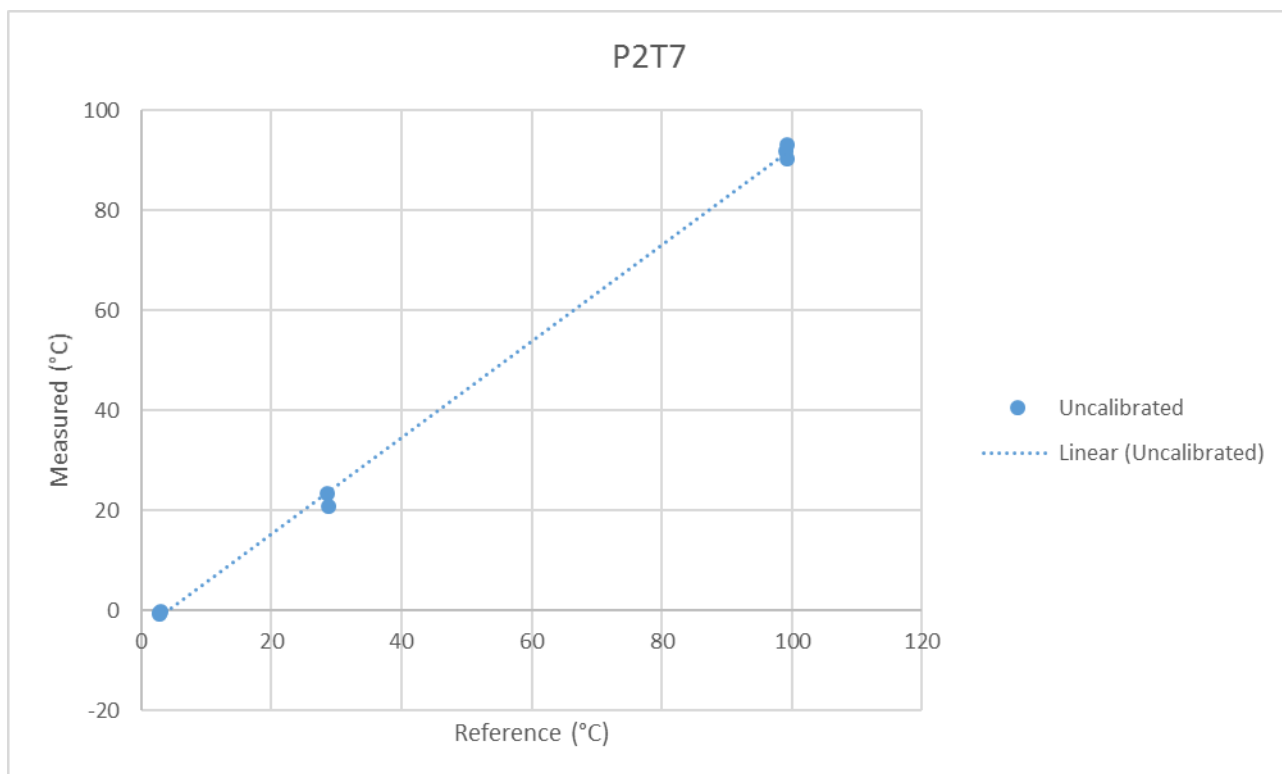
Probe 2

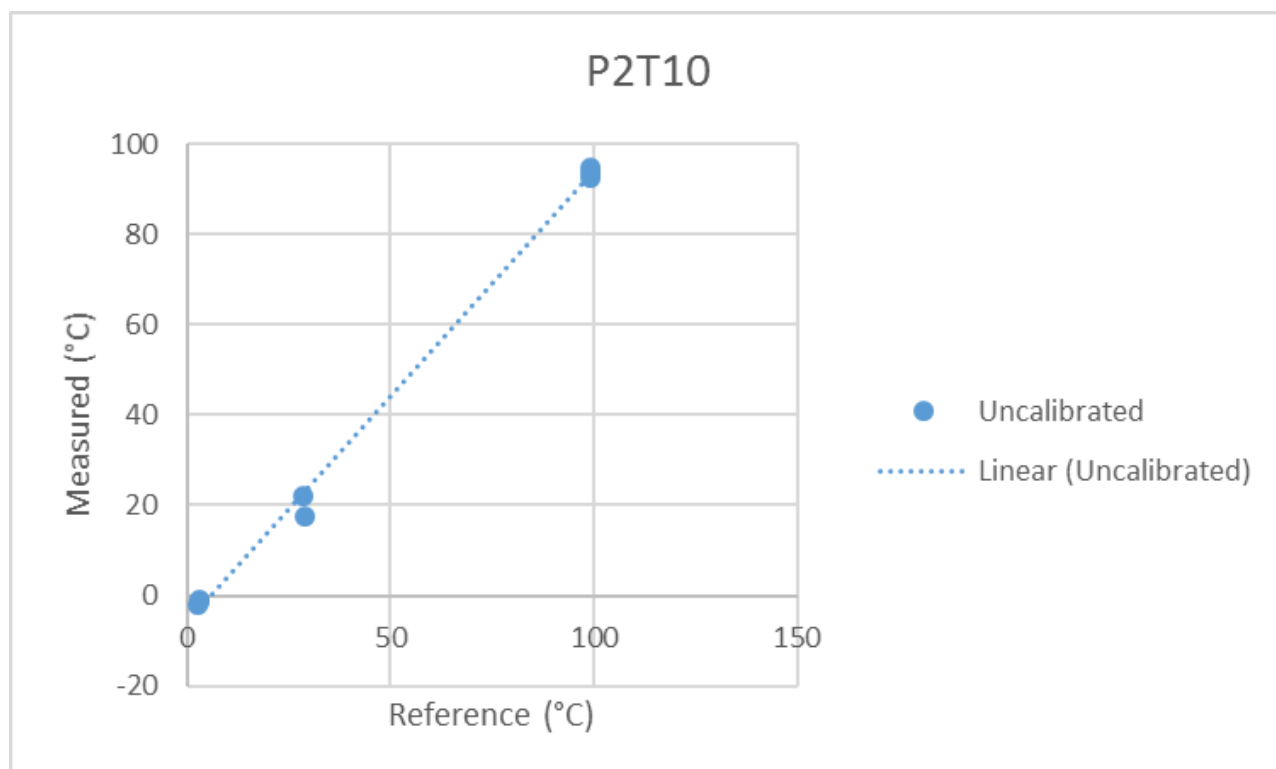
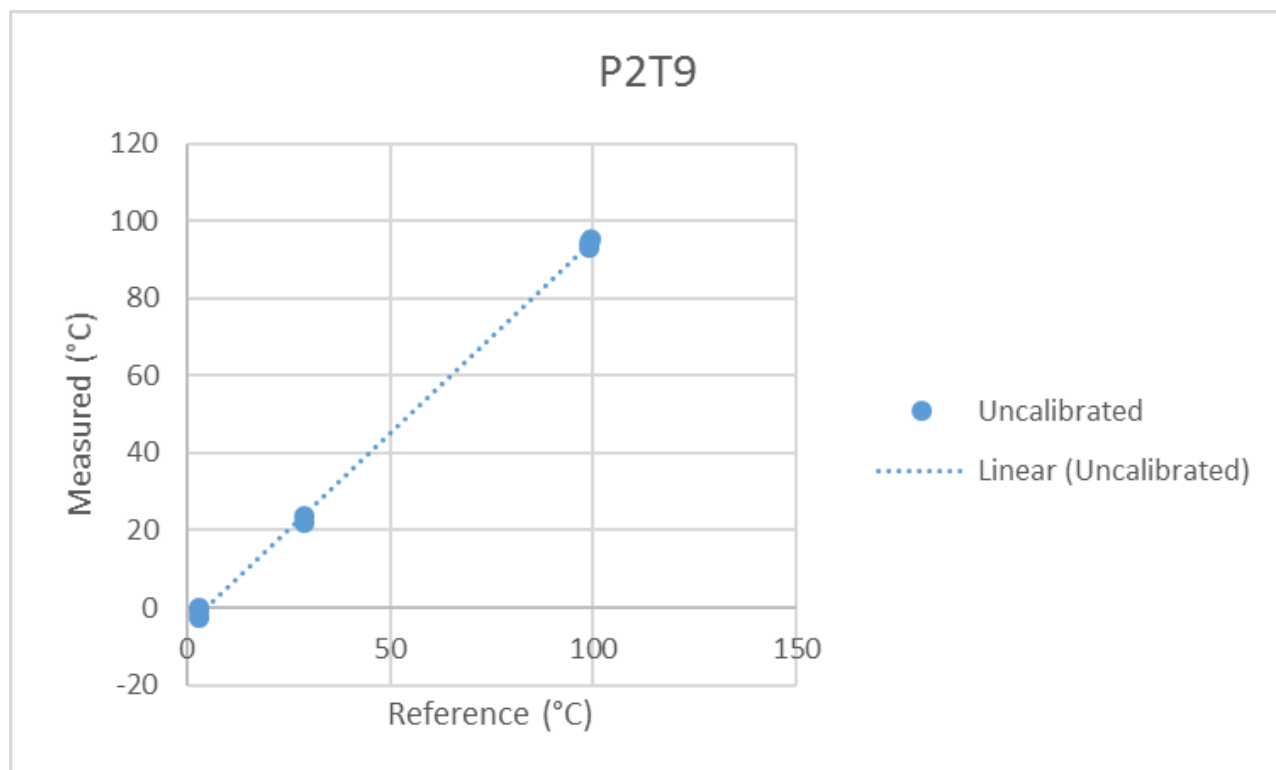












Probe 3

